Funded by the
European Union

Compact

XLS-Report-2021-010
22 December 2021

XLS Deliverable D2.3

Conceptual Design Report of the CompactLight X-ray FEL

Funded by the
European Union

Compact

G. D'Auria[1)1], E. Adli[33], M. Aicheler[12], A. Aksoy[20], D. Alesini[11], R. Apsimon[8,4], J. Arnsberg[9], R. Auchettl[6], A. Bainbridge[3,4], K. Balazs[2], D. Bantekas[18], J. Bedolla[8,4], M. Behtouei[11], M. Bellaveglia[11], M. vd Berg[5], A. Bernhard[9], A. Bignami[18,32], M. Breitenbach[27], M. Breukers[5], G. Burt[8,4], J. Cai[8,4], M. Calvi[23], F. Cardelli[11], M. Carpanese[7], H. M. Castaneda Cortes[3,4], A. Castilla[84], A. Cianchi[26], J. Clarke[3,4], L. Cowie[3,4], M. Croia[11], A. Cross[25], M. Danailov[1], G. Dattoli[7], S. Deleval[2], S. Di Mitri[1], M. Diomede[11], R. Dowd[6], D. Dunning[3,4], J. Easton[25], W. Fang[17], S. Fatehi[9], A. Faus-Golfe[22], M. Ferianis[1], M. Ferrario[11], L. Ficcadenti[11], A. Gallo[11], E. Gazis[18,30], N. Gazis[18,32], R. Geometrante[21], J. Gethmann[9], R. Gioppo[1], A. Giribono[11], D. González-Iglesias[16], V. Goryashko[13], S. Grohmann[9], Q. Gu[17], Y. Han[22], A. Hinton[3,4], A. Hobi[27], R. Hoekstra[24,31], X. Huang[17], M. Jacewicz[13], J. Jones[3,4], F. Kaertner[34], A. Karagiannaki[29], M. Kokole[28], R. Kotitsa[30], D. Kotsopoulos[29], B. Krasch[9], A. Latina[2], P. Lepercq[22], X. Liu[2], T. G. Lucas[10,24,31], O. J. Luiten[10], M. Maheshwari[3,4], J. Mahnic[28], A. Mak[13], J. Marcos[15], E. Marin[15], B. G. Martínez[16], B. Mercier[22], M. Migliorati[14,11], T. Milharcic[28], A. Mostacci[14,11], R. Muñoz[15], V. Musat[2], P. H. A. Mutsaers[10], Z. Nergiz[20], F. Nguyen[7], L. Nix[25], L. Palumbo[14,11], M. Parodi[2], R. Pavlica[21], L. Pellegrino[11], D. E. Pereira[16], F. Perez[15], A. Petralia[7], L. Piersanti[11], J. Pockar[28], K. Pramatari[29], U. Primozic[28], R. Rassool[19], S. Reiche[23], P. Revilak[27], S. Richter[2], S. C. Richter[9,2], R. Rochow[1], C. Rossi[2], P. Salén[13], T. Schmidt[23], D. Schoerling[2], D. Schulte[2], J. Scifo[11], S. Sheehy[19], B. Shepherd[3,4], B. Spataro[11], S. Stapnes[2], X. F. D. Stragier[10], C. Tabacco[1], J. Tan[17], E. Tanke[18,32], G. Taylor[19], I. Telahi[30], N. Thompson[3,4], E. Trachanas[18,32], K. Tzanetou[30], C. Vaccarezza[11], J. Vainola[12], A. Vannozzi[11], M. Volpi[19], C. Wang[17], P. Williams[3,4], X. Wu[2], W. Wuensch[2], J. Yap[19], M. Zangrando[1], K. Zhang[23], L. Zhang[25], Y. Zhao[2], Z. Zhao[17], D. Zhu[6]

On behalf of the CompactLight Partnership

Prepared on: 22.12.2021

[1] Elettra - Sincrotrone Trieste S.C.p.A., AREA Science Park, 34149 Basovizza, Trieste, Italy, [2] CERN, 1211 Geneva 23, Switzerland, [3] ASTeC, STFC Daresbury Laboratory, Keckwick Lane, Warrington, WA4 4AD, UK, [4] Cockcroft Institute, SciTech Daresbury, Warrington, WA4 4AD, UK, [5] VDL ETG Precision, Eindhoven, North Brabant 5652, NL, [6] ANSTO – Australian Synchrotron, Clayton, Australia, [7] ENEA C. R. Frascati - Fusion and Nuclear Safety Department, Via E. Fermi 45, 00044 Frascati (Roma) Italy, [8] Lancaster University, Engineering Department, Lancaster LA1 4YR, UK , [9] Karlsruhe Institute of Technology (KIT), Germany, [10] Eindhoven University of Technology (TU/e), The Netherlands, [11] INFN – Laboratori Nazionali di Frascati, Via E Fermi 54, 00044 – Frascati (Roma) Italy, [12] University of Helsinki - Helsinki Institute of Physics, Finland, [13] FREIA Laboratory, Department of Physics and Astronomy, Uppsala University, Sweden, [14] Sapienza, University of Rome, Roma, Italy, [15] ALBA Synchrotron - CELLS, Barcelona, Spain, [16] Instituto de Física Corpuscular (IFIC), University of Valencia-CSIC, Valencia, Spain, [17] Shanghai Institute of Applied Physics, Shanghai, China, [18] Institute of Accelerating Systems and Applications (IASA), Panepistimioupoli Zografou, Department of Physics, Athens, Greece, [19] The University of Melbourne, ARC Centre of Excellence for Particle

[1]Corresponding author: gerardo.dauria@elettra.eu

Funded by the
European Union

Compact

Physics, Australia, [20] Ankara University, Institute of Accelerator Technology, Ankara, Turkey, [21] Kyma S. p. A., AREA Science Park, IT-34149 Trieste, Italy, [22] CNRS, Centre National de la Recherche Scientifique, Laboratoire de Physique des 2 infinis Irène Joliot-Curie – IJCLab, 91405 Orsay cedex, France, [23] Paul Scherrer Institute, Forschungsstrasse 111, 5232 Villigen PSI, Switzerland, [24] Free University Amsterdam, De Boelelaan 1105, 1081 HV Amsterdam, The Netherlands, [25] The University of Strathclyde, 16 Richmond St, Glasgow G1 1XQ, Scotland, UK, [26] Tor Vergata University of Rome, Via Cracovia 50 – 00133 Rome, Italy, [27] Bilfinger Noell GmbH, The Netherlands, [28] Kyma Tehnologija d.o.o., Kraška ulica 2, 6210 Sežana, Slovenia, [29] Athens University of Economics and Business, 76 Patission Street, 10434 Athens, Greece, [30] National Technical University of Athens, Patission Complex 42, Patission Street, 10682 Athens, Greece, [31] Advanced Research Center for Nanolithography ARCNL, Science Park 106, 1098 XG Amsterdam, Netherlands, [32] European Spallation Source ERIC, ESS Campus, Partikelgatan 2, 224 84 Lund, Sweden, [33] University of Oslo, P.O. Box 1072 Blindern, 0316 Oslo, Norway, [34] Center for Free-Electron Laser Science, Notkestraße 85, 22607 Hamburg, Germany

This project is funded by the European Union's Horizon2020 research and innovation programme under Grant Agreement No. 777431. The contents of this report reflect only the view of the Compact-Light Consortium. The European Commission is not responsible for any use that may be made of the information it contains.

Contents

1. Executive Summary

Synchrotron Radiation (SR) is a fundamental and indispensable research tool in a wide spectrum of scientific and technological fields and their applications, including materials science, condensed-matter physics, atomic and molecular physics, life science and medicine, chemistry, and environmental sciences. For this reason, the use of synchrotron radiation has increased tremendously in the last decades, as testified by the number of synchrotron light sources built to serve the users' communities across a multitude of scientific and engineering disciplines.

The latest generation of SR sources is based on Free Electron Lasers (FELs) driven by linacs. These facilities, with sub-picosecond pulse-lengths and wavelengths down to the hard X-ray range, feature unprecedented performance in terms of peak brightness, exceeding by many orders of magnitude that of third generation synchrotrons and enabling important complementary research opportunities. Despite the great scientific and technological benefits that X-ray FELs can provide, only very few such facilities are currently in operation worldwide, due to the high costs and complexity preventing their wide diffusion. Presently only major accelerator laboratories have the resources and expertise to construct and operate them.

With the launch of this H2020 design study, funded by the European Commission under GA No. 777431, the CompactLight Collaboration aims to facilitate the widespread development of X-ray FEL facilities across Europe and beyond, by making them more affordable to construct and operate, through an optimum combination of emerging and innovative accelerator technologies. A partnership of 23 international laboratories and academic institutions, 3 private companies and 5 third parties, which brings together the world's leading experts in this field, has been created for this purpose.

The FEL specifications, on which this design study is based, have been driven by the demands of its potential users, taking into account the photon characteristics required by their current and desired future experiments. For reaching these objectives, the CompactLight Conceptual Design Report (CDR) has been based on the latest concepts for bright electron photoinjectors, high-gradient X-band structures at 12 GHz, and innovative short-period undulators.

Compared to existing facilities, for the same operating wavelengths, the technical solutions adopted ensure that the CompactLight facility can operate with a lower electron beam energy and will have a significantly more compact footprint—the total length of the facility is just over 480 m, which is, for example, more than 250 m less than the total length of SwissFEL. All of these enhancements make the proposed facility more attractive and more affordable to build and operate. Suggested by the users' wish list, the key elements considered for the design study have been the following:

- High FEL stability in pulse energy and pulse duration
- FEL synchronization better than 10 fs
- Photon pulse duration less than 50 fs
- A repetition rate from 1 Hz up to 1 kHz
- FEL pump-probe capabilities with a large photon energy difference
- Small focused spot size
- Variable polarization, linear and elliptical
- Tunability up to higher photon energies
- Two-bunch operation
- Two-color pulse generation

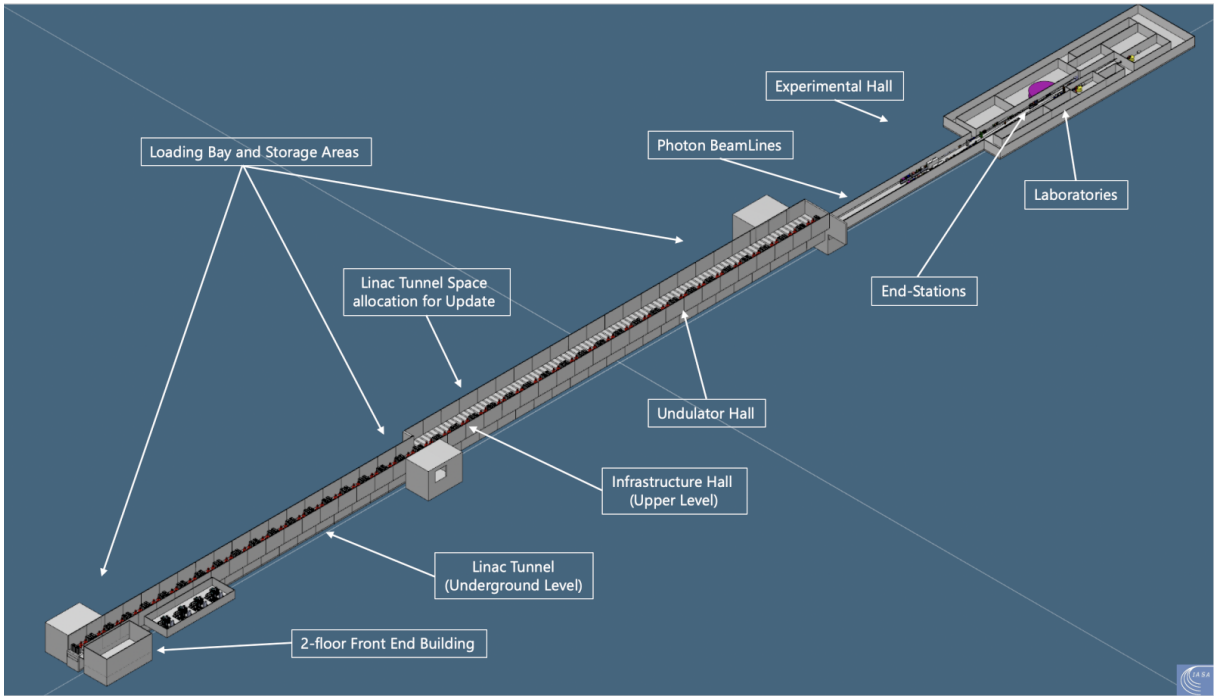

Figure 1.1.: View of the XLS facility. The total length is 483 m.

On the basis of these requirements, CompactLight has been designed as a hard X-ray facility, covering the wavelength range from 0.8 Å up to 5 nm (16 keV to 0.25 keV) with two separate FEL beamlines:

i) a soft X-ray (SXR) FEL able to deliver photons from 5.0 nm to 0.6 nm (0.25 keV to 2 keV) operating up to 1 kHz repetition rate (high rep rate);

ii) a hard X-ray FEL source (HXR) ranging from 6.0 Å to 0.8 Å (2 keV to 16 keV) with maximum 100 Hz repetition rate (low rep rate).

Key elements proposed in the design are the dual-bunch photoinjector and the two-beam deflectors adopted for the linac. Both give a huge flexibility for the facility operation, with different combinations of SXR and HXR operating modes, at high and low repetition rates, as requested by the users.

The design presented in the CDR includes a facility baseline layout and two main upgrades, with the most advanced option allowing the simultaneus operation of both FEL beamlines, in SXR/HXR pump-probe configuration, at 100 Hz repetition rate. It also includes a preliminary evaluation of the experimental hall, the photon beamlines and the X-ray optics for controlling the focus, intensity and spectral bandwidth of produced photons. An indicative layout for the buildings presented as a 3-D CAD model, an estimation of the conventional facilities, a cost estimate for the overall design and a cost comparison with SwissFEL as a reference facility, complete the design study. The 3D model is shown in Figure 1.1.

The CDR also includes preliminary evaluations of a soft X-ray FEL and an extremely compact and relatively inexpensive photon source based on Inverse Compton Scattering (ICS), both using the CompactLight technology. Compared with the full CompactLight facility, this soft X-ray FEL can be considered a quite affordable solution, in term of cost and complexity, in case of limited funding capabilities. In addition, the ICS source, with its wide range of applications, is very attractive and can be easily installed and operated in university campuses, small laboratories, and hospitals.

Various innovations and advanced systems have been designed specifically for the CompactLight facility. In particular:

- **Electron Source**

  For the electron source we have designed an innovative C-band photoinjector, with an operating gradient up to 180 MV/m, that can deliver two 75 pC e-bunches per RF pulse, with less than 0.2 mm mrad normalized emittance. The remaining part of the booster linac, up to the first bunch compression, at 300 MeV, consists of a full C-band linac.

- **Beam Linearizer**

  The development of very high frequency linearizers is of broad importance for accelerators which require short-bunches, including high frequency RF and plasma accelerators. For the XLS longitudinal phase space linearization, we have designed a Ka-band system operating at 36 GHz. The Ka-band system is based on a 300 mm travelling-wave structure, powered with 3 MW RF and operating with an integrated gradient of 12.7 MV. For the RF source we have identified two possible options: a High Order Mode Multi-Beam Klystron (HOM MBK) and a Gyro-Klystron.

- **Sub-Harmonic Deflecting System**

  An S-band (3 GHz) sub-harmonic deflecting structure, operated in the TM110 mode, has been designed to separate the two bunches before the injection into a septum magnet, which separates them into the two FEL lines. The transverse separation between the two beams at the septum is 2.5 mm. The spacing between the two bunches, 6 or 10 X-band RF cycles, is 1.5 or 2.5 RF cycles at S-band. Thus the two bunches can be placed at the crest and trough of the RF cycle of the sub-harmonic deflector so that the kicks applied to the two bunches are in opposite directions and the separation is maximized for a given kick voltage.

- **Undulator Chain**

  In the CompactLight design the same undulator line is used in both the SXR and the HXR FEL lines. Particular care has been taken to ensure that the undulator parameters are chosen appropriately to balance the output performance equally between the SXR and the HXR. This feature allows the facility to be more compact and cost-effective. The undulator chain foresees an innovative helical superconducting undulator, with 13 mm period and 4.2 mm gap followed by an APPLE X afterburner with 19 mm period and 5 mm gap. The length of each module is 1.75 m.

Each of these innovative systems can also be used ‘stand alone’ in a variety of accelerator applications (i.e. future beam colliders, compact accelerators for medicine, plasma drivers, etc.), where conventional systems cannot meet the challenging performance requested.

In conclusion, this CDR presents the design of an extremely bright and compact hard X-ray FEL, beyond today’s state of the art. It describes the technical concepts and the parameters used for the facility design, with the objective to provide a reference document for future FEL designers. It also represents an effective solution that makes X-ray FELs more affordable to construct and operate, even for small laboratories or academia with limited space and funding capabilities.

2. Introduction

In the last decades the X-ray research community has witnessed significant increases in the performances of synchrotron light sources, with a rapid succession of first, second and third generations of X-ray light source facilities constructed worldwide. From the early 1950s to the 1970s the cycling electron synchrotrons, developed for physics research, were considered the first-generation light sources. At that time, Synchrotron Radiation (SR) was mostly considered a parasitic effect responsible for unwanted energy loss and its properties were studied to validate theoretical models. The power of using SR for spectroscopy and diffraction was first realized in the 1960s and 1970s. In the mid-1970s, the demand for SR in Europe, Japan and the US led to the construction of second-generation light sources—rings fully dedicated to SR research. The bending electromagnets in the accelerator were the primary sources of the SR. In the late 1980s other specialised devices, periodic magnetic structures called wigglers and undulators, were specifically developed to generate high intensity radiation. Third-generation SR sources were based upon these devices, with dedicated straight sections in the storage rings for their insertion. The first third-generation sources began operation in the early 1990s.

The main figure of merit for SR is the brightness, which defines the intensity of radiation, within a given bandwidth around the desired wavelength, focused onto a sample of given area, within a particular solid angle. Although spectacular, the brightness of third generation sources is far from the fundamental limit in the X-ray region. Single pass Free-Electron Lasers (FELs), light sources based upon linear accelerators and long undulators, can overcome the limitations of ring-based X-ray sources. FELs can produce extremely high brightness radiation by inducing a density modulation in the electron bunch at X-ray wavelengths. This is achieved by interacting the bunch with an optical field in the spatially periodic magnetic field of the undulator. When electrons are bunched at a given wavelength, the power radiated varies as the number of electrons to the power of four-thirds, rather than linearly as for an unbunched beam. The characteristics of linac-based X-ray FELs (XFELs) are extraordinary—particularly their short pulse duration, peak brightness, and coherence. The peak brightness of the XFELs at SLAC and DESY is $\sim 10^{10}$ times higher than that of third- generation storage ring sources, with ~ 100 times shorter pulses. Linac-based short-wavelength FELs constitute the fourth-generation light-sources. Since the successful operation of FELs in Germany (FLASH [1, 2]), Japan (SACLA [3]), Italy (FERMI [4, 5]) and the USA (LCLS [6, 7]), new X-ray FELs have been built and commissioned in Germany (European XFEL [8, 9]), Switzerland (SwissFEL [10, 11]) and South Korea (PAL-XFEL [12]), whilst others are now being constructed in China (SHINE [13]) and USA (LCLS-II [14, 15]). A number of other countries have considered, or are actively considering, FEL facilities at the present time. European examples include the UK, Turkey, Sweden, The Netherlands and France. The strong scientific case for FEL beams is apparent from the inability of present facilities to meet the demands of the scientific community. At FERMI little more than 30% of the proposed experiments are currently awarded facility beam time and a similar situation exists at FLASH.

A major factor in the cost of XFELs is the choice of accelerator technology adopted. The majority of existing facilities use S-band linear accelerators, given the maturity of the technology. This technology, although consolidated through many decades of use, is not however optimal. At comparable accelerating fields, a higher frequency accelerating structure can achieve higher gradients and lower power requirements than those of lower frequency structures. The successful construction and operation of SACLA at C-band is testimony of the effectiveness of a higher accelerating frequency. In this case an 8 GeV electron beam, with the characteristics required to drive an XFEL, can be generated in the space of 400 m, compared to 600 m at S-Band (inclusive of injector and bunch compressors). Subsequently, SwissFEL also adopted C-band technology. The use of X-band technology further improves the situation and is expected to more than halve the required length of the accelerator and associated infrastructure compared to these machines. For large scale accelerator projects such as SR light sources and FELs the cost breakdown is typically 70% for the civil engineering, accelerator and the first

beamlines, and 30% for personnel and management. Simple scaling of the accelerator length can result in 20 to 25% savings. In recent years, research and development of X-band accelerator technologies has seen tremendous progress in the context of the next generation of electron-positron linear colliders, where very high gradients are necessary to achieve the multi-TeV beam energy target for particle physics. The CLIC [16] Study at CERN is the most remarkable example—here accelerating gradients three to five times larger than those in operational linacs have been demonstrated in prototype accelerating structures. Thanks to the linear collider research and development, X-band technology has reached a maturity level that encourages the envisioning of other possible applications beyond particle physics.

The CompactLight Design Study [17] enables the use of this world leading accelerator technology, developed for the most advanced particle accelerators of the future, to benefit today's society. High-frequency X-band structures can also run at low gradients and high repetition rate (kHz regime), enabling a new set of operational scenarios for higher repetition rate X-ray FELs, currently in great demand for scientific and technological applications. In parallel to X-band developments, undulators have made significant improvements in capability in recent years, with the promise of more to come. Two new undulator technologies have now been proven on light source facilities—Cryogenic Permanent Magnet Undulators (CPMUs) and SuperConducting Undulators (SCUs). Both of these continue to improve in performance as confidence and experience develops, but neither have been applied to an XFEL design—until now. Reducing the required electron beam energy through the use of more advanced undulators results in additional cost savings roughly proportional to the energy reduction. The application of both higher frequency acceleration and advanced undulators also facilitates the upgrade of existing facilities to higher energy, with the possibility of minimal or no increase in civil construction. This Design Study, based on validated high-gradient X-band and novel undulator technologies, now enables upgrades of existing FELs (e.g. FERMI) to the higher energies within physical space limitations than would otherwise not be possible. It will also allow existing facilities to expand their user communities and scientific programs, taking advantage of the higher photon energies that it will be possible to generate.

This Design Study was funded by the Horizon2020-INFRADEV 01-2017 call. The aim of this call is "to support the conceptual and technical design and preparatory actions for new research infrastructures, which are of a clear European dimension and interest. Major upgrades of existing infrastructures may also be considered if the end result is intended to be equivalent to, or capable of replacing, an existing infrastructure". The Design Study started on 1st January 2018 and ended on 31st December 2021.

The CompactLight design presented in this report now opens the way to the construction of a class of affordable regional and national FELs with world leading X-ray performance, and has helped prime the capability of industry to competitively supply components for accelerators. This Design Report discusses the major design choices that have been made, framed in terms of their scientific, strategic, and technological relevance and ambition. It enables the development of new research infrastructures and the upgrade of existing ones.

2.1. Motivation for CompactLight

SR has become a fundamental and indispensable tool for studying matter, as shown by the large number of synchrotron light source facilities in operation worldwide (close to eighty) which serve tens of thousands of users every year. The SR user community spreads across a multitude of scientific and engineering disciplines, including materials science, condensed-matter physics, atomic and molecular physics, life science and medicine, chemistry and environmental sciences. The impact of SR across these disciplines is evidenced by the five Nobel prizes awarded in the past twenty years to scientists whose research has been made possible by SR.

The latest generation of SR sources are based on FELs driven by linacs, and feature unprecedented performance in terms of pulse duration, brightness and coherence. The use of XFELs, in the short time that they have been available, has already led to significant insights in a number of scientific fields such as atomic physics, plasma physics, solid-state physics and macromolecular crystallography. As

researchers develop new exploitation techniques, increasingly based upon enhanced output from FELs such as two colour pulses, femtosecond and sub-femtosecond photon pulse-lengths, and increasingly coherent pulses, the scientific reach of FELs will continue to expand. The CompactLight aim is to facilitate the widespread development of XFEL facilities across Europe and beyond, by making them more affordable to construct and operate through an optimum combination of emerging and innovative accelerator technologies. The collaboration has designed a Hard X-ray (HXR) FEL facility using the very latest concepts for bright electron photoinjectors, very high gradient accelerating structures and novel short period undulators. The resulting facility benefits from a lower electron beam energy than current facilities, due to the enhanced undulator performance, is significantly more compact as a consequence of the lower beam energy and the high-gradient acceleration, and also has a much lower electrical power consumption. These ambitious, yet realistic, design features result in much lower construction and running costs, thus making X-ray FELs affordable, even by national institutions or academia. It is anticipated that this Design Study will enable FEL facilities to proliferate across all of Europe and beyond even more rapidly than third generation light sources have managed to do over the past decades.

In recent years there have been intense electron-accelerator developments driven by the XFEL and linear collider communities and by other applications such as Compton scattering sources. Relevant advances include:

- Lower emittance and higher repetition-rate photoinjectors
- High-gradient linacs—gradients in excess of 100 MV/m are now routinely achieved.
- High-efficiency klystrons—techniques to bring efficiencies above 60% at high frequency have been demonstrated.
- Advanced concept undulators—cryogenic permanent magnet undulators and superconducting undulators have both been demonstrated and since used operationally on 3rd generation light sources in recent years.
- Improved diagnostics—including X-band deflectors for longitudinal bunch dynamics.
- Better beam dynamics and optimization tools—including those developed for linear colliders.

It is believed that by taking these developments, as well as making other new advances, and optimising them together in this comprehensive study, a facility has been designed with significantly lower cost and size than existing facilities.

2.2. The Objectives of CompactLight

The key objective of the CompactLight Design Study has been to demonstrate, through this conceptual design, the feasibility of an innovative, compact and cost effective FEL facility suited for user demands identified with leading academics during the design study. In order to achieve this, the high-level objectives were:

- to determine the user demands and design parameters for a compact and cost effective hard X-ray FEL facility;
- to advance innovative designs for X-band and undulator technology as new standards for accelerator based compact photon sources;
- to present a flexible design that can be adapted to local implementation demands with photon source options for soft and hard X-rays as well as Inverse Compton Scattering (ICS) generated light.

All of these high-level objectives have been achieved, and are articulated in this Conceptual Design Report.

The main cost driver for every FEL is the beam energy. By taking advantage of the latest technological undulator innovations the project has been able to lower the electron beam energy requirement significantly. SwissFEL is currently the most ambitious operating XFEL in terms of undulator technology. By implementing a room temperature in-vacuum device, they are able to achieve 12 keV photon output at 5.8 GeV. The CompactLight FEL can achieve a higher photon energy of 16 keV at the lower electron beam energy of 5.5 GeV by implementing advanced superconducting undulator technology. For comparison, note that the CompactLight undulator could generate 12 keV photons at only 4.8 GeV, much lower than the SwissFEL example.

A substantial fraction of the FEL's cost, space requirements and power consumption are due to the linac that accelerates the electron beam. Normal conducting X-band technology can provide efficient, high-gradient acceleration at limited cost. Research and development in high-energy physics laboratories has developed this technology and demonstrated high performance prototypes. The CompactLight goal has been to optimize and make this technology available for FELs by adapting the design to FEL specifications. The project developed a unique concept where the linac repetition rate is traded off against accelerating gradient so that the facility can operate at 1kHz in the soft X-ray region and at 100Hz in the hard X-ray region. This exactly matches the requirements of FEL users to have a higher repetition rate at longer wavelengths.

2.3. Organisation of the Design Study

From the launch of the design study the collaboration subdivided the project into seven interlinking Work Packages (WPs). WP1 provided the overall management and coordination of the project. The overall design process was carried out by WP2. WPs 3 to 6 carried out the designs of specific technical systems (electron injector, linac, undulators, and beam dynamics) and provided the input into WP2 necessary for the overall design, optimisation, and integration. WP7 addressed the strategic and user liaison issues related to the objectives of CompactLight. Approximately half way through the design study it was appreciated that the project would benefit from an additional technical WP on diagnostics, and so WP8 was created.

The CompactLight collaboration consists of twenty five partners and five third parties. Three of the partners are from outside of Europe, two being based in Australia and one in Shanghai. Three of the partners are industrial companies that are active in the supply of components for particle accelerators. Full details of all of the partners and third parties are provided in Appendix A.4.

Excellent communication within WPs and between WPs has been key to the successful delivery of this design study. All WPs have held regular telephone and video meetings and many cross-WP video meetings have been held. In addition, two face to face meetings of the full collaboration were held per year, each being typically three days in duration, until this was prevented by the coronavirus pandemic, at which point these continued as video conferences. The face to face meetings were hosted by different members of the collaboration on each occasion. There have also been a number of smaller face to face meetings per year, either between WPs to address specific issues or for all WP leaders to address management and organisational issues. A specific meeting between members of the collaboration and leading European academic users of XFELs was held at CERN during the first year of the study to discuss the detailed user requirements for CompactLight.

A key feature of the design study has been the close involvement of industry. Three of the partners are industrial companies with experience of supplying high tech components to accelerator projects. In addition, specific companies that supply leading RF equipment were invited to face to face meetings of the full collaboration to inform their ongoing developments and to hear their views on technical limitations. The involvement of all of these companies has been extremely fruitful and has ensured that the conceptual design of CompactLight takes advantage of the latest products, benefits from industry's

wealth of experience, and pushes the technological boundaries. CompactLight has strongly influenced the future direction of product development within these companies and given them a deeper understanding of the long term requirements for the next generation of FEL projects.

2.4. The Impact of CompactLight

The ESFRI Roadmap 2016 Strategy Report on Research Infrastructures', assers 'SR facilities are very powerful attractors and contribute to European scientific and industrial competitiveness'. It further states 'Free Electron Laser sources provide a substantially novel way to probe matter and have very high, largely unexplored, potential for science and innovation'. The CompactLight facility aims to have the same scientific potential as the facilities considered for the ESFRI roadmap, but it also aims to be a pathfinder for facilities with a significantly smaller footprint and cost. The project aims at making X-ray FELs small and inexpensive enough to be within national and even university scale, yet with uncompromised scientific potential.

The currently operating facilities are significantly oversubscribed and this situation is expected to continue. Although new XFEL facilities have come on line recently, the increasing demand for FEL light (from a large variety of sciences as the user base develops) is still not met by the available facilities. CompactLight aims to promote the spread of national and international research infrastructures for photon science to help satisfy this large demand. This design study has addressed the key points that will make FELs more affordable for smaller countries or even universities. The design of CompactLight, discussed in this report in detail will have direct impact in a number of critical areas that will aid in the further dissemination of XFEL facilities across Europe and beyond:

- **Cost**: the total facility construction and operating costs have been reduced in comparison with other XFELs by making use of the most advanced injector, linac, and undulator technologies and without compromising on performance.
- **Power consumption**: the power consumption has been reduced with respect to other XFELs by making use of the more efficient X-band RF technology.
- **Footprint**: the physical scale of CompactLight has been significantly reduced in comparison to other XFELs, which further impacts the cost and also the ability of universities to host such a facility on their campuses.

3. Science Goals and Photon Output Requirements

3.1. Summary of Science Case

3.1.1. Introduction

Research at modern accelerator-driven light sources continues to deepen our knowledge of the natural world, from the subtle workings of life to matter under extreme conditions, and has a profound impact on our industrial, economic and societal evolution. A new generation of light sources based on coherent SR produced by Free-Electron Lasers enables, for example, characterization of the structure of biomolecules with sub-ångström resolution, paving the way to controlling how they function. Currently, the FEL is the brightest man-made source of light, enabling a new era of science and innovation. This section gives a few examples of groundbreaking research enabled by XFELs and points out new perspectives for X-ray science that would be opened by the highly flexible structure of double X-ray pulses from the CompactLight FEL.

3.1.2. Taste of Groundbreaking Science with XFELs

3.1.2.1. Scattering

While X-ray scattering techniques have been extensively used for decades at synchrotron light sources, the high photon flux of coherent FEL pulses opened a new regime in X-ray science—the high-resolution determination of the structure of molecules, microcrystals and matter under extreme conditions. Below, some examples of such high-resolution applications are discussed in more detail.

Bio-imaging The structure of biomolecules such as proteins, viruses or cells, is fundamental to their function. Hence, the high-resolution structure determination enabled by coherent X-ray radiation is critical in the fields of biology and life science and allows, for example, rational drug design and the understanding of human biochemistry. A key method in this context is 'diffraction-before-destruction' in which the ultrashort duration of the X-ray pulse is exploited for outrunning the sample radiation damage. It offers the opportunity to image important bio-objects that can only be formed in smaller crystals, such as membrane proteins, or even single particles, with varying resolution. In particular, hard X-rays with wavelengths in the angstrom range provide extremely high resolution [18] while soft X-rays offer useful information about larger structures, for example living cells, with high throughput. The ultrashort, intense x-ray pulses provided by FELs additionally allow measurement of the dynamics of biologically relevant molecules on their natural femtosecond timescale.

Structure determination of micrometre-sized, or smaller, crystals at FELs is often done using serial femtosecond crystallography. Typically a liquid jet provides a stream of crystals that crosses the X-ray beam and the high intensity of the FEL beam enables the collection of diffraction images of thousands of randomly oriented crystals. These can be reconstructed into a 3D image with resolution at the atomic scale [19, 20]. Major progress with respect to sample delivery has been made recently by increasing the speed of the liquid jet, which enables a fresh sample with every X-ray pulse at a MHz repetition rate [21, 22]. Simultaneous detector frame-rate development has also been carried out [23]. Another viable sample delivery method uses fixed targets and has important advantages such as an order of magnitude increase in the probability of actually hitting the sample with the X-ray pulse. This sample delivery method currently requires low kHz repetition rates.

A major scientific driver of XFELs is the potential for single-particle imaging (SPI) of biological molecules at atomic resolution [24]. Although this goal is far from being reached there have been several

measurements of biological objects at lower resolution. SPI has tremendous potential for observing the dynamics of biological, chemical and physical systems [25].

Matter under Extreme Conditions Intense laser pulses applied to solid materials can produce nanosecond or sub-nanosecond dynamic compression into extreme pressure regimes. The material response to the unexplored pressure and temperature conditions created by such compression can be uniquely explored in diffraction experiments with 100-fs temporal resolution that resolves the atomic motion. Moreover, the brightness and small focus of the XFEL pulse relaxes the pulse energy requirement of the optical pump laser, which can then also be focused to a small spot.

Studies of shock waves probed by 8 keV X-rays at FELs have measured the ultimate compressive strength, associated with a purely elastic response, of copper, and the plastic flow occurring at higher strain orders [26]. Diffraction studies have also been applied to investigations of phase transitions and melting. For example, melting of Bi was observed after a few nanoseconds upon the release of dynamically 8–14 GPa induced compression [27]. At LCLS shock pressures exceeding 120 GPa were used to demonstrate conversion of graphite to diamond and lonsdaleite phases [28], and complicated structures, including linear guest structures arranged as chains in channels of the host structure, have been observed.

High energy-density plasmas are characterized by temperatures above 1 eV (about 11600 K) and densities higher than that of a typical solid such as found in planet cores, stellar interiors, intense laser-matter interactions and fusion experiments. High-brightness (hard-)X-ray FELs are well adapted for such studies as they satisfy the requirements for both generating and detecting the hot and dense plasmas deep into the sample. The XFEL also provides the necessary spatial resolution and the temporal resolution, ranging from attosecond electron dynamics to compression processes on the nanosecond timescale.

3.1.2.2. Spectroscopy

X-ray spectroscopy provides complementary information to imaging and diffraction measurements of the chemical and electronic properties of a system, and the techniques can be performed simultaneously [29]. X-ray absorption spectroscopy (XAS) and X-ray emission spectroscopy (XES) enable element specific measurements of the unoccupied and occupied electronic states, respectively, while X-ray photoelectron spectroscopy (XPS) is highly sensitive to the chemical surroundings and offers surface sensitivity. The high peak-brightness FEL pulses allow new approaches to spectroscopic experiments such as nonlinear excitations, single-shot detection and femtosecond time-resolved measurements.

The potential for multiphoton excitation of atoms and molecules by FELs has been exploited for the formation of two-site double core-hole (tsDCH) states that could be detected using XPS [30, 31]. These states are created by the ejection of one core electron on separate atoms and require high peak intensities in order to ionize the second atom before Auger decay occurs in the first atom. These states have received attention due to the significantly enhanced chemical sensitivity compared with single core-hole states.

XES and XAS studies carried out at XFELs have been helpful in understanding important chemical processes. Electron transfer is essential in biological systems and for artificial light harvesting. XES and XAS measurements on an electron-harvesting chromophore performed at SACLA demonstrated the potential of these methods for monitoring fundamental chemical processes [32]. Moreover, resonant inelastic X-ray scattering has proven a capable tool for investigating excited state dynamics in solution via detection of orbital interaction [33]. The potential of using XAS and XES at FELs for understanding catalytic reactions has also been demonstrated at LCLS, where these techniques have enabled the observation of CO oxidation on a Ru surface [34, 35].

3.1.2.3. Time-Resolved Experiments

Ultrafast Magnetism X-ray magnetic circular dichroism (XMCD) spectra, obtained as the difference between XAS data with opposite circular polarization, offer a way to probe the magnetic properties of materials. Recently, the high peak brightness of the soft-X-ray FEL was exploited in a demonstration of time-resolved (tr) XMCD, which was applied to investigate the element specific all-optical switching dynamics in GdFeCo with femtosecond temporal resolution [36]. Moreover, sub-picosecond demagnetization dynamics were studied by tr-XMCD using hard X-rays resonant with the Pt L3 edge (11.6 keV) [37].

XFEL pulses offer an efficient tool for probing ultrafast magnetization dynamics on a femtosecond timescale with nanometer resolution. For example, soft X-ray holography using circular polarization has demonstrated 15 nm resolution [38]. Time-resolved soft X-ray resonant diffraction studies carried out at LCLS detected Gd spin reversal within the first picosecond in ferromagnetic GdFeCo. It was explained by a nanoscale flow of angular momentum from Fe-rich to Gd-rich regions induced by the optical pump [39]. The control of magnetic properties via spins opens the door to faster data storage and processing devices.

Strongly Correlated Electron Systems In strongly correlated electron systems the interaction between electrons is non-negligible and may strongly influence the character of the material. Light-induced insulator-metal transitions (IMT) dominantly driven by electron correlation effects, as opposed to large structural changes (so-called Mott transitions), are a promising route towards faster electronics. Time-resolved X-ray diffraction experiments at FELs following the structural dynamics of the THz-induced IMT in VO_2 have shown that the electronic metallization dynamics and structural phase transitions can occur on different timescales [40]. This opens the door to efficient conductivity switching in correlated-electron systems.

XFEL pulses are also useful for studying the lattice changes associated with light-induced superconductive phases. For example, THz pulses have been shown to create superconducting properties in cuprate materials, and using femtosecond X-ray diffraction the behaviour of the lattice structure was investigated for this exotic state. These studies revealed that the nonlinear excitation of the crystal lattice structure creates a displaced lattice geometry which causes drastic changes in the electronic structure, and may cause destabilization of the charge-density wave order—both may favour superconductivity [41].

Water Dynamics Water is a surprisingly complex liquid that is still far from understood. The reason for its complexity and anomalous properties is its ability to form highly disordered hydrogen-bonded networks. X-ray FELs permit resolving water structural dynamics on a sub-100-fs timescale and atomic length scale. In a recent experiment at LCLS [42] using 8.2 keV photons, water structural motion was observed from the decay of speckle contrast when tuning the pulse duration from 10 to 120 fs. The work showed that cage effects due to hydrogen bonding play an important role in the slower dynamics of water upon cooling.

3.1.3. New Possibilities Offered by the Simultaneous Use of Two FELs

The CompactLight facility offers the possibility of combining X-ray pulses from two parallel FELs, independently tunable in photon energy and temporal separation, at a single sample in a ‘dual’ endstation. This enables measurements with a large photon-energy separation between two X-ray pulses and pump-probe experiments using long and flexible time delays. The photon beamline design presented in Section 6.2 includes three dual stations that allow combining two soft X-rays, two hard X-rays or

one soft and one tender X-ray. The simultaneous access to a wide range of absorption edges with a large photon-energy separation offers the possibility to, for example, pump and probe different sites of a molecule associated with different atomic species [43] at the dual SXR station. Two hard X-ray pulses with highly tunable photon energies may be exploited at the dual HXR station for two-color diffraction, in which two datasets are recorded simultaneously for more efficient crystal structure measurements [44]. The dual soft/tender station permits concurrent spectroscopic (soft X-rays) and scattering (tender X-rays) measurements that provide simultaneous insight into chemical and structural dynamics and can be useful in, for example, heterogenous catalysis [45]. Moreover, the capability of using a soft X-ray pump that excites a specific resonance, followed by a tender X-ray pulse that probes the structural dynamics in an X-ray pump-probe scheme, will be highly beneficial.

3.1.4. User Engagement

From day one, the specifications and design of the CompactLight facility were driven by the demands of potential users and the associated Science Case. Several channels of communication with users were established and a number of interactions were undertaken. This started with two informal meetings with potential academic and industry users in the UK immediately after the project commenced. A specially developed questionnaire was then sent to over 50 FEL experts within Europe, and the CompactLight consortium sent representatives to the Science@FELs Conference in Stockholm, Sweden in June 2018 and the Attosecond and FEL Science Conference in London, UK in July 2018, to hear about the latest scientific achievements using FEL facilities and to informally interact with leading researchers to gather their views on the parameters and performance of future FELs. The interaction with FEL users culminated in a dedicated CompactLight User Meeting that was held from the 27th to the 28th of November 2018 at the European Organisation for Nuclear Research (CERN) in Geneva, Switzerland [1]. The primary objective of the meeting was to consult potential users on the photon characteristics required by their current and future experiments. The findings on the science requirements for the CompactLight FEL are summarized in the deliverable D2.1.

3.1.5. Science Requirements of a Next Generation FEL

Science opportunities with FEL light sources are far-reaching and there is an increased interest in using FELs to explore:

1. materials far from equilibrium such as in light-induced superconductivity;
2. nonlinear x-ray optics;
3. multi-dimensional attosecond spectroscopy;
4. charge migration and ultrafast x-ray damage in biomolecules;
5. surface chemistry and pathways for catalysis;
6. matter under extreme conditions.

Furthermore, the trends towards shorter pulse durations and higher photon pulse energies are clear. During the discussions with users there were also very strong requests for improving the coherence and stability properties of FEL radiation pulses as well as much better synchronization to external laser sources. The CompactLight design addresses these challenges.

In conjunction with the CompactLight User Meeting held at CERN, a preliminary survey was conducted through the use of an online questionnaire. The purpose was to gather quantitative information about the user requirements for the photon characteristics. According to the survey, the respondents

[1] https://indico.cern.ch/event/750792

expressed interest in experiments such as (i) pump-probe diffraction, (ii) serial crystallography, (iii) time-resolved spectroscopy and (iv) time-resolved scattering.

With regard to the tunability, there was a clear demand for photon energies as low as 0.2 keV and as high as 20 keV. The mean photon energy of the desired tunable range is about 4 keV. In the design, a compromise on the highest photon energy of 16 keV was made, which covers most of the user experiments. The preferable pulse energy was in the range of 3–100 μJ and the demand on the *stability* of the pulse energy was stringent with the RMS fluctuation in pulse energy requested to stay below 10%.

Most respondents preferred a pulse duration of 10–100 fs, a repetition rate higher than 100 Hz, a degree of transverse coherence higher than 70%, a coherence time of 1–100 fs, a bandwidth of 0.1–1% and a microfocus of 0.1–100 μm. For pump-probe experiments, most respondents wanted the synchronization between the FEL and the external laser to be in the order of 10 fs. Two-colour pulse operation with a wide tunability in relative photon energy and time delay between the pulses was strongly requested.

3.2. FEL Requirements

3.2.1. Introduction

This section summarizes all of the discussions and interactions that the CompactLight collaboration held with potential users of the facility during the first year of the project. The exploitation of FELs by numerous groups, covering a diverse range of research topics, highlights why FELs are fundamental engines of discovery. The diversity also means that it is not possible to meet the current and future needs of all users with a single facility. Indeed, there is a risk that by trying to satisfy all requirements the facility performance would be compromised and no users would be entirely satisfied. The CompactLight collaboration understood this issue and distilled all of the user input into a coherent specification that is fully aligned with the prime strategic objective which is to generate a compact and affordable FEL facility design.

3.2.2. CompactLight Output Specification

Table 3.1.: Main parameters of the CompactLight FEL.

Parameter	**Unit**	**Soft-x-ray FEL**	**Hard-x-ray FEL**
Photon energy	keV	0.25 – 2.0	2.0 – 16.0
Wavelength	nm	5.0 – 0.6	0.6 – 0.08
Repetition rate	Hz	1000	100
Pulse duration	fs	0.1 – 50	1 – 50
Polarization		Variable, selectable	Variable, selectable
Two-pulse delay	fs	$\pm$100	$\pm$100
Two-colour separation	%	20	10
Synchronization	fs	<10	<10

The required specification of the CompactLight FEL is summarised in Table 3.1. The following bullet points expand on this specification and explain the priorities that were used to inform the technical design work, and which were balanced against the top level objectives of compactness and low cost.

- Seeding of the FEL enhances the output quality significantly in terms of improved temporal coherence and wavelength stability and should be implemented at all wavelengths where feasible.

- Peak brightness is key to many experiments and should be maximized.
- Extreme synchronization between different photon sources for time-resolved pump-probe experiments is vital and the design should enable synchronisation of the FEL with a conventional laser to better than 10 fs.
- Two pulses and two wavelengths are essential for many experiments. The design should provide these capabilities.
- The repetition rate for the soft X-ray FEL should be 1kHz.
- The photon pulse bandwidth should be minimized to maximize the peak brightness.
- The facility output should cover the range between 250 eV and 16.0 keV with all photon energies within this range being accessible from at least one of the FEL beamlines.
- The 2 keV 'boundary' between the soft-x-ray FEL and the hard-x-ray FEL is not rigid and should be determined when considering all the technical options including electron beam energies, undulator performance, and X-ray optics capabilities.
- Tuning across photon energies should primarily be achieved by undulator scanning rather than energy scanning to maximize the efficient operation of the facility.
- The FEL output pulses should be evenly spaced in time and not provided in a burst mode.
- To maximize the efficient use of the facility, simultaneous operation of both the soft- and hard-x-ray FELs would be beneficial.
- Output pulse energies should be competitive with other facilities.
- Variable, selectable polarization is required at the sample for all photon energies.
- Generating pulses as short as 100 attoseconds is desirable but may take significant extra space and cost.
- Stability in all its aspects is important to many experiments and should be considered in all technical designs of systems and sub-systems. The RMS fluctuation in FEL pulse energy should stay below 10%.

The target performance of CompactLight in terms of peak brightness is shown graphically in Figure 3.1. The peak brightness is expected to be comparable to the state-of-the-art x-ray FEL facilities which are currently in operation.

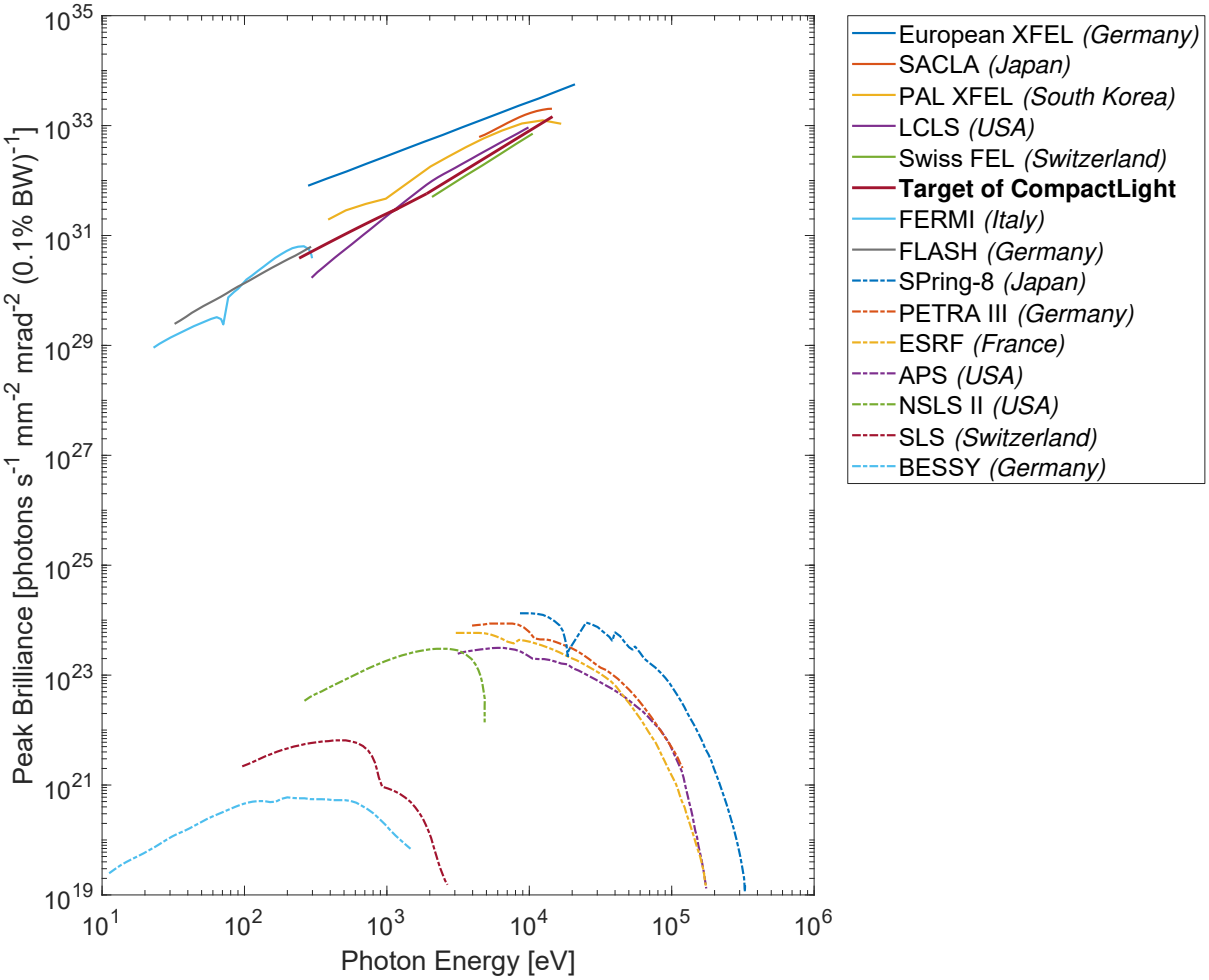

Figure 3.1.: Peak brightness as a function of photon energy for a selected set of x-ray sources. Free-electron laser facilities are shown in solid lines, and synchrotron facilities are shown in dashed lines. This figure is adapted from Figure 1 in [46].

3.3. FEL Physics

The Free-Electron Laser (FEL) was first proposed by Madey in 1971 [47] who published the seminal theory of a small gain process in a relativistic electron beam and undulator system. The first experimental demonstrations of amplification [48] and lasing [49] were achieved at Stanford a few years later. The historical development of the FEL and the theory of FEL physics are reviewed extensively in a number of excellent articles, for example [50–53]. This section provides a relatively concise general summary to convey the basic principles and give the background to the parameter choices made in the CompactLight design. Section 3.3.1 describes the FEL process, Section 3.3.2 details the basic output properties of the SASE FEL, Section 3.3.3 motivates the requirement for a high-brightness electron beam to drive the FEL and Section 3.3.4 describes how the performance of the FEL can be quantified as a function of the electron beam properties.

3.3.1. Description of FEL Process

In the FEL, a highly relativistic electron bunch with Lorentz factor $\gamma = E/mc^2 = E$ [MeV]/0.511 takes a sinusoidal path through the periodically alternating transverse magnetic field of an undulator. It emits synchrotron radiation due to its transverse acceleration. The resonant wavelength λ_r of the FEL is given

by the same expression used for on-axis spontaneous undulator radiation

$$\lambda_r = \frac{\lambda_w}{2\gamma^2}\left(1 + a_w^2\right). \tag{3.1}$$

Here λ_w is the period of the undulator magnetic field and a_w is called the undulator deflection parameter, defined as

$$a_w = \frac{eB\lambda_w}{2\pi mc} \tag{3.2}$$

with e the electron charge, m the electron mass and c the speed of light in a vacuum. For a helical undulator $B = B_0$ with B_0 the peak field, whereas for a planar undulator $B = B_0/\sqrt{2}$. Using these definitions, Equation 3.1 is true for both helical and planar undulators.

For typical undulator parameters, of a period in the tens of millimetres and deflection parameter approximately unity, it is found from Equation 3.1 that the beam energy must be in the multi-GeV range to reach sub-nanometre wavelengths. The resonance condition also shows the reason the FEL wavelength can be smoothly and continuously tuned over a fairly wide range—it is only necessary to change the on-axis magnetic field to change the wavelength. Such field tuning can typically give a factor around four in wavelength tuning while maintaining sufficient on-axis magnetic field for lasing. A much wider wavelength range is accessible by also changing the electron beam energy, although this requires adjusting multiple accelerator parameters so is less convenient (but still common). The resonance condition also shows that in order to minimise the electron beam energy required for a given wavelength, the undulator period should be made as short as possible. Minimising the electron beam energy and undulator period contribute to making the facility compact—this fact has been exploited in the CompactLight design. However, as the undulator period is reduced, relative to the undulator gap, the on axis field reduces—once the period is reduced to about the same as the gap the magnetic flux starts to flow from one magnet pole to the adjacent magnet pole of opposite polarity on the *same* side of the array, rather than across the gap where it will be seen by the electron bunch. Therefore to maintain on axis field, and hence an efficient FEL interaction, the gap must also be reduced as the period is decreased. This unfortunately has the effect of increasing the strength of resistive wall wakefields within the undulator vessel which can degrade the FEL performance, so choosing the minimum undulator period is a balance between achieving a compact design and one in which the wakefields are acceptably small. This balance has been achieved in the CompactLight design.

The resonance condition can be derived in the case of spontaneous emission by considering how the broadband synchrotron radiation emitted by the electrons from N periods of their sinusoidal trajectory interferes constructively and destructively to create a radiation pulse with bandwidth approximately $1/N$. In the case of the FEL mechanism it is more instructive to start from the fact that the average longitudinal velocity of the electrons v_z is very slightly less than c, partly due to the wiggles in their trajectory and partly because $v = \beta c$ and $\beta < 1$ by a tiny amount. As the electrons travel through the undulator they propagate in the presence of their own spontaneous emission. The transverse component of the electron velocity can then couple to the transverse component of the spontaneous emission electric field, allowing an energy transfer to occur. The resonant wavelength of the FEL is the distance the electrons slip back with respect to the light over each undulator period—this is because light at this wavelength has an electric field which *maintains a constant relative phase* with respect to the oscillating electron transverse velocity, and so this coupling between electrons and light is maintained allowing a *continuous* energy transfer. Depending on their phase, some electrons gain energy, and some electrons lose energy. This sets up a sinusoidal energy modulation along the electron bunch with period λ_r. The process is illustrated schematically in Figure 3.2.

All this time the electrons are still emitting, but because they are distributed randomly in phase their emission is incoherent with power P proportional to the number of emitting electrons N_e. However, the energy modulation in the bunch starts to convert into a density modulation due to longitudinal dispersion in the undulator—the electrons that have gained energy are now deflected less in the magnetic field

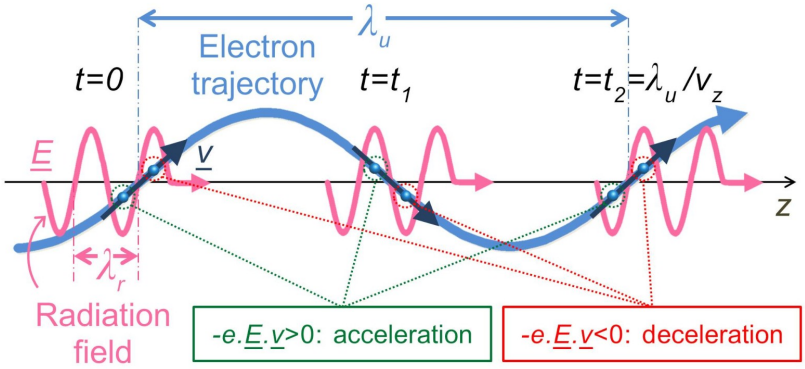

Figure 3.2.: Schematic of the undulator resonance condition. As the electrons traverse one undulator period the radiation propagates forward relative to the electrons by one radiation wavelength, allowing sustained energy transfer. Depending on their longitudinal alignment, electrons either gain or lose energy, which leads to a modulation in the electron beam energy. Figure constructed following the approach of [54]

.

and thus take a shorter path, moving ahead of the electrons that have lost energy and are deflected more to follow a longer path. In this way the electrons start to 'microbunch' themselves at the resonant wavelength. This then increases the coherence of their emission, increasing the power and amplifying the co-propagating field. Because the field is growing, the energy modulation increases, leading to increased bunching through the longitudinal dispersion, and so on in a positive feedback loop in which the radiation power grows exponentially.

Eventually the growth of the radiation power saturates. The strongest emission occurs when the electrons that are moving in one direction due to their positive energy offset meet up with the electrons moving in the other direction due to their negative energy offset and the microbunching is maximised. At this point this radiation emission power P is proportional to $N_e^{4/3}$. In a 75pC electron bunch $N_e \approx 5 \times 10^8$ so the small nonlinearity in the power scaling gives a huge increase in radiation power compared to the spontaneous emission case where $P \propto N$. After this point the dispersion continues as before, but now the positive and negative energy offset electrons move past each other and the bunching decreases which damps the radiation emission.

3.3.2. Output Properties of the SASE FEL

This section summarises the main properties of high-gain FELs in the standard Self-Amplified Spontaneous Emission (SASE) [55] operating mode. This is the mode of operation for the CompactLight baseline configuration.

3.3.2.1. Temporal Structure

As described above, the electron bunch emits spontaneous emission at the start of the undulator which is amplified exponentially by the FEL mechanism. The temporal profile of the initial spontaneous emission is noisy, because the electrons entering the undulator are randomly distributed so each electron emits radiation at a different phase. The further evolution of the radiation pulse temporal profile is then dependent on the relative slippage between radiation and electrons. At saturation the radiation pulse comprises a random superposition of many spikes with uncorrelated phases [56]. The maximum

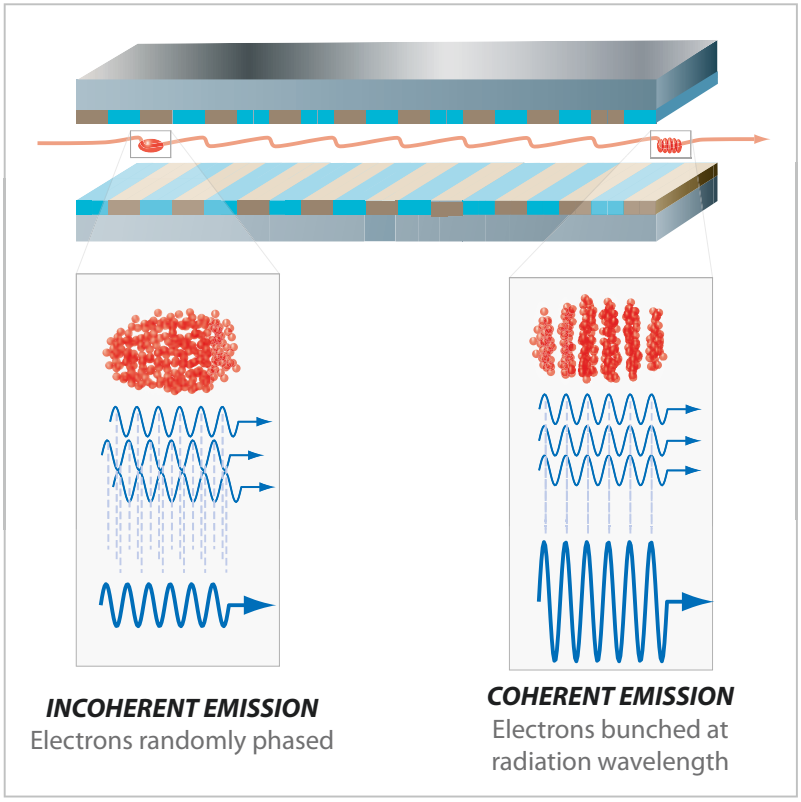

Figure 3.3.: Simple schematic of the FEL mechanism, showing the incoherent emission from the randomly phased electrons as they enter the undulator which develops into coherent emission from the microbunched electrons at the end of the undulator.

peak-to-peak distance between spikes is $2\pi l_c$ where the co-operation length is defined

$$l_c = \frac{\lambda_r}{4\pi\rho}. \tag{3.3}$$

Here ρ is the fundamental dimensionless FEL parameter [55], or Pierce parameter. This parameter expresses the strength of the coupling between the electrons and the radiation in the FEL mechanism and is very useful for predicting the output performance, as well as the required tolerances for many system parameters. It typically takes values $\approx 10^{-4} - 10^{-3}$ for SXR-HXR FELs. The FEL parameter is defined using a collection of system parameters and fundamental constants and can be expressed as

$$\rho = \frac{1}{\gamma_r}\left(\frac{\bar{a}_w \omega_p}{4ck_w}\right)^{\frac{2}{3}} \tag{3.4}$$

where

$$\omega_p = \left(\frac{e^2 n_p}{\varepsilon_0 m}\right)^{\frac{1}{2}} \tag{3.5}$$

is the plasma frequency for peak electron number density of the electron bunch n_p.

The physical interpretation of the cooperation length l_c is that it is the slippage between electrons and radiation over the so called 'nominal' gain length

$$l_g = \frac{\lambda_w}{4\pi\rho} \tag{3.6}$$

where l_g is related to the e-folding power gain length L_g as $l_g = \sqrt{3}L_g$. The co-operation length therefore defines the scale at which collective effects evolve throughout the electron beam. For a sufficiently long electron beam, different regions along the beam develop from the localised noise source autonomously and are therefore uncorrelated in phase. In this sense, the SASE process can be considered as a 'localised' collective process. Typically, in the X-ray region the electron bunch length $l_b \gg 2\pi l_c$, so there are many random spikes in the radiation pulse which has a total length similar to that of the electron bunch.

The co-operation length also then parameterises the SASE radiation coherence. The coherence time is [57]

$$\tau_{\text{coh}} \simeq \frac{1}{\rho\omega}\sqrt{\frac{\pi \ln N_c}{18}} \tag{3.7}$$

where $N_c = I/(e\rho\omega)$ with I the electron bunch current. This can be simplified using (3.3) and by noting that for typical X-ray FELs the square root term evaluates to $\simeq 1.6$ to show that the coherence length is typically about 3 co-operation lengths, $l_{coh} \simeq 3l_c$, or half the peak-to-peak spacing of the SASE spikes.

The features of a typical SASE pulse are illustrated in Figure 3.4, which shows simulation results for a high-gain SASE FEL with parameters similar to FLASH [1]. Figure 3.4 (a) shows the intensity profile comprising multiple random spikes. Figure 3.4 (b) shows the radiation phase, colour-coded to indicate the associated radiation intensity. The phase is seen to vary randomly from spike to spike but is almost constant within each spike showing that individual spikes have good temporal coherence. Figure 3.4 (c) shows the electron bunch current profile. In the simulation the current is averaged over slices one wavelength long so this shows that even if the electron bunch is perfectly smooth over this scale the output pulse will be noisy due to the shot noise at sub-wavelength scales. Finally Figure 3.4 (d) shows the spectrum of the output pulse which also comprises multiple random spikes.

3.3.2.2. Bandwidth

The pulse shown in Figure 3.4 is just one example of a typical SASE output pulse. In practice each pulse has a different arrangement of spikes, temporally and spectrally, due to the start up from noisy spontaneous emission. It is important to note that although the number of temporal spikes is approximately the same as the number of spectral spikes, there is not a one-to-one correspondence between them. Each temporal spike does not have a distinct wavelength but has the full bandwidth of the envelope which is the gain bandwidth of the FEL system. This can be seen clearly in Figure 3.5 which shows a windowed Fourier transform of the simulated FEL pulse in Figure 3.4 (a).

The gain bandwidth can be derived analytically. The result obtained is that the relative rms bandwidth narrows with distance z travelled through the undulator as $\sigma_\lambda \simeq 2\rho(\pi l_g/z)^{1/2}$. The FEL approaches saturation at $z \gtrsim 10l_g$ so the relative rms bandwidth of the saturated output is

$$\sigma_\lambda \simeq \rho. \tag{3.8}$$

3.3.2.3. Power, Pulse Energy, and Flux

As the electron bunch travels through the undulator its kinetic energy is converted into the energy of the radiation field. At saturation the mean relative electron energy loss is $(|\langle\gamma\rangle - \gamma_r|)/\gamma_r \approx \rho$ thus ρ is a fundamental indicator of FEL performance—it represents the efficiency of the conversion of electron beam power to radiation power. The peak radiation power at saturation is therefore given by

$$P_{\text{rad}} \approx \rho P_{\text{beam}} = \rho I_{\text{peak}}[\text{A}]E[\text{eV}] \tag{3.9}$$

where P_{beam}, I_{peak} and E are the electron beam peak power, peak current, and energy respectively. Typically for short-wavelength high-gain FELs, with ρ in the range 10^{-4} to 10^{-3}, the electron beam

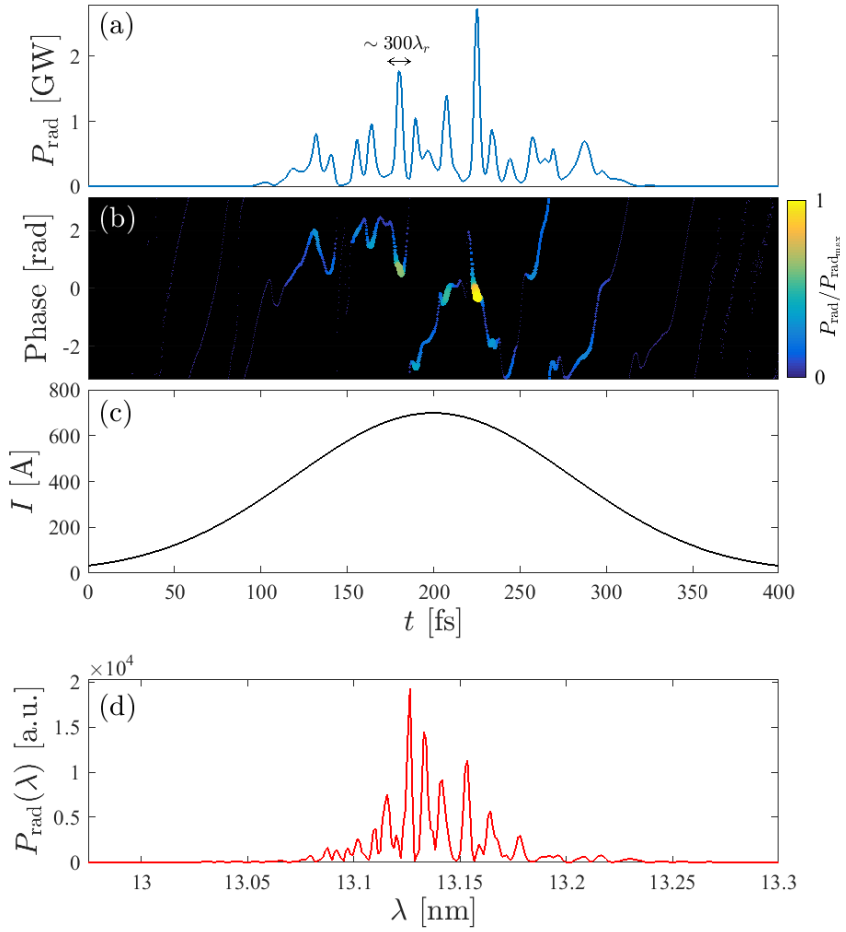

Figure 3.4.: Example SASE properties. The plots show simulation results for a high-gain SASE FEL with parameters similar to FLASH [1], results are shown at saturation: (a) radiation temporal profile consisting of multiple spikes, (b) radiation phase showing phase correlation within but not between spikes, (c) the idealised Gaussian current profile used in the simulation and (d) the radiation spectrum, also consisting of multiple spikes.

energy is in the tens of GeV and the peak current is a few kA, so FEL peak output power is in the tens of GW.

The pulse energy is the instantaneous power integrated over the pulse duration. With peak powers in the tens of GW and pulse durations 10-100 fs the pulse energy is typically 100 μJ to a few mJ. The number of photons per pulse is the pulse energy divided by the photon energy, typically 5×10^{10} to 5×10^{11}. Higher harmonics are also present in the FEL output, with intensity less than a few percent of the fundamental [58]. FEL facilities also produce spontaneous undulator radiation, the power of which can be on the order of the FEL power for hard X-ray FELs [59]. Nevertheless, the FEL radiation is many orders of magnitude brighter than this because it has narrower angular and spectral distributions.

3.3.2.4. Transverse Coherence

The radiation emission over the first few gain lengths of the FEL process has significant higher order mode content but because the growth of the field is driven most strongly on-axis this favours coupling to the fundamental Gaussian mode – higher order modes are wider or even have a minimum on axis and are therefore driven less strongly [53]. By the time the FEL is close to saturation the fundamental mode strongly dominates and the output beam is close to diffraction limited [60–62]. Beyond saturation the transverse coherence starts to degrade due to the growth in higher order transverse modes.

3.3.2.5. Brightness

As discussed, a FEL produces pulses of high peak power, narrow bandwidth and near-diffraction limited transverse coherence. This means it is possible to focus an intense flux of near-monochromatic photons onto a small area, making the X-ray FEL an extremely useful scientific tool. The flux, bandwidth and transverse coherence are collectively quantified by the spectral brightness, defined as

$$B = \frac{\Phi}{4\pi^2 \Sigma_x \Sigma_{\theta x} \Sigma_y \Sigma_{\theta y}} \tag{3.10}$$

where Φ is the spectral flux, the number of photons per second divided by the relative bandwidth and Σ represents a quadrature sum of the photon beam and electron beam rms beam sizes or divergences. Under the assumption that the FEL output is close to diffraction limited and that the FEL undulator is very long this simplifies to

$$B = \frac{4\Phi}{\lambda^2} \tag{3.11}$$

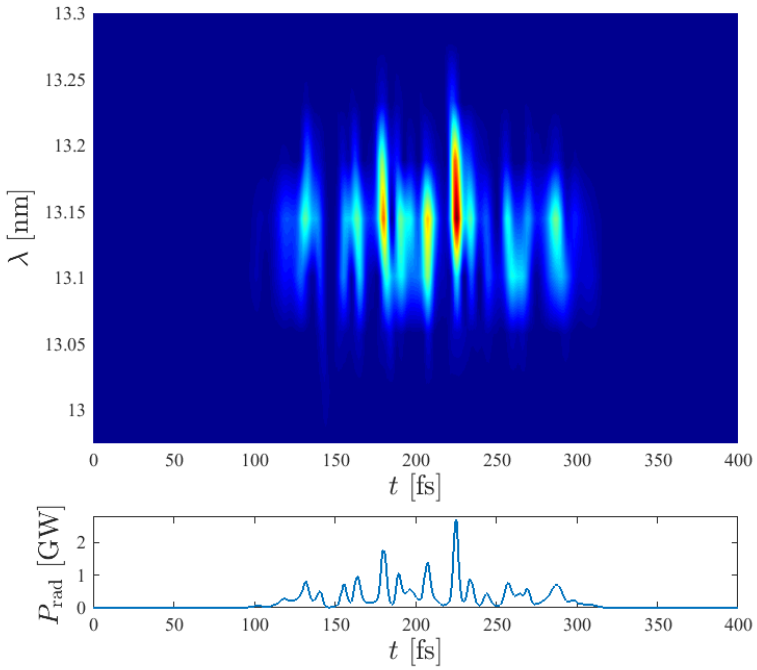

Figure 3.5.: Time-frequency plot of the simulated SASE FEL pulse shown in Figure 3.4 (a). The top panel shows a windowed Fourier transform of the output pulse and the bottom panel shows the intensity profile. Each temporal spike is seen to have the full gain bandwidth.

then using that the relative bandwidth $\sigma_\lambda \simeq \rho$ the expression for peak spectral brightness, in units of photons/s/mm^2/mrad^2/0.1% BW, becomes

$$B \simeq 8 \times 10^9 \frac{P}{\rho\lambda}. \tag{3.12}$$

For $P_{\text{rad}} \simeq 10$ GW, $\rho \simeq 10^{-3}$ and $\lambda = 0.1$ nm, this gives $B \simeq 8 \times 10^{32}$ photons/s/mm^2/mrad^2/0.1% BW, exceeding that available from storage ring sources by at least eight orders of magnitude.

3.3.3. Requirement for a High-Brightness Electron Beam

The FEL interaction requires a small initial energy spread in the electron beam. The reason for this is because, as described earlier, there is longitudinal dispersion in the undulator. This is required for the microbunching to develop from the energy modulation—without it the FEL would not work. However, if the incoming beam has an initial uncorrelated energy spread then this translates via dispersion to a longitudinal smearing of the microbunching which dampens the FEL interaction. A full analysis shows that the initial relative energy spread of the electron beam should be less than the FEL-induced modulation, which increases to ρ at saturation [59], leading to the criterion

$$\frac{\sigma_E}{E} < 0.5\rho. \tag{3.13}$$

As well as minimising the energy spread it is therefore useful to maximise the FEL parameter ρ. In fact this helps in many other ways—from (3.9) and (3.6), making ρ as large as possible maximises the output power and minimises the gain length (thus minimising the undulator length). It is also found that the allowed relative tolerances on many other system errors, such as undulator field errors, scale with ρ. It is clear therefore that the FEL parameter is fundamental and not just a convenient scaling parameter, and to obtain the best FEL performance, and maintain that performance in the presence of spreads or errors in system parameters, the FEL parameter should be maximised. It is convenient to express ρ as

$$\rho \propto \frac{1}{\gamma}\left(\frac{I_{\text{peak}} a_w^2 \lambda_w^2}{\sigma_b^2}\right)^{\frac{1}{3}} \tag{3.14}$$

where σ_b is the electron beam radius. Together, the parameters γ, a_w and λ_w define the FEL wavelength *via* the resonance condition (3.1) so for a specified FEL wavelength these are not free parameters. The FEL parameter is therefore maximised by *increasing the peak current* and *reducing the transverse beam size*. The beam size scales as the square root of the beam transverse emittance—this is a measure of the electron beam quality and is approximately the product of the beam size and beam divergence

$$\varepsilon_x = \sqrt{\langle x^2\rangle\langle x'^2\rangle - \langle xx'\rangle^2} \tag{3.15}$$

where x is the horizontal offset and $x' = \mathrm{d}x/\mathrm{d}z$ is the angle of the particle trajectory relative to the axes (assuming $\langle x\rangle = \langle x'\rangle = 0$). The vertical emittance, ε_y, is defined equivalently. A small emittance is therefore required to obtain a small beam radius σ_b and to maintain this small radius over a reasonable distance. Minimising the emittance also minimises the spread in angular divergence of the electrons in the bunch, which minimises the spread in path lengths of their trajectories which degrades the microbunching (analogous to the way in which a spread in electron energies also degrades the microbunching through longitudinal dispersion).

It is also found that for the most efficient transverse overlap of the electrons and radiation the transverse phase space of the electron beam must be less than that of the diffraction limited photon beam giving

$$\varepsilon < \frac{\lambda_r}{4\pi}. \tag{3.16}$$

so the requirement on electron beam emittance becomes increasingly stringent at shorter wavelengths.

Taken together, the peak current, energy spread, and transverse emittance can be expressed as the electron beam brightness

$$B_e = \frac{I}{c\sigma_E \gamma^2 \varepsilon^2} \tag{3.17}$$

so a *high brightness beam is necessary* to meet the requirements for high peak current, small energy spread and small transverse emittance [63]. It should be noted however that although a high brightness electron bunch is necessary it is not always sufficient – a bunch must be correctly configured, for example meeting (3.13) and (3.16), to be optimal.

To deliver high brightness beams to the FEL requires a high brightness electron source and a system for accelerating and manipulating the electron bunches to maintain brightness in the presence of degrading effects such as coherent synchrotron radiation (CSR) emission from dipole magnets in the beam transport system, wakefields, and micro-bunching instability. The fact that beams can be delivered with sufficient brightness for X-ray FELs to operate is testament to tremendous developments in numerous areas including low-emittance photoinjectors and CSR compensation and prevention.

3.3.4. Quantification of Beam Quality Effects

From the previous section is is seen that the electron bunch driving the FEL must have high brightness and that to achieve this the bunch must have high peak current, small energy spread and small emittance. The criteria given for energy spread and emittance are, however, *soft* limits. For example if the emittance criterion given by Equation 3.16 is not satisfied, the FEL might still lase but its performance will be suboptimal—the output power might be reduced somewhat from the case of an ideal electron bunch or the transverse mode quality might be degraded. It is therefore necessary to quantify exactly how the FEL performance depends on these beam quality factors.

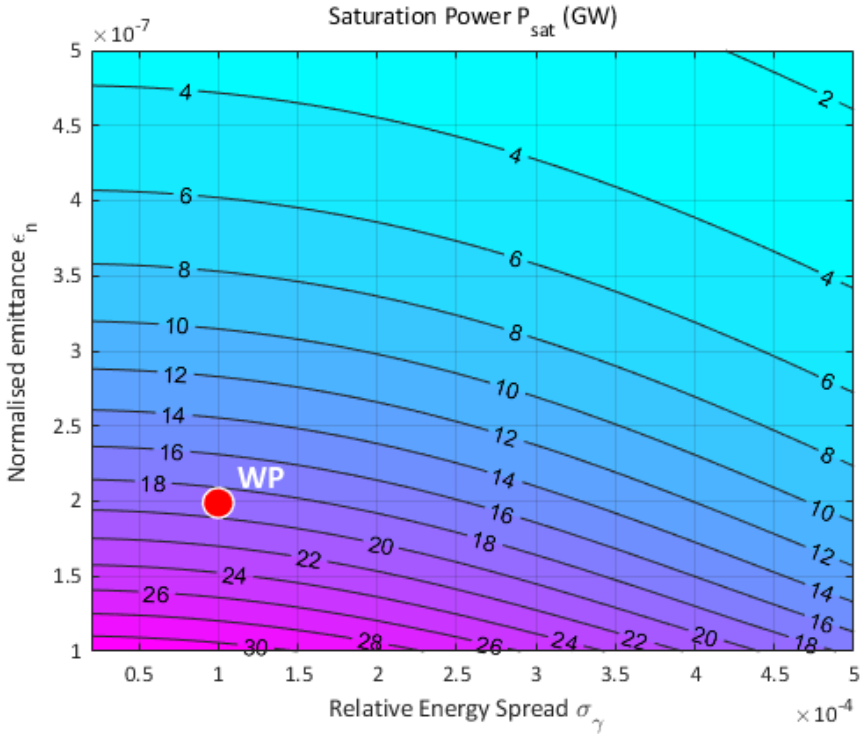

Figure 3.6.: Typical calculations, using the Ming Xie approximation, of the CompactLight FEL saturation power, for 16 keV photon output, as a function of energy spread and normalised emittance. The nominal CompactLight Working Point (WP) is marked.

In addition, the design of the undulator lattice must be optimised for best performance. This involves: determining the most suitable length for the individual modules that comprise the long FEL undulator; understanding the effect of diffraction and electron beam transport in the gaps between the modules; calculating the effect on the FEL performance of resistive wall wakefields; determining allowed tolerances for undulator misalignments and electron beam trajectory straightness. In the CompactLight design process, from the setting of initial target beam parameters to the assessment of the predicted FEL performance using a simulated bunch that has been tracked through the whole accelerator, two main approaches have been adopted.

3.3.4.1. The Ming Xie Semi-Analytical Approximation

The Ming Xie semi-analytical approximation [64, 65] is based on the basic performance formulae given above, for example those for power output and FEL gain length, but includes adjustment factors that quantify the effects of energy spread and emittance. These adjustment factors are derived from multidimensional fits to sets of FEL simulations. The approximation allows rapid estimates of FEL performance. An example is given in Figure 3.6 which shows typical calculations of the CompactLight FEL saturation power, for 16 keV photon output, as a function of energy spread and normalised emittance. The nominal chosen Working Point (WP) is marked. As can be seen, the FEL performance at 16 keV is strongly dependent on the electron beam quality.

3.3.4.2. FEL Simulation Codes

The Ming Xie approach assumes long uniform perfect undulators with electron bunches that have constant longitudinal parameters (for example current, emittance, beam size and energy spread). To include realistic bunch distributions and undulator lattices it is necessary to use FEL simulation codes. CompactLight Deliverable 6.1 presented a summary and comparison of some available codes. The FEL code used most extensively in the CompactLight design process was Genesis1.3 [66, 67]. This code is well supported, has the most functionality and flexibility, and produces reliable results which have been benchmarked against operating FELs on many occasions.

4. Systems Design and Performance

4.1. Facility Overview

4.1.1. Key Features

As discussed in Section 3.1.4 the user requirements for CompactLight were established by interacting with existing and potential FEL users in a variety of formats. The user input was distilled into a comprehensive photon output specification, summarised in Table 3.1. The facility has been designed specifically to satisfy this specification. A Baseline configuration satisfies the majority of the user case, and two upgrades fully satisfy the user requirements.

4.1.1.1. Baseline Configuration

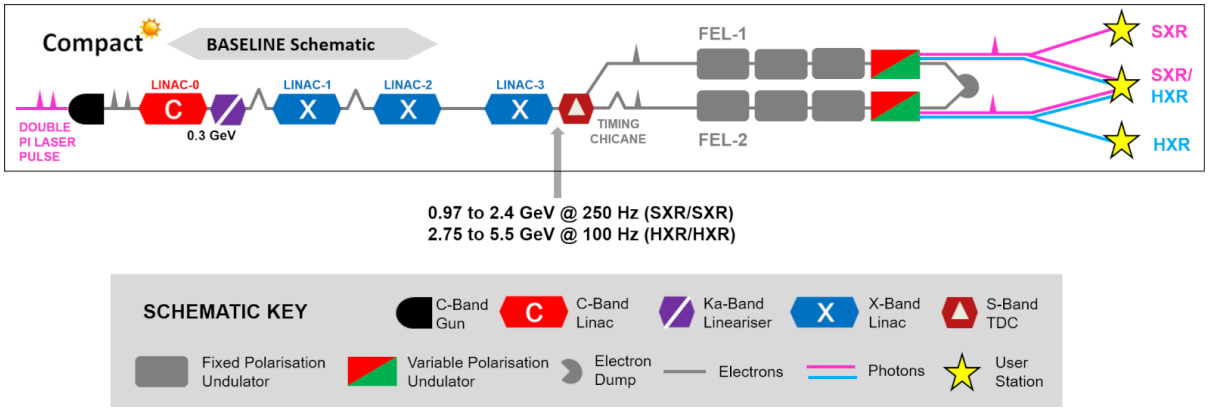

Figure 4.1.: CompactLight Baseline schematic layout.

Figure 4.1 shows the Baseline layout. The unique features and technical innovations of the Baseline are:

- **C-band RF gun and injector** with dual repetition rate and velocity bunching capabilities.
- **Compact X-band linacs** for high gradient acceleration and reduced footprint.
- **Low beam energy of 5.5 GeV** compared to existing facilities with comparable or **higher photon energy reach**.
- **Short-period in-vacuum superconducting undulators** with helical polarisation for minimisation of FEL saturation length and electron beam energy, with associated **Cryomodule structure and cooling concepts**.
- **Dual wavelength regimes using the same undulators**—soft X-rays over the range 0.25–2 keV from a low energy (0.95–2.4 GeV) electron beam, and hard X-rays over the range 2–16 keV from a high energy (2.75–5.5 GeV) electron beam.
- **Dual-mode linac** to drive the SXR FEL at 250 Hz and the HXR FEL at 100 Hz.
- **K-band 36 GHz lineariser cavity** for optimisation of electron bunch longitudinal phase space
- **K-band 36 GHz power source designs** including **multi-beam klystron** and **gyroklystron**.

- **Double FEL concept** enabling the simultaneous operation of two SASE FEL lines which can drive either FEL-pump FEL-probe experiments at a single end-station, or independent experiments at two different end-stations.
- **Sub-harmonic bunch separator** for splitting twin bunches into the twin FELs.
- **Controllable spectral separation of the twin pulses** in soft X-ray and hard X-ray by independent tuning of the two identical undulator lines.
- **Controllable temporal separation of the twin FEL pulses** at the end-station, from perfect synchronization to $\pm$100 fs.
- **Apple-X** afterburner undulators, including **solutions for magnetic force compensation**, for independent selectable polarisation of the twin FEL pulses and fast helicity switching at a single end-station.
- **Full polarisation control** from 0.25–12keV and selectable L/R circular polarisation from 12–16 keV.

4.1.1.2. Upgrade Configurations

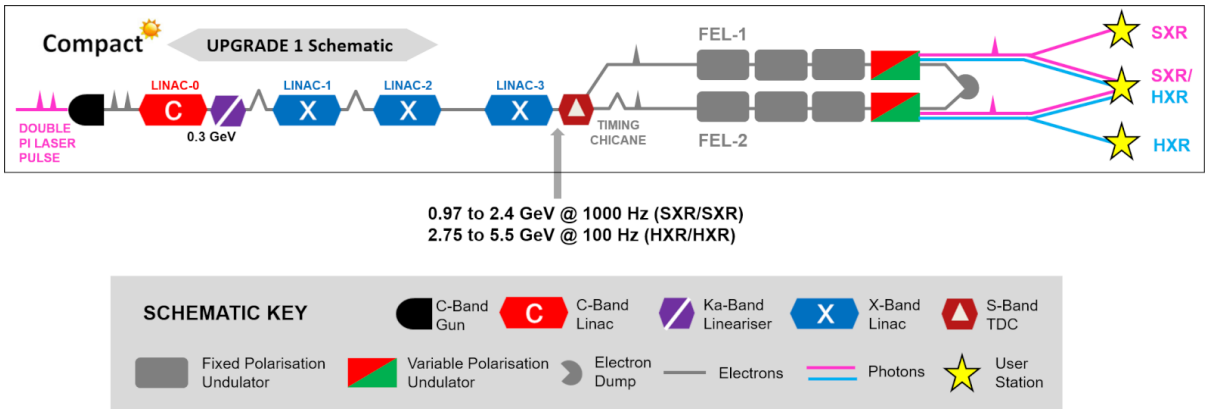

Figure 4.2.: CompactLight Upgrade-1 layout.

Further to the baseline design, two upgrade scenarios have been designed which add additional capability, in particular, higher repetition rates, improved FEL coherence and HXR/SXR or SXR/HXR FEL-pump FEL-probe capability. Taken together, the baseline and upgrades fully satisfy the user requirements. The schematic layouts of the two upgrades are shown in Figure 4.2 and Figure 4.3. The Unique features and innovations of Upgrade-1 are:

- **1 kHz repetition rate in SXR** by upgrading the linac to **dual-source** which adds additional klystron power while keeping the average RF power in the structures constant, and triggering **industrial development**.

Upgrade-2 adds three additional features beyond Upgrade-1:

- **Soft X-ray self-seeding** using a grating monochromator to provide fully coherent soft x-ray FEL output.
- **Hard X-ray Self-seeding** using a diamond crystal wake monochromator to provide much-improved longitudinal coherence in the HXR, compared to SASE.

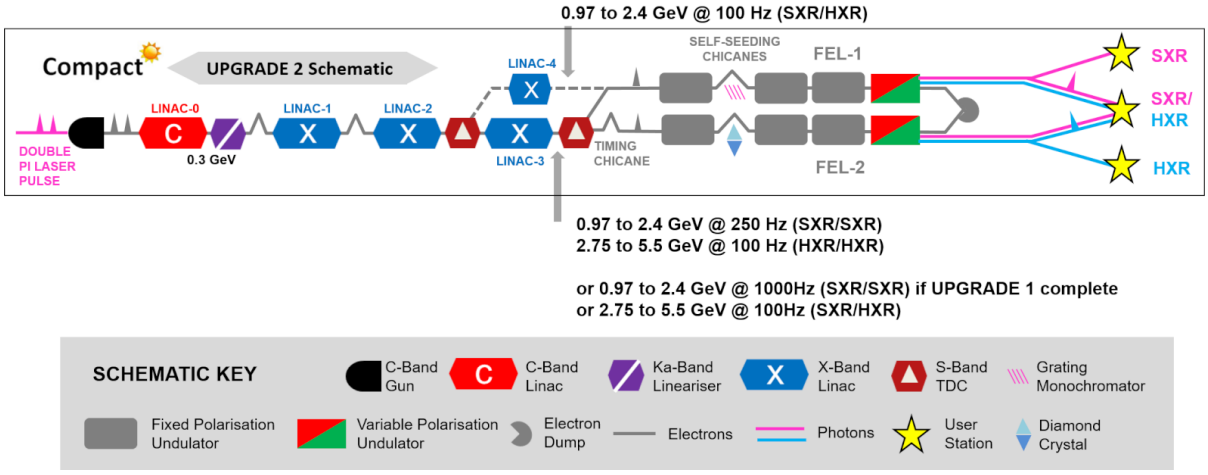

Figure 4.3.: CompactLight Upgrade 2 layout.

- **SXR/HXR FEL-pump FEL-probe capability with controllable delay of $\pm$100 fs** by the addition of a SXR bypass line containing an additional linac module to allow simultaneous soft and hard x-ray pulses at 100 Hz, with independent tuning of wavelength and polarisation. These can be used in independent experiments at two separate end stations or combined in a single end station.

Full details of Upgrade-1 are given in Section 5.2. Simulation studies of the SXR and HXR self-seeding modes of Upgrade-2 are presented in Section 4.2.4.

4.1.2. Operating Modes

The operating modes for the Baseline design and Upgrade configurations are summarised in Table 4.1. For all operating modes FEL-1 and FEL-2 can be sent to separate user stations **or** sent to the same user station with $\pm$100 fs separation.

OPERATING MODE	FEL-1 Wavelength	FEL-2 Wavelength	L0–L3 Rep. Rate (Hz)	L3 Output Energy (GeV)	L4 Rep. Rate (Hz)	L4 Output Energy (GeV)
			BASELINE			
B-HH	HXR	HXR	100	2.75–5.5	-	-
B-SS	SXR	SXR	250	0.95–2.4	-	-
			UPGRADE-1			
U1-HH	HXR	HXR	100	2.75–5.5	-	-
U1-SS	SXR	SXR	1000	0.95–2.4	-	-
			UPGRADE-2			
U2-SH	SXR	HXR	100	2.75–5.5	100	0.95–2.4

Table 4.1.: Operating Modes.

4.1.3. Layout Description

The total length of the facility, including the building, is 483 m. By comparison, SwissFEL is 740m. Figure 4.4 shows an ISO view. This section summarises the layouts and main features of the different parts of the facility. Full details and parameters are given in Chapter 5.

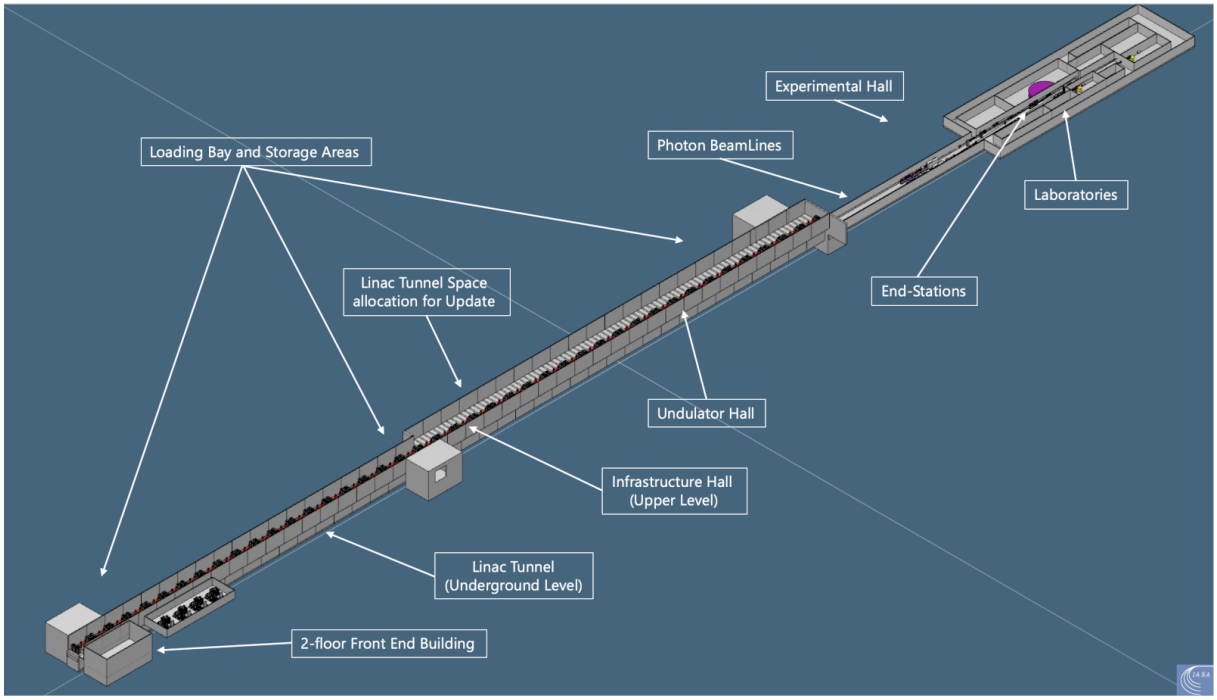

Figure 4.4.: ISO View of the XLS facility. The total length is 483 m.

4.1.3.1. Injector

CompactLight uses a normal conducting 2.5 cell C-Band photo-cathode RF gun with 160 MV/m field on the copper cathode. Space for a laser heater, to minimize the impact of micro-bunching instability on the FEL performance, is allocated. The following C-Band linac structures have gradient 15 MV/m and accelerate the beam to 300 MeV where there is a short Ka-band lineariser cavity with maximum peak accelerating voltage of 17 MV. After the lineariser is the first bunch compressor (BC1) and a small X-Band diagnostic deflector. For full details see Section 5.1

4.1.3.2. Main Linac

A two-stage magnetic compression scheme is adopted in the main linac, in addition to optional velocity bunching implemented in the injector. The main linac comprises X-band accelerating structures. The maximum beam energy is 5.5 GeV. This was chosen as it is lower than comparable facilities such as SwissFEL yet in combination with advanced short-period undulators allows a photon energy reach up to 16 keV which exceeds the highest photon energies available from SwissFEL.

The magnetic lattice of the main linac is based on a FODO cell interleaved by low-β_x insertions for the magnetic compressors. The linac fill factor is > 70% in all sections. The total linac length from cathode to exit of Linac-3 (HXR beam line) is less than 190 m, and includes 104 X-band accelerating structures in total.

The main linac is powered by standardised RF units based on the CLIC technology, which can be used in all the main and sub-design variants. The RF unit will include klystron, RF compressor and waveguide components. This choice greatly simplifies the industrialisation process, with a considerable reduction in production costs. For full details of the linac design and configuration see Section 5.2 and for details of the beam dynamics see Section 5.3.3.

4.1.3.3. Bunch Compressors

The magnetic bunch compressors are symmetric 4-dipole chicanes with beam diagnostics in the inner drift region. Small quadrupole magnets in the outer branches of the chicane are used for tweaking of residual dispersion. The local compression factors are ≈9 at BC1 and ≈5 at BC2, for a maximum total compression factor of 100 when operating the injector in velocity bunching mode. For full details see Section 5.3.3.2.

4.1.3.4. RF Distribution System Layout

The baseline configuration of the layout runs in *dual mode* where a single RF source supplies the linac in two operating modes, at 100 Hz and 250 Hz. This is the cheapest solution but limited in repetition rate to 250 Hz. The peak accelerating gradient is 65 MV/m at 100 Hz and 32 MV/m at 250 Hz with magnet strengths scaled depending on gradient to obtain the same optical functions along the linac. An X-band SLED is adopted at 100 Hz, and is bypassed at 250 Hz. Upgrade-1 and Upgrade-2 operate in *dual source mode*—here an additional klystron is connected to the RF module so two RF sources supply the linac at repetition rate 100 Hz and 1 kHz. The RF distribution connects 2 klystrons to 4 accelerating structures. These form one accelerating module of 3.6 m active length. For full details see Section 5.2.2.2.

4.1.3.5. Twin bunch system

The photoinjector laser is split into two pulses separated by 3 or 5 RF cycles of the C-band gun so the temporal spacing is either 500 ps or 833 ps. The two pulses generate identical electron bunches which have the same RF accelerating phase. The time separation corresponds to 6 or 10 RF cycles in the X-band linac. The separation of 500 ps is the minimum at which beam break up instability of the trailing bunch is kept well under control, with a projected emittance growth at the linac end below 10%. The twin bunches follow identical dynamics in the accelerator. In the Baseline and Upgrade-1 configuration, they will be separated in the horizontal plane after the linac by an S-band transverse deflecting cavity. The bunch separations correspond to a half-integer number of RF cycles of the deflecting cavity so the twin bunches will be horizontally deflected by kicks with opposite sign. About 30 MV peak deflecting voltage at the maximum beam energy of 5.5 GeV will impose angular kicks of the order of half a degree, and will allow the two bunches to be separated by ≈5 mm after a 0.5 m-long drift section. Here a DC out-of-vacuum thin septum magnet directs the leading bunch to FEL-1, and the trailing bunch to FEL-2. A schematic of this beam manipulation, showing how the twin bunches sit within the RF buckets at the three different RF frequencies, for a bunch spacing of 500 ps, is shown in Figure 4.5.

Pump-probe experiments typically require a continuous scan of the relative delay of the pump and the probe pulse by at least a few ps around synchronization. The leading bunch directed to FEL-1 has therefore to be delayed with respect to the trailing bunch. The delay required so that the pulses from the twin FELs can be synchronised at the dual end-stations for pump-probe experiments, with allowance made for the optical path lengths of the photon beamlines, is 526ps. This is accomplished by a dog-leg-like switchyard from the septum to FEL-1. The FEL undulator lines are then laterally separated by ≈2.5 m. Fine tuning of the pump-probe relative delay is done by a small 4-dipole chicane in front of the FEL-2 line and by a split-and-delay-line on the photon beam path towards the end-stations. Upgrade-2 allows the simultaneous generation of SXR and HXR FEL pulses at 100 Hz. In this case, the splitting system and dog leg are replicated at the end of Linac-2, so bringing the leading bunch to FEL-1 for SXR emission. Only the trailing bunch reaches the end of Linac3 for HXR production. The full twin bunch system is shown in Figure 4.6 which shows the spacings of the twin bunches in the linacs, the required delay in the spreaders, and the path length variations in the optical beamlines. For full details of the twin bunch system see Section 5.3.3.4.

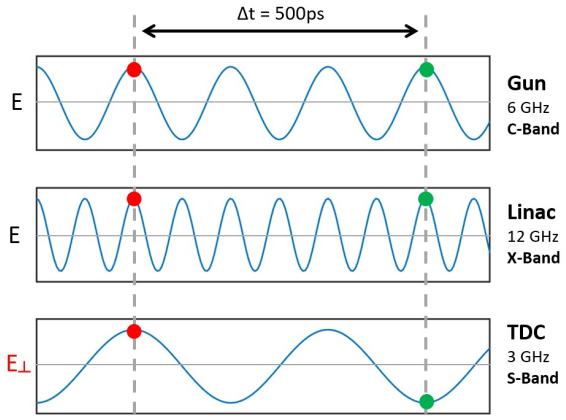

Figure 4.5.: Schematic showing how the twin bunches, separated here by 500 ps, are spaced by 3 RF cycles in the C-Band RF gun, 6 cycles in the X-Band linac, and 1.5 cycles in the S-Band Transverse Deflecting Cavity where they are deflected in opposite directions. The deflector is followed by a DC thin septum magnet.

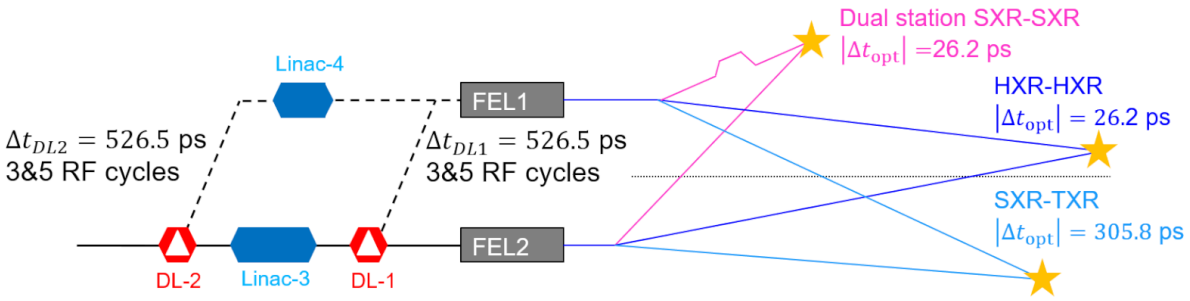

Figure 4.6.: Schematic layout of the accelerator with full upgrade, two doglegs (DL-1) and (DL-2), two undulators, and three dual endstations. The relative optical delays are indicated.

4.1.3.6. Undulator Lattice

The main undulators are 1.75m long in-vacuum helical superconducting undulators (SCUs) with period 13 mm. This undulator technology was chosen after a thorough comparative assessment of a broad range of options, reported in detail in deliverable D5.2 and summarised in Section 6.1.1. In order to cover the required wavelength range of the facility, the choice of undulator technology was made in combination with the aim of keeping the electron beam energy lower than comparable facilities. The optimisation of the undulator period and module length is detailed in Section 6.1.2. The period was optimised to obtain balanced performance across the HXR and SXR wavelength ranges which both use the same undulator beamlines. The undulator modules are separated by gaps of 0.5 m containing a quadrupole, a phase shifter and a beam position monitor. There are two identical parallel undulator beamlines with axis separation of 2.5 m. The SCUs for FEL-1 and FEL-2 have opposite helicity to allow for fast L-R polarisation switching experiments when the pulses from the two FELs are combined at a dual endstation. After the SCU undulators there are, in each beamline, two variably polarising APPLE-X afterburner undulators for production of variably polarising FEL output. For details of the undulator design and optimisation see Section 6.1.

4.1.3.7. Photon Beamlines and End Stations.

The photon transport system starts with a front-end containing a bremsstrahlung collimator, a photon shutter and a set of photon diagnostics. The front-end is followed by photon beamlines and an experimental area hosting user endstations. The SXR endstations are primarily concentrated on the FEL-1 side whereas the HXR ones are mostly located on the FEL-2 side. The path lengths in the beamlines are set to synchronise pulses from the twin FELs at the dual endstations.

The experimental area comprises 5 X-ray hutches, 2 laser laboratories, 2 control rooms and a technical gallery to access the hutches. The hutches host refocusing optics, photon diagnostics, endstations, local control electronics and data acquisition systems. The optical laser beam can be transported from the laser room, located upstream of the hutches, to incoupling mirrors positioned close to the endstations. The hutches and laser laboratories are surrounded by a technical gallery for easy access. For full details of the photon beamlines see Section 6.2.

4.1.3.8. Building Design and Infrastructure

The CompactLight building, shown in Figure 4.4, comprises a number of different sub-buildings and sections. The design follows a hybrid approach with the underground Linac Tunnel separated from the Infrastructure Hall with shielding blocks. The Linac Tunnel section is 4m wide and the Infrastructure hall is 7m wide and accommodates 50 klystrons, 50 modulators, nearly 300 electronic rack units and the necessary space for the routing of waveguides, pipes and cable trays through direct penetrations to the tunnel. Downstream of Linac-2, the widths of the tunnel and Infrastructure Hall increase to accommodate the SXR bypass line required for Upgrade-2. The Experimental Hall contains the photon beam lines with front-end diagnostics, shielded end-stations, laboratories and auxiliary spaces. Space for a laser laboratory, a magnet laboratory, a loading bay/assembly room and user laboratories has been allocated. For full details see Section 7.1.

4.2. FEL Performance

The performance of CompactLight has been analysed and optimised via detailed simulations of the accelerator and free-electron laser. This section of the report presents the results of this work. The emphasis is on performance in the Hard X-ray regime—here the demands on the electron bunch quality are most stringent. For example, from Equation 3.13 the electron bunch energy spread must be less than the FEL ρ-parameter which reduces as the photon energy increases, and similarly, from Equation 3.16 the beam emittance requirement is more stringent for higher photon energies.

At the start of the project a 'nominal' electron bunch was defined that would enable the FEL to satisfy the output requirements. The parameters of this bunch were determined through semi-analytical FEL performance calculations, initial FEL simulations, considerations of undulator technology options, estimates of emittance and energy spread at the electron source and degradation due to collective effects during beam acceleration and transport to the FEL. This process was iterative, combining input from a range of work packages. The resulting parameters for the nominal electron bunch are shown in Table 4.2. Note that the energy, emittance and energy spread are assumed to be constant along the bunch.

In Section 4.2.1 the performance of the FEL using this nominal bunch is presented via simulations using the code Genesis 1.3 at photon energies from 2 keV to 16 keV. These results give a good indication of the relative FEL performance at different photon energies and confirm that the nominal bunch parameters are satisfactory. Later in the project, once the accelerator design was complete, it was possible to simulate the FEL with a fully tracked electron bunch. Several iterations of accelerator optimisation were performed, with FEL simulations informing the quality of the FEL output. As will be seen, the performance with the final iteration of the tracked bunch exceeds the performance with the nom-

Table 4.2.: Parameters of the nominal electron bunch.

Parameter	Unit	Value
Bunch Profile		Gaussian
Energy	GeV	5.5
Peak Current	kA	5.0
Normalised Emittance	mm-mrad	0.2
RMS Energy Spread	keV	550
Bunch Charge	pC	75

inal bunch. These results are presented in Section 4.2.2 and 4.2.3. In Section 4.2.2 the performance of the FEL with the tracked bunch is compared to that of a 'static error' bunch which is an equivalent tracked bunch but with degraded emittance. The purpose is to check there is sufficient contingency in the design that the FEL can still satisfy the user specification. The FEL operation here is at 16 keV where the degraded emittance is expected to be most detrimental. In Section 4.2.3 dynamic errors are added to the bunch. The performance with the nominal tracked bunch is used as a control and realistic errors are added to the accelerator parameters, for example RF phase and gradient errors, to assess the expected performance and shot-to-shot stability of the FEL output in the presence of these dynamic errors.

In Section 4.2.4 studies are presented of the performance of the SXR and HXR self-seeded schemes introduced in Upgrade-2, using the nominal electron bunch, with the aim of clearly demonstrating the change in performance compared to the SASE operation of the baseline configuration. Finally, in Section 4.2.5 a summary is given of the predicted FEL performance at different wavelengths and in different operating modes. To obtain the best possible predictions of FEL performance at different photon energies the 16 keV results from the fully tracked bunch with dynamic errors are scaled according to the results obtained using the nominal bunch at different photon energies.

4.2.1. SASE FEL Performance with Nominal Electron Bunch

Figure 4.7 show the pulse energy growth, pulse profiles and spectra for HXR FEL operation using the nominal bunch. The pulse profiles and spectra are shown at the relevant saturation points, indicated by the coloured squares on the pulse energy plot. Saturation is taken as the point where the pulse energy growth starts to deviates from exponential. The black curves on the profiles and spectra are gaussian fits, used to determine the averaged peak power and FWHM bandwidth data which are used to calculate the peak brightness. Figure 4.8 summarises the data over the range of pulse energies. The brightness is calculated using Equation 3.11 then normalised to the measured bandwidth[1]. The calculations show that the maximum pulse energy is 225 μJ at 8 keV, but that the minimum bandwidth and maximum brightness occur at 16 keV where the FWHM bandwidth is 0.15% and the peak brightness is 3×10^{33}ph/s/mm^2/mrad^2/0.1%bw.

4.2.2. SASE FEL Performance with Tracked Bunch and Static Error Bunch

The properties of the tracked bunch are shown in Figure 4.9. The normalised slice emittance in both transverse planes is less than 0.15 mm-mrad along the whole bunch—this is significantly smaller than the normalised emittance of 0.2 mm-mrad for the nominal bunch. There is a small longitudinal energy chirp and a 20 μm transverse shear in the horizontal plane. The slice energy spread is approximately 1000 keV, double the value of the nominal bunch. To create a static error bunch the emittance was artificially increased at the laser heater to a value comparable with the average emittance obtained

[1] Calculations of the FEL transverse coherence at 16 keV, quantified via the M^2 parameter, have indicated that typically at saturation $M^2 \approx 1.5$, suggesting that the brightness is overestimated here by about this factor.

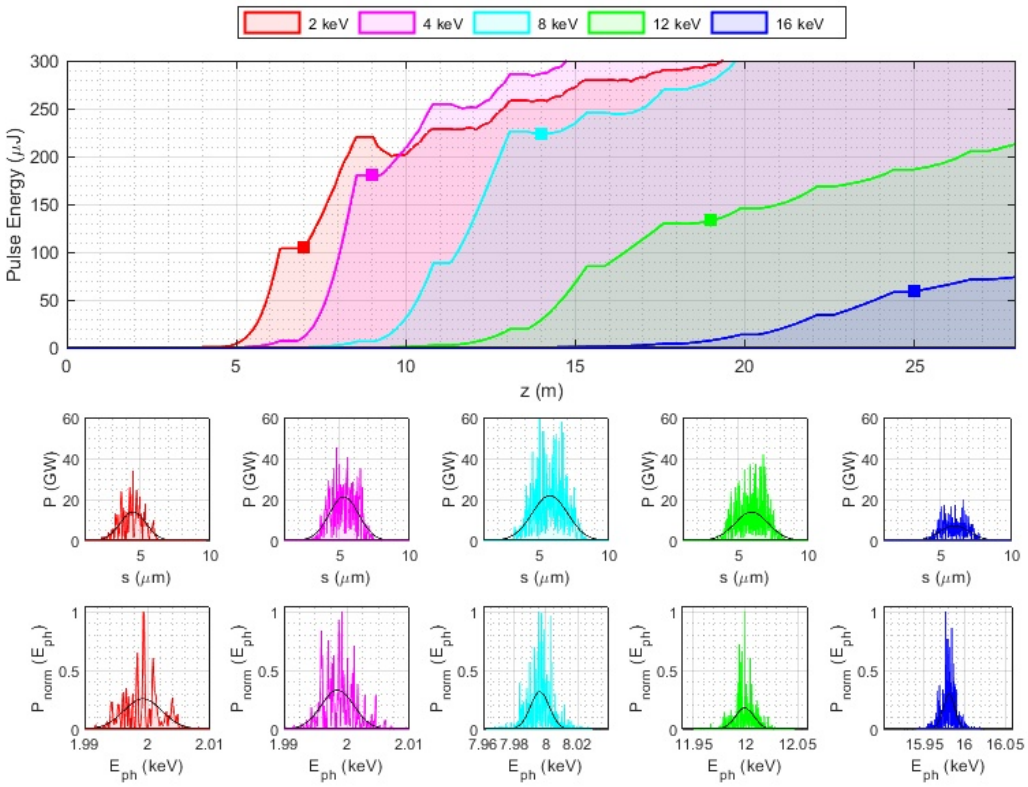

Figure 4.7.: Pulse energy growth, pulse profiles and spectra for HXR FEL operation using the nominal bunch.

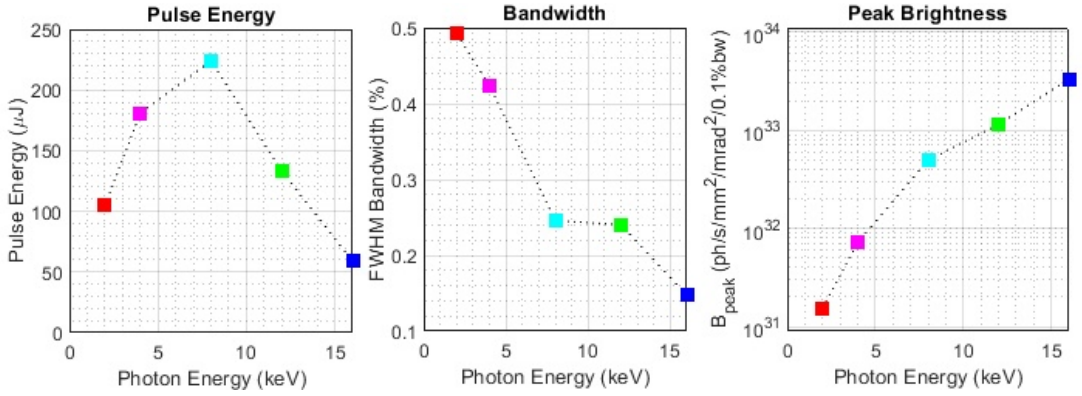

Figure 4.8.: Saturation pulse energy, FWHM bandwidth and peak brightness for HXR FEL operation using the nominal bunch.

at the end of Linac-3 from 100 random seeds of static errors and realistic beam-based alignment. The static error bunch was propagated through the machine with a rematched lattice. At the FEL the normalised emittance is less than 0.2 mm-mrad over all slices, an increase of approximately 0.05 mm-mrad over the tracked bunch. All other slice properties are unchanged.

Figure 4.10 shows a comparison of FEL performance between the tracked bunch and the static error bunch. The highest peak brightness obtained for the tracked bunch is 8.9×10^{33}ph/s/mm^2/mrad^2/0.1% bandwidth at 22.0 m along the undulator axis. Here the brightness is calculated directly from Equation 3.10 with the electron and photon beam sizes and divergences derived directly from the simulation results. At this distance, the FEL bandwidth is 0.076%. The pulse energy at highest peak brightness is

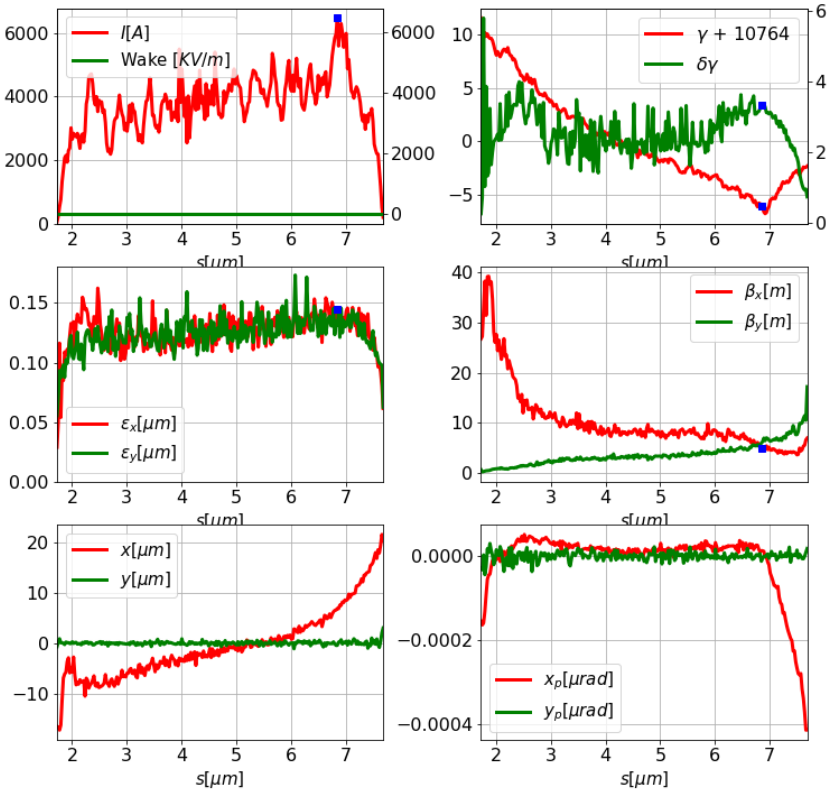

Figure 4.9.: Slice properties of the tracked bunch used for the S2E simulation.

116 μJ. The error bunch generates a pulse for which the brightness saturates later, at about 31 m, and has narrower bandwidth and reduced pulse energy. The highest peak brightness for the pulse generated by the static error bunch is 3.52 $\times 10^{33}$ph/s/mm^2/mrad^2/0.1%bw which is about 40% the value of the highest peak brightness for the tracked bunch. Clearly the performance of the static error bunch is not as good as for the tracked bunch. However it should be noted that:

- although the saturation length is slightly longer than for the tracked bunch it is still comfortably within the 36 m length of undulator included in the design;
- the brightness comfortably exceeds the user minimum requirement of 10^{33}ph/s/mm^2/mrad^2/0.1% bandwidth.

This demonstrates that sufficient contingency has been built into the accelerator design to account for a degraded emittance.

To help understand the dependence of the FEL performance on a wider range of emittance values, a set of simulations were done in which the transverse phase space of the tracked bunch, as it enters the undulator, was artificially expanded, by multiplying the x, y, x' and y' values for each electron by scaling factors. The results are shown in Figure 4.11. The left hand plot shows the peak brightness and the right hand plot shows the saturation length. The tracked bunch working point is at the bottom left corner of each plot. The dotted line in the saturation length plot is the 36 m contour which is shown because this is the length of the CompactLight undulator. The results confirm that there is an acceptable level of contingency in the design to cope with a reasonable increase in emittance over the nominal values.

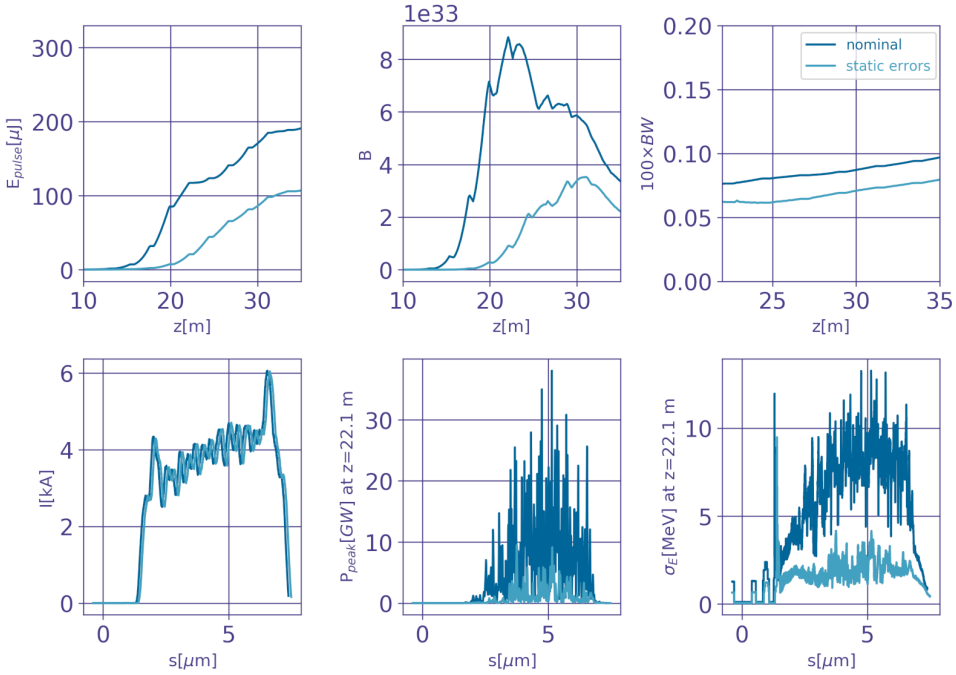

Figure 4.10.: Comparison of 16 keV FEL pulse energies (top left), FEL pulse peak brightness (top centre), pulse bandwidth (top right) as a function of distance along the undulator axis, and current profiles (bottom left), peak FEL power (bottom centre) and energy spread (bottom right) along the bunch for the tracked bunch (dark blue) and the static error bunch (light blue).

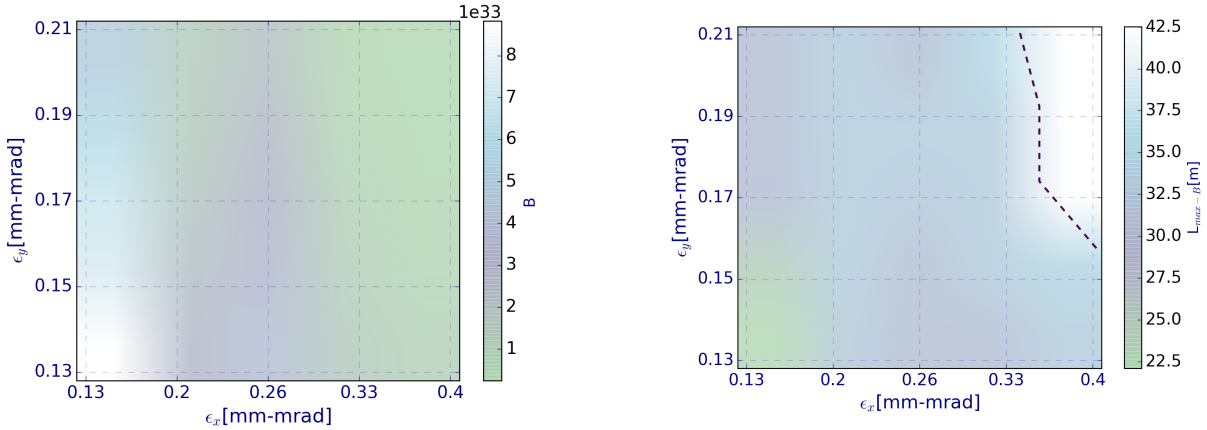

Figure 4.11.: Contour plots of FEL peak brightness (left hand side) and saturation length (right hand side) for the tracked bunch with artificially increased emittances. The dotted line on the right hand side plot corresponds to a saturation length of 36 m which is the undulator length specified in the design.

4.2.3. SASE FEL Performance with Dynamic Error Bunches

Table 4.3 shows the distribution of errors applied to the accelerator parameters to generate the dynamic error bunches. Figures 4.12, 4.13 and 4.14 summarise the results of the FEL simulations. Figure 4.12 compares the relative RMS variation of the pulse energy and peak brightness along the undulator. Each tracked bunch simulation has a different shot noise seed so that the stability of the output due to the intrinsic SASE noise can be seen. The dynamic error bunches also have different shot

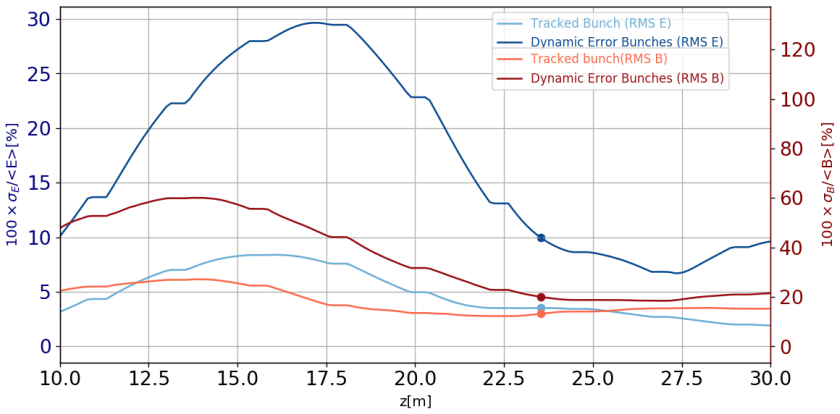

Figure 4.12.: Comparison of RMS of the pulse energies and peak brightness distributions obtained from the dynamic errors bunches and tracked bunch along the undulator.

noise seeds so the stability depends both on the intrinsic SASE noise and the errors in the accelerator parameters—these results are therefore a good indication of the predicted FEL stability as experienced by the users.

Table 4.3.: The RMS errors applied to the accelerator parameters to produce the dynamic error bunches. For the RF cavities the same error was applied to all the cavities within an RF module. The errors between modules were uncorrelated.

Parameter	**Unit**	**Value**
Charge	%	2
C-band cavity gradient	%	0.04
X-band cavity gradient	%	0.04
C-band phase	°	0.05
X-band phase	°	0.05
Gun timing	fs	25

The user requirement stated in Section 3.2 is that the RMS stability of the FEL pulse energy should be less than 10%. This value is achieved at z=23.5 m, just over 1 m further than the distance at which the highest peak brightness is reached, but at this position the peak brightness is still very close to maximum and the pulse energy is still increasing. This distance is therefore chosen as the 'point of comparison'. The distributions of pulse energies and peak brightness at the point of comparison for the tracked bunches and the dynamic error bunches are shown in Figure 4.13.

Figure 4.14 shows the evolution of pulse energy and peak brightness along the undulator. The results for the tracked bunch are shown in blue—the average over 200 SASE shot noise realisations is shown in dark blue, with the individual simulations in light blue. The results for the dynamic error bunches are shown in green—the average over 200 bunches is shown in dark green and the individual simulations in light green.

The highest peak brightness for the tracked bunch, when averaged over noise realisations, is 9.23×10^{33} ph/s/mm^2/mrad^2/0.1%bw. However at the point of comparison it has reduced slightly to 8.3×10^{33} ph/s/mm^2/mrad^2/0.1%bw. The saturation length for the dynamic error bunches is slightly longer than for tracked bunches, but the distance at which the highest peak brightness is reached is unchanged. At the point of comparison the average peak brightness is 7.9×10^{33} ph/s/mm^2/mrad^2/0.1%bw—around 5% lower than for the tracked bunches. The average pulse energy for the dynamic error bunches at the

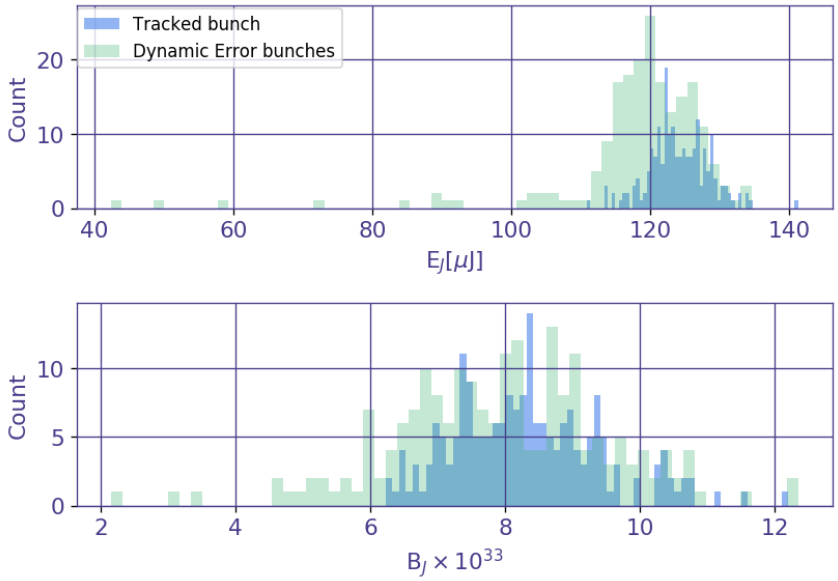

Figure 4.13.: Histograms of pulse energy (top) and peak brightness (bottom) for 200 tracked bunches with SASE shot noise and 200 dynamic error bunches.

point of comparison is 118μJ, 5% less than for tracked bunch.

It is therefore seen that the inclusion of dynamic errors in the bunch distributions causes a small decrease in averaged peak brightness and pulse energy, and does increase the fluctuations in the FEL output. However, the user requirements that RMS fluctuations in pulse energy should be less than 10% and that the peak brightness should exceed 10^{33} ph/s/mm^2/mrad^2/0.1%bw are both satisfied.

4.2.4. Upgrade-2: Self-Seeding Performance

Upgrade-2 includes self-seeding [68] options for both the HXR and SXR beamlines. The generic method is that the FEL pulse is extracted at some point along the undulator line, before saturation, and filtered to reduce its spectral width, hence increasing its coherence length. The filtered pulse is then used as a seed and injected into the second section of the undulator line to be amplified to saturation. The method used to filter the pulse depends on the wavelength regime. The CompactLight design follows the methods used in existing FEL facilities, both in the SXR [69] and the HXR [70]. In the SXR a compact grating monochromator is used. This replaces an undulator module. In the HXR a diamond crystal is used, with the crystal orientation adjusted such that a notch is taken out of the spectrum at the appropriate photon energy. The output pulse from the crystal then contains a trailing monochromatic wake which is used as the seed pulse. In both cases the electron beam must be diverted in a small chicane around the optical elements, with the path length of the electron bunch set so that it overlaps with the seed pulse in the second undulator section. The chicane has another useful function—the longitudinal dispersion, parameterised to first order by the chicane matrix element R_{56}, has the effect of smearing out the noisy FEL-induced microbunching induced in the first undulator section which otherwise would re-imprint itself upon the seed pulse in the second undulator section, reducing the coherence length.

The next sections summarise the design and simulation studies which have been done to show the feasibility of the schemes in the SXR and HXR for the CompactLight parameters and illustrate the performance enhancement compared to the baseline SASE operation.

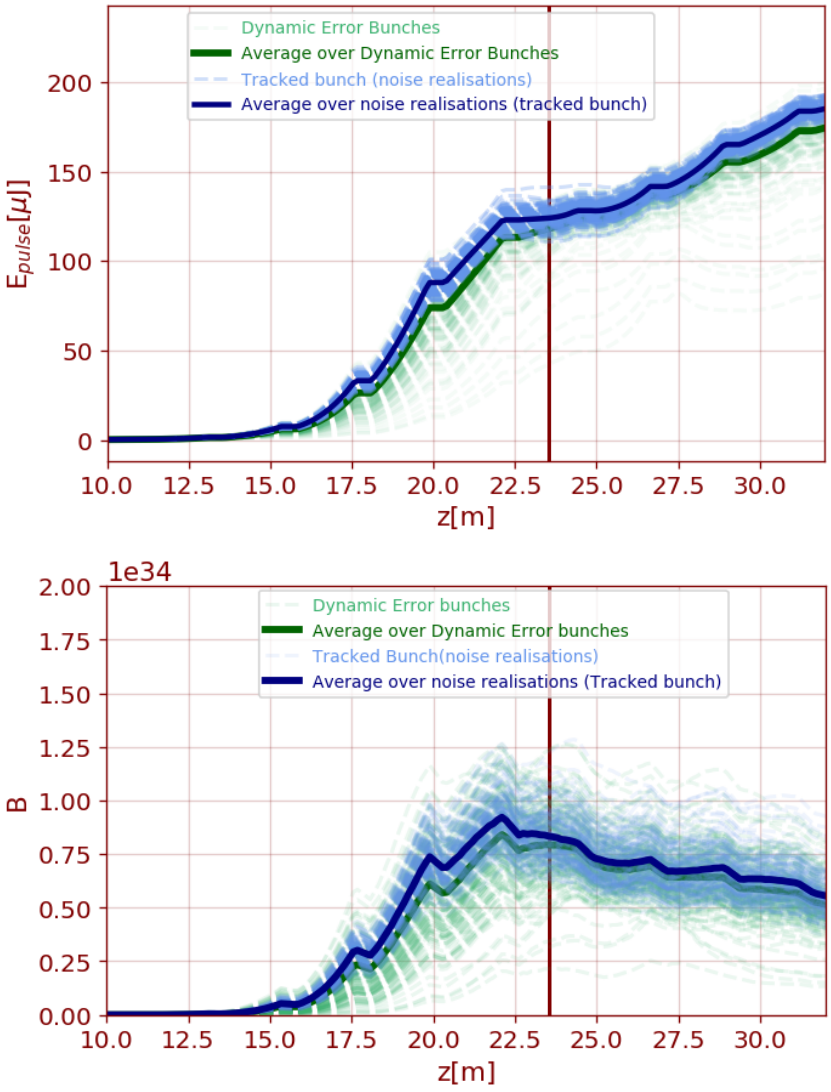

Figure 4.14.: Comparison of 16 keV FEL pulse energy (top) and peak brightness (bottom) for 200 tracked bunches with SASE shot noise and for 200 dynamic error bunches.

4.2.4.1. SXR Self-Seeding

The SXR self-seeding monochromator is based on the design described in [71] for the European XFEL, modified in order to accept a large photon-energy range (0.25-2 keV). A schematic of the layout is shown in Fig 4.15. The monochromator consists of a plane grating that creates an angular dispersion of the X-ray beam in the plane perpendicular to the electron-bunch chicane. The beam is then focused by the cylindrical mirror M1 on the exit slit, which selects a narrow bandwidth. By keeping a constant beam deviation angle at the grating, and thus a constant incidence angle on M1, a fixed focus position at the exit slit is provided for all photon energies. The beam is refocused to the undulator entrance, in the horizontal and vertical plane separately, by two cylindrical mirrors, M2 and M3. All optics are coated with platinum in order to provide sufficient damage threshold and reflectance across the photon-energy range. Two gratings with different line-densities (500 l/mm and 1000 l/mm) are used to enable high transmission over the whole photon-energy range. The resolution and transmission of the monochromator are shown is Figure 4.16.

The parameters used for the FEL simulations were the nominal ones shown in Table 4.2 with the electron bunch energy reduced to E = 2.36GeV. The undulator parameter was a_w = 1.013 giving FEL

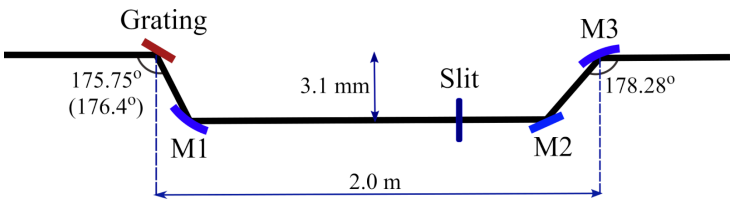

Figure 4.15.: Schematic of the SXR grating monochromator. The two beam deviation angles at the grating are associated with the 500 l/mm and 1000 l/mm (in parenthesis) gratings. The blaze angles of the gratings are 1.3° (500 l/mm) and 0.9° (1000 l/mm).

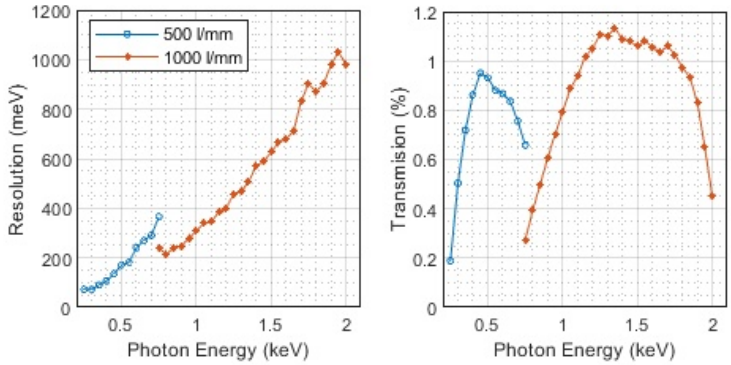

Figure 4.16.: Resolution and Transmission of the SXR self-seeding monochromator.

resonance at 2keV (λ = 0.62 nm). The optimum location to position the monochromator was found to be after the second undulator module. At this point the output pulse from the monochromator had sufficient intensity to dominate the electron beam shot noise power yet the energy spread growth in the electron bunch was not enough to prohibit exponential gain in the second undulator section. Placing the monochromator at other locations gave poorer results.

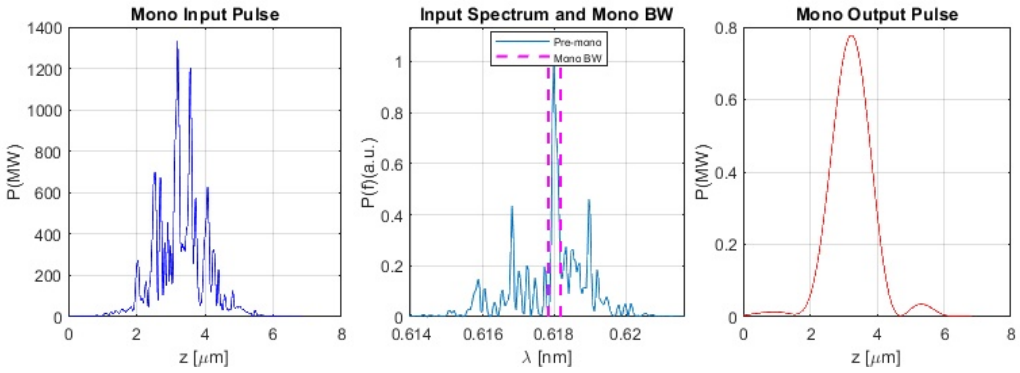

Figure 4.17.: Monochromator input pulse power profile (left), spectrum and monochromator bandwidth (centre) and output pulse (right)

Figure 4.17 shows the simulated FEL pulse profile as it enters and exits the monochromator. The centre plot shows the incident pulse spectrum and the extent of the hard-edged 1000 meV bandwidth centred at λ = 0.618 nm. The output pulse is seen to have a smooth profile with a peak power reduced from 1300 MW to 0.8 MW due to the filtering and the 0.45% transmission. Although the pulse power has been much reduced it is still sufficient to dominate the SASE shot noise emission in the second undulator section, as will be shown.

For 2keV operation the increase in the photon path length when passing the monochromator is

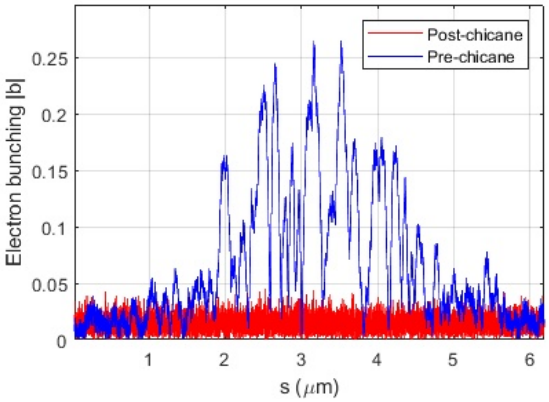

Figure 4.18.: Electron beam microbunching $|b|$ before and after the chicane

Δs = 0.144 mm. The electron is delayed by the same amount in a compact chicane. For any dipole chicane the R_{56} term is found to be twice the electron beam path length increase compared to on-axis propagation. This is applied as a simple linear transform to the electron bunch as it enters the second undulator section. The effect of the longitudinal dispersion on the microbunching induced by the FEL process in the first undulator section is shown in Figure 4.18—it is seen to be completely suppressed.

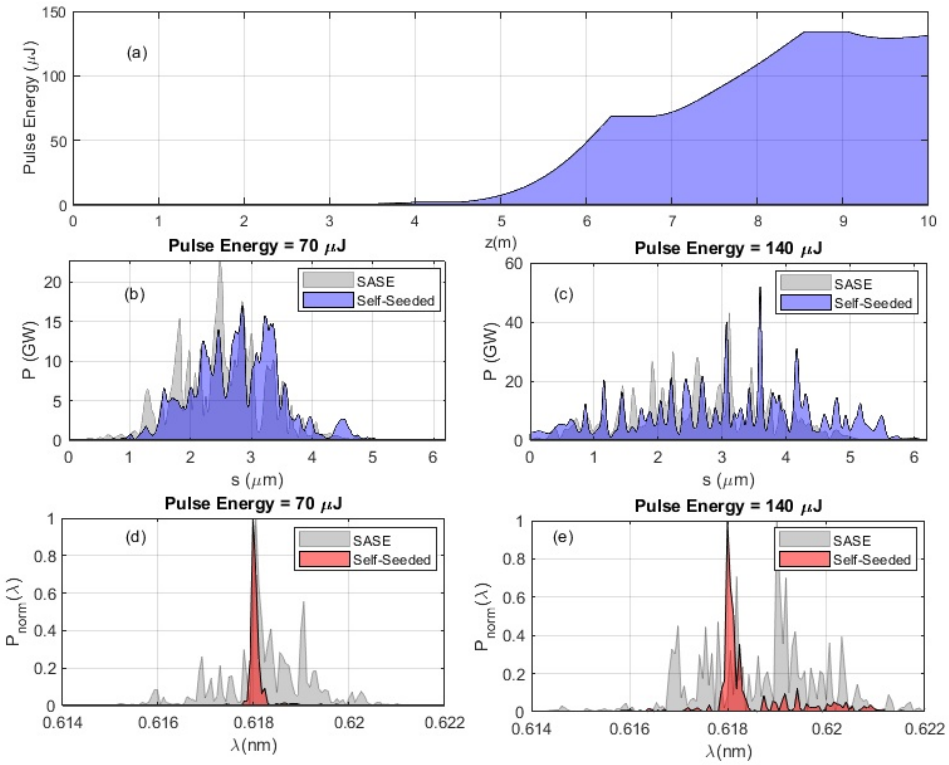

Figure 4.19.: SXR Self-Seeding simulation results for output at 2 keV: (a) Growth of pulse energy vs distance z through second undulator section (b) Self-seeded pulse profile at z = 6.5 m with pulse energy 70 μJ (in blue) and equivalent SASE pulse of the same pulse energy (in grey) (c) Self-seeded pulse profile at z = 8.5 m with pulse energy 140 μJ (in blue) and equivalent SASE pulse of the same pulse energy (d) Spectra of 70 μJ self-seeded pulse (red) and equivalent SASE pulse (grey). Both spectra normalised to peak value. (e) Spectra of 140 μJ self-seeded pulse (red) and equivalent SASE pulse (grey).

Figure 4.19 shows the FEL performance in the second undulator section, after the monochromator. The pulse energy grows to 70 μJ at a distance of z = 6.5m and 140 μJ at z = 8.5 m. The pulse profiles at these two pulse energies are shown ((b) and (c)) in comparison to SASE pulses with the same pulse energies. The SASE simulations have identical undulator, electron beam and simulation parameters. The 70 μJ self-seeded pulse has a somewhat smoother profile than the equivalent SASE pulse, but a much smaller FWHM bandwidth of $\Delta\lambda/\lambda_0 = 2 \times 10^{-4}$. At 140 μJ the self seeded pulse profile looks qualitatively similar to the equivalent SASE pulse, and again the FWHM spectrum is far narrower although not so clean. The FWHM length of the 70 μJ self-seeded pulse is $\Delta s = 1.3\mu$m. The time-bandwidth product of the pulse, a measure of how close the pulse is to the transform limit, can be estimated as

$$\Delta\nu\Delta t = \frac{1}{\lambda}\frac{\Delta\lambda}{\lambda_0}\Delta s = 0.42 \tag{4.1}$$

which is very close to the value of a gaussian pulse with constant phase. Note that the time-bandwidth product of the 140 μJ pulse has not been calculated because the pulse profile is too irregular to reasonably determine the FWHM pulse duration.

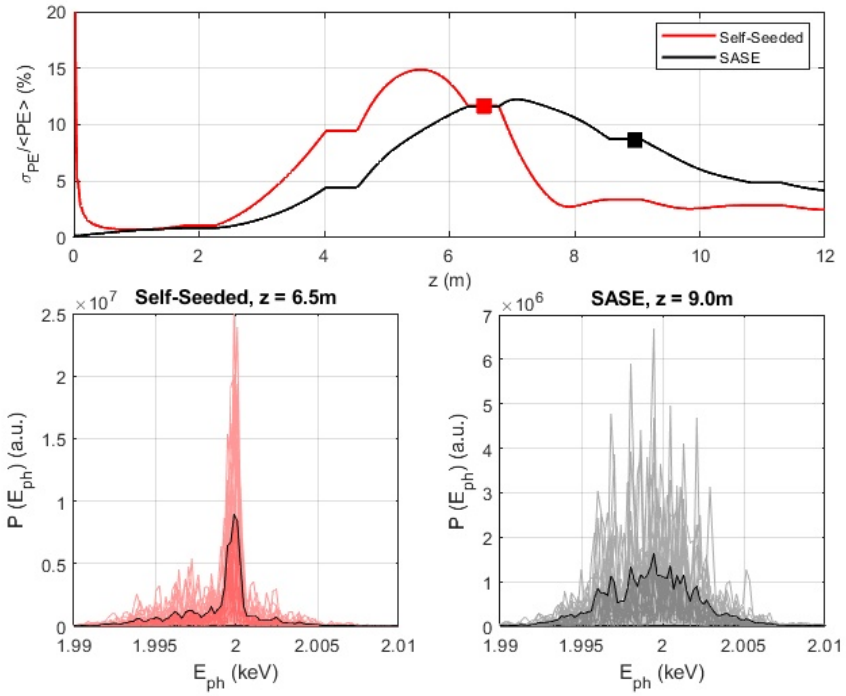

Figure 4.20.: Stability of SXR self-seeding vs SASE operation. The top plot shows the relative rms stability of the pulse energy vs distance through the undulator, for self-seeding and SASE. The coloured squares indicate the saturation points. The bottom left plot shows the spectra of 20 shot-noise realisations (light pink) and the average over all shots (darker pink). The bottom right plot shows the equivalent data for SASE.

An initial analysis of the stability of self seeding vs SASE was made, based on 20 self-seeded shot noise realisations and 20 SASE simulations. The results are shown in Figure 4.20. At saturation, the relative rms fluctuation of the self-seeded pulse energy was 12% compared to 9% for SASE. The self seeded spectra showed very good shot-to-shot reproducibility with stability of the central wavelength.

In summary, a realistic SXR self-seeding scheme has been designed and simulated. The results indicate that at 2keV photon energy near-transform-limited pulses with an energy > 70μJ can be produced.

4.2.4.2. HXR Self-Seeding

The parameters used for the FEL simulations were the nominal ones as shown in Table 4.2. The undulator parameter was $a_w = 0.6174$, giving FEL resonance at 16 keV ($\lambda = 0.0775$ nm).

As described above, the monochromator for HXR operation is a diamond crystal, with the crystal orientation adjusted for transmission at the appropriate photon energy. The output pulse from the crystal contains a trailing monochromatic wake which is used as the seed pulse [72]. The monochromator was modelled using an approach based on dynamic diffraction theory developed for SwissFEL [73, 74], which agrees well with the model by Geloni *et al.* [72].

Optimisation of the setup requires determining both the location for the monochromator and the crystal thickness. This was carried out fairly coarsely due to the computationally intensive demands of the simulations, but with promising results. FEL simulations for varying lengths of the first undulator section (up to the monochromator) were carried out for five shot noise realisations and the monochromatic wake was calculated for various crystal thicknesses. The wake is composed of a series of peaks; the peak power of which decreases with distance behind the main pulse, such that the first trailing pulse is most effective for self-seeding. Increasing the thickness of the crystal increases the peak power of the peaks in the wake, whilst reducing their duration and separation. Taking each case into the second undulator simulation stage requires the delay applied to the electron bunch to be appropriately set to overlap with the wake. Also, as described in the previous section, the corresponding R_{56} should be applied, which has the required beneficial effect of reducing micro-bunching from the first stage. For optimum performance the second undulator stage should also be detuned to take into account energy lost from the electron beam up to that point.

It was found that a combination of 8 undulator modules in the first stage, together with a crystal thickness of 0.2 mm, was suited to give good performance. Figure 4.21 shows the simulated FEL pulse profile as it enters and exits the monochromator. The central plot and its inset show the filtering effect applied by the crystal at $\lambda = 0.077566$ nm and the pulse spectrum before and after this is applied. The plot of the output pulse on the right is scaled to show the trailing monochromatic wake, which has significantly lower power than the input pulse but sufficient to dominate the shot noise emission in the second undulator section. In the right plot only are shown results for four other shot noise realisations. The required electron beam delay to overlap with the wake is 7 μm in this case, with $R_{56} = 14\mu$m applied as a simple linear transformation to the electron bunch before the second undulator section.

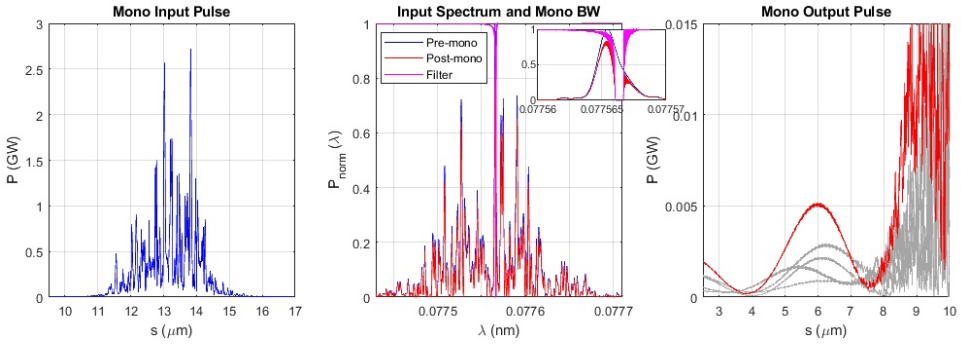

Figure 4.21.: Monochromator input pulse power profile (left), spectrum and monochromator bandwidth (centre, with zoomed horizontal axis in the inset) and output pulse (right). In the right plot only are shown results for four other shot noise realisations.

Figure 4.22 shows the simulated performance of the self-seeding scheme compared to SASE. For the self-seeded case, the pulse energy reaches ~ 50 μJ after 6 undulator modules of the second stage, and ~ 100 μJ after 8 undulator modules. The pulse temporal profiles and spectra at these two pulse energies are shown in comparison to equivalent SASE simulations results taken at the same pulse energies. Similar to the SXR results, the temporal profile for the lower pulse energy case (50 μJ here)

is somewhat smoother than the equivalent SASE pulse, whilst the bandwidth is significantly reduced to $\Delta\lambda/\lambda_0 = 2 \times 10^{-5}$. The time-bandwidth product in this case has been estimated to be 0.57, which is close to a gaussian with constant phase. The higher pulse energy case has a qualitatively degraded temporal profile whilst retaining a clean, narrow spectrum. Note that unlike Figure 4.19, the top plot in Figure 4.22 shows distance from the start of the first undulator section, in order to show a comparison with SASE, with the other four shot-noise realisations from Figure 4.21 also shown for the self-seeded case.

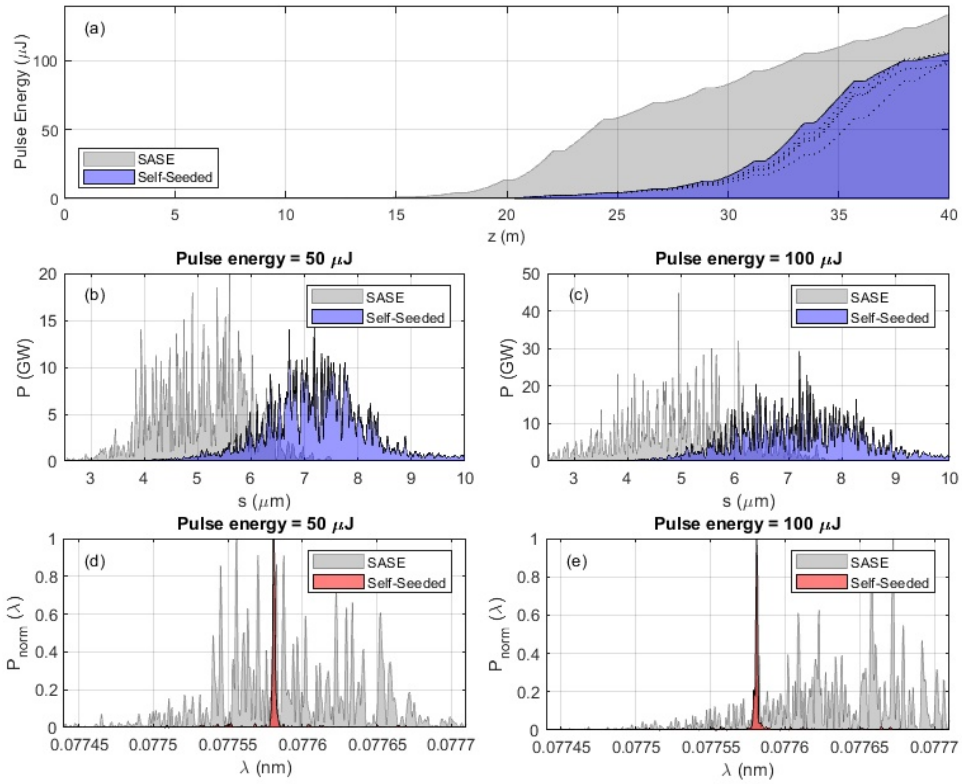

Figure 4.22.: HXR Self-Seeding simulation results for output at 16 keV: (a) Growth of pulse energy vs distance z from the start of the first undulator section (dashed lines are other shot-noise cases) (b) Self-seeded pulse profile at $z = 33.5$ m (6 modules/13.1 m in the second stage) with pulse energy 50 μJ (in blue) and equivalent SASE pulse of the same pulse energy (in grey) (c) Self-seeded pulse profile at $z = 38.0$ m (8 modules/17.6 m in the second stage) with pulse energy 100 μJ (in blue) and equivalent SASE pulse of the same pulse energy (d) Spectra of 50 μJ self-seeded pulse (red) and equivalent SASE pulse (grey). Both spectra normalised to peak value. (e) Spectra of 100 μJ self-seeded pulse (red) and equivalent SASE pulse (grey).

4.2.4.3. Self-Seeding summary

In summary, realistic SXR and HXR self-seeding schemes have been designed and simulated. The results indicate that at 2keV photon energy near-transform-limited pulses with an energy > 70μJ can be produced, and that at 16 keV photon energy single wavelength pulses with energy 100μJ can be produced. The simulations shown here indicate that self-seeding schemes can therefore introduce a significant brightness enhancement over SASE of a factor of 15-20, as shown in Figure 4.23.

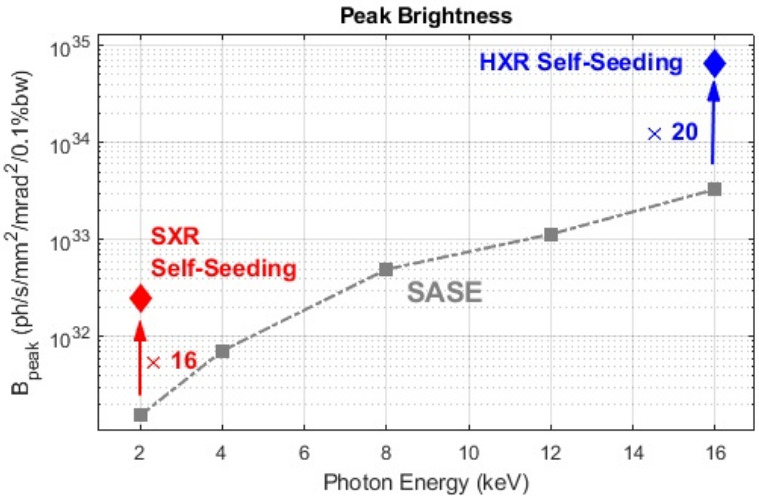

Figure 4.23.: Figure showing enhancement of peak brightness compared to SASE for the SXR and HXR self-seeding examples. The electron bunch is ideal gaussian current profile with constant nominal slice parameters.

4.2.5. Summary of FEL Performance

The predicted performance of the CompactLight FEL is summarised in Table 4.4. The SASE output figures at 16 keV are directly taken from the simulations using the tracked electron bunches with added dynamic errors, averaged over 200 bunches, and are the best available predictions of FEL performance. The SASE output figures at other photon energies are derived from the SASE results at 16 keV but scaled to the relevant photon energies according to the simulation results of the nominal bunch reported in Section 4.2.1. The self-seeded results are taken directly from the simulations which used nominal electron bunches so are not directly comparable with the SASE results.

Table 4.4.: Summary of predicted FEL performance in SASE and self-seeded modes

	SASE					**Self-Seeded**	
Photon Energy (keV)	**2**	**4**	**8**	**12**	**16**	**2**	**16**
Pulse Energy (μJ)	210	362	448	266	118	70	100
Bandwidth (% RMS)	0.19	0.17	0.13	0.10	0.07	0.01	0.001
Brightness (10^{33} ph/s/mm^2/mrad^2/0.1%bw)	0.04	0.17	1.2	2.7	7.9	0.17	47

5. Accelerator

5.1. Injector

The XLS injector system extends from the electron source to the Bunch Compressor 1 (BC-1) exit, corresponding to an upper energy of 300 MeV. At about 300 MeV the electron beam experiences a transition from the ”space-charge” dominated regime to the ”emittance dominated” regime and the emittance compensation process, performed within the injector itself, can be considered accomplished. The target injector parameters are reported in Table 5.1.

Table 5.1.: Target injector parameters

Parameter	**Unit**	**After VB and/or BC-1**
Charge Q	pC	75
Beam energy	MeV	300
RMS Bunch Duration σ_t	fs	350
Peak Current	A	60
RMS Energy Spread	%	0.5
Projected RMS Norm. Emittance	μm	0.2
Repetition Rate	Hz	100–1000

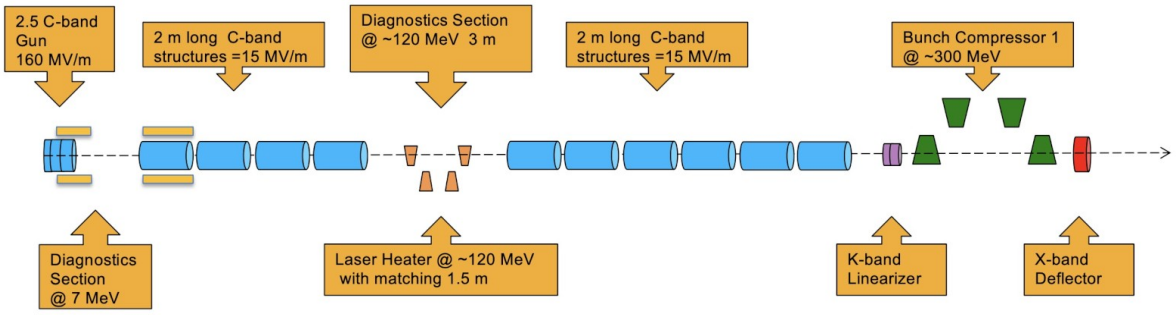

Figure 5.1.: Injector layout

To achieve these parameters the injector design incorporates various components, as shown in Figure 5.1, from the electron source (including the cathode material definition and laser system specifications), to the capture sections, needed to boost the beam energy up to 300 MeV (including the possibility of operating in Velocity Bunching configuration and/or with a magnetic compressor system). Additional components are required to provide the proper parameters optimization. These are the higher harmonics RF structure, see 5.2.9, for longitudinal phase space linearization, the X-band RF deflector system, see 5.4.1.4, to provide the adequate longitudinal diagnostics, and the Laser Heater, to prevent possible micro-bunch instabilities in BC1. Various diagnostics tools have been also considered in order to monitor the beam quality along the injector itself and are described in section 5.4.

The final injector design uses the same injector for both the operational modes, high (1 kHz) and low (100 Hz) repetition rate. This implies operating the whole injector at a moderate accelerating gradient while keeping the beam quality within the requirements. This choice is less expensive than a scheme with a dedicated injector for each operational mode. The final layout, see Figure 5.1, includes a 2.6 cell C-Band RF Gun followed by a C-Band Booster up to 150 MeV, partially embedded in a long solenoid, a laser heater, a second C-band booster up to 300 MeV, a K-Band Linearizer and a Magnetic Compressor

BC1. To fulfill the FEL operating modes, the XLS injector will use a gun and a photoinjector laser able to operate with a two e-pulses, for each RF pulse, spaced by 3 or 5 RF cycles of the C-band frequency A Copper Cathode driven by a 1 kHz Ti:Sa Laser is the choice for the electron source. This configuration meets the design goals of the XLS injector of Table 5.1, as shown in the Beam Dynamics section 5.3 . The following paragraphs describe the technical characteristics of the main components not described in other sections.

5.1.1. 2.5 cell C-band RF Gun and Solenoid Design

5.1.1.1. RF Gun Design

The strategy for the design of the 2.5 cell RF gun has been that typically implemented in the high gradient structure design, based on the reduction of the surface electric field, surface modified Poynting vector [75] and pulsed heating [76]. To this purpose, the gun is fed with short RF pulses ($\tau < 300ns$) and the coupling with the input waveguide is axial, through the last iris, with a mode launcher [77]. Standard couplers on the full cell, even if strongly rounded [78–80] cannot be used because of the high magnetic field and, as a consequence, high pulsed heating on the coupling holes. These two implementations (short RF pulses and mode launcher) reduce the pulsed heating (that scale with the square root of the RF pulse-length), the breakdown rate (that scales with τ^5), the average dissipated power and the surface magnetic field on the input coupler. The reduction of the average dissipated power is important, in CompactLight case, for the high repetition rate operation (1 kHz). Also, the geometry of the standing-wave (SW) cells has been optimized introducing an elliptical shape of the irises to reduce the surface electric field. The electromagnetic design has been performed using ANSYS HFSS [81] and the simulated gun geometry is shown in Figure 5.2. The four ports mode launcher has been designed following the criteria illustrated in [82] and the four ports allow complete cancellation of the dipole and quadrupole field components, typically induced by simple mode launchers. The main parameters of the structure are given in Table 5.2.

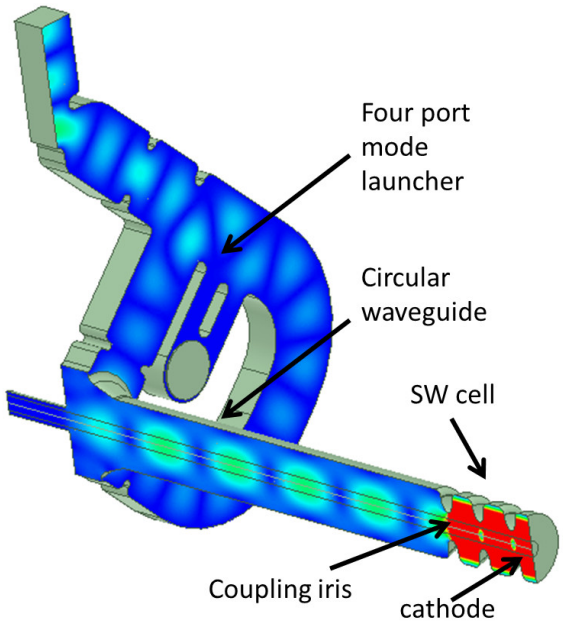

Figure 5.2.: Gun geometry simulated by ANSYS-HFSS

The structure is fed with 300 ns RF input pulses at 1 kHz repetition rate with a copper cathode peak field of 160 MV/m. The RF pulse-length and cathode peak field have been chosen as a compromise

Table 5.2.: Main parameters of the C-band gun.

Parameter	Unit	Value
Working frequency	GHz	5.996
$E_{cath}/P_{diss}^{1/2}$	MV/(mMW$^{1/2}$)	52
RF input power	MW	18
Cathode peak field	MV/m	160
Cathode type		copper
Rep. rate	Hz	1000
Quality factor		11800
Filling time	ns	164
Coupling coefficient		3
RF pulse-length	ns	300
E_{surf}/E_{cath}		0.9
Modified Poynting vector	W/μm^2	2.5
Pulsed heating	$^\circ$C	<20
Average diss. Power	W	2300

between the required peak input power from the klystron, average dissipated power into the gun and beam dynamics performance. For the same reason, instead of the original 1.5 cell gun [83, 84] the design adds one more accelerating cell to increase the beam energy at the gun exit that is now comparable with that of a 1.6 cell S-band gun operating at 120 MV/m cathode peak field [85]. The RF source is a 20 MW C-band klystron with an average power, at 1 kHz, similar to that of the klystron currently in use at SwissFEL [70]. This klystron is currently not commercially available, but from preliminary evaluations, we believe it may be available in the next 3-5 years.

The gun is directly fed by the klystron through a circulator. Commercial circulators that operate at this level of power already exist [86] and can be adopted. The coupling coefficient has been designed in order to minimize the required input power for the 160 MV/m cathode peak field operation and the average dissipated power. Figure 5.3 shows the average dissipated power in the gun and the required input power as a function of the RF pulse-length for three different coupling coefficients. The 300 ns operation with a coupling coefficient equal to 3 has been chosen as a good compromise between the required input power and the average dissipated power in the gun. The profiles of the input, reflected, dissipated power and cathode peak field are given in Figure 5.4.

The magnitude and phase of the longitudinal accelerating field on axis is reported in Figure 5.5. The plot shows the standing-wave accelerating field in the first 2.5 cells operating on the π-mode and the propagating field into the circular waveguide (phase plot). In the beam dynamics calculations, we have also taken into account the contribution of the field in the circular waveguide itself.

5.1.1.2. Thermo-Mechanical Analysis

The operation at 1 kHz with 300 ns RF pulses, results in an average dissipated power into the gun body of more than 2 kW. For this reason, a careful design of the cooling system has been performed. The gun cooling system integrates 4 cooling channels, as shown in Figure5.6: three for the cells and one for the cathode, with a total flow of about 20 liter/min for the channel. The 3D model of the gun, including cooling channels, has been implemented in the Ansys Workbench (WB) [81] environment. With this code, the fully coupled thermal, structural and electromagnetic analysis has been performed. The heat load obtained by the electromagnetic analysis has been imported in the thermal analysis module. The final temperature distribution is given in Figure 5.7(a) and the corresponding deformation is depicted in Figure 5.7(b). The deformed structure has then been simulated and the detuning has been

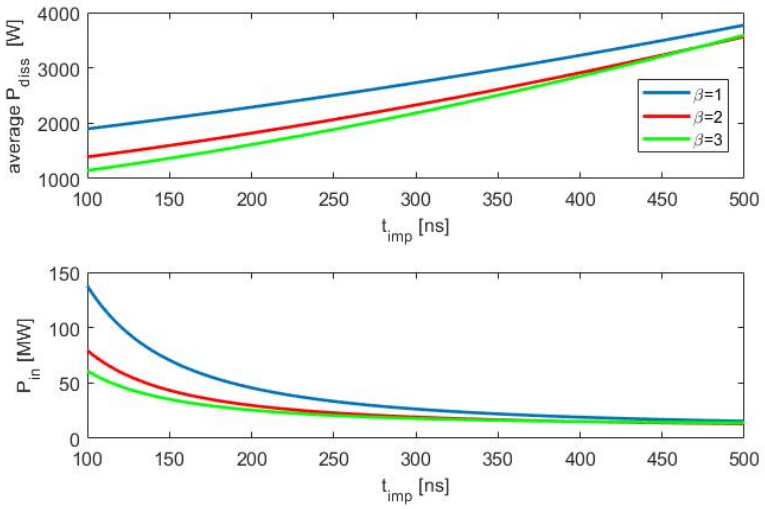

Figure 5.3.: Average dissipated power (upper plot) and required input power (bottom plot) as a function of the rf pulse-length, for three different coupling coefficients.

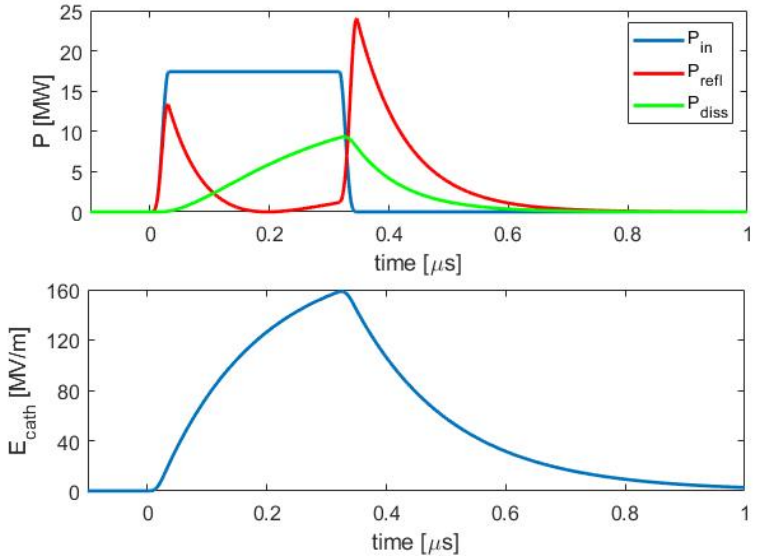

Figure 5.4.: Input, reflected, dissipated power (upper plot) and cathode peak field (bottom plot) as a function of time for a 300 ns pulse-length with 30 ns rise time.

evaluated to be about 1 MHz, while the field distribution is basically unperturbed thanks to the uniform cooling system design. This detuning can be either compensated by changing the water temperature during operation by about 15 deg, or designing the structure with a resonant frequency higher than the nominal one.

5.1.1.3. Gun Solenoid Design

The sketch of the RF gun with mode launcher and solenoid is given in Figure 5.8. The solenoid around the circular waveguide has been designed using Poisson Superfish [87]. The simulated structure and the magnetic field profiles on axis are given in Figure 5.9. The main solenoid parameters are reported

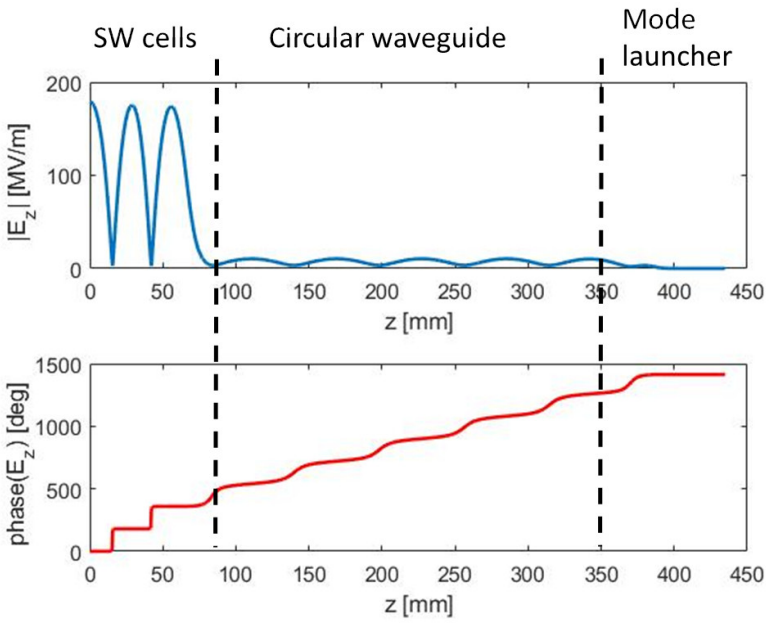

Figure 5.5.: Magnitude and phase of the longitudinal accelerating field on axis.

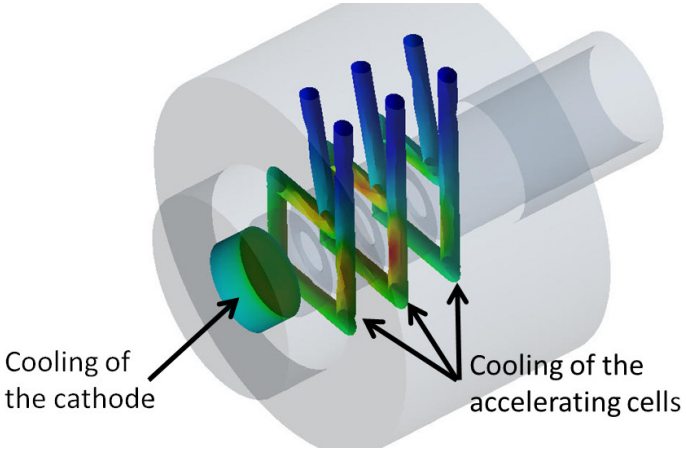

Figure 5.6.: Gun cooling system simulated in ANSYS.

in Table 5.3. In order to cancel the magnetic field on the cathode and prevent an increase of the beam emittance [88], a bucking coil is foreseen to be located at the back of the RF gun. Figure 5.9(b) shows the effect of the backing coil on the magnetic field at the cathode position at 165 mm from the coordinate z=0. Both the electromagnetic field in the RF gun and circular waveguide and the solenoid field have been inserted in the beam dynamics simulations.

5.1.1.4. Photocathode and Laser Systems

The photo-cathode is the key component of a photoinjector since the overall quality of the electron beam and the reliability of the photoinjector depends on material type, robustness, roughness and lifetime. The electron beam produced by the photo-cathode is emitted via the photoelectric effect using a laser source of appropriate wavelength. The longitudinal and transverse electron beam profiles are determined by the laser time and spatial structure [89].

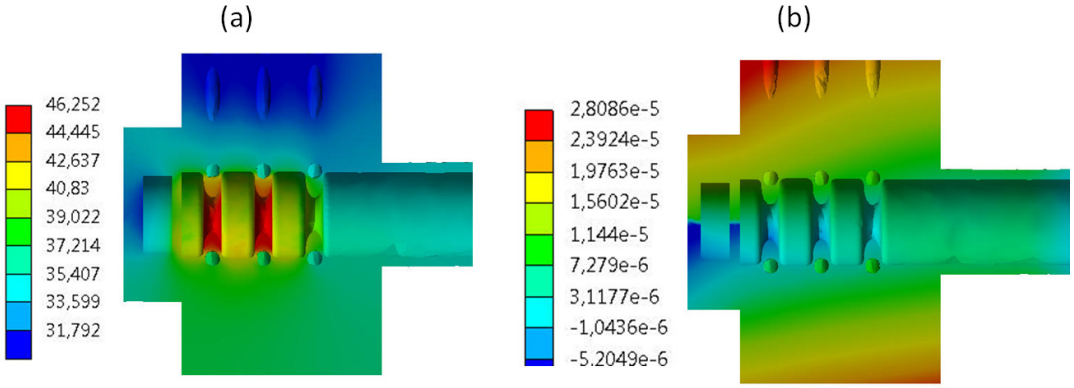

Figure 5.7.: (a) Gun temperature distribution and corresponding deformation (b)

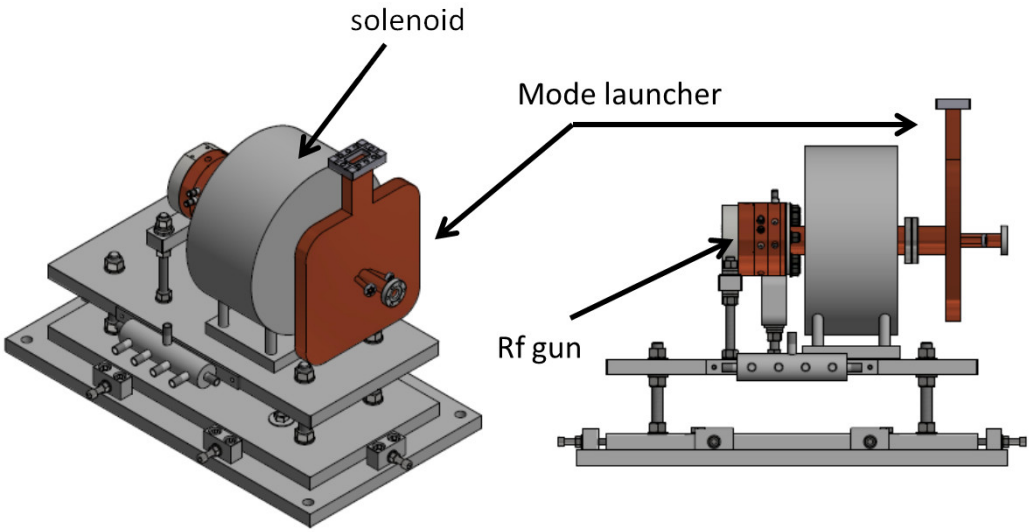

Figure 5.8.: Sketch of the RF gun with mode launcher and solenoid.

To satisfy the CompactLight requirements, the design adopts a metallic photo-cathode. This choice is based on the results obtained worldwide in different laboratories, and on the ASTRA [90] simulation studies, comparing the transverse emittance and the normalized transverse emittance between the cathode materials Cs_2Te vs Cu. The S-/C-band of the e-gun has been studied, with a solenoid after the photo-cathode, at the Ferrario working point. The proper laser parameters have been studied for final selection of wavelength, pulse duration, pulse-length, pulse energy, intrinsic emittance and QE tuning, plus the repetition rate, the longitudinal-transverse and 3D pulse profile optimization. The GIOTTO [91] code was implemented and provided optimization results of the normalized transverse emittance [92]. Simulations have been done also to optimize transverse/longitudinal emittance, beam size, bunch length, with 1.6, 2.5 and 5.6 cavity cells, with various cavity voltages and solenoid distances from the photo-cathode [93]. The most suitable candidate metal was found to be copper (Cu) [93]. The photo-cathode is centred on the flange and closes the RF gun half-cell.

The main criteria for the selection of the cathode have been the high quantum efficiency, high robustness and fast response time in addition to low intrinsic emittance, low surface roughness and high lifetime. Moreover the photo-cathode is also subject to surface modification and contamination due to

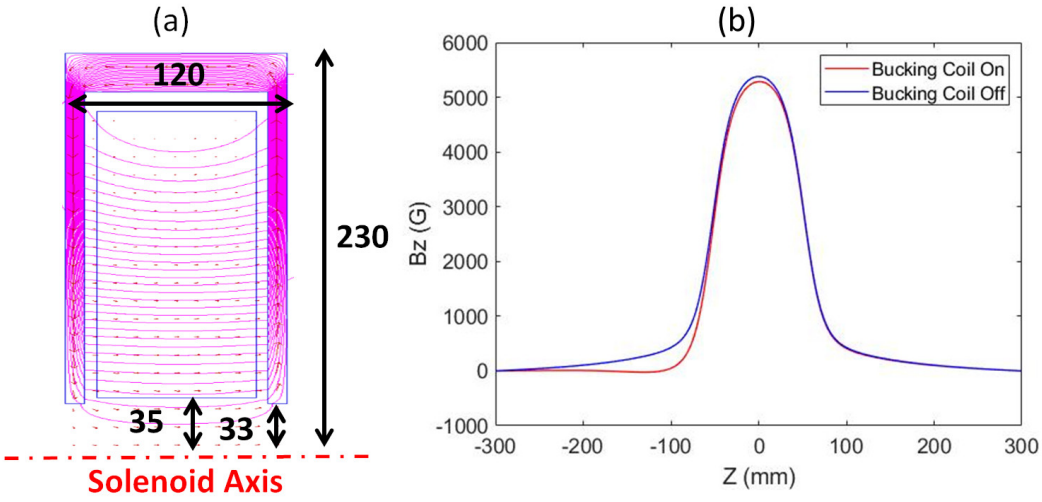

Figure 5.9.: (a) Solenoid simulated by the code Poisson and magnetic field profile on axis (b)

Table 5.3.: Main gun solenoid parameters

Parameter	**Unit**	**Value**
B_{max}	T	0.53
Bore radius	mm	33
Solenoid length	mm	120
Yoke Material		Low Carbon Steel
Integrated field	Tmm	59.4
Good field region radius	mm	10 mm
Integrated Field variation		3×10^{-5}
Number of Turns		336
Conductor dimension	mm	5.6×5.6/bore 3.6
Nominal Current	A	164
Nominal Voltage	V	40
Inductance	mH	3
Resistance	mΩ	242
Water Flow Rate	l/min	3.72
Temperature drop	$^{\circ}$C	25
Pressure drop	bar	2.72
Bucking coil conductor diameter	mm	1.6
Bucking coil radius	mm	72
Bucking coil Number of turns		700
Bucking coil Nominal current	A	7.5

laser radiation, RF field breakdown and low vacuum pressure. A Cu photo-cathode, due to its fast response time (10^{-16} s $< \tau < 10^{-14}$ s), is useful for laser pulse shaping and for its robustness and lifetime. Cu photo-cathodes are minimally reactive with respect to other materials, they require about 10^{-9} Torr vacuum level and they are compatible with the environment of the RF cavity, whose walls are also made of Cu [89]. For all these reasons an oxygen free polycrystalline Cu photo-cathode has been chosen for CompactLight.

The required electron beam distribution defines the characteristics of the laser system to be used for

the photoemission. In general metal photo-cathodes require UV light, generated from 3rd or 4th harmonic conversion from an IR fundamental wavelength. Photo-cathode drive lasers for high brightness electron beam applications must have very specific capabilities driven by two major considerations: (1) the low photoemission efficiency for robust photo-cathodes requires high UV pulse energy given the required charge; (2) the emittance compensation process is most successful with uniform temporal and spatial laser energy distribution. Additionally, low amplitude and time jitter from pulse-to-pulse, as well as stable pointing stability, are needed to ensure high performance. The laser pulses have to be synchronized with the master oscillator to extract electrons at the specified phase of the RF wave [94, 95].

The photo-cathode laser system will be based on a Ti:Sapphire laser at 800 nm with about 100 fs pulse duration. The photo-cathode pulses are up-converted via harmonic generation to the 3rd harmonic at 266 nm, the wavelength required for electron extraction out of the copper cathode. The laser system must deliver excess of 50 μJ energy per pulse at a wavelength of 266 nm to the photo-cathode at a repetition rate of 1 kHz. This energy requirement comes from the typical quantum efficiency of copper photo-cathodes, which is of the order of 10^{-5} [96]. Considering the worst case QE of 10^{-6} the requested energy per pulse will be about 100 μJ, a typical value for a Ti:Sapphire laser system. Indeed, in both cases a commercial Ti:Sapphire laser system as https://amplitude-laser.com/frequence/khz-en [97] can be used. Table 5.4 reports the technical specification of a such laser system.

Table 5.4.: The technical specification of the Ti:Sapphire laser system (ARCO)

Specifications	ARCO C (100 Hz) & ARCO M (1 kHz)					
Repetition Rate [1]	100 Hz for Arco C	1 kHz for Arco M				
Energy Per Pulse [2,3]	6 mJ @ 100 Hz	5 mJ @ 1 kHz	12 mJ @ 100 Hz	10 mJ @ 1 kHz	25 mJ @ 100 Hz	20 mJ @ 1 kHz
Pulse Width (fwhm) [4]	< 100 fs or < 35 fs or < 20 fs					
Central Wavelength (nm) [5]	800 ± 10					
Average Power (W)	5		10		20	
Pump Lasers	Terra		Terra Duo		2 Terra Duo	
Pulse To Pulse Energy Stability (RMS)[6]	0,7 %		0,7 %		0,5 %	
Power Stability (RMS) [7]	1 %					
Nanosecond Contrast [8]	$< 5.10^{-4}$					
Picosecond Contrast [9]	$< 5\ 10^{-7}$ @ 300 - 50 ps & $< 10^{-6}$ @ 50 - 10 ps & $< 10^{-5}$ @ 1 ps					
Beam Quality M^2	< 1.3					
Pointing Stability	< 10 µrad RMS					
Polarization	Linear horizontal					
Warm-up Time	< 1 hour					

[1] Please contact factory for specifications at other repetition rates
[2] 5 mJ / 9 mJ / 20 mJ @ 100 Hz or 4 mJ / 9 mJ / 16 mJ @ 1 kHz for pulse duration < 25 fs
[3] 790 nm +/- 10 nm for 100 fs pulse duration. Other central wavelengths, please contact factory
[4] Factory-set, must be specified when ordered and will be optimized prior to shipment
[5] Over 2000 pulses
[6] Over 8 hours under stable environmental conditions
[7] Pre-pulse, regenerative amplifier replicas
[8] Measured with third order cross-correlator (SEQUOIA)

The emittance compensation scheme requires that the laser pulse must have uniform transverse and flat-top longitudinal profile at the cathode to compensate the non-linear space-charge field with a proper magnetic focusing. For the longitudinal flat-top profile there is in fact a rise time of about 1 ps and a FWHM value of about 4 ps. Such a temporal and spatial laser energy distribution on the cathode has been demonstrated to reduce the emittance [98, 99]. A small portion of the laser pulse will be used for the laser heater—for details see Section 5.1.3.

It is important to use a load-lock systems for the RF gun to guarantee a fast and safe photo-cathode

exchange under vacuum conditions. Without a load-lock system, the photo-cathode exchange takes 2-3 days and the photo-cathode surface gets contaminated in the atmosphere during installation, leading to undesired QE degradation [100]. A given system must be implemented in the photo-cathode area using suitable design—Figure 5.10 shows the SWISSFEL load lock system from the photo-cathode preparation to the RF gun insertion [100].

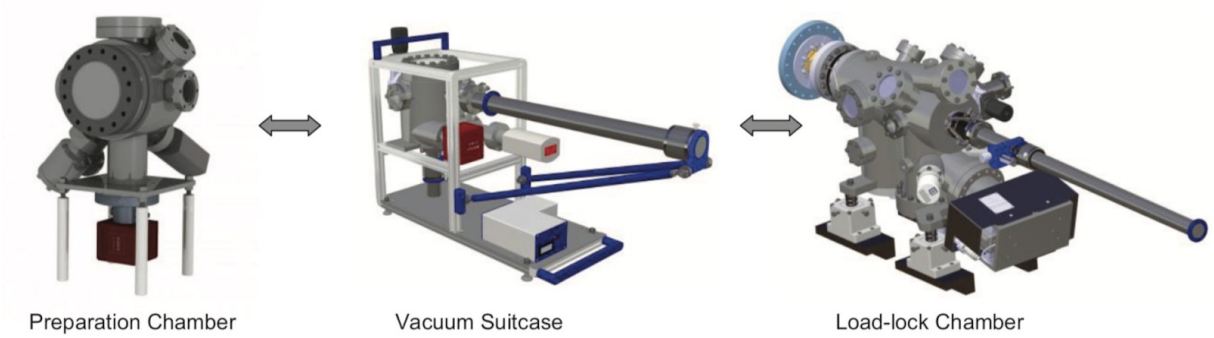

Figure 5.10.: First step is the photo-cathode plugs preparation inside the chamber(left), the photo-cathode plugs are then transported by using the vacuum suitcase (center) inside the load-lock system (right).

5.1.2. C-band Booster

5.1.2.1. C-band RF Modules

The C-band booster comprises four 2 m long travelling-wave accelerating structures installed after the photoinjector, to boost the beam energy up to 120 MeV of the laser heater, see the RF feeding system in Figure 5.11. In addition, six more structures are planned to be installed before the first bunch compressor to further increase the beam energy up to 300 MeV. The C-band structure parameters are listed in Table 5.5 and they have been determined using the algorithm in [101]. Each structure has a linear tapering of the irises. The average dimension of the iris ($< a >$) and the tapering angle have been chosen in order to maximize the structure efficiency, as given in Figure 5.12 where the effective shunt impedance has been plotted as a function of the average iris radius. In Figure 5.13 the same parameter is plotted as a function of the tapering angle for the case $< a >$ = 6.6 mm. All calculations assumed the klystron parameters listed in Table 5.6, 2 meter long structures and the BOC pulse-compressor parameters similar to those already implemented for SwissFEL [102]. The klystron operating parameters reported in Table 5.6, 15 MW peak power, 2 μs RF pulse-length and 1 kHz repetition rate, are an evolution of those of the C-band klystron currently in operation at the SwissFEL linac [70]. Currently this type of klystron is not available on the market, but, based on information received from industry, it could be available in the next 3-5 years.

5.1.2.2. C-band Structure Solenoid

For the beam emittance compensation process, a long solenoid is placed around the first accelerating structure. The solenoid has been designed using the code Poisson Superfish [87]. It is a four coil solenoid with an iron shielding, as illustrated in Figure 5.14(a), where the simulated geometry is shown. Figure 5.14(b) shows the profile of the magnetic field on axis. The main parameters of the solenoid are reported in Table 5.7.

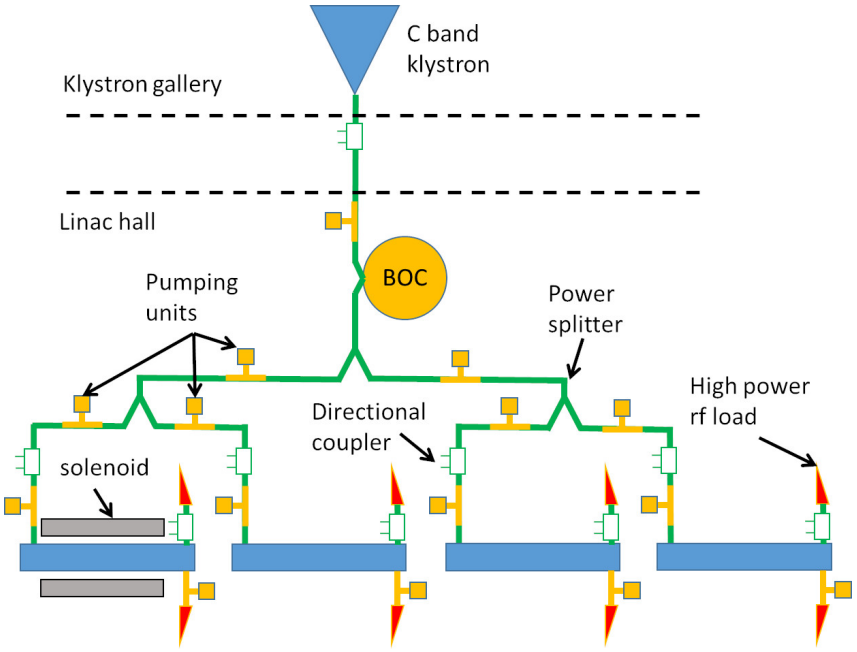

Figure 5.11.: Schematic layout of the C-band booster feeding system

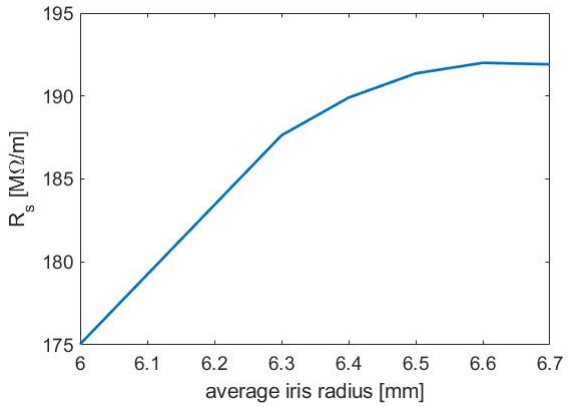

Figure 5.12.: Effective shunt impedance as a function of the average iris radius

5.1.3. Laser Heater

The brightness of X-ray FELs is affected by the uniformity of the longitudinal density and energy distribution of the electron beam injected into the undulator. Such uniformity can be spoiled by several collective processes occurring during acceleration and time-compression. Among them, the microbunching instability (MBI) is one of the most significant [103]. Driven by a combination of longitudinal space-charge force (LSC), coherent synchrotron radiation (CSR) and energy-dispersion in magnetic compressors, the MBI induces a broadband modulation of the electron beam energy and longitudinal charge distribution. This process originates with shot noise and cathode-induced non-uniformities in the particle distribution and is further stimulated and amplified by bunch length compression, in proportion to the bunch peak current. At the undulator entrance, the electron beam can have significant longitudinal energy and density modulations at micron to sub-micron scale lengths. Longer wavelength modulations can degrade the FEL spectrum, especially in externally seeded FEL schemes, while those at shorter wavelengths may appear as an increased slice energy spread and therefore translate into

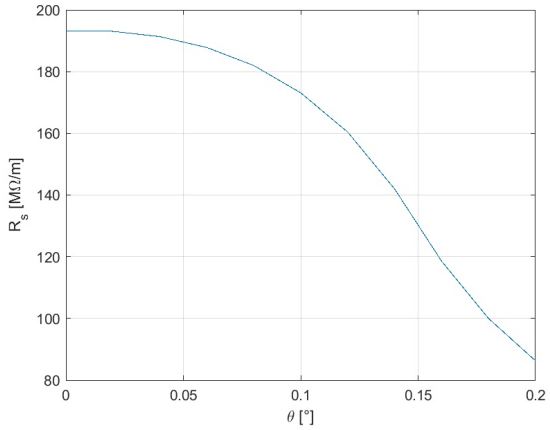

Figure 5.13.: Effective shunt impedance as a function of the tapering angle for the case $< a >$= 6.6 mm

Table 5.5.: Main parameters of the C-band structures.

Parameter	**Unit**	
Working Frequency	GHz	5.996
Phase advance per cell	rad	$2\pi/3$
Average iris radius $< a >$	mm	6.6
Iris radius **a**	mm	6.94-6.26
Number of cells per structure		120
Accelerating cell length	mm	16.67
Structure length $\mathbf{L}_s$	m	2
Shunt impedance **R**	MΩ/m	71 - 77
Effective shunt impedance $\mathbf{R}_s$	MΩ/m	190
Group velocity v_g/c	%	2.4-1.6
Filling time	ns	336
Average acceleration gradient	MV/m	15
Required input power per module	MW	9
Number of structure in the module		4

Table 5.6.: Main Parameters of the C-band Klystron

Parameter	**Unit**	**Value**
Operating frequency	GHz	5.996
Klystron pulse-length	μs	2
Klystron peak power	MW	15
Repetition Rate	Hz	1000
Q_0 of BOC		216000
Q_E of BOC		19100

reduced FEL gain and intensity.

As a means to control the MBI, Saldin et al. [104] proposed the addition of a device commonly referred to as a "laser heater" (LH). This device adds a controlled amount of incoherent energy spread to the electron beam and suppresses further MBI growth via energy Landau damping. The ability of a LH

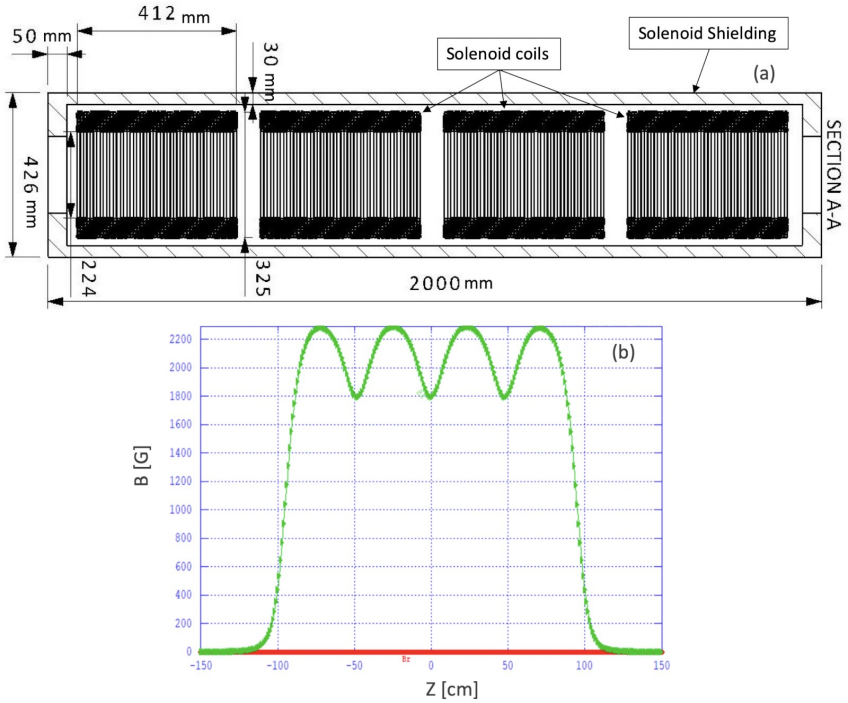

Figure 5.14.: (a) Geometry of the C-band solenoid simulated with Poisson-Superfish; (b) longitudinal magnetic field on axis.

to increase the final electron beam brightness was initially demonstrated at the LCLS hard x-ray FEL, where both a reduction of the FEL gain length and an increase of the photon flux were observed [105]. This section presents the specification of the CompactLight LH system.

5.1.3.1. Footprint

The CompactLight LH consists of a short, planar undulator located in a magnetic chicane, where an external laser pulse is superimposed to the electron beam. The electron-laser interaction within the undulator produces an energy modulation on the longitudinal scale length of the laser wavelength. The dispersion in the second half of the chicane smears the energy modulation in time, leaving the beam with a larger incoherent energy spread. The LH chicane includes two screen stations for spatial alignment of laser and electron beam, and two Beam Position Monitors for on-line electron beam trajectory control, and a screen and a BPM on each side of the undulator. A schematic is shown in Figure 5.15. The electron beam size is 80 μm in both transverse planes at the location of the LH undulator, as predicted by particle tracking runs.

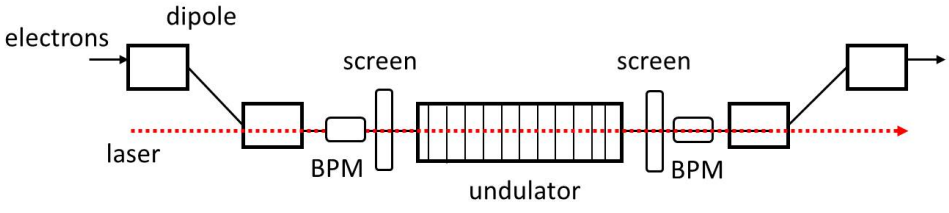

Figure 5.15.: Top view (not to scale) of the LH system. The overall length is approximately 1.5 m.

Table 5.7.: Main C band structure solenoid parameters

Parameter	**Unit**	**Value**
B_{max}	T	0.22
Bore radius	mm	100
Total solenoid length	m	2
Single coil length	mm	418
Yoke Material		Low Carbon Steel
Total integrated field	Tmm	40
Good field region radius	mm	20 mm
Integrated Field variation		10^{-4}
Number of Turns per coil		288
Conductor dimension	mm	8×8/ bore 6
Nominal Current per coil	A	278
Nominal Voltage per coil	V	153
Inductance per coil	mH	9.17
Resistance per coil	mΩ	553
Water Flow Rate per coil	l/min	2
Temperature drop per coil	$^{\circ}$C	20
Pressure drop per coil	bar	2.43

5.1.3.2. Laser

The external laser pulse consists of a small portion of the 800 nm Ti:Sa photocathode drive laser pulse, extracted before the latter is harmonically up-converted to the UV. The LH laser pulse temporal duration should completely cover the electron beam duration. It is therefore specified to be at least 20 ps FWHM. The LH laser pulse energy, expected to be up to several 10's μJ level, can be attenuated by a polarimeter. A separate shutter can completely block the pulse.

5.1.3.3. Undulator

The undulator consists of 8, 40 mm long periods and peak field of 0.4 T. The vertical gap can be remotely changed to resonantly match the external laser wavelength for electron beam energies in the range 100–140 MeV. The undulator parameter is around 1 for efficient laser-electron interaction. The relative energy bandwidth of the undulator is 12 %.

5.1.3.4. Chicane

The symmetric 4-dipole chicane has a two-fold scope. First, it allows the laser to be transversely aligned to the electron beam and perfectly overlapped with it. Second, it smears out the laser-induced energy modulation and transform it into uncorrelated energy spread. This happens by virtue of the linear transport matrix terms from the undulator to the chicane end.

Smearing becomes effective when the electrons' phase shift is larger than the laser wavelength. The design assumes the phase shift is twice the modulation wavelength for a safe operation, that is

$$\sqrt{\langle \Delta z^2 \rangle} = 2\pi \sqrt{(R_{51}\sigma_{x,W})^2 + (R_{52}\sigma'_{x,W})^2 + (R_{56}\sigma_\delta)^2} \geq 2\lambda_L \tag{5.1}$$

where, however, $R_{51} = 0$ due to the achromatic lattice. $\sigma'_{x,W} = \sqrt{\varepsilon_{n,x}/(\gamma_0 \beta_W)} \approx 10\,\mu$rad is the RMS beam divergence at the waist and $\sigma_\delta \approx 10^{-5}$ is the relative uncorrelated energy spread.

The coefficients R_{52} and R_{56} can be expressed as function of the chicane geometry:

$$\begin{aligned} R_{52} &\approx \theta \left(l_d + l_b \right) \\ R_{56} &\approx \theta^2 \left(l_d + \tfrac{2}{3} l_b \right) \end{aligned} \tag{5.2}$$

where the approximation is for small dipole bending angle $\theta << 1$, l_d is the length of the outer arms and l_b is the dipole arc length. It is apparent that the effect of energy smearing by R_{56} is θ-times smaller than the effect induced by the angular dispersion R_{52}, and the former can therefore be neglected. The minimum value of the latter can be calculated from Eq. 5.1 as ≈ 23 mm. This translates also into the value of the horizontal dispersion function η_x at the center of the chicane, and to approximately the distance of the deflected trajectory from the straight one. Thus, the chicane vacuum chamber needs to be to be 33 mm wide horizontally. The non-deflected electron beam propagates 5 mm from the right hand wall. When deflected, the beam translates 23 mm from the straight trajectory ($R_{52} \approx 23$ mm) so that 5 mm are left from the chamber left side. The chamber is assumed to be round in the outer dipole magnets, and tapered to an elliptical geometry internally to the chicane.

The dipole length is 0.1 m and Eq. 5.2 defines the length of the outer drifts for the specified R_{52} as function of the dipole bending angle. The total chicane length is the sum of the 4 dipole lengths, outer drifts, undulator length and additional 0.3 m to insert diagnostics at the undulator ends (see Figure 5.15). Such lengths are shown in Figure 5.16. The total LH system is 1.4 m long for 5 deg (0.087 rad) bending angle. The dipole field is $B_{y,b} = \frac{E[\text{GeV}]}{0.2998} \frac{\theta_b}{l_b} = 0.34$ T. Fig 5.16 also shows the horizontal emittance growth induced, respectively, by the particles' energy change in the undulator dispersive region as a consequence of the interaction with the laser beam (slice emittance growth), and by CSR in the four dipole magnets (see Eq. 5.3). The former contribution is estimated in the pessimistic assumption of full chromatic filamentation of the transverse phase space and plotted for a fixed R_{52}. The latter is the sum in quadrature of the contribution from each dipole [106]. It is shown that 5 deg bending angle ensures negligible emittance growth from both effects.

$$\begin{aligned} \left(\frac{\Delta \varepsilon_x}{\varepsilon_x} \right)_{chrom} &\leq \frac{1}{2} \left(\frac{R_{52} \sigma_{E,LH}}{\sigma_{x,W} E} \right)^2 \\ \left(\frac{\Delta \varepsilon_x}{\varepsilon_x} \right)_{csr} &\approx 7.5 \cdot 10^{-3} \frac{\beta_x}{\gamma_0} \left(\frac{N_e r_e l_b^2}{R^{5/3} \sigma_z^{4/3}} \right)^2 \end{aligned} \tag{5.3}$$

with N_e the number of electrons in a bunch, r_e the classical electron radius, R the dipole's curvature radius and σ_z the RMS bunch length.

5.1.3.5. Summary Table

Table 5.8 summarizes the laser heater system specifications. The nominal values refer to the RMS induced energy spread of 12 keV at the beam energy of 120 MeV. The ranges are evaluated for up to 30 keV RMS induced energy spread.

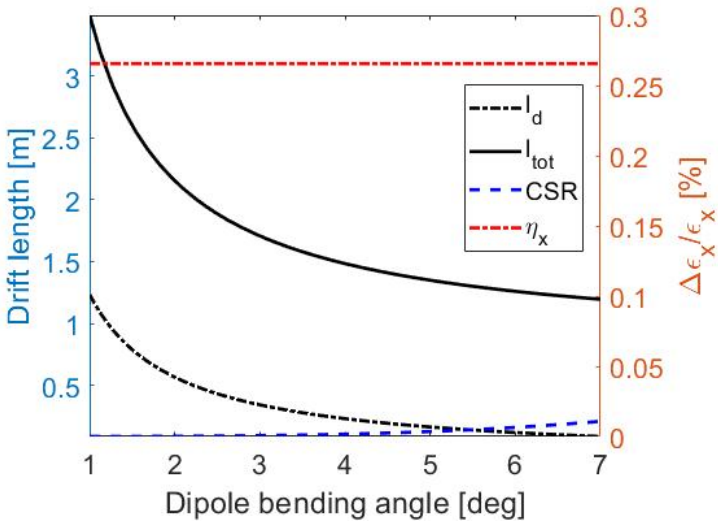

Figure 5.16.: Outer drift and total chicane length (left axis) and horizontal emittance growth induced by horizontal dispersion and CSR (right axis) vs. dipole bending angle, for fixed $R_{52} = 23\,\text{mm}$.

Table 5.8.: Laser heater specifications.

Electron beam	**Units**	**Nominal Value**	**Range**
Charge	pC	75	≥ 300
Duration, RMS	ps	3	1–3
Energy	MeV	120	100-140
Natural energy spread, RMS	%	0.001	≤ 0.2
Norm. Emittance (x,y)	μm rad	0.2	0.15–0.3
Betatron Function at Und. (x,y)	m	7.5, 7.5	≤ 25
Laser beam			
Wavelength	nm	780	760–800
Bandwidth, FWHM	%	1	<5%
Peak power	MW	0.1	≤ 5
Duration, FWHM	ps	20	10–30
Pulse energy	μJ	2	≤ 100
Repetition rate	kHz	0.1,0.25,1	
Average power	mW	2	≤ 100
Size at waist, RMS (x,y)	mm	0.15	0.05–0.300
Undulator			
Period length	mm	40	
Vertical gap, full	mm	21	15–28
Undulator parameter		1.5	1.2–1.8
Peak field	T	0.4	0.1–1.1
Number of periods		8	
Total length	m	0.32	≤ 0.36
Chicane			
Number of dipoles		4	
Bending angle	mrad	87	0–100
Arclength	m	0.1	≤ 0.15
Peak field	T	0.4	≤ 0.8
Outer drift length	m	0.15	
Total length	m	1.4	1.3–1.8
Maximum horiz. dispersion	mm	23	≤ 30
Chromatic emittance growth	%	< 0.5%	
CSR emittance growth	%	< 0.1%	

5.2. RF Systems

5.2.1. Introduction

The CompactLight linac is composed of 24 X-band RF modules which provide a beam energy of up to 5.5 GeV at a repetition rate of 100 Hz and an energy of 2.4 GeV at a repetition rate of 1 kHz. This flexibility in operation is a major innovation of CompactLight and allows a wide range of experiments to be carried out. The linac has a large impact on facility performance and represents a major part of the overall cost, consequently a significant effort was put into its design. The linac begins at the output of the injector and first bunch compressor. At this point the beam is fully relativistic, with an energy of 300 MeV, and the linac ends when the beam has achieved its final energy of 2.5 to 5.5 GeV, depending on operating mode. Two additional X-band RF modules are added in the low energy beam line as part of Upgrade-2. The linac is composed of repeated modules of standardized layout and composition, with three types that incorporate four, two and one quadrupole per module for low, medium and high energy parts of the linac respectively.

The most important design considerations for the RF module are optimising beam dynamics in the linac, maximising power efficiency, providing power source configurations with required operating modes, and minimising overall cost. The main components of the RF module are the modulator, klystron, pulse-compressor, waveguide network, and accelerating structure. The accelerating structure design is of crucial importance since it interacts directly with the beam, determining issues such as emittance growth and power efficiency of acceleration.

The RF part of the linac module is described in Section 5.2.2. The main subsystems–support and alignment, vacuum and focusing magnets–are described in Sections 5.2.3, 5.2.4, and 5.2.5 respectively. Layout summaries which describe integration are presented in Section 5.2.6. A summary of the discussion of the strategy of industrial supply is given in Section 5.2.7—for more details on this particular topic, see CompactLight deliverable D4.3.

In addition to the main X-band linac RF modules, CompactLight contains other high-power RF systems that carry out important functions: two sub-harmonic separator systems, a harmonic energy spread linear system and four POLARIX deflecting diagnostic systems. These systems were added during the design process and significant work on them was carried out. Descriptions of the former two systems have been added to this report. The POLARIX systems is described in the CompactLight diagnostics deliverable D8.1.

Two sub-harmonic separator systems are used in CompactLight to direct the two successive bunches in a train into the two respective beamlines. In one location this is so that one bunch goes into the low energy beam line and in the other so that the two bunches go into their respective undulators for double pulse light production, enabling FEL pump-FEL probe experiments. The sub-harmonic separator system operates at 3 GHz and is described in Section 5.2.8. The sub-harmonic separator is also referred to as a TDC (Transverse Deflecting Cavity)

CompactLight has implemented a harmonic lineariser system as in other XFELs. However, because the injector uses C-band accelerating structures, we have chosen a linearising frequency of 36 GHz, in the Ka-band. Such a high frequency is not found in existing user facilities however is close to the 30 GHz frequency once used by the CLIC study and thus exploits years of development. Commercial power sources are not available thus CompactLight has made comprehensive designs for two power source options, a gyro-klystron amplifier and a multi-beam klystron Ka-band power source. The associated pulse-compressor system, low-loss waveguide transport and lineariser structure have been designed as well. The Ka-band (36 GHz) harmonic lineariser system is described in Section 5.2.9.

A layout of the facility is shown in Figure 5.17 and the location of the different systems described above are indicated.

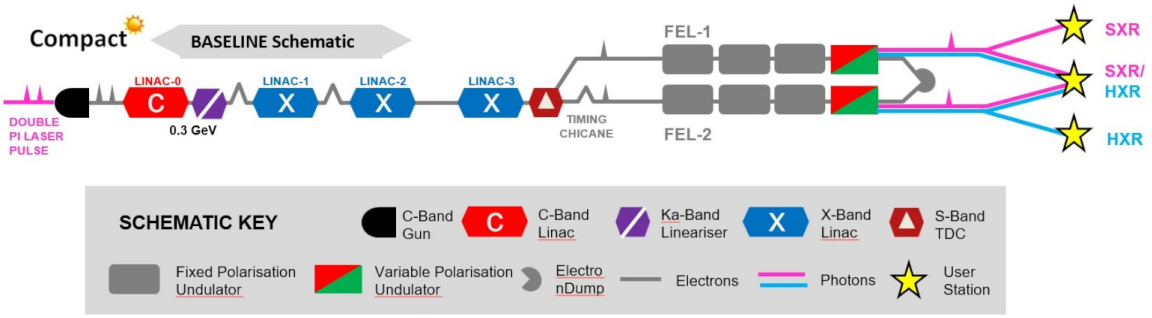

Figure 5.17.: Schematic layout of the CompactLight facility. The RF systems covered in this report are the X-band linac module, the Ka-band lineariser and the S-band bunch separator (TDC).

5.2.2. RF System

The accelerating structures must be designed to enable special operating conditions that give CompactLight unique experimental capabilities; multiple gradient and repetition rate combinations and two-bunch operation. The extreme gradient and repetition rate combinations are: a high-gradient 65 MV/m at 100 Hz mode and a high-repetition rate 30 MV/m at 1 kHz mode. The structure parameters are optimized for both radio-frequency and beam dynamics performance and have higher order transverse mode suppression for stable two-bunch operation. The cooling circuit has been designed to accommodate the high average power of the high-repetition rate mode and optimized for minimum difference between operating modes.

The CompactLight linac is composed of X-band modules, described in detail in the CompactLight deliverable D4.2, which each contain four Travelling Wave Accelerating Structures (TWASs) fed by a 50 MW klystron and pulse-compressor system. By using pulse compression, one klystron can feed several structures through a waveguide network. Thus, the X-band linac can be composed of a sequence of RF modules, each one with four structures.

There are several important parameters to be determined during optimisation, for example the structure length and the profile of the diameters of the irises along the structure length as well as their thicknesses. These parameters directly influence the total number of structures that are needed for each module and for the linac as a whole, which in turn determines the total required number of klystrons and pulse-compressors. One important goal is to maximise the RF efficiency, which has the consequence of minimising the total number of klystrons. The average accelerating gradient and the average iris radius of the structure, which defines the compactness and influences the stability of the machine respectively, are provided as input specifications to the electromagnetic design. The study of the electromagnetic design is followed by investigating the thermo-mechanical properties, which are presented in Sections 5.2.2.1 and 5.2.2.1. Finally in Section 5.2.7 the route towards an industrialisation of the accelerator is described based on a breakdown of the various production processes.

5.2.2.1. Electromagnetic Design and Optimization of the Accelerating Structure

There are many steps in the design and optimization of a linac based on traveling-wave structures. The most important parameters are the ones that directly influence the total number of structures that are needed. As already said, one important goal is to maximise the RF efficiency, which has the consequence of minimising the total number of klystrons. The most important steps used during optimisation are listed below [107]:

- Optimisation of the regular cell of the accelerating structure, with the electromagnetic simulations according to beam dynamics requirements.

The design of the regular cell has been carried out using the simulation tool ANSYS HFSS [81]. A sketch of the cell geometry is shown in Figure 5.18, where a is the cell iris radius, b the outer radius, t the iris thickness, r_0 the radius of the cell rounding and r_1/r_2 is the aspect ratio of the elliptical profile of the iris. The cell length d is determined by specification of the operating frequency of 11.9942 GHz and a cell phase advance of $2\pi/3$, and is equal to 8.332 mm.

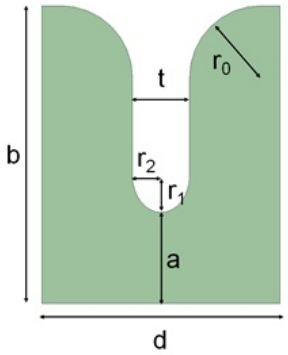

Figure 5.18.: Sketch of the single cell with main parametrized dimensions.

The design process aimed at minimising the modified Poynting vector normalized to the average accelerating gradient Sc_{max}/E^2_{acc} while maximizing RF efficiency. The latter is quantified by the shunt impedance per unit length R parameter. An elliptical shape of the irises was implemented in order to minimize the peak modified Poynting vector on its surface. It has been found that $r_1/r_2 = 1.3$ is a good compromise between expected high-gradient performance and efficiency. An r_0 equal to 2.5 mm has been chosen.

Once the iris shape was defined, the main cell parameters (shunt impedance per unit length R, quality factor Q, group velocity v_g, normalized modified Poynting vector Sc_{max}/E^2_{acc}) were calculated as a function of the iris radius a and the iris thickness t. The a value was varied in the 2 mm to 5 mm range, while t value in the 1.5 mm to 2.25 mm range. On the basis of these computed parameters, it was possible to complete the design of the accelerating structures.

- Analytical optimization of the structure length.

  With the average iris radius of the structure defined, the next step in the design of the structure as a whole was to find the optimal length of both Constant Impedance (CI) and Constant Gradient (CG) structures. This required also simulating the RF pulse-compressor, so formulae of the SLED pulse compression system [108] for constant impedance and constant gradient structures [109, 110] implemented in MATLAB code were used [101, 107, 111].

  The effective shunt impedance as a function of the accelerating structure attenuation is reported in Figure 5.19 for a CI and a CG structure, while the optimal structure length as function of the structure average iris aperture is reported in Figure 5.20. For the CI structure the optimal length is 0.890 m while for the CG structure it is 0.818 m. These values have been used as the basis for a numerical optimization of the iris tapering as described in the following section 5.2.2.1.

- Iris tapering

  Two-bunch operation in CompactLight is needed for FEL pump-FEL probe experiments. Two-bunch operation however introduces the important design consideration of the long-range transverse wakefield behaviour of the accelerating structure. This is because the long-range transverse wakefield excited by the front bunch affects the trajectory of the second bunch which causes an emmitance growth. Long-range transverse wakefield suppression is required. Fortunately this

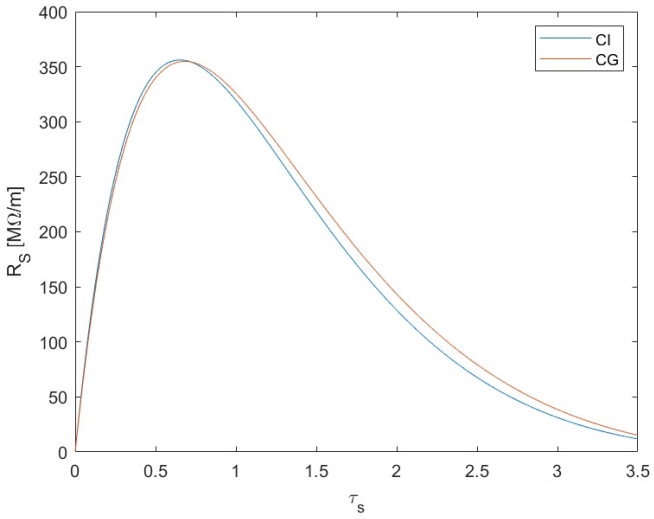

Figure 5.19.: Effective shunt impedance as a function of the section attenuation for CI and CG structures.

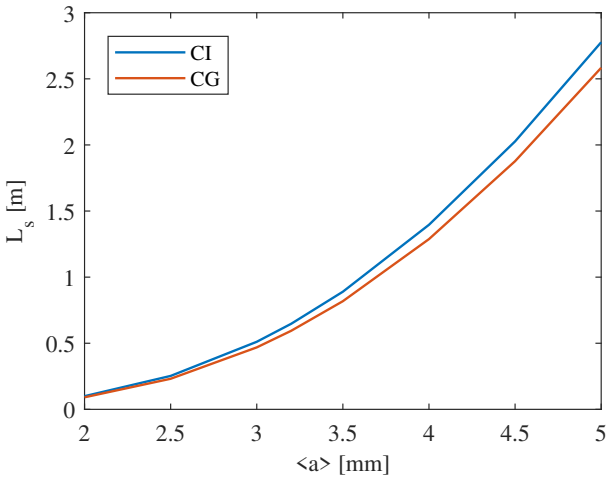

Figure 5.20.: Optimal structure length as function of the average iris radius for CI and CG structures.

can be achieved by a variation of the iris diameter along the length of the structure, which results in a detuning of the synchronous frequency of the most important transverse modes. This causes a decoherence in the transverse wake and thus a suppression of its amplitude [112–116].

The bunches will be separated and transferred into two FEL lines after the linac acceleration. The separation is achieved by a sub-harmonic transverse deflecting structure which is working at S-band (2.998 GHz). Thus the spacing for S-band between the two bunches should be $n+0.5$ rf cycles (0.5, 1.5, 2.5, etc.), where n is an integer from 0. This results in a spacing of $4n+2$ rf cycles at X-band. The rf design of the transverse deflecting structure is presented in the CompactLight deliverable D4.2.

A Gaussian-like aperture tapering combined with a linear iris thickness tapering was adopted to minimize the long-range transverse wakefield and a multi-parameter optimization of the tapering parameters was performed and compared to more standard linear iris design.

The long-range transverse wakefield of the Gaussian-like iris design is shown in Figure 5.21.

The blue line is the wakefield of the linear iris design while the red line is the wakefield of the Gaussian-like iris design. The optimum compromise between fundamental-mode performance and a minimum bunch spacing distance gives a bunch spacing of 10^{th} RF cycle. The wakefield of the new design at the second bunch is 3.65 V/pC/mm/m. The envelope of the wakefield is smaller than that of the linear iris design at the 10^{th} RF cycle, ensuring more robust operation.

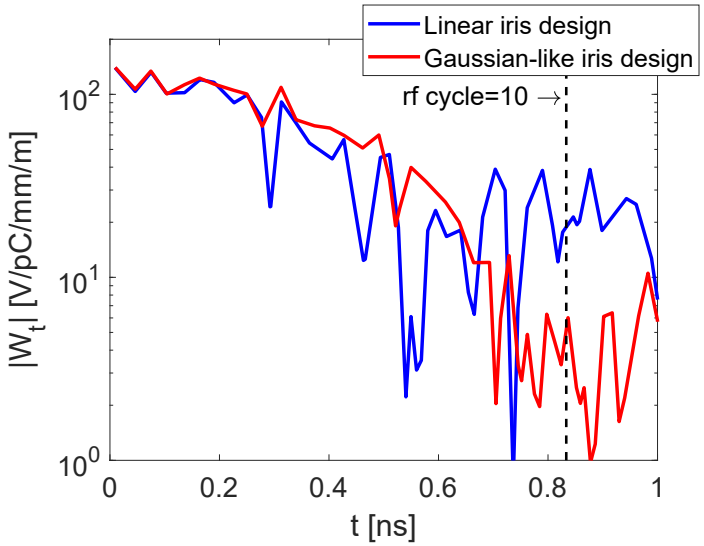

Figure 5.21.: Long-range transverse wakefields of the initial design and the gaussian-like iris design.

- Input and output RF power couplers

  The input and output RF power couplers are of the magnetic coupling type with a *z*-type geometry to minimize pulsed surface heating. A dual feed and racetrack geometry avoids dipolar, and strongly minimises quadrupolar, components of the electromagnetic fields respectively that can adversely affect beam dynamics. Full details of RF coupler design can be found in the CompactLight Deliverable D4.2.

  From a scan of coupler dimensions, the obtained reflection coefficient at the input port is -44.9 dB for the input coupler and -37. dB for the output one. For the input coupler, there is a pulsed heating of 24 °C. This value can be considered absolutely safe for high field operation.

- Mechanical and thermal design of the accelerating structure

  One important aspect of the optimised design of the accelerating structure is the thermo-mechanical simulation work, that informs the design of a cooling system to handle the average thermal load during operation. The main input for the optimisation is the calculated average dissipated power per structure. The preliminary design of the cooling system was based on 4 cooling channels distributed around the cells. The dimensions and the distribution of the cooling channels were studied with a thermal analysis performed with a commercial code. In the simulation different cooling scenarios were considered e.g. by varying the temperature, the water flux and the lengths of the channels. The maximum difference in temperature of the accelerating part of the cell is the main parameter contributing to the cell detuning. Therefore, deformation due to this difference in temperature was used to gauge the results of the simulations. The design was done in two iterations with an intermediate correction of RF dimensions based on the first iteration of the thermal results.

  The worst case heat load is expected at 1000 Hz repetition rate leading to 2.2 kW dissipated power in the structure. The deformation is mostly caused by the difference between the operating

temperature and the temperature at which the disks were made and measured (20 °C). After first verification, a second iteration of the simulations was done, again for 1000 Hz repetition rate. This iteration included variable thickness of the cavities and additional details such as thermocouple channels. The results from the study are presented in Table 5.9. The deformations due to the temperature difference within a disk are also included in the table.

Table 5.9.: Results after RF verification

	Temperature min - max (ΔT) [°C]	**Deformation due to temperature difference with the disk μm**	**Total deformation μm**
Disk 2	36.5 - 38.1 (1.6)	0.10 - 0.40	1.09 - 11.1
Disk 54	37.7 - 39.7 (2.0)	0.12 - 0.48	0.97 - 12.0
Disk 106	37.1 - 38.9 (1.8)	0.11 - 0.41	0.73 - 11.5

In the second iteration the deformation increased slightly, but can be corrected if the dimensions are adjusted for the operating temperature. The deformation due to the temperature difference in the disk itself has not changed, staying below 0.5 µm. An optimization for the 100 Hz repetition rate with the heat load of 1000 W was also studied. The full details of this modelling, as well as that for the 1000 Hz case, can be found in Deliverable D4.3.

The final, main parameters of the accelerating structure are reported in Table 5.10.

5.2.2.2. RF Module Layout

From the considerations in Section 5.2.2.1, it was found that a good compromise between RF performance and wakefield is represented by a 0.9 m structure (109 cells) with a Gaussian profile of the iris diameter. These structures are optimally powered and assembled in a groups of four, fed by a single klystron and one SLED pulse-compressor. A second klystron is added for high repetition rate operation, as will be described in more detail below. This arrangement forms the RF module, a basic unit that is repeated to achieve the desired beam energy. Full details of RF module design can be found in the CompactLight deliverable D4.2.

In Table 5.10, the main parameters of the structures and the module are reported while, in Figure 5.22, a sketch of the RF module is shown.

A symmetric binary tree layout has been adopted for the power distribution. The employment of a circular overmoded waveguide, connecting the modulator hall with the linac hall, minimises the attenuation of power. Two mode converters are then necessary at the ends.

A 50 MW klystron is used for low repetition rate operation (100 Hz and 250 Hz) while a 10 MW one is employed for high repetition rate operation (up to 1 kHz). The first RF source is the CPI VKX-8311A klystron [117] that can provide 50 MW peak power, with a pulse-length of 1.5 μs and a repetition rate of 100 Hz. This source is under routine use by the CLIC group at CERN in the X-Boxes [118, 119] and will be installed at the upcoming test facility TEX at INFN-LNF in Frascati. The second source is a prototype designed by CPI or Canon that is currently still in its development phase. Another valid option is the Canon E37113 klystron that can provide 6 MW peak power, with a pulse-length of 5 μs and a repetition rate of 400 Hz [120]. This klystron is also used at CERN, for the XBox-3 [121]. In this case, two klystrons of this kind are required for each RF module.

The external quality factor of the SLED compressor has been chosen in order to maximise the RF efficiency of the module (i.e. the effective shunt impedance) while keeping the modified Poynting vector in the accelerating structure well below the theoretical threshold of 4 W/µm^2 [75]. This value should

Table 5.10.: Main parameters of the RF structures and modules

Parameter	**Units**	**Value**		
Frequency	GHz	11.994		
Phase advance per cell	rad	$2\pi/3$		
Average iris radius a	mm	3.5		
Iris radius a	mm	4.3-2.7		
Iris thickness t	mm	2.0-2.24		
Number of cells per structure		109		
Accelerating cell length	mm	8.332		
Structure length L_s	m	0.9		
Group velocity v_g/c	%	4.7-0.9		
Filling time t_f	ns	146		
Peak klystron power (100 - 250 Hz)	MW	50		
Peak klystron power (1000 Hz)	MW	10		
RF pulse-length (250 Hz)	µs	1.5 (0.15)		
Waveguide power attenuation	%	≈ 10		
Unloaded SLED Q-factor Q_0		180000		
External SLED Q-factor Q_E		23300		
Shunt impedance R	MΩ/m	85-111		
Effective shunt impedance R_s	MΩ/m	349		
Peak modified Poynting vector	W/µm^2	3.4		
Repetition rate	Hz	100	250	1000
SLED		ON	OFF	ON
Required klystron power	MW	44	44	9
Available klystron output power	MW	50	50	10
RF pulse-length	μs	1.5	0.15	1.5
Average accelerating gradient	MV/m	65	30	30
Energy gain per module	MeV	234	108	108

not be exceeded in order to provide stable operation at the specified accelerating gradient at a pulse-length of 200 ns. In the CompactLight case, the pulse-length is 146 ns which gives a theoretical limit of 4.4 W/µm^2.

The 250 Hz operating mode can be used with the baseline layout, in which only the 50 MW CPI klystrons are present. In this case, the klystron pulse is reduced to the structure filling time and the SLED compressor is by passed. This results in a lower input power to the accelerating structures so this operating mode has a maximum accelerating gradient of 30 MV/m. 30 MV/m is also produced in the 1 kHz repetition rate.

In the **Baseline configuration**, as seen in Figure 5.17, the linac module consists of a single RF source that can run in dual mode: high-energy at repetition rates of 100 Hz and low-energy at 250 Hz. Two upgrade scenarios are foreseen for the RF system. In **Upgrade I** the same klystron can be used with higher repetition rate, 250 Hz, for providing up to 2 GeV for photon production. For **Upgrade II**, shown in Figure 5.23, a second klystron, with 10 MW output power and a 1 kHz repetition rate, is added and connected to the waveguide system via a high-power switch, shown in Figure 5.22. With such a configuration, the facility can be operated in a high-energy, moderate repetition rate mode and in a low-energy, high repetition rate mode. The primary cost drivers of the RF module are the accelerating

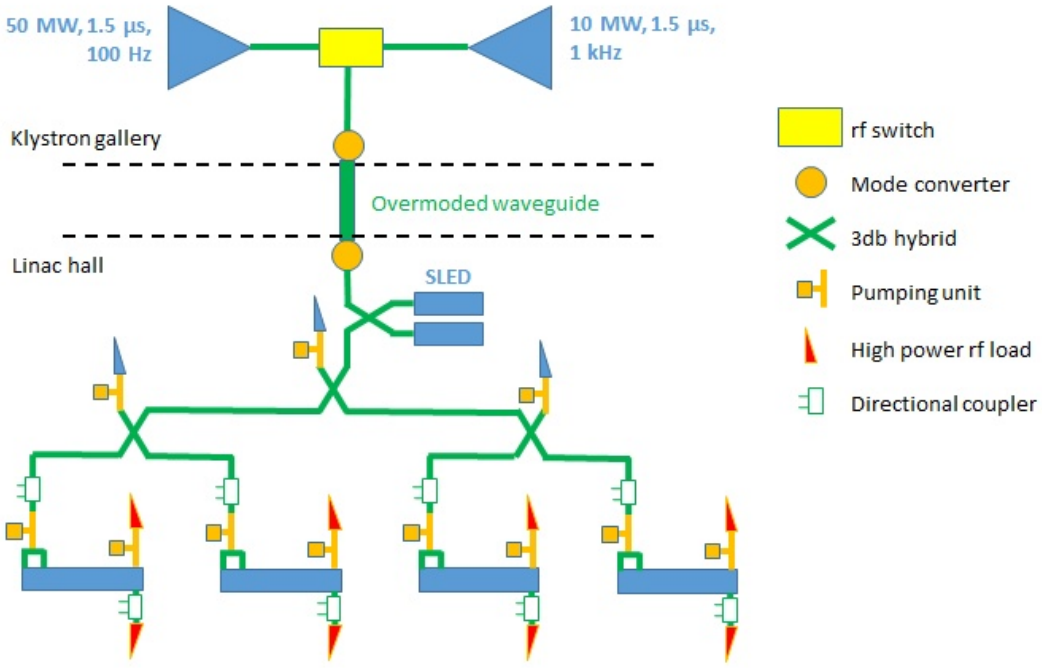

Figure 5.22.: Sketch of the RF module.

structures, klystrons and modulators. The latter two are commercial items so costs and design are well understood and they will be presented in sections below. Complete commercially supplied X-band accelerating structures are not currently available and until now producing these structures has required a combining fabrication steps at both accelerator laboratories and industrial suppliers.

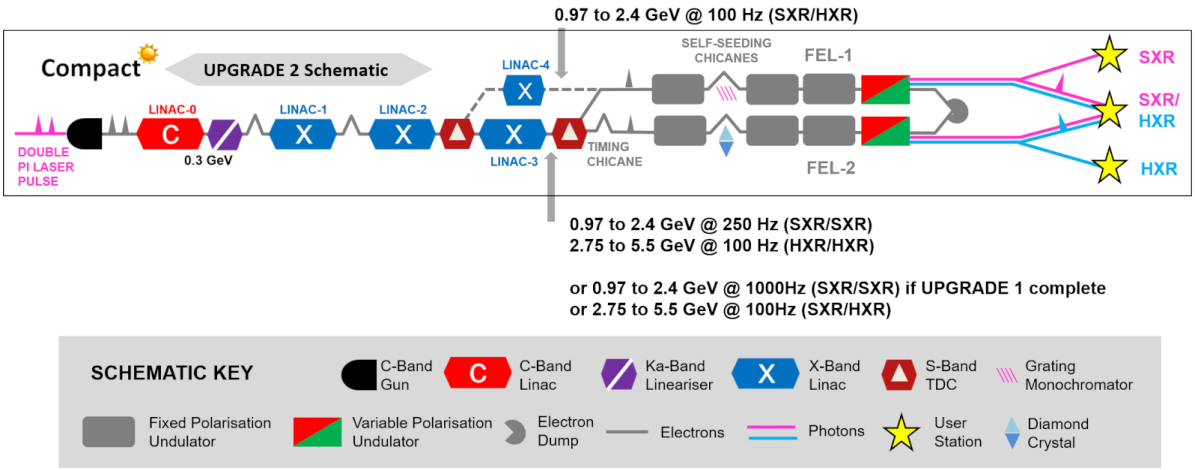

Figure 5.23.: Schematic layout of the CompactLight facility including Upgrade II.

5.2.2.3. RF Power Sources and Components

The main RF source adopted for the RF module is the CPI VKX-8311A klystron [117]. It is a pulsed klystron operating at 11.994 GHz, 50 MW peak power, 5 kW average power. It is electromagnet focused,

liquid cooled and the waveguide output is WR-90. For the high repetition rate operations two options are available: a new source from CPI and/or Canon presently still in the R&D phase, or the Canon E37113 klystron already available [120]. In case of adoption of the Canon E37113 model, 2 klystrons per module would be needed in order to guarantee the 30 MV/m gradient at 1 kHz. We remark that both the CPI VKX-8311A and the Canon E37113 klystrons have been successfully tested and are currently used in the CLIC test facilities, so they represent a reliable solution for the machine. Direct consequences of the activities of the CompactLight collaboration are the R&D activities necessary for the 1 kHz repetition rate 10 MW klystron which are now underway at the companies.

The state of the art modulator technology for pulsed linacs is based on solid state HV modulators. A reliable solution for CompactLight is the Scandinova K series modulator [122]. Thanks to the modular design, the K series is able to support RF peak power up to 100 MW. A summary of the parameters of X-band power sources relevant for CompactLight under development at the time of writing of this report can be found in Deliverable 4.2.

The main high-power RF components of the module are: 3 dB splitters, directional couplers, hybrids, phase shifters, loads, waveguides and the SLED pulse-compressor. These can be based on the high-power components developed at CERN by the CLIC collaboration and design and test of these components are described in [123]. The main components, with their key parameters, are detailed in Figure 5.24.

Two options for the RF loads are stainless steel high-power loads [124] and 3D printed loads such as the compact and spiral loads, both designed and tested at CERN [125]. Stainless steel high-power loads have reached 31 MW at 50 Hz and 30 MW at 200 Hz depending only on the power and attenuation from the upstream structure. 3D printing technology has also been successfully used to fabricate RF loads. This allows complex geometries to be produced from materials such as titanium. The power splitter is based on that developed and high-power tested in the CLIC study [126, 127].

The adopted pulse-compressor, described in [128, 129], is the SLEDX developed at CERN by the CLIC group (Figure 5.25). It is a compact device of 1 m length where the storage cavities operate in the H_{01} mode. The cavities are 45 cm long and have unloaded Q-factor of 1.8×10^5. With such a device it is possible to obtain a flat pulse with a power gain of 4.3. For CompactLight there is no need to have flat pulses so larger (average) power gains might be achieved. The simulations and design used the SLED cavity concept indicated that implementing a Barrel Open Cavity (BOC) type of pulse-compressor would result in improved performance [102].

5.2.3. Support and Alignment System

All components influencing the electron beam need to be positioned with great care in order not to degrade the beam, in particular through the generation of short-range transverse wakefields. Beam dynamics simulations indicate that the centre of each component along the beamlines needs to be positioned within a horizontal and vertical tolerance of 100 μm. By first aligning the individual components, such as the accelerating structures, beam screens and magnets relative to each other on the module girder, the entire girder can then be aligned with respect to successive girders and the beam. A 3D engineering design view of a typical XLS module can be seen in Figure 5.26.

Four 103 cm long accelerating structures are installed on top of one common girder into one CompactLight Module. Each of the structures is aligned by an individual 6 DoF adjustment system to a precision within 10 μm rms with respect to the beam axis. The module also supports quadrupole magnets and their associated Beam Position Monitors (BPMs). As described in Section 5.2.5, the magnets are equipped with integrated steering dipoles, in order to avoid an expensive motorised platform on top of the common girder for moving the quadruple magnet during operation. The girder material considered is black steel, which is supported and aligned by means of jacks that have already been used for Linac4 installation at CERN.

The survey and alignment philosophy is very similar to the one proposed for eSPS at CERN documented in the CDR [130]. Each accelerating structure and quadrupole will be fiducialised independently,

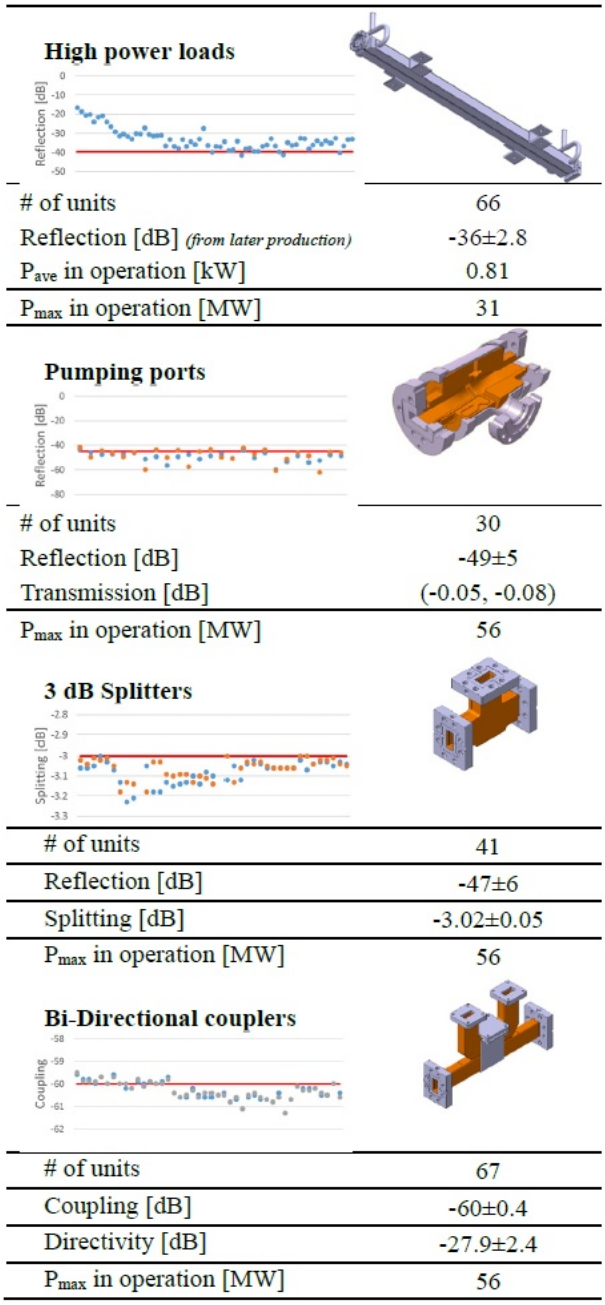

Figure 5.24.: Main parameters of RF components developed by the CLIC group at CERN.

e.g. its mechanical axis will be determined w.r.t. external targets, at a metrology lab or using a laser tracker. Once all the components are fiducialised, they will be pre-aligned on the common girder w.r.t. the geodetic network using laser tracker measurements to better than $\pm$ 0.3 mm. Different options exist for the smoothing (final relative alignment) of the modules to better than $\pm$ 0.1 mm and can be chosen at a later stage. Full details are available in Deliverable D4.2.

5.2.4. Vacuum System

The vacuum requirements for CompactLight have not been studied in detail, but similar needs were assumed as for SwissFEL. By designing the vacuum system for the various linacs based on local

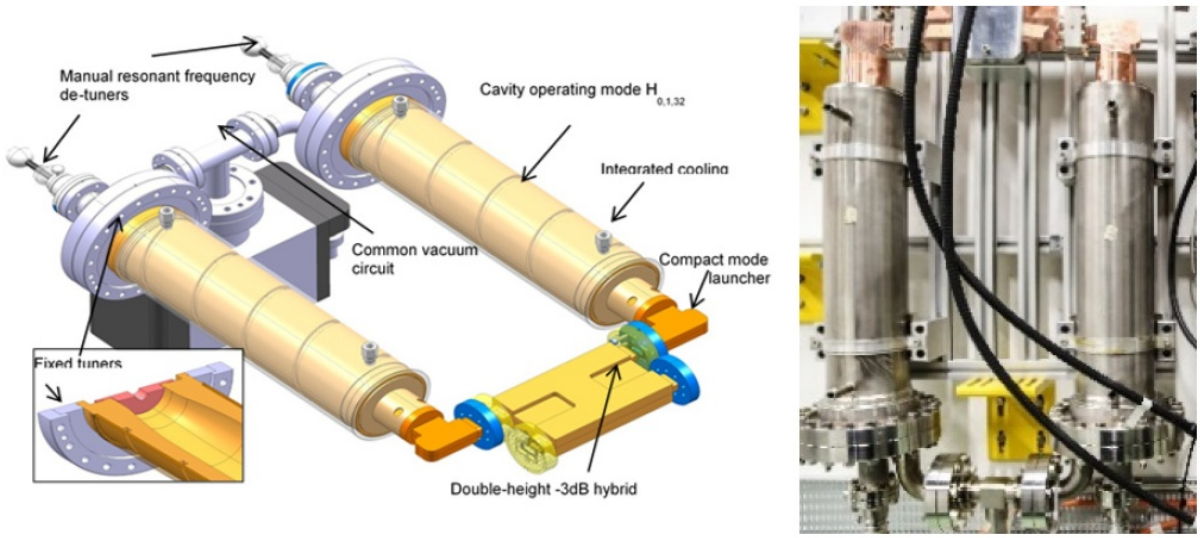

Figure 5.25.: SLED pulse-compressor 3D drawing (left) and as installed in the X-band facilities at CERN (right).

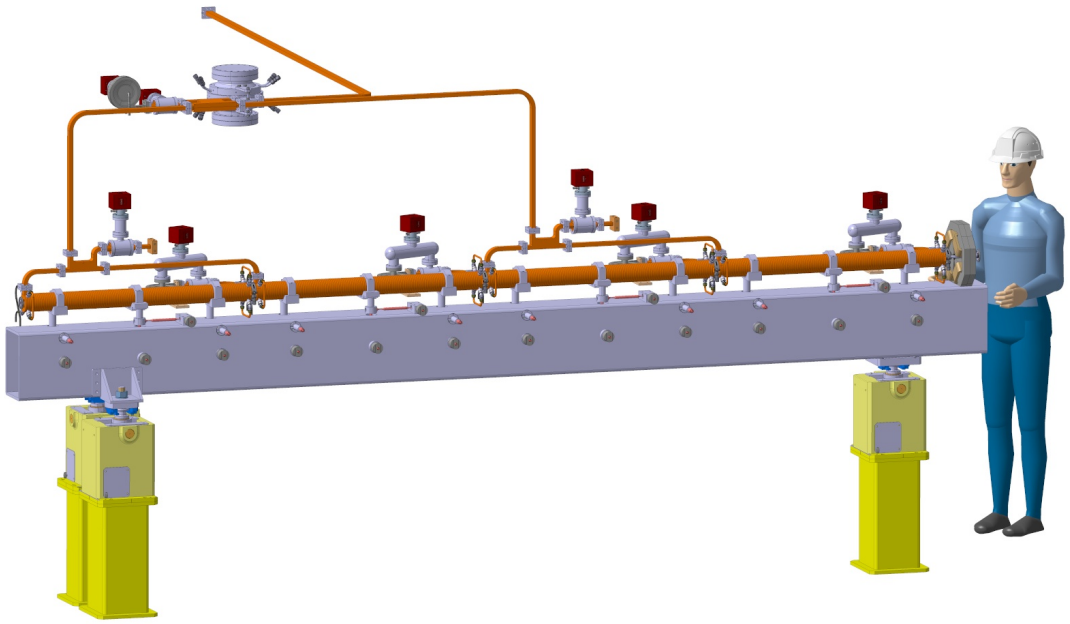

Figure 5.26.: Engineering design 3D view of a typical XLS module.

compact pumps fully integrated in the module design, these requirements can certainly be met. The resulting system is very similar to the systems considered for CLIC [131] and eSPS [130]. It consists of NEG cartridge pumps installed directly on the accelerating structure vacuum manifold. Vacuum tests have been carried out on a similar system for CLIC and documented in the Project Implementation Plan [131]. These tests were performed on dedicated accelerating structures with a NEG pump with nominal pumping speed $100\,l/s^{-1}$ combined with a sputter ion pump providing $5\,l/s^{-1}$ pumping speed. After activation of the NEG cartridge, the pressure decreased with time (1/t) and reached 3×10^{-9} mbar

along the beam axis after 100 h pumping.

In addition, a T-shape connector has to be installed on each vacuum line. Installed on the pumping port of the AS, it is equipped with a NEG pump on one side and a manual all-metal right angle valve on the other side allowing the rough pumping and an eventual leak detection procedure for each module.

Vacuum gauges, a set of Pirani and Penning gauges, are installed on each module. This allows pressure measurement from atmospheric pressure down to 10^{-10} mbar. This is needed during operation and commissioning of the vacuum system. Vacuum gauges provide also signals for interlocks of vacuum sector valves and machine protection systems.

For flexibility and safety reasons it was decided to contain each accelerator module in its own longitudinal vacuum sector. Hence, a space reservation of 10 cm is foreseen at the beginning of each module for a vacuum sector valve. These are off-the-shelf items and can be commercially provided with ease and easily integrated.

5.2.5. Magnets

Quadrupole magnets are necessary for guiding the beam during transport along the various linacs (see for example Figure 5.17). These are arranged in a FODO lattice configuration and are fully integrated in the various versions of the XLS modules (see section 5.2.6). The magnetic design for a single standard quadrupole magnet used through the facility has been developed taking into account the requirements specific to the CompactLight beams as shown in Figure 5.27. The magnet length has

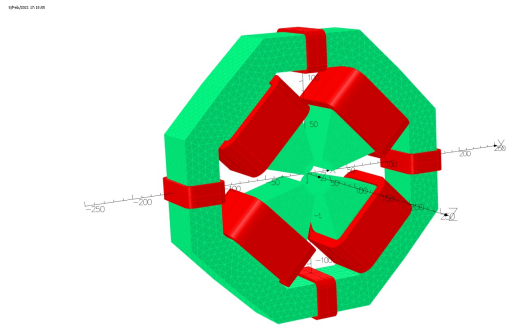

Figure 5.27.: Quadrupole design for the XLS linacs including vertical and horizontal corrector coils.

been minimized so that the filling factor for RF structures in the various different linacs can be kept high (see section 5.2.6), thus giving highest overall accelerating gradient and minimum facility length. The overall envelope of the magnet and other key numbers are summarized in Table 5.11.

The quadrupole magnets have been designed to be used at all positions, thus energies, along the linac. Hence, only one magnet design needs to be developed and manufactured reducing cost and increasing reliability. Each of the magnets needs individual powering in order to account for the different energies. Nevertheless, having one single quadrupole design for all the accelerator makes this a very economical choice.

As for the requirements of beam steering through the accelerator, given the moderate energies of the electron beam the choice was made to include corrector coils directly on the magnet yoke instead of an adjustable mechanical support capable of moving the entire magnet. This means that the magnets will be pre-positioned with respect to the accelerating structures on their common girder and then will stay in place. Beam position monitors attached are integrated in the quadrupoles and are described in detail in the ComapctLight deliverable D8.1.

Table 5.11.: XLS Quadrupole technical details.

Parameter	Units	Value
Integrated max. strength	T	2.72
Aperture	mm	25
Max. Gradient	T/m	40.5
Conductor cross-section	mm	10 x 48
Conductor current density	A/mm^2	5.4
Steel yoke length	mm	52
Magnetic length	mm	67
Total length including overhang	mm	82
Height and width	mm	302
Height and width including corrector coils	mm	310

5.2.6. System Integration

For the linacs (as can be seen for example in Figure 5.17) a specific standardised ”module” has been designed and is repeated as often as necessary for a given linac. This approach minimizes the number of variants and enables series production as much as possible. Powers for the different operation modes can be found in section 5.2.2. The accelerating structure temperature stabilisation for the various different operation modes is achieved by demineralised water circulation at the reference temperature of 28 °C. The water consumption is estimated in the order of 6 litres/min per accelerating structure.

For the various linac sections, beam dynamics imposes different distributions of the optical elements resulting in three different spacings of the quadrupoles along the entire beam line: one accelerating structure per quadrupole, two per quadrupole and four per quadrupole. Hence the module layout has to accommodate this variation and is split up into three different module layouts detailed hereafter.

5.2.6.1. Low Energy Module

The schematic module layout for the lowest energy sections of the beam line is shown in Figure 5.28. The distinct characteristic of the low energy module is that there is a single accelerating structure in between the quadrupoles. This also makes this version of the module the longest of the three with the lowest RF fill factor. The impact is limited since only a few of this module type are needed. The powering scheme (100 Hz - 1 kHz) can be switched between the two klystrons remotely, and no change in hardware is necessary. This makes the overall machine quite flexible and new operation scenarios could be applied multiple times per day.

5.2.6.2. Medium Energy Module

Figure 5.29 shows the schematic layout of the medium energy module with two accelerating structures per quadrupole which shortens the module considerably and increases the RF fill factor with respect to the low energy version.

5.2.6.3. High Energy Module

The high energy module layout can be seen in Figure 5.30 with only one quadrupole per module. This results in a slightly shorter module with respect to the medium energy version and a slightly increased RF fill factor. This will be the most common module seen in the various linac sections.

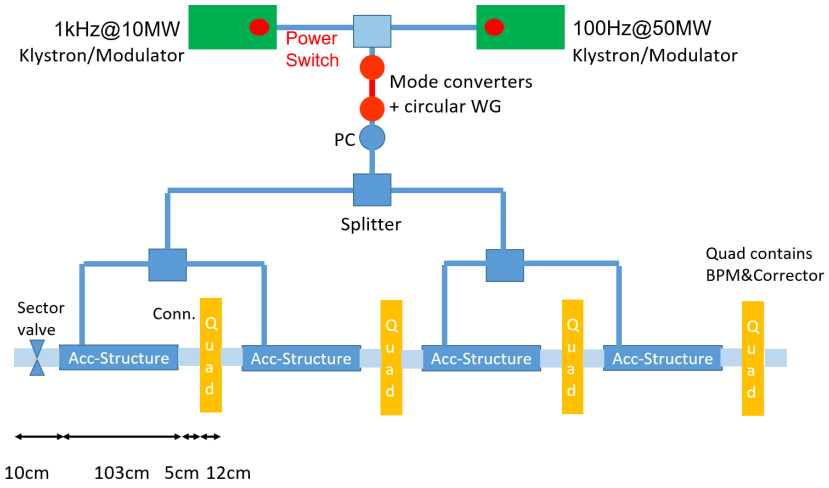

Figure 5.28.: XLS RF module layout for lowest energy section in the linac (up to 0.3 GeV). Module length: 5.10 m; RF-fill factor: 71 %.

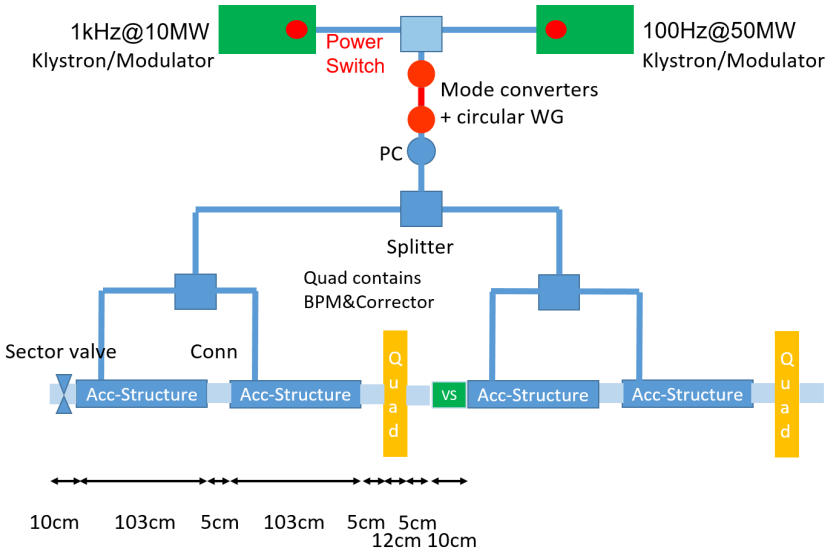

Figure 5.29.: XLS RF module layout for medium energy section in the linac (up to 2.0 GeV). VS = View Screen. Module length: 4.86 m; RF-fill factor: 74 %.

5.2.7. Industrialization

In order to produce an entire accelerator section within tolerance for minimum cost with a short lead-time, the production process has to be of an industrialized level with e.g. low rejection rate, high degree of mechanisation/automation and a high degree of reproducibility.

The challenges in the industrialization of accelerator structures are predominantly in the (sub)micrometer-machining of the copper parts and the consecutive assembly of the accelerator section due to the very strict mechanical tolerances. In state-of-the-art X-band designs these tolerances are approaching the limits of machining techniques available to date.

The typical work-flow of high precision monoparts is as follows:

- Production of bulk material

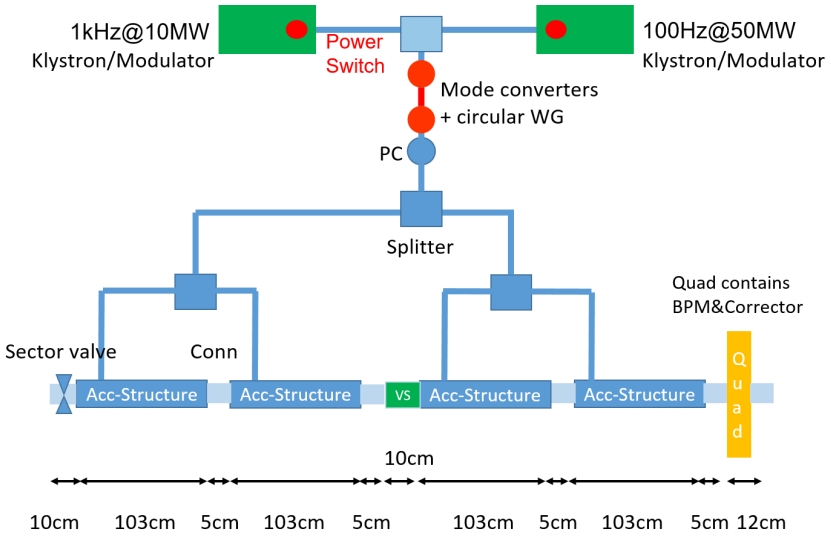

Figure 5.30.: XLS RF module layout for medium energy section in the linac (up to 5.5 GeV). VS = View Screen. Module length: 4.69 m; RF-fill factor: 77 %.

- Pre-machining by high-precision technology machines with an accuracy of 10 µm.
- Thermal annealing at 240 °C to release the stress in the material.
- Final-machining with alternating single point diamond machining and measurement steps.
- Metrology with a touch probe and interferometers to ensure that the final part is within specification.
- Cleaning by ultrasonic cleaning method, followed by a vapor degreasing
- Packaging to avoid oxidization, and damage during handling, transport and storage.

As the final machining steps are the most time- and cost-consuming, it is important to minimize the amount of material allowance after pre-machining. By this, the final machining can be done in a limited number of passes. This optimisation has to be done throughout the entire production chain i.e. from raw material until final product. Individual machined parts need to be joined into (sub)assemblies that form the accelerator structure. As the RF components need to be used in a vacuum environment, the assemblies have to be vacuum tight. There are a few techniques that are used to achieve this: bolt-connection, welding, vacuum brazing and diffusion bonding. After any joining technique, leak testing is performed as one of the last (mechanical) testing steps, often down to 10^{-10} mbar.

The production costs of the mono-parts can be divided into several categories (Table 5.12) following the manufacturing flow. The items listed under General are Non-Recurring Engineering (NRE) cost that are related to programming the CNC-machines and hence only applicable for a new design, i.e., once a particular design has been manufactured, these costs are omitted in all following production runs.

The machining steps are divided into two categories, pre- and end-machining, where the pre-machining steps take place in a regular machine shop with Precision-Technology (PT) and High-Precision-Technology (HPT) capabilities. End-machining will take place in a dedicated manufacturing area in which the Ultrahigh-Precision-Technology (UPT) machines are placed in a temperature controlled environment with a maximum temperature fluctuation of $\pm$ 0.1 °C. It is foreseen that the manufacturing strategy to date can be further optimized due to new developments in the HPT and UPT machining accuracy and combined milling/turning machine centers (Table 5.12 right two columns).

Table 5.12.: Cost breakdown.

Item	Operation	To date		Optimized	
		Costs	Total	Costs	Total
General	Work preparation	1.5%	12.3%	1.5%	12.3%
	Programming PT/HPT	3.1%		3.1%	
	Programming UPT	4.6%		4.6%	
	Programming 3D metrology	3.1%		3.1%	
Tooling	Mill	1.5%	4.6%	1.5%	4.6%
	Diamond tool	3.1%		3.1%	
Pre machining	Sawing	1.5%	22.1%	1.5%	18.0%
	Turning PT	13.0%		15.0%	
	Milling HPT	6.1%		–	
	Annealing	1.5%		1.5%	
End machining	Flycutting	5.0%	61.0%	–	54.2%
	Turning UPT Pre-machining	–		15%	
	Turning UPT End-machining	39.0%		22.5%	
	Cleaning	1.7%		1.7%	
	Metrology	15.3%		15.0%	
		100%		**90%**	

5.2.8. Sub-harmonic Deflector System

5.2.8.1. Introduction

Two-bunch operation for FEL pump and FEL probe experiments is part of the baseline specification. The spacing between the two bunches is 6 or 10 X-band RF cycles, the minimum spacing is determined by sufficient higher-order-transverse mode suppression in the accelerating structure. An S-band splitter is used to separate the two bunches and feed them into a septum magnet which separates them into the two FEL lines. The transverse separation between the two beams at the septum is 2.5 mm. A schematic is shown in Figure 5.31. A sub-harmonic deflector deflecting structure, working at S-band, is used to split the two bunches [132–134]. In contrast to the accelerating structure which operates in the TM_{010} mode, the transverse deflecting structure operates in the TM_{110} mode. The transverse magnetic fields of TM_{010} mode and TM_{110} mode are shown in Fig 5.32.

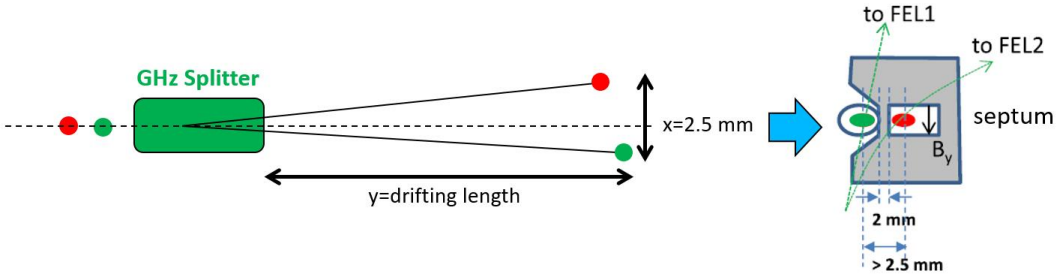

Figure 5.31.: Schematic figure of the S-band splitter system.

The magnetic field of the TM_{110} mode creates a transverse kick to the beam. The bunch will then follow an angled trajectory downstream of the deflector. The relation between transverse movement

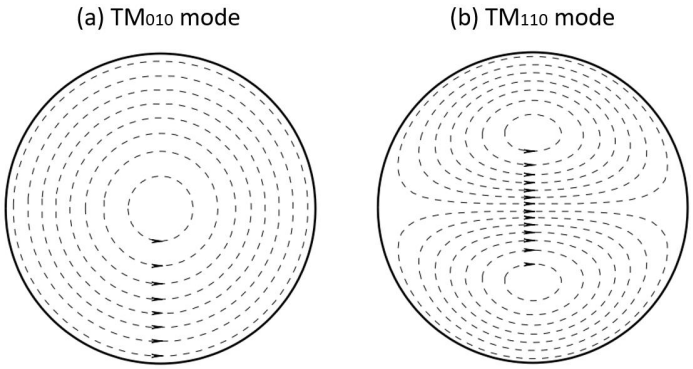

Figure 5.32.: The transverse magnetic fields of (a) TM_{010} mode and (b) TM_{110} mode.

and longitudinal movement is given by

$$\frac{x}{y} = \frac{V_{\perp} e}{E}, \tag{5.4}$$

where x is the transverse displacement, y is the drift length, $V_{\perp}$ is the transverse deflecting voltage, e is the charge of the electron, and E is the electron energy. The S-band deflector operates at 2.998 GHz. The spacing between the two bunches, 6 or 10 X-band RF cycles, is 1.5 or 2.5 RF cycles at S-band. Thus the two bunches can be placed at the crest and trough of the RF cycle of the sub-harmonic deflector so that the kicks applied to the two bunches are in opposite directions and the separation is maximized for a given kick voltage. The bunch energy in the hard X-ray mode is 5.5 GeV. The required deflecting distance for one bunch from the beam axis after drifting is 1.25 mm. The deflecting voltage can be calculated from equation (5.4). Both travelling-wave and standing-wave deflecting structures have been designed for the sub-harmonic deflector system. The power capability for the deflector system is presented next in section 5.2.8.2, followed by the details of the travelling-wave and standing-wave structure designs.

5.2.8.2. Power Source Capability

The klystron for the sub-harmonic deflector system is a CPI S-band klystron (VKS8262G1) [135]. It can reach a maximum power of 7.5 MW with maximum pulse width 5.0 μs. The maximum repetition rate is 400 Hz. This type of klystron has already been applied at IFIC S-band test-stand in Valencia. According to the manufacturer this klystron has the potential to operate at 1 kHz. An S-band spherical pulse-compressor is used to increase the peak power to the deflecting cavity. An average power gain factor of 5.29 is achieved by compressing the 4.5 μs klystron pulse to a 300 ns pulse. The pulse shape is shown in Figure 5.33. The intrinsic quality factor of the spherical cavity is 100,000. The coupling factor is set at 7. We assume that the available power for the structure in 1 kHz operation is 6 MW with consideration of the losses.

5.2.8.3. Traveling-wave Transverse Deflector Design

The traveling-wave transverse deflecting structure works at $\frac{2\pi}{3}$ mode. The single cell electrical field is shown in Figure 5.34. Constant impedance design is chosen for easy fabrication. The length of the whole traveling-wave structure can be easily modified by adding or reducing cells to achieve the required deflecting voltage at the same input power. To prevent the excitation of the modes with polarity rotated at 90°, two longitudinal rods (radius = 9.525 mm) crossing the cells off-axis have been inserted, as shown in Figure 5.34. The resonance frequencies of such modes are shifted far enough from the operating mode frequency to be negligible. The calculated frequency shift for the rotated modes due

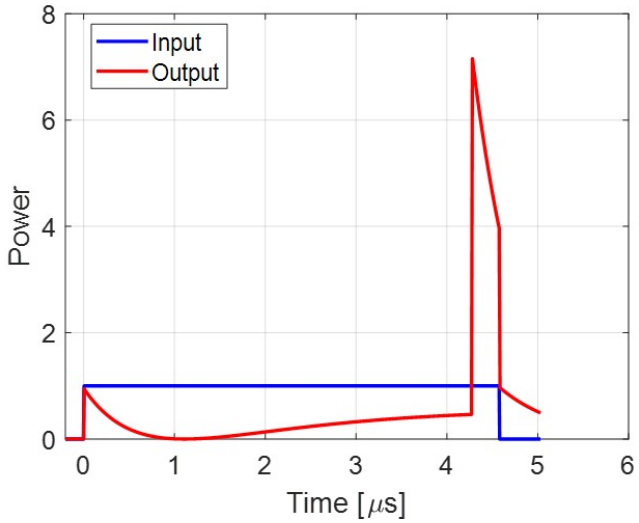

Figure 5.33.: The input and output pulse shape of the pulse-compressor.

Table 5.13.: The RF parameters of the single cell of the traveling-wave transverse deflecting structure.

Parameter	**Units**	**Value**
Cell length	mm	33.3
Operating frequency	GHz	2.998
Shunt impedance	MΩ/m	20.25
Quality factor		12369
Group velocity	v_g/c_0	0.027

to the rods is about +17.3 MHz, while the working mode is practically unperturbed. The main RF parameters are summarized in Table 5.13.

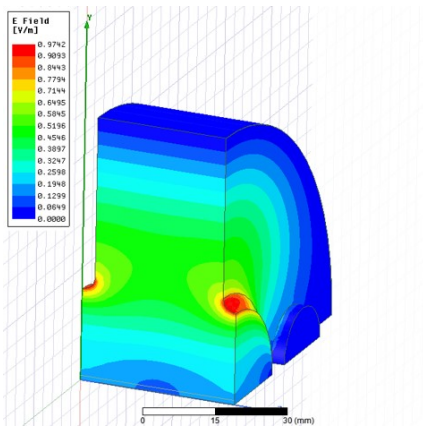

Figure 5.34.: The electrical field of single cell of travelling-wave transverse deflecting structure.

The deflecting voltage increases when increasing the cell number at the same input power. The required length of the traveling-wave deflecting structure to separate two 5.5 GeV bunches at different drift length is shown in Figure 5.35. The schematic figure of the traveling-wave deflector system is shown in Figure 5.36. The structure consists of 15 cells, with a total length of 0.5 m. The filling time is

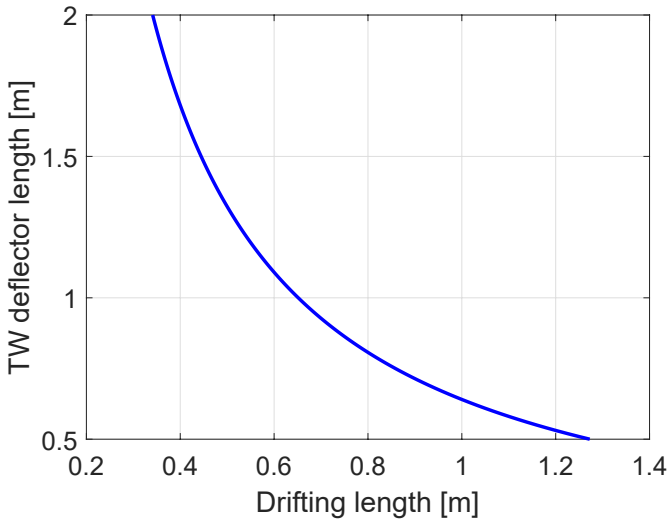

Figure 5.35.: Travelling-wave deflecting structure length versus drifting length. The input power is 31.74 MW.

62.5 ns. The pulse-compressor compresses 6 MW, 1.09 μs klystron pulse to 31.74 MW, 72.5 ns output pulse which includes the rise time of the system and the fill time of the structure. The deflecting voltage of the structure, with 31.74 MW input power, is 5.4 MV.

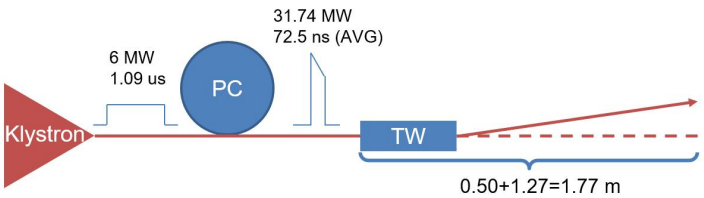

Figure 5.36.: Schematic figure of the traveling-wave deflector system. PC is the pulse-compressor and TW is the traveling-wave structure. The length of the structure is 0.5 m and the drift length is 1.27 m.

Table 5.14.: The RF parameters of the single cell of the standing-wave transverse deflecting structure.

Parameter	Units	Value
Cell length	mm	50
Operating frequency	GHz	2.998
Shunt impedance	MΩ/m	21.1
Quality factor		15642

5.2.8.4. Standing-wave Transverse Deflector Design

The single cell shape of the standing-wave transverse deflecting structure is similar to that of the travelling-wave structure, as shown in Figure 5.37. Two longitudinal rods (radius = 8 mm) crossing the cells off-axis have been inserted to suppress the excitation of the polarizing modes. The resonant frequencies of such modes are shifted far enough from the operating mode frequency to be negligible. The calculated frequency shift for the rotated modes due to the rods is +9.1 MHz. The RF parameters are summarized in Table 5.14.

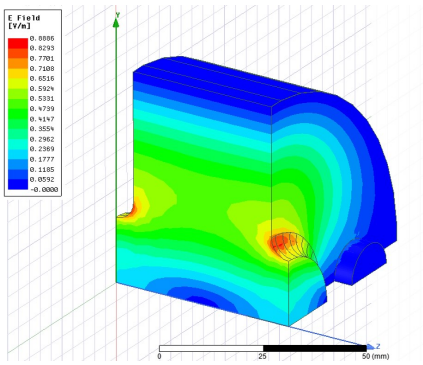

Figure 5.37.: The electrical field of single cell of standing-wave transverse deflecting structure.

Two standing-wave deflecting structures consisting of 3 cells and 5 cells have been designed. The structures are designed for critical coupling. The filling time, defined as $2Q_L/\omega$, is 830 ns. The time to fill 99 % of the maximum electrical field in the structure at a constant input power is 3776 ns. There is high reflection from the standing-wave structure during the filling period of the pulse, especially in the initial part, that represents a risk of damage to the klystron. One solution to deal with the reflected power is to use a circulator to isolate the power source and the reflection from the structure. The schematic figure of the standing-wave deflector system with circulator is shown in Figure 5.38. The pulse width of the klystron is 3.78 μs. Figure 5.39 shows a schematic of the standing-wave deflector system with 3 dB hybrid coupler. Another scheme to eliminate the reflection is to use two identical standing-wave structures and a 3 dB hybrid coupler. When the two structures are filled with a relative 90° phase shift, the 3 dB hybrid coupler can separate the wave from the klystron from the wave that leaves the cavities. The input power of each structure is 3 MW. The comparison between the two schemes of 3-cell and 5-cell standing-wave structures is summarized in Table 5.15.

5.2.9. Harmonic Linearizer System

5.2.9.1. Introduction

To compress the bunch length an energy chirp in the longitudinal phase space of the bunch is used combined with a magnetic chicane. The C-band RF system of the injector introduces an energy chirp

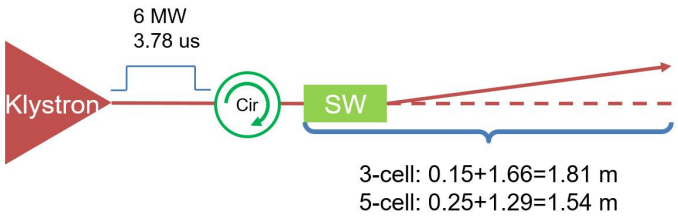

Figure 5.38.: Schematic figure of the standing-wave deflector system with circulator. The length of the 3-cell standing-wave structure is 0.15 m and the drifting length is 1.66 m. The length of the 5-cell standing-wave structure is 0.25 m and the drifting length is 1.29 m.

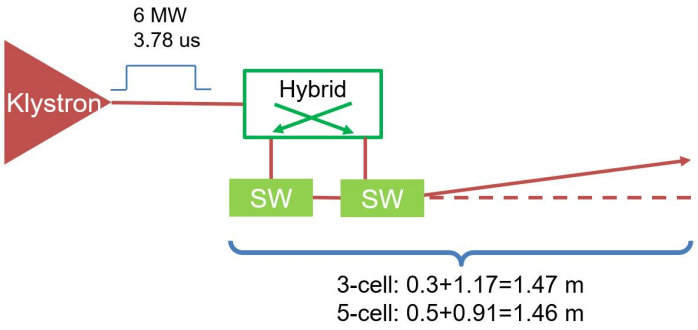

Figure 5.39.: Schematic figure of the standing-wave deflector system with 3 dB hybrid coupler. The length of the two 3-cell standing-wave structures is 0.3 m and the drifting length is 1.17 m. The length of the two 5-cell standing-wave structures is 0.5 m and the drifting length is 0.91 m.

in the bunch by operating off-crest. However this chirp can be non-linear due to the curvature of the RF wave over the bunch length. This nonlinearity can cause temporal current spikes and longitudinal wakefields in the undulator section which may hinder FEL performance. To linearize the energy chirp a higher harmonic RF system is used. The higher the harmonic used the lower the RF voltage required, with the required voltage scaling approximately with the square of the harmonic number. Most injectors use a 3^{rd} or 4^{th} harmonic, but this is mostly due to those harmonic numbers being standard RF frequencies for L and S band injectors. However in the case of CompactLight, which has a C-band injector, this frequency would be a 18 GHz or 24 GHz RF system, neither of which is widely available and requires the development of bespoke RF amplifiers. While higher frequencies result in lower required voltages there are potential issues associated with high frequency. A higher frequency means a larger ratio of the aperture to the wavelength (as the aperture is fixed by impedance limits) resulting

Table 5.15.: Information of various standing-wave deflector systems.

	Number of structures	Length of the structure [m]	Drifting length [m]	Deflecting voltage [MV]
3-cell SW structure with circulator	1	0.15	1.66	4.15
5-cell SW structure with circulator	1	0.25	1.29	5.33
3-cell SW structure with 3 dB hybrid	2	0.15	1.17	5.87
5-cell SW structure with 3 dB hybrid	2	0.25	0.91	7.53

in a lower shunt impedance and higher group velocity. A higher frequency in theory requires tighter tolerances (although that is partially offset by the higher group velocity), and the available RF power drops sharply with frequency. A 12 GHz RF system would be a 2^{nd} harmonic which would require a high voltage. A detailed study of periodic cells at all sensible harmonics converged to 36 GHz (Ka-band) as being the optimum choice for Compactlight. This frequency choice also means that experience with 30 GHz RF technology early in the CLIC study can be applied to CompactLight [136]. The development of very high frequency linearizers is of broad importance for accelerators which require short-bunches, including high frequency RF and plasma accelerators. Further information about the injector and its optimization can be found in the ComapctLight deliverable D3.4.

The requirements of the linearizer system The requirements for the linerizer are fairly complex as the linearizing effect is perturbed by the short-range longitudinal wakefield. As such, the required voltage depends strongly on the structure length and aperture.The structure should provide a peak accelerating voltage of 12.75 MV (which includes a 20 % overhead) at a frequency of 36 GHz for a 30 cm structure, however as the wakes act in tandem with the structure, the required voltage depends on the cavity length and aperture. The required voltage for a 2 mm aperture radius as a function of cavity length is shown in Figure 5.40. Under the effect of transverse short-range wakefields, the bunch

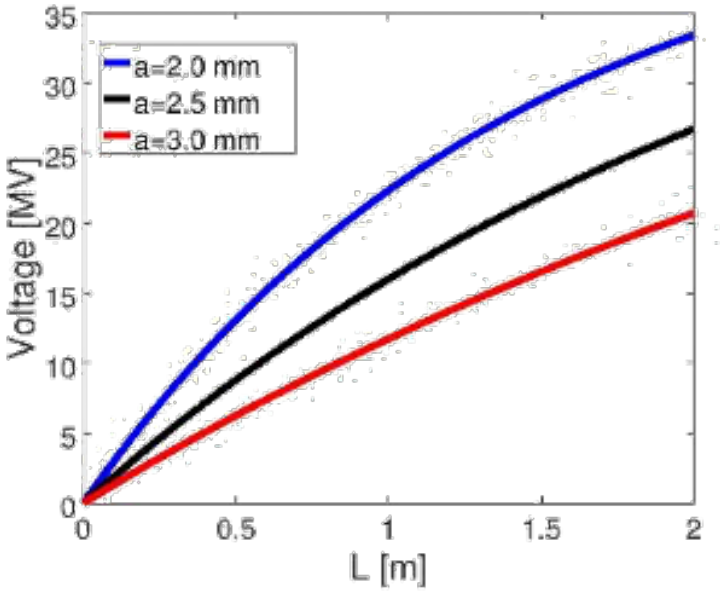

Figure 5.40.: Analytical estimate of the required voltage as a function of the Ka-band length, for different iris aperture radii.

tail gets a transverse deflection due to the wakefield excited by the bunch head. Given the relatively long bunch at the Ka-band and the small iris aperture, this deflection can induce beam breakup. The action amplification factor, A, allows estimation of the deflection amplitude as a function of the distance from the head of the bunch, z,

$$A(z) = \frac{J_f}{J_i} = \sqrt{1 + \left(\beta \frac{eQL_{\text{cav}} w_\perp(z)}{E_{\text{beam}}}\right)^2} \tag{5.5}$$

In this formula, J_i and J_i indicate respectively the action before and after the Ka-band, β is the optical beta function at the Ka-band (assumed to be 5 m), e is the electron charge, Q is the total bunch charge, L_{cav} is the length of the Ka-band, E_{beam} is the beam energy, and $w_\perp(z)$ is the wake potential

expressed in V/pC/m/mm following the approximation defined in [137]. Due to wakefields, the aperture size is limited by a minimum radius which is dependant on the cavity length, as given in Figure 5.41. Acceptable amplification factors are defined here as below 1.1, i.e., < 10 % amplification.

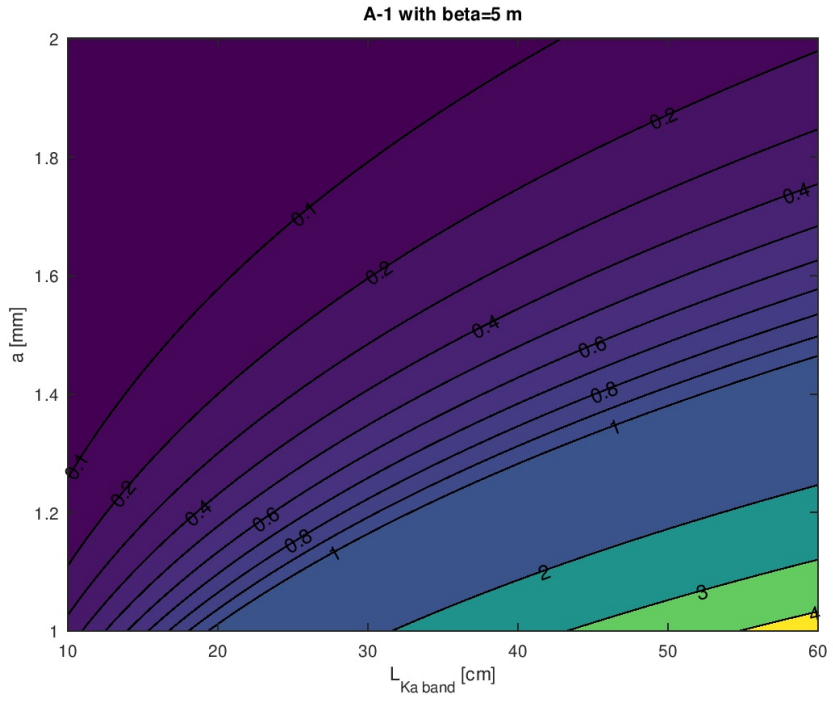

Figure 5.41.: The fraction of the action amplification factor exceeding one under the effects of short-range wakefields in the Ka-band lineariser, as a function of the Ka-band length and of the aperture radius.

The phase stability of the RF system is limited by charge stability, with a 30 cm structure requiring a phase stability of 0.25 degrees. The amplitude stability is limited by variation in arrival time to 0.25 %.The phase and amplitude jitter/stability will be dominated by the variation in the modulator voltage. We assume a 0.005 % variation in voltage hence the RF source should not have its amplitude or phase vary by more than the specified amounts with a 0.005 % voltage variation.

5.2.9.2. Ka Band Power Sources

A rough estimate of the likely pulse compression factors and structure parameters led to a power requirement of around 3 MW from the RF amplifier for a 300 mm long structure, with pulse-lengths of around 1000 μs and a repetition rate of 1 kHz. Traditional single-beam klystrons commonly used at RF frequencies to drive accelerators are unlikely to be able to produce this power at Ka-band hence bespoke amplifiers are required. Two approaches have been identified—a Higher-Order-Mode Multi-beam Klystron (HOM MBK) and a Gyro-Klystron. In both devices Higher-Order-Mode cavities are utilised allowing better power handling. In both cases extensive numerical Particle-in-Cell code modelling has validated the novel designs. RF amplifier development is a long risky process so a single technology has not been selected at this stage and both options require further commercial development and prototyping.

A third amplifier concept has been identified to generate very high powers which would allow far higher gradients and hence shorter linearizer structures. This is the use of a klystron up-converter. In this concept a high power X-band klystron is used, but the output cavity is replaced with a 36 GHz

cavity to generate RF power using the third beam harmonic current. As the cavity is a monopole, cavity peak fields and power density would be much higher in this design, and there seems no requirement for shorter linearizers hence this option was not selected as baseline. Further development of this concept is required.

Multi-beam klystron As klystrons scale in frequency the aperture sizes in the cavities decrease and as such the beam must have a smaller radius, increasing the current density in the beam, in turn decreasing the RF efficiency. A multi-beam klystron allows the beam current to be spread across many beams reducing the current density in each. However it would be impossible to fit a large number of cathodes in an area consistent with a standard Ka-band cavity. In addition, the peak fields would be very high for a TM_{110} mode cavity and would be very high at Ka-band with a power of 3 MW. Hence in order to create a high power klystron in the frequency range of interest we need to move to a Higher-Order Mode (HOM) cavity which would be oversized compared to the wavelength. A coaxial HOM cavity was chosen to base the design upon, However one problem to be considered is ensuring the beam excites the correct mode and not one of the many others at nearby frequencies.

In order to make the device compact and avoid the use of an oil tank a beam voltage of 60 kV was chosen. Assuming the klystron would be around 35 % efficient and produce an RF output power of 3 MW, a beam current of around 120 A is required. For limiting the current in each beamlet to 6 A twenty beamlets are required. Finally, for having a round 12 mm between each cathode a mean radius of around 38 mm is necessary. After optimisation of the cavity geometry the final radius was 37.6 mm with operation in the the $TM_{20,0}$ and a beam tunnel aperture of 2 mm, and width = height = 5.9 mm. With a 2 mm aperture the required magnetic field is 0.55 T (3-4 times the Brillioun field) which can be generated with a normal conducting magnet.

One issue with the HOM cavity was detuning. When exciting the cavity with a single port or beam the excited mode was found to have a varying field amplitude around the ring as nearby modes were excited. Figure 5.42 shows the operating mode and one of the nearby modes. However, it was also found that exciting with multiple beams, or with a distributed coupling, the other modes field components were completely cancelled out leaving only a pure $TM_{20,0}$ mode. A study was performed to understand the tolerance to beam current variations or failure of beamlets. This showed that the cavity was largely insensitive to very large fluctuations or multiple failed beamlets.

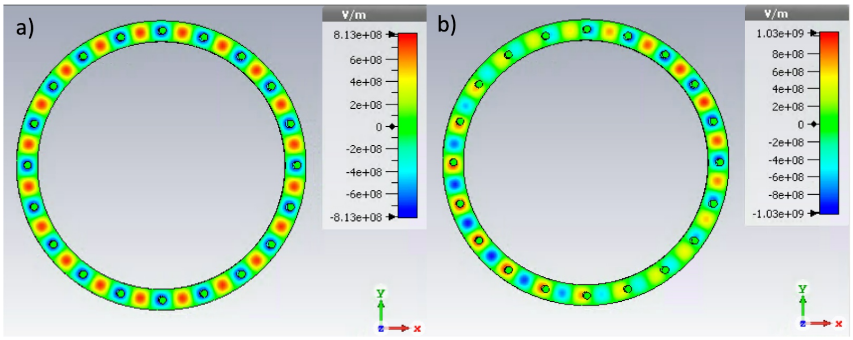

Figure 5.42.: TE20,1,0 mode (a) and TE21,1,0 mode (b) in the coaxial cavity with integrated beam tunnels.

With the basic cavity geometry designed the exact positions and frequencies of each cavity wewre optimised using the disk-model code KlyC, with final verification in CST Studio Suite. The optimized tube provided 33.3 % efficiency (2.4 MW peak power), 50 MHz frequency bandwidth at a level of -3 dB and a power gain of 40.7 dB. The parameters are listed in Table 5.16. The effect of a single beamlet being turned off was studied to ensure stability. The observed RF power reduction in this case was only 7 % which is consistent with the reduction in beam current of 5 %. The spectrum of the output signal

Table 5.16.: The HOM-MBK parameters.

Parameter	Units	Value
Operating frequency	GHz	36
Output power	MW	2.4
Bandwidth	MHz	50
Electron beam voltage	kV	60
Electron beam current	A	120
Beamlet Current	A	6
Magnetic field strength	T	0.55
Small-signal linear gain	dB	40.7
Efficiency	%	33.3

was observed up to 100 GHz and did not show any other major frequency component apart from the input 36 GHz. The electric fields in the HOM MBK are shown in Figure 5.43.

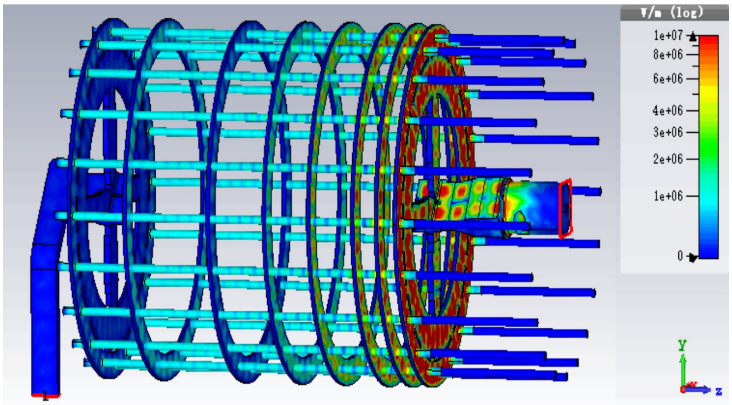

Figure 5.43.: The electric field plot on the HOM MBK surface.

As CompactLight has very tight tolerances on phase variations of RF cavities a study was performed to assess the variation in output RF phase with variation of the modulator voltage. Variation of the cathode voltage by 1 part in 10,000, which is believed to be a conservative estimate of modulator stability, resulted in a phase shift of 0.36 degrees. While this is greater than the specification it should be noted that most modulators achieve a greater stability than the conservative estimate used here. The required manufacturing tolerance was also assessed and was found to be 5 μm which is similar to that of an X-band RF cavity and so feasible.

An upgrade requirement of CompactLight is operation at 1 kHz. The main limitation to achieving this is the average power density in the collector. A new code was developed to calculate this. This code was then used to optimise the collector geometry in order to minimise the heat load for two cases: 1) no RF input (DC mode) and 2) saturated RF output. While the beam power is higher for the DC case, in the saturated RF output case the location of the heat deposition on the collector wall is shifted with respect to the DC case and hence the maximum power density in both modes of operation must be assessed. The maximal power density is below 70 W/cm^2 which is below the standard limit of 100 W/cm^2 typically used in collectors with water cooling systems. The final HOM MBK geometry is shown in Figure 5.44. A detailed description of on the design of this multi-beam klystron has also been published in [138].

Gyroklystron The gyrotron klystron is a vacuum electronic based amplifier that relies on the fast beam-wave electron cyclotron maser interaction for its operation [139]. Compared with a conventional

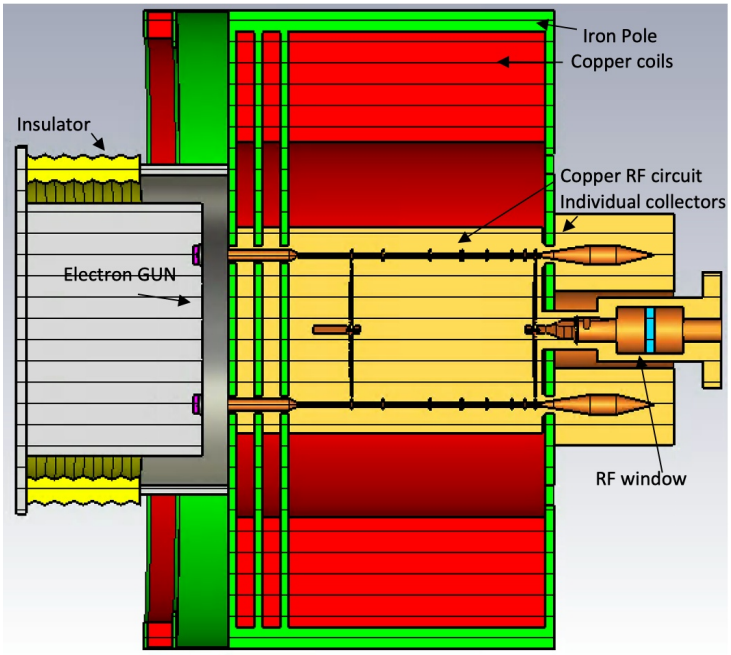

Figure 5.44.: Artistic view of the Ka-band HOM MBK.

klystron normally used in accelerators, the electron beam interacts with the TE resonant mode in the gyro-klystron cavities and the bunching is mainly in the azimuthal direction. The small gap length in a klystron which determines the operating frequency is no longer a constraint in a gyroklyston which allows it to produce high power at the higher operating frequency, for example, to achieve MWs of power at high (Ka-band) frequency. A schematic drawing of a gyroklystron is shown in Figure 5.45. Its main components include: (1) the magnetron injection gun (MIG) to generate a rotating electron beam with optimised transverse to axial velocity ratio and small velocity spread; (2) beam wave interaction circuit to effectively convert the power in the electron beam into the microwave radiation; (3) a cryogen-free superconducting magnet system to properly guide the electron beam and maintain the electron beam cyclotron frequency; (4) the input and output microwave window to couple the input and output radiation; (5) the ultra-high vacuum system; and (6) the depressed collector to reduce the thermal load when operating at high pulse repetition frequencies of 100 Hz or greater.

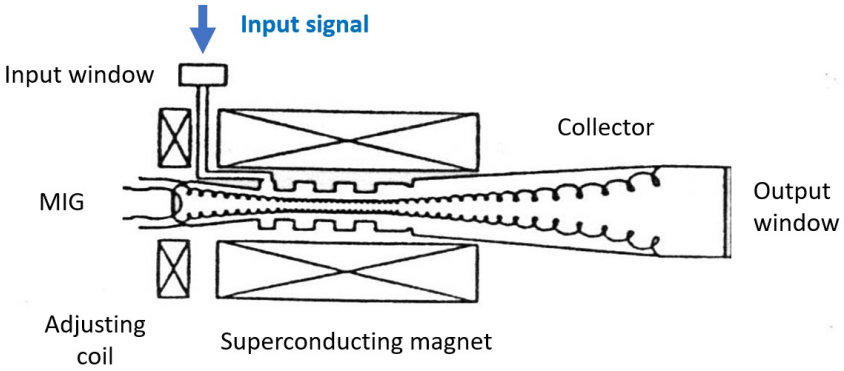

Figure 5.45.: Schematic drawing of a gyroklystron.

Table 5.17.: The requirements and initial parameters from the linear theory.

Parameter	Units	Value
Operating frequency	GHz	36
Output power	MW	3.2
Bandwidth	MHz	200
Electron beam voltage	kV	150
Electron beam current	A	50
Magnetic field strength	T	1.5
Beam transverse-to-axial velocity ratio		1.4
Small-signal linear gain	dB	48
Efficiency	%	42

Design of the interaction circuit

During the design of the 36 GHz gyroklystron with 3 MW output power, a three-cavity configuration was chosen as a trade-off between gain improvements using more cavities, thermal issues, design complexity and bunching quality. It included an input cavity to couple in the driving RF signal, a bunching cavity to enhance the electron bunch, and an output cavity to induce a strong resonance with the bunched electron beam for effective beam-wave interaction. The input and bunching cavities are operating with the TE_{01} mode, and the output cavity operates with a TE_{02} mode in order to improve the power capability.

The design of the gyroklystron interaction circuit follows an iterative process [140, 141]. Firstly, a small-signal linear theory based on the point-gap approximation was used to find the constraints of the initial parameters, such as the beam voltage, current, the transverse-to-axial velocity ratio α, and the magnetic field strength at the interaction region, as shown in Table 5.17. The dispersion curve of the operating modes of the output cavity based on the interaction principle is shown in Fig 5.46. The possible competing modes are the TE_{11} and TE_{01}.

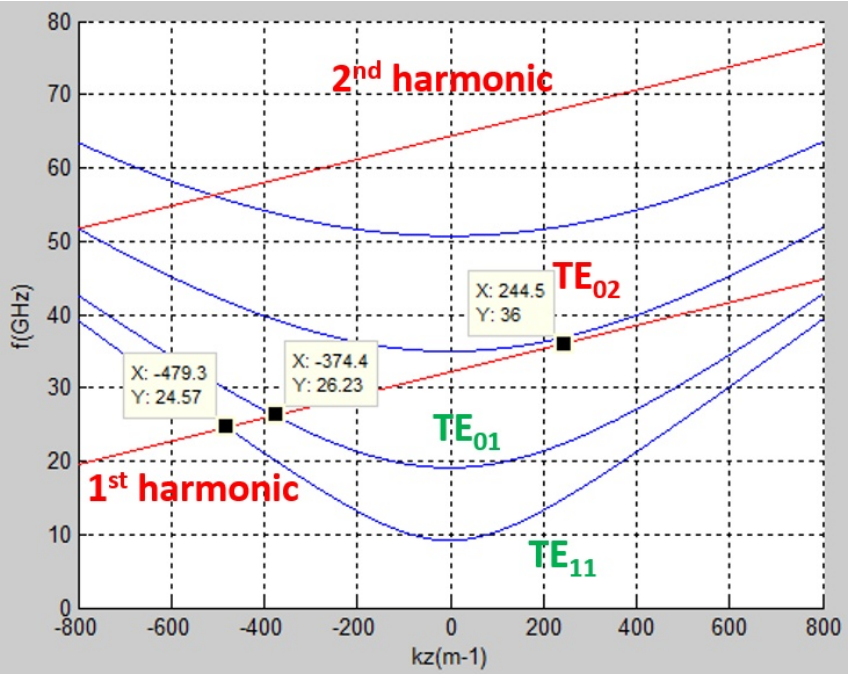

Figure 5.46.: Dispersion relation of the operating mode of the output cavity.

After selecting the core beam parameters, the proper eigenfrequencies and the quality factors for the cavities, the dimensions of the cavities could be decided. The resonant frequencies of the input and intermediate cavities, f_1 and f_2, were chosen using the following equations:

$$f_1 = f_0 + f_0/(3Q_0) \tag{5.6}$$

$$f_2 = f_0 - f_0/(3Q_0) \tag{5.7}$$

where f_0 and Q_0 are the eigenfrequency and quality factor of the output cavity. The dimensions of the cavities and the radius of the guiding center can be determined from:

$$f = c/\lambda_0 = c/2\pi\sqrt{(\nu_{mp}/R)^2 + (n\pi/L)^2} \tag{5.8}$$

$$C_{mp}(r) = (J^2_{m\pm1}(k_{\perp r})/((\nu^2_{mp} - m^2)J^2_m(\nu_m p)) \tag{5.9}$$

where f is the eigenfrequency of the operating mode $TE_{m,p,n}$, R and L are the radius and length of the cavity, J is the Bessel function of the first kind and ν_{mp} is the Bessel root corresponding to the mode in question.

The parameters chosen from these equations were then put into the nonlinear theory, which can include the accurate field profiles of the cavities in the calculation enabling the beam-wave coupling equation to be solved. The nonlinear theory provides a balance between accuracy and simulation time. It provides useful information on the bunching process and the trends that occur when changing the parameters. The initial dimensions of cavities, as well as the length of the drift tube sections from the linear theory, were then further optimized using the nonlinear theory calculations to achieve optimal efficiency. The maximum interaction efficiency was about 40 %. Figure 5.47 shows the interaction efficiencies at the intermediate and output cavity as a function of the cavity positions.

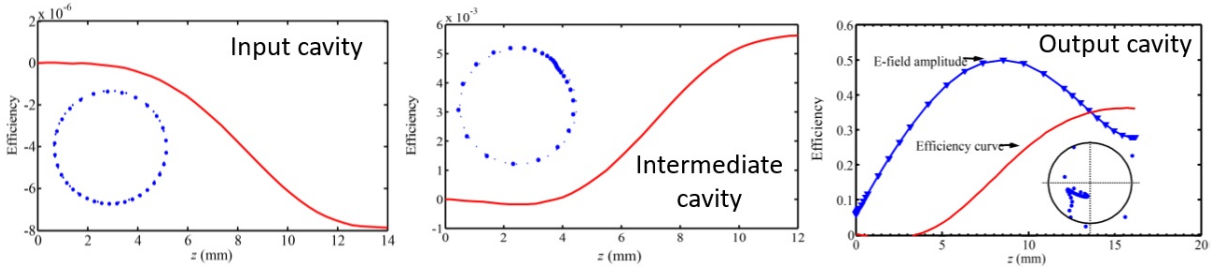

Figure 5.47.: The efficiency as the function of the cavity position for each cavity from nonlinear theory results.

The most accurate simulation of the beam-wave interaction is based on Finite-Difference Time-Domain Particle-in-Cell simulations carried out using the optimal geometry suggested by the nonlinear theory calculations. This enables the space-charge effect in the gyro-klystron cavities, the beam energy spread and velocity spread to be included in the simulations. The design goal is to achieve the required output power, frequency and efficiency from a gyrotron klystron amplifier that can be manufactured with acceptable tolerances. The Particle-in-Cell simulation requires large computation time. This makes it suited only for final optimization and validation, sweeping across a range of parameters suggested by the nonlinear simulations. Figure 5.48(a) shows the structure of the gyroklystron and the phase space of the electrons. The phase space of the electron energy is shown in Figure 5.48(b), where at the output cavity most of the electrons lose their energy to the electromagnetic wave which results in the amplification of the input signal.

The simulation showed that more than 3 MW output power can be generated, satisfying the requirements. The Fourier transformation of the amplitude of the electric field at the output port showed that a distinct frequency component of 36 GHz exists in the frequency spectrum. No other frequency components were found except a relatively weak second harmonic. Further PIC simulations were carried

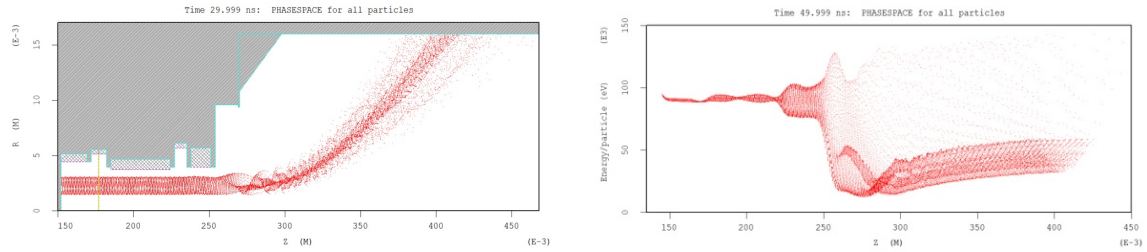

Figure 5.48.: Simulated gyroklystron structure and the simulated phase space of the electrons.

out to investigate the effect of the electron beam velocity spread and the variation of the magnetic field strength. The output power remained greater than 3 MW if the variation of the transverse-to-axial velocity ratio was less than 4 %. The output power as the function of input power and bandwidth are shown in Figure 5.49.

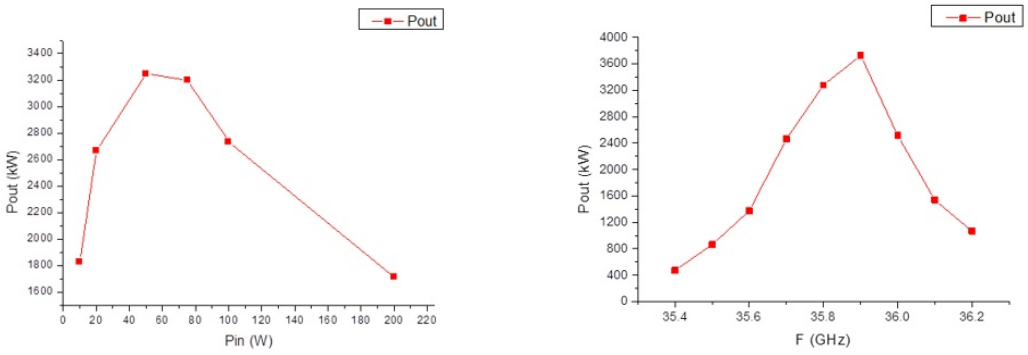

Figure 5.49.: the output power as the function of input power and bandwidth.

The MIG gun design for the 36 GHz gyroklystron

The small-orbit gyrating electron beam used for the gyroklystron is generated from a magnetron injection gun (MIG). A triode-type gun that can provide better control of the beam velocity ratio by adjusting the modulating anode voltage was designed. The initial parameters of the MIG were derived from the theoretical model using the final optimized beam parameters of the gyroklystron, as listed in Table 5.18. The geometry dimensions were further optimized using the particle tracking code EGUN. The optimized beam velocity spreads were about 4 % for the desired beam parameters. The simulation results were also validated using other simulation codes MAGIC and CST particle studio. The trajectory of the electron beam of the optimized MIG is shown in Figure 5.50. The beam transverse-to-axial velocity ratio can be adjusted by varying the modulation anode voltage, as shown in Figure 5.51.

Magnetic field design

The simulation showed that the variation of the magnetic field strength at the interaction region was required to be less than 1 % in order to maintain the desired output power. Although it is possible to generate a magnetic field strength of 1.5 T using a water-cooled copper coil the cooling requirement and field stability are challenging. A better choice is to use a cryo-cooled closed-loop superconducting magnet. A magnet system composed of four solenoids was used to generate the magnetic field, as shown in Figure 5.52. It included one main coil and two shim coils to compensate for the field decrease

Table 5.18.: The optimized beam parameters of the gyroklystron.

Parameter	Units	Value
Electron beam voltage	kV	150
Electron beam current	A	50
Magnetic field strength	T	1.46
Beam transverse-to-axial velocity ratio		1.4
Gain	dB	39 (max. 42)
Efficiency	%	44
Beam guide radius	mm	2.3
Magnetic field compression ratio		10.5
Modulation anode voltage	kV	38.5

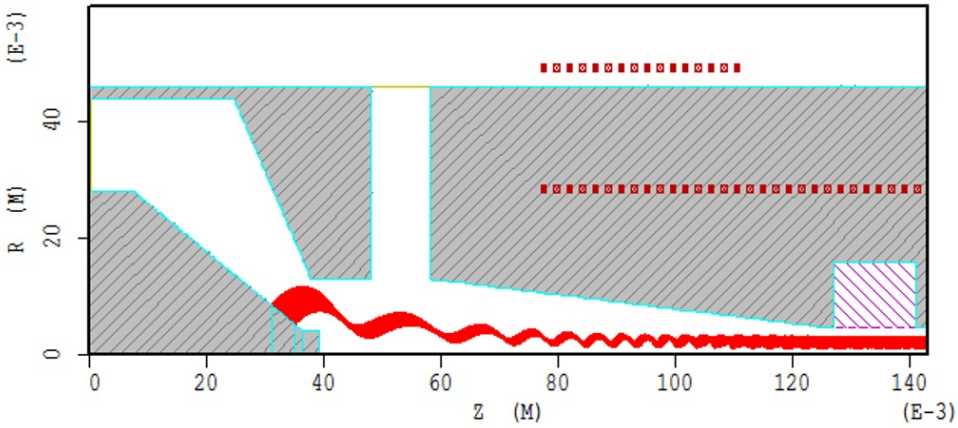

Figure 5.50.: The trajectories of the electron beam in the MIG.

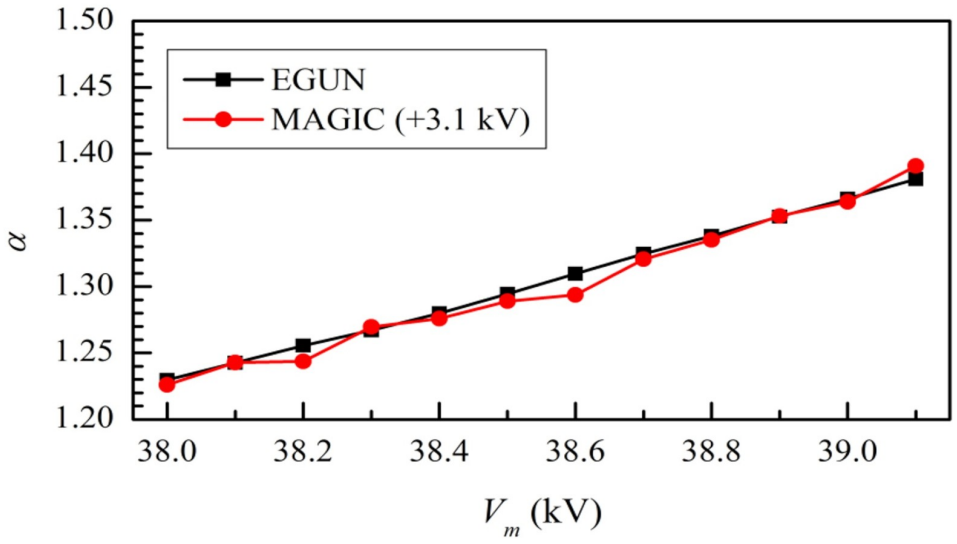

Figure 5.51.: The beam transverse-to-axial velocity ratio as the function of modulation anode voltage.

at both ends of the main coil. The reverse coil was used to accurately adjust the magnetic field strength at the emitter surface. The magnet system was initially designed and optimized by analytical equations. Then the solenoid configurations were modelled and verified by the magnetic field solver using the finite

Table 5.19.: The specifications of the 36 GHz gyroklystron.

Parameter	**Value**
Beam voltage / Beam current	150 kV / 50 A
Output power / 2^{nd} harmonic component	3.2 MW / 2.3 %
Output power stability	0.4 % @0.5 % variation of the modulator voltage
Output frequency / 3 dB bandwidth	36 GHz / 108 MHz (0.3 %)
Magnetic field and frequency drift	1.46 T and < 1 MHz drift due to magnetic field drift
Frequency drift due to beam voltage	4.8 MHz @0.1 % variation of the modulator voltage
Pulse repetition rate / Duration	1000 Hz / 1.5 us
Drive power / Gain	400 W / 39 dB
Input / output waveguide mode	Input TE10 (Rectangular) mode, output TE02 (Circular) mode
Efficiency	42.7 % (without energy recovery), 58.0 % (with single stage depressed collector)
Average spent beam power	6.5 kW
Dimensions	60 cm (W) * 60 cm (L) * 1200 cm (H)
Phase stability	3.4 deg@0.1 %, 0.34 deg@0.01 % variation of the modulator voltage

element method. The on-axis magnetic field profile is as shown in Figure 5.52.

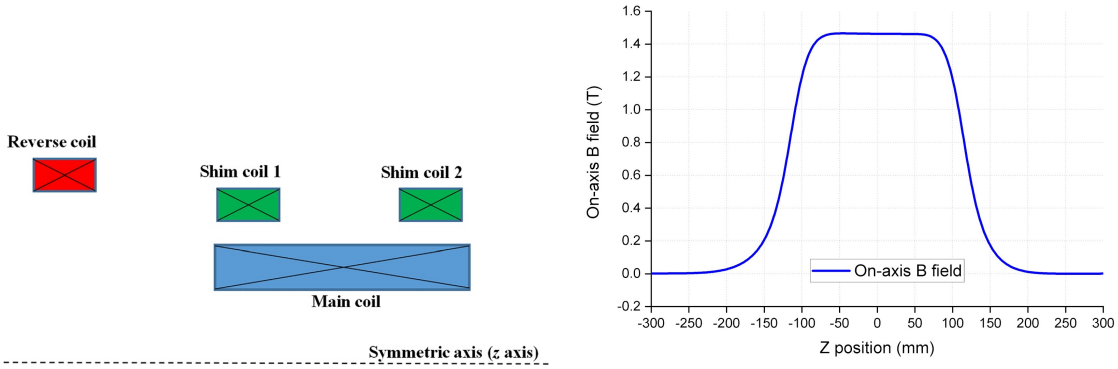

Figure 5.52.: The superconducting magnet system and the on-axis magnetic field profile.

Specifications of the 36 GHz gyroklystron

A full summary of specifications of the gyroklystron from the simulations are summarized as in Table 5.19, which also details the footprint and the phase stability. Specifications of the commercial superconducting magnet used for the gyrotron are summarized as in Table 5.20, which is based on the user manual from the potential vendor [142]. The specifications of the power modulator which satisfies the requirements to drive the gyroklystron are summarized as in Table 5.21, which is based on the user manual from the potential vendor [143].

Table 5.20.: Specifications of the commercial superconducting magnet.

Parameter	Value
Guide magnetic field	1.46 T
Type	Cryogen Free Superconducting Magnet
Possible vendor	Cryogenic Ltd.
Magnetic field accuracy	0.08 %
Stability over time	0.002 %/hour
Stability over temperature	0.002 %/K

Table 5.21.: Specifications of the commercial power modulator.

Parameter	Value
Operating voltage	150 kV
Operating current	50 A
Possible vendor	ScandiNova
Product model	K Series K100
Typical pulsed voltage range	115 – 190 kV
Typical pulsed current range	90 – 140 A
RMS Voltage stability	0.02 %
Dimensions	166 cm * 70 cm * 220 cm

5.2.9.3. Pulse Compression System

Waveguide system

As waveguide losses increase at higher frequencies it is necessary to use a an overmoded waveguide operating in a lower-loss TE_{01} mode to limit the RF losses between the RF source and the RF structure. With such a scaling, the circular waveguide diameter is 12 mm. In such a waveguide the Ohmic losses are -0.255 dB/m (5.7 %/m). For the long straight WG sections this diameter can be increased (matched taper) to 20 mm (-0.035 dB/m; 0.8 %/m).

The HOM MBK is very compact, and does not require an oil tank and hence could be installed in the tunnel next to the structure further limiting transmission loss. The Gyroklystron is larger and requires both an oil tank and a superconducting magnet making it more difficult to place in the tunnel, and will likely need to be in a separate service tunnel or plant room. In both cases the modulator will have to be in the plant room. The Gyroklystron requires a TE_{02} to TE_{01} mode converter while the HOM MBK has a TE_{01} output. The proposal is to use an existing rectangular TE_{20} mode hybrid coupler on the pulse-compressor, which requires a simple circular TE_{01} to rectangular TE_{20} mode converter.

Pulse compression

The Gyroklystron and multi-beam klystron can provide 3.2 MW and 2.5 MW respectively as Ka-band RF sources. This power level is smaller than the required input power for the linearizer, which means that more than one RF power source is needed for the system if pulse compression is not implemented. However, the required pulse width for the linearizer is much shorter than the output of the power source. Hense pulse compression can be used to reduce the number of power sources and increase the peak power of the RF source to meet the required input power of the linearizer. The passive pulse-compressor consists of a cavity based SLEDI and a delay-line based SLEDII [108, 144–146]. The Q factor of the SLEDI cavity needs to be around 100,000. However, the Q factor of the resonant cavity at 36 GHz could not reach that value. A SLEDII pulse-compressor could have a good performance at

a higher frequency range. A 30 GHz pulse-compressor with resonant delay-lines has been built and installed in the CTF3 (CLIC Test Facility) and obtained the high peak power of 150 MW, as shown in Figure 5.53 [147]. A delay-line based dual-moded SLEDII pulse-compressor is proposed for the CompactLight linearizer system.

Figure 5.53.: 30 GHz SLED2 pulse-compressor in CTF3.

The length of the delay-line of SLEDII pulse-compressor is proportional to the output pulse width. Reflective delay-lines transmit the RF power in several modes by utilizing the transmission lines several times [148–150]. This can reduce the required delay-line by a factor of n, where n is the number of modes used simultaneously. The dual-moded SLEDII pulse-compressor utilizes two modes which are circular TE_{01} and TE_{02} modes in the same delay-line, as shown in Figure 5.54. This cuts the delay-line length by a factor of 2.

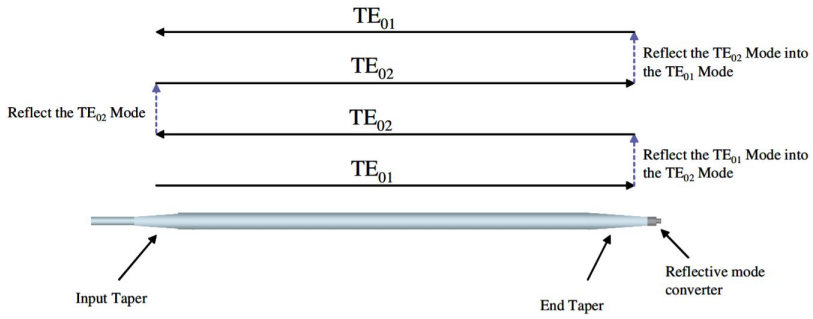

Figure 5.54.: The delay-line of dual-moded SLEDII pulse-compressor.

The baseline of CompactLight aims at a two-bunch operation with a spacing of 6 or 10 X-band RF cycles (0.5 or 0.83 ns). The required input pulse width for the linearizer should ensure the two-bunch operation. As the spacing is much smaller than the filling time of the linearizer, the output pulse width from the pulse compression system is mainly dominated by the filling time. This drives a shorter length of the delay-line compared with the those designed for colliders with wider pulse widths.

The filling time for a 0.3 m traveling-wave linearizer which operates at $2\pi/3$ mode is 9 ns. The dual-moded delay-line needs to have an approximate length of 1.71 m which includes the filling time and rise/fall edge of the RF power source. The diameter of the waveguide for the delay-line is 50 mm. The average power gain of the pulse-compressor as a function of RF source pulse width is shown in Figure 5.55.

An average power gain of 7.37 is reached when the RF power source width is 984 ns. The input and output pulse shape is shown in Fig 5.56.

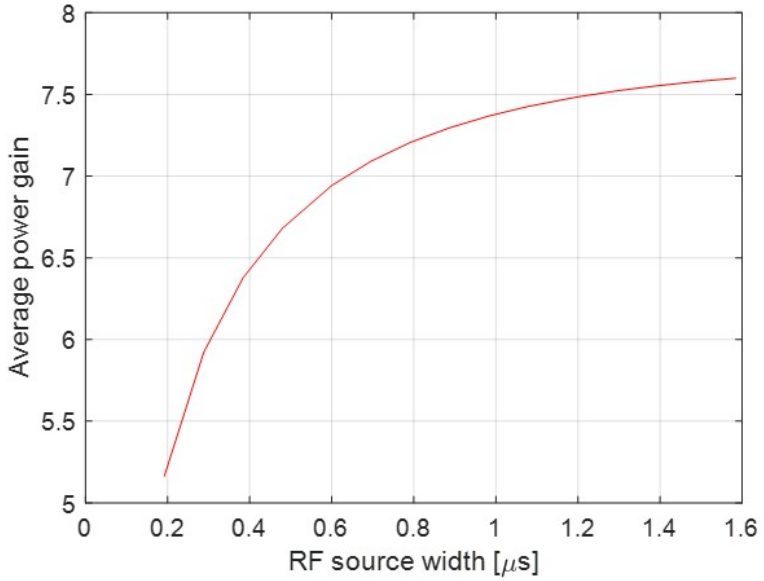

Figure 5.55.: Average power gain from the pulse-compressor as a function of RF power source pulse width.

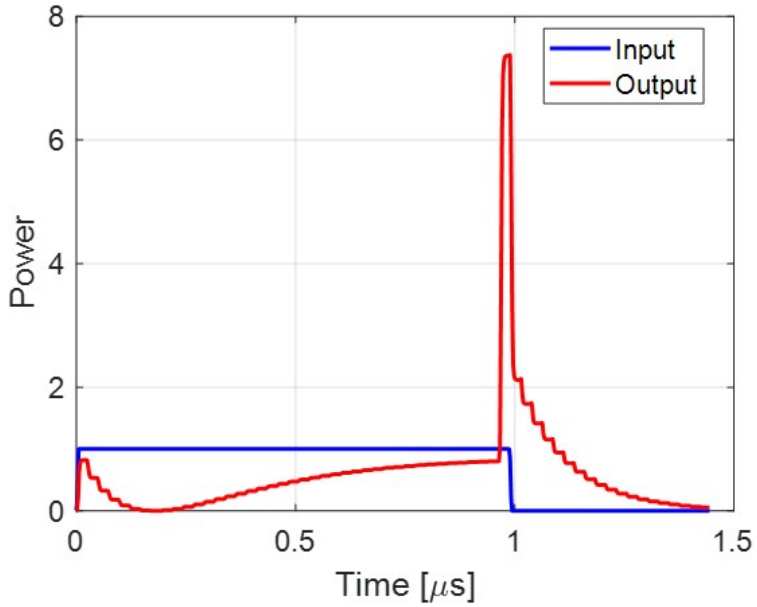

Figure 5.56.: Input and output pulse shape of the pulse-compressor. The input pulse width is 984 ns and the output pulse width is 24 ns including the rise/fall edge.

5.2.9.4. Traveling-wave Linearizing Structure

At Ka-band the power available from RF amplifiers is much smaller that that at lower frequencies. While higher powers could potentially be realised in a klystron upconverter the complexity, size, cost and peak field requirements of such a device would be more risky than other devices. Also, since the lineariser is a single cavity and hence space is not a driving constraint, there was no real requirement for high gradient and hence high power. This led to an initial limit of 3 MW from the RF source for the purpose of designing the RF structure. A preliminary investigation on SLED-II pulse-compressors

suggested that this would lead to around 22 MW of RF power being available for the RF structure.

The aperture of the RF structure is limited by short-range wakefields to around 2 mm, although this is weakly dependant on the structure length. The limit thickness of the iris at Ka-band is not well known hence a conservative width of 0.6 mm was chosen based on experience in the CLIC study. One issue with a travelling-wave structure at Ka-band is that the requirement to have a large aperture compared to the wavelength leads to a very high group velocity which can limit the structure's efficiency. Initially travelling-wave structures with phase advances $2\pi/3$ and $5\pi/6$ were investigated. With smaller apertures the higher phase advance normally has a lower group velocity for a given aperture size, however it was found that where the aperture is large compared to the wavelength the $2\pi/3$ structure had the lower group velocity of 11.9 % the speed of light. This resulted in minimum structure length of 300 mm in order to achieve a voltage of 12.75 MV with the available RF power.

Using a standing-wave structure would initially appear to be more efficient as there is no power flow out of the structure. However there are two issues with a standing-wave cavity. The first issue is that there are no Ka-band 3 MW circulators, hence the structures would need to be split and fed through hybrid couplers to cancel out the reflections in pairs by choosing the correct phase delay between each structure. Several structures are also required as there is a limit to the number of cells that can be used in a standing-wave structure and the Ka-band cells are very short. The second issue is the longer filling time of the structure leads to significantly longer SLED-II pulse-compressor delay-lines. This second issue can be avoided by partly filling the structure but in doing so the performance of the standing-wave structure becomes comparable to the travelling-wave structure. Due to the added complication of the standing-wave scheme the baseline structure design was chosen to be a $2\pi/3$ travelling-wave structure with a length of 300 mm.

Cell design

The single cell geometry (see Figure 5.57) was optimized for 3 different phase advances of the travelling-wave structure (TWS) at 36 GHz, and the general parameters of each one are presented in Table 5.22, for comparison.

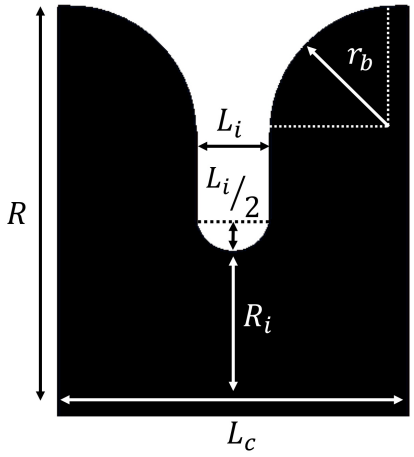

Figure 5.57.: single cell geometrical parameters.

From Table 5.22 we observe that for a structure with relative large apertures such as this one (where $R_{iris} \approx \lambda/4$), going from phase advances (ϕ) of $2\pi/3$ to $6\pi/7$, the change of the shunt impedance and group velocity are minimal, ~ 3 % and ~ 2 %, respectively. Although the attenuation factor changes by ~ 40 % and the Q factor by ~ 22 %, the shunt impedance remains virtually the same. The peak surface magnetic field increases by close to 19%, while the peak surface electric field increases by less than 9%. Finally, and as expected, the length per cell increases by up to a 28%, between $\phi = 2\pi/3$ and $6\pi/7$.

Table 5.22.: The TWS single cell parameters.

Parameter	$\phi = 2\pi/3$	$5\pi/6$	$6\pi/7$	**Units**
Frequency f		36		GHz
Q factor	4392	5251	5365	- -
Shunt impedance r_L	106	109	109	MΩ / m
Group velocity v_g	0.119	0.138	0.145	c
Attenuation α_0	0.7	0.5	0.5	m^{-1}
Peak surface field E_p^*	2.57	2.99	3.05	MV/m
Peak surface field B_p^*	4.45	4.76	4.83	mT
Cavity radius R	3.96	3.86	3.85	mm
Iris radius R_{iris}		2.00		mm
Cell length L_c	2.78	3.47	3.57	mm
Iris thickness L_i		0.60		mm
Cavity blending radius r_b		1.00		mm

*normalized to $E_z = 1$ MV/m

All of these factors make the lower phase advance option more attractive to reach the target integrated voltage (i.e. 12.75 MV), with lower power requirements for a given structure length (see Figure 5.58), which is not the expected result when dealing with structures with smaller apertures.

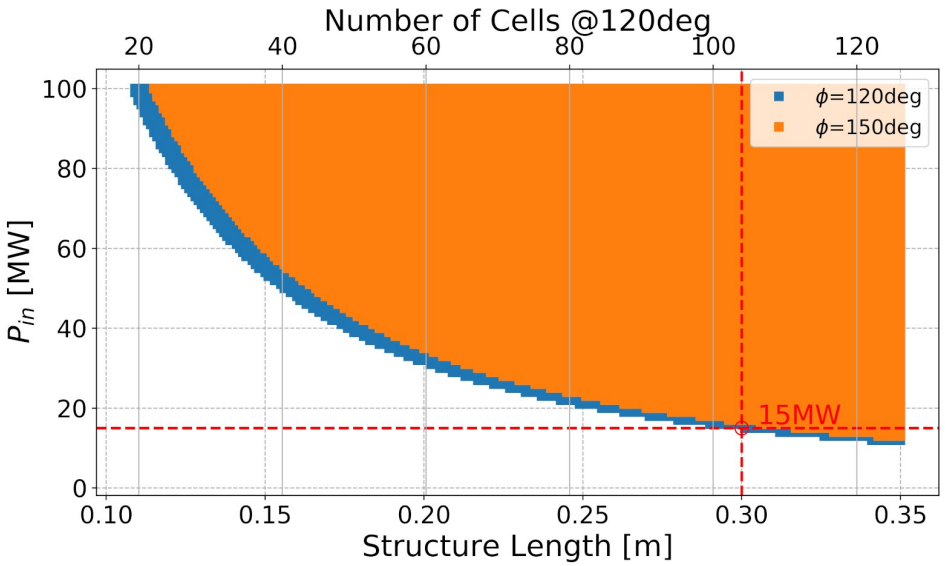

Figure 5.58.: Power requirement as a function of structure length at 36 GHz to provide 12.75 MV integrated voltage for $2\pi/3$ and $5\pi/6$ phase advance options.

Figure 5.58 shows: in orange, all the possible combinations of input power (after compression) and structure length ($\phi = 6\pi/7$) that deliver at least 12.75 MV of integrated voltage, and in blue, the same for $\phi = 2\pi/3$. This makes the lower border of the colored areas the optimal front, where a minimal input power is needed to deliver the required voltage, for a given structure length. Highlighted in red dashed lines is the point where 15 MW of input power after compression provides the 12.75 MV, for a 30 cm long TWS with $\phi = 2\pi/3$. This point is chosen as a trade off between the available power and a reduced number of cells (108 cells in this case). It is obvious that a structure with phase advance greater than $2\pi/3$, will fail to provide the linearising voltage for the input power available based on both RF source designs and the performed pulse-compressor studies. From this graph, it is clear that to reduce the

total structure length by one third (i.e. from 30 cm to 20 cm), would mean doubling the required input power, making it unpractical to go to shorter structure lengths.

Finally, preliminary thermal analysis simulations have been done on the single cell geometry to understand the thermal losses. An interesting outcome of the simulations is that, since the iris is the highest temperature point, and because this design has a large aperture, the thermal path between the tip of the iris and the cavity body remains relatively short and wide, making the heat transfer to the copper, and eventually the cooling channels, easy and quick. Therefore, using 10 mm diameter for the cooling channels and water at 27 deg C at peak gradient (42.5 MV/m), the increment is only 1 deg on the iris at the CW steady state (see Figure 5.59). For all these reasons the cooling should not present a considerable challenge for the operation of this structure.

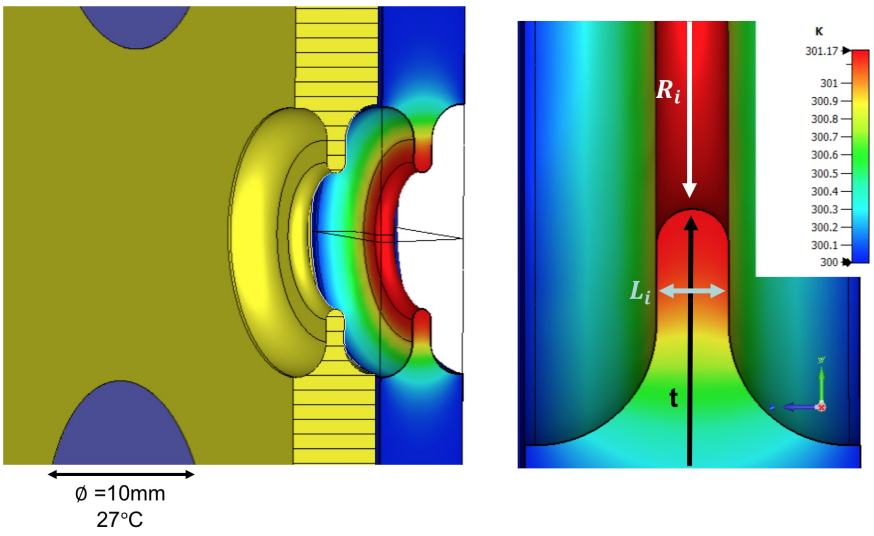

Figure 5.59.: Setup on CST® (left) and results of the steady state thermal simulations at peak gradient (right).

Couplers

A double feed mode launcher was designed for the Ka-band TWS. Figure 5.60 shows both the mode launcher topology (top) and the S-parameters for a 10 cm long structure (bottom), as an illustration of its performance. Inductive notches are included in the mode launcher's rectangular waveguides. These notches, along with a matching cell after the mode launcher's circular waveguide, are used to tune the coupling and eliminate any residual standing-wave due to internal reflections in the structure.

A mode converter option was designed in an effort to simplify a low loss transport network. Such a converter couples to a TE20 mode coming directly from a low loss waveguide, and feeds symmetrically a TE01 circular mode to the structure's mode launcher (see Figure 5.61). This mode converter requires the feeding paths to the mode launcher to be asymmetrical, which allows for the correct power flow into the structure. Inductive notches are introduced at the side of the splitting bifurcation to control and reduce any standing-wave trapped in this section. There is, however, a residual standing-wave that stays present in such a TE20 to TE01 mode launcher. Nevertheless, this has been reduced to a practical level and can be further optimized.. Figure 5.61 (bottom) shows the linear magnitude of the mode converter's S_{11} parameter. It is centered at 36 GHz and its broad bandwidth makes it a suitable coupler for the TWS.

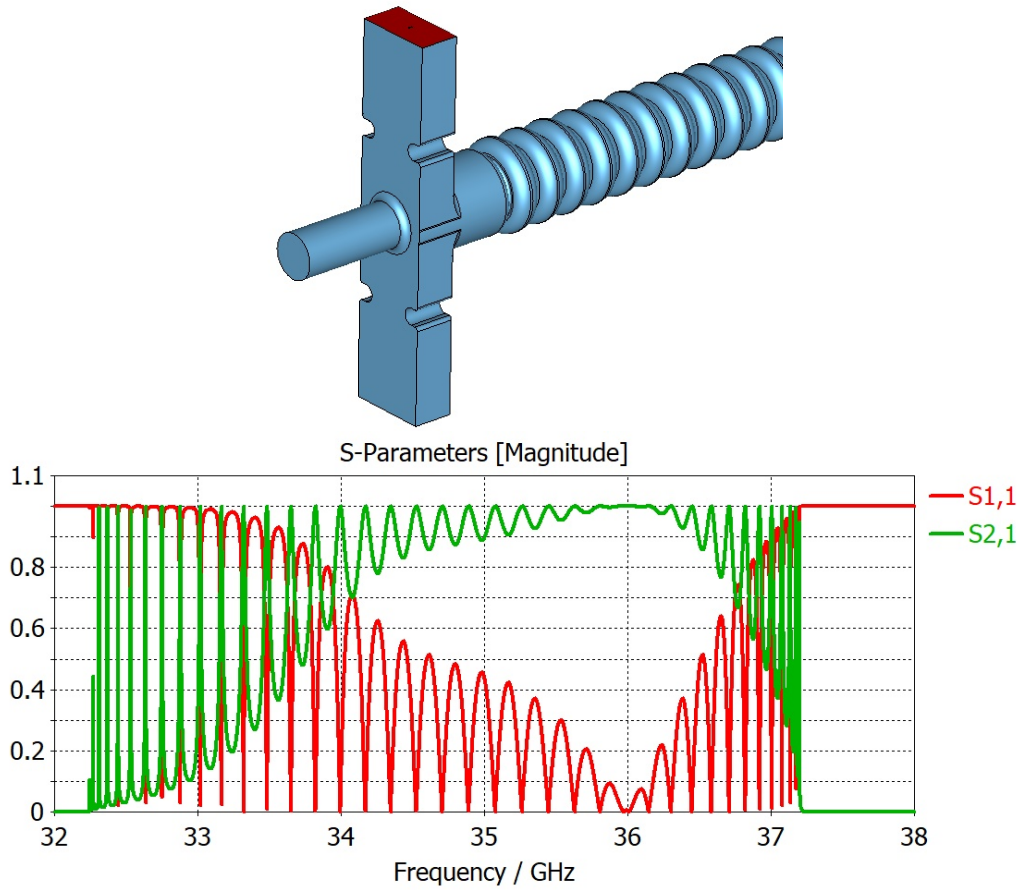

Figure 5.60.: Mode launcher geometry (top) and S-parameters for a 10 cm long structure (bottom).

Full structure

Following the comparison presented in Table 5.22, we propose a $2\pi/3$, 30 cm long (108 cells), constant impedance TWS as the lineariser baseline. This structure can reach the required 12.75 MV of integrated voltage, for a feasible input power of 15 MW after compression (see Figure 5.58). Table 5.23 shows the operational parameters of the baseline structure at the required integrated voltage for the bunch linearisation.

Table 5.23.: Ka-band travelng wave structure parameters at nominal voltage.

Parameter	**Value**	**Units**
Active length l	300	mm
Phase advance ϕ	$2\pi/3$	rad
Number of cells	108	–
Filling time τ	8.4	ns
Frequency f	36	GHz
Compressed power P	15	MW
Design gradient E_{acc}	42.5	MV/m
Peak surface field E_p	109.2	MV/m
Peak surface field B_p	189.1	mT
Modified Poynting vector S_c	4.84	W/μm^2

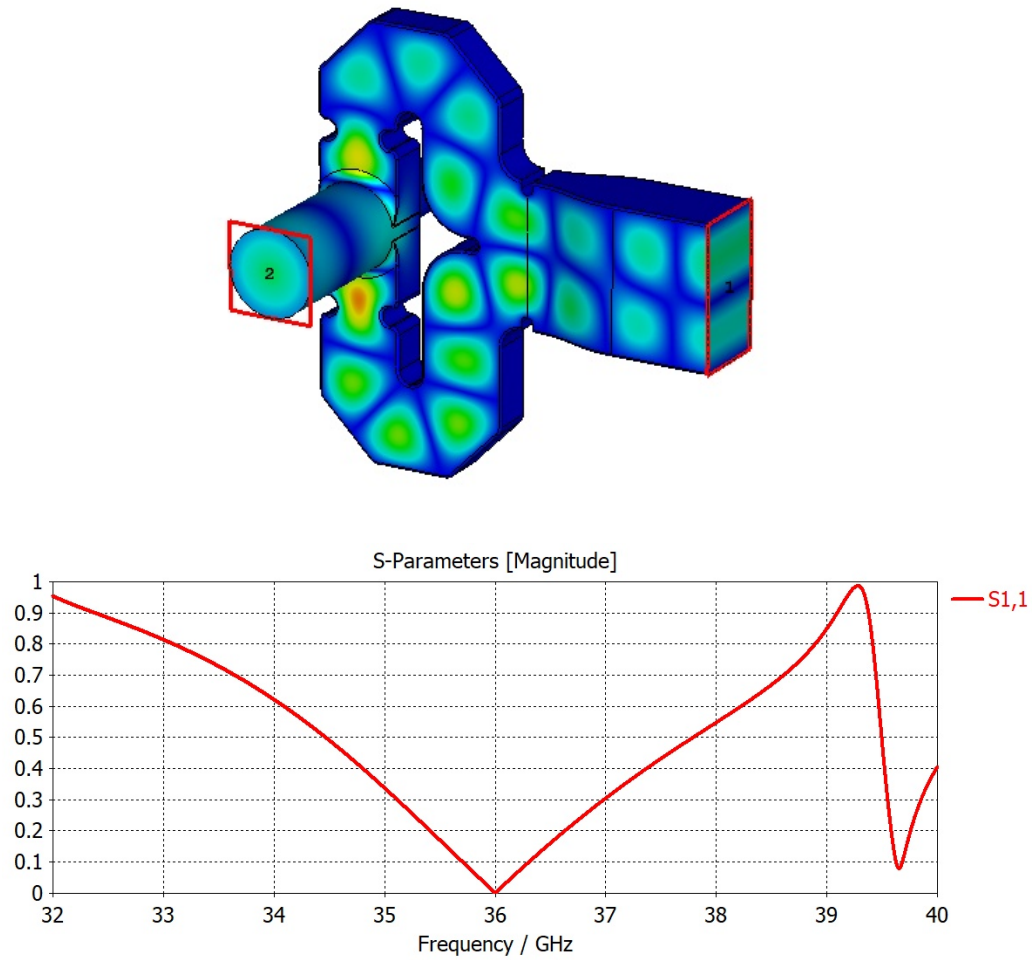

Figure 5.61.: TE20 to TE01 mode converter (top) and its matched S_{11} parameters (bottom).

The peak fields of $E_p \approx 109\,\text{MV/m}$, $B_p \approx 189\,\text{mT}$, and $S_c \approx 5\ \text{W}/\mu\text{m}^2$ at nominal gradient, are all within the practical limits of operation. A 108 cell structure is deemed feasible from the manufacturing view point, and a filling time of 8.4 ns allows for good performance of the pulse-compressor, see Figs. 5.55 and 5.56.

Table 5.24 shows a comparison of the power dissipation of the Ka-band linearizer to two X-band examples. The power dissipation at the Ka-band (2.5 kW/m) is comparable to that of the CompactLight main linac (2.4 kW/m), when both are operating at 1kHz repetition rate. This makes the Ka-band TWS a consistent option, in terms of its power dissipation, for this application.

Table 5.24.: Comparison of average dissipated power.

Structure	**Rep. rate [Hz]**	**Ave. dissipated power [kW/m]**
CLIC	50	3.06
CompactLight main linac	1000	2.44
Ka-band 300 mm TWS	1000	2.47

In order to benchmark the wakefield effects discussed in Section 5.2.9.1 long-range and short-range wakefield simulations have been done for a 10 cm long structure with couplers. Figure 5.62 shows the

magnitude of the longitudinal wake fields for a single, 75 nC, 300 μm electron bunch, up to 216 GHz. A more advanced analysis of this work will include the calculated wakefields on the beam dynamics studies for proper benchmarking of the codes used and their results. The long-range transverse wakefield of a 30 cm long structure was simulated by GdfidL [151]. The transverse wake potential for a 300 μm electron bunch is shown in Figure 5.63. Further studies are required to include long-range wake fields and gain trust in the codes employed for the beam dynamics calculations.

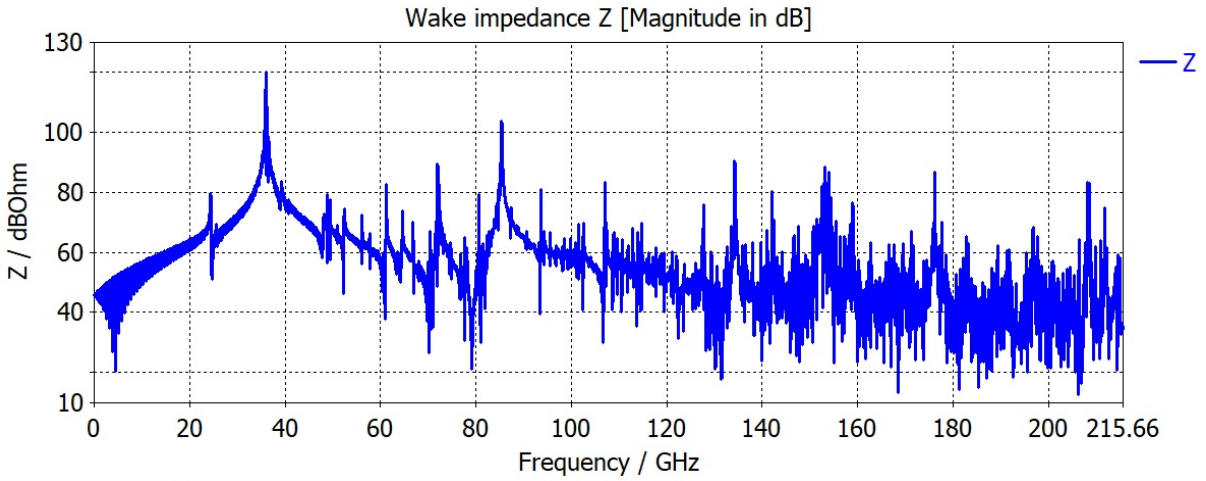

Figure 5.62.: Magnitude of the longitudinal wakefields on a 10 cm TWS for a single XLS nominal electron bunch.

5.2.9.5. Alternatives

Standing-wave linearizing structure

Using a standing-wave structure would initially appear to be more efficient as there is no power flow out of the structure. However there are two issues. The first issue is that there are no Ka-band 3 MW circulators hence the structures would need to be split and fed through hybrid couplers to cancel out the reflections in pairs by choosing the correct phase delay between each structure. Several structures are also required as there is a limit to the number of cells that can be used in a standing-wave structure and the Ka-band cells are very short. The second issue is the longer filling time of the structure leads to significantly longer SLEDII pulse-compressor delay-lines. This second issue can be avoided by partly filling the structure but in doing so the performance of the standing-wave structure becomes comparable to the travelling-wave structure.

A standing-wave structure option is retained as an alternative structure due to its lower average power requirement. The travelling-wave structure requires around 16 MW of input power to the structure, which needs a 1 microsecond pulse from the klystron/gyroklystron, resulting in an average power dissipated per unit length along the structure of 2.5 kW/m at a 1 kHz repetition frequency which is similar to the main linac. Initial studies of structure heating suggest that the maximum allowable heat load per unit length is independent of the cavity frequency however further studies are required to confirm this. In the event that the smaller K-band structures cannot handle the same power per unit length as the main linac then we would require an option with a lower heat load.

The standing-wave structure design is based on four 19-cell standing-wave structures. An aperture of 2 mm is chosen which is the same as that in traveling-wave option. Cell geometry is shown in Figure 5.64 and the general parameters are presented in Table 5.25.

A length of 2.08 m is chosen for the dual-moded SLEDII pulse-compressor delay-line to increase the input power to the standing-wave structures. This length is comparable with that for the traveling-wave

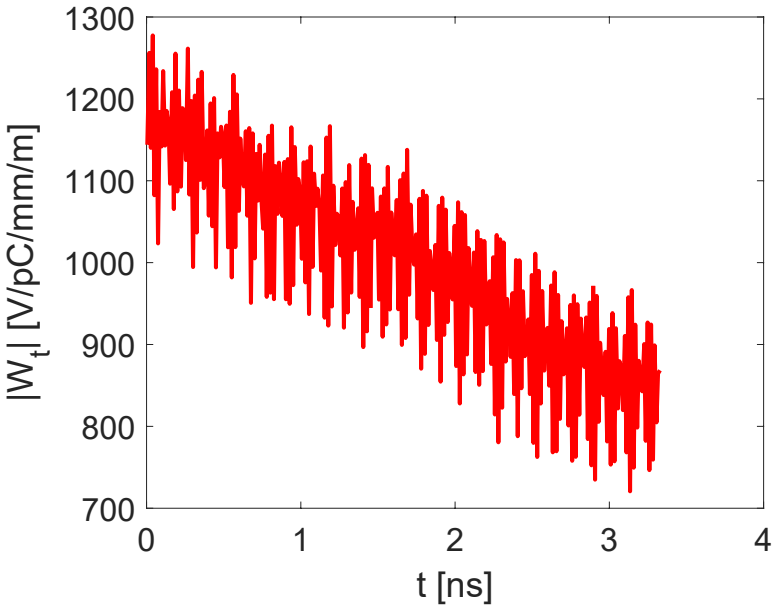

Figure 5.63.: Magnitude of the long-range transverse wakefield on a 30 cm TWS for a single XLS nominal electron bunch.

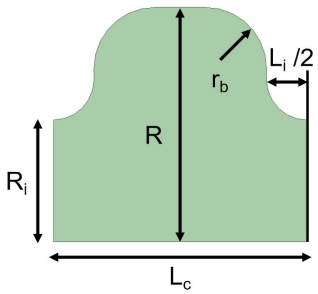

Figure 5.64.: Geometry of the standing-wave structure cell.

option and will give a flat top width of 30 ns. The standing-wave structure could be partially filled to 68 % of the steady state voltage with the compressed pulse. Each structure would require a peak input

Table 5.25.: SWS single cell parameters

Parameter	Value	Units
Frequency f	36	GHz
Q factor	5941	- -
Shunt impedance r_L	97	MΩ / m
Peak surface field E_p^*	2.67	MV/m
Filling time T_{fill}^{**}	121	ns
Cavity radius R	3.86	mm
Iris radius R_i	2.00	mm
Cell length L_c	4.16	mm
Iris thickness L_i	0.667	mm
Cavity blending radius r_b	1.00	mm

*normalized to E_z = 1 MV/m

**time to fill 99 % of the the steady state electrical field

power of 2.70 MW to achieve total integrated voltage of 12.43 MV, requiring only a 240 ns pulse from the amplifier. This results in a much lower heating per unit length of 1.6 kW/m. However, three hybrid couplers are needed to cancel out the reflection which makes the whole setup complicated.

Ka-band cryo-cooled structures

The amplifier development is a complex project and there is a risk that it is not successful and results in a much lower saturated output power in practice. If that occurs a more efficient structure would be required. One option would be to make a longer structure, however this would use more cells, and using multiple amplifiers would increase the cost significantly. Another option is to use a cryogenic-cooled copper standing-wave cavity. A 10 cm long structure, operating at 77 K, would have an estimated shunt impedance of 349 $M\Omega/m$, so two 10 cm structures could be utilised with a hybrid to cancel reflections to protect the amplifier. These structures could alternatively be used to reduce the length of the lineariser by increasing the gradient, however there seems to be little need to reduce the length at present. It would require significant additional development to design a cryostat and prototype and hence this is reserved as a future option rather than an alternative. It should be noted however that this technology can potentially deliver very high gradients and hence could be a future route to high gradient accelerators.

The use of cryogenic structures to both diminish the RF dissipation and to mitigate breakdown is by now well established, particularly through testing of X-band and S-band devices. In these experiments, the scaling of RF dissipation according to the theory of the anomalous skin effect (ASE) [152] has been verified, and surface fields over 500 MV/m have been achieved before breakdown is observed [153]. The advantage in dissipation effects diminishes somewhat at high frequency, but is still notable up to Ka-band. This component is critically important for applications such as the MaRIE XFEL [154], the CompactLight FEL and the Ultra-Compact XFEL at UCLA [155]. Paired with the CompactLight sponsored initiative to develop a preliminary design of a 15 MW-class klystron at 36 GHz, a compact, high gradient cryogenic linearizer in this frequency range now seems within reach [156].

This section reviews the scaling laws that allow approximate prediction of the performance of such a linearizer, based on a derated 5 MW input. To orient the expected performance, it is noted that the shunt impedance calculated for an optimized 36 GHz structure at room temperature is 158 MΩ/m. The expected behavior of this shunt impedance can be scaled from detailed calculations of ASE enhancement at low temperature in S-band by a factor of 5. To extend this to Ka-band, it is noted that the ohmic model scaling of surface resistivity is $R_{s,\Omega} \propto \omega^{1/2}$, while for ASE, the scaling in the low temperature limit is $R_{s,ASE} \propto \omega^{2/3}$. This means that the expected enhancement in the quality factor has a scaling

$Q_{enh} \propto \omega^{-1/6}$, and for low temperature (below 40 K), one may expect in Ka-band $Q_{enh} \simeq 3.3$. For less ambitious cooling designs, operating with liquid nitrogen at 77 K, an enhancement of 2.2 may be foreseen.

To give an idea of what is possible with this approach, the assumption is made, as stated above, of a 5 MW matched input into a 10 cm long structure, operating at 77 K, with estimated shunt impedance of 349 $M\Omega/m$. In this case, the accelerating field is 130 MV/m, which is well below the breakdown limit of 250 MV/m. The corresponding surface field of 260 MV/m is also below the threshold of dark-current emission of $\sim$ 300 MV/m that is strong enough to beam load the structure [157]. Further, at this frequency, the normalized vector potential is a factor of three below that needed to capture and accelerate dark current, further mitigating potential issues with spurious field emission effects.

For a cryogenic structure with a/λ = 0.12 (or a = 1 mm radius) and $r_1 = r_2$ = 5/7 ellipse semi-axes ratio and assuming an input power of 8 MW, with only one cryogenic structure it is possible to achieve an integrated voltage of about 15 MV. It should be noted that this structure's iris radius does not meet the CompactLight beam dynamics specification hence further work would be required to redesign the cavity to meet the requirements should a cryo-cooled option be utilised.

High gradient Ka-band structures

There is a strong demand for accelerating structures able to achieve higher gradients and more compact dimensions for the next generation of linear accelerators for research, industrial and medical applications. In the framework of the CompactLight project, an ultra-high gradient higher harmonic RF accelerating structure was also developed. The aperture chosen for this design is smaller than the minimum value dictated by beam dynamics requirements for CompactLight so is not considered for the lineariser, but may have applications in other X-band FEL projects with less stringent impedance requirements. In order to minimize the input power requirements for a given accelerating gradient, the RF accelerating structures have to be designed with the aim of maximizing the shunt impedance.

Table 5.26.: RF parameters list of the SW Ka-band structure

Parameter	**Unit**	textbfValue
Frequency	GHz	35.982
Operating Mode		π
Input power	MW	8
E_p/E_a		1.55
H_p/E_a	mT/MV/m	2.68
Effective accelerating Electric field	MV/m	125
Shunt impedance	MΩ/m	188
Unloaded quality factor, Q		5628
Build-up (coupling beta = 1)	ns	12.5
RF Pulse-length flat top	ns	50
Repetition rate	kHz	1
Average RF power per meter	KW/m	4.2
Structure length	cm	8
Iris radius a/λ ratio		0.12
Coupling coefficient, K	%	0.83
Iris thickness	mm	0.667
Ellipse semi-axes iris ratio shape		5/7
Cavity radius	mm	3.628

Presented here is a discussion of the electromagnetic design of an ultra compact Ka-band standing-wave (SW) linearizer, 8 cm long, working on π mode. It has an ultra-high accelerating gradient (beyond 100 MV/m) and minimum surface electric field for minimizing the probability of RF breakdown without affecting the beam dynamics quality [156, 158, 159]. It is assumed the beam energy is about 300 MeV, a bunch charge of 75 pC and an emittance of ε = 0.18 μm rad. As a result, from a compromise among the beam dimensions and the RF parameters, in order to minimize the peak surface electric field and to get a satisfactory surface magnetic field for the optimum design [156], the geometry chosen has an iris radius a/λ = 0.12 (or a = 1 mm radius), a cavity radius b = 3.628 mm and r_1/r_2 = 5/7 ellipse semi-axes ratio for the optimum design [156]. While this iris radius does not meet the CompactLight beam dynamics specification, it may well be suitable for other future projects. The main RF properties of the structure are summarized in Table 5.26.

A practical tolerable limit on the higher gradient operation came out recently from experimental activity [75, 160, 161] by estimating the Modified Poynting Vector (MPV) and pulse heating (PH) effects. The Breakdown Rate (BDR) is a measure of the RF sparks per unit time and length inside an accelerating structure. Estimations of the MPV by assuming a RF 50 ns flat top length pulse and HV in case of the cavity geometry are reported in Table 5.27.

Table 5.27.: MPV and PH as function of the accelerating gradient

E_{acc} [MV/m]	EF [MV/m]	HF [MA/m]	MPV [MW/mm^2]	PH [$^\circ$C]
100	155	0.2205	1.88	8
132	204	0.2911	3.27	14
150	232	0.3308	4.23	18

EF: surface electric fields; HF: surface magnetic field

In all cases, both the MPV and PH are well below the safety thresholds [160, 162, 163]. In order to achieve an integrated voltage of at least 15 MV, two separated normal conducting SW structures provide an integrated voltage of 20 MV. The average RF power per meter is 4.2 kW/m which, while double the other designs, is believed to be below the safety threshold, although further simulations are required to confirm this. The RF power source can be provided by a RF amplifier plus a SLED system [164]. Assuming a compression of 4, it is possible to achieve 12 MW. A hybrid device should give no problem for the power reflection to power source.

5.3. Beam Dynamics

5.3.1. Introduction

The user requirements for CompactLight were established by interacting with existing and potential FEL users in a variety of channels, and the required parameters are given in Section 3.2. Key requests from the user community, which affect the facility layout significantly, are:

- Wide range of photon energy (0.25-16 keV)
- Repetition rate 100 Hz and up to 1 kHz for the soft X-ray option.
- Simultaneous HXR/SXR operation at 100 Hz
- Pulse duration 1-50 fs

The facility is proposed in three stages as a baseline layout and two upgrade scenarios to satisfy various user requirements. Figures 4.1, 4.2 and 4.3 show the schematic layout of the machine for

different upgrade and operation modes. The target photon parameters of CompactLight are given in Table 3.1 and the corresponding electron beam repetition rate and energies for various operation modes are given in Table 4.1. To achieve the requested photon beam parameters the electron beam must have parameters as given in Table 5.28 below.

Table 5.28.: Main Parameters of the CompactLight FEL.

Parameter	Unit	Hard X-ray	Soft X-ray
Beam Energy	GeV	5.5–2.75	2.35–0.95
Photon Energy Range	keV	16.0–2.0	2.0–0.25
Peak Current (minimum)	kA	5.0–1.5	0.92–0.35
RMS Sliced Emittance	mm.mrad	0.2	
RMS Sliced Energy Spread	keV	550	
Bunch Charge	pC	75	

As can be seen in Table 5.28, the electron beam energy tuning range is large (i.e. 5.5 GeV - 0.95 GeV), the implications of which must be considered for the linacs operating at X-band frequency. Operation at different repetition rates brings another challenge to the facility design: multi-bunch operation and adjustment of the bunch spacing. To avoid over-complex operation, due to tuning different sections of the facility at different settings for different operating modes, the beam parameters at various locations have been fixed. Figure 5.65 shows the beam energies at different locations along the beamline.

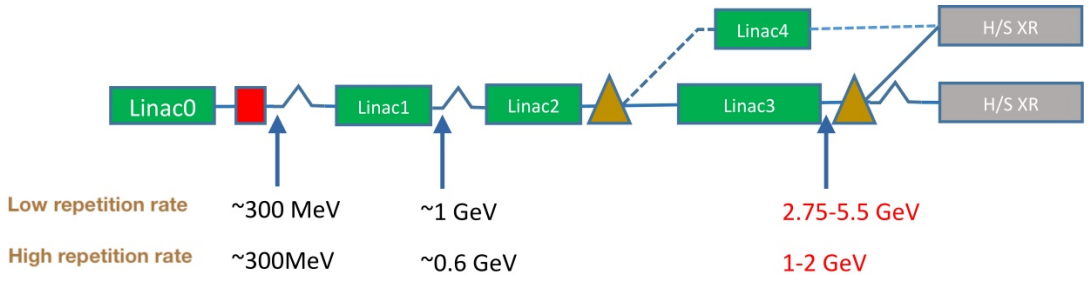

Figure 5.65.: Electron beam energy for various operation modes of the facility for different operation frequencies

In order to determine the performance of the machine for all operating modes, it is sufficient to simulate the following operating modes.

1. Soft-X-ray 100 - 250 - 1000 Hz 0.97 GeV targeting shortest bunch length for SXR (nominal + bba + jitter coh & inc)
2. Hard-X-ray 100 Hz 5.5 GeV targeting shortest bunch length (nominal + bba + jitter coh & inc)
3. Hard-X-ray 100 Hz 2.75 GeV targeting shortest bunch length (only nominal performance)
4. HXR/SXR Linac 4 (only nominal performance)

This section of the report summarises the integrated performance studies of the facility using the simulation tools discussed in [165]. Start-to-end (S2E) simulations have been performed from the cathode to the end of the undulator, including space-charge effects, coherent synchrotron radiation in magnetic compressors, wake field effects in the X-band linac and FEL performance. The injector optimization is reported in Section 5.3.2 while the lattice optimization and beam transport along the main accelerating sections is given in Section 5.3.3. The beam dynamics simulations also include the study

of key tolerances and mitigation strategies to deal with imperfections. The beam distribution obtained by the linac optimization has been imported into FEL simulations and the expected FEL performance is reported in Section 4.2.

5.3.2. Beam Dynamics in Injector

The proposed final injector design consists of a C-band RF gun and C-band accelerating structures operating for both the operational modes, high (1 kHz) and low (100 Hz) repetition rate, which implies operating the whole injector at the same accelerating gradient while keeping the beam quality within the requirements. The final layout, (see Figure 5.1), includes a 2.6 cell C-Band RF Gun (see Section 5.1.1) followed by C-Band Booster structures (see Section 5.1.2.1) for acceleration up to 120 MeV. This configuration meets the design goals of the CompactLight injector of Table 5.1

The reference working point for the CompactLight injector is a 75 pC electron bunch that reaches the laser heater entrance with $< 0.15\,\mu$mrad transverse normalised emittance and $\sim$ 100 MeV energy. For this reason the photoinjector is operated on-crest, nearly according to the invariant envelope criteria [166], imposing at the entrance of the first C-band structure a laminar envelope ($\sigma'_{x,y} = 0$) with the beam spot size $\sigma_{x,y}$ matched to the accelerating structures. The generation of the electron beam has been studied in detail by means of beam dynamics simulations. The layout reported in deliverable D3.4 was used (up to the laser heater) in simulations using the multi-particle codes Astra [167] and GPT [168], which take into account the space-charge effects relevant at very low energies and the beam features defined by the emission from the cathode. It was found that the bunch length at the entrance to the laser heater has to be $\sim$ 300 μm in order to achieve a final peak current up to 1 kA at end of BC1. It was assumed that the copper cathode is excited by a laser pulse with a flat-top longitudinal profile of 4 ps RMS duration with 0.5 ps rise/fall time. The transverse spot size is considered as a uniform distribution of $\sigma_{x,y}$ = 180 μm. With these laser parameters and a peak field at the copper cathode of 160 MV/m, the transverse intrinsic emittance is of the order of 0.1 mm mrad.

To perform precise simulations, particularly to understand CSR effects in dispersive sections, 1 million macro-particles were considered as a good compromise between reliability and computational time. The position of the first C-band structure, the strength of the solenoids to match the beam to the first structure, and the phase of the RF structures, were optimized to obtain the minimum slice and projected emittances. The simulated projected emittance is ε = 0.13 mm.mrad and the bunch length is $\sigma_z \approx 1$ ps. Figure 5.66 shows the energy gain, bunch length variation, normalized horizontal emittance and transverse beam size along the beamline, after optimization .

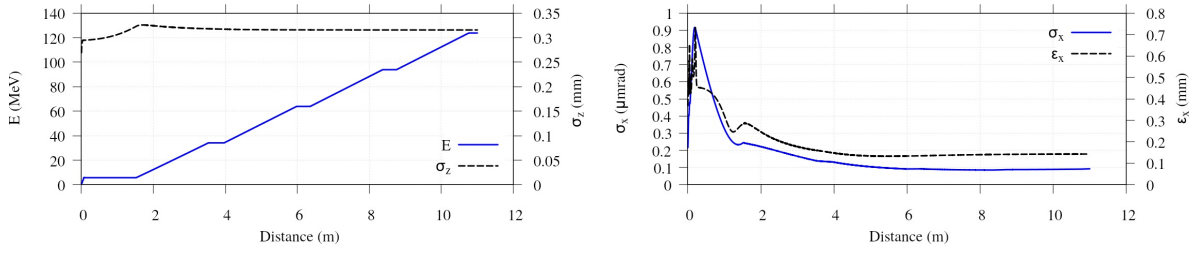

(a) (b)

Figure 5.66.: Evolution of 5.66(a) the RMS bunch length and energy gain 5.66(b) the transverse normalized emittance and transverse spot size along the photo-cathode RF gun and first C-Band section of the injector.

Figure 5.67 represents horizontal and longitudinal and beam parameters of the bunch at the exit of first C-band section of injector. The structures are operated on-crest in order to minimize relative energy spread.

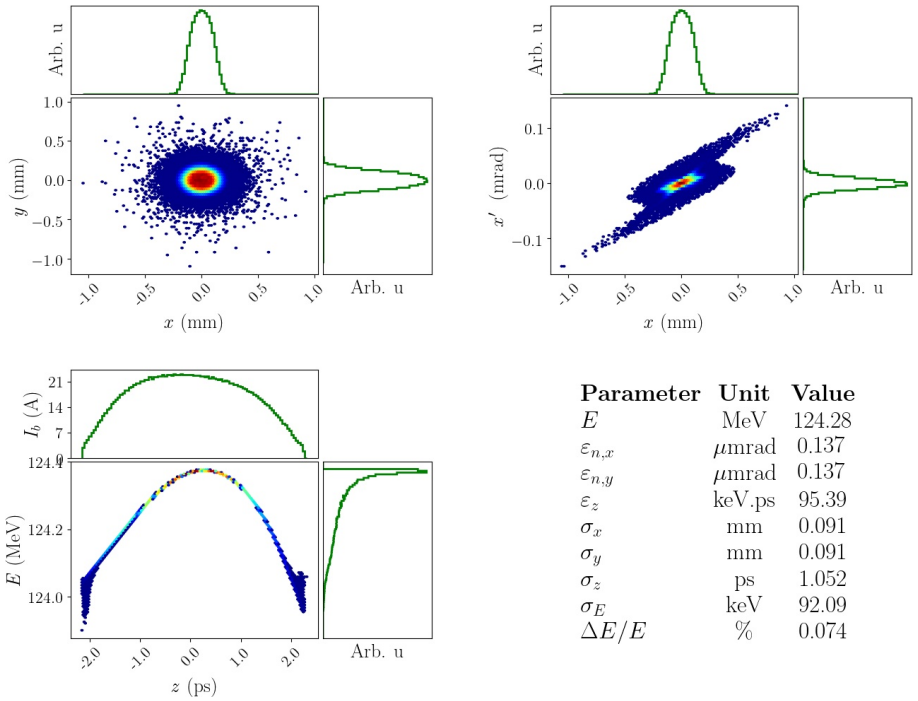

Parameter	Unit	Value
E	MeV	124.28
$\varepsilon_{n,x}$	μmrad	0.137
$\varepsilon_{n,y}$	μmrad	0.137
ε_z	keV.ps	95.39
σ_x	mm	0.091
σ_y	mm	0.091
σ_z	ps	1.052
σ_E	keV	92.09
$\Delta E/E$	%	0.074

Figure 5.67.: Transverse beam distribution (top left), and horizontal (top right) and longitudinal (bottom left) phase spaces with associated histograms representing the projection along the respective axis and beam parameters of the bunch at the exit of first C-band section of injector.

5.3.3. Beam Dynamics in Main Linac

The CompactLight FEL will operate within a range of wavelengths from 0.08 to 5 nm, covered by two distinct undulator beamlines at electron beam energy between 5.5-0.95 GeV. Two operation modes have been developed: “short bunch length mode” to achieve 5 kA peak current for HXR production and “long bunch mode” to achieve 1.5 kA for SXR production. The main accelerator has to be designed with sufficient flexibility to accommodate these operational modes. The main linac must be able to operate at three repetition frequencies: 100 Hz, 250 Hz, and 1000 Hz, while providing an electron beam with constant peak current and a small slice energy spread. Since the RF photocathode gun produces 75 pC over a bunch length of 1 ps, the bunch must be compressed by a total factor of more than 100 before it enters the undulator. The acceleration and compression is achieved in the main linac sections, as shown in Figure 4.1. The two bunch compressors (BCs) consist of symmetric magnetic chicanes.

The layout and the compression factor of the two chicanes have been optimized to minimize the 6D emittance dilution due to space-charge forces and wakefields in the linacs. The electron energy at the first chicane (BC1) was fixed to $\sim$ 300 MeV to avoid space-charge effects while compressing the bunch to increase the peak current and reduce the effects of transverse wakefields in the downstream linacs. The energy of the second compressor (BC2) depends on the operation mode: it is $\approx$ 1 GeV when the machine operates at low repetition rate, or $\sim$ 600 MeV at high repetition rate. Table 5.28 reports the beam parameters in HXR operation mode. Compressing the bunches at $\sim$ 1 GeV balances the conflicting requirements of minimizing the transverse and the longitudinal emittance dilution due to coherent synchrotron radiation (CSR), the final energy requirement, and cancellation of the final correlated energy spread by means of the downstream longitudinal wake field after BC2. By using a weak chicane with a bending angle smaller than 5 degrees per dipole, and a large initial correlated energy spread, the CSR effects can be reduced, but the chromatic aberrations make the tolerances on the magnetic field quality tighter.

A short Ka-band RF structure is used prior to the first compressor to linearize the longitudinal phase space, as discussed in Section 5.2.9.4. A laser heater is also foreseen at $\sim$100 MeV just after the photoinjector to avoid the micro bunching instability, as described in Section 5.1.3. Dedicated diagnostic sections after the laser heater, the BCs and beam delivery sections are also included in the beamline. Start-to-end simulations have been carried out to evaluate the emittance growth in the linacs due to transverse wakefields, CSR, and unwanted dispersion due to element misalignment. These simulations, which included realistic imperfections and correction techniques, successfully demonstrated that the required level of transverse emittance preservation is achievable. Jitter studies implemented in full start-to-end simulations have been performed and a tolerance budget of the linac stability has been defined according to the FEL specifications.

The beam delivery system ends with a transfer line located between the end of the linac and the entrance of the FEL. This sections includes the emittance diagnostic section, the electron beam switchyard for the two FELs, called the "spreader", and the matching sections. The design meets the constraints imposed by the existing and planned building boundaries, by the desire to utilize existing equipment and by the demands for various diagnostic instruments. To cover all operation options either a single bunch per pulse, or a train of two bunches per pulse, have to be transported through the following sections of the facility:

Option-i HXR/HXR: Two bunches @ 100 Hz

a - 1st bunch (E_f =2.75-5.5 GeV): LN0 $\mapsto$ BC1 $\mapsto$ LN1 $\mapsto$ BC2 $\mapsto$ LN2 $\mapsto$ LN3 $\mapsto$ SP1 $\mapsto$ FEL1

b - 2nd bunch (E_f =2.75-5.5 GeV): LN0 $\mapsto$ BC1 $\mapsto$ LN1 $\mapsto$ BC2 $\mapsto$ LN2 $\mapsto$ LN3 $\mapsto$ TC $\mapsto$ FEL2

Option-ii SXR/SXR: Two bunches @ 250 Hz

a - 1st bunch (E_f =0.95-2.4 GeV): LN0 $\mapsto$ BC1 $\mapsto$ LN1 $\mapsto$ BC2 $\mapsto$ LN2 $\mapsto$ LN3 $\mapsto$ SP1 $\mapsto$ FEL1

b - 2nd bunch (E_f =0.95-2.4 GeV): LN0 $\mapsto$ BC1 $\mapsto$ LN1 $\mapsto$ BC2 $\mapsto$ LN2 $\mapsto$ LN3 $\mapsto$ TC $\mapsto$ FEL2

Option-iii HXR/SXR: Two bunches @ 100 Hz

a - 1st bunch (E_f =0.95-2.4 GeV): LN0 $\mapsto$ BC1 $\mapsto$ LN1 $\mapsto$ BC2 $\mapsto$ LN2 $\mapsto$ SP2 $\mapsto$ LN4 $\mapsto$ FEL1

b - 2nd bunch (E_f =2.75-5.5 GeV): LN0 $\mapsto$ BC1 $\mapsto$ LN1 $\mapsto$ BC2 $\mapsto$ LN2 $\mapsto$ LN3 $\mapsto$ TC $\mapsto$ FEL2

Here LN*i* represents Linac-*i* $\{i = 0, 1..4\}$; BC*i* represents Bunch Compressor-*i* $\{i = 1, 2\}$; SP*i* represents Spreader Beamline-*i* $\{i = 1, 2\}$ for high and low energy, respectively; FEL*i* represents Free Electron Laser Beamline-*i* $\{i = 1, 2\}$ and TC represents timing chicane (See Figure 4.3). **Option-i** and **Option-ii** beamlines are valid for the Baseline while **Option-iii** is possible after Upgrade-2. The target beam parameters for all these operation modes are summarized in Table 5.28.

This chapter describes the accelerator physics aspects and the choice of parameters that led to the design of the CompactLight accelerator. The accelerator covers the region from the exit of the first C-band section of the injector to the entrance of the first FEL undulator. The tracking results of the electron beam dynamics from the photocathode to the end of different beamlines are discussed in the following sections.

5.3.3.1. RF Module Configuration

When a beam enters the linac with an offset, for example due to transverse jitter or an alignment error, the head of the bunch experiences a normal betatron transverse oscillation, whereas the tail feels the kicks due to the rf structure wakefields excited by the bunch head. At the end of a linac of length L, the amplitude of such transverse deflections of the bunch tail due to all structures is proportional to

$$\Delta x_{\text{tail}} \propto \int_0^L \frac{\beta(s)}{E(s)} \Delta V_{\perp}(s) ds, \tag{5.10}$$

where $\beta(s)$ is the beta function along the linac, $E(s)$ is the beam energy, and $\Delta V_{\perp}(s)$ is the transverse deflection due to transverse wakefield kick at location s [169]. For a particle at relative position z, one can write:

$$\Delta V_{\perp,\parallel}(s,z) = Ne^2 \int_{-\infty}^{z} W_{\perp,\parallel}\left(s, z'-z\right) \lambda\left(z'\right) dz', \tag{5.11}$$

where N is number of particles per bunch, $\lambda(z)$ is the longitudinal charge distribution. $W_{\perp}(z)$ and $W_{\parallel}(z)$ are the RF structure single-particle transverse and longitudinal wake potentials, respectively [170]. In the evaluation of Equation (5.11), $W_{\perp}(s)$ has been calculated using the analytic approximation of the wake potential presented in [137], applied to a two-particle beam model such as

$$W_{\perp}(s) = \frac{4Z_0 c s_{\perp 0}}{\pi a^4}\left[1-\left(1+\sqrt{\frac{s}{s_{\perp 0}}}\right)\exp\left(-\sqrt{\frac{s}{s_{\perp 0}}}\right)\right], \quad W_{\parallel}(s) = \frac{4Z_0 c}{\pi a^2}\exp\left(-\sqrt{\frac{s}{s_{\parallel 0}}}\right) \tag{5.12}$$

where $Z_0 = 120\,\pi\Omega$ is the impedance of free space, a is the average aperture radius of the structure, g is the gap length, d is the length of the cell, $s_{\parallel 0} = 0.41 a^{0.18} g^{1.6}/d^{2.5}$ and $s_{\perp 0} = 1.69 a^{1.79} g^{0.38}/d^{1.17}$. Equation (5.10) implies that the amplification factor is proportional to the beta function along the beam line. Therefore, in order to enhance the beam stability, the betatron function of the lattice has to be small enough to minimize the effect introduced by wakefields. A FODO-type lattice was chosen, optimized in the number of structures per module, and calculating the transverse deflection, in normalized coordinates, for different type of charge distributions along the X-band structures of the linac.

Space-charge effects in the linacs have been deemed negligible, following the indications in [171], where it is stated that the transition energy, γ_{tr}, between the space-charge dominated regime and the thermal regime, is approximated by the following equation:

$$\gamma_{\text{tr}} = \frac{\hat{I}}{2I_A}\frac{\sigma^2}{\varepsilon_n^2} \tag{5.13}$$

where $\hat{I}$ is the peak current, and I_A is the the Alfvén current ($\sim$ 17 kA). With an average β function of 5 m, a bunch length of about 300 μm, a bunch charge of 75 pC, and a normalized emittance of 0.2 μm, one obtains: $E_{\text{tr}} = m_e\gamma_{\text{tr}} \sim 120$ MeV. As it can be seen on Figure 5.66(b) the change in emittance due to space-charge is negligible by the end of the second structure. In order to further minimize the effect of space-charge forces in the injector, the beta functions were minimised ($\sim$ 5 m) up to the first BC, using 2 structures per FODO cell. The lattice is relaxed in the second stage of acceleration where the bunches have a length of $\sim 20\,\mu$m, with 2 structures between each pair of quadrupoles in Linac-1, Linac-2 and Linac-4. The beta functions in the last stage of acceleration can be even larger since the bunch is quite short. Thus we have chosen 4 X-band structures between each pair of quadrupoles in Linac-3. The Twiss functions and phase advances per FODO have been optimized by considering the following factors:

- Offsets of the structures (thus offset of the beam inside the structures) cause increasing wakefield effect (minimum deflection requires a strong lattice).
- Quadrupole misalignment causes transverse deflection of the beam and introduces dispersion, thus increasing the emittance growth. Various alignment techniques are used to align the beam (requiring a weak lattice and fewer quadrupoles).

5.3.3.2. Bunch compression scheme (from Booster 2 to BC2)

The overall CompactLight design parameters are motivated by the goal of 75 pC bunch charge, accelerated to 5.5 GeV and compressed to a peak current of about 5 kA. To maximise the FEL brightness a flat top longitudinal current profile is required so that the maximum number of electrons contribute to the FEL lasing and all longitudinal slices of the bunch reach FEL saturation at the same distance throught

the undulator. A two-stage bunch compression system is used to achieve this goal. The whole bunch compression system comprises, apart from the two magnetic chicanes, two linac sections (Linac-0 and Linac 1) to imprint the energy chirp on the beam, and an X-band section to linearise the energy–time correlation along the bunch. After compression, the energy chirp is reduced by virtue of the longitudinal wakefields in Linacs 2 and 3.

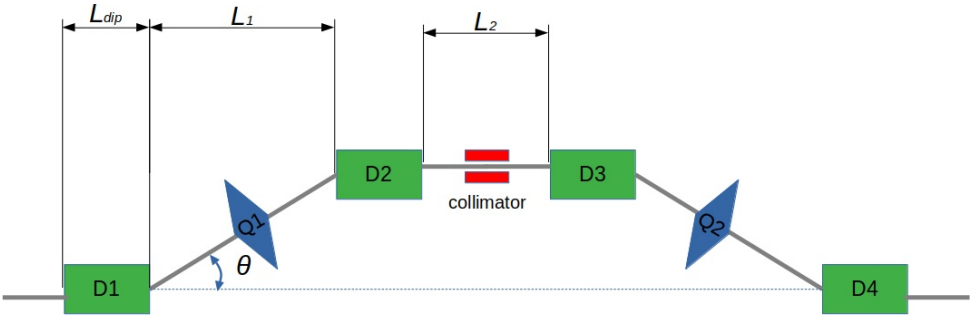

Figure 5.68.: A schematic of the bunch compressors

A 4-dipole chicane geometry has been selected for BC1 and BC2 to achieve the required bunch length at the entrance of the undulators. A schematic of the bunch compressor is shown in Figure 5.68. The chosen geometry has been identified as the most compact and suitable. Because of its symmetry, this bunch compressor is a perfect achromat. Nevertheless, leakage of the dispersion function after the last bend may occur due to errors. For this reason, trim quadrupoles (shown in the figure between the first and second bends and the third and fourth bends) are added for fine tuning the dispersion function. The electron bunch undergoes compression in the BCs according to the following equation:

$$\sigma_{z,f} = \sqrt{\left(\frac{\sigma_{z,i}}{C}\right)^2 + \left(R_{56}\sigma_{\delta,i}\right)^2 + \left(3T_{566}h_i{}^2\sigma_{z,i}{}^2\right)^2} \tag{5.14}$$

where $\sigma_{z,i}$ and $\sigma_{z,f}$ are initial and final RMS length of the electron bunch, R_{56} and T_{566} the first and second order chicane matrix elements, h the linear energy chirp of the electron bunch, and C the linear compression factor defined as:

$$C = \frac{1}{|1 + hR_{56}|}. \tag{5.15}$$

An initial 2D optimization was performed using fast Track1D. This code was developed within the CompactLight collaboration [172] and described in D6.1. It follows a similar approach to LiTrack [173], without taking into account the CSR effects. However one needs to consider CSR and indirect emittance excitation via longitudinal-to-transverse coupling as in

$$\varepsilon = \varepsilon_0\sqrt{1 + \frac{H}{\varepsilon_0}\sigma_{\delta,CSR}}, \tag{5.16}$$

where $\sigma_{\delta,CSR}$ is the energy spread due to CSR wake, $H = \left(\eta^2 + \left(\beta\eta' + \alpha\eta\right)^2\right)/\beta$ is the optics function for coupled betatron and dispersive motion, and β, α and η are the Twiss parameters [174].

In order to reduce the relative effect of CSR on emittance growth, Eq. 5.16 indicates that the BC lattices need to have small H. One can minimize H by choosing small bending angle (thus used large energy spread) and minimizing β-function considering beam divergence angle, in the latter half of the chicane.On the other hand, while the emittance excitation due to CSR requires small H, the micro bunching instability might need larger H. To address both problems, an integrated optimization of both bunch compressors has been performed using ELEGANT [175] taking into account both CSR and space-charge.

The simulations in the injector booster have been described previously, in 5.3.2. The second part of the Linac-0, consisting of 6 C-band structures, generates the necessary longitudinal chirp, through off-crest operation, for the bunch compression. An harmonic linearizer operating at K-band frequency (see Section 5.2.9) is employed at the end of Linac-0 to control energy modulation of the bunch. Chirp adjustments between the compressor chicanes are carried out on the X-band structures of Linac-1. Linac-0, Linac-1 and the BCs are optimized simultaneously in order to have quasi uniform charge distribution at the end of BC2. The transverse beam optics are controlled by quadrupoles downstream of each bunch compressor in order to minimize the effect of CSR. Parameters such as RF gradient, RF phase or bending angle are only slightly different for different operating modes.

The electron bunch profiles (horizontal phase space, energy spread, current and emittance) directly after the second bunch compressor BC2 are shown on Figure 5.70 and Figure 5.71 for low and high repetition modes, respectively. In the low repetition mode, the bunch is compressed from initially σ_t = 1 ps to σ_t = 65 fs after the first chicane, and to σ_t = 5 fs final bunch length, with a peak current of 5.0 kA at 75 pC. In the case of high repetition mode, since the Linac-0 (injector) has fixed operation parameters for both modes, the compression scheme is identical to up the BC1 and the bunch is compressed to final bunch length of σ_t = 18 fs at BC2 with a peak current of 1.2 kA. Figure 5.69 shows the Twiss parameters through the first and second bunch compressors. Three quadrupole magnets are used to match the optics functions and optimize the H parameters for both compressors. The CSR effect on the slice emittance is mitigated by obtaining a waist in the horizontal beam size in the fourth dipole of the chicane. The optimization results for both BCs are reported in Table 5.29 for different operating modes. Peak currents of 5 kA and 1.2 kA are obtained for low and high repetition rate modes, respectively.

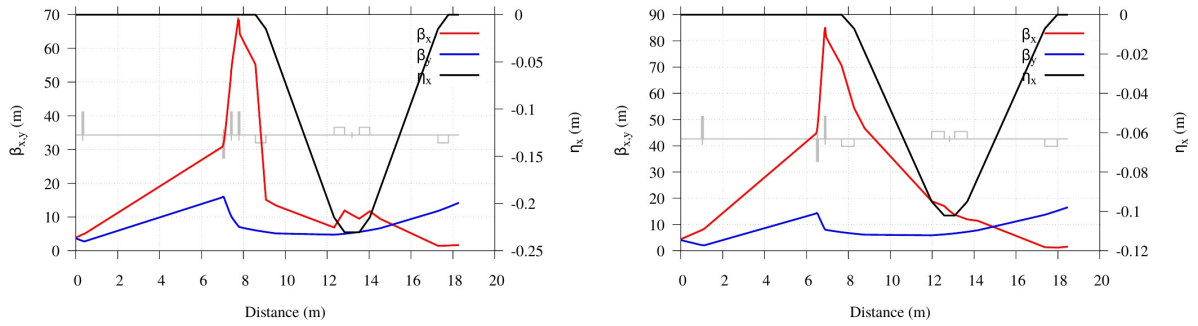

(a) BC1 (b) BC2

Figure 5.69.: Twiss functions along BC1 and BC2

Table 5.29.: Chicane parameter table for low and high repetition mode operation.

Parameter	**Units**	**Low rep-rate**		**High rep-rate**	
		BC1	BC2	BC1	BC2
Beam Energy	GeV	0.28	1.1	0.28	0.68
Initial rms bunch length	μm	315	26	315	26
Final rms bunch length	μm	18	1.5	18.6	5.56
RMS relative energy spread	%	1.09	0.41	1.08	0.44
Bending angle	deg	3.83	1.375	3.83	1.25
Dipole Lenght (L_{dip})	m	0.4	0.6	0.4	0.6
Outer drift length (L_1)	m	3.25	3.7	3.25	3.7
R_{56}	mm	-31.58	-4.72	-31.58	-3.9
T_{566}	mm	47.58	7.09	47.58	5.86

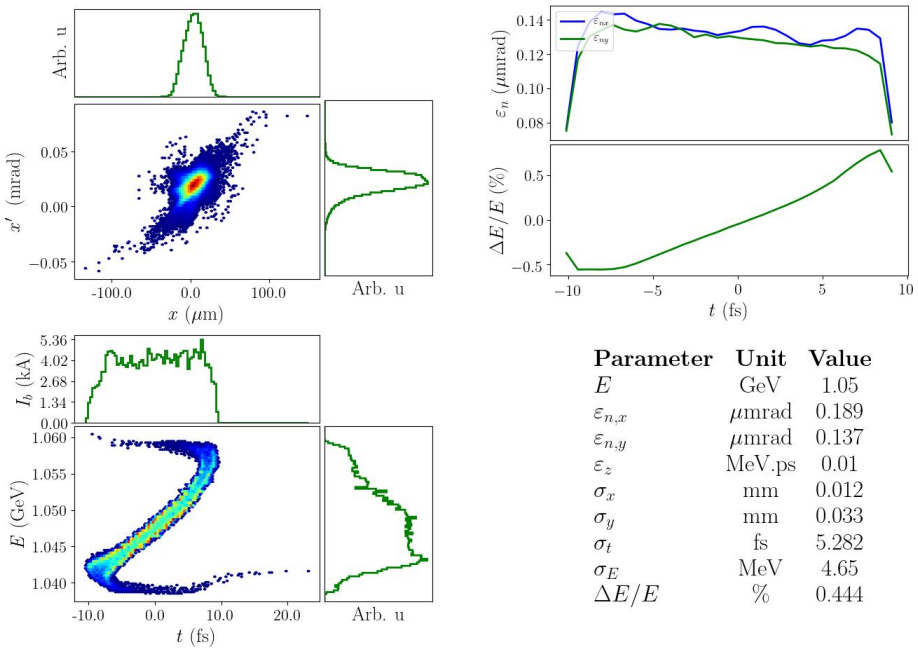

Parameter	Unit	Value
E	GeV	1.05
$\varepsilon_{n,x}$	μmrad	0.189
$\varepsilon_{n,y}$	μmrad	0.137
ε_z	MeV.ps	0.01
σ_x	mm	0.012
σ_y	mm	0.033
σ_t	fs	5.282
σ_E	MeV	4.65
$\Delta E/E$	%	0.444

Figure 5.70.: Horizontal (top left), and longitudinal (bottom left) phase spaces with associated histograms representing the projection along the respective axis and sliced emittance/energy spread and beam parameters of the bunch at the exit of BC2 for low repetition operation.

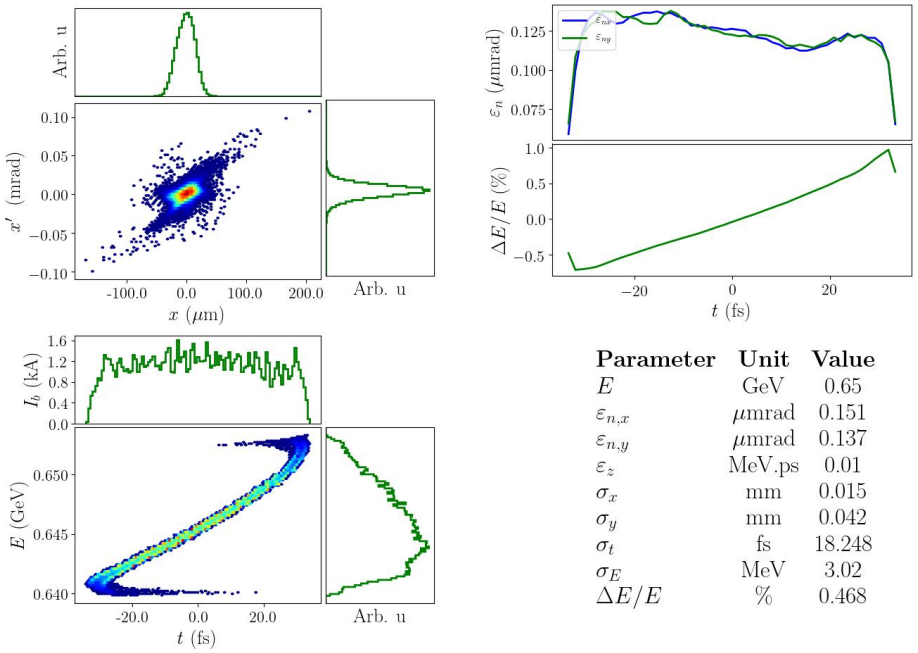

Parameter	Unit	Value
E	GeV	0.65
$\varepsilon_{n,x}$	μmrad	0.151
$\varepsilon_{n,y}$	μmrad	0.137
ε_z	MeV.ps	0.01
σ_x	mm	0.015
σ_y	mm	0.042
σ_t	fs	18.248
σ_E	MeV	3.02
$\Delta E/E$	%	0.468

Figure 5.71.: Horizontal (top left), and longitudinal (bottom left) phase spaces with associated histograms representing the projection along the respective axis and sliced emittance/energy spread and beam parameters of the bunch at the exit of BC2 for high repetition operation.

5.3.3.3. Linac-2 to Linac-4

The main bunch acceleration is driven by three X-band linacs (Figure 4.1). The first of these (Linac-1) is located between the bunch compressors and has already been described in Section 5.3.3.2. Downstream of the second bunch compressor, Linac-2 defines the energy at the spreader through to

Linac-4, with the extraction point to the simultaneous SXR/HXR operation. Final acceleration to the short wavelength FEL line is achieved in Linac 3. A simple FODO type of lattice is proposed which has the advantage of easy operation. The detailed configurations of the Linac FODO cells are given in Section 5.2.6.2 and 5.2.6.3. As discussed in Section 5.3.3.1 the Twiss functions are optimized along the linacs in order to minimize wakefield effects, considering the trade off between sensitivity to quadrupole errors. The parameters of the main linac sections are summarised in Table 5.30.

Table 5.30.: Parameters of the main linac sections

Parameter	**Unit**	**Linac-1**	**Linac-2**	**Linac-3**	**Linac-4**
Cell Layout			FODO		
Cell Length	m	4.91	4.91	9.23	4.91
Phase Advance	deg	81	81	101	81
Cavities per half cell		2	2	4	2
Number of cells		4	2	17	2
Cavity frequency	GHz		X-band (12 GHz)		
Max cavity gradient @high rep.	MV/m		30		
Max cavity gradient @low rep.	MV/m		65		
Quadrupole length	cm		16.5 (8cm effective)		

Despite its technical challenges, an X-band linac does present some advantages for the beam dynamics in comparison to an C-band linac. At higher frequencies, a higher effective gradient is possible, allowing a shorter linac length. The lower iris diameter of X-band structures, compared to C-band, results in stronger wakefields. While wakefield effects on the transverse emittance are tolerable, the longitudinal component helps in the reduction of the energy chirp generated for the compressors, resulting in FEL bandwidth reduction.

The phases in Linac-1 are optimized for maximum compression and for a flat top current profile with peak current above 5 kA. The phases in Linacs 2 and 3 are chosen to be on crest for maximum acceleration. Note that the choice of the phases takes into account longitudinal wakefields. To reach 5.5 GeV, Linac-3 requires a large number of structures. The matching condition for the FODO lattice is 81° and 101° phase advance (which is not a strong condition) per cell for Linacs 1/2/4 and 3, respectively . It can be adjusted if needed, to ease the matching from, or to, other sections. Diagnostic sections after BC1 and Linac-2 have been foreseen in order to diagnose the longitudinal profile of the bunch before it is transported to Linac-4 and Linac-3 (see Section 5.2.5). Profile monitors are foreseen per linac cell to measure the optical functions. The measurement is completed by the orbit response function using the BPMs located inside Quadrupole chamber (see Section 5.4).

During the transport from BC2 to the FEL-2 undulator beamline, the Linac-2 and Linac-3 wakefields are used to shape the current profile for optimum FEL lasing. The final longitudinal bunch current profile before the FEL2 beamline, for shortest wavelength operation, has a quasi-flat top profile together with small slice emittance.

The beam optics design comprises FODO channels in each linac section through to the undulators, and a diagnostic line downstream of BC1. Four quadrupoles between these sections enable beam matching during transition to another section and to special elements such as the chicanes or the spreader beamlines. The overall beam optics through to the FEL-2 beamline are shown in Figure 5.73.

5.3.3.4. Spreader beamlines

The low energy spreader for CompactLight diverts the the first bunch coming from Linac-2 to Linac-4 for SXR/HXR operation, while the high energy one is used to deliver the first bunch to FEL1 beamline for SXR/SXR or HXR/HXR. At the entrance of both spreaders is a TDC operating at S-band frequency

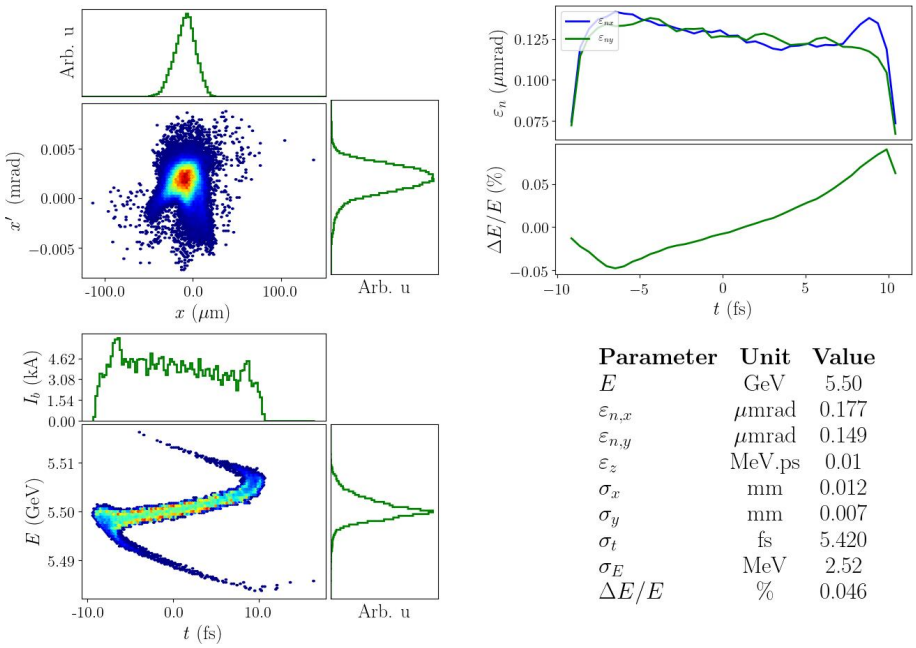

Parameter	Unit	Value
E	GeV	5.50
$\varepsilon_{n,x}$	μmrad	0.177
$\varepsilon_{n,y}$	μmrad	0.149
ε_z	MeV.ps	0.01
σ_x	mm	0.012
σ_y	mm	0.007
σ_t	fs	5.420
σ_E	MeV	2.52
$\Delta E/E$	%	0.046

Figure 5.72.: Horizontal (top left), and longitudinal (bottom left) phase spaces with associated histograms representing the projection along the respective axis and sliced emittance/energy spread and beam parameters of the bunch at the entrance of FEL2 undulator beamline for low repetition operation.

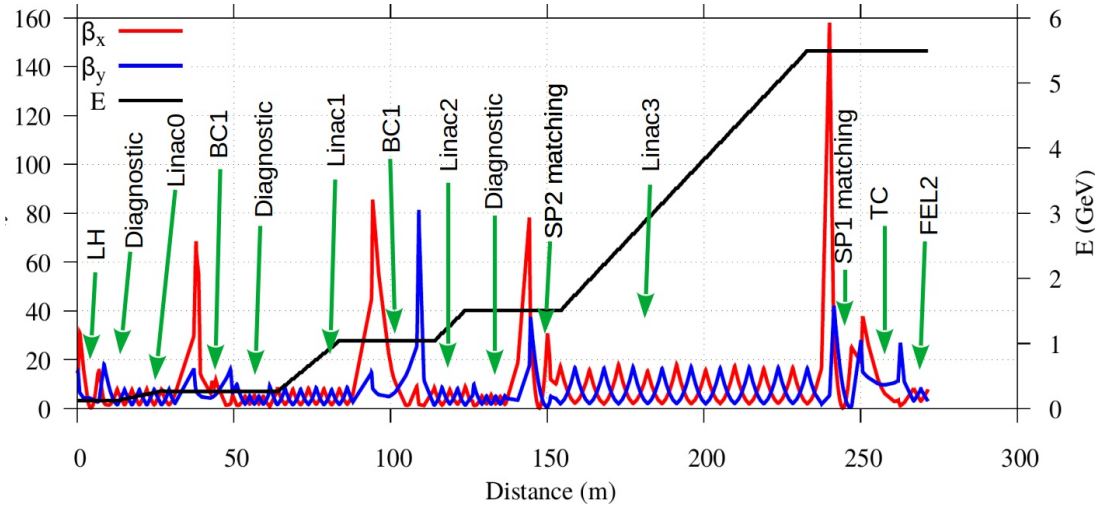

Figure 5.73.: Start-to-end beta functions and energy gain of the bunch through to the FEL-2 beamline.

(see Sections 5.2.8 and 4.1.3.5) followed by septum magnet. For the former case the nominal bunch length is desirable however for the latter case the beam goes through a series of dispersive sections and CSR effects spoil the beam quality so that a slightly longer bunch is preferable. In view of these requirements, and to allow some flexibility for this beamline it is possible to set up the spreaders for a range of values of R_{56}.

The electron bunches are longitudinally compressed below 5 fs (rms) and the peak current reaches about 5 kA . When such high peak current bunches pass through the dogleg, electron beam orbit instability and projected emittance growth in the deflecting plane can occur. The use of two sets of Double-Bend Achromat (DBA) structures is the simplest solution to cancel out the CSR effects of the

dogleg [176]. If one adjusts the betatron phase advance between adjacent dipoles to an odd multiple of π in the deflecting plane, the sum of the CSR dispersion becomes zero at the end of the dogleg. Since the betatron phase advance between the two dipoles of the DBA is naturally π, only the phase advance between the two DBA structures is adjusted close to π. To control the bunch length along the spreaders, quadrupoles are tuned for adjusting R_{56}. The design is similar to that in [177]. The total length is approximately 20 m and the separation between the FEL-1 and FEL-2 beamlines is 2.5 m, with a net bending angle equal to zero, making the two beamlines parallel to each other as shown schematically in Figure 5.74 for first and second spreaders.

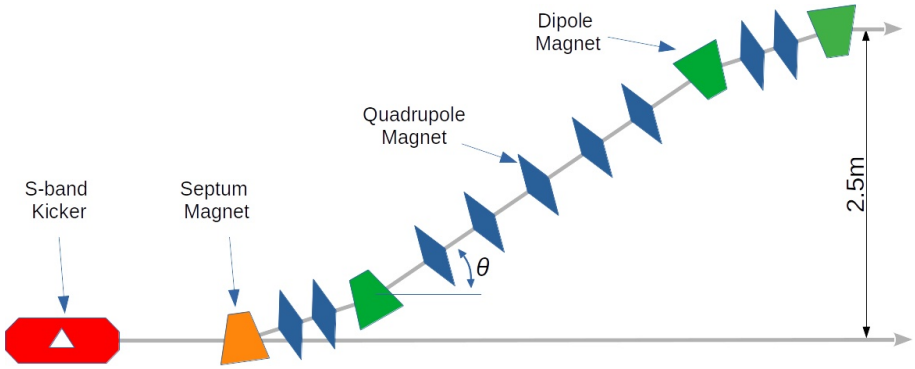

Figure 5.74.: Schematic layout of the spreader which is compposed two DBA with opposite bending angle.

In order to evaluate emittances and beam size changes throughout the spreaders, simulations have been done with an electron distribution at the entrance of the septum magnet. The initial beam conditions are shown in Table 5.31.

Table 5.31.: Beam parameters at the entrance of low and high energy spreaders

Parameter	**Units**	**Low energy spreader**	**High energy spreader**
Beam Energy	GeV	1.5	5.5
Rms bunch length	μm	1.5	1.5
RMS relative energy spread	%	0.25	0.02
RMS relative energy spread	%	0.25	0.02
Horizontal beta function	m	0.33953	1.1547
Horizontal alpha function		0.8569	1.6341
RMS Horizontal emittancee	mm.mrad	0.178	0.181

Another consideration for the spreader design is the synchronization of dual bunch operation, as discussed in Section 6.2.2.3. The twin bunches will follow identical dynamics in the accelerator before being separated by the S-band TDC. By virtue of the odd number of C-band cycles in the injector, the twin bunches will be horizontally deflected by kicks with opposite sign at the deflector. About 30 MV peak deflecting voltage at the maximum beam energy of 5.5 GeV will impose angular kicks of the order of half a degree, and will allow the two bunches to be separated by $\sim$ 5 mm after a 0.5 m-long drift section. At this position, a DC out-of-vacuum thin septum magnet will direct the leading bunch to FEL-1, and the trailing bunch to FEL-2. The same scheme is proposed for low energy spreader in order to transport first and second bunch through Linac-4 and Linac-3, respectively.

The leading bunch directed to FEL-1 (or Linac-4) has to be delayed by 526 ps w.r.t. the trailing bunch. Note that this value is not the same at the timing separation of the twin bunches as they enter the spreader which is either 3 or 5 cycles of X-band (500ps 0r 833ps). However, this 526 ps delay,

in combination with the path length delays in the optical beamlines, allows all permutations of HXR and SXR FEL pulses to be combined in one user station for pump-prope experiments. The 526p̃s delay is accomplished by means of a dog-leg-like switchyard from the septum to FEL-1. This has to satisfy a minimum longitudinal occupancy of 20 m, for a lateral separation of the undulator lines by $\sim$ 2.5 m. On the other hand, in order to minimize impact of CSR on the beam emittance, parasitic energy dispersion and energy distribution, the bending angle needs to be smaller than 5 degrees at the minimum beam energy of 0.95 GeV. From the schematic given with Figure 6.58, and as descibed earlier, the optical delay partly compensates for the electron delay in the spreaders. The required time delay on the spreaders can be simply computed by

$$\Delta t_{DL} - \Delta t_{opt} = nT \tag{5.17}$$

where Δt_{DL} is the time delay in dogleg, Δt_{opt} is the time delay in optical beamlines and T = 166 ps is the period of the C-band frequency.

The bunches meeting the same beam dynamics conditions through the accelerator will have identical bunch length when they leave BC-2. Therefore the most challenging beam transport for both spreaders, due to strong CSR, is the 5 kA case which is required for SXR/HXR with HXR in the range of 8-16 keV (i.e. E_{LN4} = 0.95 GeV E_{LN3} = 5.5 GeV, see Table 5.28). For this case, as it can be seen in Table 5.31, the projected energy spread at the entrance of the low energy spreader is too large due to less wakefield compensation in Linac-2. Defining the derivative of the dispersion function in the middle of the bending magnet as D', the kick to the electron trajectory at the end of the bending magnet is

$$\Delta x' = D' \delta E \tag{5.18}$$

where δE is the energy spread of the bunch which can be the initial energy spread or the energy spread introduced by CSR in dispersive sections. For that reason it is useful to increase the bunch length in the low energy spreader by tuning the R_{56}. On the other hand, in the case of the HXR/HXR operation, if both FEL lines are operating close together in wavelength, the length of the bunches has to be identical, thus the lattice needs to be achromatic and isochronous. The quadrupoles located at the center of the DBA allows tuning of the R_{56} of the beamline (see Figure 5.74).

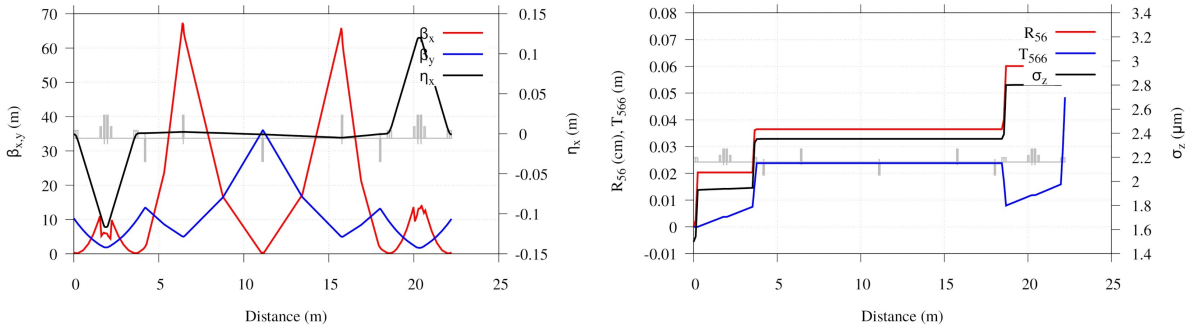

(a) (b)

Figure 5.75.: Lattice function for the low energy spreader 5.75(a) twiss functions along beamline 5.75(b) first and second order momentum compaction factors

Figures 5.75 and 5.76 shows the lattice functions and first and second order momentum compaction factors of the low and high energy spreaders, respectively. The beta functions are designed to be symmetric with respect to the center of the dogleg and the horizontal beta function takes its minimum at the dipoles. As it can be seen on the figure, the R_{56} of the beamline is tuned with the central quadrupoles between bending magnets and both spreaders are achromatic, while the high energy spreader is isochronous and the low one is not.

The tracking results are shown in Figures 5.77 and 5.78 for low and high energy spreaders, respectively. Since the beam energy spread is too high in the low energy spreader, due chromatic aberrations

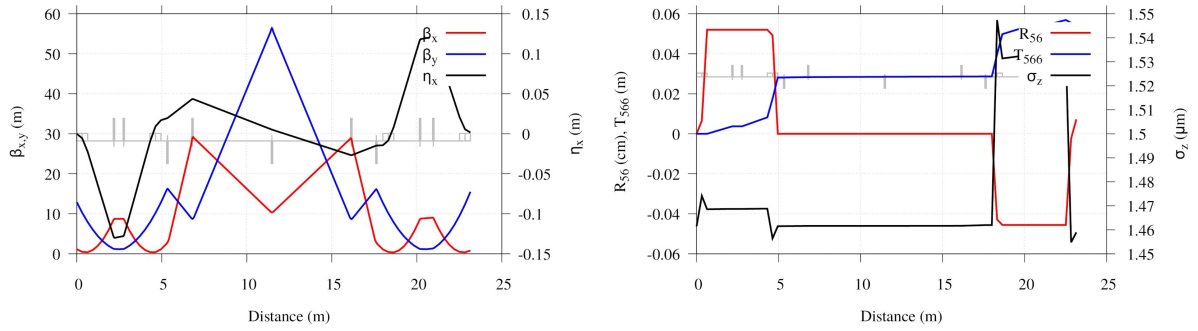

Figure 5.76.: Lattice function for the low energy spreader 5.76(a) twiss functions along beamline 5.76(b)

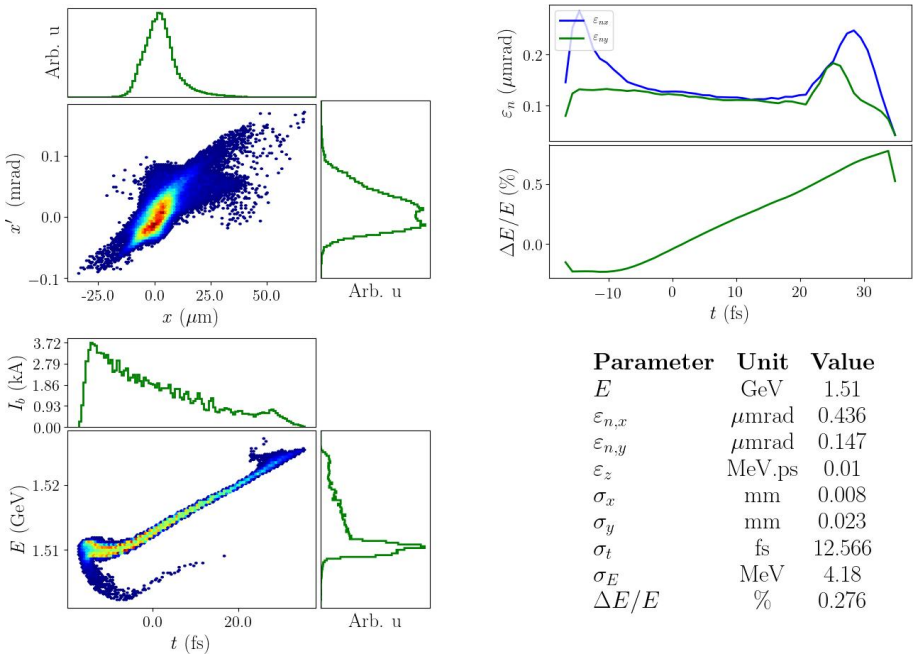

Figure 5.77.: Horizontal (top left) and longitudinal (bottom left) phase spaces with associated histograms representing the projection along the respective axis and sliced emittance/energy spread and beam parameters of the bunch at the exit of low energy spreader.

coming from the quadrupoles cause high non-linear effects. To correct this, 2 sets of sextupoles were placed in the bending sections (maximum dispersion, Figure 5.75 left). The corrections are localized (closing dispersion and minimizing the beta-beat) at the end of each bending section so as to minimize the sextupole strengths. However, the emittance growth is still larger than in the high enegy beamline. Same approach can be used for high energy spreader as well. The spreaders provide 526 and 535 ps delay for low and high energy, respectively. The main parameters are given in Table 5.32 for shortest bunch length operation of CompactLight.

In Figures 5.77 and 5.78 it is possible to see the distortions in longitudinal phase space caused by CSR. The current profile is fixed for the high energy spreader while it is distorted by nonzero R_{56} in the high energy one. The total effect of CSR on the emittance is not negligible, however the amount of projected emittance growth can be minimized by changing the phase advance between the two bending sets. Although the projected emittance is very sensitive to the phase advances, the slice emittance, which is the important parameter to minimise for best FEL performance, is conserved at the end of the spreaders. For longer bunch lengths the operation would be much easier because of the low CSR effect

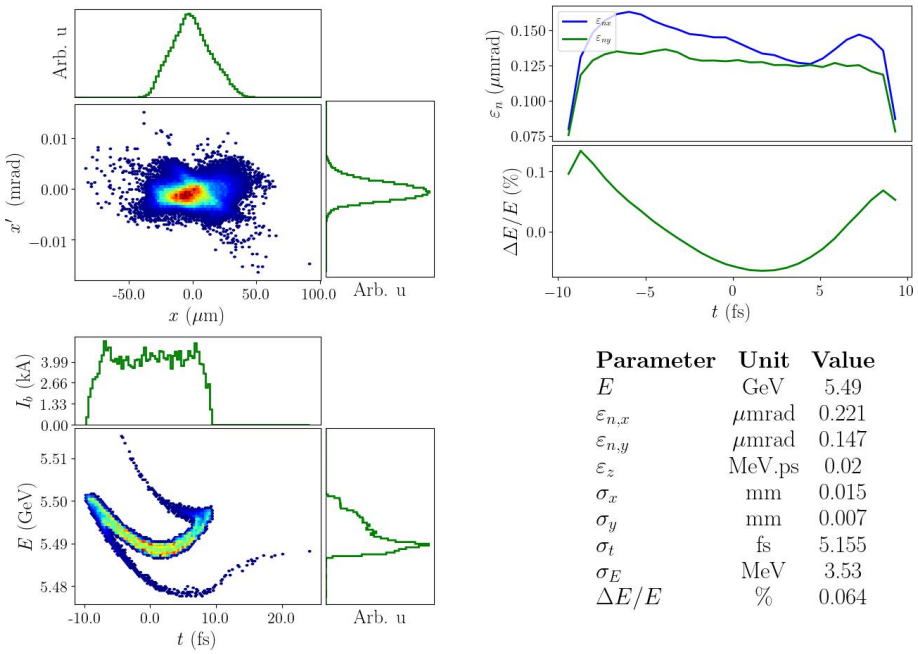

Parameter	Unit	Value
E	GeV	5.49
$\varepsilon_{n,x}$	μmrad	0.221
$\varepsilon_{n,y}$	μmrad	0.147
ε_z	MeV.ps	0.02
σ_x	mm	0.015
σ_y	mm	0.007
σ_t	fs	5.155
σ_E	MeV	3.53
$\Delta E/E$	%	0.064

Figure 5.78.: Horizontal (top left) and longitudinal (bottom left) phase spaces with associated histograms representing the projection along the respective axis and sliced emittance/energy spread and beam parameters of the bunch at the exit of high energy spreader.

Table 5.32.: Lattice parameters for low and high energy spreaders

Parameter	**Units**	**Low energy spreader**	**High energy spreader**
Maximum beam Energy	GeV	1.5	5.5
Bending angle	deg	4	4
Length of septum magnet	m	0.3	0.7
Length of dipole magnet	m	0.3	0.7
R_{56}	mm	0.7	0.0
T_{566}	mm	53	48
Time delay	ps	526	535
Final RMS bunch length	μm	3	1.5
Final RMS Horizontal emittance	mm.mrad	0.41	0.28

in the present dogleg designs in which the R_{56} can be tuned.

5.3.3.5. Start-to-end simulation through different beamlines

Start to end Twiss functions for the FEL-2 beamline (**Option-i b**, **Option-ii b** or **Option-iii b**) are given in Figure 5.73 and beam phase space for shortest wavelength at matching location is shown in Figure 5.72.

In the Baseline and Upgrade-1 configuration, the accelerator drives both HXR/HXR and SXR/SXR FELs. FEL-1 will be generated through **Option-i a** or **Option-ii a** beamlines by the first bunch deflected by the S-band TDC after Linac-3. The twin bunches in the RF pulse will follow identical dynamics in the accelerator up to end of Linac-3. Figure 5.79 shows the Beta functions and energy variation through Linac 3 to FEL-1 beamline for shortest wavelength operation while Figure 5.78 shows the phase space at the matching location to the FEL-1 undulator line. According to this plot, the projected emittance growth is about 50% while the sliced emittance growth is smaller. Due to the short bunch, and therefore

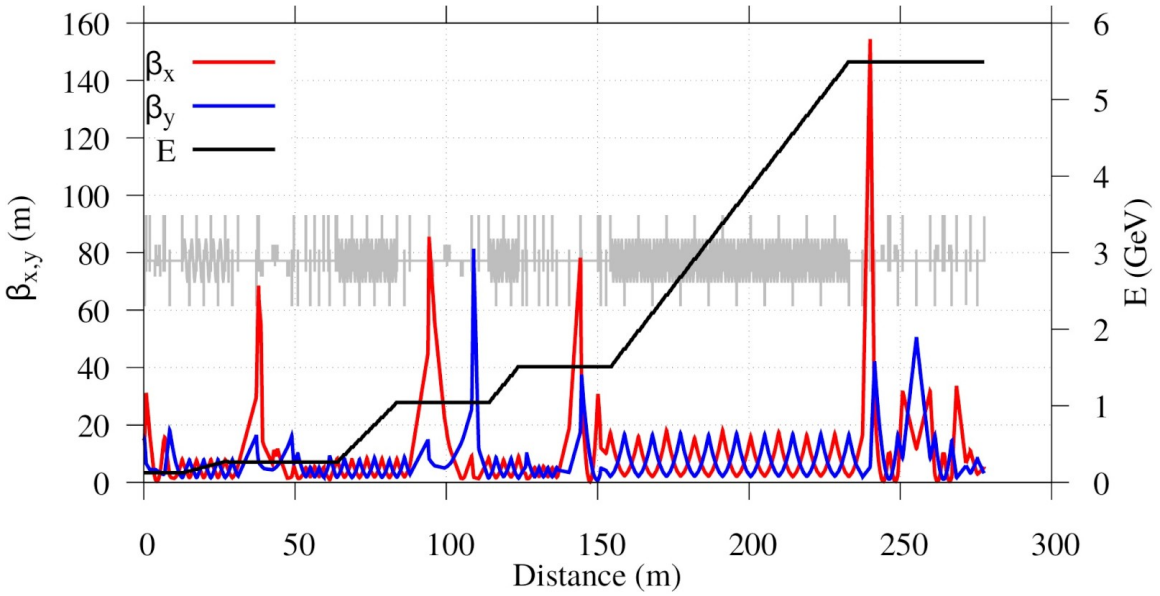

Figure 5.79.: Twiss functions and beam energy through Linac 3 to FEL-1 beamline (**Option-i a**)

strong CSR, the energy spread is increased by almost 100%. Since the peak current requirement is smaller for longer FEL wavelengths, transportation through the high energy spreader would be relaxed.

In the case of the second upgrade (See Figure 4.3) a low energy spreader and Linac-4 are added. Similar to the high energy spreader, the first bunch will be deflected horizontally by an S-band TDC after Linac-2 at about 1.5 GeV. Linac-4 will be used to accelerate the bunch up to 2 GeV or decelerate down to 1 GeV for driving the FEL-1 beamline (**Option-iii a**). As discussed in Sec. 5.3.3.4, similar to the case of simultaneous HXR/HXR generation, for short wavelength HXR FEL generation on FEL-2 beam transport through the low energy spreader becomes challenging because of strong CSR wake due to high peak current. Figure 5.80 shows the Beta functions and energy variation along **Option-iii a** beamline.

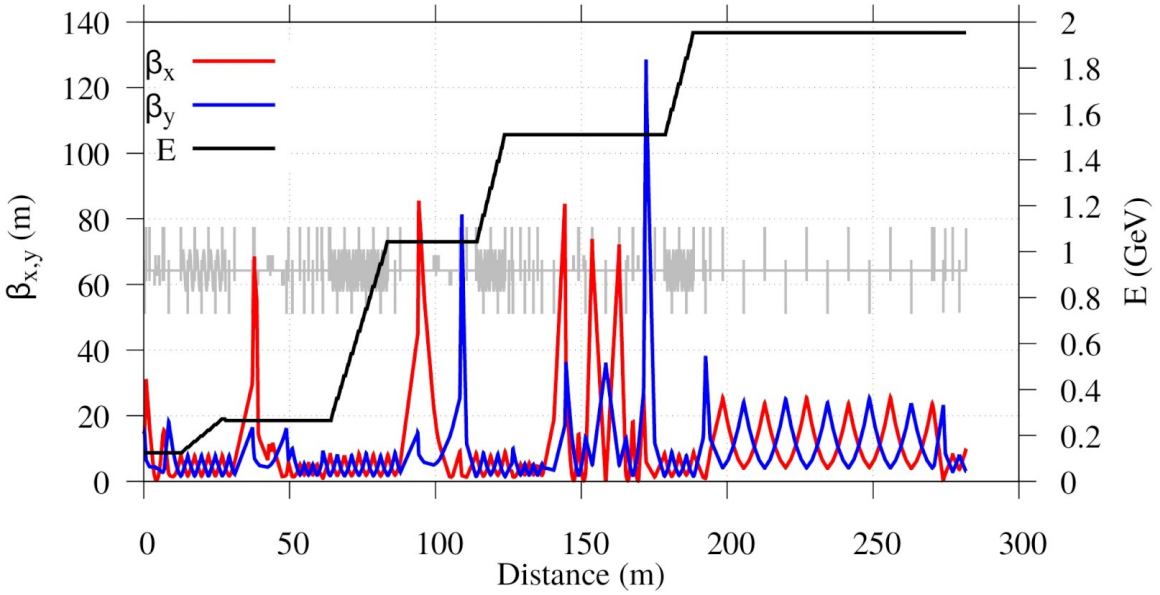

Figure 5.80.: Twiss functions and beam energy through Linac 4 to FEL-1 (**Option-iii a**)

Linac-4 consists of 8 structures (2 modules) and has the same lattice configuration as Linac-2. It is

only about 20 m length therefore one needs to have a 75 m long transport line for matching the beam to the FEL-1 undulators. This section can also be used for diagnostic purposes. Figure 5.81 shows the final phase space of the first bunch at the matching position to the FEL-1 undulators. It is possible to see the distortions in longitudinal phase space and current distribution caused by the strong CSR effect due to the short bunch. The length of the bunch is increased due to a positive value of the R_{56} in the low energy spreader, which can be tuned to smaller values. For this particular case, since the 2^{nd} bunch of the train is optimised for shortest wavelength, the energy profile of the 1^{st} bunch is set at the extraction point to the low energy spreader, and the total wakefield experienced in Linac-4 is not sufficient to remove the chirp. It is also noted that the smallest sliced emittance is at the center of the electron bunch which has sufficient current for lasing in the SXR regime. The head of bunch, which has about 0.35 mm.mrad sliced emittance, has current up to 5 kA. The FEL performance of this bunch is discussed in Section 4.2. Transportation of longer bunches would simplify the situation and one can also try to accelerate the 1^{st} bunch at a different phase on the beamline which is adjusted for 2^{nd} (nominal) bunch for HXR lasing.

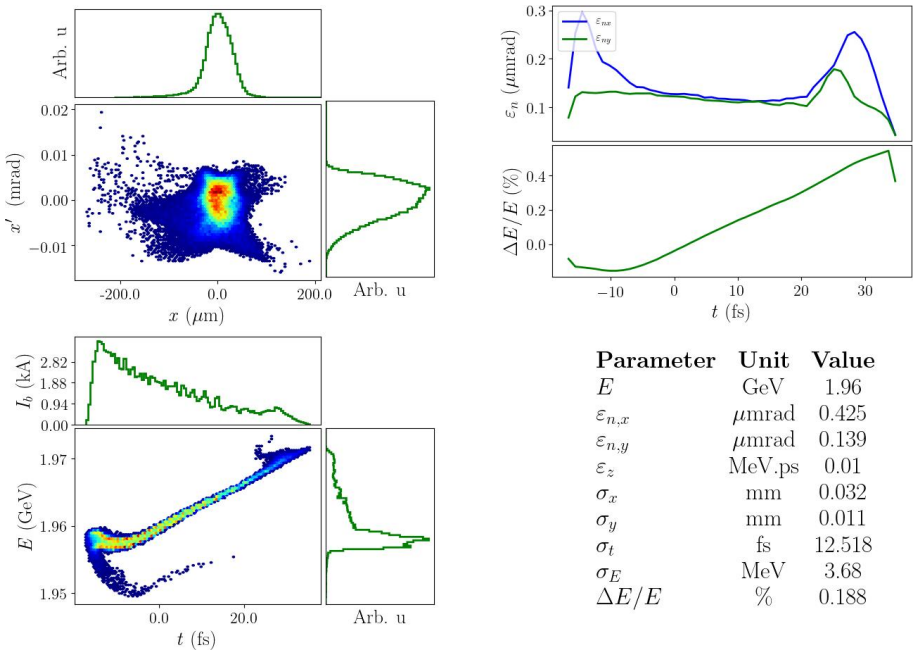

Parameter	Unit	Value
E	GeV	1.96
$\varepsilon_{n,x}$	μmrad	0.425
$\varepsilon_{n,y}$	μmrad	0.139
ε_z	MeV.ps	0.01
σ_x	mm	0.032
σ_y	mm	0.011
σ_t	fs	12.518
σ_E	MeV	3.68
$\Delta E/E$	%	0.188

Figure 5.81.: Horizontal (top left) and longitudinal (bottom left) phase spaces with associated histograms representing the projection along the respective axis and sliced emittance/energy spread and beam parameters of the bunch at the matching location of FEL undulators after Linac-4.

5.3.4. Linac performance

To achieve excellent FEL performance, the beam quality must be preserved along the accelerator. The emittance growth must be kept at a minimum, and the energy spread and peak current of the bunch must be preserved. Several effects harm the beam quality during its passage through the linacs, the bunch compressors and spreaders. The geometric and chromatic aberrations of the lattice, beam break up (BBU) instability, CSR-induced energy spread are all effects that contribute to emittance degradation or bunch current fluctuations. In particular, trajectory distortions caused by element misalignment errors at installation, which are typically of the order of 100 μm and 100 μrad RMS, are the source of a number of detrimental effects, as well as variations of the operational conditions with time. These effects can be classified as static and dynamic imperfections. In order to counteract them, a set of horizontal and

vertical magnetic correctors and beam position monitors are attached to each quadrupole magnet to apply beam-based alignment.

Other unavoidable effects, such as the emission of coherent synchrotron radiation in the bending magnets, introduce emittance growth and an increase of the energy spread. These effects are mitigated by optimized design of the magnetic chicanes and of the spreaders. As previously described, a laser heater is inserted before Linac-0 to dampen the micro-bunching in the bunch compressors.

5.3.4.1. Static imperfections

Static imperfections include the effects of element misalignment, which can harm the beam in different ways. We list the effects focusing on their impact on the beam.

Quadrupole misalignment Quadrupole misalignment introduces transverse deflections and unwanted dispersion, which respectively cause trajectory deflections and emittance growth. These effects can be cured in two different ways: improving the quadrupole alignment during the installation process, or using beam-based correction techniques. This latter technique is the preferred choice of CompactLight, as it will be needed anyway for routine operation. The detail of the beam-based alignment (BBA) techniques will be outlined in the following paragraphs.

Accelerating structure misalignment. The off-axis passage of the beam through the accelerating structures can excite short-range wakefields. The strength of the wakefields depends on the iris aperture inside the structures. The CompactLight accelerator features structures in the C, X, and Ka band of frequencies. It is well knows that wakefield effects depend non-linearly on the inverse of the iris aperture. In the approximations presented in [170], one can find the following relations:

$$W_{\parallel}\ [\text{V/pC/m}] \quad \propto \frac{1}{a^2}, \quad W_{\perp}\ [\text{V/pC/m/mm}] \quad \propto \frac{1}{a^4} \tag{5.19}$$

The smaller the aperture is, the stronger the effect. The X-band structures, which constitute nearly 80% of the entire linac, are characterized by small iris apertures. In the longitudinal plane, the short-range wakefields introduce a correlated momentum spread that must be compensated by operating the RF off-crest. In the transverse plane, the head-to-tail deflections that can introduce single-bunch beam-breakup can be mitigated by design using BNS damping, and in operation using BBA techniques. Even though the CompactLight X-band structure has been designed to provide a relatively large aperture (see CompactLight Deliverable 4.3) to mitigate these effects, the impact on the beam is strong due to the large number of structures in the linacs.

The off-axis passage of the beam through the accelerating structures excites also long-range wakefields, that is, high-order modes that can persist in the structure for long enough to affect the trailing bunches. This can induce bunch-to-bunch transverse deflections, potentially leading to beam breakup. The simplest solution to mitigate this effect is to space the bunches sufficiently for the wakefields to be damped below the harmful threshold. Figure 5.21 shows the evolution of the transverse long-range wakefields in the CompactLight X-band structure.

Element roll Roll installation errors of dipole magnets, quadrupoles, and correctors introduce horizontal to vertical coupling. Roll errors in BPMs mislead the beam-based alignment algorithms and hamper their effectiveness. An RMS error of 200 μrad has been assumed in the simulations.

All the imperfections simulations were performed using the code PLACET [178] on the lattice created by ELEGANT for optimization of ideal bunches.

5.3.4.2. Beam-based alignment

In order to preserve the beam quality under the effects of static element misalignment, three steps of beam-based alignment are applied.

1. Orbit correction: the beam is steered using all correctors to minimize the bpm readings. This is the first step and allows the beam to travel along the accelerator.
2. Dispersion-free correction: the beam dispersion is measured by running the RF structures in Linac-0 and Linac-1 off-crest by 10 deg in order to obtain a small energy difference. Then, the measured dispersion is minimized using all available correctors.
3. Wakefield-free correction: the impact of short-range wakefields is assessed using a test beam with 90% of the nominal charge and measuring its relative deflection to the nominal beam using the BPMs; then, the deflection is minimized using all available correctors.

Each step uses the beam position information from each quadrupole BPM and corrector magnet. A simulation study of the performance has been performed, using the errors reported in Table 5.33, for the shortest hard X-ray FEL and longest soft X-ray FEL modes. Figures 5.82 and 5.83 show the emittance growth along the CompactLight accelerator after each step of beam-based alignment for HXR and SXR operation, respectively. Each curve is the average of 100 random machines featuring the imperfections reported in Table 5.33.

Table 5.33.: Table of RMS static imperfections considered in the simulations.

	RMS position offset Δx, Δy **[μm]**	**RMS angle error** $\Delta x'$, $\Delta y'$ **[μrad]**	**RMS roll error [μrad]**
Quadrupoles	100	100	200
C-band structures	100	100	-
Ka-band structure	100	100	-
X-band structures	100	100	-
BPMs	100	100	200
BPM resolution	5	-	-
Correctors	-	100	200

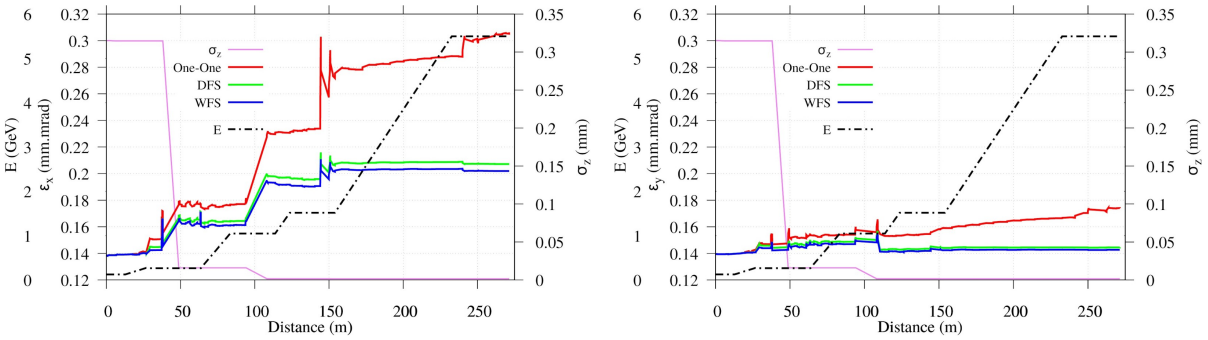

(a) Horizontal (b) Vertical

Figure 5.82.: Horizontal and vertical emittance growth, energy and bunch length variation along the CompactLight accelerator, for shortest wavelength operation mode, after three consecutive steps of beam-based alignment.

Each curve in the plot is the average of 100 randomly misaligned machines. The figure shows that WFS gives the best results in terms of final emittace, whilst One-to-One (orbit) correction does not meet the CompactLight requirement of achieving a final emittance below 0.2 mm.mrad. The emittance increase visible at about $\approx$ 100m is due to CSR effects in the second bunch compressor, when operating in HXR mode. In SXR operation, since the bunch length is longer than in HXR mode, the emittance growth at the end of the linac is smaller.

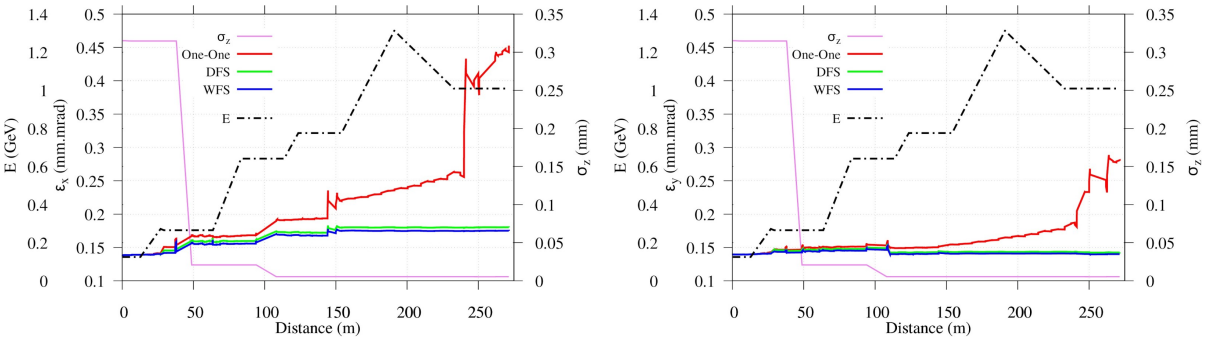

(a) Horizontal (b) Vertical

Figure 5.83.: Horizontal and vertical emittance growth, energy and bunch length variation along the CompactLight accelerator, for longest wavelength operation mode, after three consecutive steps of beam-based alignment.

5.3.4.3. Dynamic imperfections

The FEL operation requires stringent specifications for the stability of the linac output parameters: electron bunch arrival time, relative peak current and relative mean energy. Dynamic effects which can harm the on-line operation of the accelerator, may result variation on these parameters. Sensitivity studies have been performed to determine the variation of the linac output parameters with respect to the phase and amplitude jitters of the accelerating fields, electron bunch charge and electron emission time at the cathode. We summarize the impact of these imperfections below.

Beam transverse jitter: If too strong, the long-range wakefield effects in the accelerating structures can lead to jitter amplification, or ultimately beam breakup. The extent of the jitter amplification can be evaluated through the action amplification experienced by the second bunch due to the wakefield excited by the first bunch, as a function of the amplitude of the transverse long-range wakefield kick. Figure 5.84 shows the action amplification factor. The plot shows that kicks up to about 35 V/pC/m/mm can be tolerated, as they induce an action amplification factor less than the threshold, fixed at 1.15 (i.e., 15% action increase). The maximum kick tolerable, in our case 35 V/pC/m/mm, determines the minimum bunch spacing: this about 500 ps, as visible in Figure 5.21. The threshold

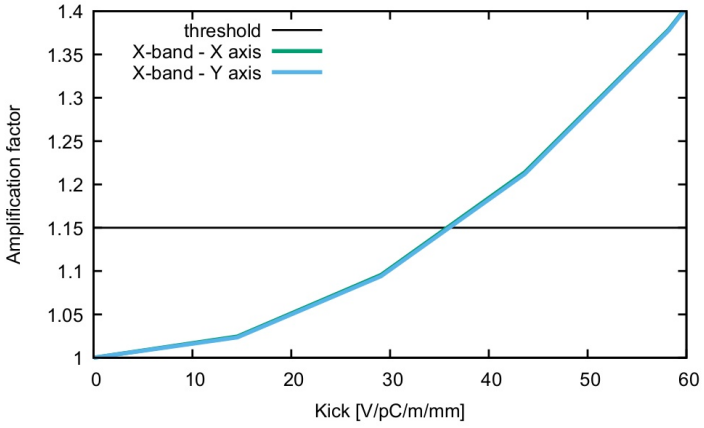

Figure 5.84.: Action amplification factor as a function of the amplitude of the transverse long-range wakefield kick at the 2nd bunch.

has been fixed to 1.15 on the basis that the FEL can tolerate a electron beam jitter up to 20% of the beam size and divergence at the undulator – this is therefore satisfied by the 15% action increase

and an assumed beam jitter of 5% at the injector.

Injector laser variations: Injector laser variations include laser timing errors and intensity variations (which result in bunch charge variations) induce variation on acceleration phase and wake potential introduced inside accelerating structures.

RF variations. RF variations such as RF phase offset and gradient errors impact the beam transport and induce timing errors, energy offsets and energy spread variations.

All these dynamic imperfections, in addition to mismatched bunch transport, can cause large oscillation on peak current and mean energy. To obtain the sensitivities for each segment of the machine, the sources of errors need to provide a collection of tolerances that need to be met.

The stability goals given in the tables below are determined from the SASE dynamics by analyzing intrinsic fluctuations of the FEL process given in Section 4.2.3. To define the level of allowed peak current fluctuations a series of Genesis runs were accomplished. Beam arrival time jitter is assumed to be on the order of the photon pulse-length ($\sim$ 10 fs). A jitter of 0.035 % in the mean energy would keep the resonant condition within the FEL bandwidth.

The stability goals of the machine can be divided by the corresponding sensitivity to obtain the allowed deviation from the design parameter (jitter budget or tolerance). Since some components are driven by uncorrelated jitter sources, such as for the linac RF stations, one can take the square root of the number of independent sources (3 klystrons for the C-band injector, 4 klystrons for the X-band linac 1, 2 klystrons for the X-band linac 2, 17 klystrons for X-band linac 3, and 1 klystron for K-band linearizer). In order to evaluate if those stability goals can be met, we used expected jitter values (Table 5.34) for all critical accelerator components and run 500 simulations for the shortest wavelength generation case.

Table 5.34.: Table of RMS dynamic imperfections of CompactLight subsystems considered in the simulations.

Parameter	**Unit**	**Value**
Incoming bunch energy jitter	%	0.01
Incoming bunch charge jitter	%	1
Incoming bunch timing jitter	fs	25
C-band phase stability	deg	0.04
C-band voltage stability	%	0.02
X-band phase stability	deg	0.08
X-band voltage stability	%	0.02
Ka-band phase stability	deg	0.16
Ka-band voltage stability	%	0.02

Figures 5.85 and 5.86 shows the variations of some beam parameters

Table 5.35.: Summary of dynamic jitters of some beam parameters

Parameter	**Units**	**Value**
RMS mean energy error	%	0.016
RMS arrival time error	fs	8.52
RMS energy spread	(keV)	165
RMS bunch length error	(μm)	0.28
RMS horizontal emittance	mm.mrad	0.029
RMS Peak current error	kA	1.05

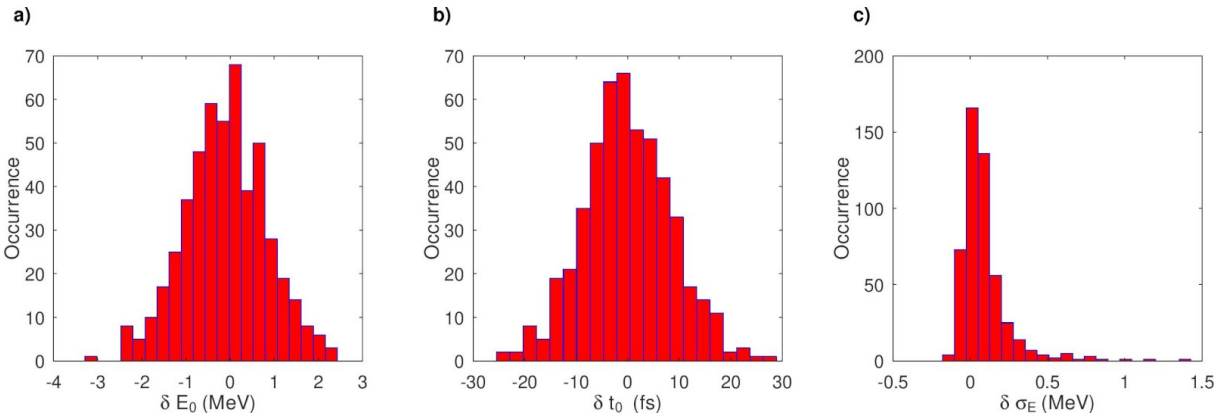

Figure 5.85.: Simulated distribution of average energy variation, arrival time difference, and energy spread difference at linac end for 500 jittering machines.

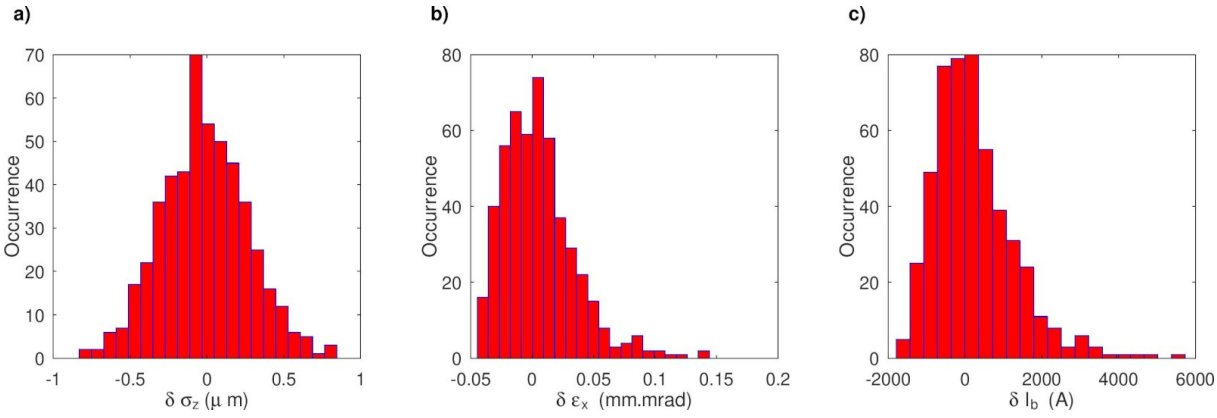

Figure 5.86.: Simulated distribution of bunch length variation, horizontal normalised emittance difference, and peak current difference at linac end for 500 jittering machines.

5.4. Electron Beam Diagnostics

There is an old statement which says that an accelerator is only as good as its diagnostics. In machines where high brightness is essential in order to drive a light source, particular care has to be taken at the ”beginning of the story”, where the beam is just born.

A great advance in high brightness accelerators was the introduction of photoinjectors, allowing the possibility to shape transversely and longitudinally the beam using a laser. The space-charge-dominated beam leaving the photocathode is immediately focused by a solenoid, providing emittance compensation [99] to reduce the emittance growth due to slice misalignment in the phase space. It was noted that an unexpected emittance oscillation in the drift downstream of the rf gun showed a double emittance minimum [179]. The experimental validation of this behaviour ([180] [181]) opened the way for the so-called Ferrario’s working point, in order to drive high brightness machines that produce high brilliance light beams. However, this solution is a delicate equilibrium between several parameters, for example beam transverse spot size, bunch length, solenoid field, drift length, injection phase and total charge. During the acceleration process precise control of the beam envelope, correct manipulation of the longitudinal phase space, and correct matching (in order to preserve the transverse emittance) are mandatory to achieve a beam with high enough peak current and small enough slice energy spread to drive an X-ray FEL.

The diagnostics detailed here allow some flexibility in the machine working point. Here the beam rigidity is considered at the highest energy of 5.5 GeV, this is particularly important when considering

the drift of the active elements like transverse deflecting structures.

5.4.1. Beam Instrumentation

The right choice of device is the basis for accurate measurements of the beam parameters. This section discusses the principal devices that will be used for CompactLight.

5.4.1.1. Charge Measurement

Charge measurements are performed using ICT (Integrated Current Transformer) devices. These can measure down to fC (in the Turbo-ICT variation), they are easy to implement and very compact, using only 10 cm of space.

Conventional ICTs measure both the beam charge and the dark current. In a state-of-the-art machine the main source of dark current is the RF-Gun. Only a small fraction of the dark current is transported—that which occurs at the right phase to be accelerated. Usually the poor transverse properties of this current produce just a halo in the beam. Switching off the laser in a photoinjector allows the dark current to be isolated. In CompactLight the X-band linac structures can be an additional source of unwanted dark current.

It is too early to understand if dark current can perturb the charge measurements. However, there are solutions that can be implemented for the mitigation of both gun and linac dark current. Conventional ICTs can measure charges from a few pC up to several nC and they will be extensively used in the accelerator. In recent years Bergoz Instrumentations has introduced a new toroid, called Turbo-ICT, which operates in the frequency domain rather than the time domain. This means the detector is insensitive to the dark current and the measurement is very precise, down to very small charges of tens of fC. This device is very useful, but in modern accelerators radiation safety usually requires an online and full time measurement of the dark current. As this device is not suitable for this task another ICT is needed. In order to save space and to integrate both functions in a single device, Bergoz Instrumentations have recently developed an integrated device which is under test at SPARC_LAB at INFN-LNF. It combines conventional ICT and turbo toroid, and is named Combo-Turbo-Toroid. This device will be placed in the CompactLight injector area where the dark current is likely to be an issue.

For the rest of the machine a decision will be made later, after clear characterization of the dark current emitted by the X-band structures at high gradient, on whether to install conventional toroids or combo ones. The cost estimation assumes the use of combo toroid only in the injector area.

Faraday cups (FC) are another charge diagnostic. They use an absorber block (usually made of copper) to stop the beam. The block is connected to ground through an ammeter to measure the total charge deposited by the beam. Unlike ICTs, FCs intercept the beam and thus can only be installed at the end of the beam line. Because all the charge is absorbed it is an absolute measurement requiring no calibration. The size of the absorber has to be adjusted depending on the beam energy. An FC will be very useful, especially in the commissioning phase. One will also be placed in the injector.

5.4.1.2. Position Measurements

Beam Position Monitors (BPMs) are essential for non-invasive monitoring of the beam trajectory. Several types of monitor are available—buttons, striplines and cavity BPMs. The relatively low charge of the CompactLight bunches means that buttons are not considered suitable due to their limited sensitivity and poor single pass. Stripline BPMs are often used. They give reasonable sensitivity to the beam position—about tens of microns at tens of pC—and their cost is acceptable. Cavity BPMs are the only type that can offer micrometer resolution, even at only a few pC. For much of the accelerator, where 1 μm resolution is not required, stripline BPMs are simpler and cheaper. However striplines are longer than cavity BPMs. So far one of the shortest striplines working in an accelerator is in PAL-XFEL [182] and is 16 cm long. Several labs are developing shorter striplines—for example Figure 5.87 shows the

mechanical drawings of a project running at LNF-INFN. The length of this device is just a couple of cm more than a cavity BPM.

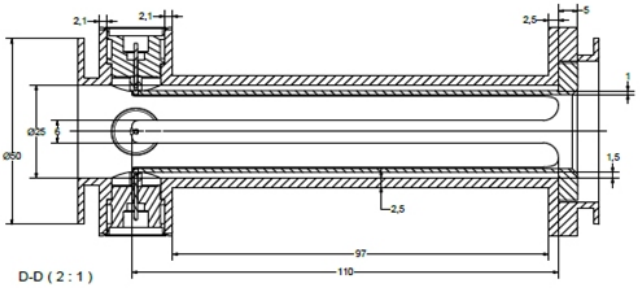

Figure 5.87.: A compact stripline BPM in development at LNF-INFN (courtesy G. Di Raddo).

The striplines also offer the possibility of being integrated inside the quadrupoles. The model in Figure 5.87 has a diameter of 30 mm, whilst the quads in CompactLight have an inner diameter of 25 mm. However the BPM diameter can be reduced by more than 5mm without changing the technology so a more compact design is certainly achievable.

A different approach is considered for the beam position monitors between the undulator modules. The main issue is the low temperature. There are several examples worldwide of cavity BPMs operating at cryogenic temperatures [183], [184]. These are usually embedded in cryostats and are between accelerating modules. Being very close to superconducting modules even a single dust particle can severely affect the cavity performance and eventually drive it to a quench. For such a reason the choice of a low frequency cavity BPM, usually in L-band, has the advantage of larger dimensions, easing the cleaning of these devices. These dimensions impact also the longitudinal occupancy of the devices, which is in the order of 170 mm. However, in CompactLight these devices are used between undulators and there are not superconducting cavities nearby, so the constraint on the dimensions is different. In this case the longitudinal dimension is the most important factor. While there is not a single example of a cold BPM working at cryogenic temperature in X-band, there is also no evidence that it is not possible to rescale the device to such smaller dimensions.

Usually cavity BPM modules are about 100 mm long [185]. One of the main concerns about these devices working at such low temperature is the material choice. In particular the feedthrough has to be well designed because the ceramic must work not only under vacuum conditions but also in a low temperature regime. A R&D program is needed to develop these devices, but there is no evidence that they cannot be developed in a few years.

5.4.1.3. View Screens

View screens are particularly important where an intercepting diagnostic is allowed. Their use is widespread: for envelope measurements; for transverse emittance measurements by means of quadrupole scans; for longitudinal phase space measurements in which the beam is imaged after a transverse deflecting structure and a dipole.

There are only two type of screen that are routinely used—scintillators and optical transition radiation (OTR) monitors. Several materials can be used for the scintillators screens [186]. Their main advantage is the strong photon yield, which makes these devices suitable for imaging beams with charges as low as a few pC. However, the bulk emission can result in resolution degradation if the geometry is not properly chosen and the crystal is not very thin.

A compact accelerator must have also compact diagnostics. A small vacuum chamber of 80 mm length can host several screens on a mobile actuator. A thin scintillator, like for instance YAG:Ce, can be mounted orthogonal to the beam direction with a 45 degrees mirror on the back to prevent blurring. The emitted radiation is then collected through an optical window by a camera. A drawing is

shown in Figure 5.88. On the same holder, unplugging the scintillator, an optical transmission radiation

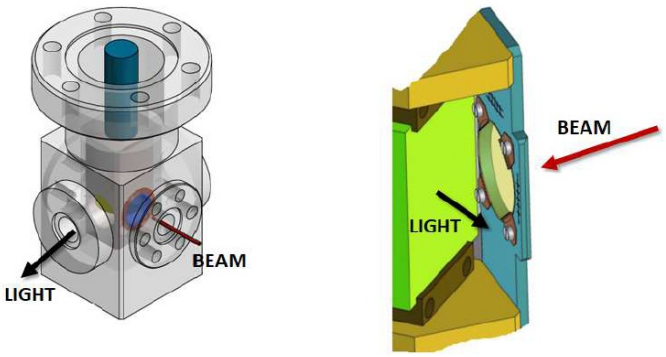

Figure 5.88.: Drawing of a compact view screen. A thin scintillator (typically 100 μm) is placed normal to the beam direction. A 45 degree mirror on the back reflects the emitted radiation towards a detector outside the vacuum chamber.

(OTR) screen, usually an aluminium coated silicon plate, can be placed at the mirror position. OTR is emitted when a charge crosses the boundary between two media with different refractive indices. The radiation is emitted backward and forward in a narrow cone with angular aperture of about $2/\gamma$, with γ the relativistic factor. The main advantages of OTR screens are their linearity, even with strong signals, their fast response with respect to the beam structure, and their resolution which is close to the diffraction limit. Their main limitation is the number of emitted photons. In visible light it is possible to estimate somewhere between 10^{-3} and 10^{-4} photons per incident electron.

OTR screens are therefore used for high resolution transverse measurements and for all applications of coherent transition radiation, including longitudinal diagnostics. In CompactLight the resolution is not an issue, so scintillator screens will be used extensively and OTR screens will only be employed to produce radiation useful for longitudinal diagnostics using coherent emission.

One problem associated with photoinjectors with high current and magnetic compression is the possibility of microbunching. This can affect the FEL performance but the induced CSR emitted in the bunch compressor can also interfere with the optical diagnostics [187].

Several solutions, with different levels of success, have been proposed and implemented. For CompactLight space is the priority, so the choice must be the scheme that prevents the detection of CSR and at the same time is the most compact. Coherent OTR (COTR) is emitted in a narrow cone, even with a scintillator. However, the scintillator light has a very wide distribution. The solution implemented in [188] and reported in Figure 5.89 makes use of a mask to suppress the COTR contribution, while the rest of the radiation is collected by a lens. This is the best choice for CompactLight, and it has other important advantages—the whole device is outside of the vacuum chamber so can be easily installed if there is evidence of microbunching, and there is no impact on machine layout.

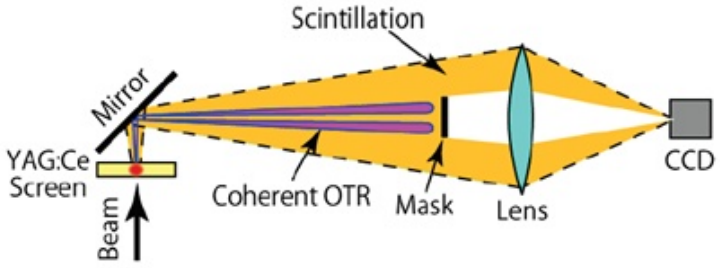

Figure 5.89.: COTR suppresion system in use at SACLA [188]

5.4.1.4. Transverse deflecting structure

The longitudinal properties of the electron bunch are very important. Often the right parameters to drive the FEL effectively are not reached along the whole bunch but only in some longitudinal slices. The bunch peak current (the charge divided by the bunch duration) is also a parameter of paramount importance in a FEL, so the correct evaluation of the beam length is fundamental. There are several techniques that can be used. Some of them are single shot, others are not intercepting. Usually a certain redundancy is needed in every machine, hence it makes sense to use multiple different techniques.

Transverse Deflection Structures (TDS) ([189],[190]), often called RF-deflectors, are RF cavities providing a time-dependent transverse force which can be exploited to measure the bunch longitudiunal properties. These are powerful devices, able to attain measurements with few-femtosecond resolution in the X-band [191]. The working principle is shown in 5.4.1.4. A time-dependent transverse deflecting voltage is present in a standing or travelling-wave structure. Different parts of the beam, in different longitudinal positions, experience a correlated transverse force that imprints a transverse momentum on the bunch. After a drift, imaging the bunch on a screen reveals the longitudinal charge distribution.

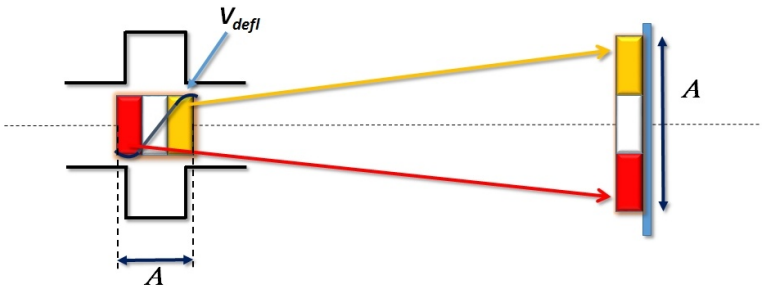

Figure 5.90.: Principle of operation of RF deflector. The longitudinal structure is mapped on the transverse profile because different longitudinal positions experience different transverse kicks.

The measured bunch length, using the average between the results obtained at the two zero cross phases separated by 180 degrees, as stated in [192], is:

$$\sigma = \sqrt{\sigma_0^2 + \sigma_z^2} \tag{5.20}$$

The dimension of the beam on the screen, with no power in the TDS, is indicated with σ_0 and

$$\sigma_z^2 = \beta\beta_0 \sin^2\Delta \left(\frac{qV_0}{pc}k\right)^2 \langle z^2 \rangle \tag{5.21}$$

where β and β_0 are respectively the betatron function at the TDS and on the screen, Δ is the betatron phase advance between the TDS and the screen, V_0 is the integrated voltage along the TDS, p is the particle momentum, q is the charge, c is the speed of light and z is the longitudinal position inside the bunch. This term contains the required quantity, the second moment of the longitudinal charge distribution $\langle z^2 \rangle$ multiplied by a calibration factor. Equating the two terms under the square root in Equation 5.20 it is possible to find the resolution

$$\sigma_z^{res} = \frac{E}{q}\frac{\sigma_0}{V_0 L}\frac{\lambda}{2\pi} \tag{5.22}$$

where λ is the wavelength of the RF.

To increase the resolution of the device the term σ_0^2 must be much smaller than σ_z^2, so the spot on the screen with the TDS off must be as small as possible. From 5.22, other methods to improve the resolution are to increase the deflecting voltage V_0 or the device length L, or to decrease the RF

wavelength. Working in X-band can therefore give the best resolution although for beams of only a few hundred MeV C-band or S-band structures can be considered.

A new transverse deflecting device called PolariX [193], [194] has an innovative feature that allows the polarization of the field to be rotated. The streaking direction can then be rotated allowing the characterization of the slice emittance [195] in both planes. This feature, together with the high resolution and the availability of X-band RF power when the downstream linac structures are not in use, make Polarix a suitable design choice for CompactLight. It is used in several positions along the machine, at energies of 120 MeV, 1 GeV, 1.5 GeV and 5.5 GeV. Figure 5.91 and Figure 5.92 show the resolution versus voltage for these four different energies.

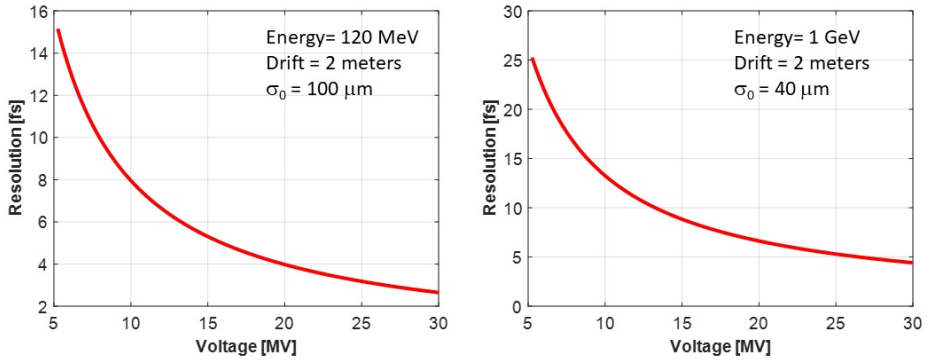

Figure 5.91.: Resolution vs voltage for 120 MeV (left) and 1.0 GeV (right). Beam size and drift between TDS and the screen are shown on the plots.

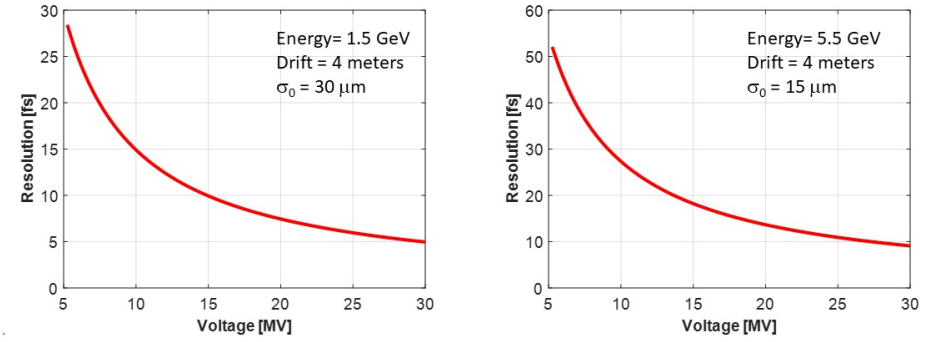

Figure 5.92.: Resolution vs voltage for 1.5 GeV (left) and 5.5 GeV (right). Beam size and drift between TDS and the screen are shown on the plots.

To obtain the best resolution the drift between the TDS and the screen can be optimised, increasing the length at high energy. The natural decreasing of the beam spot helps also at high energy. At low energy an integrated voltage of 10 MV is enough for 10 fs resolution, well beyond the bunch length. This value can be reached with a shorter structure, for example 0.5 meters long, while at larger energy the use of a 1 meter structure is foreseen, due to the larger beam rigidity.

The Polarix can be used not only in the main linac, but also after the undulator chain, following the experience at SLAC [196]. The measurement of the longitudinal phase space after the undulators allows a precise reconstruction of the light pulse giving an insight into the radiation emission process.

5.4.1.5. Coherent Radiation Monitors

Ultra-short electron bunches allow the use of coherent radiation spectroscopy techniques in the infrared, where well established spectrum characterization methods exist. Such schemes have been demonstrated in single shot diagnostics, either measuring the CTR spectrum directly with an far-infrared spectrometer based on a dispersive prism [197] or with a cascaded grating setup in [198].

When a bunch of N electrons emits radiation, whether synchrotron radiation, transition radiation, or Smith-Purcell radiation, for example, the spectral-angular distribution of the produced radiation is given by

$$\left.\frac{d^2W}{d\Omega\, d\omega}\right|^{\text{total}} = \left[N + N(N-1)|F(\lambda)|^2\right] \left.\frac{d^2W}{d\Omega\, d\omega}\right|^{\text{single}} \tag{5.23}$$

Here $\left.\frac{d^2W}{d\Omega\, d\omega}\right|^{\text{single}}$ is the spectral-angular distribution of the radiation produced by a single particle, strongly dependent on the particular physical process but well known, λ is the observed radiation wavelength and $|F(\lambda)|^2$ is the squared amplitude of the bunch form-factor which is represented by the Fourier transform of the normalized longitudinal bunch distribution $\rho(z)$:

$$F(\lambda) = \int_{-\infty}^{\infty} \rho(z) \exp\left(\frac{-2\pi i z}{\lambda}\right) dz \tag{5.24}$$

The contribution of the transverse bunch size to the form-factor is negligible for high energies ($\gamma \gg 1$) and small observation angles ($\theta \ll 1$). The radiation is considered to be coherent if the second term in Equation 5.23 dominates. From Equation 5.24, the information about the longitudinal bunch profile is contained in the form-factor and can be retrieved from it by measuring the coherent radiation spectrum.

In general the form-factor defined by Equation 5.24 is a complex-valued function and can be represented as $\mathscr{F}(\lambda) = F(\lambda)\exp[i\Phi(\lambda)]$. In order to achieve a unique reconstruction of the longitudinal charge distribution both amplitude $F(\lambda)$ and phase $\Phi(\lambda)$ must be known. By measuring the spectrum of coherent radiation only the absolute value $F(\lambda) = |\mathscr{F}(\lambda)|$ of the longitudinal form-factor can be obtained leaving the phase $\Phi(\lambda)$ undefined. There are two methods for obtaining this: analytical, such as Kramers-Kronig or Blashke phase retrieval, and iterative methods, for example weighted greedy sparce phase retrieval (WGESPAR) [199]. A very good overview of the different bunch shape reconstruction algorithms can be found in [200] and references therein.

The advantage of using coherent radiation, rather than a deflecting structure, is the compactness of the system. A simple screen for OTR is sufficient. A spectrometer (the specification depending on the type of measurement required) can be placed outside the vacuum chamber and sometimes even outside the linac hall. However, the main drawback of the technique is an unavoidable cut in some frequencies, or simply a frequency dependent system transfer function up to the detector, that can influence the bunch reconstruction algorithm. However, the coherent radiation can be very effective as a *relative* compression monitor. Because the signal intensity depends on the form factor, which increases as the bunch length decreases, it is possible to monitor the compression factor without the need to reconstruct the bunch profile—this can be done online, for every shot, and in a non-intercepting way. Such an online compression monitor can be used for RF feedback, using the output as a probe of RF phase stability. In CompactLight there is a relative compression monitor after Bunch Compressor 1 (BC-1) and another station for full bunch length reconstruction after BC-2.

5.4.1.6. Time of Arrival Monitors

Measuring the bunch arrival time supplies crucial information for the beam-based feedback system. The best result in this field, a resolution of a few fs, is achieved with the BAM (Beam Arrival Monitor) developed at DESY for XFEL. We refer mainly to this system [201, 202].

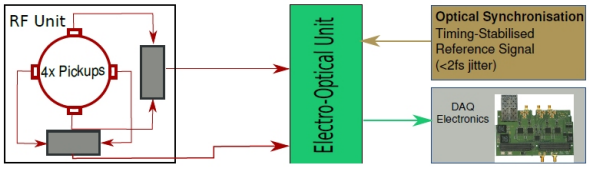

Figure 5.93.: BAM main components.[201]

The BAM system comprises three parts, as shown in Figure 5.93—the RF unit, the electro-optical unit and the data acquisition system. The electromagnetic field induced by the electron bunch is captured by four broadband pickups. The electro-optical unit (EOM), see Figure 5.94, combines the signals from the RF unit and a reference signal provided by an external source to perform the measurement. The result is then stored in the DAQ system. Modulation occurs via a Mach-Zehnder-type interferometer. If no RF signal is encountered by the probe laser pulse, or if the laser pulse is perfectly synchronized with it, no change in the laser pulse height is observed. If the two signals are not synchronized, the pulse height is modulated. The working principle of the EOM is shown in Figure 5.95.

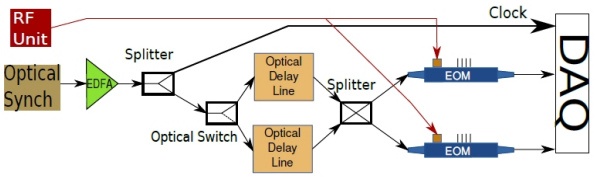

Figure 5.94.: Layout of the electro-optical unit.[201]

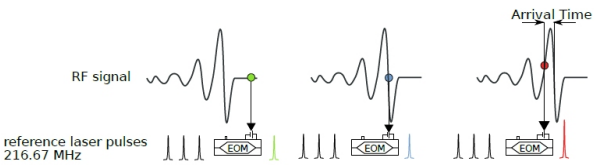

Figure 5.95.: Working principle of the electro-optical unit (EOM).

5.4.1.7. Intensified CCD Camera

The diagnostics should be able to discriminate the longitudinal and transverse properties of two different bunches at the same energy, produced for the two FEL lines, with a temporal separation of about 883 ps, equal to ten wavelength periods. The TDS in X band cannot separate these two bunches, because they are separated by exactly an integer number of periods and so they sees the same phase in the device. Using a device in the other band will allow their separation but it will also reduce the measurement resolution following the formula (5.22). Also their distance is quite large with respect to the usual time window of a TDS, in the order of ps. The only way to select a single bunch is the use of an Intensified CCD camera (ICCD). This device can expose its sensor for few nanoseconds. The idea is to collect two different images, one in the first window containing only the first bunch and the second having the last one. It will work because the jitter in the start and stop of the exposure in the multi channel plate (the intensifier), is smaller than the time separation between bunches.

Two ICCDs can be considered, one at the spreader position and one after BC-1. The radiation will be produced by OTR screens which have a fast response, shorter than the bunch time separation.

5.4.2. Layout Integration

In this section the integration of the diagnostics with the machine layout is introduced. The injector is covered comprehensively in deliverable D3.3. Presented here is a schematic layout, although adequate space for each component is allocated. The principles used for determining the layout positions of the elements within the machine are as follows.

For transverse phase space diagnostics, for example emittance measurements with the quad-scan method,

- The best choice is using only one quadrupole at time. Every quads increase the error, giving mostly by chromatic effect and depending on the beam size, beam divergence and beam energy spread at the quadrupole entrance [203]. However, if we use only one quadrupole the beam could be largely defocused in the other plane. Considering reasonable screen size and camera magnification, a spot larger than 3 mm rms it will be quite difficult to image. So, if we run in this situation we have to use two quadrupoles.
- What is important in the quad scan is the region around the minimum spot size. To have realistic measurement it is important to have an increase in the spot size at least of a factor 2.5, changing the magnet current accordingly.
- The distance between quad and screen is chosen in order to fulfill these conditions. About the minimum spot size it depends mostly by the optics and the camera. But as a rule of thumb if we want to have better measurements with more sampling points, going much lower than 20 um, even if it is possible, it is not recommended. We can measure a spot down to few microns, but with much more uncertainties.

For longitudinal phase space measurements the main rules followed for the design are:

- To improve the resolution of the TDS the beam focus should be on the screen where the measurement is made.
- The focus should be mainly in the streak plane. However, if the beam is large in the other plane, poor signal to noise ratio could be a problem, therefore a small round beam is preferable.
- With the use of Polarix, which adds the possibility of rotating the polarization, the optics should have the flexibility to make a small spot in both planes.
- The phase advance between the TDS and the screen must be 90 degrees or a value very close to it. Again the use of the deflector with rotating polarization means that this condition must be fulfilled in both transverse planes.

In order to give a clearer definition of each single part of the machine, and the related measurements, the layout has been divided in several parts that do not reflect the usual subdivision into Linac-0, Linac-1 and so on. However, for clarity the nomenclature used in the other CompactLight deliverables is always shown.

5.4.2.1. Injector

In this area, due to the reduced space availability, the layout is considered in more detail, with reasonable estimates given of the length of every device to demonstrate the feasibility of the design (see sketch in Figure 5.96).

The lengths of the elements are assumed as follows: for view screens 100 mm including flanges, for stripline BPMs 200 mm including bellows and flanges. Starting from the gun, after a solenoid and a vacuum valve to separate the cathode from the rest of the machine, there is the laser port, to allow

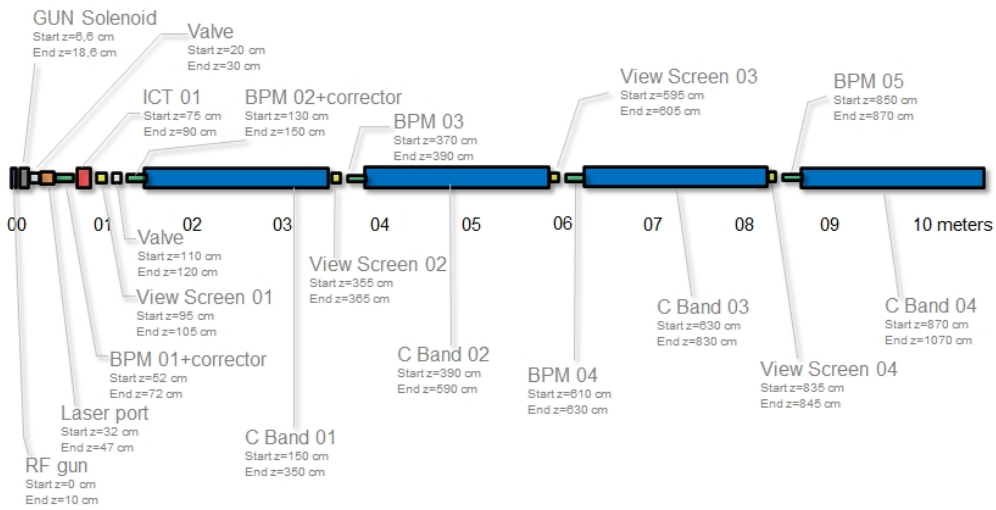

Figure 5.96.: Sketch of the injector layout including quotes and diagnostics up to the end of the C band structures.

the laser light to arrive on the cathode. In this device a mirror is also included to make an image of the cathode that is visible from the window opposite the laser input. Then there is the first stripline embedded in a corrector to reduce the space occupancy. The Combo-Turbo-ICT toroid is placed just after the stripline and before a view screen where it is possible to measure the beam envelope. The energy measurement is performed using the first corrector and measuring the change in the beam position vs current. Another stripline embedded in a corrector is placed before the entrance of the first accelerating module. In this way the trajectory is determined from the start and the entrance point in the accelerating structure is monitored. Between every accelerating structure there is a view screen, to monitor the envelope, and a stripline BPM inside a corrector.

5.4.2.2. Laser Heater Region

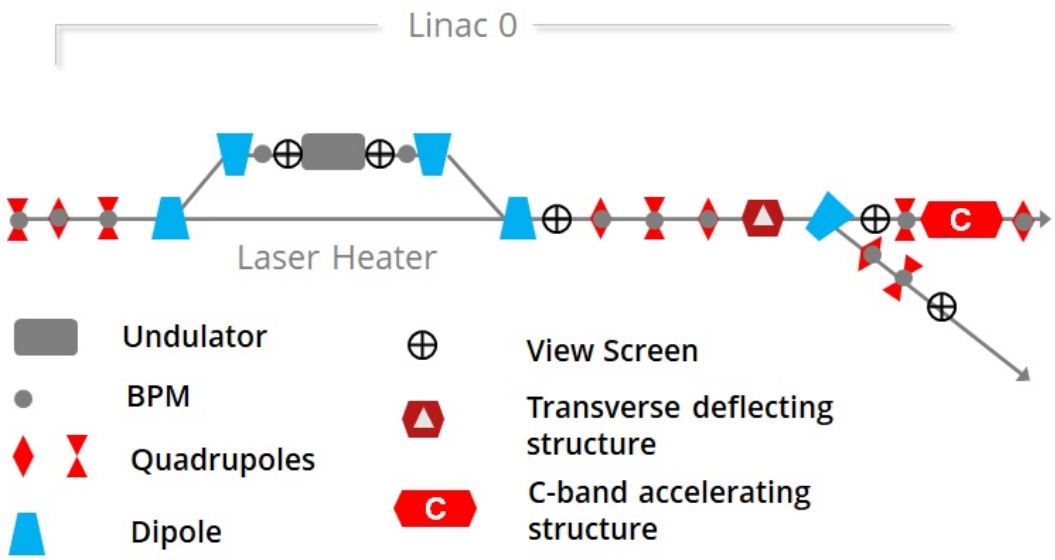

Figure 5.97.: Schematic definition of the diagnostics layout in the laser heater, including the full 6D phase space characterization region.

A complete 6D phase space reconstruction is considered here. Refer to Figure 5.97 for a schematic definition of the diagnostics layout. Inside every quadrupole is a stripline to measure the beam trajectory. The correctors are also embedded in the quadrupoles. The envelope is monitored using the view screens before and after the undulator. Two striplines are placed to measure the beam trajectory before and after the undulator. After the chicane a full 6D phase space characterization is implemented. A triplet of quadrupoles, used also to match the beam in the following accelerating sections, can be used for a quadrupole scan and to tune the beam for the spectrometer arm. On the view screen in the spectrometer it will be possible to perform a longitudinal phase space measurement, while the screen before the accelerating structure will be used for emittance measurement.

5.4.2.3. Bunch Compressor 01 Region

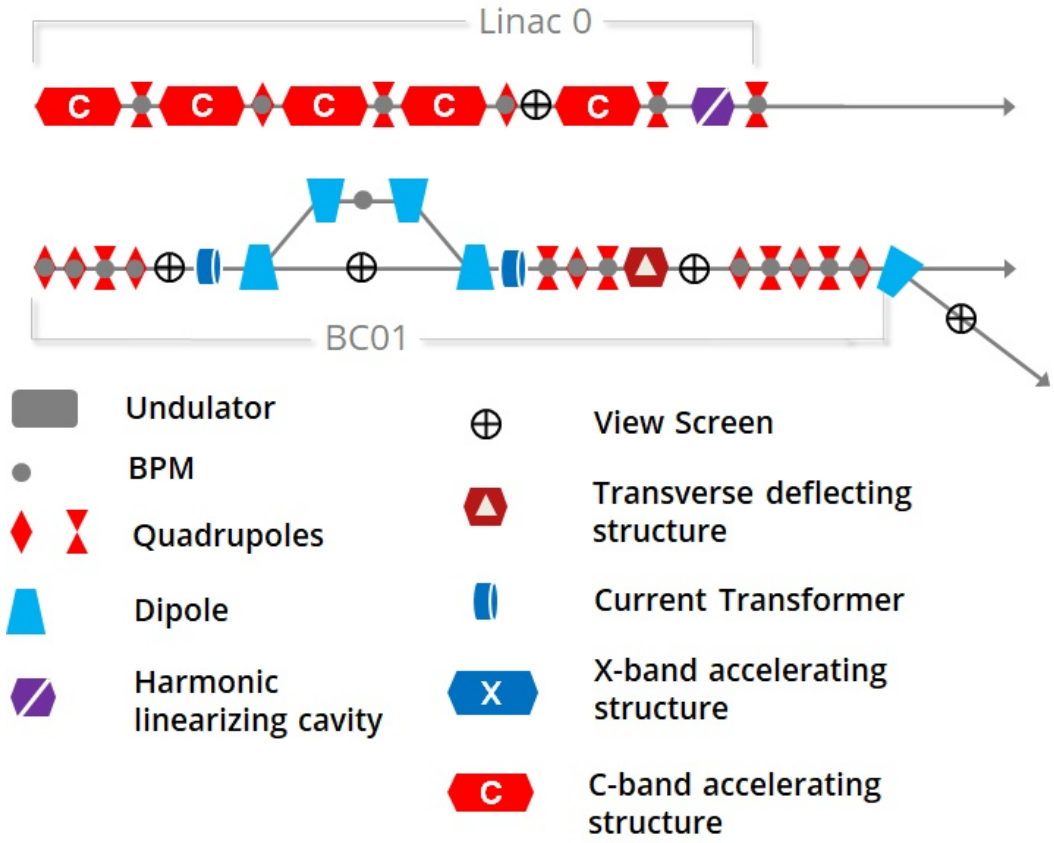

Figure 5.98.: Schematic definition of the diagnostics in the region surrounding the bunch compressor 01.

Refer to Figure 5.98 for a schematic of the diagnostics layout in this sector. In Linac-0 the striplines are inside the quads and every four accelerating modules there is a view screen for beam envelope measurement. Before the bunch compressor other view screens are placed to check the envelope during and after the process of longitudinal bunch length linearization with the K-band structure. In the bunch compressor a stripline is placed between the two upper dipoles. There is also a screen which can be used for emittance measurement in the straight line. The charge is monitored by means of an ICT before and after the compression.

After the bunch compressor the first part of Linac-1 is dedicated to the full 6D characterization of the beam, by means of a TDS and emittance measurement. The spectrometer is also placed here to measure energy, energy spread and longitudinal slice properties. The first view screen location in

Linac-1 will also be equipped with a diffraction radiation radiator to produce coherent radiation for a non-invasive online compression monitor, useful for feedback purposes.

5.4.2.4. Bunch Compressor 02 Region

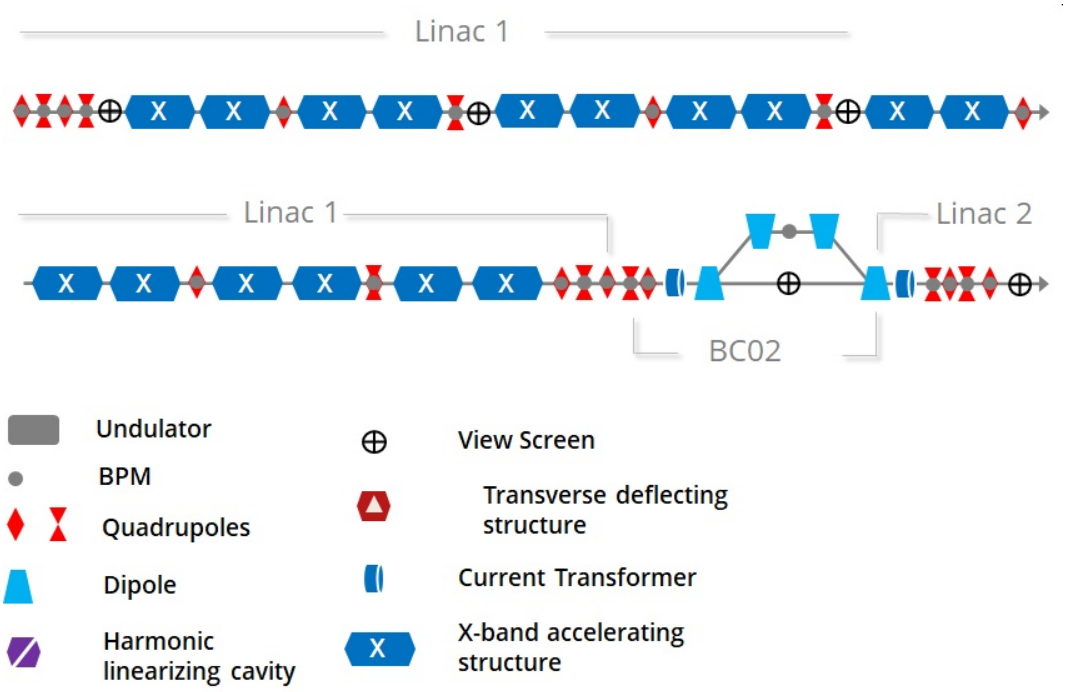

Figure 5.99.: Schematic definition of the diagnostics in the region surrounding the bunch compressor 02.

Refer to Figure 5.99 for a schematic definition of the diagnostics layout in this sector. In Linac-1 the same scheme is used—a view screen every four accelerating modules and striplines inside the quadrupoles. At the end of Linac-1 is BC-2, with diagnostics similar to those for BC-1. However, in this sector there is not a full 6D characterization of the phase space, instead this is done after Linac-2. The last screen of the scheme shown in Figure 5.99 can be also used for coherent radiation measurement to monitor the compression.

5.4.2.5. Spreader Zone to Linac 4

Refer to Figure 5.100 for a schematic definition of the diagnostics layout in this sector.

In this region the beam is divided between Linac3 and Linac4. For better matching in the dogleg the full 6D characterization is placed here rather than after BC-2. A transverse deflecting cavity and spectrometer are used for longitudinal characterization. An ICT is placed after the beamline separation for charge measurement. Transverse emittance, as well slice emittance, can be monitored with the view screen at the beginning of Linac3.

5.4.2.6. Linac 03

Refer to Figure 5.101 for a schematic definition of the diagnostics layout in this sector. This section is fully dominated by the presence of X-band accelerating structures. Stripline bpms are inside the quadrupoles, while view screens are now placed every 8 sections for beam envelope checking.

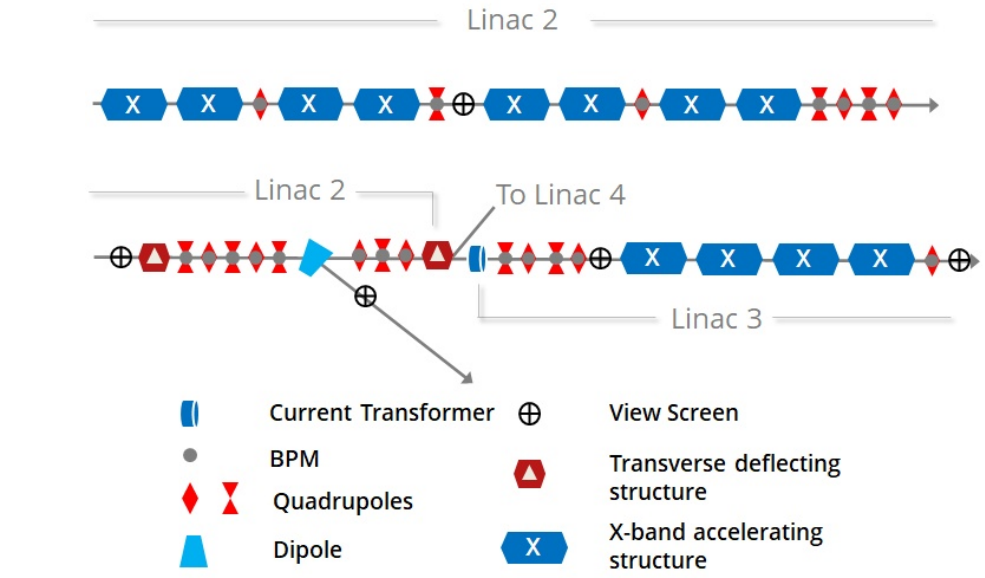

Figure 5.100.: Schematic definition of the diagnostics in the region surrounding the spreader.

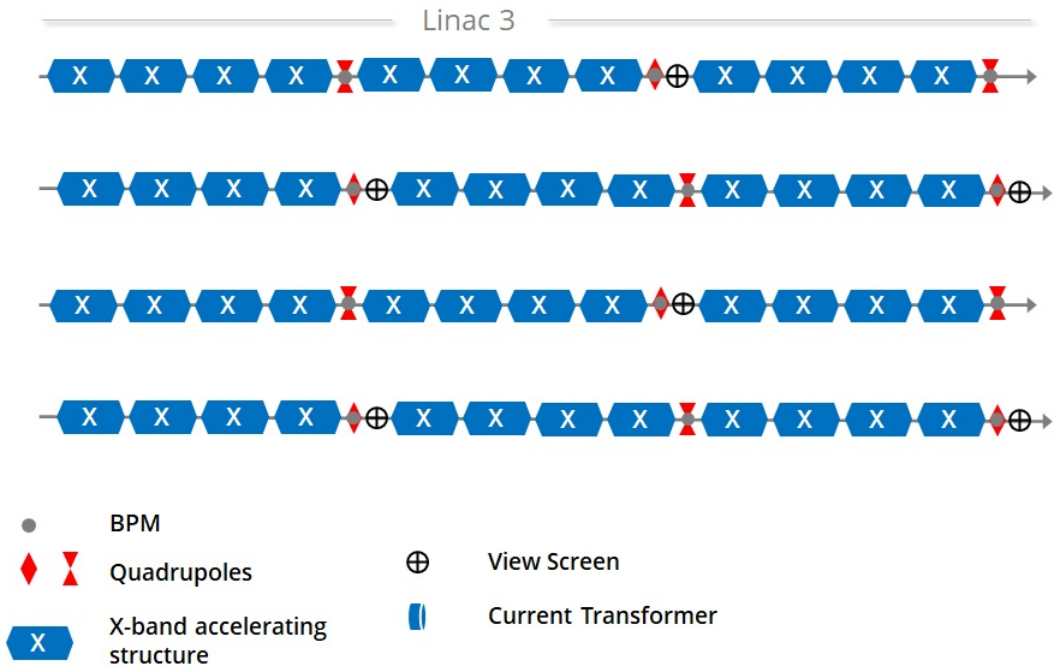

Figure 5.101.: Schematic definition of the diagnostics layout in Linac03

Spreader and Matching Area Refer to Figure 5.102 for a schematic of the diagnostics layout in this sector. At the end of Linac-3 there is another 6D phase space characterization area. Quadrupole scans are used for measuring transverse emittance, and a spectrometer with TDS allows the longitudinal phase space measurement. Both of these are fundamental in order to properly match the beam inside the undulator. The charge is monitored by an ICT just in front of the undulator.

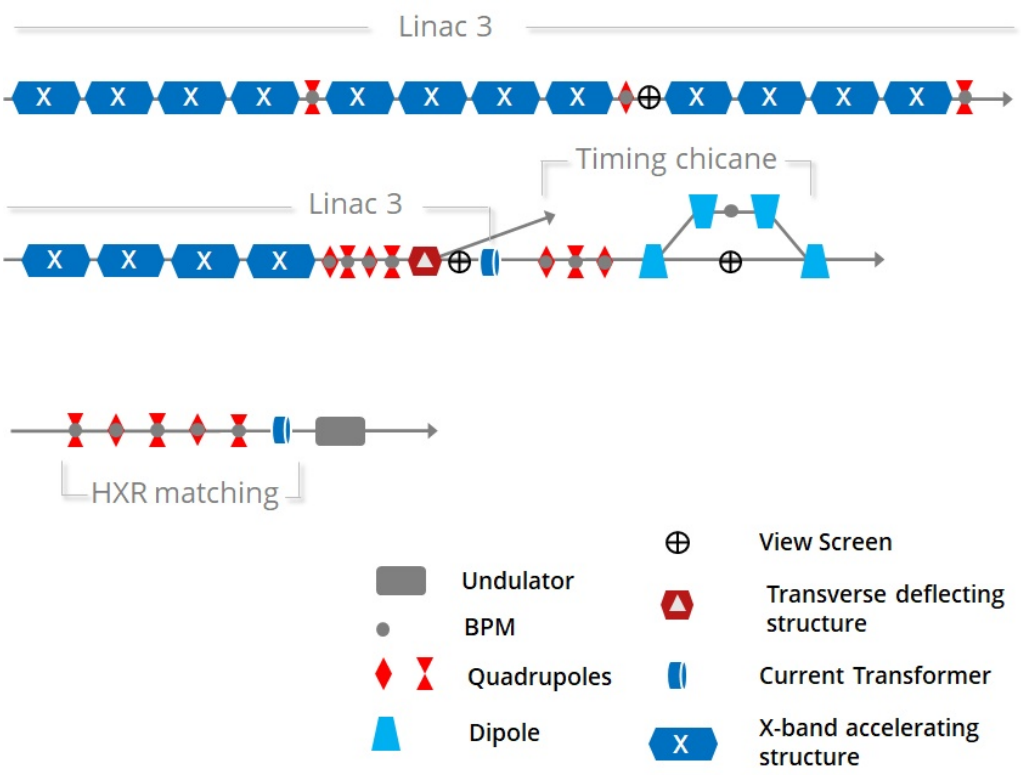

Figure 5.102.: Schematic definition of the diagnostics in the last part of the machine, before the undulator in the high energy line.

5.5. Timing and Synchronisation

The timing system in a modern light source determines the timing of all time-critical subsystems, with stability of a few femtoseconds. Over the last 15–20 years, several 4th generation light sources have been brought into regular user operation. Different timing system solutions have been adopted in these facilities, depending on the specifications and the local expertise available at the laboratory. Currently deployed solutions still include mixed copper/fibre schemes. Optical timing systems have been in operation for ten years, with FERMI being the first fully optically synchronised light source.

Frequently, timing is used as a synonym for synchronisation as these two systems work in close connection. Often the term T&S is used, for timing and synchronisation. However, these are well separated systems as the ‘timing’ system takes care of the generation and ultra-stable distribution of the ’phase reference’ signal, which needs to be femtosecond class in a 4th generation light source, plus some ancillary triggers. Synchronisation systems are mainly local optical or electro/optical devices which ‘lock’ the timing system client to the phase reference. These units are typically laser locking or Low Level RF (LLRF) devices.

In a timing system, a single ultra-stable phase clock oscillator generates the phase reference signal for the whole facility. The phase reference information is distributed throughout the facility, and is transmitted using either RF-modulated CW light, best suited for RF system synchronisation, or as pulsed light, which may be directly used in laser system synchronisation. The overall design may incorporate different synchronisation methods, optimised for their particular application. The main ‘clients’ of a timing system are:

- Injector
- LLRF electronics for stabilisation of the accelerating voltages

Table 5.36.: CompactLight RF operating frequencies. The RF degrees are shown in time units.

Item	**Frequency** MHZ	***n* factor** X-band / *n*	τ_{RF} ps	**1 deg** fs	**0.5 deg** fs
X-Band	11,994.0	master	83.38	231.60	11.58
C-Band	5,997.0	$\div 2$	166.75	463.19	23.16
S-Band	2,998.5	$\div 4$	333.50	926.39	46.32
Ka-Band	35,982.0	$\times 3$	27.79	77.20	3.86
f_{laser}	399.8	$\div 30$	2501.25	6,948	347

- Harmonic linearizer
- Various local laser oscillators used throughout the machine, such as in the photoinjector and end-station lasers
- Femtosecond class longitudinal diagnostics

The fiber optical components used in optical timing systems are, as much as possible, standard 1550 nm wavelength telecommunication devices, for enhanced reliability. Controls are implemented digitally and communicate via internet connections, to enable easy optimization as well as facilitate remote control and diagnostics. Also, trigger signals defining the coarse machine repetition rate, used in coarsely timed low repetition rate devices throughout the facility, are usually considered as part of the timing system.

5.5.1. CompactLight Specifications Relevant to the Timing System

The CompactLight design is quite innovative as it deploys different frequencies for electron acceleration while providing FEL radiation over a broad spectrum. The FEL pulses repetition rate varies over a large interval from 100 Hz to 1 kHz, both in single pulse or twin pulse configuration.

The FEL radiation production includes different schemes, implemented at the different phases of the project, ranging from SASE FEL to self-seeding schemes. A brief outline of the CompactLight timing system is presented in [204]. Typically in 4th generation light sources, three main sections are present: the linac, the undulator line and the experimental section. The phase reference signal has to be distributed to, and used within, all three sections.

A peculiarity of CompactLight is the combination of a C-band gun and Linac0, with the CLIC based, 12 GHz, accelerating structures, operating at a frequency which is the 4th harmonic of the normal S-band. In Table 5.36, the operating frequencies are listed; it is assumed that the Reference Master Oscillator (RMO) is set at the X-band frequency. The various *n* factors needed to divide, or multiply, the RMO X-band frequency to obtain all the operating frequencies are indicated. The Ka-band harmonic linearizer is set to operate at 35.3982 GHz. A possible integer divider (30) of the X-band is also indicated yielding a possible repetition rate for the laser oscillators, equal to 374.750 MHz [205].

An important feature to be addressed is the ability to trigger (generate) two laser pulses within the same shot to create two closely spaced radiation pulses. Given the limited delay between the two pulses (100 fs), it seems convenient to handle this feature using optical delays using stabilised optical delay-lines.

5.5.2. Specifications for the CompactLight FEL Timing system

The main specifications of the CompactLight FEL Timing system are listed in Table 5.37. From the 'topological' view point the number of clients and key facility parameters are listed in Table 5.38.

Table 5.37.: CompactLight Timing system main specifications.

Parameter	Value	Unit	Comment
f_{RUB}	10.00	MHz	
f_X	11.994	GHz	
$Jitter_{XRMS}$	0.05	deg	at delivery point; t=11.5 fs
f_C	5.997	GHz	
$Jitter_{CRMS}$	0.05	deg	at delivery point; t=23.1 fs
f_{LASER}	339.8	MHz	
t_{JIT}	≤ 10	fs	Laser Clients f_{off}=100HZ-10HZ
t_{DRIFT}	≤ 20	fs	24h

Table 5.38.: CompactLight Timing system topological parameters.

Timing Clients	n	Comment
S-Band	1	sub-harmonic deflector
C-Band Clients	≤ 20	gun, linac0
X-Band Clients	≤ 30	linac1-3, deflectors
Ka-Band	1	harmonic linearizer
Laser Clients	≤ 5	
Diagnostics	≤ 10	

5.5.3. Proposed Layout for the CompactLight FEL Timing System

Given the above specifications, both in terms of:

- absolute jitter values
- adopted RF frequencies
- physical extension of the facility

an optical timing system is the most appropriate for ultra-low phase noise distribution of the reference phase signal. As is typically the case for linac driven FEL sources, two main categories of timing system clients may be identified, which are intrinsically either pulsed or CW. At the very end of the timing path, the signal used as the phase reference by the remotely synced device has necessarily to have the features listed in Table 5.39.

The ultra-low phase noise source used in the timing system consists of a tightly locked electronic oscillator and a femtosecond laser. It offers both pulsed and CW-RF reference signals at a central location with the help of short (*leq* 2 m) phase stabilised and temperature compensated coaxial cables, all operated inside a temperature and humidity stabilised timing hutch. The number of Electro/Optical (E/O) conversions should be minimised and performed in a controlled environment. Finally, these cent-

Table 5.39.: List of Timing system clients.

Timing Clients	Synced Device Type	Regime	Comment
Klystron	electronic	CW	LLRF board
Laser	optical	pulsed	X-Correlator
Long Diagnostic	optical	pulsed	BAM, EOS

ral phase reference signals should adopt the physical layer that best suits the specific remote timing client, adopting the optimum stabilised link technique to transfer them to the end point.

A characteristic of CompactLight is the number of different frequencies involved in the bunch creation and acceleration processes. This poses some extra requirements on the source signal implementation. This is particularly true for the most critical generation of ultra-stable phase carriers at C-band and X-band in order to achieve an overall facility stability by design. In fact, the adopted frequencies are direct sub/multiple of each other. Both signals can be conveniently generated either from the same optical reference pulse train in a completely phase stable way, or by deducing the C-band signal from the X-band signal by simple frequency division, which is phase preserving. Ka-band carrier may be generated using even multipliers.

The proposed layout for the CompactLight timing system is shown in Figure 5.103. There are two main sections in this schematic: on the left, the femtosecond class ultra-low phase noise part and on the right, the low jitter picosecond class event system for the trigger distribution.

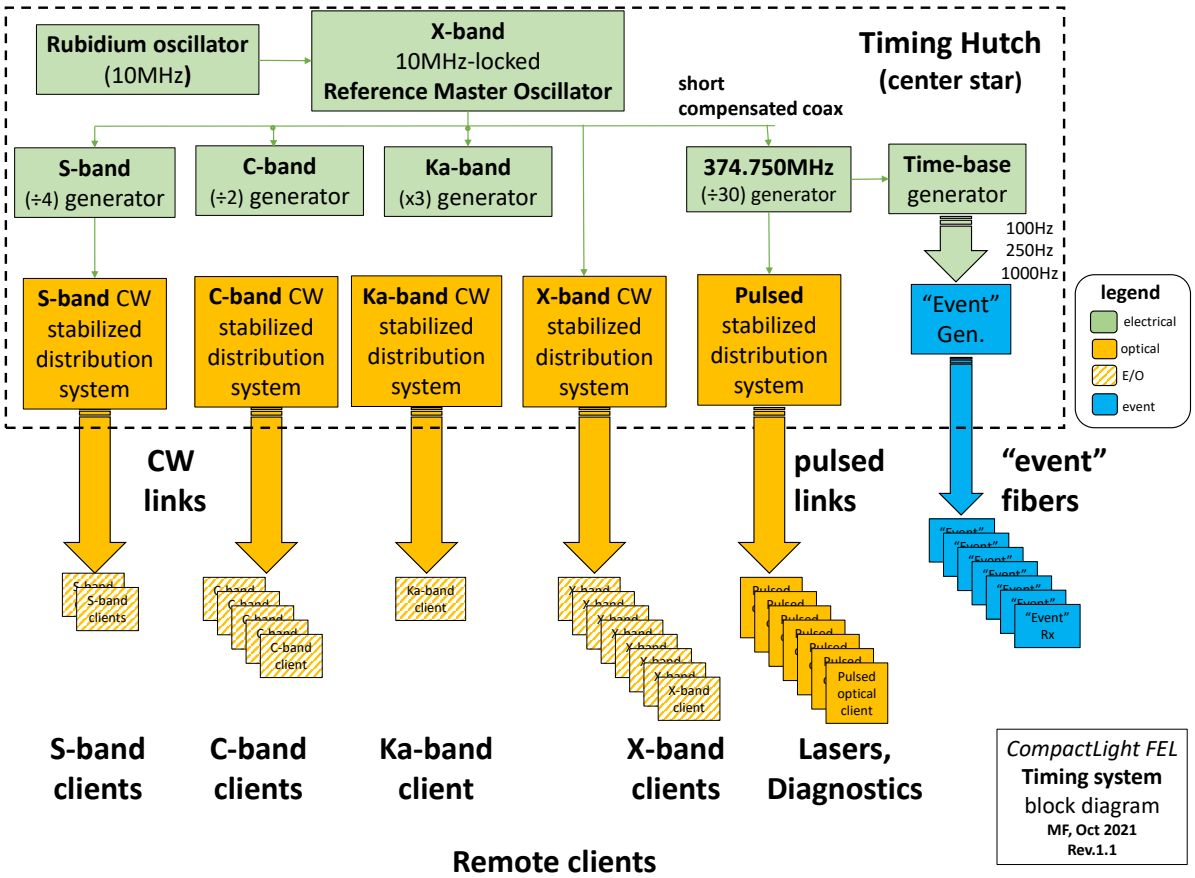

Figure 5.103.: CompactLight Timing system schematic layout; the number of "clients" is merely indicative.

The devices indicated in the layout are colour-coded:

- green for electronic / μ-wave ultra-low phase noise devices
- orange for optical ultra-low phase noise devices
- patterned orange for electro / optical devices
- blue for event class devices

The same colour code applies also to the links, indicated as large arrows.

The centralised devices are within the dashed line. This indicates the so-called timing hutch which will be located in a central position for minimising the lengths of the different optical links. In the lower part of the schematic the remote clients are indicated. These are typically optical devices (for the pulsed reference clients) and electro/optical for the CW clients and for the diagnostics.

As stated above, the overall timing system performance is critically related to the ultra-low phase noise performance of the Reference Master Oscillator (RMO). The RMO is a RF/μ-wave ultra-low phase noise generator at X-band, locked to the 10 MHz reference provided by the Rubidium Reference Oscillator, for improved long term stability. From this reference frequency both the C-band and S-band can be obtained by even division. The Ka-band is obtained by an odd multiplier ($\times 3$). The laser repetition rate has been set equal to 374,750 MHz, directly obtained by division. This frequency is a value compatible with current state-of-the-art laser products [205]. Finally, the actual low frequency bunch clock signals at 100, 250 and 1000 Hz may be obtained by dividing the laser repetition rate. The triggers are then distributed to the facility using an event like system, based on the low noise transmission over MM fibre of a given frame.

5.5.4. Timing Distribution

Due to the short reference pulses, typical 100 fs, of optical timing distribution systems and high resolution timing detectors based on integrated Balanced Optical Cross-Correlators (BOC), today's optical timing detectors have easily a resolution of 0.1 fs. If ultra-low noise seed oscillators for optical amplifier systems are used, such as low noise Er- and Yb- lasers, few femtosecond synchronisation of different oscillators over km distances is possible [206]. A possible implementation scheme of an optical distribution system is shown in Figure 5.104. With the new generation of the Menhir ultra-low jitter oscillators [205], with a repetition rate of 400 MHz, one can also co-integrate out of loop delay stages that can be used for precise tuning of all optical pulses without excessively long delay stages, up to 2.5 ns only.

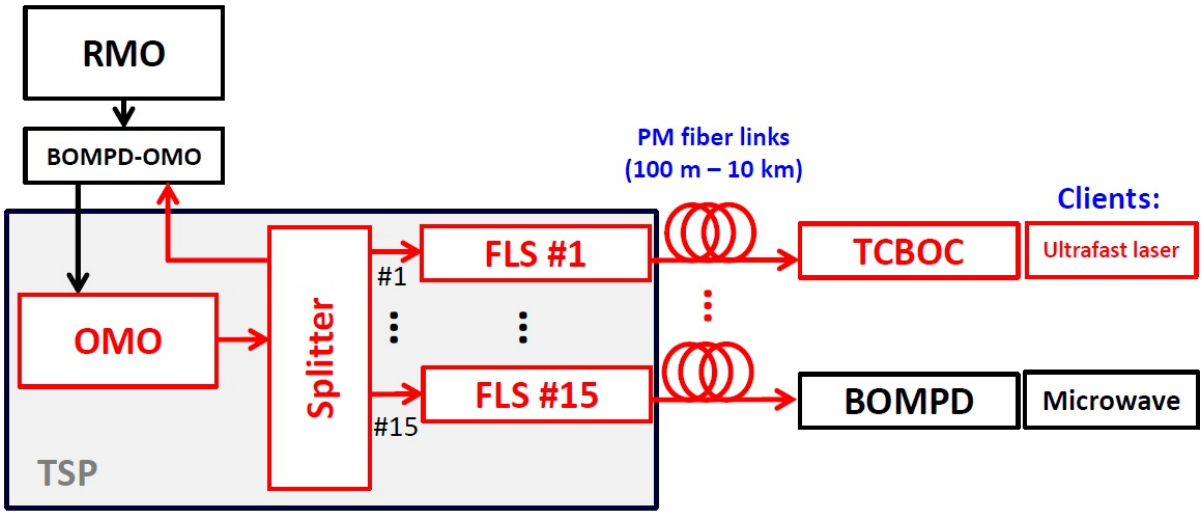

Figure 5.104.: CompactLight optical timing system schematic layout.

The low power consumption of integrated BOCs, up to 20 times less than previous BOCs, allows powering up to 20 times more timing links from the same laser source than for earlier timing systems, thus greatly simplifying pulsed optical timing systems. RF signals are conveniently transferred via RF over fibre delivery systems, with the required precision of a few tens to few femtoseconds. Also, using a pulsed optical timing distribution system RF signals may be regenerated at the far end node using a Balanced Optical Microwave Phase Detector (BOMPD) assuring the lowest-noise synchronisation

between laser and RF sources.

In Figure 5.105 a possible scheme of a (commercial, by Cycle GmbH, [207]) pulsed optical timing system feeding both pulsed and CW clients is shown.

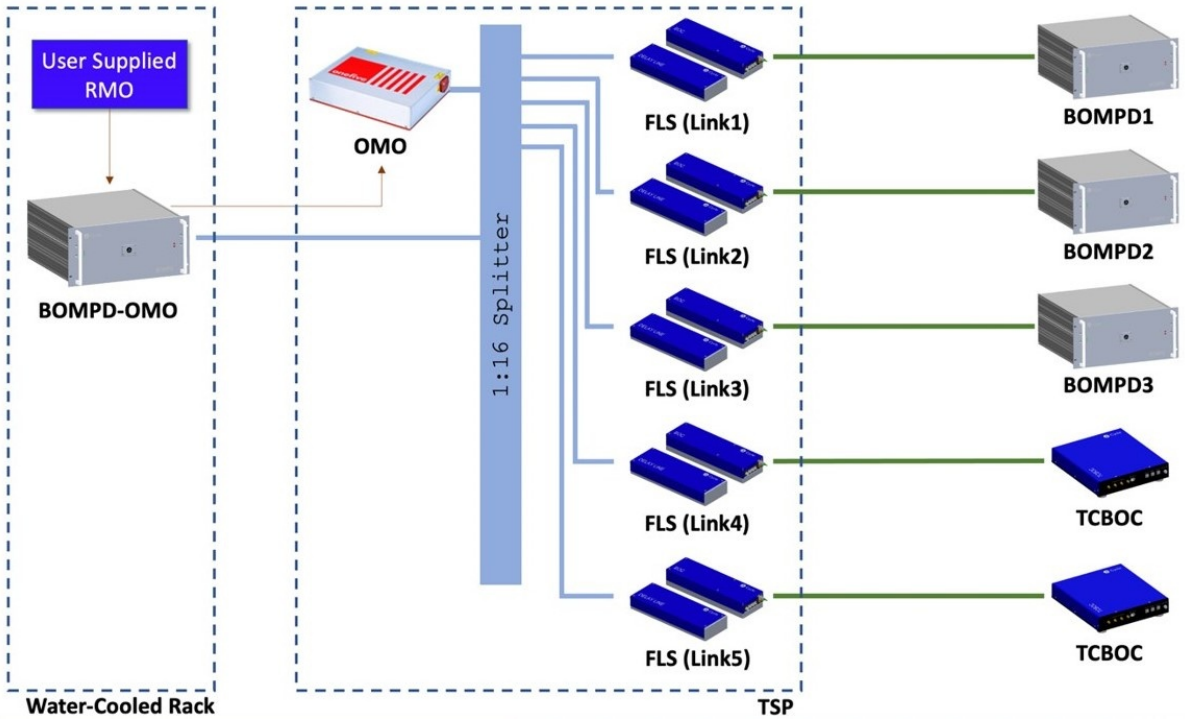

Figure 5.105.: Layout of an optical pulsed timing system with stabilized distribution fiber links.

Here, the optical master oscillator (OMO) is phase stably locked to the user supplied reference master oscillator (RMO) (here the X-band RMO) via a BOMPD-OMO. The OMO output is split via an 1:16 splitter to possibly 16 outputs or more, driving up to 16 fibre links. The fibre links are length stabilised to better than 1 fs (RMS) via fibre stabilisation units (FLS). Two possibilities at the output of each fibre link could be considered: a) regeneration of an ultra-low noise CW-microwave signal from the optical pulse stream with the help of a BOMPD at frequencies equal to a harmonic of the laser's repetition rate, or b) another laser at a different wavelength (0.8, 1 or 1.5 μm) can be synchronised to the output pulse stream at 1.5 μm with a BOC or two-color BOC (TC-BOC).

6. Light Production

6.1. Undulators

6.1.1. Choice of Undulator Technology

In this section a quantitative comparison is made of a comprehensive range of current and emerging undulator technologies, using the parameterisations of the estimated field, as a function of undulator period and gap, reported in Deliverable D5.1. Two approaches are combined. First, the semi-analytical model of Ming Xie [65] is used. The model, briefly described in Section 3.3.4.1, extends the one-dimensional FEL theory, which applies in the limit of a 1D monoenergetic beam, to the case where degradation of performance due to finite emittance and energy spread is included. This model reliably predicts the FEL saturation power and saturation length via the FEL ρ-parameter using corrections based on a parameterisation of a set of 3D numerical simulations. The results from the Xie analysis are combined with the analytical theory of Saldin [57] which allows the FEL longitudinal and transverse coherence to be calculated. Hence the FEL spectral brilliance can be determined. This is a key parameter of interest to users because it tells them how many photons per second within a given bandwidth they can focus onto a sample of given transverse dimensions - i.e. it tells them how *useful* the light is.

One figure of merit chosen for the quantitative comparison is the ratio between the FEL peak brilliance and the saturation length as this is a convenient measure of performance vs compactness. The second figure of merit chosen is the FEL peak brilliance itself (i.e. not normalised to the saturation length) because there is a specific user requirement for a minimum brilliance of 10^{33}ph/s/mm^2/mrad^2/0.1% bandwidth. The analysis of both figures of merit is conducted as a function of electron beam energy to illustrate the advantage obtained by using the undulator technologies with the strongest fields and to determine the required electron beam energy that would be required so that the peak brilliance exceeds the user requirement. This allows us an upper limit to be set on the electron beam energy for CompactLight that allows the following criteria to be satisfied:

- The electron beam energy of 5.5 GeV is lower than any other X-ray FEL facility
- The photon energy reach of 16 keV is higher than that of SwissFEL which has a beam energy higher than CompactLight
- There are a number of viable options for undulator technology which can be reserved as technology alternatives.

For the figure of merit calculations the beam energy was varied in small steps. Snapshots of the calculations are shown in Fig 6.1 where the top plot is for beam energy 4.5 GeV, the middle plot is for 5.5 GeV and the bottom plot is for 6.5 GeV. The electron beam parameters used in the calculations are peak current $I = 5$ kA, normalised emittance $\varepsilon_n = 0.2$ mm-mrad, relative RMS energy spread $\sigma_\gamma/\gamma_0 = 10^{-4}$ and average β-function $\bar{\beta} = 9$ m. In each plot the horizontal axis is the undulator period λ_u and the vertical axis is the undulator K_{rms}. Each line shows the dependence of K_{rms} vs λ_u for a different undulator technology, as represented in the legend. For some technologies a full parameterisation over the space is not available—these technologies (for example the Microwave undulators) are represented by single points on the plot. The coloured region represents the $[K_{rms}, \lambda_u]$ parameter space in which the undulator resonant wavelength lies between $\lambda_r = 0.155$ nm (top edge) and $\lambda_r = 0.0775$ nm (bottom edge). The colour represents the value of the figure of merit B/L_{sat}.

The interpretation of these plots is as follows. The intersection of each undulator curve with the $\lambda_r = 0.155$ nm line defines the period required for that undulator, at that beam energy, to be resonant at $\lambda_r = 0.155$ nm. To tune to $\lambda_r = 0.0775$ nm the undulator K strength is then reduced. For beam energy 4.5 GeV (top plot) it can be seen that for a number of technologies, for example APPLE-II,

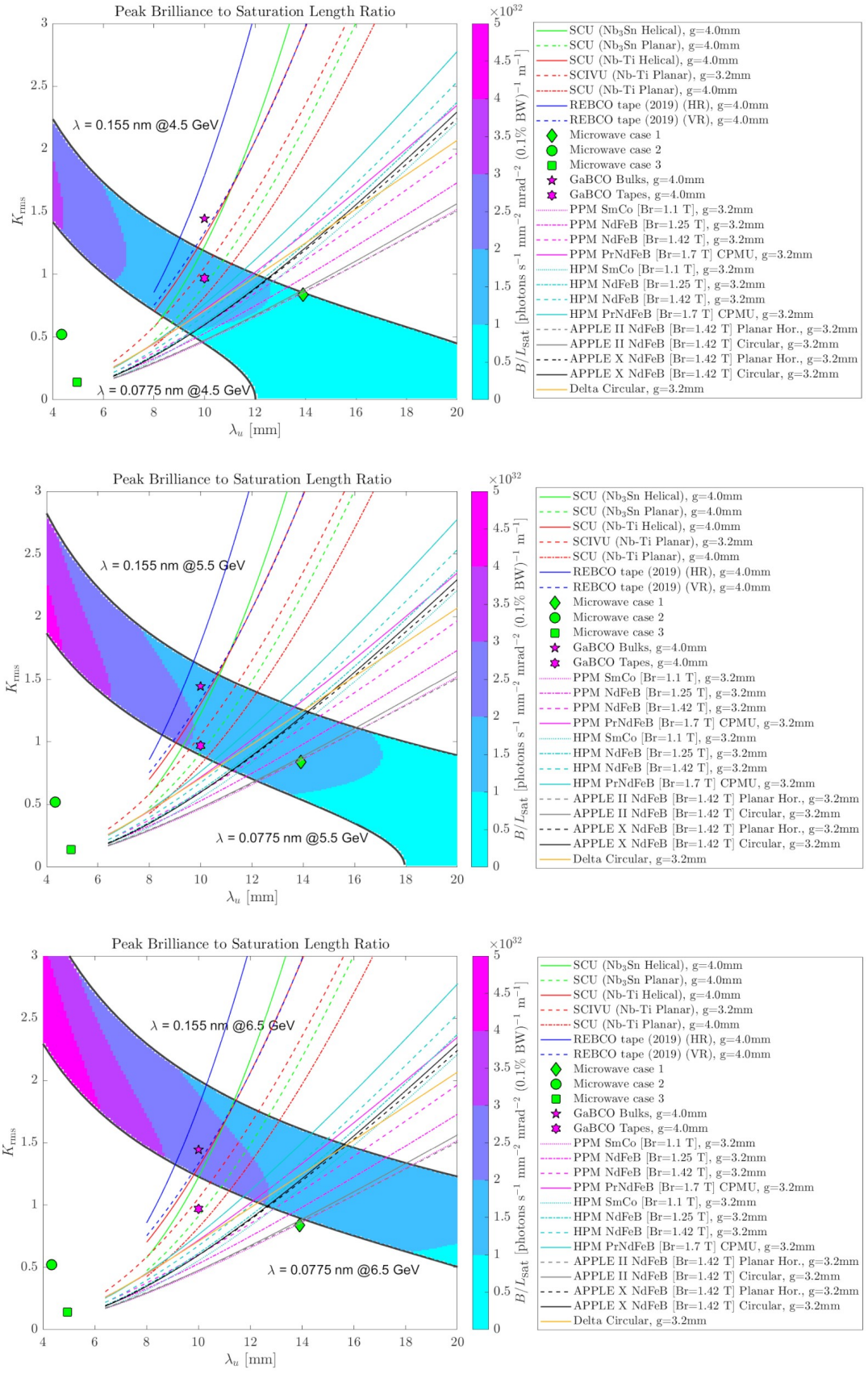

Figure 6.1.: Figure of merit B/L_{sat} for electron beam energies 4.5 GeV (top), 5.5 GeV (middle) and 6.5 GeV (bottom)

the merit function drops to zero at λ_r = 0.0775 nm, indicating that these technologies are unviable at 4.5 GeV—they provide insufficient field to cover the required tuning range. In fact, at 4.5 GeV only those technologies for which the $[K_{rms}, \lambda_u]$ curve intersects the λ_r = 0.155 nm line at λ_u < 12mm provide any output at λ_r = 0.0775 nm.

By increasing the beam energy to 5.5 GeV (middle plot) all of the technologies are able to tune across the required range, but the merit function is low for those technologies with weaker field, indicating that a threshold could be defined in principle. Finally, at 6.5 GeV, the trend continues of improving performance.

In general then, it is seen that:

- the undulator technologies that provide the strongest K as a function of period, or the 'strongest' undulators, have the highest merit function;
- at low beam energies only the strongest undulator can give any photon output across the whole tuning range;
- as the beam energy is increased more technologies become viable and the merit function increases for all technologies.

Therefore the beam energy must be chosen appropriately—it must be as low as possible to enable a compact facility but high enough to provide the required FEL output. Also the decision was made that the beam energy choice must allow a number of undulator technologies to remain viable alternative technology options.

To further assess the required beam energy the peak brilliance is calculated for the different technologies at three different beam energies. The user specification is that peak brilliance should satisfy $B > 1 \times 10^{33}$ph/s/mm^2/mrad^2/0.1% bandwidth at higher photon energies. It is noted that the calculations here are for an ideal case and that in reality there are effects that may degrade the performance—for example the bunch may have an energy chirp, or there may be bandwidth broadening or power reduction due to undulator wakefields. Therefore, a factor of two contingency is added to the required peak brilliance, i.e. the choice of undulator tecnology and beam energy must provide $B > 2 \times 10^{33}$ph/s/mm^2/mrad^2/0.1% bandwidth. The calculations are shown in Fig 6.2, where the yellow region corresponds to the peak brilliance exceeding the threshold including contingency. Clearly at E =4.5 GeV, none of the technologies provide sufficient brilliance, whereas at $E \geq$ 5.5 GeV, all of the undulator technologies are satisfactory.

Based on the previous analysis, a nominal CompactLight beam energy of 5.5 GeV was chosen. As has been shown, this is the minimum beam energy at which all undulator technologies considered will provide sufficient FEL brilliance, but this energy is also lower than that of SwissFEL at PSI which has a lower photon energy reach. In addition it is reiterated that as clearly shown in Fig 6.1 and ensuing discussion, the merit function is always stronger for those undulator technologies which provide the highest field which is a critical factor in determining choice of undulator technology, together with the analyses of the risks and costs of each technology presented in Deliverable D5.1.

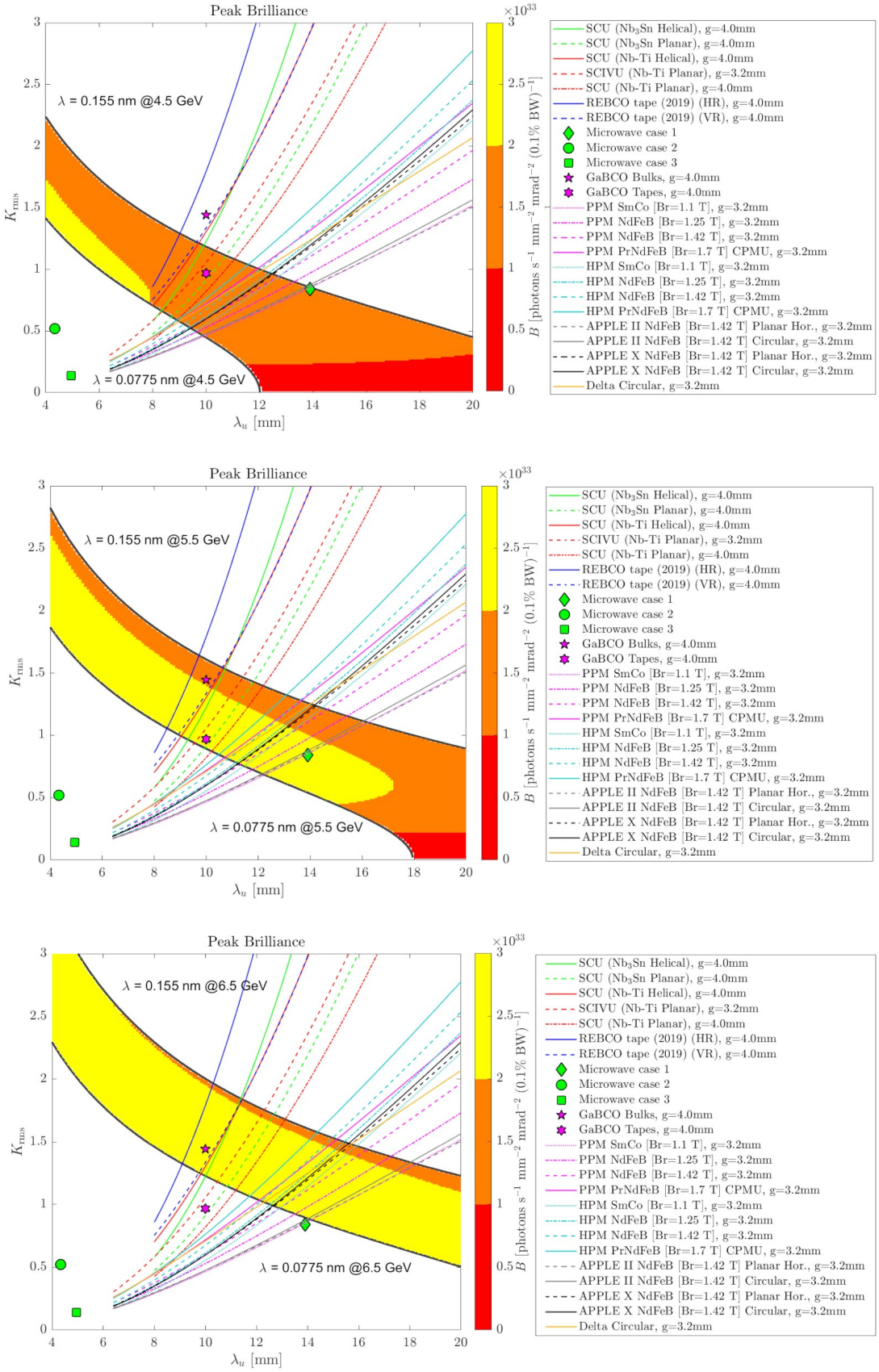

Figure 6.2.: Peak brilliance for electron beam energies 4.5 GeV (top), 5.5 GeV (middle) and 6.5 GeV (bottom)

The semi-analytical predictions in the figures were later supported by initial time-dependent FEL simulations using ideal nominal electron bunches and selecting a specific design from four groups of the technology options assessed - a CPMU design, a DELTA design, a Hybrid design and a helical SCU design. The results are summarised in Table 6.1. The conclusion drawn from the analysis and simulations was that CompactLight should adopt helical SCU undulator technology as the baseline technology choice.

Table 6.1.: Results of GENESIS time-dependent simulations.

Parameter	**Units**	**CPMU**	**Delta**	**Hybrid**	**SCU**
Saturation power	GW	9.1	8.9	7.6	9.8
Saturation length	m	24.5	26.5	29.1	15.6
Sat. pulse energy	μJ	49	48	29	54
FWHM bandwidth	10^{-3}	0.987	0.975	0.996	1.16
Peak brightness	$\times 10^{33}$ ph/s/mm^2/mrad^2/0.1%bw	2.39	2.37	1.98	2.18

The selectable polarisation is varied by means of two APPLE-X type afterburners positioned downstream of the SCU devices. The analysis that informed this design choice is described later in Section 6.1.2.5. The electron beam becomes microbunched by the FEL at the required wavelength in the SCU and then, just prior to saturation, when the level of microbunching is sufficient, yet the energy spread growth is still modest, it enters the afterburner and radiates strongly producing coherent output with the required polarisation. The afterburner can have a longer period λ_{AB}: it is important that the resonant energy range of the afterburner is matched to that of the SCU. The maximum period length is limited by the maximum photon energy and the minimum period length is given by enough field strength to meet the minimum photon energy. The λ_{AB} value is selected so that when the SCU and the afterburner are both at maximum field, they are resonant at the same wavelength. The caveat is that the afterburner cannot produce output at 16 keV because here the resonance condition cannot be satisfied. However, as will be shown in Section 6.1.2.5, the afterburner can provide satisfactory polarised output at photon energies as high as 12 keV, in line with the science case requirements, and crucially the decision to employ an afterburner for variably polarised output enables the SCU device to be optimised to produce output at photon energies exceeding that available from variably polarising devices, i.e. up to 16 keV. It should be noted that obtaining variable polarisation in the HXR range by means of optical manipulation in the photon beamline is still considered very inefficient and deemed too high-risk for a user facility.

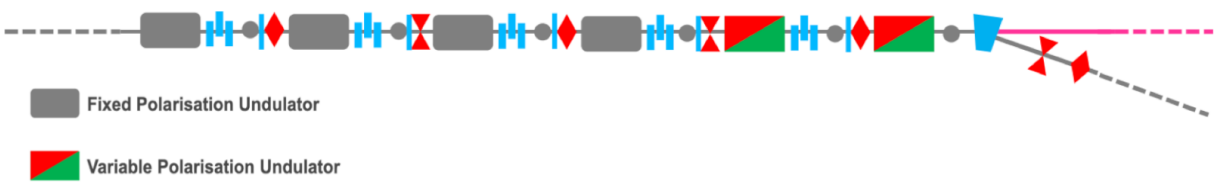

Figure 6.3.: Schematic of the XLS undulator line for both HXR and SXR FEL layouts.

Therefore, the FEL concept consists of identical undulator lines for both SXR and HXR operation regimes, supplied by different electron beam energies. Figure 6.3 shows a schematic view of these lines. Given the simultaneous requirement of large wavelength tuning and two-colour operation with close photon energies, both undulator lines are constrained to have identical parameters and tunability, with the exception that the two SCU undulators will have opposite helicity, as already discussed.

The next section presents the derivation of the main parameters of the SCU and the afterburner. Unless otherwise stated, the electron beam parameters assumed for all subsequent calculations and

simulations are the nominal parameters given in Table 4.2: charge 75 pC, peak current 5 kA, normalised emittance 0.2 mm mrad, bunch length 5 µm, energy range 2-5.5 GeV and rms energy spread 1×10^{-4} at 5.5 GeV. The following major sections concern the detailed design of the helical SCU devices (Section 6.1.3) and associated beamline elements and finally the afterburner devices (Section 6.1.4).

6.1.2. Derivation of Undulator Specification

This section presents a summary of the analysis which was used to determine the required specification of the SCU and the afterburner. The parameters determined are the SCU aperture, which is dependent on the degrading effect of wakefields on the FEL performance, the SCU period, the SCU module length, the SCU field tolerances and the required length of afterburner.

6.1.2.1. SCU Aperture

The electron beam generates an image current on the finite conducting vacuum chamber which, due to the small size, acts back to the electron bunch. This effect is known as the resistive wall wakefield effect and has magnitude inversely proportional to the aperture and bunch duration. Wakefield effects inside the undulator can cause significant electron beam energy loss and energy spread growth, which can degrade the performance of the FEL by reducing the saturation power and increasing the bandwidth. The wakefields therefore determine the minimum SCU aperture for effective FEL performance. The analyses in this section of the effect of the wakefields on the FEL performance, and the effectiveness of the mitigating strategy of applying a longitudinal taper to the undulator field, estimate that a full aperture of 4.2 mm is aggressive, yet acceptable.

For an accelerator operating at room temperature, the vacuum chamber material is generally assumed to be in the regime of the normal skin effect (NSE). The effects of resistive wakefields in the NSE regime have been detailed in several studies for round and flat beam-pipes [208–211]. In the case of (ultra-)cold metal surfaces, the resistive wall effects enter the anomalous skin effect (ASE) regime, where the AC conductivity of metals is different from in the NSE. The effect of resistive wall in the ASE regime has been studied for long and short beams in [212, 213]. For a bunch of a few µm duration, the resistive wakefield effect is essentially independent of the skin regime (i.e. temperature) and material choice (i.e. aluminium or copper): any difference due to skin effect regime and material choice is negligible.

The wake potential, i.e. the wakefield induced energy loss per meter along the single bunch, can be calculated by convolving the single particle wake function $\omega(z)$ with the electron longitudinal line charge density $\rho(z')$ [214],

$$E_\omega(z) = \int_{-\infty}^{z} \omega(z-z')\rho(z')dz' \tag{6.1}$$

where z is the position along the undulator and z' is the electron longitudinal coordinate with respect to the head of the bunch. The generated current distribution and wake potentials along the bunch for different apertures are shown in Figure 6.4.

The effect of the wakefield on the FEL was investigated by importing the calculated wake potential (Equation 6.1) into the Genesis 1.3 simulation code [215]. The undulator period was the nominal 13 mm and the wavelength was 0.76 Å (photon energy 16 keV). The simulation was performed for a helical undulator and the vacuum chamber was assumed to be copper and round.

It is seen that the energy loss due to the wakefield can be compensated by gradually tapering the undulator field strength. The left panel of Figure 6.5 shows the evolution of the FEL power for different apertures and tapering options, while the right panel shows the evolution of the bandwidth. It is seen that the saturation power decreases for smaller aperture values. For a 4 mm aperture (r=2 mm), linearly tapering the undulator field by 0.9% along the undulator (from the beginning to the end) compensates the negative effect of the wakefield on the saturation power, with only a small increase in bandwidth. It

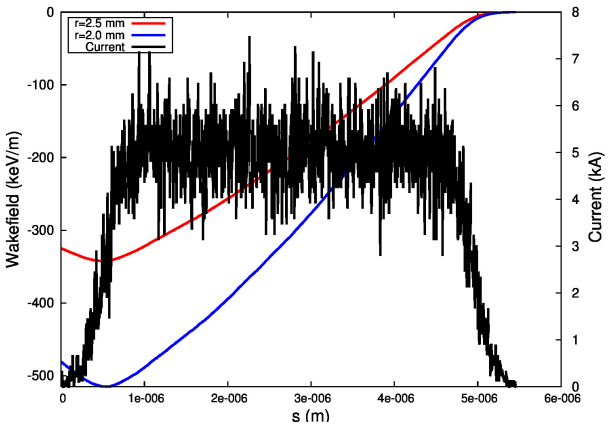

Figure 6.4.: Generated current distribution of 5.5 GeV electron bunch and the wake potentials along the bunch for different beam-pipe radii (the head of the beam is to the right).

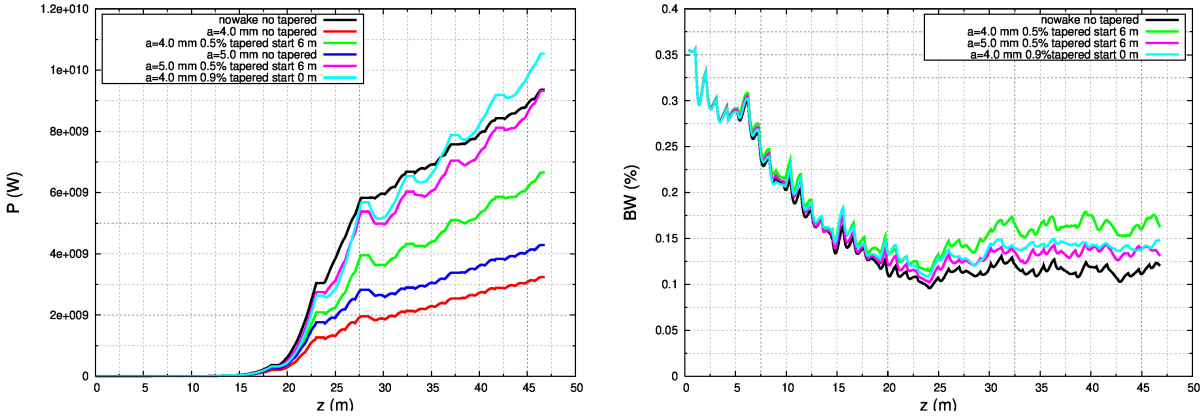

Figure 6.5.: Left: evolution of power in undulator region for different apertures (averaged over the full FEL pulse). Right: bandwidth along the undulator for different apertures.

is therefore concluded that an aperture of 4 mm is in fact a realistic design choice – the wakefields are seen to have an effect on the FEL but a practical mitigating technique is effective.

6.1.2.2. SCU Period Length

In the XLS design the same undulator line is used in both the SXR *and* the HXR – this feature allows the facility to be more compact and cost-effective than other FEL facilities which have separate undulator lines for different wavelength regimes, but it does mean that care has to be taken to ensure that the undulator parameters are chosen appropriately to balance the output performance equally between the SXR and the HXR. As will be shown, pushing to shorter undulator periods is better for the HXR, but this is at the cost of reduced performance in the SXR, which favours longer periods. An assessment has therefore been made of the required undulator period to properly balance the FEL output performance across the whole SXR and HXR tuning range.

The assessment was done using the widely-used semi-analytical model developed by Ming Xie [64], described in Section 3.3.4.1, which provides a rapid comparison of relative FEL performance for different undulator periods. The results of the calculations are shown in Figure 6.6. The top plot shows the pulse energy as a function of photon energy, the middle plot shows the estimated saturation length, neglecting the length of any gaps between the undulator sections, i.e. the active undulator length. The bottom plot shows the electron beam energy. The calculations assume the nominal electron bunch

parameters. The pulse energy is calculated as $\Delta_t \times P_{sat} \times FF$, where Δ_t is the full pulse duration, P_{sat} is the saturation power and $FF = 0.6$ is an empirical 'filling factor' accounting for the spikiness of the SASE radiation pulse. To maximise the pulse energy at each wavelength, both electron beam energy and undulator field should be maximised fulfilling the already defined resonance condition:

$$\lambda_r = \frac{\lambda_w}{2\gamma^2}\left(1 + a_w^2\right) \tag{6.2}$$

so to operate at maximum beam energy for a given wavelength the undulator parameter a_w must therefore also be as large as possible. However, the beam energy for CompactLight is capped at 5.5 GeV

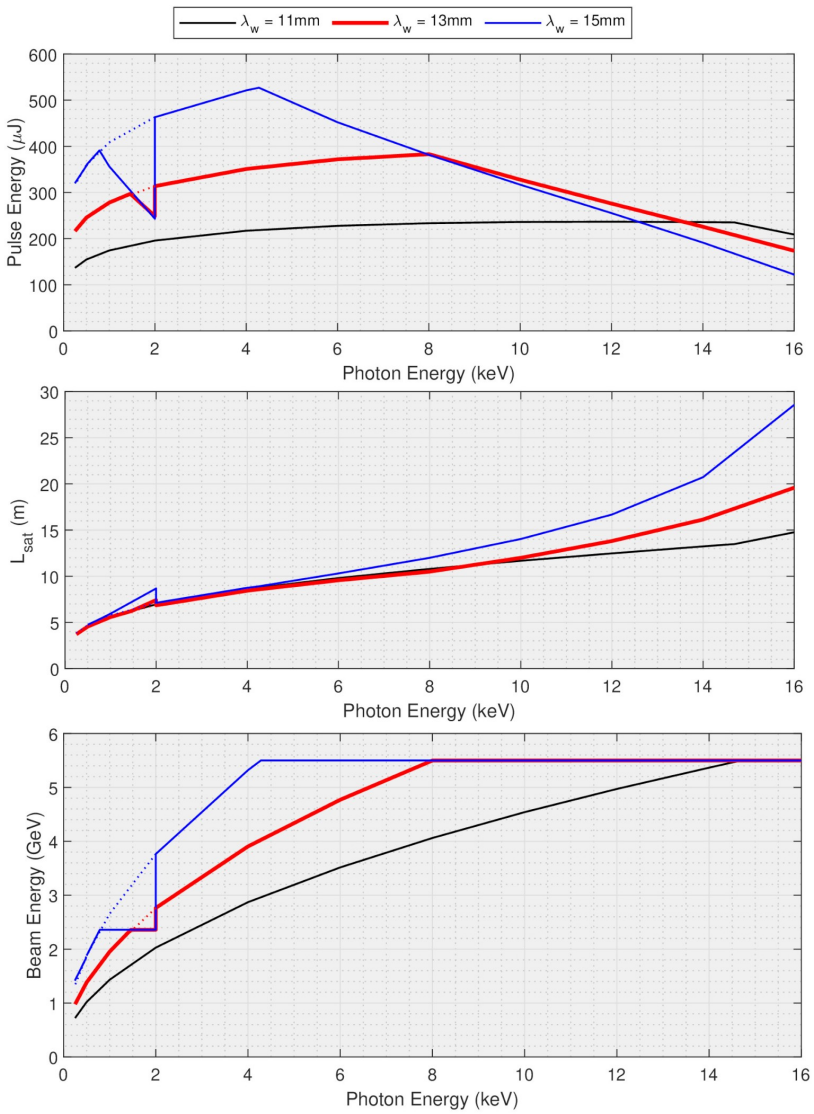

Figure 6.6.: Semi-analytical performance calculations, showing comparison between 11 mm SCU period, 13 mm SCU period (baseline choice) and 15 mm SCU period, showing pulse energy (top), saturation length (middle) and electron beam energy (bottom). The solid lines are relevant to the case where the electron beam energy in the SXR is limited to 2.36 GeV which is required for operation at 1 kHz repetition rate. The dashed lines at photon energies less than 2 keV are for the case where SXR operation is at 100 Hz in which case the 2.36 GeV energy limit does not apply.

for 100 Hz operation and 2.36 GeV for 1 kHz operation, so at some point as the wavelength is reduced (the photon energy is increased) it becomes necessary to start reducing the undulator parameter which gives weaker performance. For example, for 11 mm undulator period, this occurs at a photon energy of approximately 15 keV. Figure 6.6 therefore shows the *maximum* pulse energies obtainable by freely varying the electron beam energy – in reality, it is more convenient to operate at a set of fixed beam energies. The dotted lines relate to the case where CompactLight operates in the SXR at 100 Hz.

The calculations show that compared to the baseline period choice of 13 mm, 11 mm only gives higher pulse energy at photon energies greater than 14 keV and reduced saturation length at photon energies above 10 keV, whereas 15 mm gives progressively lower pulse energy and longer saturation length above 8 keV. However, at lower photon energies the situation is reversed – below 12 keV the 11 mm period is significantly worse and below 8 keV the 15 mm period offers the best performance. It is anticipated that will be fewer users for photon energies above $\approx$ 14 keV where the 11 mm period is the best choice, and the 15 mm period would require another 10 m of undulator, compared to the 13 mm period, to reach saturation at 16 keV. The optimum choice for balanced performance across the whole operating range is therefore λ_w = 13 mm.

6.1.2.3. SCU Module Length

The long undulator required for the FEL will comprise a number of individual modules in series. This is to allow the periodic insertion between modules of focusing quadrupoles, phase shifters, diagnostics and vacuum components. A study was done to determine the optimum length of the individual undulator modules. The primary consideration was the output performance of the FEL, with secondary consideration given to compactness, cost and ease of construction and operation.

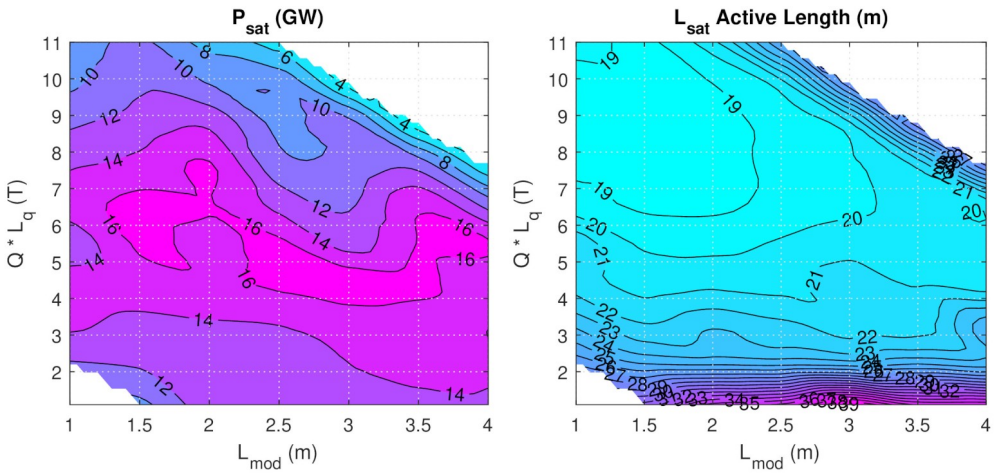

Figure 6.7.: HXR saturation power and *active* undulator length (i.e. excluding the length of the gaps between the modules) as a function of module length and integrated quad strength.

Simulations were performed using Genesis 1.3. Module lengths from 1 m to 4 m were considered, and for each module length the quadrupole focusing was scanned over a range to determine the maximum saturation power and minimum saturation length for each length of undulator module. The gap between modules was fixed at 0.5 m. This study was done using nominal electron beam parameters, once in the HXR for 16 keV photon output, and once in the SXR for 2 keV photon output. More weighting was given to the HXR results when choosing the optimum module length. Figure 6.7 shows the results for the HXR with the left plot showing the saturation power and the right plot showing the *active* undulator length (i.e. excluding the length of the gaps between the modules) which is a more useful measure for cost optimisation than floor length. Figure 6.8 shows the same data but expressed in terms of undulator 'efficiency', i.e. saturation power normalised by the active saturation length.

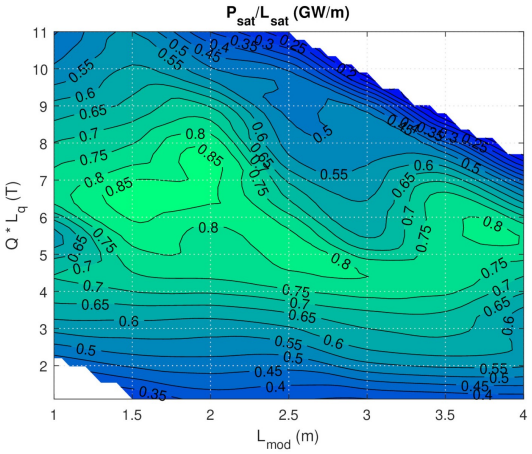

Figure 6.8.: Saturation power normalised by active saturation length, as a function of module length and integrated quad strength.

The data shows that to obtain maximum saturation power the module length can be between 1.25 m and 4 m, but to minimise the active undulator length, and hence the total cost of the undulator, the module length should be less than 2.1 m. To obtain maximum undulator efficiency, P_{sat}/L_{sat} the optimum length is 1.75 m. The equivalent data for the SXR (not shown) indicated that for maximum saturation power the module length should be 2.25 m but the optimum is broad and for a module length of 1.75 m the reduction is only 5%. The data for SXR saturation length is not relevant, because the saturation lengths are much shorter in the SXR and so do not determine the total length of undulator required for the facility. The conclusion therefore is that the optimum module length is 1.75 m.

6.1.2.4. SCU Field Tolerances

The mechanism of exponential gain in the FEL is a resonant process that amplifies a narrow bandwidth of radiation. The radiation bandwidth at saturation σ_λ/λ is approximately equal to the FEL ρ-parameter, with typical value $\rho \approx 5 \times 10^{-4}$ at HXR wavelengths. The FEL wavelength is given by the resonance condition, Equation 6.2, and any variation during the exponential gain process of parameters in this equation acts to broaden the bandwidth and degrade the FEL gain. It is therefore critical that errors of the undulator parameter a_w along the beamline are within a satisfactory tolerance level.

An estimate of the tolerable variation in the undulator parameter can be derived by differentiating the resonance condition to find

$$\frac{\sigma_{a_w}}{a_w} = \frac{1+a_w^2}{2a_w^2}\frac{\sigma_{\lambda_r}}{\lambda_r} \approx \frac{1+a_w^2}{2a_w^2}\rho \tag{6.3}$$

and using CompactLight parameters for 16 keV operation, this gives an estimated field variation tolerance of $\sigma_{a_w}/a_w \approx 8 \times 10^{-4}$.

Simulations were also done using Genesis 1.3 with the FEL operating at 16 keV. The code allows random field errors to be added to each period, with the errors correlated to minimise the field integrals. This ensures that any degradation in FEL performance is due to perturbations of the resonance condition rather than trajectory wander. The results are shown in Figure 6.9. This shows that errors in the undulator parameter exceeding $\sigma_{a_w}/a_w \approx 1 \times 10^{-3}$ could give a reduction in output power of more than 5% and increase in the saturation length of more than 0.6 m. This level of error is close to the analytically derived specification.

The baseline tolerance is specified as $\sigma_{a_w}/a_w < 1 \times 10^{-3}$. From SCU modelling this translates to a tolerance in the placement of the windings of approximately 20 µm which is acceptable. Reducing field errors below 1×10^{-3} would provide a small advantage for FEL performance, but this would have to be balanced against the feasibility and cost of the tighter tolerance.

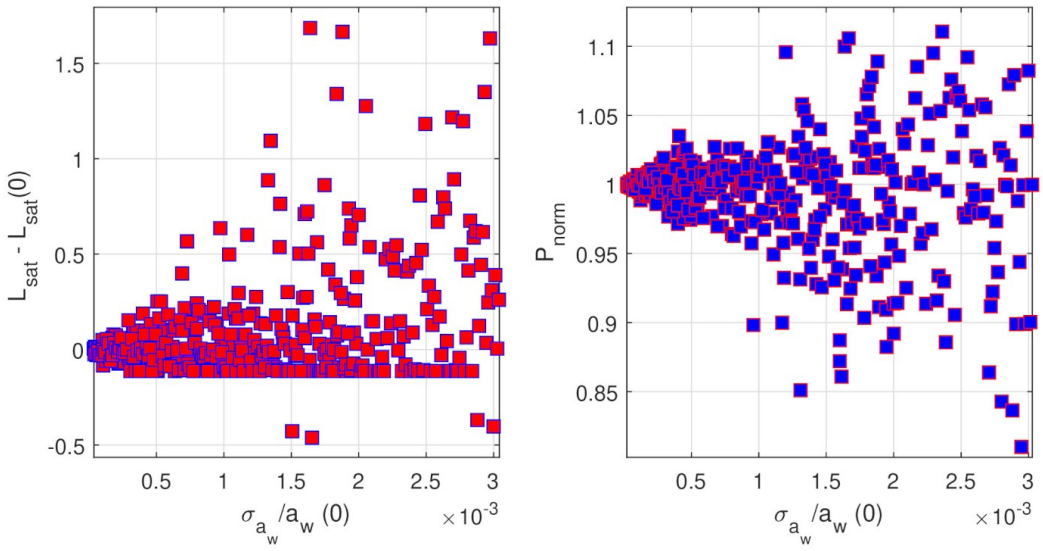

Figure 6.9.: Increase in saturation length and peak power degradation due to random errors in the undulator parameter a_w.

6.1.2.5. Afterburner Requirements

As described in Section 6.1.1, the baseline design comprises a helical SCU followed by a variably polarising APPLE-X afterburner. This section presents a simulation study (using Genesis 1.3) that optimises the output performance of the afterburner in the SXR and the HXR and determines the length of afterburner required to produce useful output. A comparison is also made between the baseline configuration and an alternative scenario for providing variably polarised FEL output, comprising an undulator line built entirely from APPLE-X devices.

In the simulations, the microbunched electron beam from the SCU section is propagated into the afterburner section, but the radiation is not—it is artificially blocked. This means that the degree of polarisation of the afterburner output can be assumed to be near perfect (in fact this cannot be proven from the simulations because polarised fields are not supported by Genesis 1.3). In practice, the radiation from the SCU can be 'blocked' by setting the afterburner at a small angle and kicking the electron beam onto its axis with a corrector [216] or by applying an inverse taper in the SCU which allows the electron beam bunching to develop but suppresses the radiation output [217].

To obtain optimum flux from the afterburner, the level of microbunching in the beam as it enters must be sufficient to create an initial intense burst of coherent output, but not so great that the associated energy spread growth prohibits further exponential growth. This optimisation was studied in the SXR at 250 eV and in the HXR at 12 keV. The afterburner period is set to 19 mm. This assumes an in-vacuum device of gap 5 mm, and means that the resonant photon energy at maximum field is the same as that of the SCU at maximum field, so that the tuning ranges of the two devices are matched to each other. Note that out-of-vacuum and cryogenic versions of the APPLE-X design are also under consideration, as will be discussed in Section 6.1.4.2. These versions might require a slightly different period choice, but the results of this section are still relevant. The peak brilliance, total length of the undulator line and the pulse energy at the end of the afterburner are used as the figures of merit to characterise the FEL performance.

The results in the HXR, at 12 keV resonant photon energy, are summarised in the top plot of Figure 6.10 which shows the pulse energy and peak brightness as a function of the number of SCU modules and number of afterburner modules. Peak brightness of 9×10^{32} photons/s/mm^2/mrad^2/0.1%bw can be obtained using 6 modules of the SCU and two modules of the afterburner. This configura-

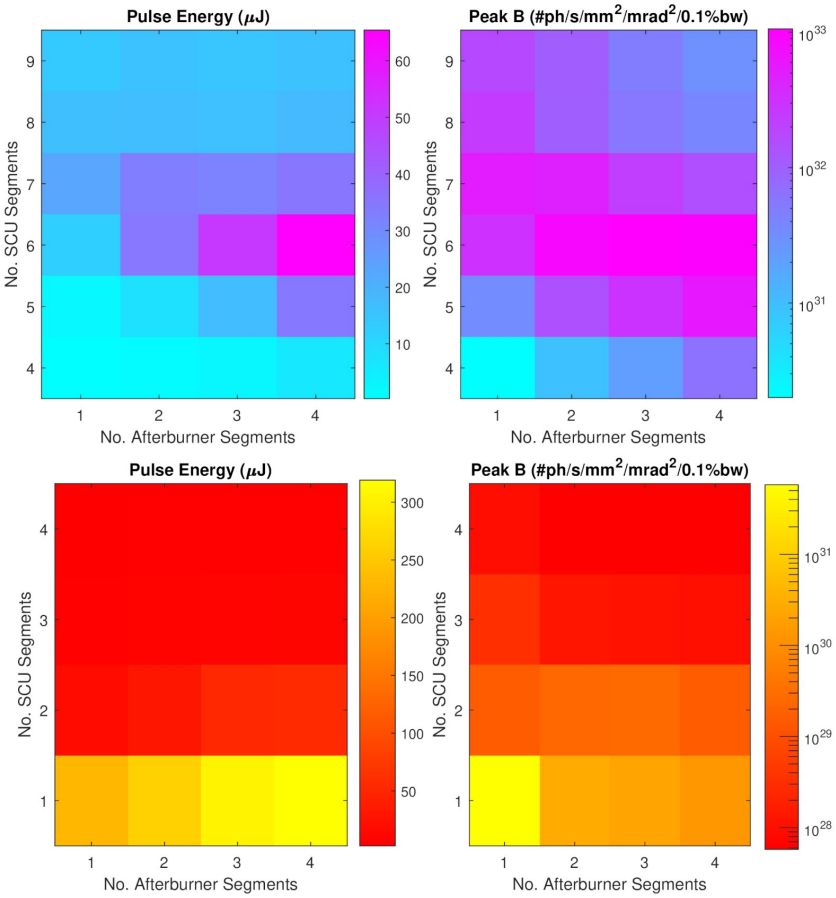

Figure 6.10.: Top: Afterburner pulse energy and peak brightness in the HXR at 12 keV photon energy, as a function of the number of SCU modules and number of afterburner modules. Bottom: Equivalent results in the SXR at 250 eV photon energy.

tion generates a pulse energy of 35 µJ. Adding another afterburner module increases the brightness slightly to 10×10^{32} and the pulse energy to 50 µJ. The equivalent results in the SXR, at 250 eV photon energy, are shown in the bottom plot of Figure 6.10. At this photon energy only a single SCU module and a single afterburner module are required to obtain the maximum peak brightness of 6×10^{31} photons/s/mm^2/mrad^2/0.1%bw and a pulse energy of 230 µJ. Using a second afterburner module does not increase the brightness but increases the pulse energy to 260 µJ.

From these results in the HXR and SXR, a single afterburner module is insufficient—two are required to achieve near maximum brightness. The extra brightness and pulse energy that could be obtained in the HXR by adding a third afterburner is modest. The baseline configuration is therefore specified to comprise the helical SCU followed by two APPLE-X afterburner modules. It is also proposed, for contingency, to consider leaving an empty slot in the lattice for later installation of a third afterburner device if required.

The SCU + APPLE-X baseline configuration is now compared to alternative scenarios where the entire undulator line is a helical SCU or an APPLE-X. The HXR results are shown in Figure 6.11, and for completeness the SXR results are shown in Figure 6.12. The z-axis is the distance through the undulator line. In the HXR baseline, the SCU extends to 13.6 m and the two modules of APPLE-X afterburner are from 13.6 m to 18.1 m. In the SXR baseline configuration, the changeover from SCU to APPLE-X occurs earlier because there is only one SCU module in use. It is clear that in the HXR the baseline configuration has the advantage of being significantly more compact than the alternative

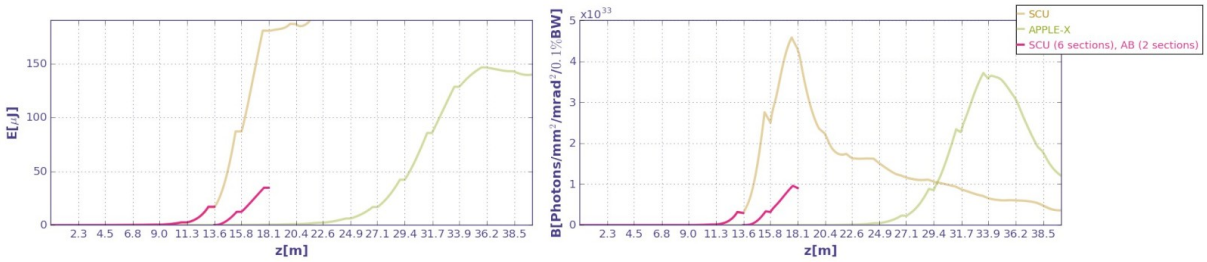

Figure 6.11.: HXR: Comparison of 12 keV pulse energy (left) and peak brightness (right) for three different scenarios: an SCU, an APPLE-X in vertically planar configuration, and the baseline SCU and APPLE-X configuration. The tick marks and labels on the z-axis correspond to the locations of the ends of individual undulator modules.

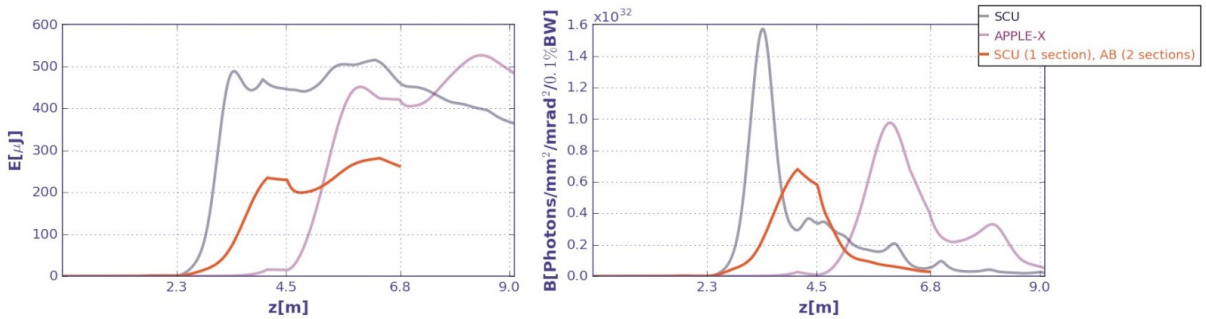

Figure 6.12.: SXR: Comparison of 250 eV pulse energy (left) and peak brightness (right) for three different scenarios: an SCU, an APPLE-X in vertically planar configuration, and the baseline SCU and APPLE-X configuration.

scenario of using an APPLE-X undulator for the whole FEL line. The disadvantage is that the peak brightness obtained is only 25% of that obtainable from the APPLE-X on its own, and the pulse energy is only 27%. However, the baseline configuration allows the FEL to operate at much higher photon energies – the SCU is effective at up to 16 keV whereas the APPLE-X cannot reach much above 12 keV without operating at very weak a_w values which give very poor performance.

To conclude, the baseline configuration of a helical SCU followed by two modules of APPLE-X afterburner is a significantly more compact solution for the production of variably polarised FEL output in the HXR than the alternative scenario of using a variably polarising APPLE-X undulator for the whole FEL line. Variably polarised light can be produced at photon energies up to about 12 keV which satisfies the user requirements. A disadvantage is that the pulse energies and brightness are reduced to less than 50% of that available with a stand-alone APPLE-X, but this is more than offset by the fact that using the SCU section on its own circularly polarised FEL light can be produced with pulse energies in the 100s of μJ at photon energies up to 16 keV.

6.1.2.6. Parameter Summary

The main parameters of the SCU and APPLE-X afterburners are summarised in Table 6.2.

6.1.3. The Self-Amplified Spontaneous Emission Lines

The investigations reported in the deliverable report D5.1 [218], comparing a wide range of undulator technologies in terms of achievable key parameters determining both the performance and compact-

Table 6.2.: Summary of the main undulator parameters.

	Main Undulator	**Afterburner**
Technology	NbTi Superconducting	APPLE-X
Polarisation	Helical	Variable
Period length λ_w	13 mm	$\approx$ 19 mm
Maximum a_w	1.33	1.80
Beam gap	4.2 mm	5 mm
Module length	1.755 m	1.75 m

ness of the facility, lead to the choice of helical superconducting undulators as the baseline for the Self-Amplified Spontaneous Emission (SASE) lines for CompactLight. Table 6.3 summarises the main functional parameters of the SASE line according to the specifications derived in Section 6.1.2.

In terms of electron beam optics, the SASE lines form a FODO lattice with one undulator magnet inserted into each half cell. In addition, each half FODO cell is equipped with a phase shifter in order to keep the phases of radiation field and undulating particle motion matched between subsequent undulator modules, and a cavity beam position monitor for minimal beam diagnostics. A balancing of the optimisation objectives for the hard and the soft X-ray cases (see Section 6.1.2) led to the Pareto optimal choice of geometric and focusing parameters and subsequent requirements for the focusing and phase shifting magnets described in the following sections.

Superconducting undulators have been considered for the Linac Coherent Light Source upgrade (LCLS-II) [219], and the conceptual design for the CompactLight SASE line adopts conceptions developed in the conceptual design phase of the LCLS-II superconducting undulators [220, 221].

For the superconducting undulator, the phase shifters and the quadrupoles, for the cooling scheme of each of these components, as well as for the overall layout of the supporting and cooling infrastructure, there are a number of technological choices. The choice was made to use virtually iron-free designs for all magnetic components, i.e. they are laid out as coil-dominated superconducting magnets based on NbTi technology. That implies that the magnets at least of each half FODO cell, including the beampipe, form a cold mass which needs to be maintained at an operating temperature range below 4.5 K. For the cryomodule design, as well as for the refrigeration scheme and infrastructure, a set of different options was considered. Each of these options comes with advantages and disadvantages in terms of investment, running costs, efficient use of resources, downtimes due to maintenance, and likely also overall reliability of operation.

6.1.3.1. Basic Concept Layout

From the multi-objective optimisation of the undulator module length and the integrated FODO quadrupole strength described in Section 6.1.2.3 it was concluded that the optimum undulator module length is L_u = 1.75 m with an integrated focusing gradient of about 7 T. The gap between undulator modules was fixed at 500 mm: this value has to accommodate quadrupoles, phase shifters, diagnostics and transitions between cryomodules. For the conceptual undulator design an undulator module length of L_u = 1.755 m is chosen, corresponding to 135 periods of 13 mm length, including the matching periods at both ends of the undulator. According to the simulations of the E_{ph} = 16 keV photon energy working point described in Section 4.2, FEL saturation would be reached after 11 undulator magnet units. Accounting for contingency, the design includes 16 units per SASE line.

Each of the two SASE lines consists of 16 identical, 2.255 m long cryomodules, each housing one undulator module plus the components for focusing, phase matching, diagnostics and beam-based alignment, all operated at liquid helium temperature. These modules can either be minimally sectioned, i.e. forming together one long, continuous cryostat, or sectioned, i.e. intercepted by cold-warm trans-

Table 6.3.: General functional parameters of the CompactLight SASE lines.

Undulator	**Value**	**Units**
Period length	13	mm
Length (incl. matching periods)	1.755	m
(Periods)	135	
Magnetic gap	5.0	mm
Beam-pipe bore diameter	4.2	mm
a_w (8 keV)	1.33	
a_w (16 keV)	0.617	
B_{max} on axis (at 80% on the load line)	1.09	T
Phase shifter		
Phase Integral	2000	$T^2\,mm^3$
Geometric length	≤ 170	mm
FODO Quadrupole magnet		
Integrated field gradient	10	T
Active length	60	mm
(Geometric length)	≤ 100	mm
Alignment Quadrupole magnet		
Integrated field gradient	2	T
Geometric length	≤ 50	mm
FEL lines		
Cryomodule length	2.255	m
Number of modules	2×16	

itions. In the former case, two additional short transition modules at the entrance and the exit of the minimally sectioned cryostat are required. The two options for the cryostat layout will be discussed later on in more detail

A unique property of the CompactLight facility is enabled by applying different winding schemes for the undulators in FEL-1 and FEL-2, respectively, namely a left-handed helical winding scheme for FEL-1 and a right-handed for FEL-2. This arrangement will allow for ultra-fast helicity switching in that sub-set of photon beam lines which is served by both FEL lines.

Cryomodule structure. The general structure of the cryomodules is sketched in Figure 6.13. The cold mass consists, in the order upstream to downstream, of a superconducting short alignment quadrupole magnet, the superconducting helical undulator magnet, a superconducting phase shifter, which also serves as a vertical and horizontal field integral corrector magnet, a superconducting FODO quadrupole magnet and a cold, i.e. capable of operation at $\sim$4 K, cavity beam position monitor.

The beam-pipe is an integral part of the cold mass. The pipe is made of aluminium and has a round aperture with 4.2 mm bore diameter. It is sectioned in at least four parts, (1) undulator section, (2) straight section, (3) BPM section and (4) cryostat interconnection section.

In the undulator section, the winding body incorporates the beam-pipe meaning that the pipe is directly cooled to the SCU operation temperature level. The other parts of the beam-pipe not in direct mechanical contact with the phase shifter and quadrupole magnet apertures are indirectly cooled by contact with the undulator section and, if required, through additional thermal connections to directly cooled parts. Details have to be elaborated in the course of the technical design for the particular

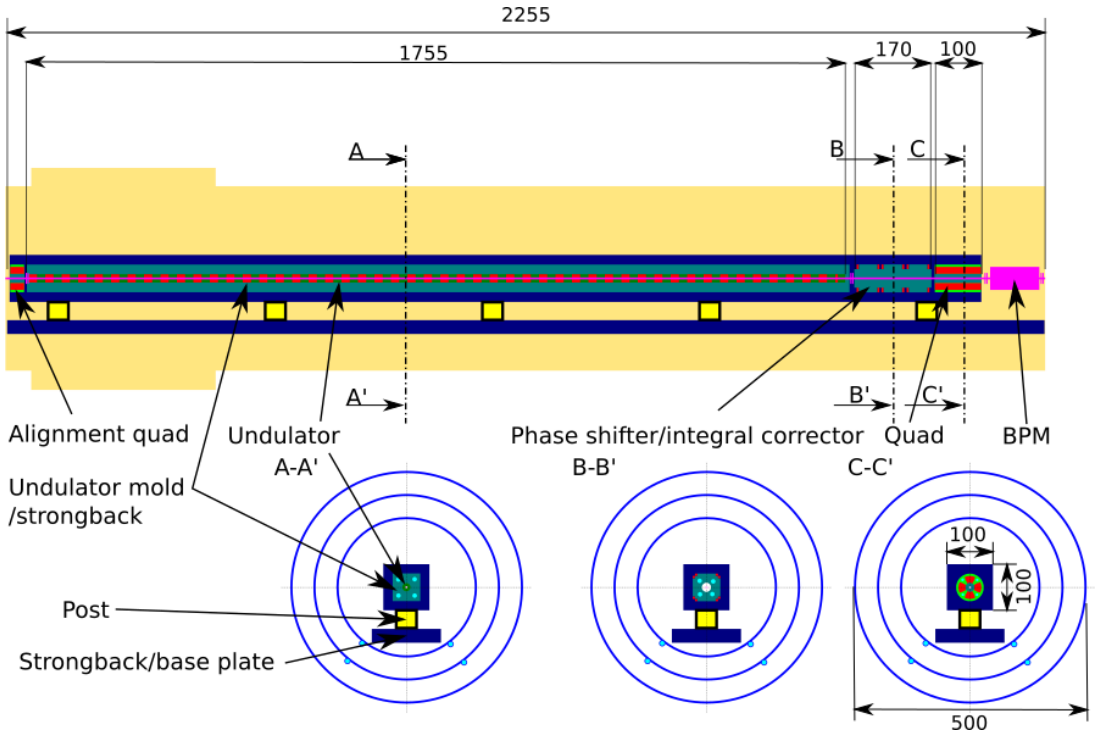

Figure 6.13.: Basic layout of the SCU cryomodule.

cryogenic concept chosen. The BPM section will accommodate a cold cavity beam position monitor which for the sake of compactness is assumed to operate in the X-band, as will be discussed in more detail in Section 6.1.3.4.

The design of the cryostat interconnection section depends on the chosen overall cryostat layout options. In the case of a minimally sectioned cryostat layout, the interconnection section of the beam pipe is designed for compensating the thermal contraction of the cold mass. In the case of a sectioned layout, cold-warm transitions have to be realised in addition.

In the following subsections, the conceptual designs for the elements forming the cold mass are described, along with the underlying design principles and considerations on the design requirements and general considerations for the integration of these components into a complete, modular system.

Superconducting undulator design features. A helical superconducting undulator (HSCU) is chosen for use in the CompactLight undulator lines. For the hard X-rays, the HSCU must be able to produce photons in the energy range 8–16 keV from an electron beam of energy 5.5 GeV. Given this photon energy range, the undulator must be capable of producing a peak transverse field on axis of 1.09 T, corresponding to an a_w value of 1.33. The undulator will have a beam-pipe bore diameter of 4.2 mm and a magnetic inner winding diameter of 5 mm. The parameters of the HSCU are summarised in Table 6.3.

The undulator fields can be generated by a bifilar winding of superconducting wire. The winding consists of two helical coils separated by half an undulator period, with current flowing in opposite directions in the two coils. There are several choices for the use of superconducting wire for the HSCU. Given the short period and winding diameter, niobium titanium (NbTi) wire, which is more malleable than niobium tin (Nb_3Sn) wire, was chosen. For the design work, the choice of superconducting wire was chosen to be SuperCon VSF-678 0.44 mm diameter NbTi wire.

The choice of material for the HSCU former and poles was investigated. The use of ferromagnetic helical poles between the undulator windings can be used in bifilar undulators to boost and shape the field on-axis. However, due to the short undulator period, the pole thickness would be very short, res-

ulting in saturation of the poles at low currents. Also, it would be difficult to manufacture a ferromagnetic double helix and mount it separately on a non-ferromagnetic tube. It would be easier to machine a single ferromagnetic piece into a helix with a remaining thickness. The fields on axis for different wire currents and the corresponding load lines for three cases are shown in Figure 6.14 left and right respectively. The cases are for conductors with no iron poles, a model with iron poles but non-ferromagnetic beam tube, and poles and beam tube made from iron. The models assume a coil stack consisting of 100 wires, poles which are 2 mm thick and a beam tube of 0.5 mm thickness.

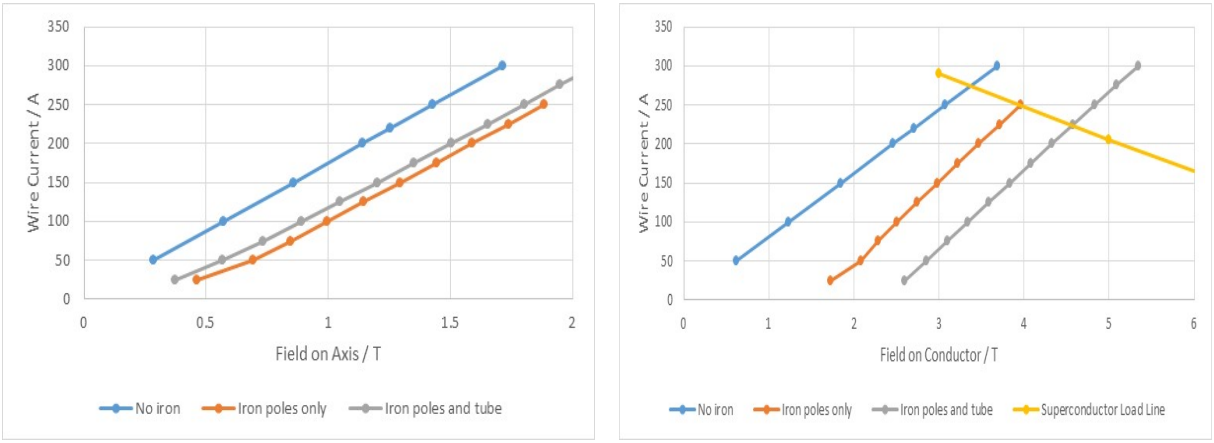

Figure 6.14.: Fields on axis for different wire currents for models with and without iron (left). Superconductor load lines for models with and without iron (right).

From Figure 6.14 left, it is apparent that the presence of iron poles can help to boost the undulator field on axis. However, the iron also increases the field on the conductor at a given wire current and hence increases the operating point of the superconductor at a given current. Given the boost to the fields from the poles, an undulator with iron poles could achieve the target field at lower current than an undulator without iron poles.

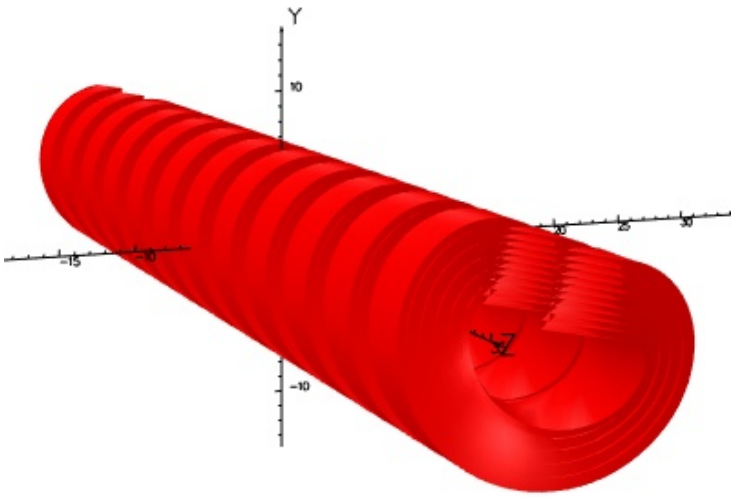

Figure 6.15.: Image of the Opera-3D conductor model used to investigate the load lines of different winding stack configurations.

However, for the case where both the poles and beam-pipe are made from iron, the field on axis is reduced compared to the case where only the poles are made from iron. This is because the iron beam-pipe partially shields the bore from the undulator field. Also, for a given wire current, the peak

field on the conductor is higher for the case with the iron beam-pipe than for the case with iron poles only. Manufacturing a double helix with an iron beam-pipe will reduce the field on axis and increase the operating point of the superconductor for a given current. Although a non-ferromagnetic former would not increase the field generated by iron poles, the effects of the iron beam-pipe shielding the field and increasing the field on the conductor could be avoided.

Therefore, the superconducting undulator windings were assumed to be wound onto an aluminium helical former. As well as reducing the superconducting operating point, an aluminium former would be beneficial due to its high heat conductivity, allowing the former to be cooled to indirectly cool the superconducting wires.

Given the choice of an aluminum winding former, different winding stack configurations were investigated. A model in which the layers of conductors were modeled as conductor bricks of different thickness (depending on the number of turns of wire in the layer) was developed to investigate the load lines of different stack configurations. Figure 6.15 shows an image of the model used. The model does not contain any end effects.

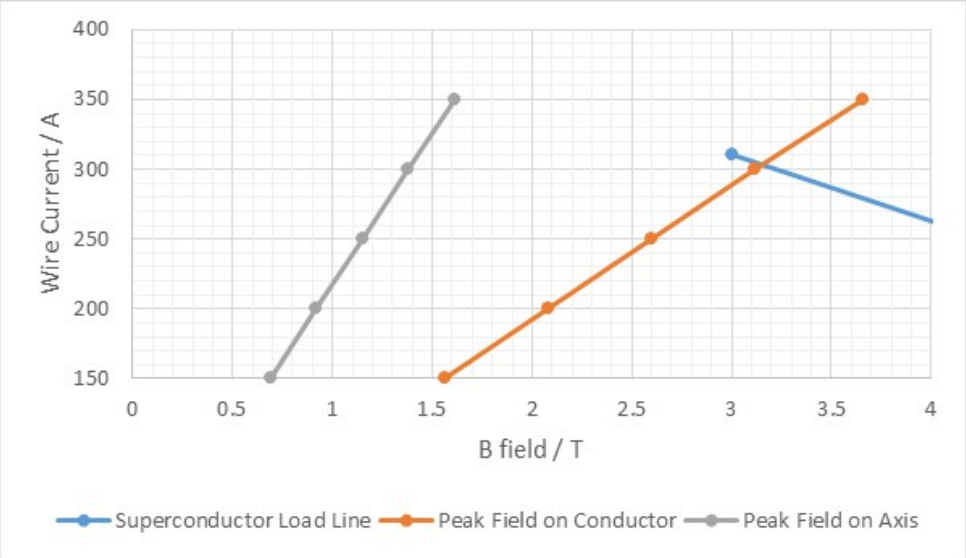

Figure 6.16.: Load line for chosen wire stack arrangement.

Figure 6.17.: Cut through of undulator winding, showing the winding stack.

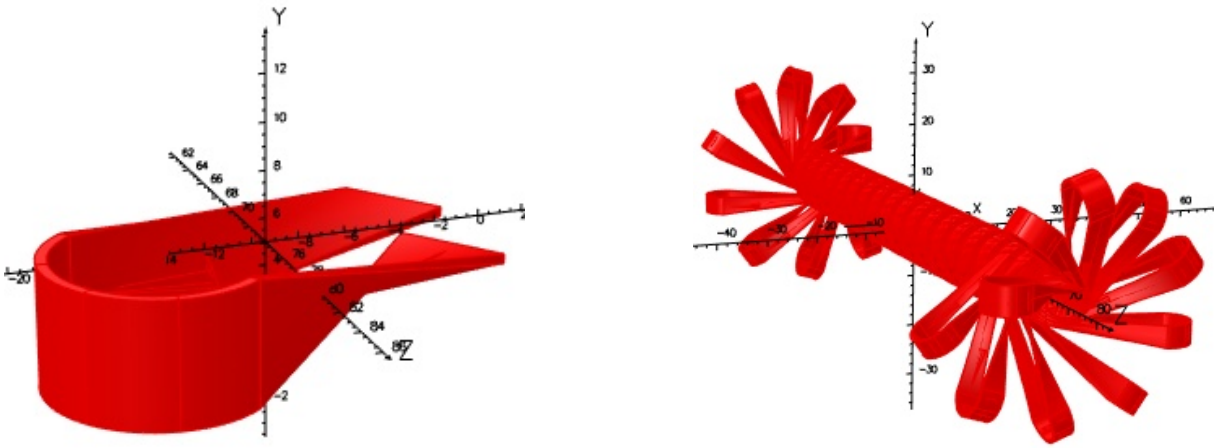

Figure 6.18.: Left: image of a single turnaround model. Right: image of 10-period long undulator module with turnarounds modeled.

A winding stack consisting of 10 layers of NbTi wire with a 9-8-9-8 turn arrangement was chosen. This arrangement would produce the maximum field of 1.09 T on axis at 78.9% of the NbTi wire critical current. The load line for this stack arrangement is shown in Figure 6.16. For this stack configuration, the winding stack would have a width of 4.98 mm at the bottom and a radial height of 3.87 mm. Therefore, the minimum wall thickness between the grooves will be 1.52 mm. Figure 6.17 shows an image of a cut through of the undulator, showing the winding stack.

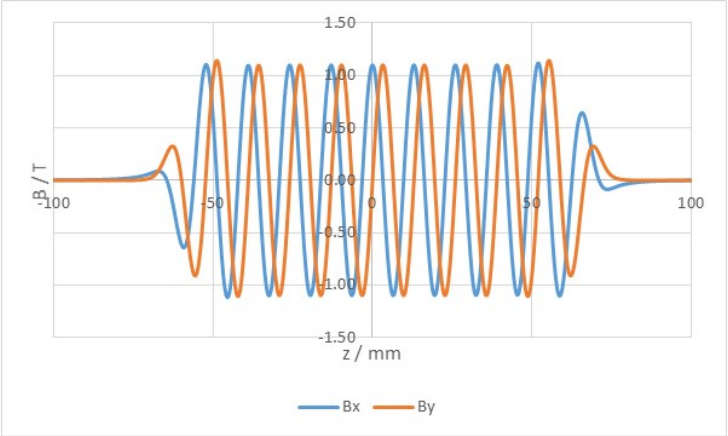

Figure 6.19.: Example field profile through an Opera 3D model of the superconducting undulator containing 10 full periods.

A turnaround design has been developed to allow the undulator to be wound from a single length of superconducting wire without the need for superconducting joints between wire sections. At the ends of the undulator, the wires come away from the helix at a tangent to the helix. The wires are turned around a non-ferromagnetic pin which is perpendicular to the winding direction, and then returned into the adjacent winding groove. There are ten turnaround pins at each end of the undulator former, spaced 36° apart from each other. There is one turnaround pin per layer of wire in the winding stack. The turnarounds are spaced by one-tenth of the undulator period in the axial direction. The turnarounds occur over a single period at each end of the undulator. In this way, the magnitude of the transverse field is decreased over the end undulator period. In Figure 6.18, the left panel shows the Opera-3D conductor model of a single 20 mm long turnaround, while the right panel shows the complete 10-period long model with all turnarounds.

Figure 6.19 shows an example field profile generated by the HSCU model with the turnarounds

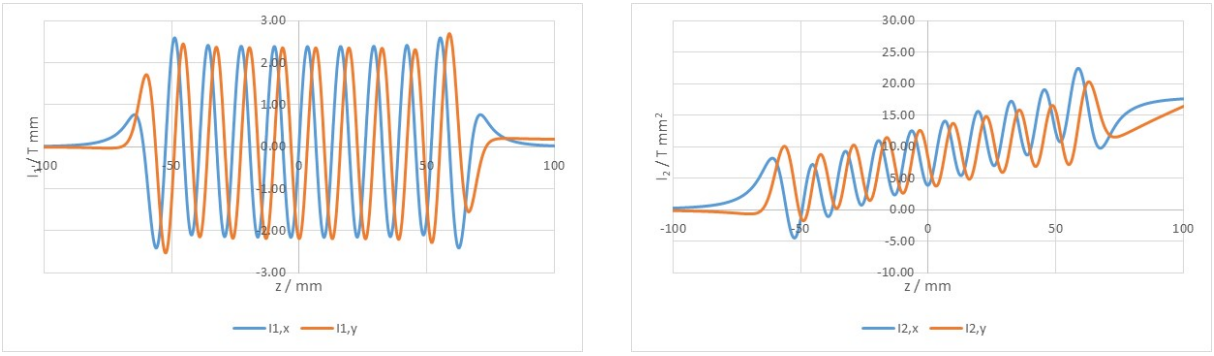

Figure 6.20.: First (left) and second (right) field integral of the field profiles shown in Figure 6.19.

modeled. The peak transverse field in the undulator main body is 1.10 T. The perpendicular distance from the undulator axis to the centre of the turnaround pin was 20 mm. Figure 6.20 shows the first (left) and second (right) field integrals through this model field profile. From the figures, it is apparent that the field integrals through the undulator with the turnarounds would be non-zero. Therefore, correction magnets would be needed outside the HSCU to correct the trajectory of the electron beam. These correction magnets can be integrated into the design of the phase shifters between undulator modules.

The magnitude of correction depends on the distance of the turnaround pins from the undulator axis. The larger the distance, the smaller the effect of the turnarounds on the field on axis and hence the small correction required. From the average first field integrals measured in the main body of a 10 period undulator model as a function of the turnaround length, it results that a maximum first field integral correction of approximately 0.3 T mm will be required. Increasing the turnaround length decreases the necessary field integral correction, but it will make it harder to cool the wires at the turnarounds. If the turnarounds are kept close to the undulator body, they can be kept cold in order to prevent the turnarounds from quenching.

6.1.3.2. Phase Shifters

General considerations. The radiation phase, $\Phi(z)$, in an undulator is defined by Equation 6.4 [222], where λ_r is the wavelength of radiation produced in the undulator, z is the coordinate on the longitudinal axis where the phase is measured, γ is the relativistic Lorentz factor of the electron beam, e is the electron charge, m_e is the electron rest mass, c is the speed of light in vacuum and the term PI is referred to as the Phase Integral and is defined in Equation 6.5 [223], where $B_x(z')$ and $B_y(z')$ are the field profiles in the x and y directions respectively.

$$\Phi(z) = \frac{\pi}{\lambda_r}\left(\frac{z}{\gamma^2} + \left(\frac{e}{\gamma m_e c}\right)^2 \times PI\right) \tag{6.4}$$

$$PI = \int_{-\infty}^{\infty}\left(\left(\int_{-\infty}^{z} B_x(z')\mathrm{d}z'\right)^2 + \left(\int_{-\infty}^{z} B_y(z')\mathrm{d}z'\right)^2\right)\mathrm{d}z. \tag{6.5}$$

Equation 6.4 can also be rewritten in terms of the undulator wavelength, λ_u, and the undulator deflection parameter, K (defined in Equation 6.7 [222]).

$$\Phi(z) = \frac{2\pi}{\lambda_u(1+K_{rms}^2)}\left(z + \left(\frac{e}{m_e c}\right)^2 \times PI\right) \tag{6.6}$$

$$K_{rms} = \frac{eB_{rms}\lambda_u}{2\pi m_e c}. \tag{6.7}$$

In an ideal undulator, the phase advances by 2π per period [222].

Undulator lines in an FEL or synchrotron require many periods to reach saturation, and hence need to be many metres long. It is not practical to construct undulators which are many metres long due to manufacturing tolerances and strict requirements on the electron beam properties [224]. Instead, undulator lines are designed with undulator modules with break sections between the undulators. These break sections contain elements including quadrupoles, beam position monitors and phase shifter magnets [225].

Over a break section, the transverse magnetic field profile is different to that inside an undulator; therefore, the phase advance over the break section will be different to the phase advance through the body of the undulator. This will cause a phase difference between the photons produced in one undulator module and those produced in subsequent modules. This change in phase results in an interruption to the amplification process by causing electrons to gain energy from the radiation field. This phase mismatch then results in an increase in saturation length [226] and decrease in pulse energy for the undulator system [227].

If an electron traverses a break section of length L which has no transverse magnetic fields, the phase advance can be calculated using Equation 6.8:

$$\Phi(L) = \frac{2\pi L}{\lambda_u(1 + K_{rms}^2)}. \tag{6.8}$$

In a simplified picture with no undulator fringe fields, there are two cases of undulator cells that need to be considered. These are the symmetric case when the last pole of one undulator segment and the first pole of the following segment have the same polarity (Figure 6.21a) and the antisymmetric case when the first and last poles of subsequent sections have opposite polarity (Figure 6.21b) [224]. In order to

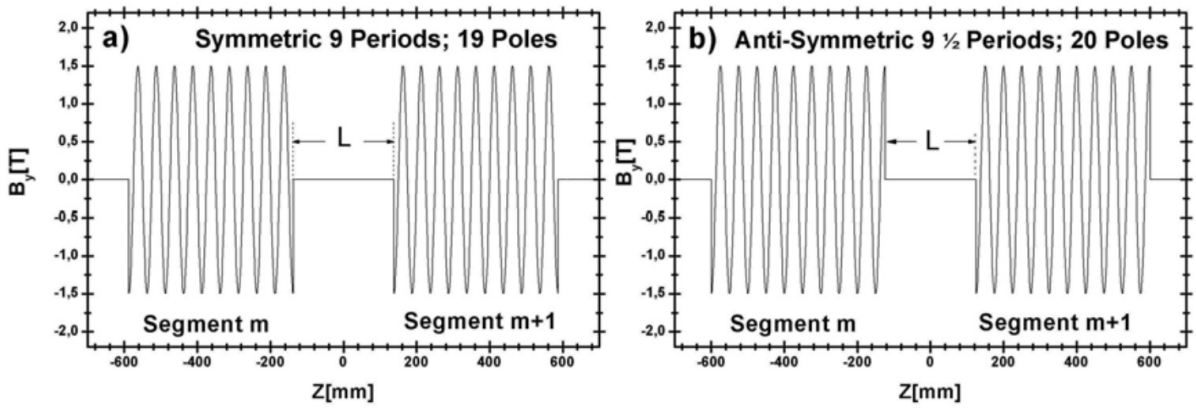

Figure 6.21.: Examples of simplified symmetric and antisymmetric undulator arrangements. These figures assume no undulator fringe fields [224].

maintain the condition for constructive interference of radiation between separate undulator modules, the phase advance over the break section must meet the condition specified in Equation 6.9,

$$\Phi(L_b) = \nu\pi, \tag{6.9}$$

where ν is called the Phase Number [224]. For even symmetry, ν must be a positive, even integer; for odd symmetry, ν must be a positive, odd integer.

If the undulator K value is changed, the phase advance over a break of fixed length L_b will change. In order to maintain the constructive interference condition in Equation 6.9 for multiple undulator K values, the phase advance over the break section needs to be variable.

A variable phase advance over a break section can be achieved using a magnetic structure known as a phase shifter. This structure creates a magnetic chicane which causes a phase delay across a break

section without affecting the overall trajectory of the electron beam. The standard requirement for phase shifters to ensure no overall effect on the electron trajectory is that the first and second field integrals through the undulator go to zero [224]. The first and second field integrals are directly proportional to the angle between the electron beam and the axis and the transverse displacement of the beam from the axis respectively [222]. If the break section contains a transverse magnetic field profile, the phase advance over the break section can be calculated from Equation 6.6.

The phase integral term is a useful metric for quantifying the phase delay imparted by a phase shifter magnetic field in an undulator break section. Equations 6.6 and 6.9 can be combined to define the minimum necessary phase integral of a phase shifter as a function of the break length L_b and undulator deflection parameter K,

$$PI = \left(\frac{m_e c}{e}\right)^2 \left(\frac{\nu\lambda_u(1+K_{rms}^2)}{2} - L_b\right) \geq 0 \tag{6.10}$$

The inequality in Equation 6.10 must be met because the phase shifter can only impart a positive phase delay on the electron beam [228]. To allow for a constant range of tuning of the undulator K parameter, the phase number ν should be chosen so that the same value of ν can be used for all undulator parameters and that the phase integral will always be greater than 0 [224]. Therefore, the largest phase integral needed for a device will be determined by the smallest undulator K parameter that will be used in the undulator lines (i.e. the highest energy radiation).

In reality, the actual phase integral required for an undulator line will be more complicated than Equation 6.10. The fringe fields at the ends of the undulator modules will need to be accounted for. The actual phase advance between main body poles in the undulator modules would be calculated by integrating the field data, and the necessary phase integral in the break section to achieve constructive interference would have to be determined. Equation 6.10 provides a good first estimate for the magnitude of the phase integral required for a given undulator break section.

XLS phase shifter requirements. The preliminary specifications give an intersection length between undulator modules of 500 mm. Assuming that 500 mm is the distance from the end pole of one undulator to the first pole of the next undulator, the phase advance over the intersection can be calculated using Equation 6.6. The actual phase advance between modules would have to be measured, to account for the end fields of the undulators.

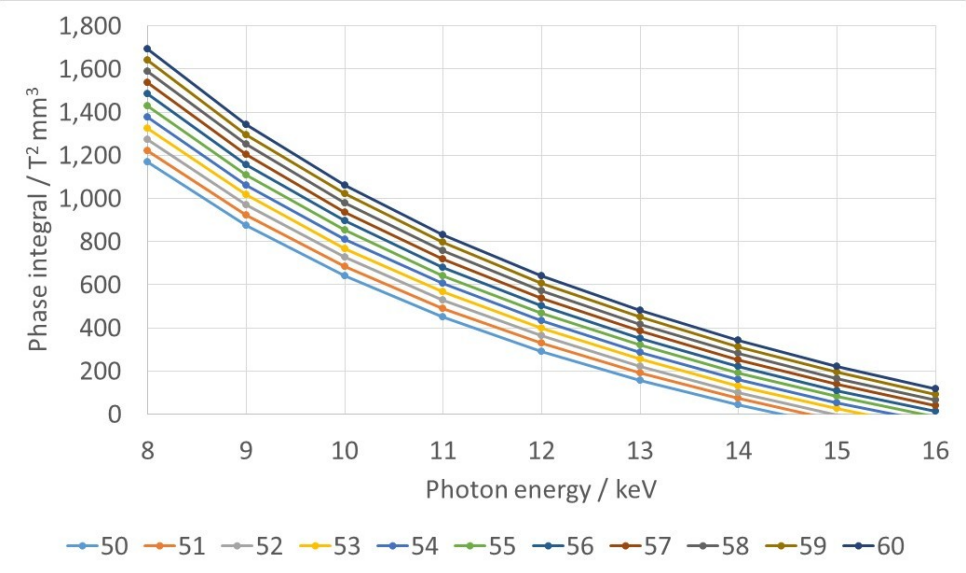

Figure 6.22.: Required phase integral to reach different phase numbers, as a function of photon energy.

Equation 6.10 can be used to determine the phase integral that is required through a phase shifter magnet in order to satisfy Equation 6.10 as a function of the undulator K parameter for different values of the phase number, ν. Assuming a break length, L_b, of 500 mm, the required phase integral as a function of the XLS radiation energy range for different phase numbers is shown in Figure 6.22.

Figure 6.22 shows that for a given photon energy, a larger phase integral is required to achieve a larger phase number, ν. For lower phase numbers, the required phase integral for a given photon energy may be negative. A phase shifter cannot generate a negative phase integral because the chicane can only delay the electron beam. The minimum even phase number (referring to the symmetric case in Figure 6.21) that requires a positive phase integral for the whole tuning range is 56. The minimum odd phase number (referring to the asymmetric case in Figure 6.21) that requires a positive phase integral for the whole tuning range is 57.

The maximum required phase integrals for values of ν of 56 and 57 are 1482 $T^2\,mm^3$ and 1535 $T^2\,mm^3$ respectively, which are the phase integrals required for the lowest photon energy of 8 keV. Therefore, if the end fields of the undulator are not considered, the maximum phase integral through a phase shifter for the XLS FEL will be 1535 $T^2\,mm^3$. To allow for some tolerance on this value and to potentially account for an extra delay required due to the undulator end fields, a maximum target phase integral of 2000 $T^2\,mm^3$ was considered for the phase shifter conceptual design. The requirements for the XLS phase shifters are summarised in Table 6.4.

Table 6.4.: Summary of the phase shifter requirements.

Parameter	**Value**	**Units**
Maximum Phase Integral	2000	$T^2\,mm^3$
Maximum Overall Length	170	mm

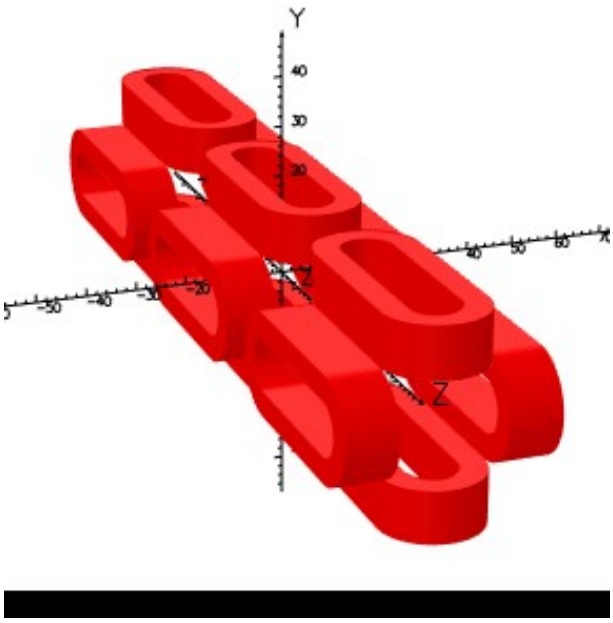

Figure 6.23.: Image of Opera 3D model of phase shifter conceptual magnetic design. The red rings represent superconducting coils.

Phase Shifter Conceptual Design. The basic conceptual magnetic design for the CompactLight phase shifters consists of six pairs of superconducting coils oriented to create a three dipole chicane in

the horizontal (x) and vertical (y) directions simultaneously. A model of the basic conceptual magnetic design as modeled in Opera 3D is shown in Figure 6.23.

In the arrangement shown in Figure 6.23, the current in the central coils would be twice that in the corresponding end coils. This would provide a magnetic field profile consisting of three dipole kicks in the x and y directions, where the central kick would be of twice the magnitude and in the opposite direction to the end kicks. The result to the electron trajectory would be to introduce a non-zero phase shift whilst imparting no overall change to the direction or displacement of the electron beam (the first and second field integrals measured through the phase shifter would go to zero).

Figure 6.24 shows example field profiles, first field integrals, second field integrals and phase integrals respectively for the conceptual magnetic design. This arrangement causes the first and second field integrals to go to zero, whilst providing a non-zero phase integral. Figure 6.24 (b) and (c) show that the first and second integrals of both the B_x and B_y fields go to zero when measured through the length of the phase shifter. This shows that the change to the angle of the electron beam trajectory from the axis and the corresponding transverse displacement of the beam from the axis would not be affected by the presence of the phase shifter. This is one of the common requirements for a phase shifter magnet. Figure 6.24 (d) shows that whilst the first and second field integrals through the magnet can be made to go to zero, the phase integral through the magnet is non-zero. Therefore, this coil arrangement can provide a phase shift and hence provide the necessary correction to maintain the condition for constructive interference of the synchrotron radiation.

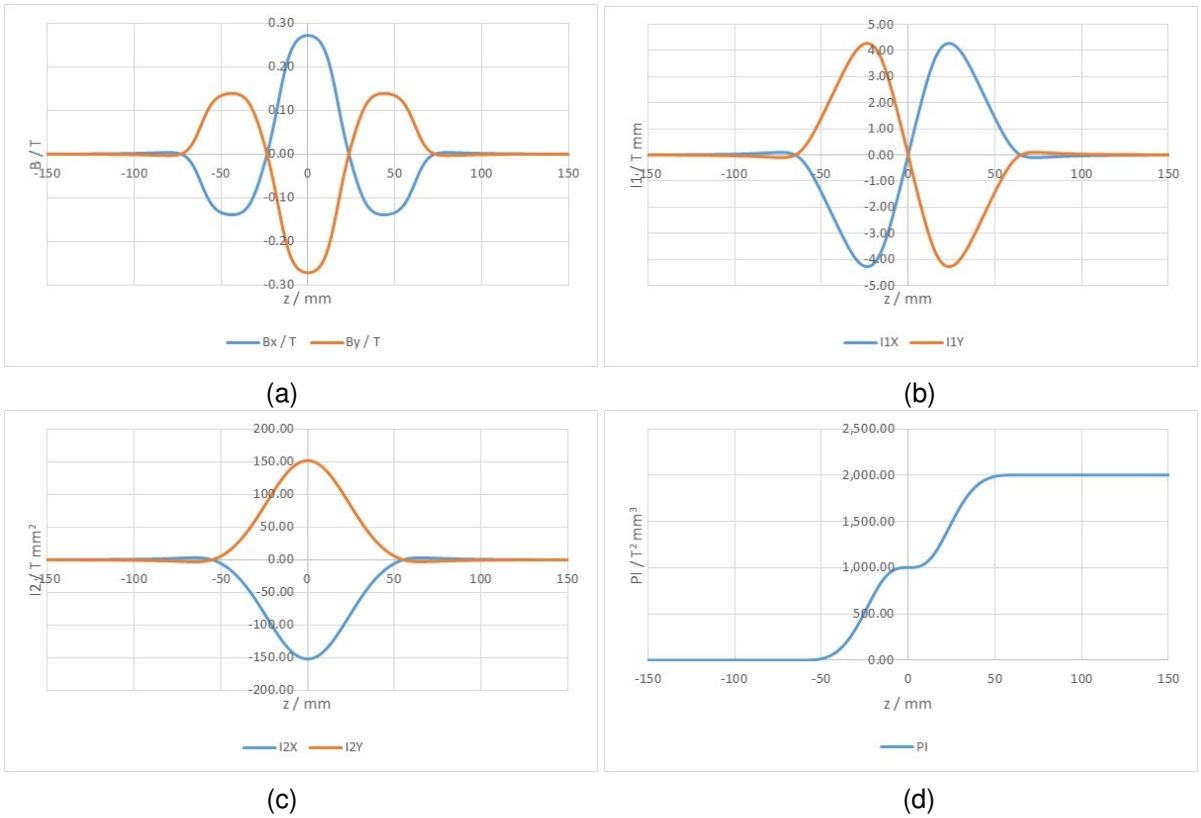

Figure 6.24.: Field profile (a), first field integrals (b), second field integrals (c) and phase integral (d) through an example coil dominated phase shifter model.

The conceptual design could also be used as an integrated phase shifter and trajectory corrector. If the 6 coil pairs are all powered individually, it should be possible to tune the field and phase integrals across the undulator break section to give any desired combination of first and second field integral and phase integral. This would allow correction to angular and positional displacements of the electron beam caused by the non-periodic fields at the ends of the undulators. If the field strengths can be

tuned independently, then any combination of trajectory correction (in both planes) and phase correction should be achievable.

This design produces fields using superconducting coils only. The field is not boosted by iron poles. The use of iron poles would boost the fields produced by the phase shifter at low currents. However, at higher coil currents, the pole pieces would become saturated. Saturation of the iron poles would change the field integrals through the phase shifter and make it difficult to achieve zero field integrals because each of the poles would saturate differently. It was decided that a current dominated design would allow larger phase integrals to be achieved whilst maintaining the condition for cancellation of the first and second field integrals. Also, with a current dominated design, the fields on axis scale linearly with coil current and the phase integral scales linearly with the square of the coil current. This would make it easier to tune the value of the phase integral through the phase shifter.

Size considerations. Several example coil geometries and current densities – as required in the central coils (assuming same current density in Bx and By coils) – have been considered to achieve the target phase integral of 2000 $T^2\,mm^3$. The different geometrical parameters of the coils will have an influence over the current and size requirements of the phase shifter:

- Decreasing the physical length of the phase shifter will provide more space for other components in the inter-undulator sections, such as quadrupoles and beam position monitors. Minimising the current in the coils will reduce the heat load from the current leads and reduce the operating point of the superconducting coils, making them less likely to quench.
- Increasing the inner length of the coils allows the fields to cover a longer axial distance. Consequently, the fields on axis can be lower to achieve a given phase integral and the current density in the coils can be reduced. However, the total physical length of the phase shifter will increase.
- Increasing the coil width increases the minimum separation between coils and the total length of each coil but increases the number of turns in the coils.
- Increasing the coil thickness also increases the number of turns. Increasing the number of turns in the coils allows larger fields (and hence phase integrals) to be achieved for lower current densities in the coils. The current can be minimised by increasing the coil cross-sectional area, at the cost of using more superconducting wire to wind the coils.
- Increasing the inner width of the coils, the minimum face to face separation between a coil pair increases, and therefore decreases the magnitudes of the fields on axis (and hence phase integrals) for a given current density. However, the inner radius needs to be large enough to allow for a sufficiently large bend radius at the ends of the coils for the wires to be turned around.
- Increasing the axial separation between coils increases the phase integral through a phase shifter at the cost of increased total length.
- The coil dimensions can be optimised for the space and cooling power available in the XLS SCU cryostat. The general trend is that longer phase shifters require smaller current densities to achieve the target phase integral of 2000 $T^2\,mm^3$.

Overall, this coil design would be capable of simultaneously correcting the phase shift and trajectory errors between undulator modules by providing tuneable dipole chicanes in the horizontal and vertical directions. The exact coil dimensions would need to be optimised. Total lengths as short as 85 mm could be achieved using NbTi wires, but would require higher currents in the coils. This would require more cooling power and the coils would operate closer to their quench point. This would provide less margin for tuning the fields for combined phase and trajectory correction. Increasing the coil dimensions

would reduce the required currents in the coils; this would reduce the heat loads and operating points of the superconductor.

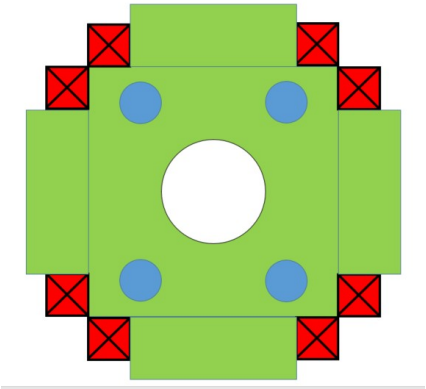

Figure 6.25.: Proposed method for mounting and cooling phase shifter coils.

Proposed mounting and cooling structure. The coils shown in Figure 6.23 would need to be mounted and cooled. The proposed mounting method is shown in Figure 6.25. Each coil would be wound onto a former made from non-magnetic material with high thermal conductivity, which would act as a heat sink. Aluminium would be a desirable choice for this heat sink. The coils could then be potted in these aluminium formers. Pipes containing a forced flow of liquid helium through the heat sink would provide cooling to the coils.

The conceptual magnetic design presented here is of six superconducting coil pairs, which could act as a simultaneous phase and trajectory corrector between the undulator modules for the CompactLight FEL. At the nominal physical length of 170 mm, the phase shifter would be able to achieve phase integrals larger than the target maximum of 2000 $T^2\,mm^3$ at low coil current densities. The coil dimensions could be reduced and hence the total physical length of the phase shifter could be reduced below 170 mm. At physical lengths of 85 mm, the arrangement would still be able to reach the target maximum phase integral. However, if the coil dimensions and total physical length are reduced, the coil currents required to achieve the target phase integrals will increase. Therefore, there will be a larger heat load from the coil current leads that needs to be cooled.

6.1.3.3. Quadrupoles

The undulator line FODO cells are composed of a focusing quadrupole (F), a defocusing quadrupole (D) and the virtually non-focusing superconducting undulators which for the beam optics in first order can be treated as drift spaces. Superconducting coil-dominated quadrupole magnets are proposed. These consist of four current-carrying coils which create a magnetic flux density that grows proportionally to the radial distance:

$$B_x = gy, \qquad B_y = gx, \tag{6.11}$$

where g is the nominal field gradient.

In the following the multipole expansion of the transverse magnetic field in the complex plane is used:

$$B = B_y + iB_x = \sum_{n=1}^{\infty} (B_n + iA_n)(x + iy)^{n-1}. \tag{6.12}$$

with B_n and A_n are the normal and skew multipole components, respectively, $n = 2$ refers to the quatrupole component. The field gradient is related to the multipole component of order $n = 2$ by

$$g = \frac{B_2}{R_{\text{ref}}} \tag{6.13}$$

with the reference radius R_{ref} which is typically chosen to be 2/3 of the magnet aperture.

The main parameters for the FODO quadrupoles are specified in Table 6.5. The design should be accurate enough to achieve $\Delta g/g \leq 0.1\%$ over the specified good field region. In order to meet this field quality requirement and to minimize the content of higher order multipole components, a coil configuration of sectors and wedges of 12°–18°–30° has been developed for the SASE FODO quadrupole magnets, following concepts described e.g. in [229, 230]. The coil configuration is depicted in Figure 6.26. Calculations and optimisations were carried out with the magnet design software OPERA [231].

Table 6.5.: FODO quadrupole main parameters.

Parameter	**Value**	**Units**
Integrated field gradient	10	T
Field gradient	167	$\mathrm{T\,m^{-1}}$
Effective length	60	mm
Inner aperture radius	7	mm
Horizontal good field region	± 5	mm

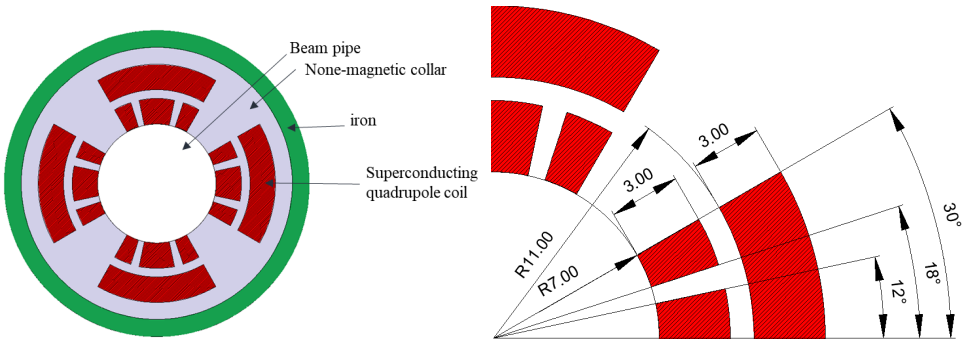

Figure 6.26.: Geometry layout (left) and coil configuration in one quadrant of the magnet (right).

The four superconducting coils forming the quadrupole winding are held together by means of laminated none-magnetic collars which are surrounded by laminated iron yokes.The inner radius of the coils and the coil width are considered to be 7 mm and 3 mm, respectively. Simulations were done for a NbTi coil-based quadrupole with a field gradient of $167\,\mathrm{T\,m^{-1}}$ and magnetic length of 60 mm. The current density to achieve the desired field strength is taken to be $380\,\mathrm{A\,mm^{-2}}$ which is well below the limitations of NbTi for the applied magnetic field at 4.5 K.

The modulus of the magnetic flux density in the central plane $z = 0$ is shown in Figure 6.27.

For calculating the field gradient at $x = 5$ mm versus the longitudinal direction in Opera 3D, the field is calculated on circles with radius 5 mm which are moved in the beam direction in steps of 2 mm. Using a Fast Fourier Transformation, the magnetic field, the field gradient and higher order harmonics are obtained in each location. Having the field gradient at different longitudinal locations, one can calculate the integrated field gradient at $x = 5$ mm to be 9.898 T. The field gradient uniformity in terms of $\Delta g/g_0 = (g - g_0)/g_0$ in the central plane $z = 0$ is displayed in Figure 6.28. The relative deviation is within a few units of 10^{-4} in the good field region up to 5 mm. The strength and relative strength of nominal and the first three allowed higher order multipole components for the FODO quadrupole are summarised in Table 6.6.

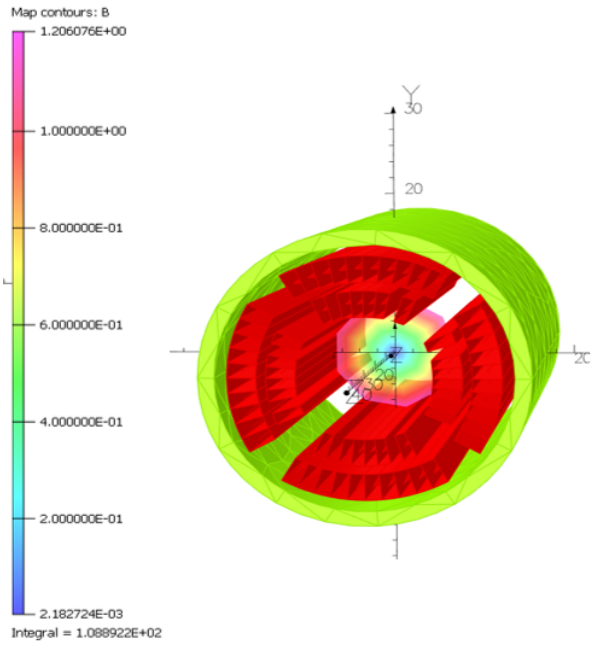

Figure 6.27.: Magnetic flux density in the central plane $z = 0$.

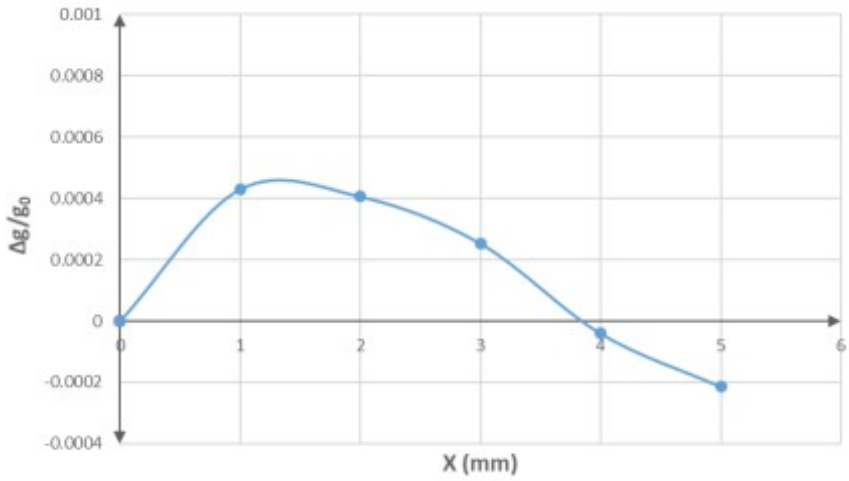

Figure 6.28.: Field quality in terms of relative gradient deviation as a function of x in the centre plane $z = 0$.

Table 6.6.: FODO quadrupole field coefficients.

n	type	$B_n(5\,\text{mm})$ [T]	$\lvert B_n/B_2\rvert(5\,\text{mm})$
2	Q	8.23×10^{-1}	1
6	Q	5.48×10^{-3}	6.65×10^{-3}
10	Q	1.67×10^{-3}	2.03×10^{-3}
14	Q	9.55×10^{-5}	1.16×10^{-4}

6.1.3.4. Integrated diagnostics.

The electron beam diagnostics in the SASE line will consist of a set of cavity beam position monitors (BPMs), one in each cryomodule. These BPMs will provide the feed-back signal required for the intra-module beam steering as well as for the inter-module beam-based alignment. The BPM will be operated in the cold environment. Cold cavity BPMs are currently in operation in superconducting linacs, for example at the European XFEL [184, 232]. State-of-the-art cold cavity BPMs are L-band structures. Since the size of these structures is directly related to their operation frequency, L-band cavities seem not optimally suited for the integration into the CompactLight SASE undulator cryomodules. The limited space in the gap between the undulator units favours more compact structures. For the conceptual design of the CompactLight FEL lines, we foresee cold X-band cavity BPMs. The length of these BPMs could be 100 mm (as compared to 180 mm for the L-band cavities).

Such devices do not exist today. For the application of superconducting linacs, L-band cavities are preferred due to the extremely demanding requirements on surface cleanliness for operation in proximity to the superconducting cavities. For application in the superconducting undulator cryomodules, however, vacuum and cleanliness requirements will be much less demanding. It is reasonable to assume that X-band cavity BPMs for this application are in principle feasible and could become available on the five-year development time horizon considered for CompactLight.

6.1.3.5. System Integration

It is likely the design concept for the cryomodules will follow a bottom-up approach similar to that suggested by Leitner et al. [221]. A room-temperature strongback at the bottom forms the basis of the supporting structure, which is directly supported by the girder outside the cryomodule. The cold mass is mounted onto this strongback on thermally intersected fibreglass posts. These thermal interceptions at three temperature levels ($\sim$80 K, $\sim$20 K and $\sim$4 K from outer to inner) are connected to concentric radiation shields at the same temperature levels. The cold mass elements, SCU, quadrupole magnets, phase shifter magnet and BPM are integrated into a common, stiff frame which will also provide magnetic shielding. Within this frame, the components are mutually aligned to the required precision (see Section 6.1.3.7). To avoid internal cooling channels with interconnecting tubes, contact cooling of the cold mass elements, e.g. through heat exchanger plates on top and/or at the base of the common frame, is favoured.

No active internal alignment of the cold mass elements is foreseen. The inter-module alignment is achieved through motorised stages as part of the outer girders, to which the room-temperature strongback inside the cryomodule is rigidly connected. The design of the cryostat interconnection region has to account for the mechanical flexibility required for the alignment of the entire cryomodule with neighbouring cryomodules.

6.1.3.6. Cooling Concept

Requirements and conceptional options – overall facility layout. For the cooling of the beam lines, three basic options are considered. These include a *segmented design* approach, where liquid helium (LHe) is re-condensed by cryocoolers located at a number of individual cryostat modules, a *minimal segmentation concept* with LHe provided by a central LHe cryoplant, and a novel *hybrid approach* that provides LHe individually for each cryomodule. In the latter case, cryocoolers and Joule-Thomson cycles shall be combined in order to enhance the cooling capacity of cryocoolers and to enable forced-flow LHe cooling. In the following, these options are presented in greater detail and their individual benefits are discussed.

Cryostat layout I – segmented design cooled by cryocoolers

The segmented design rests on the idea of separating the beam line into 16 individual modules

comparable to the suggestion for storage ring application by Fuerst et al. [220]. Following this design, each module is surrounded by a thermal shield and installed inside a vacuum cryostat. The components inside each module are submersed in a LHe bath, where the boil-off gas is re-condensed at the second stage of pulse tube cryocoolers. Figure 6.29 depicts a scheme of one module of the segmented cryostat layout.

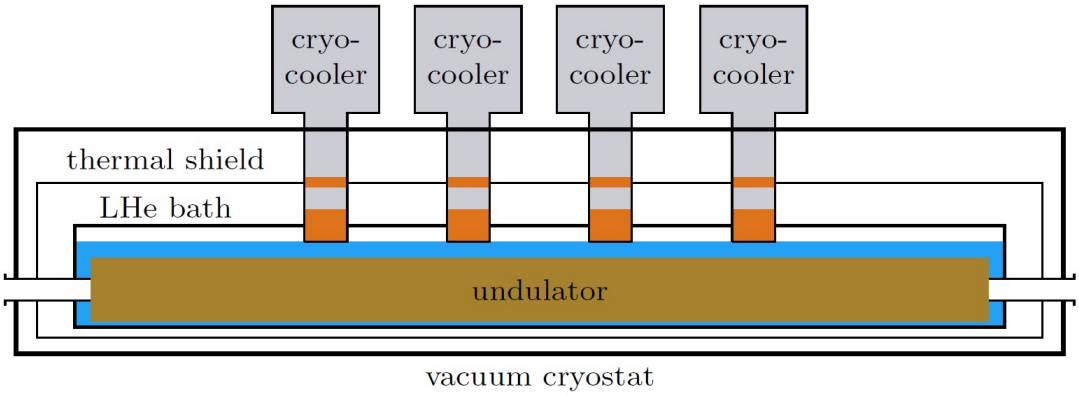

Figure 6.29.: Proposed Cryostat layout I – segmented design cooled by cryocoolers.

Based on the assumptions of Fuerst et al. [220], the heat load onto the LHe by the components alone can be estimated to be in the order of $1\,\mathrm{W\,m^{-1}}$ module length. For the planned modules with length 2.3 m, this would sum up to a total heat load of $\dot{Q} \approx 2.3\,\mathrm{W}$ @ 4.2 K per cryomodule. This estimation does not include the heat load originating from the cold-warm transitions between the individual modules. As these heat loads depend on the beam line design, the contribution of cold-warm transitions must be optimised during the technical design phase. In any case, the most powerful cryocooler available today provides 2 W @ 4.2 K [233], resulting in the need of about two to four cryocoolers per module, or 32 to 64 cryocoolers per beam line, respectively.

The main benefit of the segmented design approach is its flexibility in terms of maintenance and alignment. During maintenance, only the individual module needs to be warmed up to ambient temperature, while the rest of the beam line remains at 4.2 K, minimising the overall beam downtime [234]. Moreover, following the design suggestions provided by Emma et al. [234], the components can be aligned precisely within each module and the position of the modules to each other can be adjusted independently.

The main drawbacks of the segmented design approach are the higher overall heat load due to the transitions from 4.2 K to ambient temperature between the modules, and the large amount of helium needed for helium bath cooling. A certain helium infrastructure will also be necessary for initial cool-down, LHe filling and helium recovery. Since cryocoolers have a periodic working principle, the large number of cryocoolers is expected to cause vibrations onto the system and acoustic noise. Moreover, the system cost due to the more complex design of the cryostat modules should be considered.

Cryostat layout II – minimal segmented cryostat design cooled by a cryoplant

Following the minimal segmentation design suggested by Emma et al. [234] for the LCLS-II Hard-X-Ray FEL, the beam line with all its components is housed inside one single long stretched vacuum chamber with an integrated LHe distribution system along the undulator string. Unlike the segmented design option, there are no cold-warm transitions for the beam line between the single undulator passages, reducing the overall heat load onto the LHe. Figure 6.30 depicts a scheme of one undulator module of the suggested minimal segmented cryostat layout.

In case of the minimal segmented cryostat design, the LHe is provided by a helium refrigeration plant located offside, reducing both acoustic noise and vibrations onto the beam line. Moreover, the LHe plant provides a pressure gradient for fluid circulation inside the cooling channels along the strongback

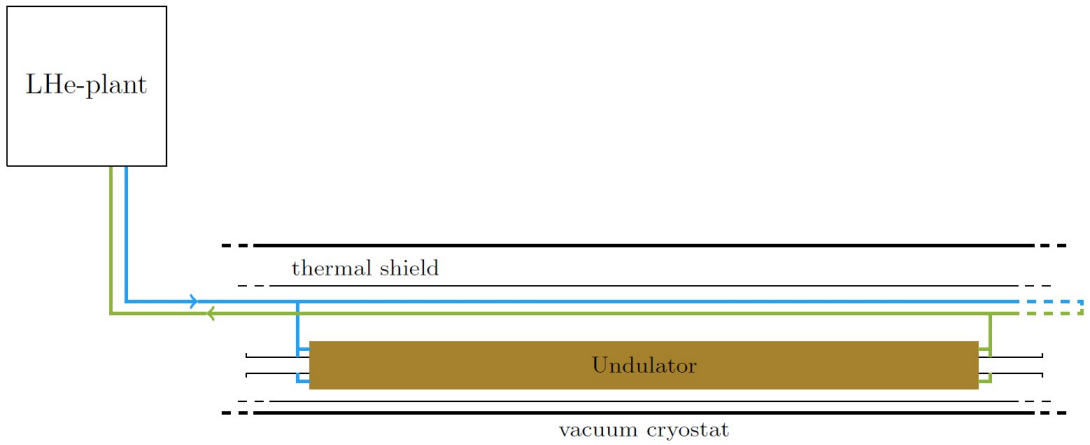

Figure 6.30.: Proposed Cryostat layout II – minimal segmented cryostat design cooled by a cryoplant.

according to the design presented in Figure 6.25. Due to the enhanced heat transfer in forced-flow convection, the amount of LHe inside the cryostats can be reduced compared to cryostat layout I, reducing the size of pressure relief devices to ensure the cryostat safety. In addition, the cooling system inside the cryostat is maintenance-free, an advantage compared to the cryocoolers according to layout option I. Due to the less complex cryostat design, the system cost is expected to be lower than for the segmented design discussed before [234]. The disadvantage of the minimal segmented design is its limited flexibility concerning maintenance of individual parts of the beam line. Due to the single piece cryostat design, accessing one of the magnets along the beam line requires a warm-up of the whole system to ambient temperature. The cooling power provided by the smallest standard helium refrigeration plants is in the range of 130–210 W [235]. The cooling capacity of one helium plant will hence be compatible with the requirements of one entire beam line, which are to be defined in the technical beam line design phase.

Cryostat layout III – segmented design cooled by a hybrid cryoplant

Besides the established cryostat designs discussed before, current developments in the field of cryogenic mixed-refrigerant cycles (CMRC) provide the basis for a novel hybrid cooling system design. CMRC are refrigeration systems using a wide-boiling mixture instead of a pure fluid as a working fluid. By adjusting the mixture's composition, the efficiency of a refrigeration process can be increased significantly, as the heat exchanger performance is enhanced and the pressure ratio lowered [236]. In previous years, CMRC technology evolved towards the temperature range of high-temperature superconducting (HTS) applications [237], making it an interesting option especially for the cooling of current leads [237, 238]. A novel heat exchanger technology combining large heat transfer areas with compact dimensions [239] promises a compact modular design.

Cooling current leads with CMRC, a major fraction of the overall heat load can be absorbed by this new technology [238]. In addition, it can be used for efficient pre-cooling of helium in a Joule-Thomson cycle, which is cooled further by a cryocooler operated at an elevated temperature of e.g. 10 K with larger cooling power, before the helium is expanded to the 4.2 K temperature level (cf. Figure 6.31). This combination may extend the 4.2 K cooling power limitation of cryocoolers such that significantly fewer cryocoolers are needed in a segmented design. The main advantage of such a hybrid cooling system is the scalability, enabling forced-flow LHe supply for medium-power applications, where typically several cryocoolers are needed and LHe cryoplants are oversized. It is important to note, however, that this novel refrigeration strategy is still in development and its potential for 4.2 K applications yet needs to be investigated. Therefore, the achievable performance is not yet clear and there is no prototypical application today. From a thermodynamic point of view though, CMRC technology is the only feasible way to

close the cooling power gap of about two orders of magnitude between cryocoolers and cryoplants.

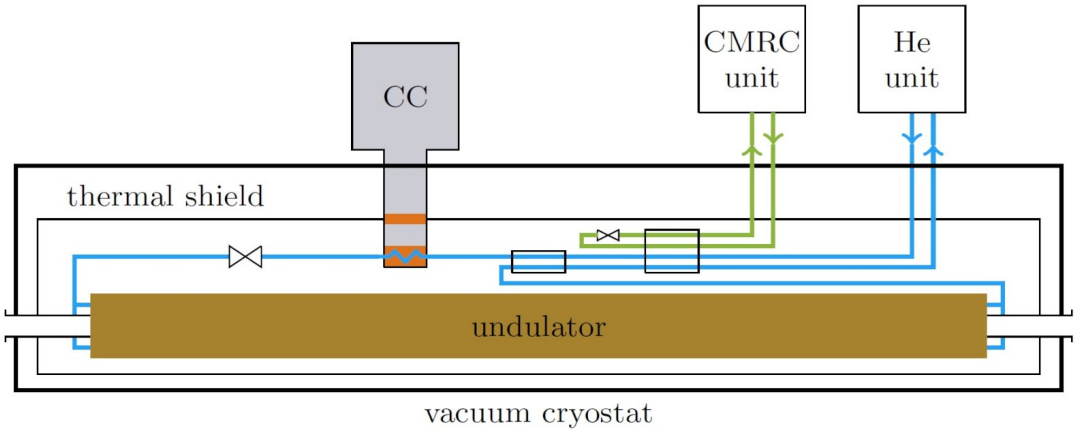

Figure 6.31.: Proposed Cryostat layout III – segmented design cooled by a hybrid cryoplant.

Components Cooling Options. Besides the LHe cooling of the magnets along the beam line, the current leads as well as the thermal shield inside the vacuum cryostat have to be cooled. Strategies for these components shall be presented in the following.

Cooling of current leads

In order to reduce the heat load onto the cryogenic system, the usage of high-temperature superconducting (HTS) current leads is recommended. To keep the HTS current leads below their transition temperature, conduction cooling to the first stage of cryocoolers is an option for the cryostat layout I. For cryostat layout II, the current leads might be cooled by either conduction or convective gas cooling with cold helium gas, flowing back to the LHe cryoplant. For cryostat layout III, CMRC cooling is the ideal option for the current leads. The required cooling power in these cases has to be calculated on the basis of the total power consumption and the required current of the magnets along the beam line. This is expected to be done during the technical design phase.

Cooling of the thermal shield

For cryostat layout I, thermal shielding is typically cooled via conduction by the first stage of the cryocoolers [240]. For cryostat layout II, a convective cooling circuit with either He of liquid nitrogen (LN_2) is possible [240]. For cryostat layout III, the shield cooling can be realised by the first stage of the cryocooler in combination with the CMRC system. Moreover, Xu et al. [241] reported an optimisation of the shielding temperature for the FRIB cryomodule. A similar study should be performed during the technical design phase in order to minimise the static heat load onto the beam line.

Summary on cooling requirements In order to evaluate and compare particularly the layout concepts I and II, which are based on currently available technologies, the heat loads on the cold mass and shields due to radiation and heat conduction particularly through the required current leads have been preliminarily estimated [242]. Table 6.7 summarises the results. The estimates are clearly in favour of the minimally segmented SASE line supplied by a central cryoplant.

6.1.3.7. Tolerance Considerations and Alignment strategies

The specification of accuracy requirements is a work in progress, as well as the development of design strategies for achieving the required tolerances. Three levels of accuracy requirements need to

	Segmented layout	Minimally segmented layout
Per SASE line:		
Heat load shields / W	2625	2620
Heat load @ 4 K / W	67	70
Refrigeration infrastructure	48 cryocoolers, 2 W@4 K	cryoplant, 100 W@4 K
Wall plug power / kW	550	45 - 75

Table 6.7.: Comparison of the overall cooling requirements for the segmented and minimally segmented layout of the SASE SCU cryostat.

be addressed: (1) field quality requirements for the individual magnetic components which are related, but not necessarily limited to mechanical accuracy requirements for these components; (2) mutual alignment tolerances of the components forming the cold mass; (3) mutual alignment of the cryomodules forming the SASE line. At all levels, alignment accuracies are subject to mechanical variations upon cooling due to thermo-mechanical stress and subsequent deformation. Above that, also magnetic forces have to be taken into account.

Mechanical variations upon cooling. A detailed investigation of forces occurring due to thermal contraction upon cooling, subsequent stresses and deformation has to be performed in the course of elaborating a detailed technical design for the cryomodules. General design strategies to cope with thermo-mechanical effects include, but are certainly not limited to a careful choice of materials, appropriate pre-stressing of composed components, and avoiding stresses by design, e.g. by allowing elements to slide against each other in a well-defined way.

Magnetic field quality requirements. Magnetic field quality requirements are the same for the main FEL undulators as for the afterburner undulators: Most important is a straight trajectory and a reasonable phase error. Trajectory straightness requirements differs with wavelength. Because the XLS undulators and afterburner will serve both soft X-ray and hard X-ray, the requirements need to fulfil the demands for the hard X-ray case. Trajectory straightness of 2 µm is required. Beam wander in addition depends on the frequency. Long-range beam wander is more forgiving in the exponential growth regime, because the electron beam can take the light with it. Short range trajectory errors such as kicks can stop the FEL process and must be avoided [243]. The phase error of the FEL undulators and afterburner as well are not very stringent. As only the fundamental harmonics are used, the maximum rms phase error can be specified to 10°.

Specifications on multipoles which mainly refer to off-axis field quality are less important. The only possibility which might need to be controlled is the presence of gradients over the undulator axis. Such gradients would for example appear systematically in circular mode in a fixed gap undulator.

In an SCU, the described field properties are determined by the accuracy of the winding placement, both locally and long-range. How the requirements stated here and in Section 6.1.2.4 translate into specifications for mechanical tolerances is to be investigated and their practical feasibility to be proven. If necessary, additional coil-based field integral correctors along the SCU can be employed to actively control trajectory straightness.

Intra-module component alignment. The components forming the cold mass, which are the relevant components with respect to the FEL performance, will be mutually aligned in warm conditions within a common, stiff frame. Magnet centres have to be aligned through mechanical reference only, since no fiducialisation of individual components with respect to their magnetic axis will be available. The aforementioned design strategies have to be applied such that the mutual alignment is maintained upon cooling as far as achievable. To correct for residual deformations and alignment changes, settings

for the field integral correctors providing zero beam offset in the quadrupole centres and zero overall beam deflection can be found by means of stretched- or pulsed-wire based magnetic field integral measurement methods. That has to be done offline for each individual cryomodule and over the entire tuning range of the undulator.

The accuracy of the internal alignment and the external alignment control achieved by these methods has to be good enough that the K variation requirements described in Section 6.1.2.4 can be met across the modules through their mutual alignment. To first order, that requires that the components of the cold mass are aligned to each other within 20 µm.

Cross-module mutual alignments. Each individual cryomodule will be fiducialised with reference to e.g. pulsed-wire measurements for the alignment and FODO quadrupoles only. An advantage of the iron-free design of all magnets inside the cryomodule is that such measurements will not be disturbed by remanent fields. The external fiducials will allow for an initial mutual alignment of the cryomodules with respect to the quadrupole centres, which will be sufficient for the beam to pass through the FODO lattice along the SASE line. That will enable a refined beam-based alignment employing the FODO and alignment quadrupoles.

6.1.4. The Afterburner Undulators

The afterburners are undulators which are placed after the main FEL undulator which generates the electron microbunching and the exponential growth in intensity of the emitted light. The afterburners use the microbunched electrons to generate either background-free higher harmonics [244] or allow polarisation control [217]. An alternative approach for polarisation control is to build the entire FEL undulator line with variably-polarising undulators like the SwissFEL Athos beamline [245] at PSI. However, in terms of compactness and overall costs the afterburner allows FEL undulators with the shortest possible period length to be used, while the afterburner may have relaxed parameters. This is espe-

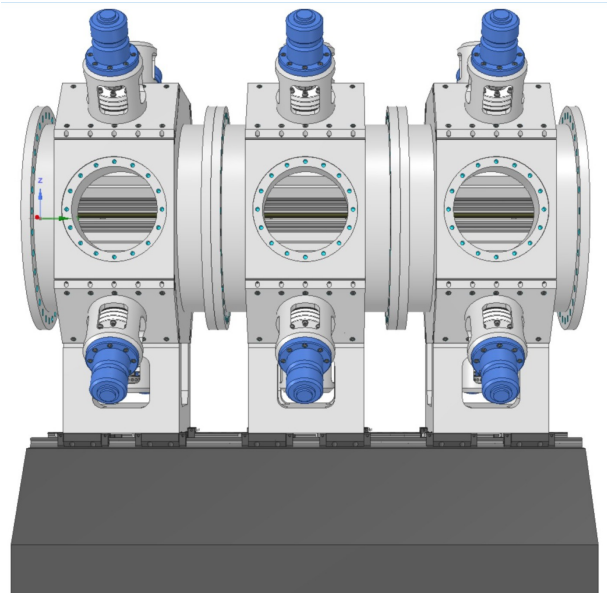

Figure 6.32.: Permanent Magnet based in-vacuum APPLE-X undulator as afterburner.

cially true if polarisation control is not required over the entire photon energy range. Simulations of the expected afterburner performance, including a study determining the required number of afterburner modules, were presented in Section 6.1.2.5.

Variably-polarising undulators have been dominated by APPLE-type permanent magnet undulators [246] for more than 25 years now. Figure 6.32 shows an example of an in-vacuum APPLE-X

undulator. Electromagnetic undulators are used for very long periods only. For short period length, recently a variably polarising superconducting undulator named SCAPE (Superconducting Arbitrarily Polarising Emitter) has been proposed. [247]. Figure 6.33 shows the design principle of the SCAPE undulator; it consists of two planar undulators shifted by a quarter of a period.

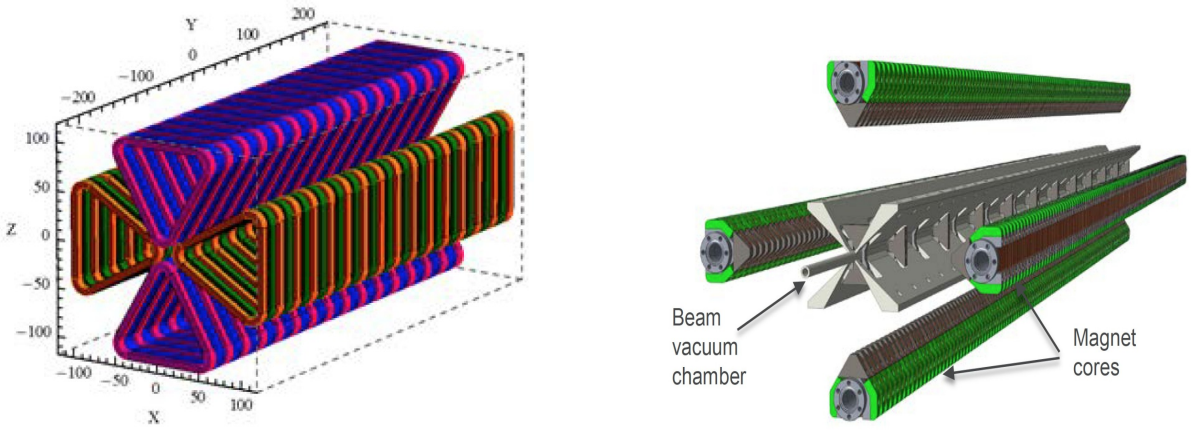

Figure 6.33.: Superconducting arbitrary polarised emitter SCAPE. Radia model (left) and assembly (right) (courtesy Yuri Ivanyushenkov, ANL).

A 0.5 m long SCAPE prototype with a period length of 30 mm has been successfully tested. A study for fast helicity switching with this device is under study [248] as well. This is a very interesting device with high potential also for shorter period length. But based on a great deal of experience in Europe with APPLE-type undulators on one hand and in-vacuum and cryogenic planar undulators on the other hand, for CompactLight it was decided to use in-vacuum or even cryogenic APPLE-X undulator technology as the baseline. However, this decision can be revisited in the future as technology evolves.

APPLE undulators have been used so far only for soft X-ray applications and have therefore in general a longer period length (mostly between 38–70 mm). Also, only recently a first in-vacuum APPLE with period length of 32 mm has been realised at HZB for the storage ring BESSY II [249, 250]. For FEL applications, the vacuum stay clear apertures can be smaller, which will allow for shorter period length.

Besides strong vertical forces, APPLE type undulators in general have also strong forces in the horizontal and longitudinal directions. To handle these forces, APPLE type undulators are large. Classical C-shape undulators for storage rings have widths of up to 2 m. The already compact design for the Athos UE38 APPLE-X undulators with a closed support structure still has a width of 1.4 m. Similarly to CompactLight, SwissFEL has two parallel beamlines and the width of the undulators defines the separation as 4 m to allow the installation and eventual replacement of undulators. For CompactLight, a smaller separation of only 2.5 m is required. This not only reduces the building volume but allows a feasible design for the electron beam spreader and photon beamlines which are used to combine light from the two parallel FELs in the endstations for pump-probe experiments.

6.1.4.1. Basic Concept

The FEL undulators will be superconducting helical undulators with 13 mm period length and K-value ranging between 1.85 and 0.85. The period length of the afterburner is not necessarily the same as the main undulators—it can be longer, but needs to cover the same photon energy range. The initial study of afterburner performance in Section 6.1.2.5 used a provisional period of 19mm. Hence, the afterburner needs also to be linked to the FEL undulator by

$$\lambda_{AB}\left(1+\frac{K_{AB}^2}{2}\right)=\lambda_U\left(1+\frac{K_U^2}{2}\right), \tag{6.14}$$

with λ the wavelength and $K = 0.934\ B[\mathrm{T}]\ \lambda_{U/AB}[\mathrm{cm}]$ the product of field and period length. The lowest energy is defined by the achievable field strength or K value of the afterburner at a given period length, and the highest energy by the chosen period length at the lowest acceptable K value. The main SASE undulators yield circular FEL light, but they provide no polarisation control. The helicity is implemented with the winding direction of the superconducting wire. It is worth noting that the emitted light is therefore circularly polarised - in contrast to the horizontally-polarised light from conventional vertical undulators. LCLS-II provides vertical polarisation in the hard X-ray beamline and horizontal polarisation in the soft X-ray.

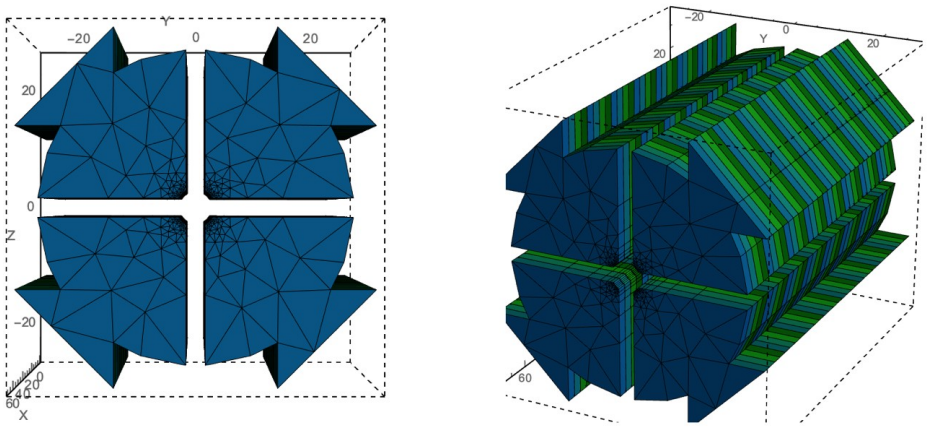

Figure 6.34.: RADIA [251] model of the APPLE-X magnet configuration. The magnetic gap, here, the free diameter depends on in- or out-of vacuum solutions. For a 5 mm inner diameter vacuum chamber, a magnetic diameter of 6.5 mm is required. For in-vacuum undulators this can be reduced to about 5.2 mm. The slit can be minimum 2.5 mm to allow magnetic measurements and support of a vacuum chamber.

The APPLE-III, DELTA and APPLE-X designs are optimised for use in single-pass accelerators with round vacuum chambers giving equal space requirements in horizontal and vertical directions. They all enclose the beam-pipe with four magnet arrays, but DELTA and APPLE-X maximise the on-axis field by radial magnetisation. While the polarisation is changed by symmetric or antisymmetric shift of diagonal magnet arrays, the field amplitude can be changed by a gap variation or with fixed gap and longitudinal shift of adjacent magnet arrays. This results in a simplified design, but results in operation always at the lowest gap and thus higher risk of radiation-induced demagnetisation of the magnets. Another aspect to be considered is the appearance of field gradients over the beam axis in the circular mode. The APPLE-X provides a radial gap drive which has symmetric conditions in all polarisation modes. In addition, this device has the feature of producing controlled gradients [245] and is the most flexible APPLE-type undulator. This type is chosen as baseline for the afterburner. Figure 6.34 shows a model of the APPLE-X magnet.

The possible remanent magnetic field B_r, especially of NdFeB magnets, has increased over the last years. Techniques such as Dysprosium (Dy) and recently Terbium (Tb) diffusion enable an increase in the coercivity H_{cj} without decreasing B_r which can be up to 1.35 T with sufficiently high stability against radiation damage. The diffuse heavier rare earth materials replace the Nd at the grain boundaries from where demagnetisation starts. So with a cost-effective low concentration, the coercivity can be increased sufficiently without reducing the remanence. This works well for thin magnets, for instance those used in short-period undulators. The strength of the magnets can be further increased by operating the undulator under cryogenic conditions at liquid nitrogen temperatures. Stronger grades of the

magnetic material can be used because both coercivity and remanence show a negative temperature gradient. It is only necessary to control demagnetisation effects during assembly. Radiation effects in operation are not harmful any more. The material of choice is PrFeB. NdFeB also works, but shows a spin reorientation below 135 K which reduces the fields when the temperature is further lowered. The cryogenic design needs to be careful to meet this maximum, but it has shown stable operation on the flat top with temperature gradients. With both materials, remanent magnetic fields of 1.65 T are achievable. Room temperature devices can be built in or out of vacuum. The thinnest vacuum chambers so far have been used for the Athos beamline at SwissFEL with a wall thickness of only 200 µm. The magnet gaps of in-vacuum undulators can be slightly reduced, since for impedance reasons they need to be covered by a thin copper-nickel foil with a typical thickness of 100 µm. But the effective loss in gap is larger for out-of vacuum undulators because of the required alignment tolerances. At PSI, a vacuum chamber of 5 mm is used, but the minimum magnetic gap is 6.5 mm, so the effective loss in gap is 1.5 mm, compared to 0.2 mm for in-vacuum applications. Cryogenic undulators are mandatory in-vacuum, of course.

6.1.4.2. Magnetic Optimisation of the Afterburner

The optimisation parameters for the magnetic design of the afterburner are the

- B_r, depending on cryogenic or room-temperature
- Magnet dimensions
- Gap / slit
- Number of magnets per period
- Field shape

In the APPLE-X design, the shape of the magnets makes effective use of the available volume. Variations are possible, mainly in the clamping and symmetry. For the studies for CompactLight the SwissFEL Athos UE38 design is used, scaled from a period length of 38 mm to the much shorter period length of 16 to 20 mm. While the gap is determined by wakefield considerations to 5 mm, the distance of the magnet blocks (slit) is determined by the practical consideration of allowing magnetic measurements from the side. So, a minimum slit is 2.5 mm (UE38: 3 mm). The classical Halbach approach uses 4 magnets per period. However, using more magnets increases the effective field. Using 8 magnets per period, the peak field can be increased by 8%. Field shaping, an inhomogeneous magnetisation of the magnets, has been used for the UE38 in combination with SmCo magnets, which are however not an option where maximum fields are required.

Table 6.8 shows possible K-values as function of the period for a round vacuum gap of 5 mm for the three options. The K-values assigned are required to match the tuning range. Full tuning is only possible for period length of less than 17 mm. Longer periods reduce the maximum energy of polarisation control for XLS. For all models, a 5 mm diameter vacuum stay clear aperture is assumed. A period length of 18 mm could just be feasible even at out-of vacuum with 4 magnets per period (1^{st} number) and 8 (2^{nd} number) respectively. An afterburner with a period length of 18 mm would just match the nominal tuning range of the FEL undulator. However, for high energies the K-value would be unusually small which will have an impact on the efficiency (see Section 6.1.2.5). Therefore, studies of in-vacuum technology including the cryogenic option are required. However, polarisation control is mandatory for the entire soft X-ray range starting from 250 eV. In the hard X-ray regime, circular dichroism is limited to the K_α absorption lines up to about 12.5 keV. Afterburners with periods longer than 20 mm reduce successively the high-energy part, meaning that only circular polarisation is available. In principle, this is not a problem, but the standard the users would expect and find anywhere else is linearly polarised

Table 6.8.: Link between the FEL undulator with 13 mm period and a range of the K-value of 1.85 to 0.85 and the longer period afterburner (left). Maximum K-values calculated with RADIA [251] for APPLE-X undulators in and out of vacuum and cryogenic in-vacuum technology (right).

$\lambda_{U/AB}$ [mm]	K_{max}	K_{min}	$E_{ph,max}$ [keV]
13	1.85	0.85	16
14	1.74	0.73	16
15	1.64	0.6	16
16	1.55	0.46	16
17	1.47	0.3	16
18	1.38	0.3	15.3
19	1.30	0.3	14.4
20	1.23	0.3	13.7

λ_{AB} [mm]	out-vac B_r = 1.37 T	in-vac B_r = 1.37 T	cryo B_r = 1.65 T
13			
14			
15			1.29 / 1.39
16	1.07 / 1.16	1.23 / 1.32	1.48 / 1.60
17	1.23 / 1.31	1.38 / 1.50	1.68 / 1.82
18	1.39 / 1.51	1.56 / 1.69	1.89 / 2.04
19	1.57 / 1.68	1.75 / 1.88	
20	1.74 / 1.87	1.93 / 2.07	

light. This limitation would need to be explicitly indicated to the users. However, from magnetic calculations it seems to be possible to cover the entire wavelength range at the expense of efficiency. From the point of pulse energy a longer period length might be favourable (see Section 6.1.2.5 for details). For systematic studies, it is helpful to parametrise the gap dependence of the field.

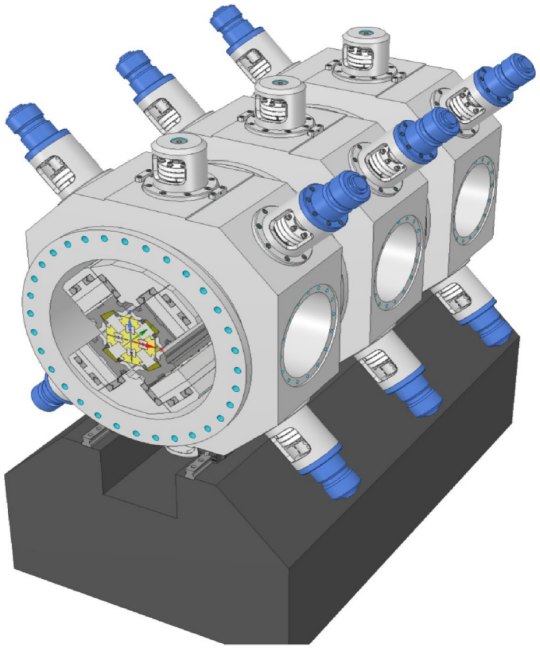

Figure 6.35.: Design study for a compact and modular, in-vacuum APPLE-X undulator.

Support mechanics. A design study has been explicitly carried out for this project by Kyma for a compact, modular, in-vacuum APPLE-X undulator as shown in Figure 6.35. This study follows a compact and modular design for the next generation in-vacuum undulators for SLS2.0 at PSI. A vacuum chamber machined out of a massive aluminium block plays the role of the support structure. In the APPLE-X configuration, every magnet array is adjustable in radial and longitudinal direction. A very compact drive system can be realised with hydraulic cylinders. The intelligent valve (Bosch-Rexroth) can provide sub-µm resolution. The undulator is segmented in modules, and each of the modules has its own drive system, which can allow even for a segmented taper inside the undulator. The compact

modules will be placed on a girder similar to the multipole magnets. Various options have been analysed, which follow various concepts. All drive systems are out-of-vacuum. The design shown here combines elements such as external longitudinal shifts. The magnet arrays are here internally connected to increase stiffness to handle the large magnetic forces and to allow fine alignment of the magnetic axis. The magnet keeper is equipped with force compensating magnets, which could make the internal connection between the magnet arrays obsolete.

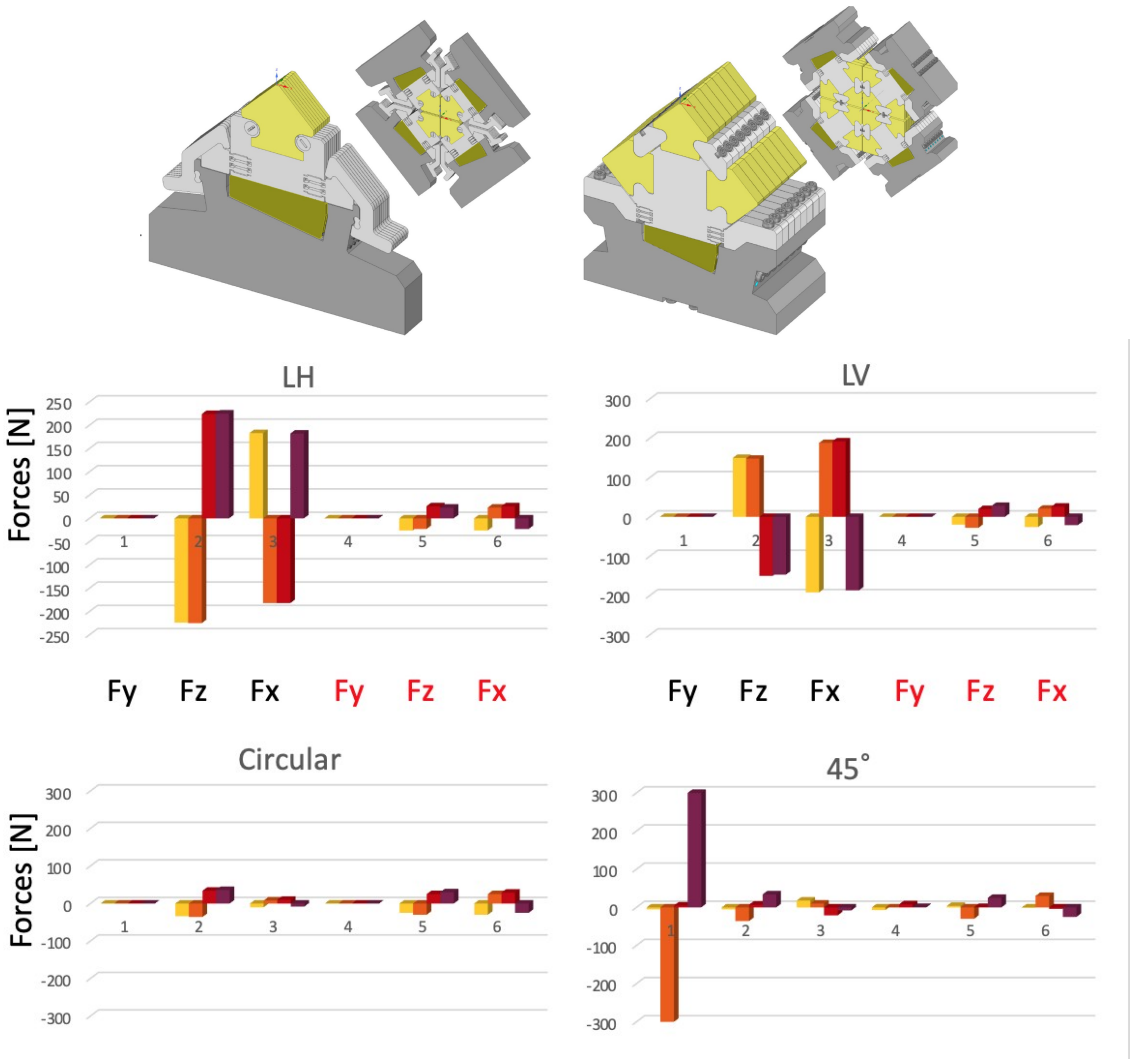

Figure 6.36.: Force compensation for the APPLE-X design. On top is shown a possible field compensation using identical magnets without increasing the complexity of the keeper by additional clamps. The graphs plotted below show the forces on the individual magnet arrays for the different operation modes linear horizontal and vertical (LH, LV), helical and inclined. On the left are the forces (calculated for a few periods only) for the standard APPLE-X configuration and on the right, marked in red, for the force compensation case. The reduction is remarkable, even though it is not zero. But it is drastically reduced and is identical for the major operation modes. The forces further reduce with radial opening of the gap.

Magnetic force compensation solutions. As already mentioned above, the challenge of APPLE type undulators is coping with three-dimensional forces which can even change sign with mode of operation. In addition, these forces act differently on the individual magnet arrays, which results in moments through the entire support structure. The forces are responsible for the large dimensions of

the support structures for these devices and are a major obstacle for designing in-vacuum solutions. The key idea seems to be magnetic field compensation as proposed for the BESSY-II in-vacuum APPLE and studied for APPLE type undulators at ALS at LBNL in Berkeley. For planar undulators magnetic field compensation has been also successfully tested.

Figure 6.36 shows a possible implementation for the APPLE-X configuration using identical magnets for field compensation. It is obvious that the number of magnets increases significantly, by a factor of 3. However, the field quality is not so stringent as for the centre magnets, so that the specification could be relaxed for the field compensation magnets only. Alternatively, the specification could be relaxed for all the magnets which could then be sorted to find the best magnets for the centre. However, it is interesting to see that the field compensation is very successful. In contrast to planar undulators the field compensation cannot be 100% because there is only compensation to the neighbouring magnet arrays, but no compensation to the diagonal magnet array. However, the forces are drastically reduced as seen from the graphs in Figure 6.36, and are constant for the major polarisation modes of linear vertical, linear horizontal and circular with both helicities. Only in the inclined mode are the remaining forces different, but of the same small level. It is certainly worth studying carefully the field compensation for in-vacuum applications.

6.1.4.3. Analyses of the Mechanical Support Structure

The mechanical structure is exposed to three-dimensional forces as described above. The use of compensating magnets is proposed to minimise the undulator support structure. The load analyses of the proposed support structure was carried out by Kyma, where the magnetic load without compensating magnets was simulated, and the results were compared to the simulations with the reduced magnetic load achieved with the compensating magnets. Simulations were carried out for the four main modes of operation:

- Linear horizontal mode.
- Circular mode.
- Linear vertical mode.
- 45° mode.

Mechanical structure main features. A detailed description of the support structure presented by Kyma is shown in Figure 6.37. The magnetic forces acting on the array are transferred to the magnet holder support (1) screwed onto the in-vacuum girder (2), transferred across the girder onto the radial pistons (3) with linear bushings (4). Part of the load would be transferred via linear bushings onto the guiding plate (5), whereas the remaining load would be transferred onto the radial frame plate (9) via locking nuts (10). Part of the loads would be (vertically) compensated, by the means of a preloaded linear bearing with needle bearing elements (6), with inner rails screwed onto the radial guiding plate (6.1) and outer rails screwed onto the top frame (6.2). The top and radial connecting rods would be mounted onto the frame and radial frame plates using a bolted connection.

The structural response chain extends further onto the radial actuator assembly (12), external linear rail guides (13) and the vacuum chamber housing (14). Given several vacuum chamber housing segments within this design concept, the longitudinal loading extends along the beam axis across the entire vacuum chamber. Figs. 6.38 and 6.39 show the vacuum chamber with radial and phase actuation mechanism and the vacuum chamber bottom support with bottom linear rail guides, respectively. The response chain extends further down across the vacuum chamber support (15) and across bottom linear rail guides (16) onto the foundation. Results of simulations for the four main modes of operation are presented in the next section.

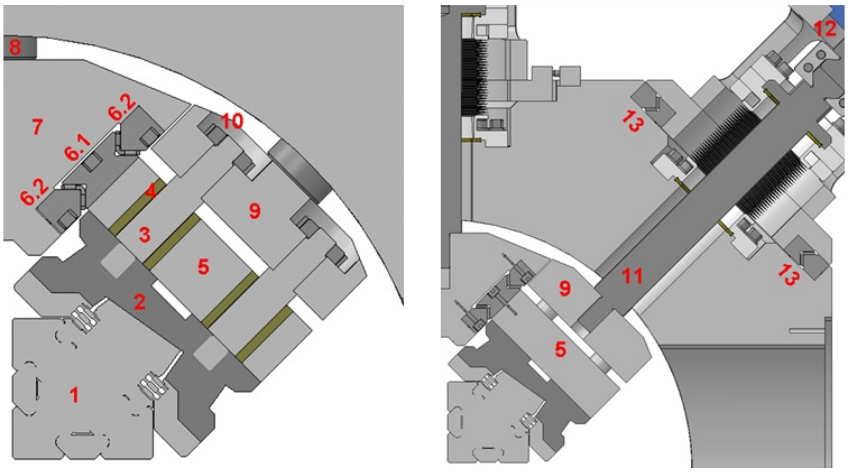

Figure 6.37.: Cross-section at radial piston (left) and at radial acting rod axis depth (right).

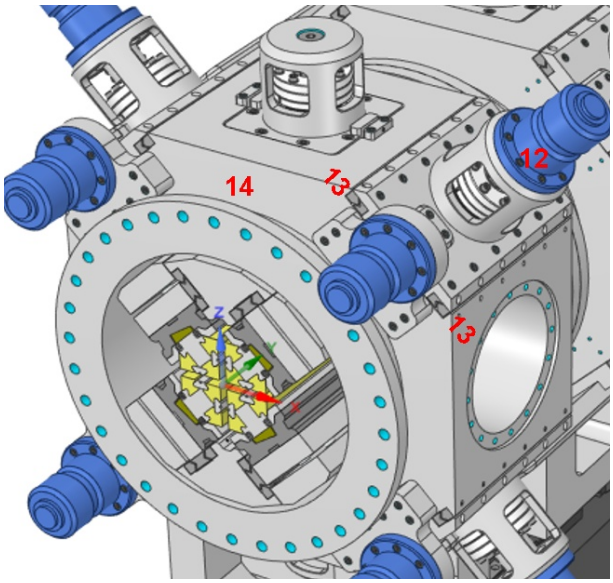

Figure 6.38.: Vacuum chamber with radial and phase actuation mechanism.

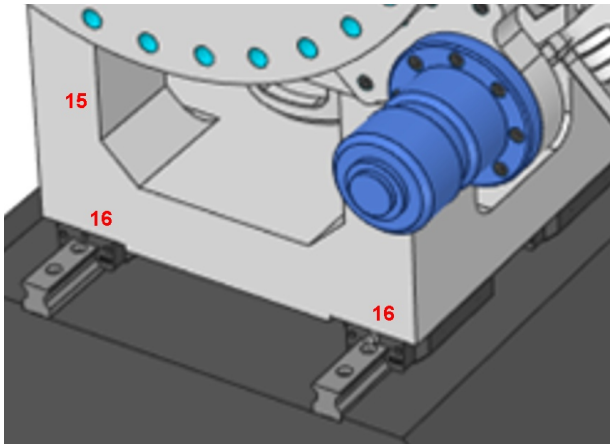

Figure 6.39.: Vacuum chamber bottom support with bottom linear rail guides.

Mechanical simulation results. The proposed APPLE-X undulator is mechanically symmetrical across the vertical longitudinal plane and horizontal longitudinal plane. The advantage of this symmetry is that only one-quarter of the whole structure can be considered when performing the simulations. Although the simulated model is very complex, the symmetry minimises the complexity and greatly reduces the simulation time without losing the precision of simulation results.

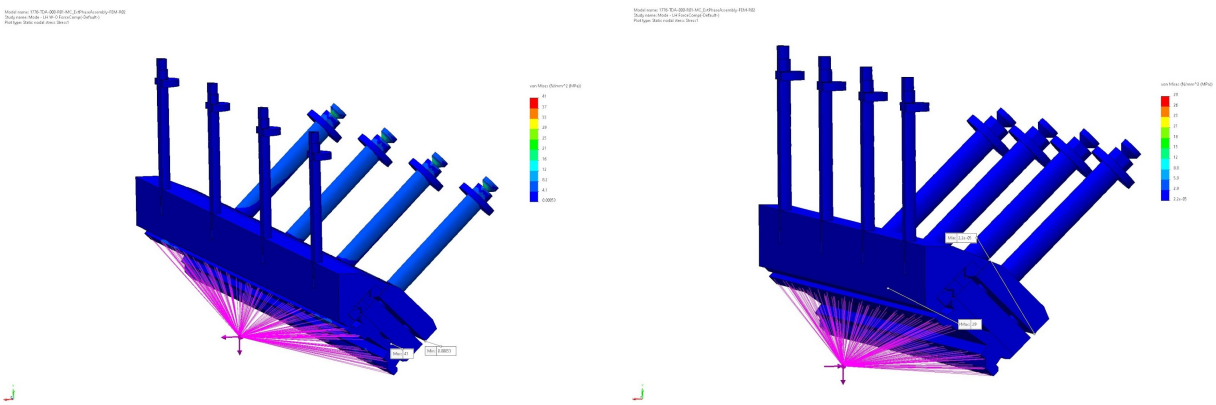

Figure 6.40.: von Mises stress without (left) and with (right) force compensation in linear horizontal mode.

Linear horizontal mode. Figure 6.40 shows the von Mises stress without (left) and with (right) compensation in the case of linear horizontal mode. Figure 6.41 shows the URES displacement in the same configurations. The overall improvement in stress reduction and deformation by using compensating magnets is presented in Table 6.9.

Table 6.9.: Linear horizontal mode with and without compensating magnets.

	von Mises stress [$\mathrm{N\,mm^{-2}}$]	**Overall deformation [µm]**
Without compensating magnets	41	123
With compensating magnets	29	47
Improvement	29%	62%

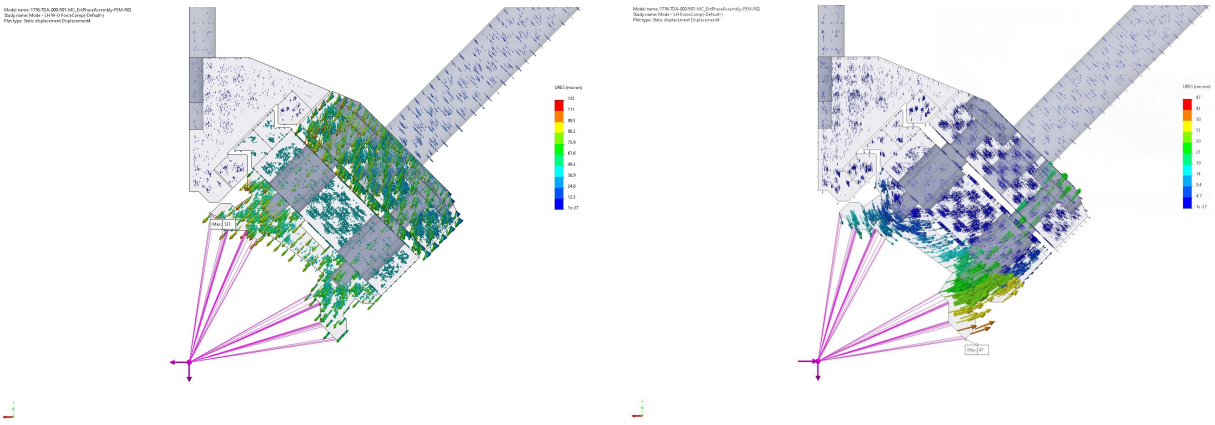

Figure 6.41.: URES displacement without (left) and with (right) force compensation in linear horizontal mode.

Circular mode. Figure 6.42 shows the von Mises stress without (left) and with (right) compensation in the case of circular mode. Figure 6.43 shows the URES displacement without (left) and with (right) compensation. The overall improvement in stress reduction and deformation by using compensating magnets is presented in Table 6.10.

Table 6.10.: Circular mode with and without compensating magnets.

	von Mises stress [$\mathrm{N\,mm^{-2}}$]	**Overall deformation [µm]**
Without compensating magnets	34	54
With compensating magnets	24	50
Improvement	29%	7.4%

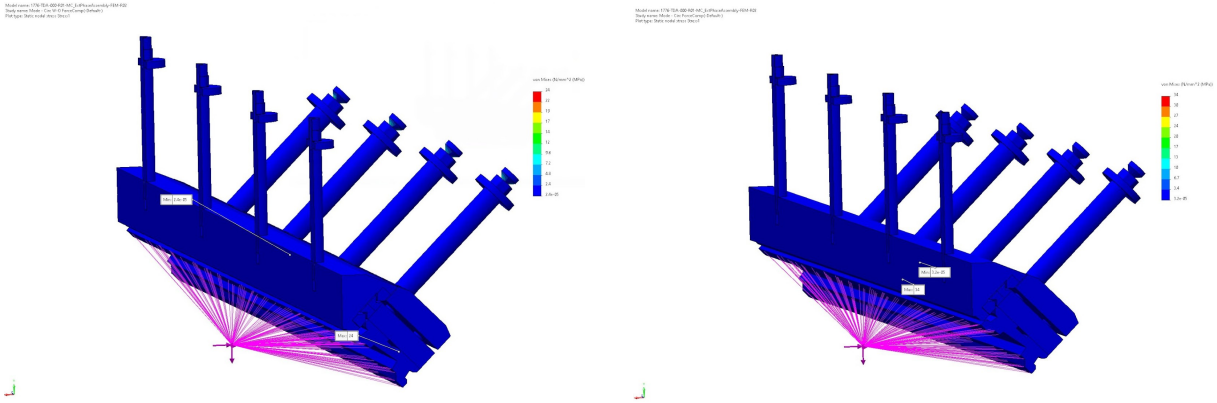

Figure 6.42.: von Mises stress without (left) and with (right) force compensation in circular mode.

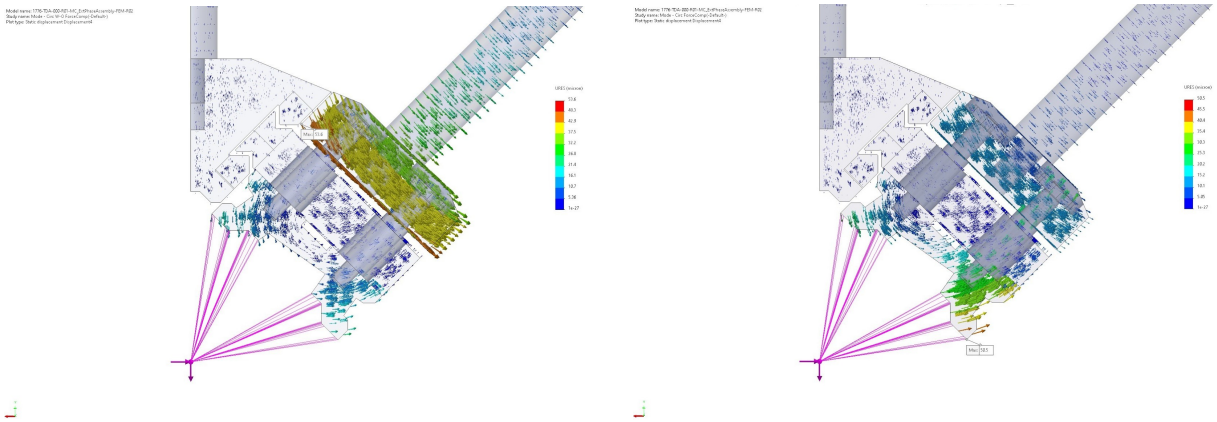

Figure 6.43.: URES displacement without (left) and with (right) force compensation in circular mode.

Linear vertical and 45° modes In both configurations, the proposed mechanical solution can only be used with compensating magnets. In the case where compensating magnets are omitted, the longitudinal force acting on the girder is too large for these proposed solutions. The overall performance in stress reduction and deformation by using compensating magnets in both modes is presented in Table 6.11.

Figs. 6.44 and 6.45 respectively show the von Mises stress and the URES displacement with compensation in linear vertical (left) and 45° (right) mode.

Table 6.11.: Stress reduction and deformation performance.

	von Mises stress [$\mathrm{N\,mm^{-2}}$]	**Overall deformation [µm]**
linear vertical mode	28	42
45° mode	36	64

The proposed mechanical solution can only be used with compensating magnets for the linear vertical mode of operation. In the case where compensating magnets are omitted, the longitudinal force acting on the girder is too large for the proposed mechanical solution.

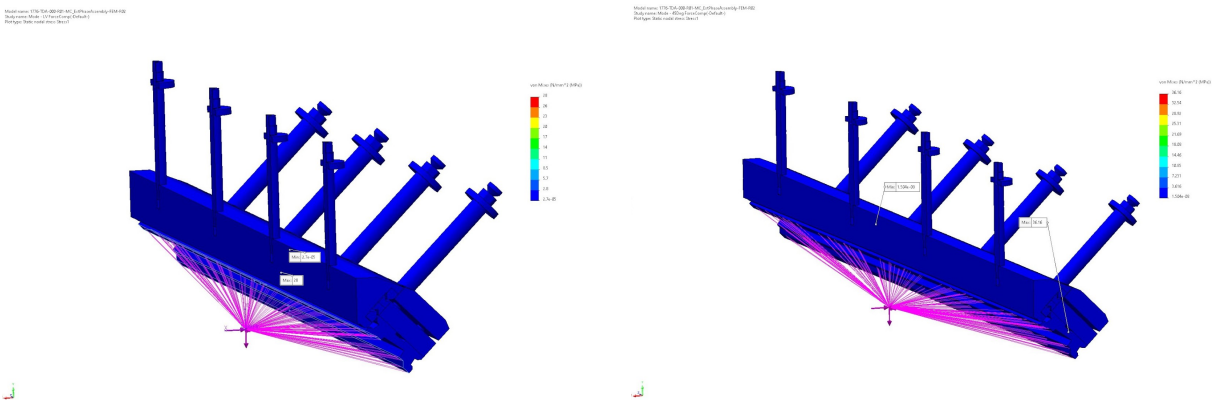

Figure 6.44.: von Mises stress with force compensation in linear vertical (left) and 45° (right) mode.

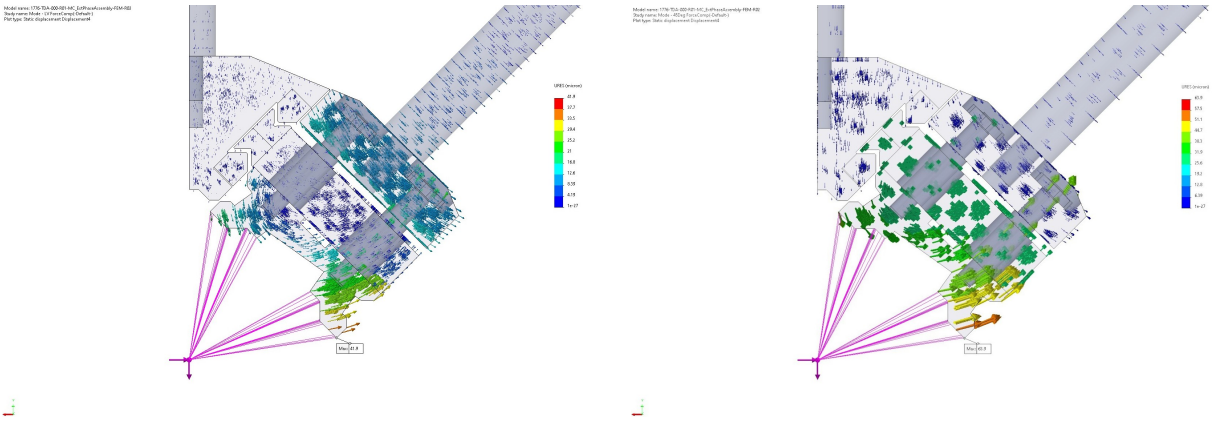

Figure 6.45.: URES displacement with force compensation in linear vertical (left) and 45° (right) mode.

Simulation results conclusion. As shown, the load on the support structure is significantly reduced with the use of compensating magnets. In the case of linear vertical and 45° polarisation modes, the use of compensating magnets is even mandatory for such a structure to withstand the magnetic load. The deformations of the structure are much lower, and the central magnets maintain their theoretical position better in all modes of operation. In theory, such a device could perform better magnetically, because the magnets will better maintain their positions. Consequently, the magnetic errors should be lower in different modes of operation in respect to a device without magnetic compensation.
The presented mechanical structure is a conceptual idea which should be further developed, evaluated and optimised, before a prototype of such a device could be built. Nevertheless, the benefit of using compensating magnets has been confirmed using mechanical simulations.

Layout of the afterburner section. The afterburner line will consist of two undulator modules with an intersection, which continues the layout in the undulator section. The intersection hosts a phase matcher, quadrupoles, beam position monitors, corrector magnets and bellows. The vacuum chamber in the intersection should be small and has a diameter of 6 mm, which would allow the quadrupole magnets to have a full gap as small as 8 mm. The periodicity of the quadrupoles should remain the same as shown in Figure 6.13 for the SCU cryomodule, hence a length of 2255 mm. The length of the afterburner module will be given then by the space required for the intersection elements. The goal is to use also only 500 mm for the intersection elements so that the length of the afterburner module will around 1700 mm. For comparison, the intersection in the SwissFEL Aramis beamline is 750 mm. This is already quite compact, and the major components can be used either directly or as an initial design concept. As the in-vacuum undulators allow already a distributed pumping along the entire undulators, no additional space is required in the intersection. However, a sector valve would be helpful in case of a possible failure and repair demand. Figure 6.46 shows the intersection between the two afterburners.

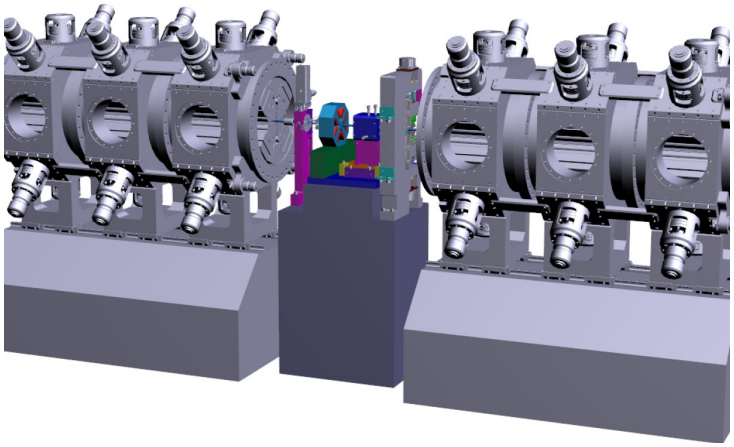

Figure 6.46.: Intersection between the two afterburners with sector valve, quadrupole, BPM and bellows.

Drive and control system. For the drive system for the radial and axial adjustments of the magnet arrays a hydraulic drive system is proposed, because it combines compactness, force, and precision. The heart of the system is an electronic valve from Bosch-Rexroth, which adds high resolution of less than 100 nm. The system has been tested for applications in APPLE undulators in a framework of a Master's thesis in co-operation of PSI and Fachhochschule Nordwestschweiz and is currently under test in a prototype study for SLS2.0 planar compact in-vacuum undulators. The digital valve of the 4WRPH series (see Figure 6.47) is compatible with the ENDAT 2.2 interface for direct integration of Heidenhain encoders and fast field bus i.e. EtherCAT bus for integration into the control system.

The APPLE-X undulators have a good field region of about 50 µm in both directions. A remote alignment system is therefore highly recommended for the afterburner, with control of the horizontal and vertical position and pitch and yaw angles. The concept of dedicated alignment quadrupoles allows for a beam-based alignment strategy. It has been used in LCLS where undulator and quadrupole were placed on the same girder table, and by SwissFEL with dedicated, small fixed permanent magnet quadrupoles. After magnetic optimisation the quadrupoles will be aligned to the magnetic axis. Placed on a simple pneumatic stage with two hard stops, a reproducibility of less than 10 µm can be achieved. For beam-based alignment, these quadrupoles are brought successively into the beam. Misalignment results in kicks, which can be detected with downstream beam position monitors. Therefore, the FODO optics scheme needs to be extended beyond the afterburner. After alignment, the quadrupoles are pushed back to minimise distortion of the electron beam. A compact mover system allowing for five

Figure 6.47.: Digital regulation valve for the hydraulic drive system.

degrees of freedom is based on cam-shaft movers, which allows for sub-µm resolution.

6.1.4.4. Tolerance Studies

The main requirements on field quality and tolerances for the main FEL undulators as well as for the afterburners are described in Section 6.1.3.7. The trajectory in the afterburner undulators can be optimised only in one setting (K parameter and polarisation state). The mechanics of the undulator structures then determines the dynamic errors coming with load change. In addition, permanent magnet based undulators show systematic errors because of the permeability of the magnet material. Although this value is low, especially compared to iron, it is a source of kicks especially caused by the end magnets due to the change of the magnetic environment coming along with changes in gap and shift. There are shimming techniques which can reduce these kicks, but in general active correction by coils in the x and y directions is required at both extremities of an undulator. In practice therefore, there are no specifications for the end-kicks as long as the strength of the correction coils is sufficient.

In order to avoid field gradients over the undulator axis, the afterburner concept is based on a variable-gap APPLE undulator. The APPLE-X concept, on the other hand, would be able to produce gradients, but in an intentional and controlled way. The algorithms to control field and gradients in APPLE-X undulators can be found in [252].

6.1.4.5. Afterburner Quadrupoles

In the following sections, the design of the small normal conducting FODO quadrupole magnets with solid conductor air-cooled coils is explained.

Table 6.12.: FODO quadrupole main parameters.

Parameter	Value	Units
Integrated field gradient	10	T
Field gradient	165	$\mathrm{T\,m^{-1}}$
Effective length	60	mm
Aperture radius	4	mm

Pole and yoke design Using the three-dimensional code OPERA and the two-dimensional codes Poisson and FEMM, a pole and yoke geometry was developed for the FODO quadrupoles which met

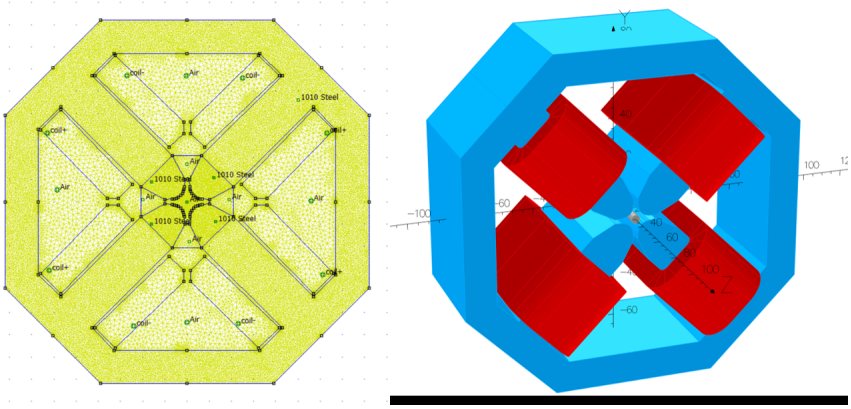

Figure 6.48.: 2D (left) and 3D (right) models of the FODO quadrupole magnet

the magnets' operational requirements. Simulations were done for a quadrupole with a field gradient of 165 T m^{-1} and effective length of 60 mm using the following equation for the pole profile:

$$xy = R^2/2 \tag{6.15}$$

The main parameters for the FODO quadrupoles are specified in Table 6.12 and simulated 2D and 3D geometries are shown in Figure 6.48. Applying the low-carbon steel AISI-1010, the magnetic field intensity inside the quadrupole is shown in Figure 6.49. Figure 6.50 shows the magnet dimensions (left) as well as the coil specifications and geometry (right). Figure 6.51 shows the obtained magnetic field gradient with respect to the longitudinal axis.

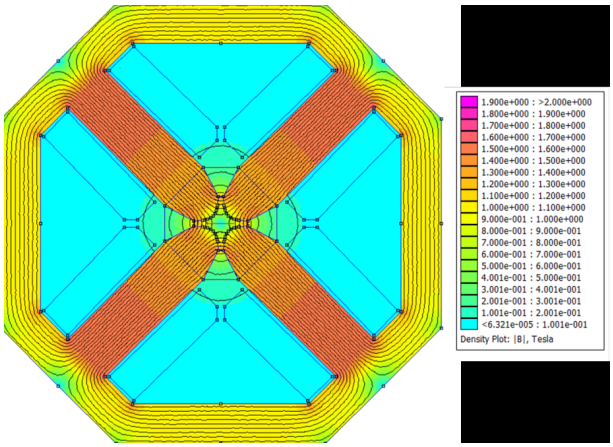

Figure 6.49.: Magnetic field intensity inside the FODO quadrupole magnet.

In order to calculate the field gradient at $x = 2$ mm versus the longitudinal direction in Opera 3D, the field is calculated on circles with radius 2 mm moving along the beam direction in steps of 4 mm. Using a Fast Fourier Transformation, the magnetic field, the field gradient and higher order harmonics are obtained in each location. Having the field gradient at different longitudinal locations, the integrated field gradient at $x = 2$ mm is calculated to be 10 T.

Harmonic analysis The strength and relative strength of nominal and the first three allowed higher order multipole components for the FODO quadrupole are summarised in Table 6.13 and Figure 6.52.

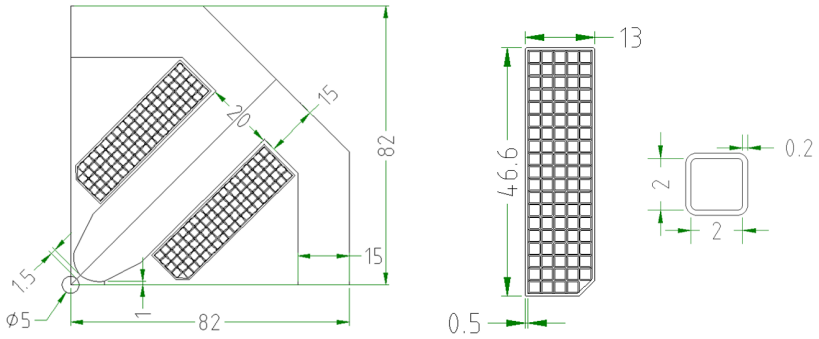

Figure 6.50.: Left: FODO quadrupole magnet. Right: coil cross-section for the FODO quadrupoles. Dimensions in mm.

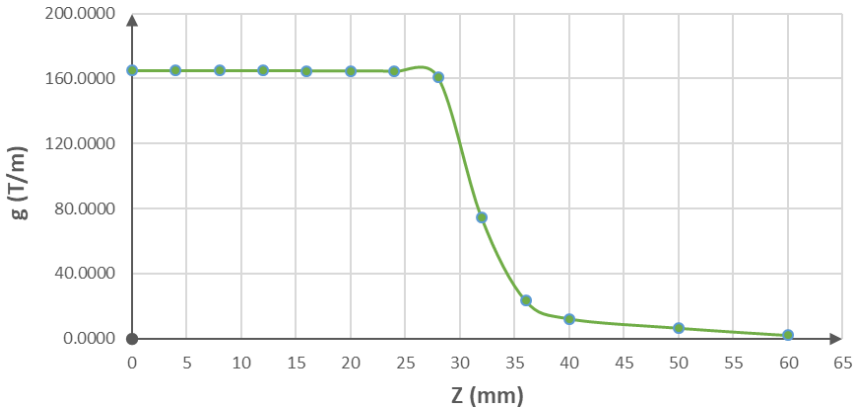

Figure 6.51.: FODO quadrupole field gradient versus longitudinal distance z.

Table 6.13.: FODO quadrupole field coefficients at 2 mm.

n	type	B_n(2 mm) [T]	$\lvert B_n/B_2\rvert$(2 mm)
2	Q	3.300×10^{-1}	1
6	Q	-1.271×10^{-5}	3.85×10^{-5}
10	Q	1.937×10^{-6}	5.87×10^{-6}
14	Q	7.029×10^{-9}	2.13×10^{-8}

6.1.4.6. Electrical and Cooling Parameters

FODO quadrupole magnets in the afterburner line have a small gap radius of 4 mm, which increase the quadrupole strength significantly. So, having a small amount of current in each coil and a dissipated power of 100 W per magnet, the coils can be wound from solid copper conductors, rather than hollow conductors. Table 6.14 shows the FODO magnets electrical and cooling parameters.

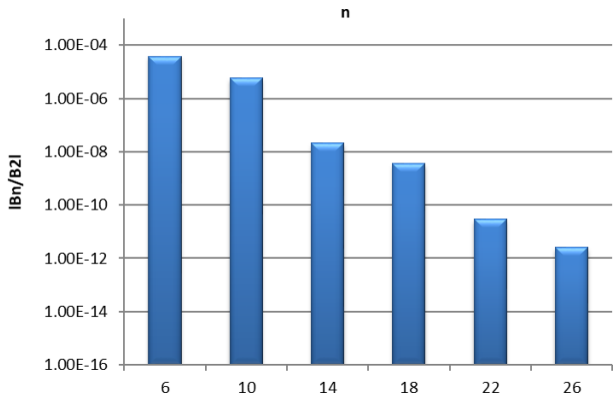

Figure 6.52.: Absolute normalised multipole errors in the 2 mm radius. The quadrupolar component, $n = 2$, is not shown.

Table 6.14.: Afterburner FODO quadrupole magnets electrical and cooling parameters.

Parameter	**Value**	**Units**	**Parameter**	**Value**	**Units**
Effective length	0.06	m	Conductor dimensions	2×2	mm
Field strength	165	$\mathrm{T\,m^{-1}}$	Copper area	4	$\mathrm{mm^2}$
Full gap	8	mm	Current density	3.27	$\mathrm{A\,mm^{-2}}$
Total Ampere-turns per coil	1230	At	Voltage drop per magnet	7.41	V
Operating current	13	A	Resistance per magnet	0.56	Ω
Number of turns per coil	94	-	Power per magnet	97	W

6.2. Photon Beamlines

6.2.1. Overview

Experiments performed at FEL facilities can be broadly divided into two distinct categories: time-resolved microscopy and photon energy-resolved spectroscopy. In the first category of experiments, fs FEL pulses are used to follow the temporal dynamics of the system in question. Meanwhile in the second category, sub-eV energy resolution is employed to study, for instance, element-specific X-ray absorption peaks with respect to position and spectral line shape. To enable the second category, the photon beam is monochromatised to a sub-eV spectral width using a dispersive optical element and a system that allows for transmission of X-rays only in the desired photon energy range. The corresponding beamline is referred to as a mono beamline. For time-resolved experiments, the full bandwidth of photon pulses is used to maximize the photon flux on the sample. The corresponding beamline must provide high transmission and is commonly referred to as a pink beamline. The CompactLight design provides mono and pink beamline capabilities in the whole operation range from 0.25 to 16 keV.

The CompactLight design has a unique feature of two independently-tunable undulator lines driven by twin bunches from the same accelerator. The twin-bunch approach creates an opportunity for X-ray pump/X-ray probe experiments in a wide range of photon energies not accessible with any other existing or planned FEL. The time and energy separation between the photon pulses from twin bunches can be varied to a large extent. To utilize these unique X-ray pump/X-ray probe capabilities, three *dual* endstations are foreseen: (i) a Soft X-ray (SXR) endstation, 0.25-2 keV, for SXR pump/SXR probe experiments; (ii) a SXR/Tender X-ray (TXR) endstation with a SXR pump and a probe in the TXR, 2-8 keV, range; and (iii) a Hard X-ray (HXR) station with the pump and probe being both either in the TXR or HXR, 8-16 keV, range. In addition, two standalone endstations (one SXR, one HXR endstation) are also foreseen to efficiently utilize the available beam time.

6.2.1.1. Optical Layout

Figure 6.53 shows the optical layout (not to scale) of a photon transport system for the FEL-1 and FEL-2. The photon transport system starts with a so-called front-end containing a bremsstrahlung collimator, a photon shutter and a set of photon diagnostics. The bremsstrahlung collimator removes non-coherent, strongly-divergent bremsstrahlung radiation and broadband spontaneous undulator radiation. The photon shutter is the first element of a safety system and must withstand full FEL fluence in case of a sudden beamline shutdown.

The front-end is followed by photon beamlines and an experimental area hosting user endstations. To facilitate the discussion of individual photon beamlines, Figure 6.54 introduces a *naming convention for beamlines*. The SXR endstations are primarily concentrated on the FEL-1 side whereas the HXR ones are mostly located on the FEL-2 side. This choice is dictated by the fact that after the complete upgrade, FEL-1 can be independently operated in a SXR range of 0.25-3.1 keV at 1 kHz repetition rate (the corresponding electron energy range is 0.95-2.4 GeV). Hence, it is convenient to place SXR endstations close to FEL-1. Three SXR beamlines serving FEL-1, $B_{1s,S,m}$, $B_{1d,S,m}$ and $B_{1d,S/T,m}$, share the same monochromator based on variable-line-spacing gratings. Two interchangeable gratings are available in the monochromator to cover the 0.25-2.2 keV photon energy range[1]. These beamlines can also operate in pink mode by retracting the gratings. In addition, a HXR beamline up to 16 keV, $B_{1d,H,m}$, from FEL-1 is used for X-ray pump/probe experiments at the central dual endstation. FEL-2 is served by 4 beamlines: (i) one SXR beamline, $B_{2d,S,p}$, providing the beam to the dual SXR endstation, (ii) one HXR pink/mono beamline, $B_{2s,H,p/m}$, providing the beam to a standalone station, (iii) two HXR and TXR beamlines, $B_{2d,H,m}$ and $B_{2d,S/T,p}$ providing the beam to the other two dual stations. The hard beamlines contain mirrors with two types of coatings to cover the whole range from 2 to 16 keV.

The beamlines include steering mirrors that direct the X-ray beam into corresponding endstations, refocusing Kirkpatrick-Baez (KB) optics to refocus the beam at the sample position and monochromators in monochromatic mode. The mirrors are operated in the regime of total external reflection with incidence angles of a few tens of milliradians for SXR and a few milliradians for HXR. Incoupling of attosecond UV pulses from a high-harmonic generation (HHG) source is foreseen for some pink beamlines for ultrafast pump-probe experiments.

6.2.1.2. Overview of the Performance of Beamlines

Table 6.15 summarizes the performance of photon beamlines based on simulations performed with RAY [253]. To realize efficient total external reflection by the beamline mirrors, different mirror materials depending on the photon energy range are used. Based on the simulation results for different materials, it is convenient to define three photon energy ranges: (i) SXR from 0.25 to 2.2 keV with Au mirrors, (ii) TXR from 2 to 8 keV with B_4C mirrors, and (iii) HXR from 8 to 16 keV with mirror coating composed of 5 nm B_4C on 25 nm of Rh. The successful deposition of B_4C on Rh is demonstrated for the European XFEL [254]. The mono beamlines can also be operated in pink mode by retracting dispersive elements (a grating or a crystal).

6.2.1.3. Overview of the Photon Transport Area and Experimental hall

The CompactLight experimental area of 24.5 by 85 m (2060 m^2) is located 65 m away from the undulator end. The area comprises 5 X-ray hutches, 2 laser laboratories, 2 control rooms and a technical gallery to access the hutches. For comparison, the total area of the SwissFEL experimental facility is also around 2000 m^2 with 1200 m^2 allocated for X-ray hutches. The hutches host refocusing optics, photon diagnostics, endstations, local control electronics and data acquisition systems. The optical laser beam can be transported from the laser room, located upstream of the hutches, to incoupling mirrors positioned close to the endstations. The hutches and laser laboratories are surrounded by a

[1] the acceptance range of photon beamlines in terms of photon energies is designed with some margin

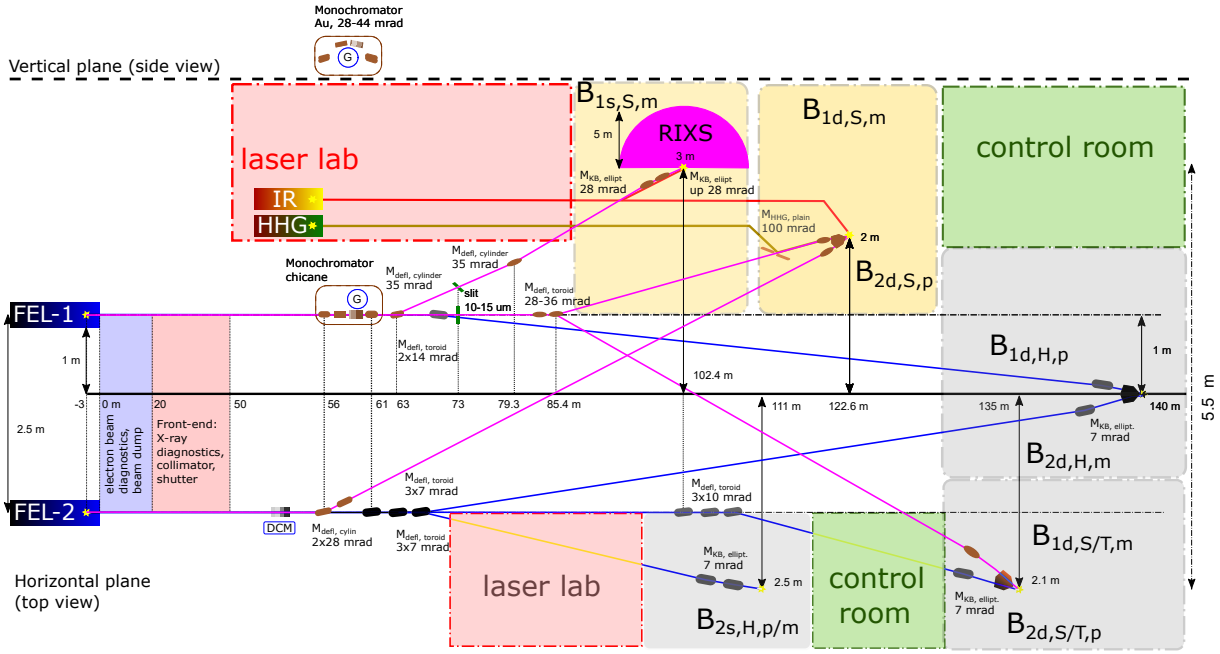

Figure 6.53.: Schematic of the optical layout of the photon beamlines. The two virtual sources of FEL-1 and FEL-2, correspondingly, are depicted by the yellow stars (on the left). The photon beam path is shown by the blue (hard X-rays) and pink (soft X-rays) lines. The beam is focused into five endstations: three dual stations and two standalone ones. The main optical elements are mirrors denoted by "M" (the deflection angle and the type of curvature are indicated in the subscript) and monochromators (grating-based, "G", or double-crystal-based, "DCM"). The hutches (shaded areas) hosting the endstations are also schematically indicated. External lasers for pumping the sample in the IR and VUV ranges will be available.

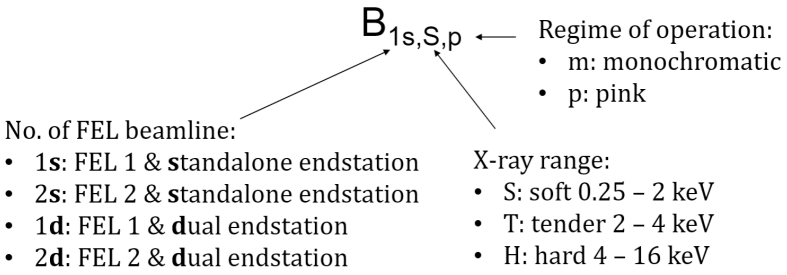

Figure 6.54.: Naming convention for photon beamlines: the numeral in the subscript indicates the FEL from which the photon beam comes. The letter, next to the numeral, indicates whether the beamline serves a standalone endstation or a dual one. The capital letter after the first comma specifies the operation photon energy range of the beamline. The last letter indicates whether the beamline is operated in monochromatic mode or pink mode (unaltered photon energy range of the FEL beam).

technical gallery for easy access. Note that the walls of two hutches are positioned in such a way that they are exactly on straight lines from the accelerators. Partly, this naturally prevents personnel of being illuminated by neutron radiation from the accelerators.

Table 6.15.: Overview of the performance of photon beamlines. The results are obtained with software RAY [253]. Note: a relative FEL bandwidth of 0.1% is assumed in the simulations.

X-ray range	Mode of operation	Beamline	Mirror material	Transmission (%)	Photon energy resolution (meV)	Pulse stretch (fs)	Beam size FWHM (μm)
Soft: 0.25-2 keV	Pink	$B_{2d,S,p}$	25 nm Au	75-85	-	-	6.5-2; 4-3
		$B_{2d,S/T,p}$		53-82	-	-	2.8-1.1; 2-1.1
	Mono	$B_{1s,S,m}$		1-4	40-500	200-10	8-5; 4-2
		$B_{1d,S,m}$		1-6	40-500	200-10	9-4; 7-3
		$B_{1d,S/T,m}$		0.6-3	40-500	200-10	4-2.4; 3.2-1.6
Tender: 2-8 keV	Pink	$B_{2s,H,p}$	25 nm B_4C	83-97	-	-	0.99; 0.83
		$B_{2d,H,p}$		68-98	-	-	0.77; 0.65
		$B_{2d,S/T,p}$		73-97	-	-	0.83; 0.7
	Mono	$B_{2d,H,m}$		1.2-11.2	120-1000	-	0.77; 0.65
Hard: 8-16 keV	Pink	$B_{2s,H,p}$	5 nm B_4C on 25 nm Rh	85-69	-	-	0.71
		$B_{1d,H,p}$		86-75	-	-	0.55
	Mono	$B_{2d,H,m}$		2.1	230-470	-	0.55
		$B_{2s,H,m}$		2	230-470	-	0.71

6.2.2. General Aspects of Photon Transport

6.2.2.1. Virtual FEL source

FEL lasing occurs over an extended interaction length in the undulator but in the far-field zone the emitted radiation can be approximated as the one emitted by a localized source [255]. This source is called a virtual FEL source and its use simplifies the design of beamlines. The calculation of the FEL source parameters requires massive simulations, which were carried out at 12 keV. To calculate the FEL source parameters over the whole photon range a simple analytical model is used. Most of the FEL pulse energy is emitted in the last undulator modules. The electron beam is usually well prebunched and emits strong coherent undulator radiation. Then, the FEL intensity is approximately constant and the virtual source position can be estimated as

$$z_{\text{vir}} = \frac{\int_0^L z\mathrm{d}z \int_0^\infty I_{\text{und}} r\mathrm{d}r}{\int_0^L \mathrm{d}z \int_0^\infty I_{\text{und}} r\mathrm{d}r} \approx \frac{L}{2}\left(1 + \frac{L^2}{6z_R^2}\right). \tag{6.16}$$

Here, I_{und} is the intensity of undulator radiation with a transverse Gaussian distribution and $z_R = 4\pi\sigma_u^2/\lambda$ is the Rayleigh length, σ_u is the rms size of the radiation mode. For coherent undulator radiation [256], $I_{\text{und}} = I_{0,\text{und}}\exp(-r^2/\sigma_u^2)$ and $\sigma_u^2 = \sigma_b^2\left(1 + z^2/z_R^2\right)$, where σ_b is the electron beam size.

The rms size of the virtual undulator source is defined as

$$\sigma_{\text{vir}}^2 = \frac{\int_0^L \mathrm{d}z \int_0^\infty r^2 I_{\text{und}} r\mathrm{d}r}{\int_0^L \mathrm{d}z \int_0^\infty I_{\text{und}} r\mathrm{d}r} = \sigma_b^2\left(1 + \frac{1}{3}\frac{L^2}{z_R^2}\right). \tag{6.17}$$

The virtual source size σ_{vir}^2 scales with the wavelength as $(1 + \alpha\lambda^2)$, where α is a scaling parameter. The divergence of the virtual source is calculated as $M^2\lambda/(4\pi\sigma_{\text{vir}})$, where M^2 is the optical beam parameter.

Figure 6.55 shows the estimated virtual source parameters over the entire CompactLight operation range. There are jumps in the photon beam size because of different electron beam energies and different focusing conditions.

6.2.2.2. Material X-ray Absorption and Damage

An important consideration in the beamline design is the choice of the material of the optical components and the operational angle of incidence on them. Figure 6.56 shows the absorption coefficient for different materials in a range from 0.25 to 16 keV. Because of absorption edges several materials have to be used: (i) gold (Au) for SXR (0.25-2.2 keV) with a critical incidence angle of around 25 mrad;

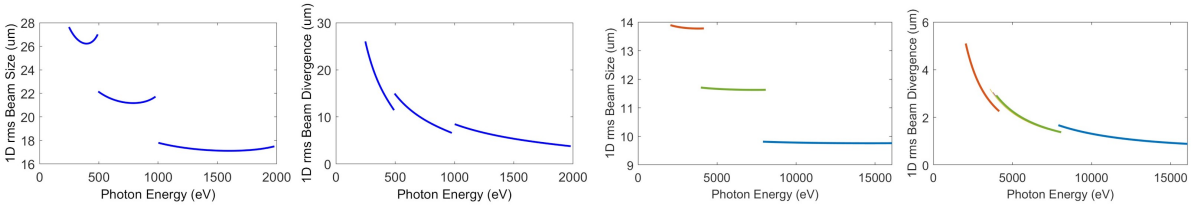

Figure 6.55.: Analytically estimated parameters of the virtual FEL source.

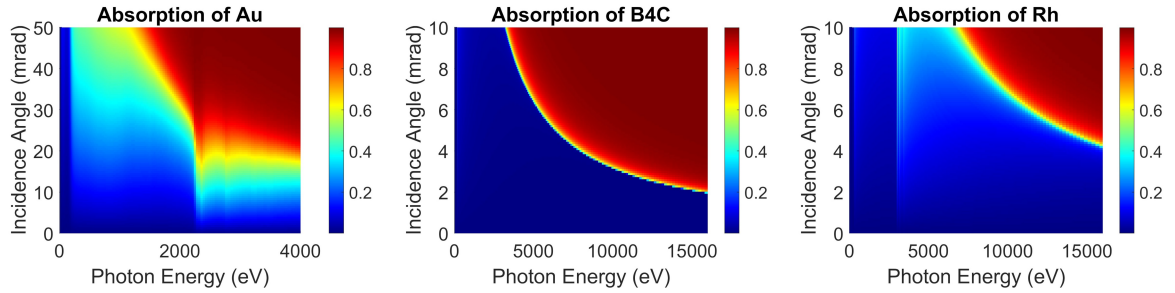

Figure 6.56.: Absorption of materials vs photon energy and incidence angle.

(ii) boron carbide (B_4C) for TXR (2-8 keV) with a critical angle of 4 mrad; and (iii) rhodium (Rh) for HXR (8-16 keV) with a critical angle of 4 mrad. Boron carbide has the lowest absorption coefficient in the entire operation region compared to many other materials. It has also the highest X-ray damage threshold, but simultaneously exhibits a sharp absorption peak at 285 eV due to the carbon edge. In addition, B_4C has a small critical angle at 16 keV. Hence, B_4C is used only for TXR. For transportation and incoupling of VUV pulses for pump-probe experiments, Au is a suitable material.

Some nonlinear experiments require a very clean spectrum without harmonics. For that the incidence angle on KB mirrors can be increased beyond the critical angle of the harmonic. The sample position and detectors must, however, be adjustable to accommodate for a change in the focus position that might reach a few millimetres.

The left plot in Figure 6.57 shows the maximum incident fluence of X-ray radiation that Au, B_4C and Rh can handle depending on the incidence angle and photon energy. Note that the damage threshold considerably increases with photon energy because of the increased attenuation length, i.e. the material becomes transparent and the energy deposition is distributed over a larger volume. The right plot in Figure 6.57 presents the calculation results for the fluence of FEL pulses 50 m away from the undulator. The FEL fluence is on average one order of magnitude below the damage level.

It is noted that the SASE FEL process is stochastic and pulse energies much higher than the mean pulse energy are statistically possible [57]. The statistical analysis of SASE pulses shows that within a ten-year operation period at 100 Hz repetition rate, the statistically possible maximum energy of the FEL pulse may exceed the mean pulse energy by around 50%. However, the resulting fluence would still be one order of magnitude lower than the damage limit. Hence, there is room for increasing the FEL pulse energy in the future.

6.2.2.3. Dual Endstations and Synchronization

Figure 6.58 shows a simplified layout of the electron and optical paths in the CompactLight facility. Consider the synchronization of HXR pulses. From the schematic it follows that the optical delay, Δt_{opt}, partly compensates for the electron delay in the dogleg DL-1. This allows one to write a condition $\Delta t_{DL1} - \Delta t_{opt} = nT$, which determines the required electron delay Δt_{DL1} depending on the number of RF cycles n and an RF period, T, of 166 ps. For 5 RF cycles, $\Delta t_{DL1} = 860$ ps. For the synchronization of SXR either of dog-legs can be used, $\Delta t_{DL2} - \Delta t_{opt} = nT$ and for 3 RF cycles, $\Delta t_{DL2} = 526.5$ ps. For

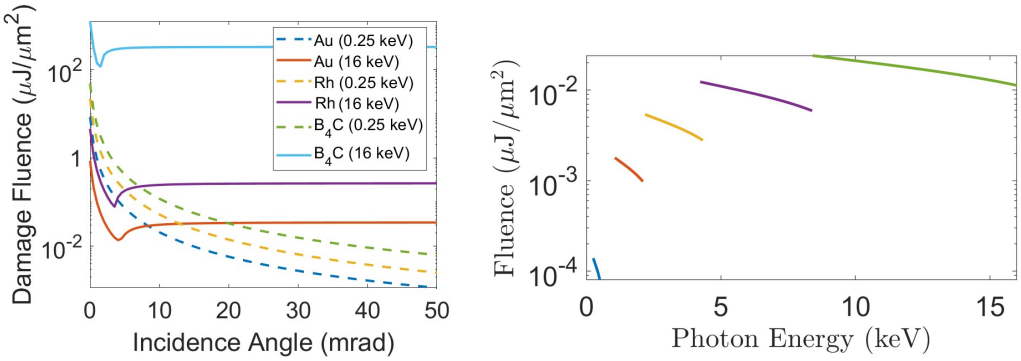

Figure 6.57.: Maximum tolerable fluence vs incidence angle for Au, B_4C and Rh (left plot). The FEL fluence vs photon energy at 50 m away from the virtual source (right plot).

S/TXR, the optical delay increases the electron delay so that $\Delta t_{DL1} + \Delta t_{opt} = nT$. Hence, DL-1 can be used to synchronise photon pulses at all three dual endstations. Meanwhile DL-2 adds additional flexibility of tuning the photon energy range by means of the Linac-4. Any residual differences between the photon pulses will be compensated for with a small timing chicane for electron bunches.

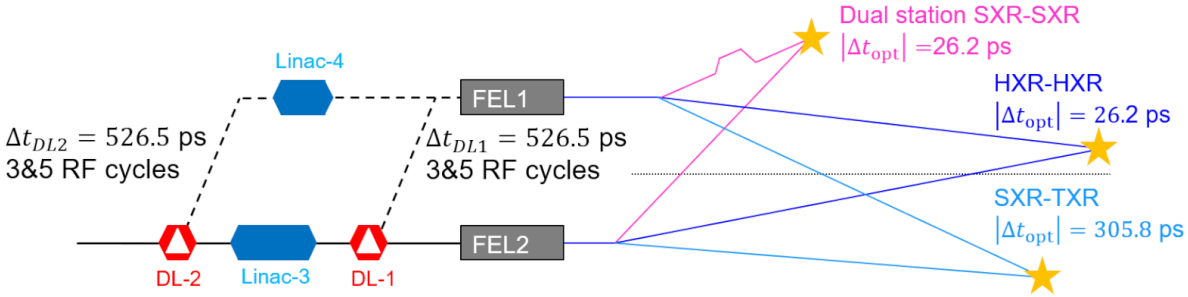

Figure 6.58.: Schematic layout of the accelerator with full upgrade, two doglegs (DL-1) and (DL-2), two undulators, three dual endstation. The relative optical delays are indicated.

6.2.2.4. External Laser Incoupling

For pump-probe experiments with external lasers, pumping capabilities in the IR and VUV regions are foreseen and a high-harmonic generation source in the laser laboratory is planned. While IR pulses can easily be focused on the sample from the side, VUV pulses usually require refocussing and a more complex incoupling scheme. In this design, VUV pulses are incoupled via a holed mirror placed in the X-ray beam path, see Figure 6.53. A sufficiently large hole in the center allows the X-ray beam to pass through and simultaneously sends the oversized VUV beam onto the KB mirrors. In order to balance the losses of the incoupled VUV beam and the transmission of the X-ray beam through the incoupling mirror, the mirror aperture will have a diameter corresponding to 5σ of the maximum X-ray beam size. The VUV-incoupling setup will be located approximately 2 m before the corresponding first KB mirror. In the beamline $B_{2d,S,p}$ the holed mirror will collimate the VUV beam so that its focus matches that of the X-ray beam, which is also collimated.

6.2.3. Soft X-ray Beamlines

6.2.3.1. Grating Monochromator

The central element of the SXR mono beamlines is a monochromator composed of a grating, a monochromator mirror and an exit slit. The CompactLight design makes use of a regular grating combined with a cylindrical mirror focusing in the dispersive plane, Figure 6.59(A). The grating is used in the regime of a constant-deviation mount, i.e. the deflection angle of the grating is independent of the wavelength. This allows the focusing mirror to be kept in a fixed position. The photon energy scan (selection) is done by changing the yaw angle of the grating. In this type of mount, the illuminated grating area changes during an energy scan so that the resolving power also slightly varies. The focal length of the system is independent of the wavelength. Compared to other configurations of the grating type and mount, Figure 6.59(B) and Figure 6.59(C), the mount presented in Figure 6.59A provides the simplest operation. Note that the configuration (C), based on a varied-line-spacing (VLS) toroidal grating, provides almost wavelength independent focusing via a linear chirp of the local grating period. The configuration (C) is widely used in synchrotron beamlines. However, in a wide photon energy range, the effect of wavelength-dependent focusing is noticeable and the position of the slit must be adjusted to compensate for a shift in focus. This makes the configuration (C) more difficult to operate compared with the configuration (A).

Downstream in the mono beamline, the monochromator is followed by a spectral diagnostic unit. A set of KB mirrors is used to refocus the monochromatised beam onto the sample in the mono endstation.

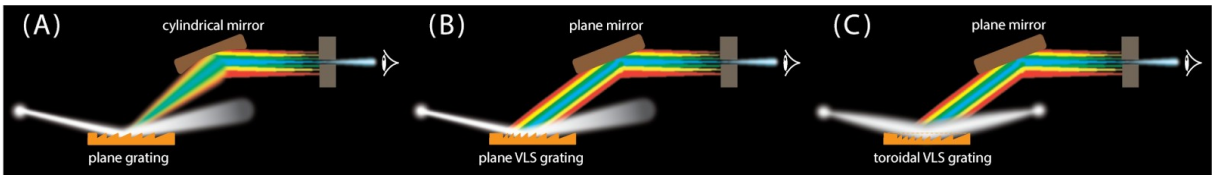

Figure 6.59.: Types and mount of a grating-based monochromator.

6.2.3.2. Photon Beam Parameters on the Sample

The main parameters of the SXR beamlines are summarized in Table 6.15 and Figure 6.60 presents further details of the photon beam parameters for the $B_{1s,S,m}$ and $B_{1d,S,m}$ mono beamlines. Two gratings with line spacings of 50 and 100 lines/mm are used in order to maximize the transmission over the whole photon energy range, while allowing high resolution and limited pulse stretching. By switching from the 50 l/mm grating to the 100 l/mm grating at photon energies above 1 keV, pulse stretching below approximately 100 fs is provided in the 0.25-2 keV photon energy range, while the transmission and resolution are high. In order to further increase the resolution, a grating with a higher line spacing can be used. The gratings have blaze angles of 0.15° (50 l/mm) and 0.2° (100 l/mm) and are roughly 0.5 m long. Note that nowadays blazed SXR gratings as long as 0.5 m can be produced [257].

6.2.4. Hard X-ray Beamlines

6.2.4.1. Photon Beam Parameters at the Sample

Similarly to the SXR beamlines, the main parameters of the HXR beamlines are summarized in Table 6.15, and Figure 6.61 presents two illustrative cases of the performance of the $B_{2d,H,m}$ and $B_{2s,H,p}$ beamlines. A double-crystal monochromator based on a Si crystal cut either in the (111) or (311) orientation is used to cover the operational range from 2 to 16 keV.

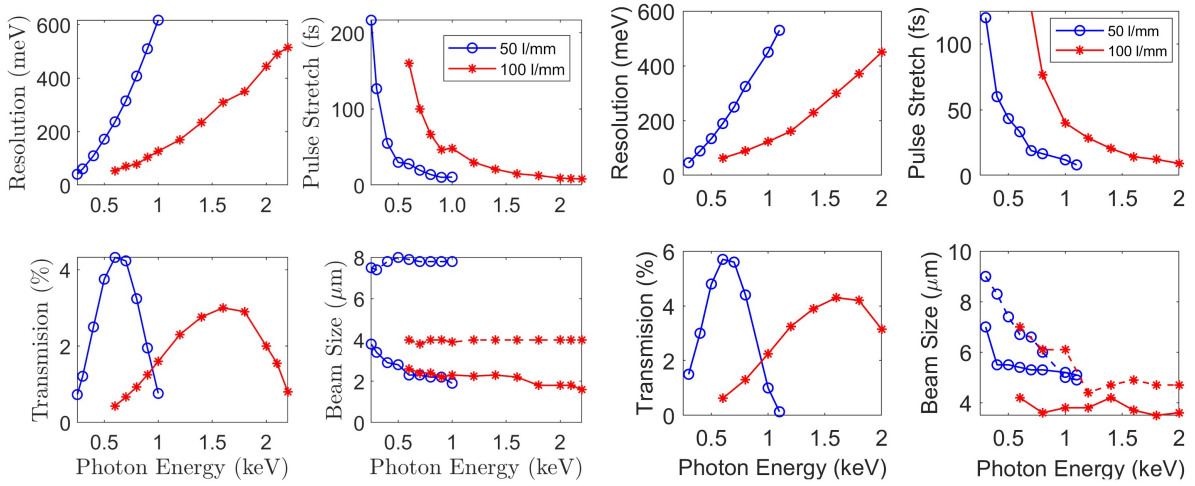

Figure 6.60.: Photon beam parameters on the sample for the $B_{1s,S,m}$ (left) and $B_{1d,S,m}$ (right) beamlines.

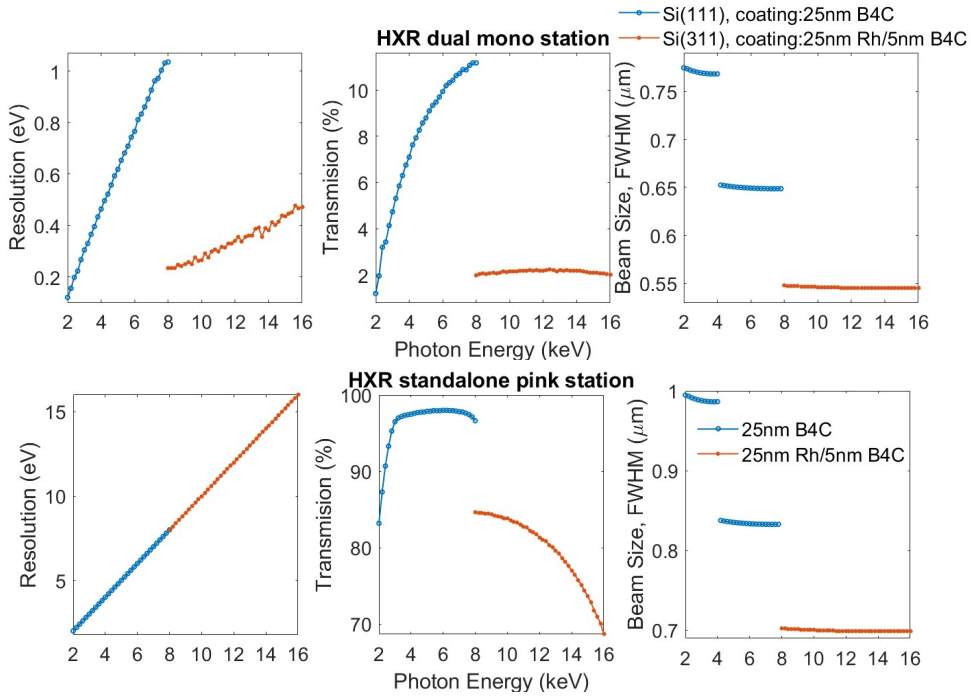

Figure 6.61.: Photon beam parameters on the sample for the $B_{2d,H,m}$ (top) and $B_{2s,H,p}$ (bottom) beamlines. The drop in transmission towards the lower photon-energy range, particularly visible for the bottom figure, is due to clipping of the X-ray mirrors at large beam divergence.

6.2.4.2. X-ray Mirrors

FEL radiation possess a high degree of transverse coherence (typically 90%) and an optical transport system must preserve this coherence. To this end, the optical system must satisfy the Marechal criterion that an overall rms wavefront distortion is smaller than 1/14 of the wavelength of interest. For a transport system composed of N mirrors, the condition for preserving the wavefront is $\lambda/14 = \sqrt{N}2h\sin\alpha$, where α is the grazing incidence angle and h is the rms surface roughness [258]. In the CompactLight design, α is around 15 mrad so that the maximum acceptable peak-to-valley surface roughness is 2.5 nm at 2 keV. For comparison, for the LCLS SXR beamline, the surface roughness requirement is 1.5 nm. For

HXR, the maximum acceptable roughness is 1.24 nm. The simulation results for the intensity reduction due to the surface roughness of a single mirror are depicted in Figure 6.62. The result is somewhat dependent on the mirror coating material. It is noted that, for example at LCLS, thickness uniformity better than 0.14 nm rms has been demonstrated for B_4C coatings on top of a Si substrate [259].

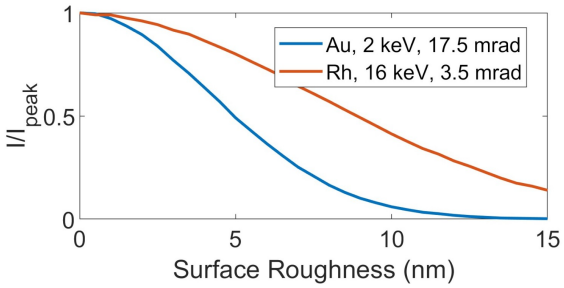

Figure 6.62.: Simulation of the normalized intensity transmitted by a mirror for different heights of surface roughness. The simulations are performed with RAY.

6.3. Photon Beam Diagnostics and Instruments

6.3.1. Overview of Diagnostic Methods

The CompactLight source (XLS) will deliver an X-ray photon beam with wavelength 5 to 0.08 Å (photon energy: 0.25 - 16 keV) and pulse-length 0.1 - 50 fs at repetition rate 0.1 to 1 kHz.

The machine physicists and the experimental users groups will need to know as completely as possible the characteristics of the photon beam. For the machine physicists the information about the FEL radiation will be used for setup, operation and optimization of the accelerator, undulators and X-ray optics during every phase from commissioning to user operation. Similarly, the knowledge of the photon beam properties will be necessary for users for experimental data normalization and interpretation. Consequently, in order to provide the most useful information about the FEL photon beam,

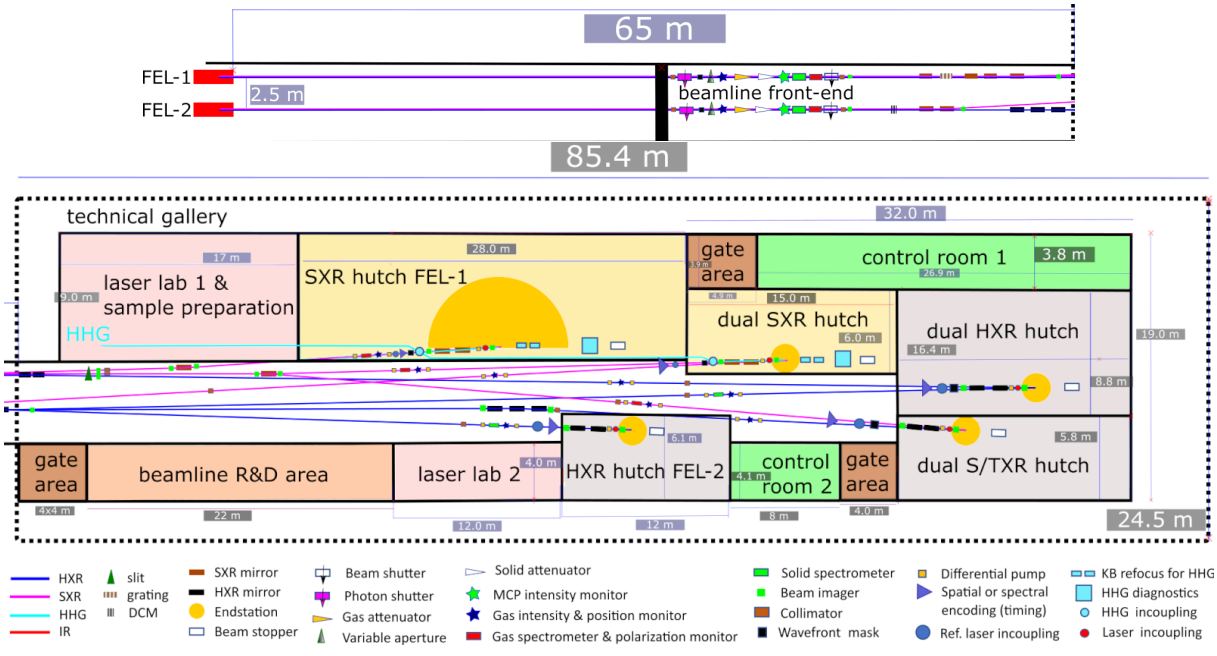

Figure 6.63.: Beamline front-end, experimental area and diagnostics

dedicated diagnostics should be implemented to assess properties such as intensity, position, shape, lateral dimensions and spectrum. A further mandatory request is that the beam properties should be determined on a pulse-to-pulse basis and, whenever possible, in a non-invasive or quasi-non-invasive fashion. Of course, especially at the beginning of the commissioning process and for specific checks and verifications, invasive diagnostics will also be implemented.

Besides the already-mentioned properties that will be characterized and monitored by diagnostics installed all along the photon beam transport (starting from the undulators), other diagnostics will be integrated in the experimental hall, close to the endstations. In particular, temporal diagnostics, devoted to monitor the pulse arrival time, the pulse duration and possibly the temporal shape, will be employed together with wavefront- and coherence-dedicated instruments in the experimental hall. Figure 6.63 shows an overview of the instruments and diagnostics along the beamlines. Most of these can operate parasitically in order to enable online characterization and monitoring of the FEL beam.

After the front-end hall the beamlines split into several branchlines as shown in Figure 6.63 (bottom). The branchlines are equipped with diagnostics suitable for the photon-energy range of the specific branch. An online spectrometer, intensity monitor and positon monitor are included in every mono-branch in order to characterize the FEL beam after passing through the monochromator. An arrival-time monitor is placed relatively close to the endstation of each branch in order to accurately characterize the femtosecond-scale FEL pulses. The arrival-time monitor will use spatial or spectral encoding with a temporal resolution of $\sim$10 fs. Higher Harmonic Generation (HHG) diagnostics are placed after endstations that can couple the FEL and the HHG beam. The HHG beam is coupled out and directed towards the diagnostics station after the endstation using a holed mirror, exploiting the larger spot size of the HHG beam compared to the FEL beam that passes through the hole. Refocusing of the HHG beam after the endstation is obtained by KB mirrors. A Resonant Inelastic X-ray Scattering (RIXS) spectrometer, equipped with a 5 m rotatable spectrometer arm that allows angular resolved RIXS experiments with a resolving power of approximately 10000, is forseen at one SXR beamline.

6.3.2. Intensity and Position

The determination of the intensity of the FEL photon beam (*i.e.*, pulse energy in μJ or number of photons per pulse) is mandatory and, at least during user operation, should be exploited non-invasively and shot-to-shot. To accomplish this task the most important instrument is the X-ray Gas Monitor (XGM), which is used during normal operation. Besides the XGM, other intensity diagnostics can be employed during early stages of machine preparation and optimization, such as MCP-based detectors.

For monitoring of the photon beam position the same XGM can be used, together with invasive diagnostics such as imagers (of several kinds) useful for initial commissioning with spontaneous radiation (synchrotron radiation), for FEL commissioning, or for the setup of measurements.

6.3.2.1. X-ray Gas Monitor

The X-ray Gas Monitor is a gas-based system that operates employing a photoionization process induced by the FEL beam in a gas-filled vacuum chamber [260–263]. The X-ray pulse, travelling through the XGM, ionizes the gas, which is dosed into the vacuum chamber at a base pressure of about 10^{-5} mbar, and photo-electrons and photo-ions are generated and collected. The system, using rare gases (Xe, Kr, Ne) or nitrogen, to cover the X-ray beam wavelength range, is thus practically transparent and indestructible, and is well suited for high average flux and peak energies since there is no damage or heating. Moreover, this diagnostic has no influence on the wavefront and coherence of the transmitted pulses, and can be operated at very high pulse repetition rates (up to MHz).

An XGM consists of at least two vacuum chambers containing one X-ray Gas Monitor Detector (XGMD) each, one dedicated to measure the single-shot-resolved photo-electron signal and the other dedicated to measure the averaged calibrated photo-ion signal. Each chamber also includes also electrodes for measuring the X-ray beam position in one transverse direction: combining two of them (as

in one XGM) then gives the beam position in the transverse plane. As a consequence, individual X-ray pulses with fs-durations containing from 10^7 to 10^{15} photons can be measured with <10 %-absolute accuracy and $\leq$ 1 %-relative (pulse-to-pulse) accuracy. For the same pulses, moreover, it is possible to determine the position in both transverse directions with an accuracy about $\pm 10\,\mu m$ over a range of $\pm 1\,mm$.

Figure 6.64.: CAD rendering of the XGM used at the European XFEL. Figure from [263].

The XGM developed by a joint effort of DESY and European XFEL operates seamlessly up to 12 keV. For higher energies it could be necessary to implement two additional modules to the XGM girder hosting two Huge Aperture open Multipliers (HAMP), which measure the single-shot-resolved photo-ion signal at higher sensitivity for harder X-rays than the XGMDs [263]. Figure 6.64 shows the sketch of the actual XGM used at the European XFEL (including the HAMPs). The implementation of the HAMPs into the CompactLight source will have to be discussed in more detail—the DESY group that developed the XGM are confident that it might not be necessary and the XGMDs would be enough.

6.3.2.2. Imagers

In order to determine the position, trajectory and/or transverse intensity profile of the FEL beam, some invasive diagnostics can be used [263]. This is especially true in the early stages of machine and transport commissioning as well as during beam finding/alignment procedures. Because they are dedicated to different purposes, imagers offer different resolutions, fields of view (FOV) and geometries, and can be located in different part of the facility. Typically, every imager contains at least one Ce:YAG crystal that is viewed through a lens+camera system. Then there are:

- Transmissive imagers: these are put close to the FEL sources and employ thin scintillators in order to allow the beam transmission to another downstream-placed scintillator so to provide beam pointing and beam offset data.
- Spontaneous radiation imagers: these present high photon sensitivity as they are supposed to detect spontaneous synchrotron radiation generated by single undulators during the commissioning phase. In particular, they should be operated together with a monochromator system (K-mono) used to analyze the radiation and measure the angular pointing and the a_w-parameter of single undulator segments.
- FEL imagers: these are used to determine precisely the transverse spatial intensity distribution of the FEL beam, thus providing parameters such as position, size and shape. There will be one for each FEL line.
- Insertable imagers: they are used all along the photon beam transport system to find and align the beam. They should be typically placed after each major optical elements (mirrors, monochromators, etc.).
- Exit slit imagers: they are installed on the exit slit of the monochromator for beam alignment and single-shot spectra acquisition.

6.3.2.3. MCP Based Detectors

During the initial commissioning of the undulators, when all the undulator sections are inserted, this kind of detector can measure the intensity signal from the initial stage up to the saturation regime [263]. It can employ either MCP-discs + photodiode or a MCP-intensified phosphor screen to detect the integrated intensity and help operators in setting up the FEL emission process. Moreover, during normal operation, they can provide pulse-resolved intensity monitoring in a parasitic way: they can be placed just outside of the direct FEL beam and detect a signal coming from the scattered radiation from the mirrors.

6.3.3. Spectrum

The determination of the spectral content of the FEL photon beam is mandatory, and it should be obtained non-invasively, online (during machine operation) and on a shot-to-shot basis. The instruments dedicated to this task are energy spectrometers that should cover the whole wavelength range delivered by the source. To efficiently cover it three different spectrometers are envisioned, ranging over the following intervals: 0.25 - 3 keV, 2 - 4 keV, and 3 - 16 keV.

6.3.3.1. Photoelectron Spectrometer (0.25 - 3 keV)

To cover the lower energy part of the FEL emission, a photo-electron spectrometer (PES) can be used [264, 265]. This instrument can measure the spectrum (and polarization) of the photon pulse based on an angular resolved time-of-flight measurement of photo-electrons. In particular, to be non-invasive, it uses a low-density gas target that is ionized by the passing photon pulse, generating ions and electrons that are collected and linked to the pulse intensity. The collection is realized by means of 16 electron time-of-flight (TOF) spectrometers oriented perpendicularly to the X-ray beam (see Figure 6.65).

Each TOF spectrometer has a drift-tube with tunable voltage that decelerates the electrons. The (fast) electronics measures the time difference between ionization and detection which is dependent on the photoelectron kinetic energy. The ionization takes place in a gas medium, which can be either a rare gas (Ne, Kr, Xe) or N_2, which is injected into the interaction volume via a capillary. By using these

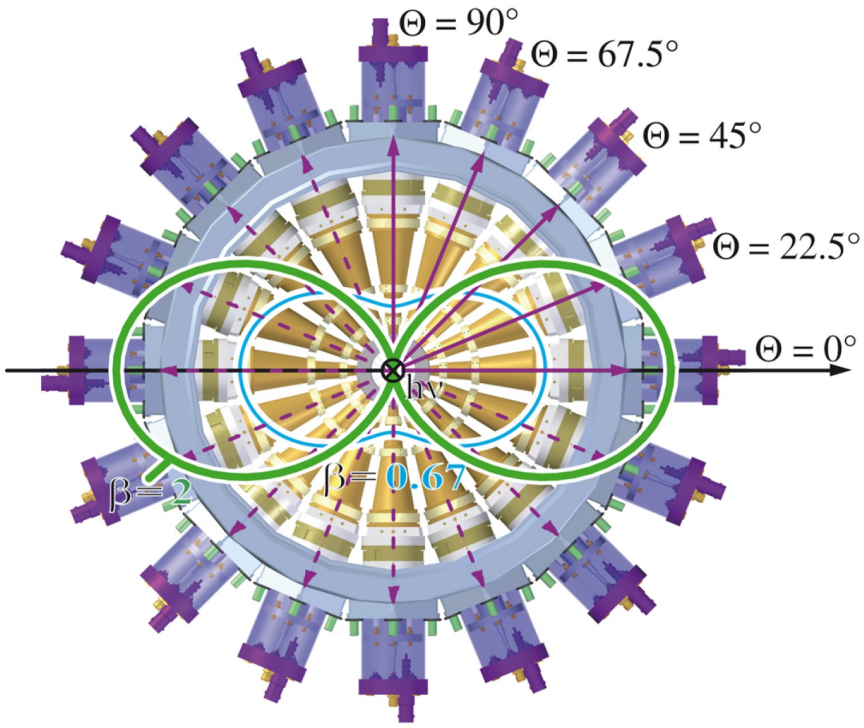

Figure 6.65.: Geometry of the 16 TOF spectrometers employed in the PES. The FEL beam enters perpendicularly with respect to the plane of the figure. As an example, the angular distributions of Ne 2p (blue) and He 12 (green) are reported. Figure from [265].

gases it is possible to cover the 250 - 3000 eV X-ray region with enough cross-section for single-shot measurements, low photoelectron kinetic energies assuring good energy resolutions, and the ability to efficiently measure the polarization. The injection pressure of the gas is typically in the 10^{-5} - 10^{-7} mbar range, while the base pressure is about 10^{-8} mbar. These values guarantee the near transparency of the instrument with respect to the passing FEL beam. Finally, the PES is capable of determining the spectral content with a relative photon energy resolution of 10^{-3} - 10^{-4}.

Besides the spectrum characterization, since the 16 TOF spectrometers of the PES can determine the photoelectron angular distribution, the PES can also non-invasively measure the (linear) polarization in a pulse-resolved way.

6.3.3.2. Tender X-ray Spectrometer (2 - 4 keV)

The so-called tender X-ray range (from 2 to 4 keV) can be characterized with a spectrometer currently used at SwissFEL (PSI) [266]. The instrument is based on a dispersive von Hamos geometry-spectrometer combined with the use of a scattering sample to be inserted into the FEL beam. The sample, being a low atomic number and density material, once hit by the photon beam gives rise to an elastic Rayleigh scattering spectrum that replicates the incoming FEL pulse spectrum. The sample should be thin enough to guarantee the maximum possible transparency to the FEL beam and absorption edges should be avoided in the scatterer. Figure 6.66 shows the working principle and mechanical scheme of the spectrometer. The setup presents a single interaction point with the FEL beam and the generated photons are scattered over a large angle hitting an optical element made by a cylindrically bent substrate that has Si crystals glued on it. Working in a back-scattering geometry, the spectrometer can collect enough signal and determine the FEL spectrum with 10^{-4} energy resolution and a 2 % bandwidth.

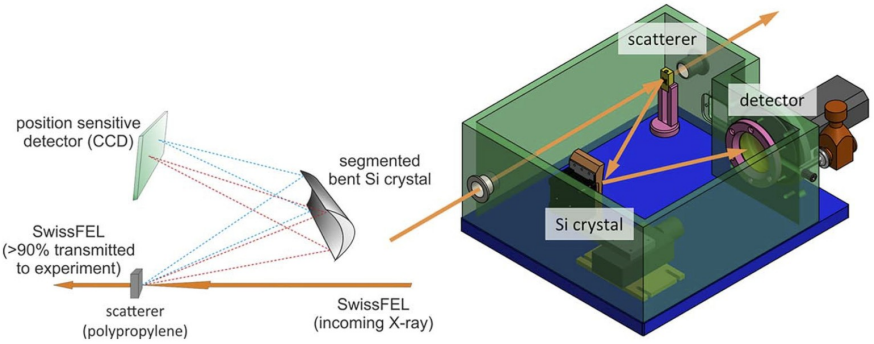

Figure 6.66.: Scheme of the von Hamos spectrometer used for the diagnostics of tender X-rays at the SwissFEL. Figure from [266]

6.3.3.3. High Resolution Hard X-ray Spectrometer (3 - 16 keV)

In the hard X-ray range of the FEL emission, above 3 keV, a different energy spectrometer should be employed, based on a system of elements that utilize just a small fraction of the photon beam to determine the spectral content. Such an instrument, called a HIgh REsolution hard X-ray single-pulse diagnostic (HiREX) spectrometer at the European XFEL [267], is made of a diamond diffraction grating used in transmission to split off a small fraction (0.1 %) of the photon beam, a bent crystal as a dispersive element, and a 1D MHz-repetition rate detector. The working principle is sketched in Figure 6.67. Typically,over the whole range of operation of this spectrometer, about 95 % transmission is achieved, while five percent is spread into all diffraction orders.

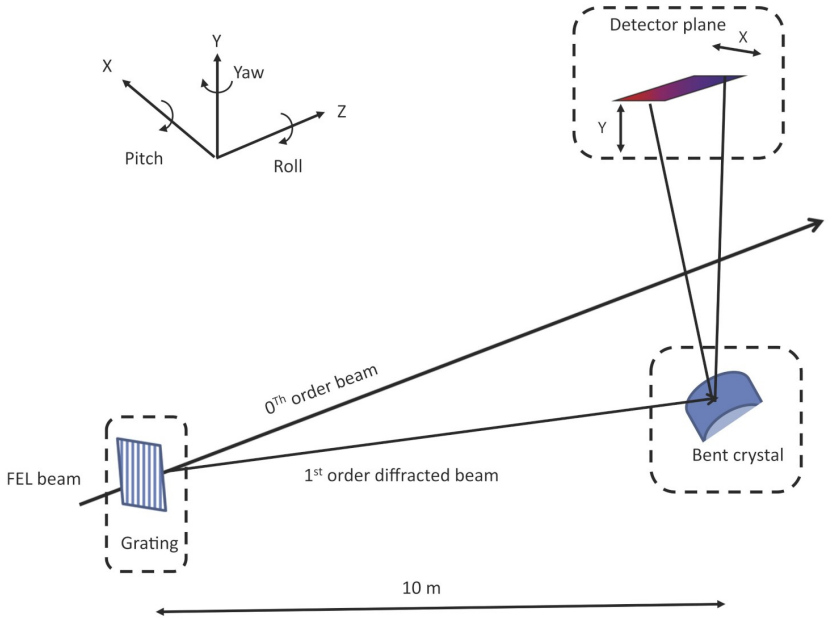

Figure 6.67.: Schematic of the HIREX spectrometer at the European XFEL. The grating lines are oriented in the vertical direction perpendicular to the FEL so that the diffraction takes place in the horizontal plane. The bent crystal, then, deviates the radiation vertically onto the detector. Figure from [267].

The initial diffraction of the FEL beam is realized by a diamond transmission grating that is inserted

directly into the beam, splitting a portion of it while leaving the transmitted beam almost unchanged for the experiments in the endstations. In order to cover efficiently the entire photon energy range a set of gratings has to be used with different pitches. Diamond is chosen as the material for grating fabrication as it presents high thermal conductivity (2052 W/mK at 300 K), low absorption for hard X-rays, and higher single-shot damage threshold as compared to silicon.

Once the first diffraction order has been generated, it hits a bent silicon crystal where it is Bragg-reflected and thus dispersed spectrally. To cover the whole photon energy range different crystals with different bending radii are employed, which are then optimized to match the detecting camera parameters (pixel size, detector chip dimension, and detector distance).

The overall performance of such spectrometer includes a transmission of about 95 %, energy resolution in the 10^{-5} range and a bandwidth of 0.5 %, working on a shot-to-shot basis during normal operation.

6.3.4. Temporal Monitors

Precise determination of the X-ray pulse arrival time is necessary for accurate analysis of pump-probe experiments as it allows one to compensate for the temporal jitter of the SASE pulses. In addition, characterization of the pulse duration can be useful for obtaining the X-ray pulse peak intensity, which is of importance, e.g., for nonlinear experiments. Table 6.16 provides a comparison of different methods for temporal characterization of FEL pulses. All these methods have already been demonstrated at other FEL facilities. The streaking techniques are relatively complicated methods that require overlapping an IR or THz pulse with the X-ray pulse in a gas. The X-ray generated photoelectrons experience different E-fields depending on the relative delay between the IR/THz fields and X-ray pulses, which results in a varying kinetic energy with the delay. Thus, the delay, as well as the pulse duration, of the X-ray pulse can be obtained by measuring the photoelectron kinetic energies. Angular streaking uses circularly polarized streaking fields, which permits higher temporal resolution because the pulse delay is imprinted in the angle of the ejected photoelectron. In contrast, spatial and spectral encoding are less complicated methods in which the X-ray induced reflectivity change of an optical pulse, overlapping with the X-ray pulse on a solid sheet, is measured. In spectral encoding the delay between the pulses is encoded in the spectrum of a chirped optical pulse, while spatial encoding relies on the varying delay along the beam cross-sections of two beams at an angle.

In the baseline design the X-ray pulse arrival time will be measured using spatial and spectral encoding. Both of the methods have advantages and disadvantages and it is common to implement them both for better accuracy and reliability as done, for example, at the SACLA FEL. Since the arrival time will be measured for all beams individually, nearly overlapping pulses from two beams entering a dual station can be resolved, and therefore the possibility of resolving double-pulses, offered by streaking experiments, is not critical. Streaking experiments may however be included as a future upgrade as a tool to monitor the pulse profile. In the baseline design the XLS pulse duration will be obtained indirectly. The measured parameters of the electron beam such as the emittance, current and duration will be fed into a computer program simulating the XLS performance and calculating the XLS pulse duration. Such an approach was taken at the SACLA FEL before their implementation of THz streaking. The subsequent comparison of the FEL pulse duration from the THz streaking measurement results, and from the simulation results based on experimental measurements of the electron beam, showed a very good agreement. Hence, one can expect the indirect approach to work also for CompactLight.

6.3.5. Other elements

6.3.5.1. Wavefront Monitors

The wavefront of the X-ray beam is subject to shot-to-shot fluctations associated with the statistical FEL process and with changes in beam alignment on the optics that occur every shot, or as drifts.

Table 6.16.: Overview of methods for temporal characterization of X-ray pulses. The left column lists the names of the methods described in the references specified in the last column. The second column lists the measured rms accuracy of the arrival time of X-ray pulses with respect to the reference laser pulse. The third column gives the rms resolution of the pulse duration measurement when this is applicable. The fourth column specifies the time window, in which the arrival time and pulse duration of X-ray pulses can be measured. This time window is defined by the reference laser pulse duration and is the full length of the measurement interval, in which the specified accuracy can be achieved. The fifth column specifies capabilities for measurements of double FEL pulses with the same photon energy and for measurements of FEL pulses with different photon energies called two-colour pulses. The dash in the cell implies that the measurement capability is not available. The principle of these methods is generally applicable to both soft and hard X-rays, however, VMI streaking has only been demonstrated for soft X-rays.

Method	Arrival time, accuracy (fs)	Pulse duration, resolution (fs)	Measurement interval (ps)	Double pulses, accuracy (fs)	Ref.
Spatial encoding	1.5	-	2	-	[268]
Spectral encoding	4.5	-	3	-	[269]
Spectrogram	<1	-	4	-	[270]
THz streaking	10	10	0.5	25	[271]
IR angular streaking	1	0.25 (0.1 for double pulses)	0.34	1	[272]
VMI streaking	< 50	0.1	0.3	-	[273]

The wavefront quality affects the shape and the minimum size of the focussed beam at the sample. Therefore, it is useful to be able to characterize the wavefront as part of the FEL optimization and optical alignment procedure. These monitors will be placed in the front-end before all other optical components in order to measure the direct output from the FEL, and just before the KB mirrors to observe the influence of the optics.

A simple and highly accurate wavefront-sensor setup operating on single-shot basis has recently been developed, (see Figure 6.68) [274]. It is based on Talbot interferometry, which exploits the phase sensitivity of the Talbot effect, i.e., self-images of a coherently irradiated periodic structure occuring in the near-field. By using a single grating and detecting the Talbot image on a scintillating screen, high quality measurements can be obtained. The demonstrated sensitivity and accuracy are both at the level of $\lambda/100$.

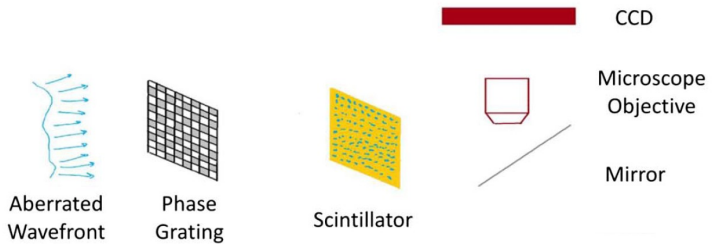

Figure 6.68.: Sketch of a setup for a sensitive wavefront measurement based on single-grating Talbot interferometry [274].

Table 6.17.: Summary of the beamline diagnostics including their approximate accuracies.

Diagnostic	**Type**	**Accuracy**
Intensity and position monitor (parasitic)	X-ray gas monitor detector [260–263]	1% rel. intensity, 10 μm
Spectrometers (parasitic)		
0.25-3 keV	eTOFS (cookie box) [264, 265]	10^{-3} - 10^{-4}
2-4 keV	Bent crystal [266]	10^{-4}
3-16 keV	Bent crystal [267]	10^{-5}
Polarization monitor (parasitic)	Cookie box [264]	10^{o}
Arrival-time monitor (parasitic)	Spatial and spectral encoding [268, 269]	10 fs
Beam profile and position monitor (destructive)	YAG screens [263]	10 μm
Wavefront sensor (destructive)	Talbot interferometer [274] or Hartmann sensor [275]	λ/100 λ/10

6.3.5.2. Beam Shutters and Stoppers

Beam shutters are part of the personnel safety system that prevents radiation from the FEL entering a downstream hutch where access is permitted. The beam shutters will be composed of a B_4C layer in front of a thicker tungsten block. The B_4C layer blocks the soft X-rays and the tungsten blocks the hard X-rays. Upstream of all optical components there will also be a photon shutter of B_4C that can quickly be inserted when moving optics in and out in order to protect them from harmful soft X-rays. Beam stoppers are similar to beam shutters but are permanently placed typically at the end of a beamline to stop the beam. Burnthrough monitors are connected with the beam shutters and stoppers in order to be able to shut off the FEL in case of failure to block the beam.

6.3.5.3. Slits and Collimators

Slits and collimators limit the transmittance of the spontaneous radiation, which has a large angular spread, and thus predominantly filter out the FEL beam. Like the beam shutters they have to tolerate the full FEL power and will have a similar layer structure.

6.3.5.4. Attenuators

Attenuators that permit adjustable reduction of the X-ray flux will be installed in the front-end. Different designs are required for the SXR and HXR beamlines. The SXR beamlines will use a gas attenuator. It comprises a gas volume set to specific pressures to reduce the X-ray flux, and differential pumping on each side. The apertures of the gas volume and the differential pumping need to be sufficiently large to transmit 5σ of the beam size. For hard X-rays the gas attenuator becomes ineffective. Instead the HXR beam will be attenuated by solid samples of e.g. B_4C or Silicon with a thickness adjusted to the desired attenuation level. The attenuating crystals need to be of sufficient quality with respect to density uniformity and thickness variations across the beam in order not to degrade the wavefront.

6.4. Experimental Hall

6.4.1. Layout of the Experimental Area

The beamline branches end up in separate hutches in the experimental area, shown in Figure 6.63. The experimental area also hosts the laser labs that produce the IR and VUV pulses used for pump-probe experiments, gate areas for bringing in large equipment, and control rooms. The control room areas are sufficiently large so that they can accommodate one control room for each endstation. The three gate areas are located as to enable easy transport of equipment to the hutches and to the beamlines. Transverse cranes in the ceiling can also move components along the beamlines.

6.4.2. X-ray Hutches and Endstations

The endstations are marked with yellow circles or half-circles in Figure 6.63. The radius of the circles is 1 m to indicate the required space around the endstations. The half-circle represents the available space for the spectrometer arm of the RIXS instrument, which is $\sim$5 m long and can be moved almost 180 degrees. There is space in the X-ray hutches to fit equipment such as electronics racks and computers, and some beamline components before and after the endstations. The endstations comprise both the standard single stations dedicated to one FEL beam, as well as, dual station that can couple in two FEL beams. The new scientific applications offered by the dual stations is described in section 3.1.3.

6.4.3. Laser Laboratories

Two laser labs are forseen committed to the beamlines of each FEL. The laser labs house the IR lasers that can be used for IR pump/X-ray probe experiments. VUV laser pulses can also be produced by HHG in laser lab 1. This hutch will have additional space for sample preparation.

6.4.4. Timing and Synchronisation

Synchronization between the external, IR or VUV, lasers and the X-ray FEL pulses is crucial for pump-probe experiments. In such measurements a synchronization level below the FEL-pulse duration is typically desired in order to avoid a significant influence of the timing jitter between the external and FEL pulses, on the temporal resolution. The total timing jitter results from both electron bunch arrival time jitter and external-laser to optical master oscillator jitter. An overall synchronization level on the order of 10 fs has been demonstrated at present FELs [276].

7. Civil Engineering

7.1. Buildings and Infrastructure

The CompactLight facility building consists of different sub-buildings, and sections for accommodating the different accelerator parts and corresponding infrastructure. The names of the different main building sections correspond to the different parts of the electron and photon beamline following the naming scheme proposed below:

Table 7.1.1.: XLS Building Naming convention with indicative dimensions.

Name	Length (m)	Width (m)	Height (m)
Linac Tunnel/Undulator Hall	329	4.0/8.5	3.2
Infrastructure Hall	329	7.0/11.0	5.5
Experimental Hall	154.6	5.9/24.9	4.0
Total:	483.6		

The design follows a hybrid approach with the underground Linac Tunnel separated from the Infrastructure Hall with shielding blocks. The facility building has total length of approximately 484 m (7661.59 m^2) with an increased width downstream to accommodate the future machine upgrades, the two undulator lines and Experimental Hall. Figure 7.1.1 presents the 2D drawing of the building with estimated indicative dimensions. Figures 7.1.2, 7.1.3, 7.1.4 present ISO and top 3D views of the total facility.

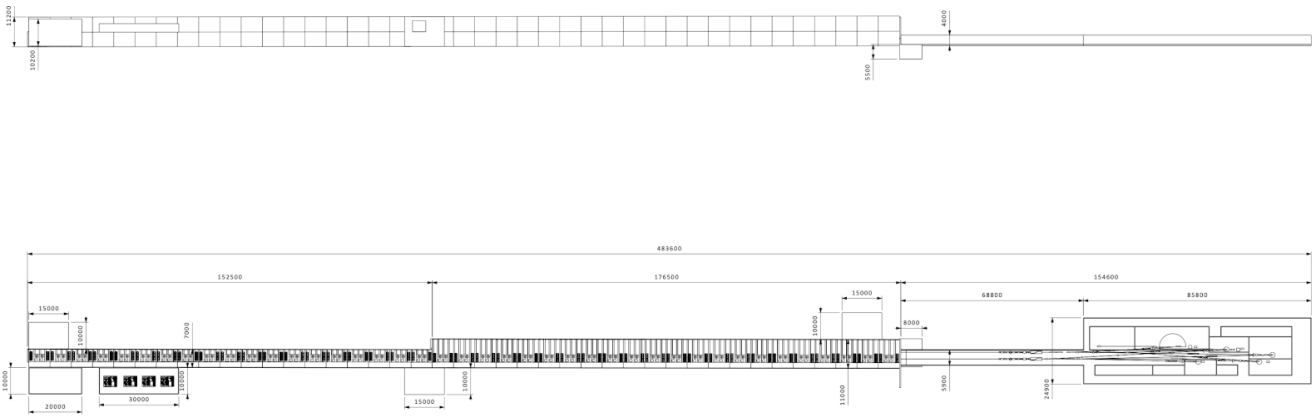

Figure 7.1.1.: 2D side and top view of XLS building facility with indicative dimensions (Scale 1:350)

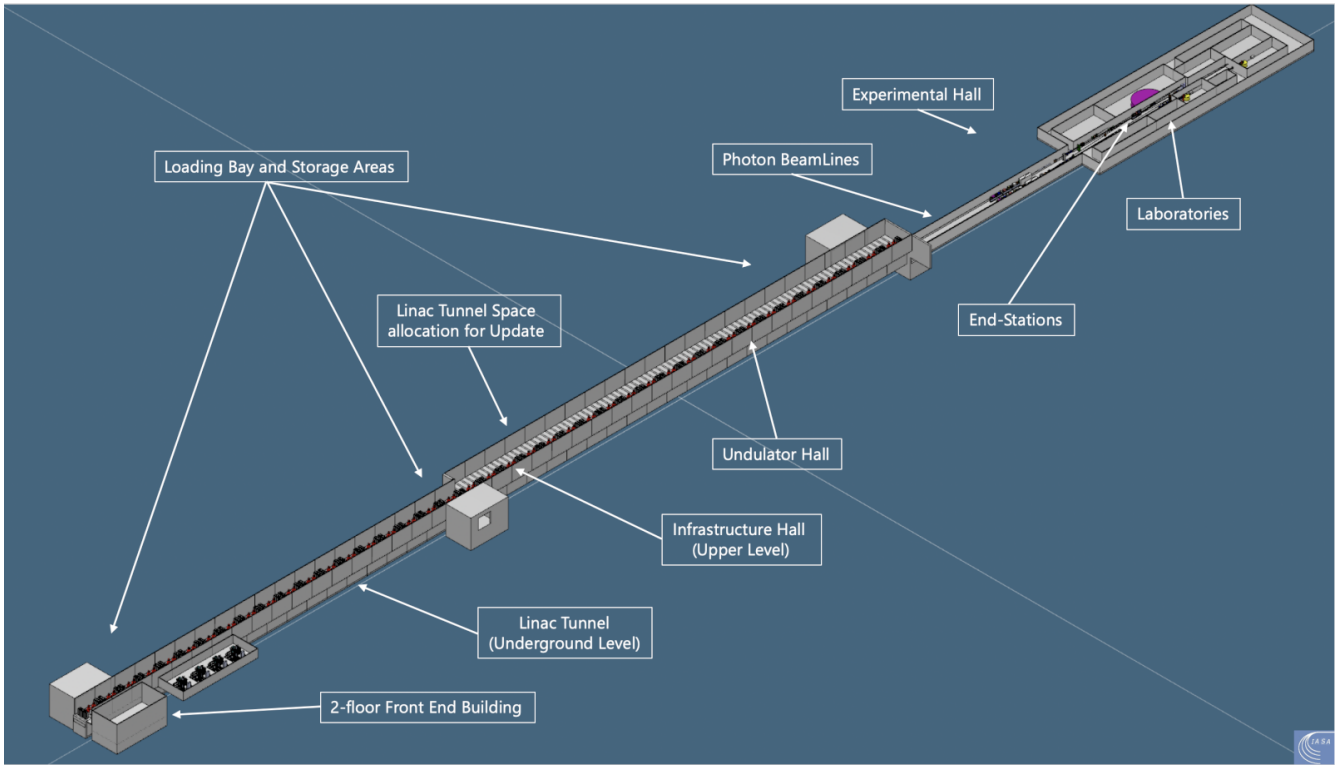

Figure 7.1.2.: ISO View of the XLS facility with the proposed buildings Naming scheme. Facility building is depicted with the shielding blocks covering the Linac Tunnel.

Figure 7.1.3.: Top View of the XLS facility.

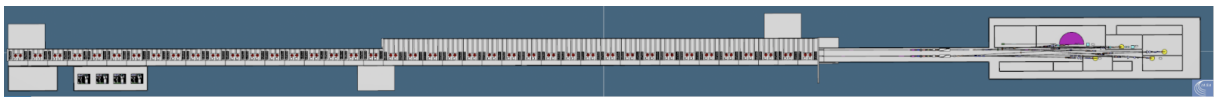

Figure 7.1.4.: Top view of the Infrastructure Hall, Linac Tunnel and Undulator Hall with the shielding blocks removed revealing the linear accelerator.

The design incorporates a 2-floor (200 m^2 each floor) front-end building at the beginning of the Linac Tunnel that can be used as Control Room/Offices, Rack space and Laser/Photocathode/Gun laboratory. The Linac Tunnel section consists of a tunnel of 4m width, allowing 2m for a transportation corridor on the right hand side, 1m for the electron beamline, 1m for piping, waveguides and cable trays on the left hand side and 3.2 m of height. The electron beam axis is situated 1.5 m from the left-side wall of the tunnel (Figure 7.1.5). The linac tunnel is covered with cement blocks in T-inverted T configuration for shielding purposes. The T-shaped shielding blocks, with short and long versions, weigh less than 40 tons each (Figure 7.1.6 shows the short version), permitting a flexible and modular construction, blocking direct line of sight, and can be modified using the double 10 tons crane installed at the top of the building.

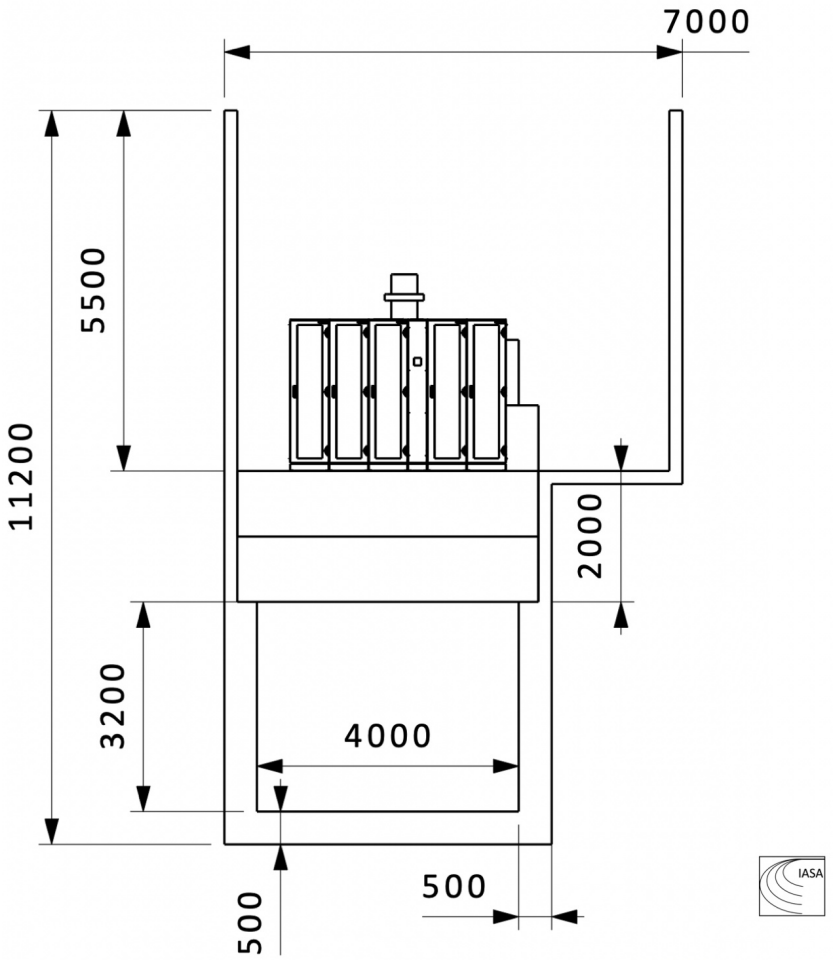

Figure 7.1.5.: Cross-section drawing of the Linac Tunnel and Infrastructure Hall.

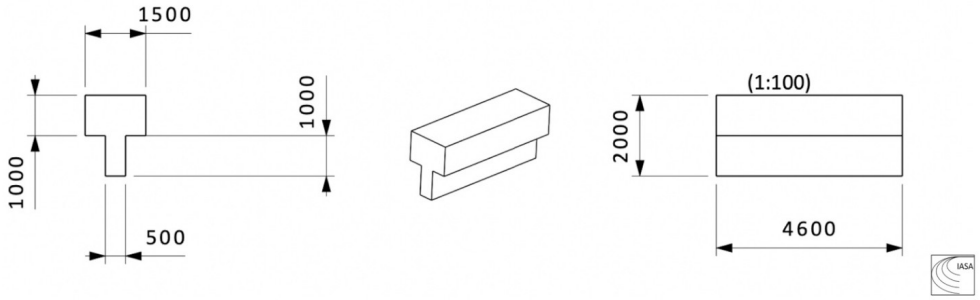

Figure 7.1.6.: Design of the T-shaped shielding block covering the 2-beam line part of the tunnel.

The Infrastructure hall is 7m wide and accommodates the Klystrons (50), Modulators (50), Electronic Rack rows ($\sim$320) and the necessary space for the routing of waveguides, pipes and cable trays to accelerator components through direct penetrations to the tunnel. The number and configuration of the RF modules selected takes into account the RF design for C-band cavities (one klystron per four structures) and X-band cavities (two klystrons per four structures). Figure 7.1.7 shows a close-up view of the infrastructure hall. As mentioned, the left hand part of the Linac Tunnel can be used for the connection of waveguides, cables and pipes to the components. Waveguides and pipes can be

routed through direct penetrations placed in the left-side wall of the accelerator tunnel and in trenches on the floor of infrastructure hall. Cables can be routed in cable trays above and/or below the racks in similar floor depressions or trenches perpendicular to the beam line axis (Figure 7.1.7), ensuring adequate signal separation, and guided to the tunnel through the same direct openings. The area of the Infrastructure Hall close to the right wall can be used for the electrical distribution system, routing the power cables from substation buildings (not presented currently in the design) to the modulators and racks.

The primary water circuit piping can be routed from the facility water building using the right side of the Infrastructure Hall area and from there to the tunnel components water manifolds using the direct penetrations. Furthermore, for storage, preparation and transportation of goods and components in and out of the tunnel and Infrastructure Hall, three ground-level loading bays are foreseen close to the electron gun and undulator areas. Components can be unloaded from trucks, stored in these areas and moved to the tunnel using drop hatches.

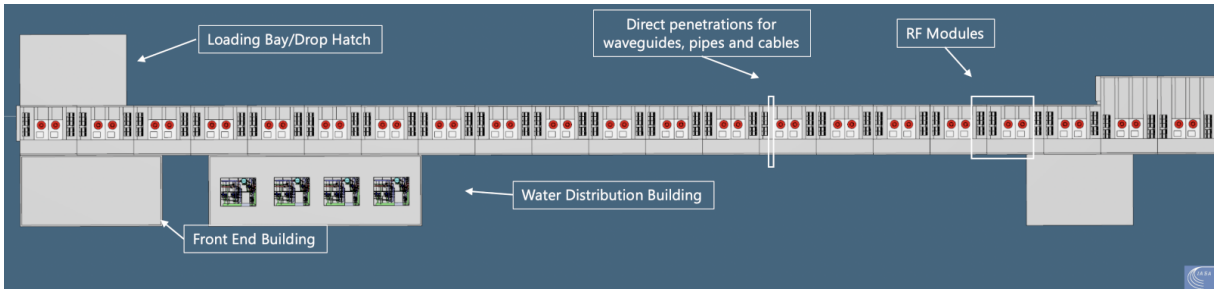

Figure 7.1.7.: Top view of the Infrastructure Hall with the trenches for waveguides, pipes and cables.

Downstream of Linac 2, the width of the tunnel and infrastructure hall increases to accommodate the future XLS update 2.0 (Linac4 and SXR bypass line) and the two undulator beamlines (Undulator Hall section) (Figure 7.1.8). After the undulators the electron beam can be vertically diverted and guided to the double beam dump comprised of copper cores embraced with radiation shielding (Figure 7.1.9). The total area of the Linac tunnel until the end of undulator line is 2110.25 m^2 and for the Infrastructure Hall 3009 m^2.

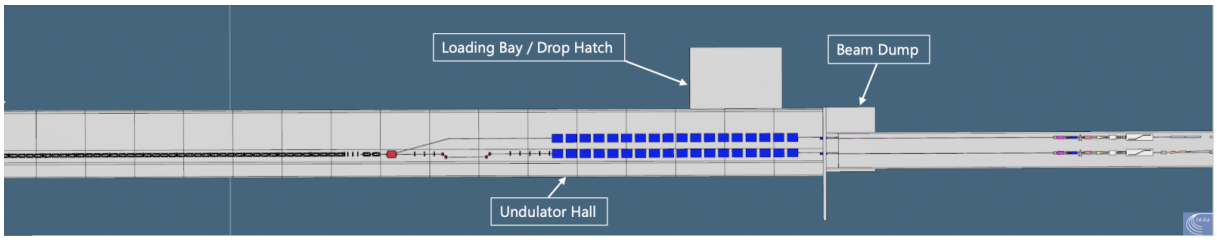

Figure 7.1.8.: Top View of Linac3, Undulator Hall and beginning of the Experimental Hall Area. The tunnel is enlarged in parallel to Linac3 to accommodate future upgrades.

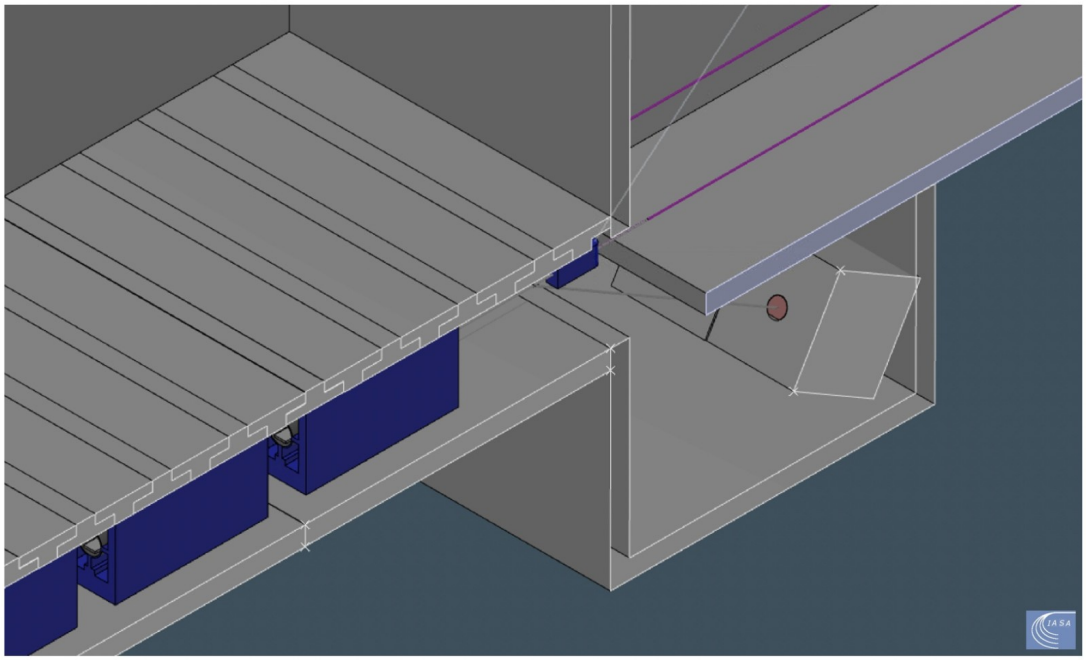

Figure 7.1.9.: Cross-section view of the dogleg area and beam dump.

The Experimental Hall (2542.34 m^2)(Figures 7.1.10, 7.1.11) contains the photon beam lines with front-end diagnostics, shielded user end-stations, laboratories and auxiliary spaces. Space is allocated for a laser laboratory, a magnetic laboratory, a loading bay and assembly room and user laboratories. The design of the facility building will be further updated according to radiation shielding requirements and introducing any necessary sub-buildings

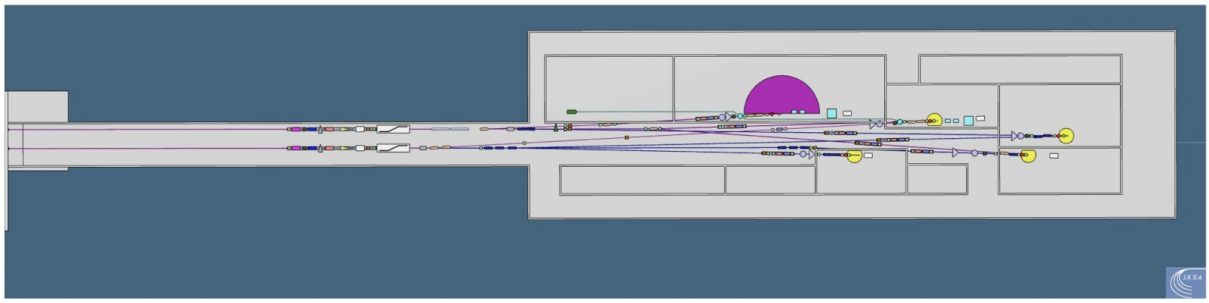

Figure 7.1.10.: Top View of the Experimental Hall with the segregated sections configuration and the end user stations.

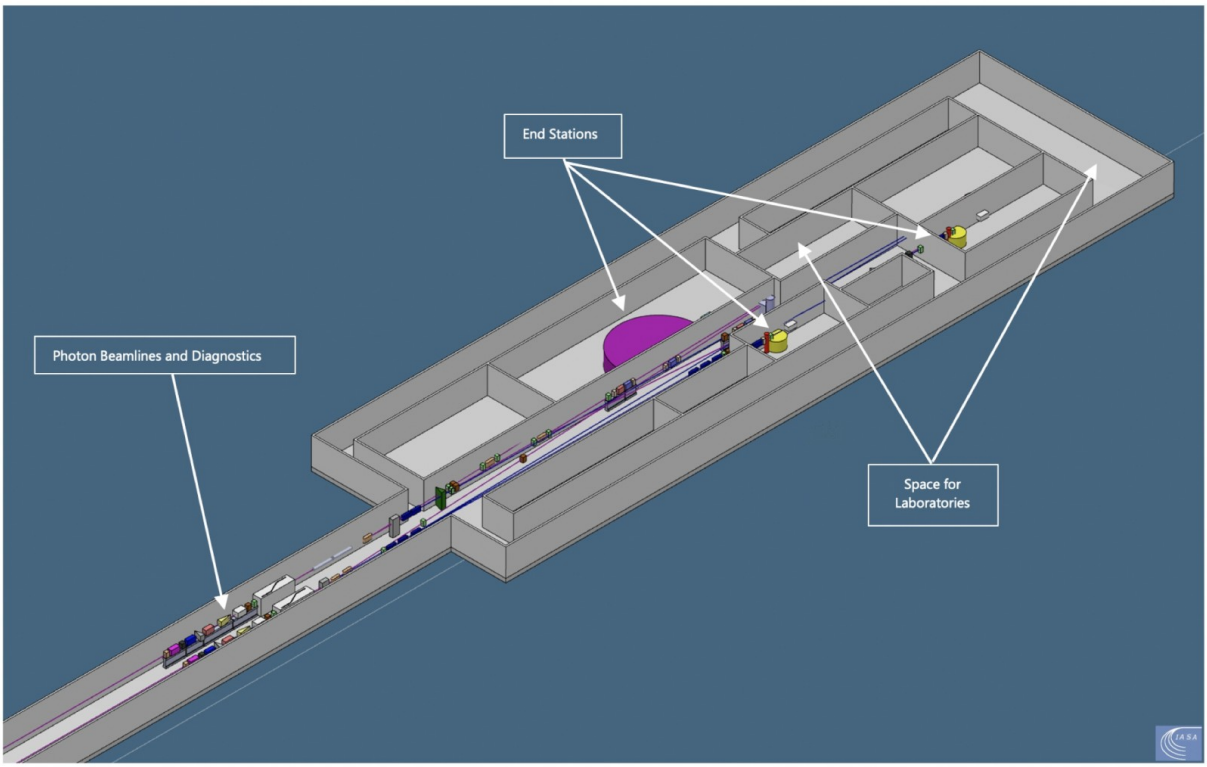

Figure 7.1.11.: ISO view of the Experimental hall area.

7.2. Accelerator Layout

7.2.1. Gun and Injector Layout

The 3D CAD model covers design, development and relevant sequencing from the beginning of the design phase and up to installation, assembly, commissioning and operation, obtained with a methodology which is based on processing from physical to engineering parts of the injector via verification, validation and traceability. Maintenance aspects will be addressed in the future.

The layout is divided in separate Modules for each sub-assembly of the injector. The Modules are defined as sub-assemblies that can undergo stand-alone commissioning. The Modules are numbered in tens so that new Modules can be inserted if needed in the future without changing the numbering scheme. The 3D CAD model has been designed with the help of commercial CAD s/w (CATIA) and in sequence based on the consolidated baseline reference of the provided injector layout.

Figure 7.2.1 shows the general layout of the injector 3D CAD model and Figures 7.2.2, 7.2.3, 7.2.4, 7.2.5 and 7.2.6 show close-up views of the designed components. The first part is a 2.5 cell RF gun with a solenoid (design provided by INFN) and 0.7m of space reserved for diagnostics such as two BPMs and correctors, viewport and ICT (Figure 7.2.3). Subsequently, the injector is comprised of four C-band travelling-wave cavities of 120 cells with solenoid magnets on the first one, a laser heater and then Linac0 follows with additional six C-band modules, K-band linearizers, the bunch compressor BC1, the X-band deflector and quadrupole focusing magnets (Figures 7.2.5, 7.2.6).

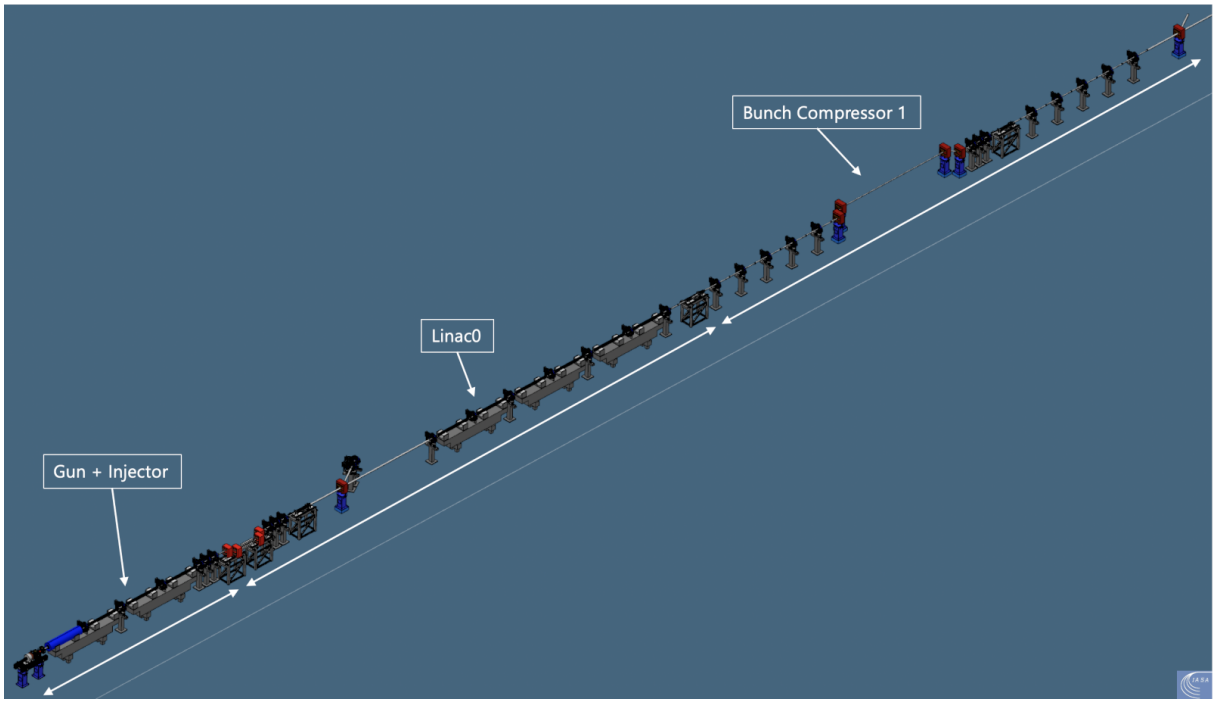

Figure 7.2.1.: The 3D CAD layout of the injector, Linac0 and Bunch Compressor 1 area.

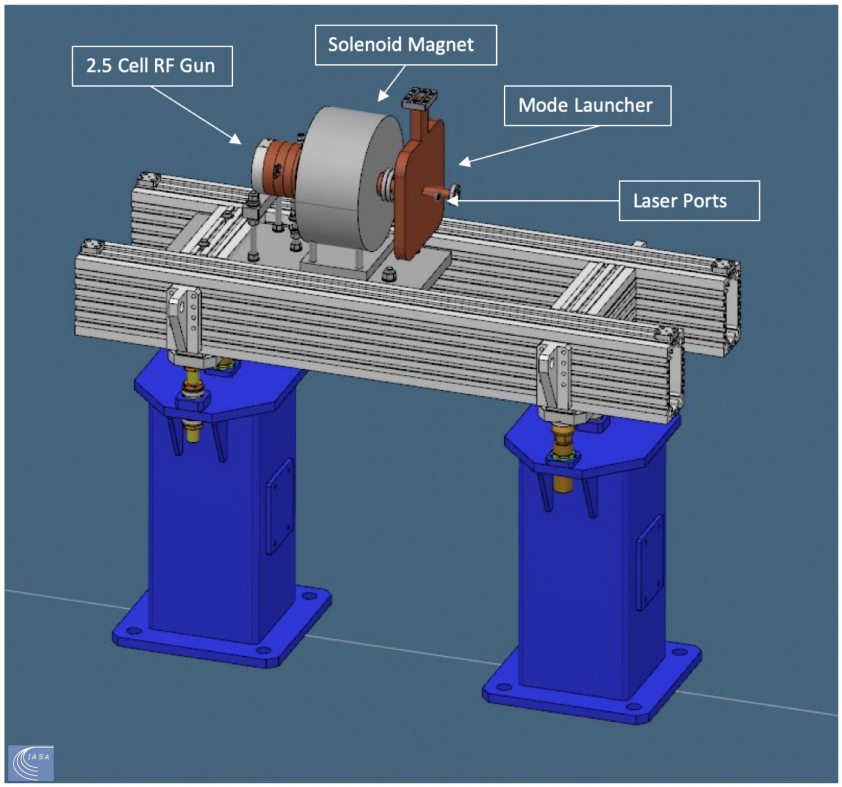

Figure 7.2.2.: 2.5 Cell C-band gun parameters and 3D design , with solenoid , mode launcher ,laser ports and supports provided by INFN.

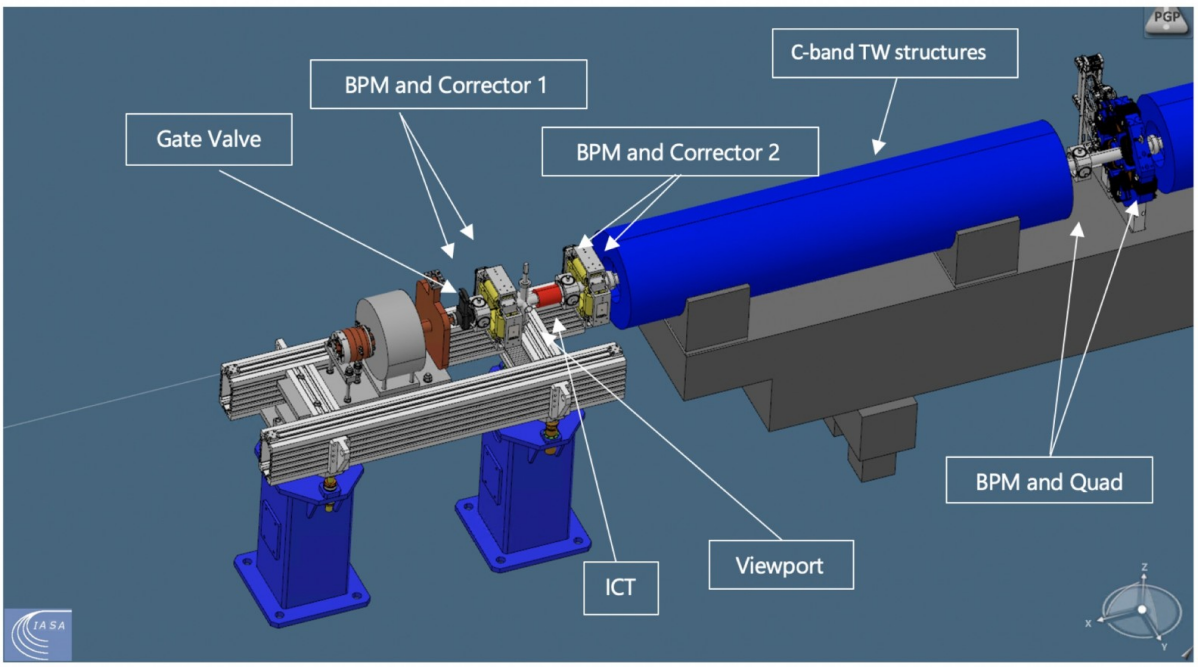

Figure 7.2.3.: Close up view of the 2.5 Cell C-band gun, the diagnostics section and the first TW C-band structure.

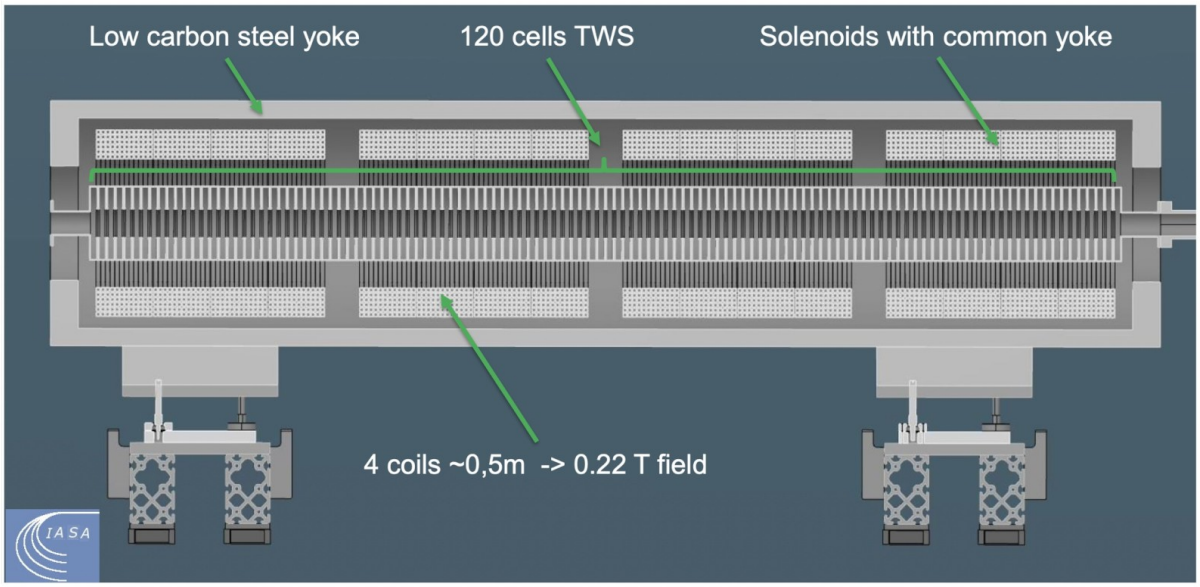

Figure 7.2.4.: Cross-section view of the first 120 cell Travelling-wave structure with the embracing common-yoke solenoid. 3D model of the solenoid follows the Electromagnetic design from IASA/INFN.

Figures 7.2.3, 7.2.4 present the C-band TW structure embraced from a 4-coil common yoke solenoid. The robust girder, containing 2 C-band cavities was inspired by the SwissFEL design [262].

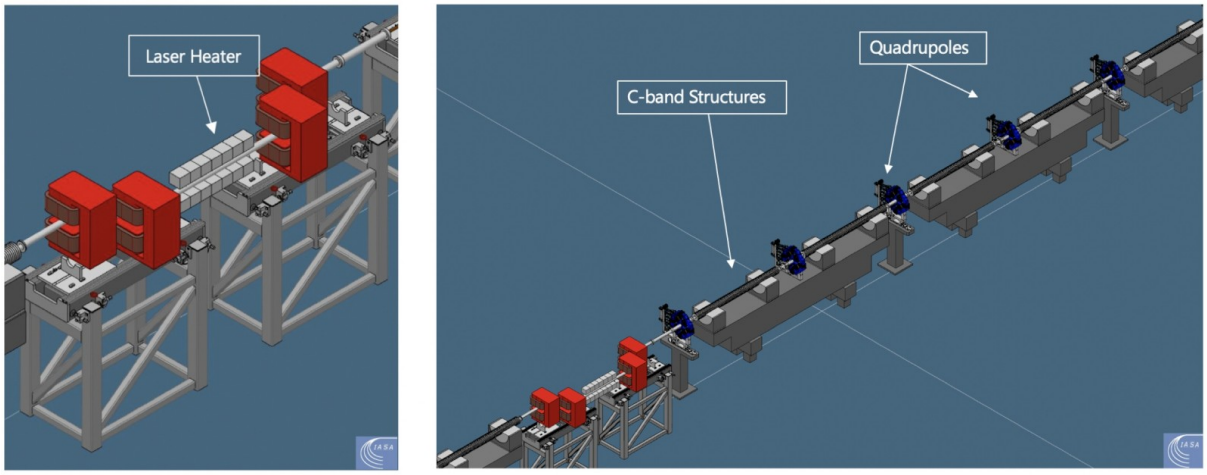

Figure 7.2.5.: Preliminary design of the laser heater, and the C-band cavities of the injector with focusing and defocusing quadrupole magnets.

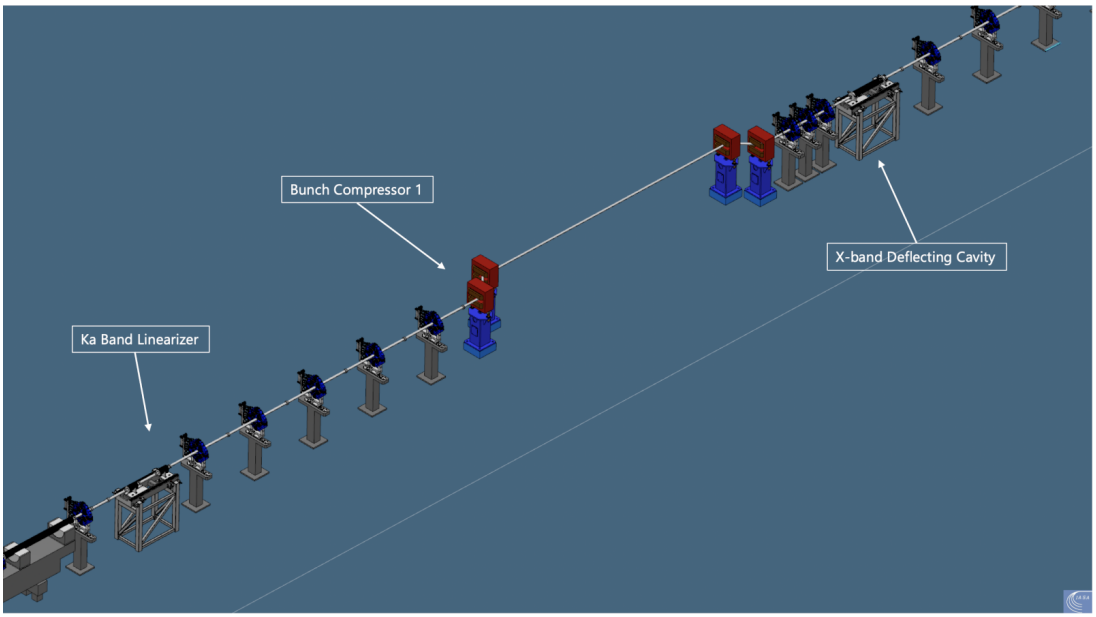

Figure 7.2.6.: Close up view at the end area of the injector with the K band linearizer, the bunch compressor 1 and the X-band deflecting cavity.

The preliminary 3D design for the quadrupole magnet for the injector and linacs, in Figure 7.2.7, was based on the parameters and design of the European Spallation Source (ESS) Medium Energy Beam Transport (MEBT) quads provided by ESS Bilbao [277]. It consists of a common yoke with embedded horizontal and vertical steerer magnets.

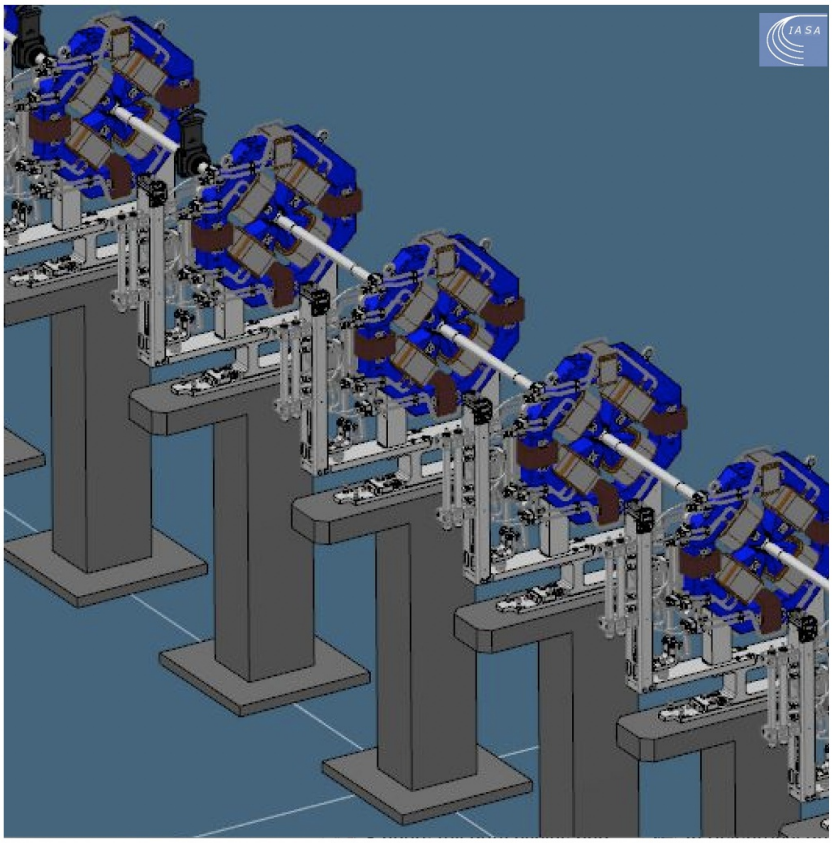

Figure 7.2.7.: Close up view of the quadrupoles with embedded steerers. .

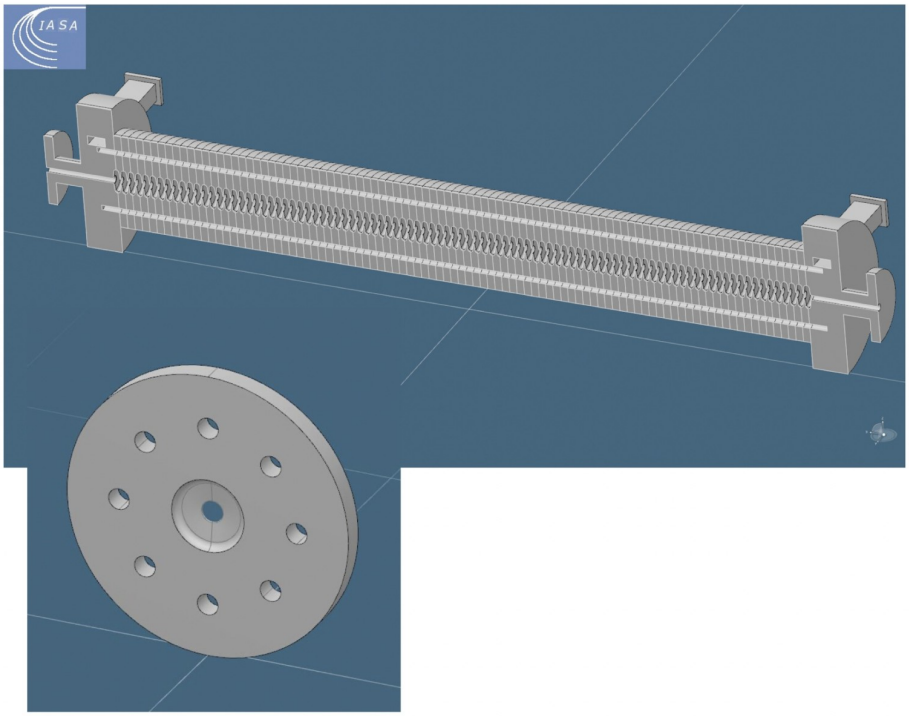

Figure 7.2.8.: The X- band transverse deflector cavity design for XLS.

The Transverse Deflecting cavity for XLS (Figure: 7.2.8, 7.2.9) has been designed following the design and parameters of the Polarix TDS X-band cavity [278] (96 cells, 0.8 m length, 8 cooling channels).

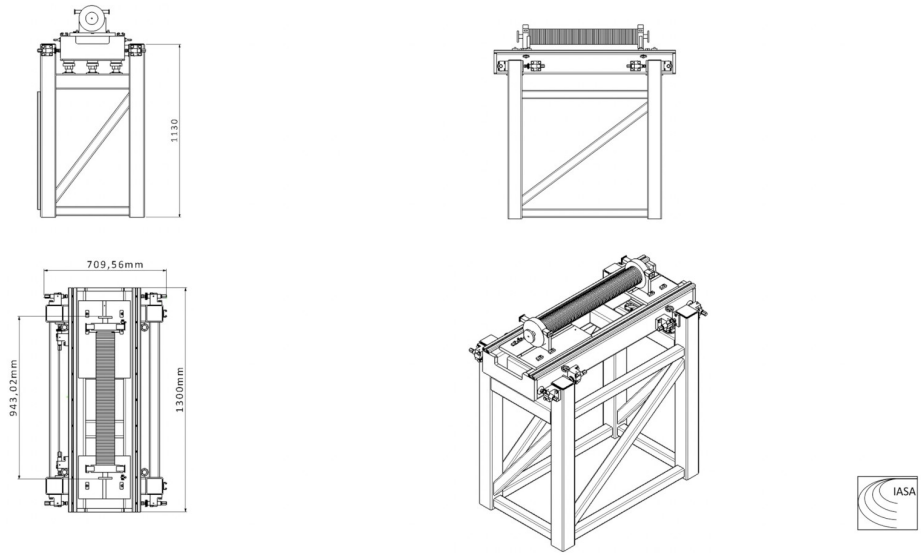

Figure 7.2.9.: Adaptation for XLS of the 0.8 m ,96 cell X-band transverse deflecting cavity.

Four TDS cavities are foreseen, one after the laser heater, one after the first bunch compressor (BC1), one at the end of Linac 2 and one before the undulators. Figure 7.2.10 (a),(b),(c) shows the main X-band module used in all sections. Based on design efforts by INFN-LNL and VDL ($\sim$1.3m, $\sim$109 cells, with coupler and adapter discs) a preliminary model was created and integrated in the facility 3D model. Additionally, Figure 7.2.11 shows the first proposed solution for the X-band cavity (72

cells, 965mm) based on the design by SwissFEL [262].

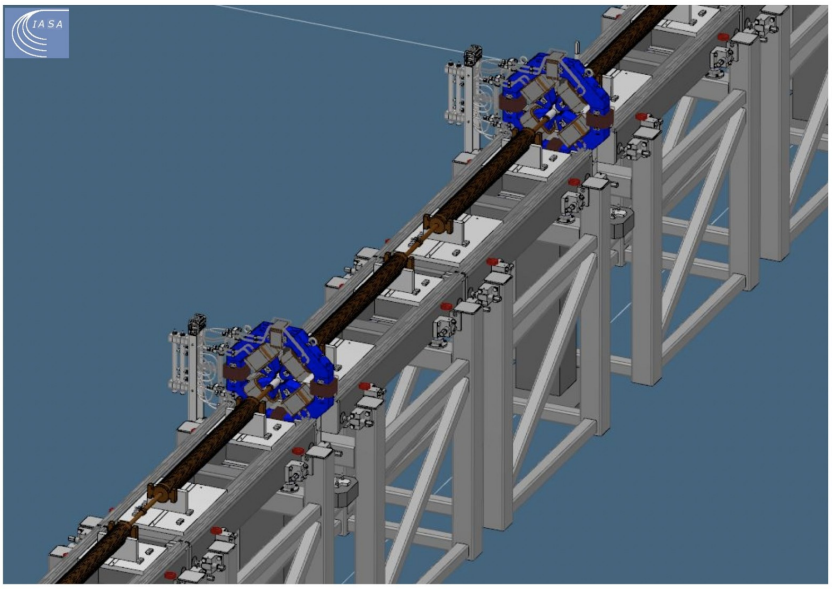

(a)

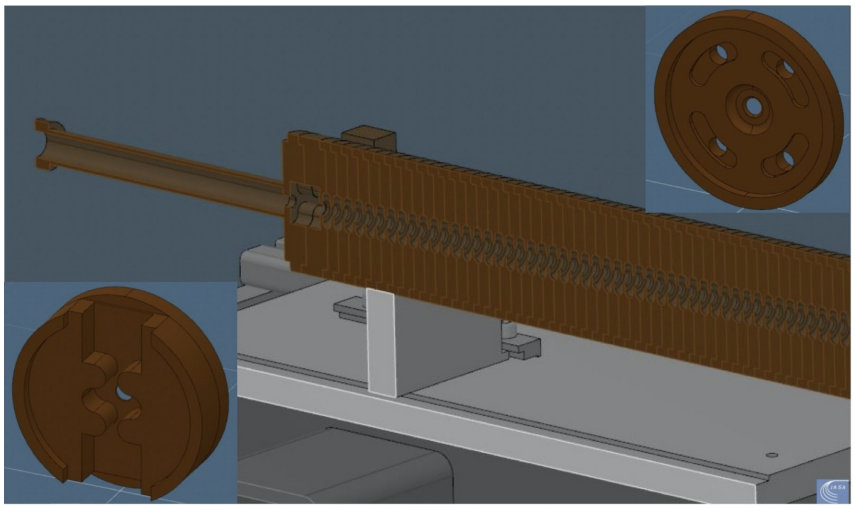

(b)

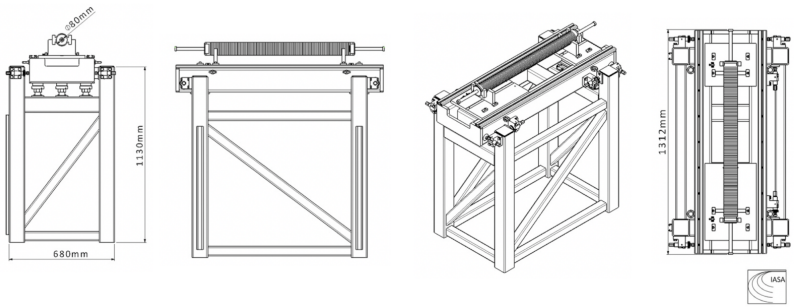

(c)

Figure 7.2.10.: (a), (b), (c) Preliminary design of the XLS 108 cell X-band cavity with coupler and adaptor discs based on the design by INFN/VDL-ETG.

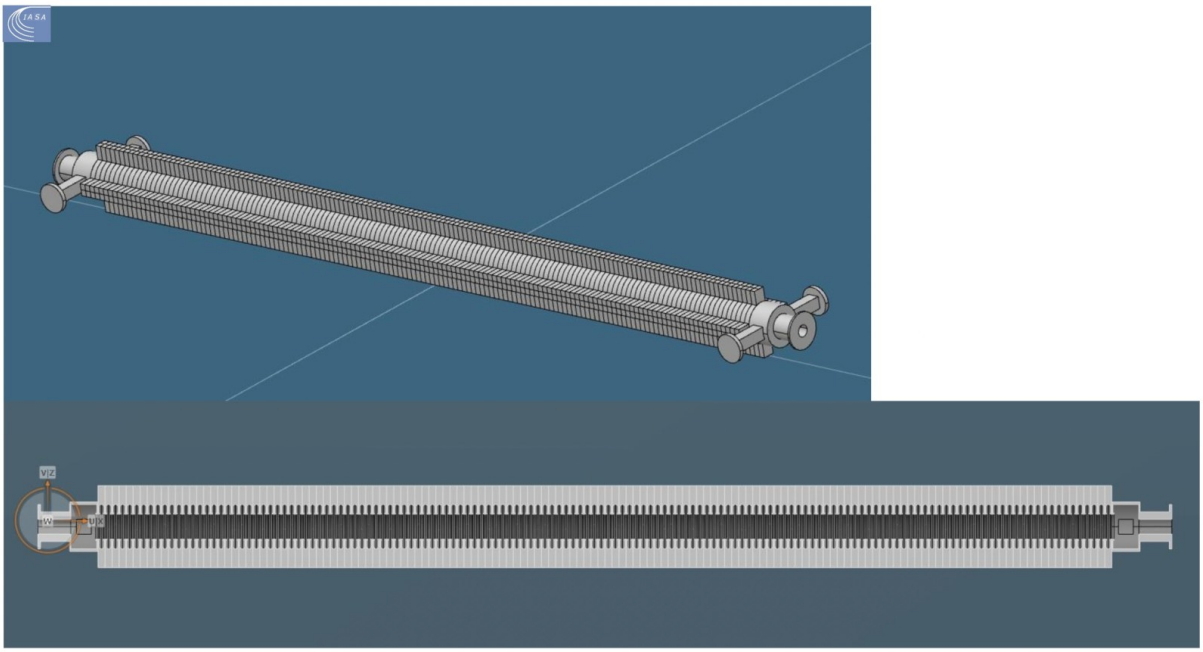

(a)

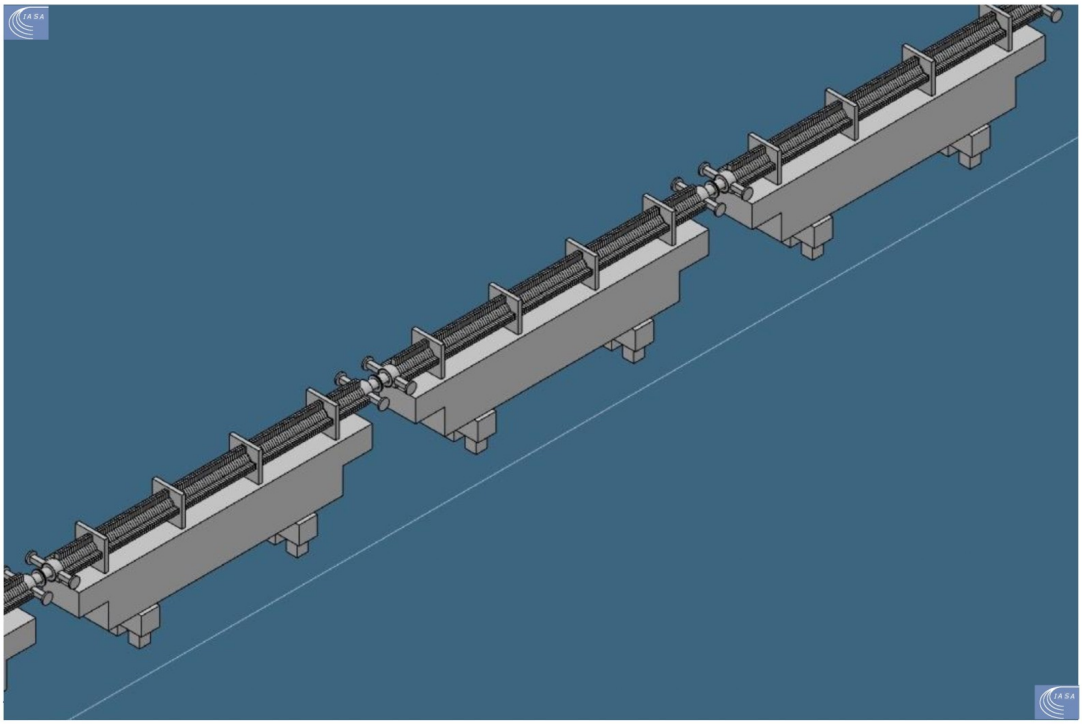

(b)

Figure 7.2.11.: (a), (b) Preliminary design options of the X-band modules cavities (72 cells , 965mm) and girders based on SwissFEL design [262]

Figures 7.2.12, 7.2.13, 7.2.14, 7.2.15, 7.2.16,7.2.17 present the accelerator layout comprised of Linac 1,2,3 and FEL lines 1,2. FEL lines contain focusing and defocusing magnets, phase shifters, electron and photon beam diagnostics, sixteen (16) undulators per beamline with fixed polarisation and two (2) per beamline with variable polarisation. Using dipole magnets the beam lines can be split downstream

and guided to the beam dump or towards the Experimental Hall.

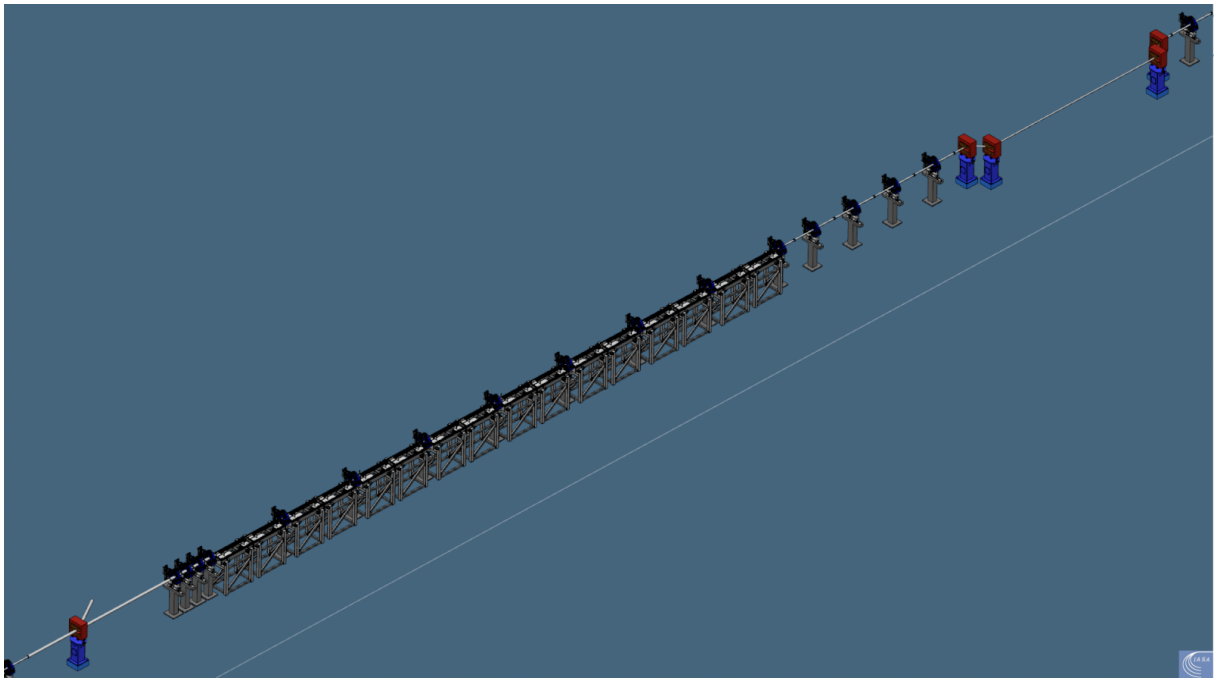

Figure 7.2.12.: Linac 1 Preliminary 3D model Layout and Bunch Compressor 2.

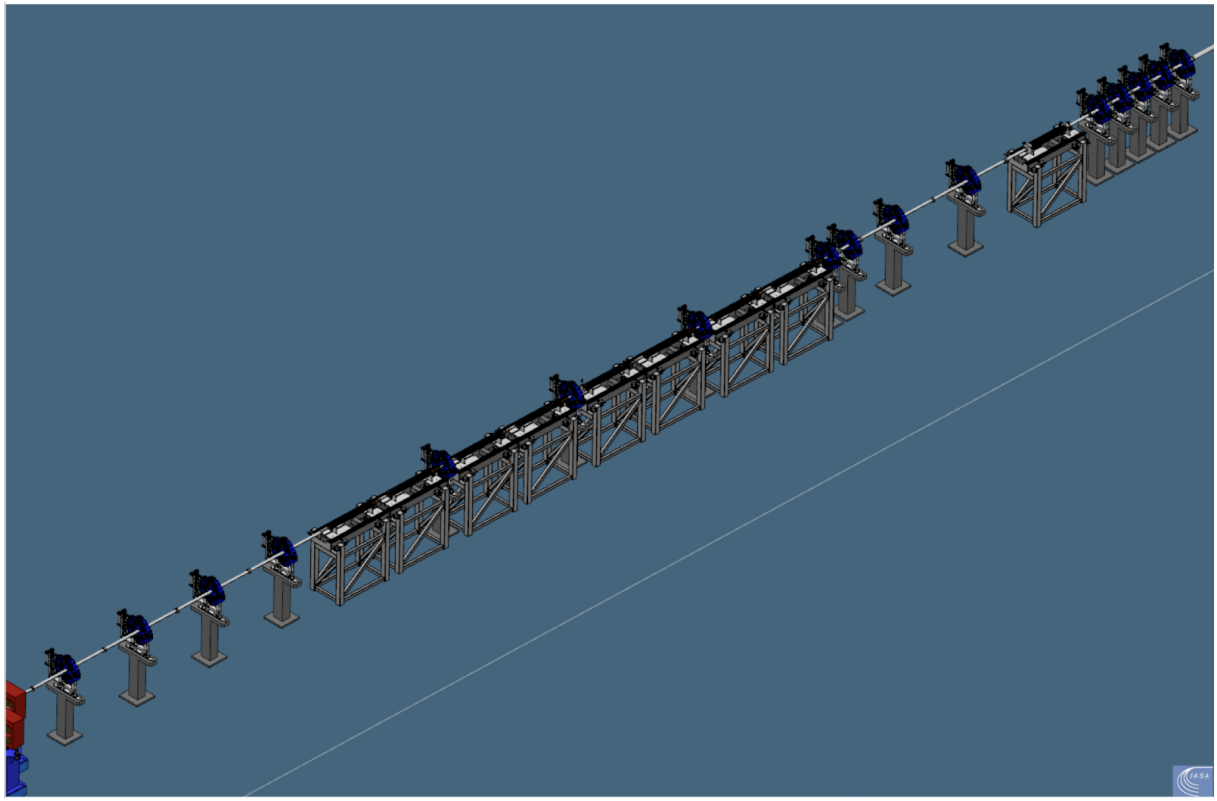

Figure 7.2.13.: Linac 2 Preliminary 3D model Layout.

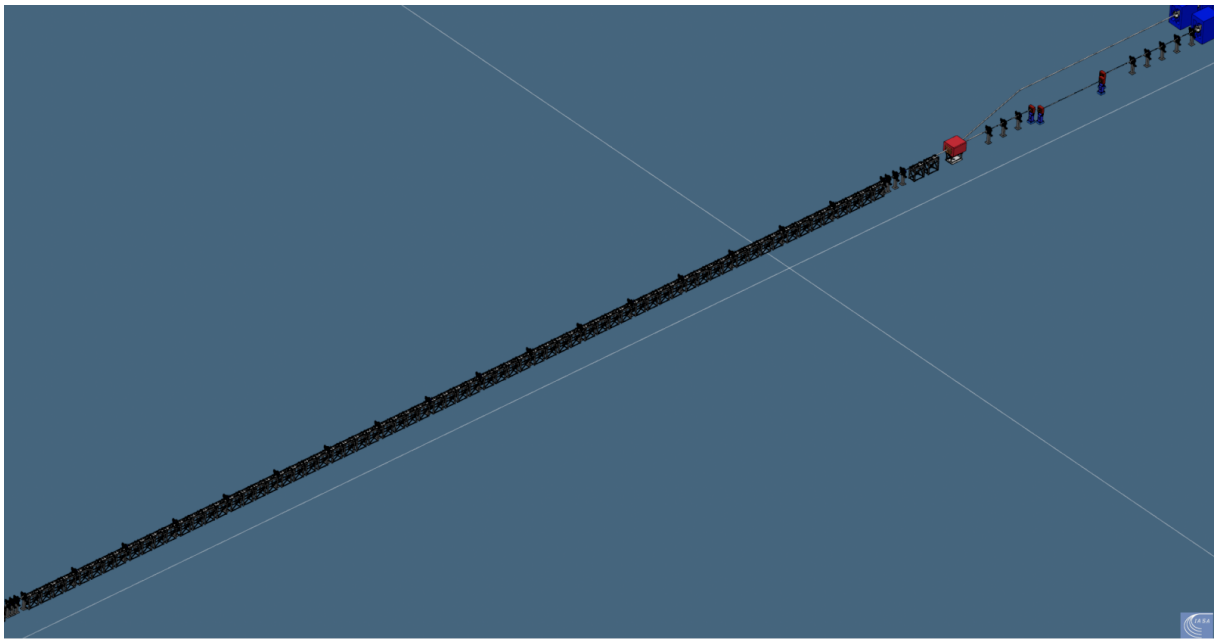

Figure 7.2.14.: Linac 3 Preliminary model Layout.

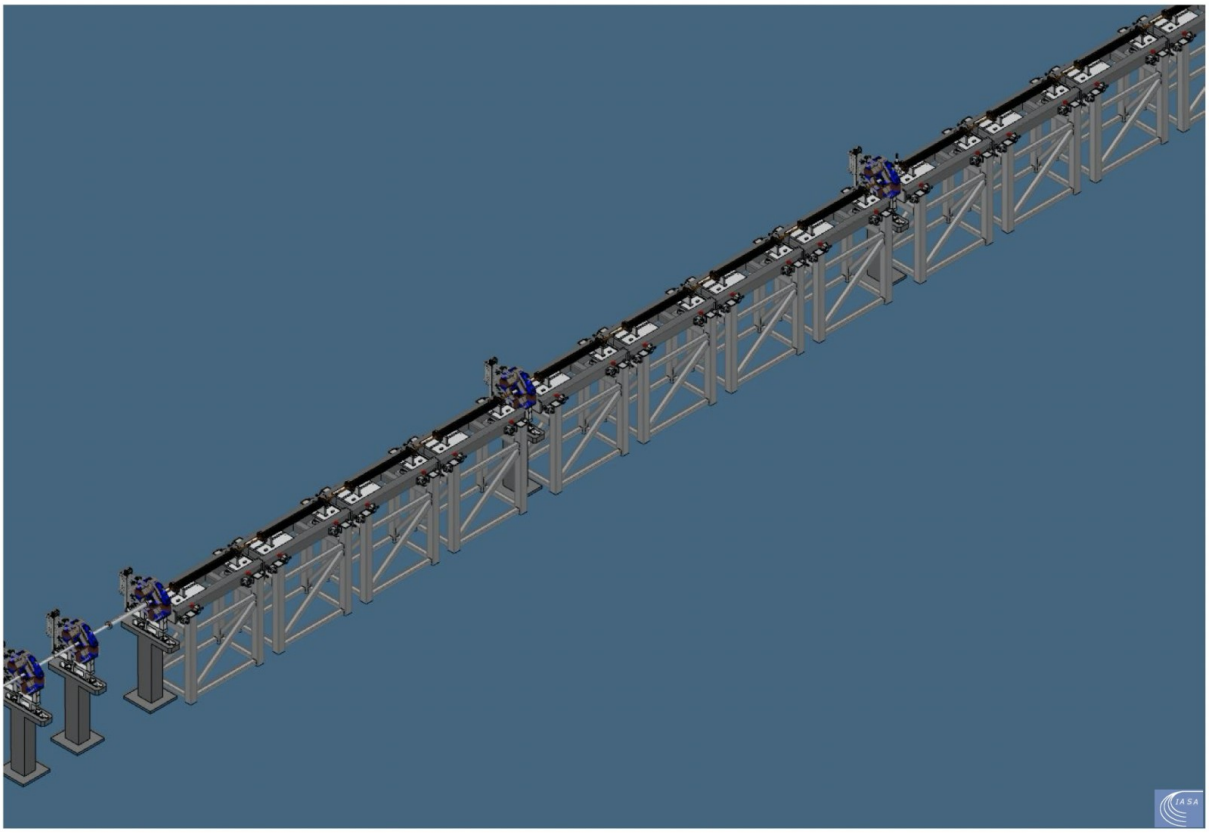

Figure 7.2.15.: Close-Up view of the X-band modules of Linac 3.

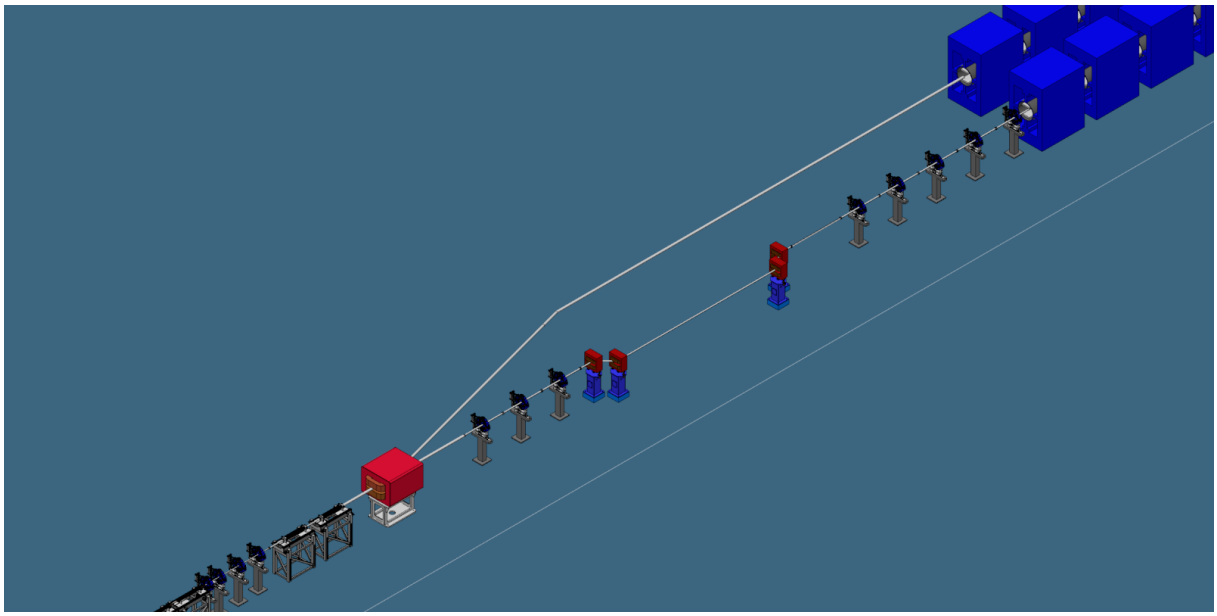

Figure 7.2.16.: Close up view of the 2 X-band TDS at the end of linac 3, beam splitting, timing chicane and HXR line on FEL 2.

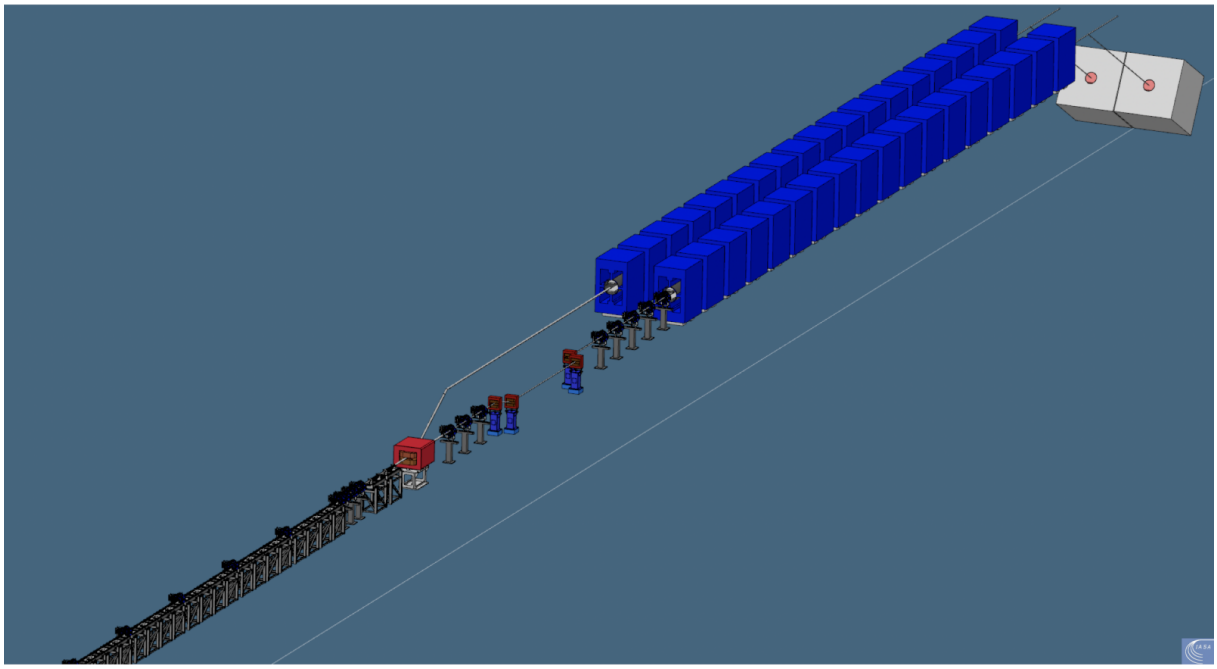

Figure 7.2.17.: Preliminary design of the FEL 1 and FEL 2 photon beamlines and beam dump.

7.3. XLS Facility 2D Drawings

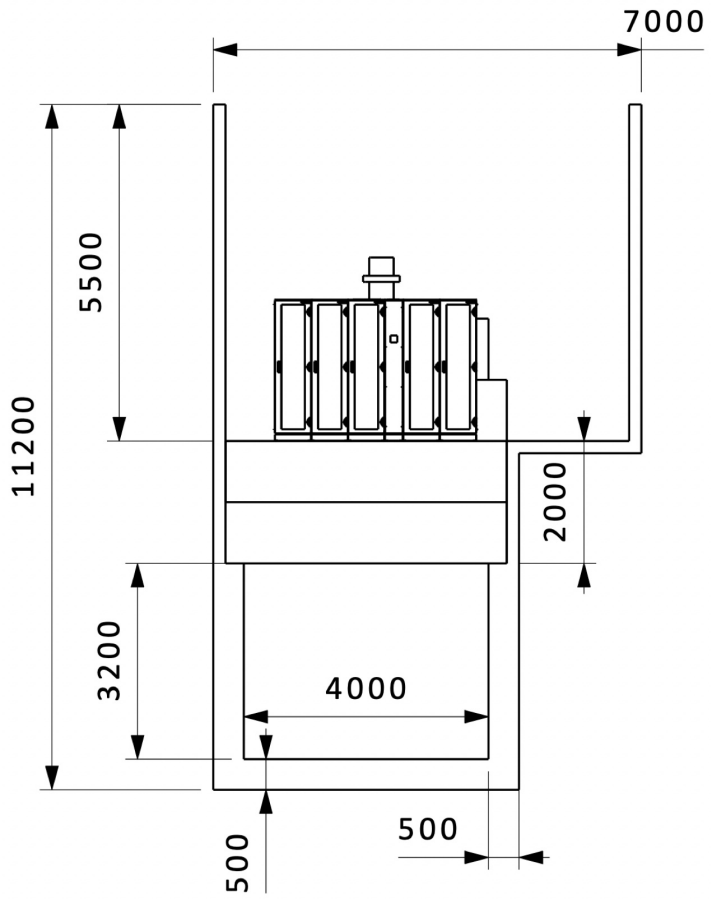

Figure 7.3.1.: Draft 5.0 XLS Tunnel and Infrastructure Hall cross-section (1:100)

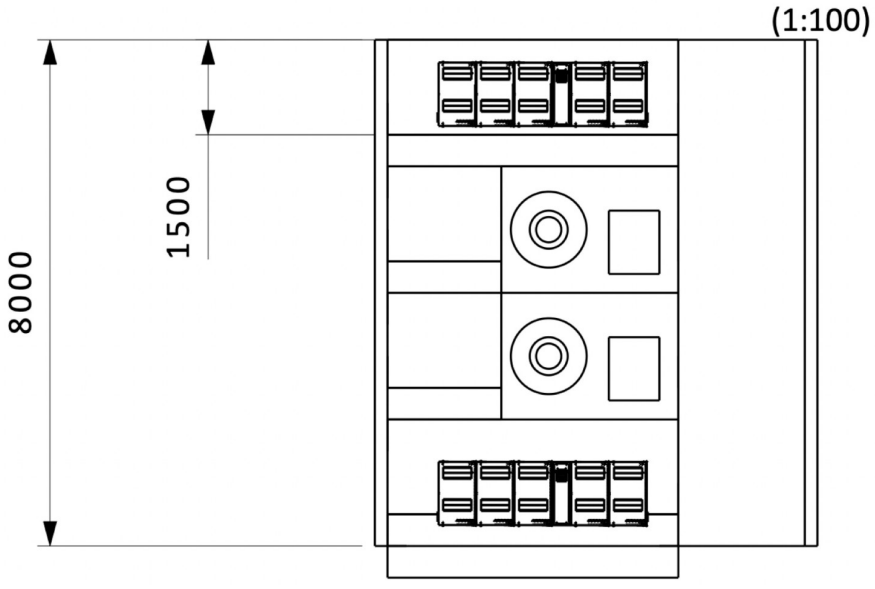

Figure 7.3.2.: Infrastructure Hall - RF cell top view (1:100)

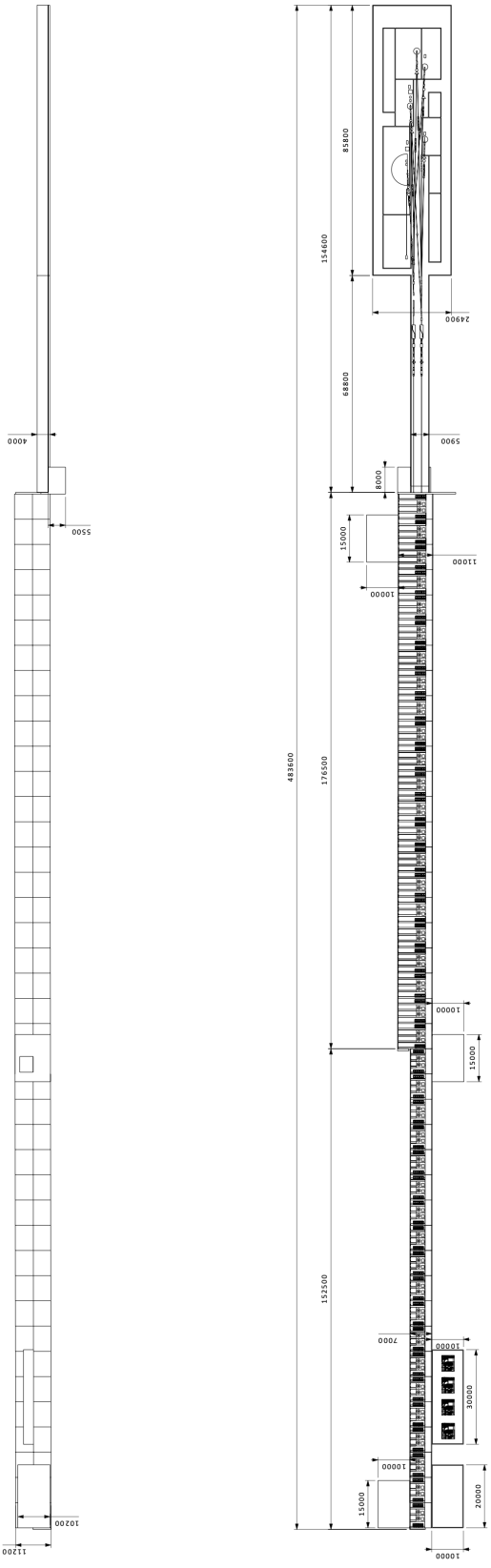

Figure 7.3.3.: XLS facility building Layout (1:350)

8. Strategy and Implementation

8.1. Cost Estimates and Comparison

8.1.1. Introduction

For the CompactLight cost analysis a bottom-up approach has been chosen, starting at the lowest level with the identification of the component cost and of their multiplicity. The cost in the estimate is expressed in Euros and considers the value of manufactured components, which already includes the cost of personnel by the supplier. The uncertainty of the cost estimate has been evaluated by taking into account on the one hand the technical maturity of the adopted solutions and on the other hand the uncertainty in the industrial procurement process [279]. Three levels of uncertainty have been associated to the technical risk, by assuming 10% uncertainty when the technology is already available, 20% uncertainty when an extrapolation is needed from a known technology and finally 30% uncertainty when a technology requires additional R&D. The uncertainty in the industrial procurement process has been extracted from the model following the study of procurement during the LHC realization, which was previously used in the frame of the cost estimate for the CLIC facility [131]. The standard deviation of the cost distribution has been considered as $\sigma = 0.5/n$, with n the number of valid offers received. The total uncertainty is then calculated by adding quadratically the two standard deviation values for the two classes of uncertainty. In the visualisation of the uncertainty band of oscillation around the estimated value the total uncertainty is used on the positive side, while only technical uncertainties are adopted for the negative side [280].

The CompactLight project aims at providing a site-independent facility design, however Civil Engineering costing has been estimated on the basis of CERN SCE Department guidelines and compared to other projects and studies performed at CERN. This estimate should then be scaled to the site specific cost of civil engineering construction and infrastructure when a particular country is considered for the facility. The cost of land acquisition is not included into this study.

A preliminary layout has been proposed with an associated design of tunnels and buildings that could host the facility, which is used here as a reference for the cost estimate. Figure 8.1.1 provides an overview of the CompactLight facility, with a view of the areas dedicated respectively to the accelerator, the FEL generation and experimental stations.

For some critical components a range of cost has been provided and the analysis shows the impact that such variations may have on the final cost of the facility. The estimates for the required manpower are purely indicative, they have been extrapolated from projects having a comparable budget. The cost estimate for operation is calculated on the assumption that the facility is running 7000 hours/year.

8.1.2. Construction Costs

The data of cost are analysed by considering three different areas in the machine:

1. the accelerator;
2. the undulators and beamlines;
3. civil engineering and technical infrastructure.

This approach is justified by the existence of different levels of uncertainty of the estimate for the three areas.

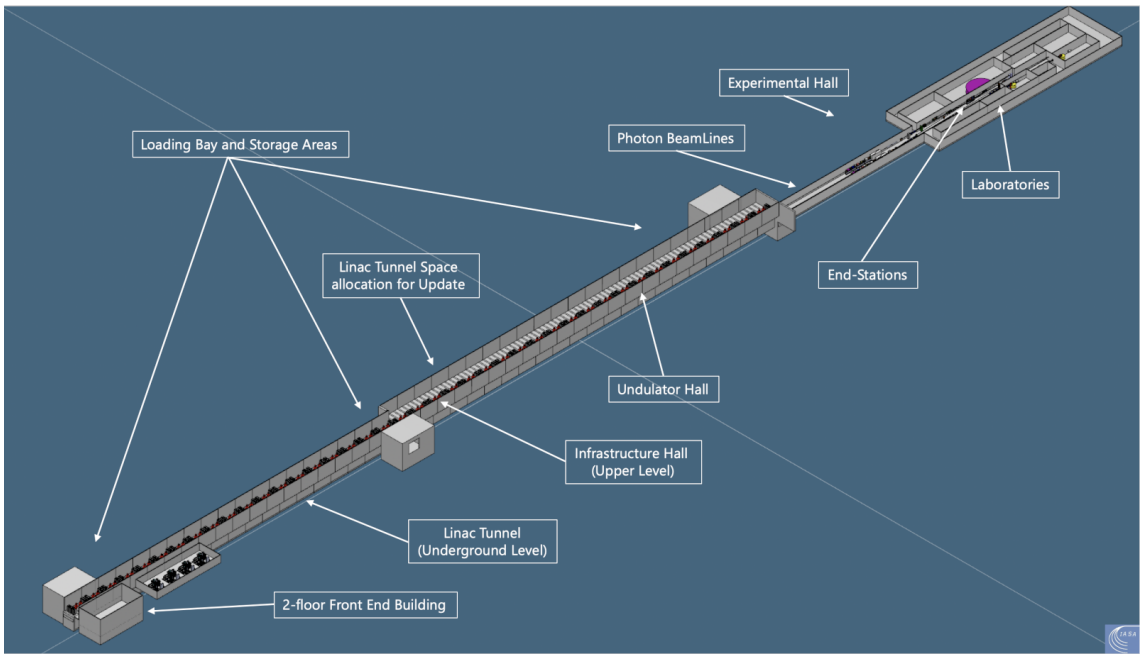

Figure 8.1.1.: Overview of the CompactLight facility

8.1.2.1. The Accelerator Sector

The accelerator layout is accurately described in this Conceptual Design Report and it is sketched in Figure 8.1.2. The cost of the accelerator sector is summarised in Table 8.1.1, which provides figures referring to the baseline design.

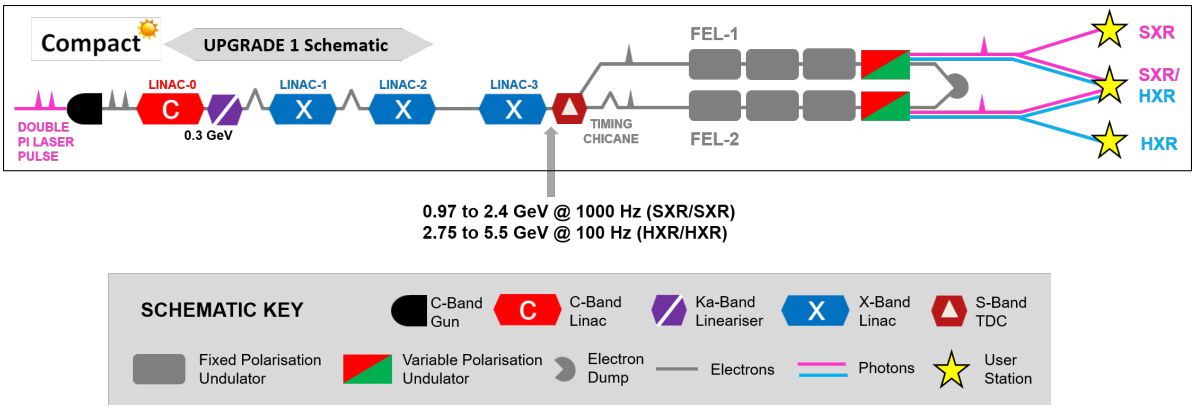

Figure 8.1.2.: Schematic layout of the CompactLight facility.

Running the facility at a higher repetition rate of 1kHz would imply a significant upgrade of the RF system. The cost increase for the different areas of the accelerator is detailed in the following Table 8.1.2.

For some of the components the average unit cost has been calculated by applying a learning curve of the form:

$$\langle c(n) \rangle = \frac{C(N)}{N} = c(1) \times \frac{N^{\log_2 \alpha}}{1 + \log_2 \alpha},$$

with $c(1)$ = prototype cost and α = learning factor, which was chosen equal to 0.9 in the case of X-band accelerating structures. In this case, $N = 100$. Since RF components are expected to have an

Table 8.1.1.: Distribution of cost for the accelerator sector of the CompactLight project baseline

Area of the facility	**Cost (MEUR)**	**Uncertainty (MEUR)**
Injector	14.886	+3.8 / -2.5
Linac 1	9.972	+2.5 / -1.5
Linac 2 - 3	43.746	+10.1 / -6.6
Bunch Compressors 1 and 2	1.633	+0.6 / -0.3
Kicker and Spreader	2.487	+0.6 / -0.4
Machine Timing, Controls and Protection	4.0	+0.6 / -0.6
Accelerator TOTAL	76.724	+18.3 / -11.9

Table 8.1.2.: Cost to upgrade the CompactLight baseline to 1kHz operation

Area of the facility	**Baseline Cost (MEUR)**	**Upgrade Cost (MEUR)**
Injector	14.886	0.500
Linac 1	9.972	2.020
Linac 2 - 3	43.746	9.595
Bunch Compressors 1 and 2	1.633	-
Kicker and Spreader	2.487	-
Machine Timing, Controls and Protection	4.0	-
Accelerator TOTAL	76.724	12.115

important impact on the overall cost of the facility, it is interesting to perform a sensitivity analysis that can illustrate how the cost may evolve by adopting different approaches in the estimate. Also, with the upcoming availability of high efficiency klystrons, it is worth showing how important the impact may be of that technological advance on the overall construction cost.

In Figure 8.1.3 the range of variation for some of the critical components is shown, with respect to the accelerator cost that was retained. The lowest side of the range of possible variations considers more aggressive choices that may be made for the cost estimate. For example, by considering that klystrons could go through HV processing at the laboratory, after delivery and under the lab's responsibility. The highest side of the range is reached if no learning curve is applied for the average cost calculation.

Figure 8.1.4 shows the impact that the adoption of high efficiency X-band klystrons may have on the overall accelerator construction cost.

8.1.2.2. The Undulators and Photon Beamlines

The cost of undulators and photon beamlines has been summarized in Table 8.1.3. The cost estimate for this area of the facility considers a total number of 4 photon end stations. This area equally includes electron beam instrumentation and photon diagnostics for the beamlines and the end stations. The choice of a single cryoplant feeding the 32 cryostats, which house the undulator segments, has been adopted for this estimate, since it has been considered as the economically most advantageous option, when compared to the adoption of individual crycoolers.

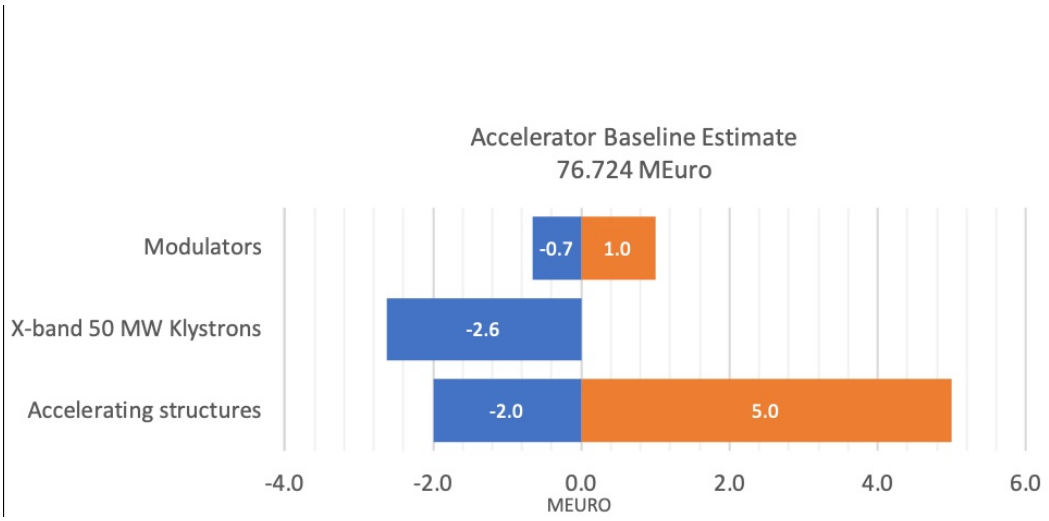

Figure 8.1.3.: Range of variation of the final cost for the accelerator area as a function of how the cost of critical items is evaluated.

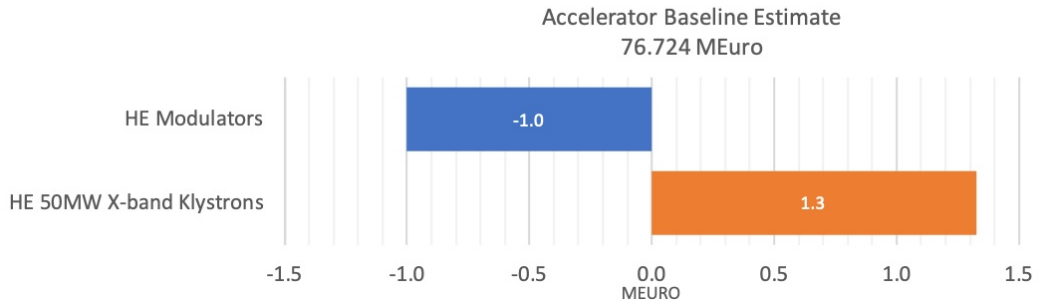

Figure 8.1.4.: Range of variation of the final cost for the accelerator area in the hypothesis that high efficiency klystrons become available on the market (cost estimate for prototype and small series provided to CERN and to EuPRAXIA@SPARC_LAB).

Table 8.1.3.: Distribution of cost for the undulator and photon beamline sector

Area of the facility	**Cost (MEUR)**	**Uncertainty (MEUR)**
FEL1 and FEL 2	39.450	+12.928 / -10.396
Photon Beamlines	29.990	+10.292 / -8.997
Photon End Stations	25.0	+5.0 / -5.0
FEL and Beamlines TOTAL	94.440	+28.220 / -24.393

8.1.2.3. Civil Engineering and Technical Infrastructure

This part of the cost estimate is more difficult in the absence of a detailed design of the facility and of the choice of a specific construction site. In order to provide a proper estimate, different projects that have been realised or studied at CERN in recent years have been taken as a reference and scaling laws have been applied based on fundamental parameters like surface and volume of the buildings,

power needs and power dissipation across the facility. In the case of civil engineering realisations, the cost estimate has been considered as a Class 5 estimate, in accordance with the definition provided in [281], where a summary table of the different classes of estimate can be found.

The proposed facility layout shows a total footprint of approximately $5000m^2$ and a total surface of $6600m^2$ for an overall volume of $28150m^3$. The construction technique proposed in the reference study is based on cut and cover tunnel. For the cost estimate two different scenarios have been considered, which could be alternately adopted depending on the nature of the ground and of the surroundings: either open cut excavation or excavation using diaphragm walls along the tunnel length. A different value of the unit cost has been considered for surface buildings with respect to underground tunnels. Depending on the adopted scenario the cost may range between the extreme values of 36 MEUR and 50 MEUR; it is proposed here to adopt an intermediate value for this estimate at 43 MEUR.

The cost estimate for the heating, ventilation and air conditioning (HVAC) systems considers the overall volume of the buildings as provided above, also taking into account that 60 % of the volume is represented by buildings that require, like the Linac Tunnel, a stable temperature during the year. A water cooling capacity of 3.5 MW is estimated for the dimensioning of the cooling plant. The assumption is made that the cooling system can rely on an open wet cooling tower for the primary water production with two secondary circuits filled with demineralised water for the klystrons, kickers and power converters' cooling. A chilled water plant would supply the more demanding accelerator cooling, in terms of temperature stability, and for the air conditioning.

The estimate has been produced based on external conditions of the Geneva Region in Switzerland. Following ASHRAE and SIA Standards, the wet bulb temperature taken for the estimate is 21.1 °C , 99.9 % of the time. In summer dry temperature is 34 °C with a Relative Humidity of 33 %. In winter dry temperature is –8.4 °C with a Relative Humidity of 72 %. Depending on the region where the facility is realised, this could lead to important deviation in the final estimated cost.

For the cost estimate of the electrical distribution system a total electrical power need of 4.5 MW has been considered. The facility is divided into two independent electrical areas, one including the Linear accelerator and the second area feeding the FEL lines and the experimental area, which is reflected in the tentative scheme proposed in Figure 8.1.5.

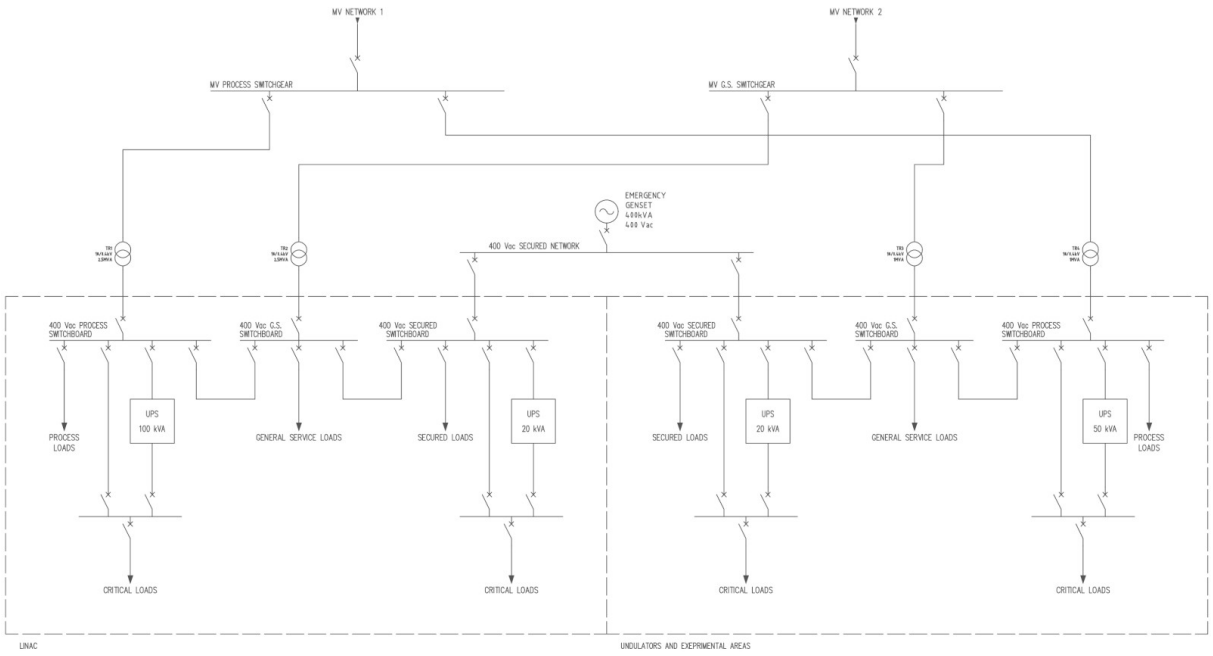

Figure 8.1.5.: Proposed topology for the Compact Light electrical network.

From an electrical supply point of view the Compact Light facility shall be supplied by an electrical substation connected to a medium voltage distribution utility or included into an existing medium voltage network. In order to keep a functional separation between process-related loads and general services, two medium voltage switchgears supplied by two different lines are considered here. The adoption of a single switchgear would simplify the installation, reducing the cost, but preventing the possibility of a back-up. Four load classes are fed by the envisaged distribution network, as summarised in Table 8.1.4.

Table 8.1.4.: Load Classes in the Compact Light Electrical Network

Load Class	**Load Type**
Machine	Power converters, cooling and ventilation motors, radio-frequency, klystrons, vacuum, cryogenics
General Service	Lighting, pumps, general ventilation, wall plugs
Secured	Personnel safety: Emergency lighting, pumps, elevators, smoke/extraction, secured ventilation
Uninterruptable	Personnel safety and Machine safety

In the analysis performed for the electrical network and for the cooling system, the option of running the facility at the 1kHz repetition rate is already partially included and will require an additional 15% with respect to the indicated budget at the moment of the upgrade. If the 1kHz option was discarded, a cost reduction of the initial budget can be expected of the order of 15%. Table 8.1.5 summarizes the cost that is estimated for the Civil Engineering and the Technical Infrastructure.

Table 8.1.5.: Distribution of infrastructure cost for the CompactLight project

Area of the facility	**Cost (MEUR)**	**Uncertainty (MEUR)**
Civil Engineering	43.0	+7.0 / -7.0
Electrical System	6.5	+2.3 / -1.0
Cooling and Ventilation	11.0	+1.0 / -1.0
Buildings and Technical Infrastructure TOTAL	60.5	+10.3 / -9.0

The cost for the electrical network assumes that an upstream infrastructure (medium voltage switchgears and networks, emergency genset station) is already available in the installation site, if this was not the case an additional cost that could vary from 0.5 to 1.3 MEUR could be considered. This possibility has been taken into account by adding 1.3 MEUR on the positive side of the range of uncertainty.

8.1.3. A Preliminary Resources Profile

A preliminary estimate of the manpower profile required for the construction can be proposed by looking into similar projects, similar in scale, such as the realisation of the Linac4 at CERN, a project that was completed in 2017. For Linac4 a manpower need of about 1.9 FTE-year/MCHF had been initially estimated, corresponding approximately to 2.1 FTE-year/MEUR. One can consider that the CompactLight facility is a project whose nature is very similar to Linac4, with comparable sizes between the two facilities, such that the same fixed ratio between personnel and material expenditures may apply. With a total cost of the baseline project of about 207 MEUR, the labour cost can be estimated at 435 FTE-years. A tentative resource distribution along the project duration may show a profile such as in Figure 8.1.6, where the material cost for the baseline facility and the associated labour have been normalised to their respective estimated amounts and the distribution profiles expressed as a percentage

of them. In this graph, year 1 must be considered as a project preparation year and year 8 as a facility commissioning year.

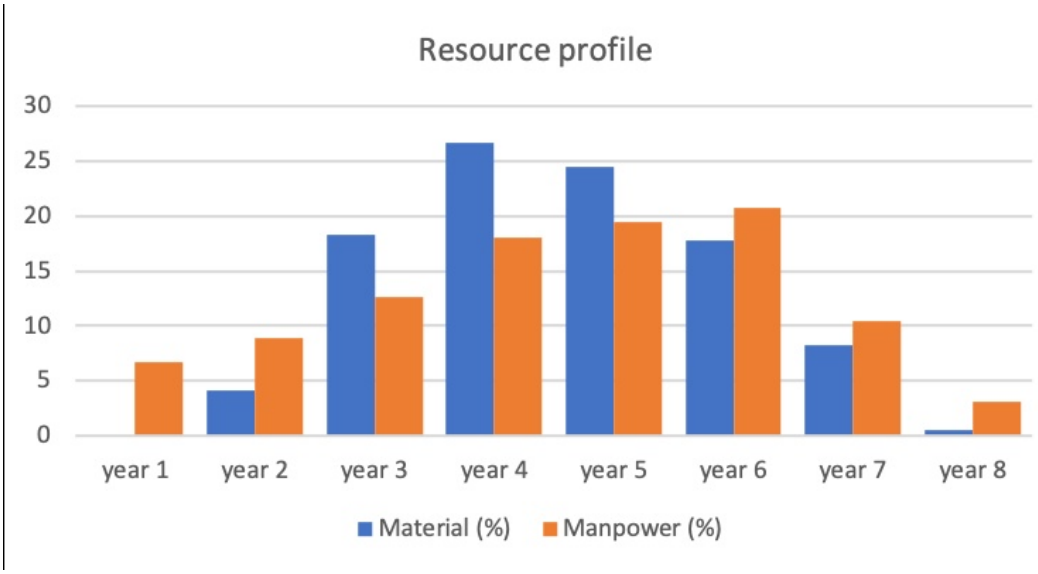

Figure 8.1.6.: Tentative resource profile distribution in percentage of the estimate material cost and needed labour.

8.1.4. Comparison to a Real Case: SwissFEL

SwissFEL is the X-ray Free Electron Laser facility hosted at the Paul Scherrer Institute in Villigen (Switzerland) [282]. The facility provides X-ray radiation in the range 1 to 50 Å by means of two beamlines, named Athos and Aramis, which are fed by a single Linac. The facility started regular user operation in 2018. The compact linear accelerator, which mainly relies on C-band RF technology, delivers single and twin bunches of electrons at an energy up to 5.8 GeV with a repetition rate of 100 Hz. Having considered its design characteristics and performance, SwissFEL is the natural reference to compare with the CompactLight baseline in terms of cost for the realisation and the operational budget. The fabrication cost for SwissFEL, originally expressed in CHF, has been translated into EUR currency by assuming an exchange rate of 1 CHF = 0.9508 EUR. By considering the different areas of the facility, the result of the comparison is summarised in Table 8.1.6. It must be noted that the cost corresponding to preliminary studies and preparation for SwissFEL has been included in the Infrastructure cost while for CompactLight it is spread over the cost of the three areas of the facility and reflected in the associated margin of uncertainty.

Table 8.1.6.: Comparison of CompactLight and SwissFEL project cost per area

Area of the facility	**XLS Cost (MEUR)**	**XLS Uncertainty (MEUR)**	**SwissFEL (MEUR)**
Accelerator sector	76.724	+18.3 / -11.9	88.860
FEL and Beamlines	94.440	+28.2 / -24.4	85.670
CE and Infrastructure	60.500	+10.3 / -9.0	131.630
Facility TOTAL	231.664	+56.8 / -45.3	306.160

8.1.5. Operation Costs

The power need for the different operation modes has been estimated and the energy consumption has been calculated on the basis of a yearly operation of 7000 hrs. A cost of energy at 60 EUR/MWh has been assumed for this calculation. Table 8.1.7 provides an overview of the operation cost related to energy consumption, in the different operating modes.

Table 8.1.7.: Power needs, energy consumption and estimated operation cost for the two main operation modes of CompactLight

Operation mode	Power (kW)	Energy (MWh)	Cost (EUR)
Baseline operation 100Hz	2503	17521	1051260
Upgraded operation 1kHz	3153	22068	1324080

The introduction of high efficiency klystrons would bring a non-negligible reduction in the yearly operation cost. By considering a 20% increase in the klystron efficiency, the operation cost reduction would be in the order of 50 kEUR/year for 100 Hz operation and would rise to 150 kEUR/year in the case of 1 kHz operation. The material cost for operation, required for spare parts as a yearly replacement cost, can be estimated as a percentage of the overall cost of consumable components. We can estimate a need of 1% of the hardware parts in general, 7% of RF components, which have a well known life cycle, and 5% of the infrastructure cost, covering the cooling and ventilation and electrical systems spare parts. Overall the material cost for operation is estimated at 6.2 MEUR/year.

8.1.6. The CompactLight Ultimate Upgrade

An ultimate upgrade, or upgrade 2, has been envisaged for the CompactLight facility with the addition of a SXR bypass line that integrates two additional accelerator modules, which will enable the possibility of producing simultaneous soft and hard X-ray pulses at 100 Hz repetition rate. The optional upgrade introduces the possibility of FEL pump FEL probe capabilities and a self seeding scheme for higher harmonic operation. The layout is sketched in Figure 8.1.7. More technical details are provided in the CompactLight CDR document. The cost estimate for the facility upgrade is summarised in Table 8.1.8.

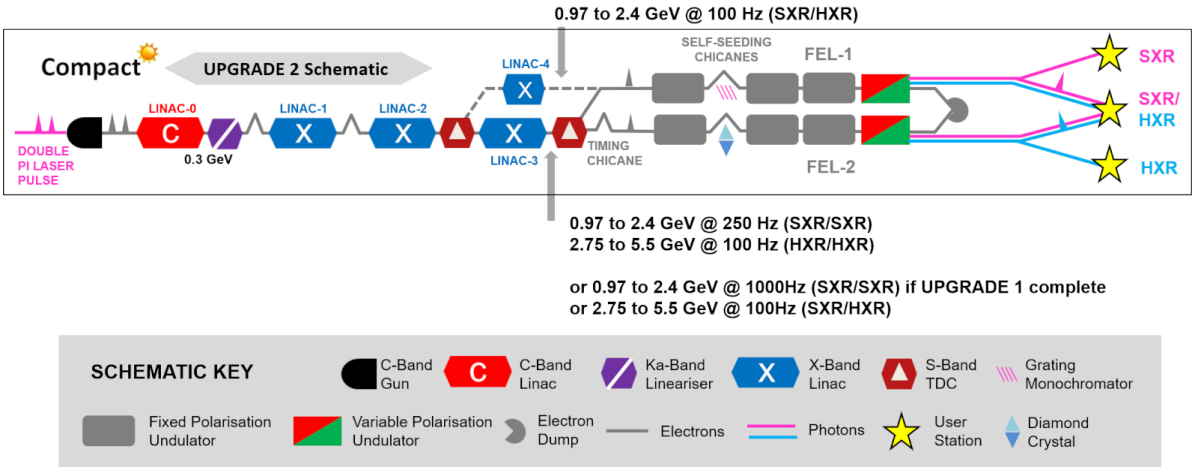

Figure 8.1.7.: Schematic layout of the CompactLight facility with Upgrade 2.

Table 8.1.8.: Estimated cost for the ultimate upgrade of the CompactLight facility

Elements in the Upgrade	Cost (MEUR)	Uncertainty (MEUR)
SXR 2nd Upgrade bypass	1.322	+0.32 / -0.22
Linac4 RF and Vacuum	4.384	+0.99 / -0.65
Linac4 Magnets	0.640	+0.13 / -0.09
Linac4 Beam Instrumentation	0.424	+0.10 / -0.08
CompactLight Upgrade 2 TOTAL	6.770	+1.54 / -1.04

8.1.7. Methodology

The data have been organized by means of a costing tool that was originally developed to estimate the CLIC project cost, in preparation of the European Strategy document. The tool provides the interface to a large database where the information is stored and secured. The CERN Advanced Information Systems team (AIS) has provided a dedicated interface specifically prepared for the CompactLight project. The costing tool includes features for fixed and variable costs, currency conversion, escalation and uncertainty, as well as full traceability of input data and production of tabulated reports which can be exported for further processing. The chosen currency for this estimate is the Euro.

Since the CompactLight study considers a baseline facility and additional optional upgrades for higher performance, with increasing complexity, the tool can be used to to separately estimate the cost of the baseline and of the upgrades, with the possibility to include the options of choice in the overall cost of the facility. At the end of the project, the database will remain accessible for consultation in a simplified form.

The cost information has been organised in a project breakdown structure (PBS), which considers four levels of complexity providing increasing detail starting from the Machine Sector down to System, sub-System and Component. A bottom-up approach has been used. Each Machine Sector has been associated to a work package and the work package leader was asked to provide the cost information for the items under his responsibility, starting from unit cost at the component level and then upwards. An iterative process has been followed, which provided an increasing completeness and accuracy of the estimate while the study progressed. In Figure 8.1.8 the PBS structure is shown for the CompactLight facility baseline.

A very limited use of learning curves has been made for some components, such as klystrons as an example, for which a prototype cost estimate exists and an extrapolation is required for providing a cost value for the relatively small series production needed by the CompactLight design. For the critical items where learning curves have been applied, the cost analysis reports a sensitivity study that shows the possible oscillation range. Specifically for klystrons and modulators budgetary offers were collected in the context of this study and of the EuPRAXIA@SPARC_LAB project and have been used as a reference to evaluate the possible band of cost oscillation. More generally, the costing is based on the experience gained with previous installations by different experts contributing into the work package technical development. In some cases it was decided to produce the estimate at the system level, without going into the details of the components, when a cost scaling law was possible by comparing similar items. R&D activities and the development of prototypes have not been explicitly included in the cost estimate, however they are implicitly considered, partially, in the margin of uncertainty of the estimate itself [279].

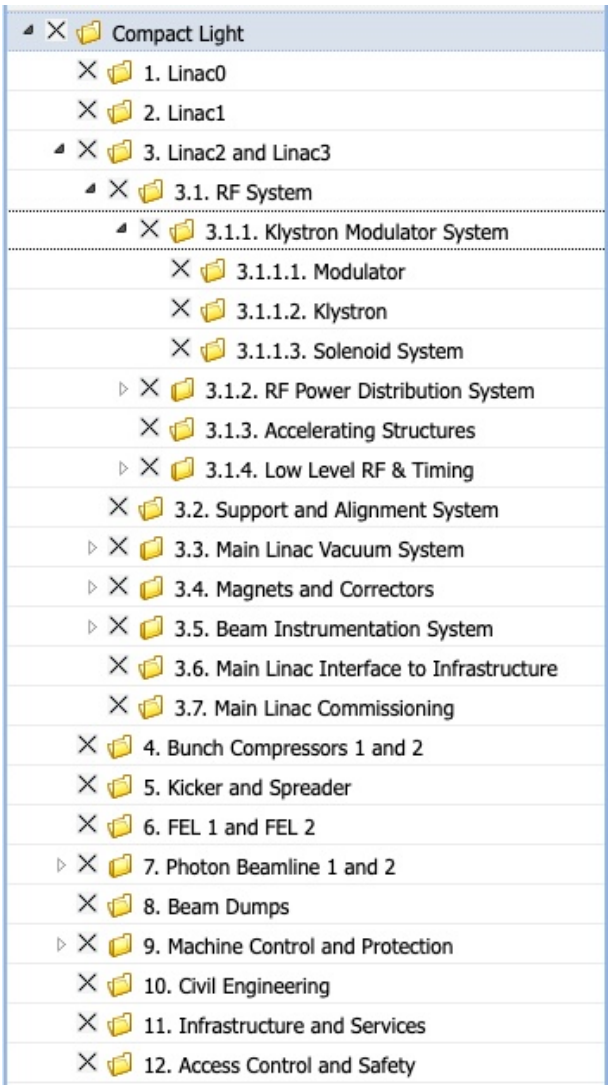

Figure 8.1.8.: PBS structure for the baseline layout of the CompactLight facility. The multi-level organisation is highlighted.

8.2. Global Integration

CompactLight is not a design study for a concrete research infrastructure development project, but the project has the intention to support communities in developing their own project for a flexible, more compact and resource-efficient and therefore more sustainable FEL facility than those that can be constructed with existing technologies. The hope is that CompactLight will be the basis for a new generation of FEL light sources with a considerably reduced footprint, cheaper and more affordable for communities with less resources, that it will also pave the way for smaller machines that can be used for new applications and that it will, last but not least, fuel the development of innovative, resource-efficient technologies for other types of accelerator-based infrastructures. This section gives a brief insight into the communities that might benefit directly and indirectly from the work: the global accelerator community, the community of accelerator-based light-sources that is part of it, and the user community of FELs and Synchrotrons. These communities are, as possible applicants and end users of CompactLight technologies, the direct beneficiaries of the project results, but also the actors required to push them on together with the CompactLight partners during the coming years and make CompactLight

facilities become real in a not too far future.

8.2.1. The Global Accelerator Community

8.2.1.1. Methodology

In order to obtain information about the global accelerator community, the participation of research institutions, universities and companies in the International Particle Accelerator Conferences (IPAC) of the years 2015-2019 has been analysed.

The IPAC has been organised for the first time in spring 2010 in Kyoto/Japan (IPAC 10) with the aim to create a joint event for the global community and boost the international collaboration. Since then, more than 1000 delegates from the major scientific institutions, universities, and companies in the field world-wide are annually participating in the conference, which is meanwhile recognized as the main event of the global accelerator community.

To get information about the community, the participation in the latest five pre-COVID-19 emergency events, which took place in Richmond (USA, IPAC 15), Busan (Korea, IPAC 16), Copenhagen (Denmark, IPAC 17), Vancouver (Canada, IPAC 18) and Melbourne (Australia, IPAC 2019), has been analysed. The analysed data have been extracted from participation and contribution lists of the different events that have been downloaded from the conference websites and the Accelerator Conference website of JACoW at CERN [283]. In the collected data sets, the participant institutions have been identified one by one and the different names used by different participants for the same institution during subscription have been harmonized. In this process, the institutions have been categorized as ‘university’, ‘research institute’, ‘company’ and ‘others’, where ‘others’ refers to all participants that could not be classified in the other three categories. Participants classified as ’others’ have not been considered in the further analysis. More information and methodological details as well as the links to all the event websites are given in D7.2, which will be published on the CompactLight website after approval by the European Commission and which will also be archived and made available in Zenodo.

8.2.1.2. Data and Results

The collected participation data have been analysed separately for each year and also in total for the whole considered period. A detailed table with the results of this analysis can be found in deliverable D7.2. In this part, the main results of the analysis, which provide some insights into the global accelerator community, will be presented.

Countries. The data shows that each of the considered IPAC Conferences has been attended by participants from between 30 and 39 distinct countries. These countries changed somewhat according to the location of the event, but many countries have consistently participated in all the considered conferences, in particular those with major accelerator-based facilities. Figure 8.2.1 shows that 48 distinct countries have participated in the five selected events, of which 56% have been European. This European prevalence can probably be understood by the large number of European countries running own accelerator-based infrastructures.

Table 8.2.1 provides a full list of all participating countries in the IPAC 2015-2019 events for each continent. The data show clearly that the accelerator community is a real global community, except for the lack of African representation.

Institutions. The total number of distinct institutions that have participated in the events has been 905, namely 355 companies, 268 research institutes, 242 universities and 40 others. This is shown in Figure 8.2.2(a).

The category “others” gathers external services for event organisation, political administrations, foundations, funding agencies, publishers, commercial and trade offices, private persons and others and is

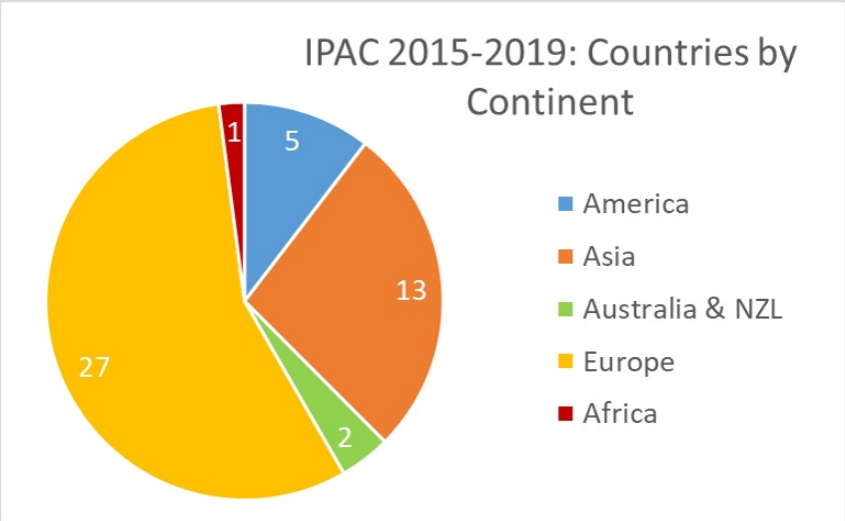

Figure 8.2.1.: Number of distinct countries by continent participating in the IPAC conferences 2015-2019.

Table 8.2.1.: Countries represented in IPAC 2015-2019 by continent.

Continent	**Number**	**Countries**
Africa	1	South Africa
America	5	Brazil, Canada, Columbia, Mexico, USA
Asia	13	China, India, Indonesia, Iran, Israel, Japan, Jordan, Korea, Pakistan, Saudi Arabia, Taiwan, Thailand, Viet Nam
Australia	2	Australia, New Zealand
Europe	27	Austria, Armenia, Belgium, Belarus, Czech Republic, Denmark, Finland, France, Germany, Greece, Hungary, Italy, Latvia, Malta, Netherlands, Norway, Poland, Portugal, Romania, Russia, Slovenia, Spain, Sweden, Switzerland, Turkey, Ukraine, United Kingdom
World	**48**	

not further considered in the analysis. Of the remaining 864 distinct institutions attending the conferences, 41% have been companies, 31% research institutes and 28% universities. These numbers might roughly outline the size of the community, although there are indications that in particular for the companies the IPAC participation might underestimate the number of actively involved players considerably due to cost-benefit considerations concerning their participation.

Figure 8.2.2(b) provides the number of participating institutions by continent. The data indicate a strong European accelerator community that represents half of the global actors in this field. The Asian and American communities amount roughly to one quarter each, the community in the Australian continent is small and limited to Australia and New Zealand, while South African has been the only African participant, despite the large size of the continent and probably a real African community does not exist currently.

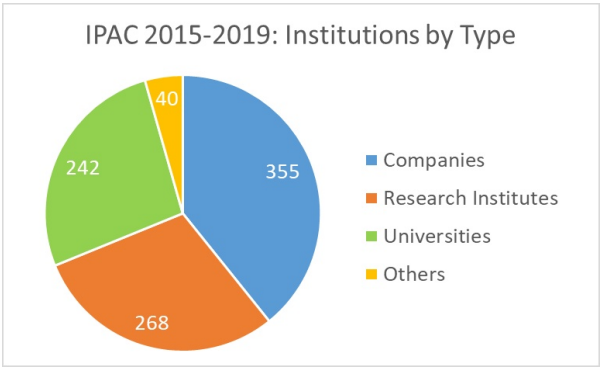

(a) Number of institutions participating in the IPAC conferences 2015-2019 by type.

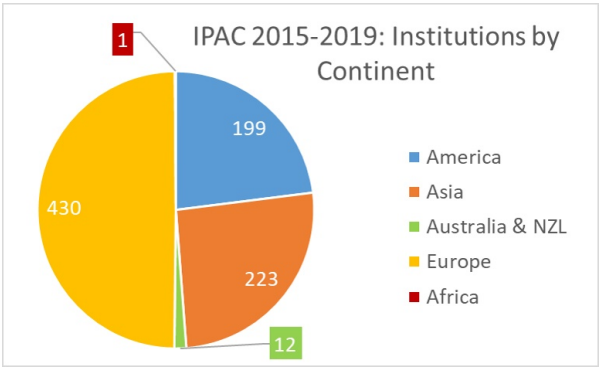

(b) Number of institutions participating in the IPAC conferences 2015-2019 by continent.

Figure 8.2.2.: Institutions participating in the IPAC conferences 2015-2019.

Companies. The analysed data show that the participation of companies in the events is closely related to their geographic location. The number of European companies at IPAC 17 in Denmark is more than twice that of events organised in other continents, and the same trend is observed for Asian companies in Korea, and American companies in the USA and Canada. This leads to the assumption expressed above, that cost-benefit considerations might limit the participation of companies in the events, which is also supported by the observation that among the 355 distinct companies attending the IPAC events, only 15% have been present 3 times and more.

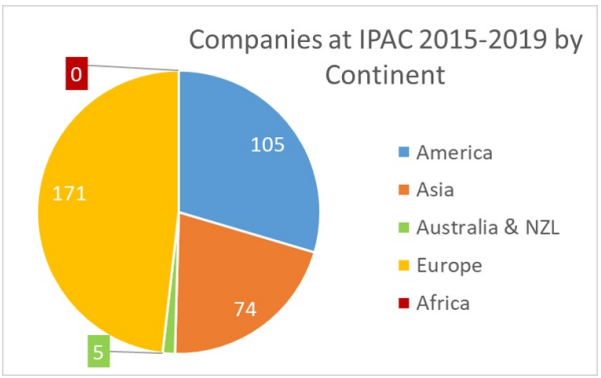

(a) Attendance of companies by continent.

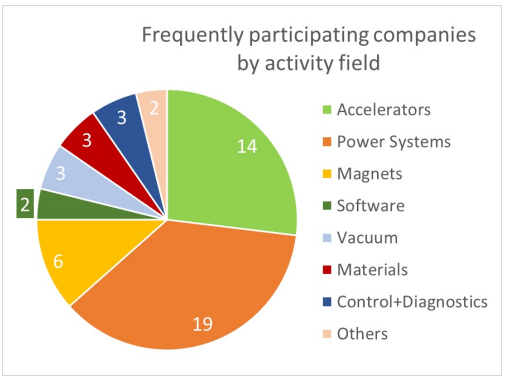

(b) Frequently participating companies by activity.

Figure 8.2.3.: Companies participating in the IPAC conferences 2015-2019.

Figure 8.2.3(a) illustrates that 48% of all participating companies are from Europe, 30% from America, 21% from Asia, and a small number of firms from Australia and New Zealand is also observed. The ratio of American companies is higher than the fraction of all American institutions in the five events. In America and Asia, the participating companies are concentrated in the economically strongest countries. 90% of the American enterprises are from the USA, 10% are Canadians. 49% of the Asian companies are Japanese, 35% are Korean and 15% are Chinese. The European companies come instead from 15 large and small countries across the whole continent.

Figure 8.2.3(b) shows a distribution of the 52 companies that participated 3 times or more in the analysed events according to their major activities as described on the companies' websites. The largest numbers of these companies are observed in Power Systems (including power systems and components, RF and microwave technologies; 19) and Accelerators (including commercial accelerators and components, precision engineering, accelerators for special applications, and services; 14). All other categories are less represented, as shown in the figure.

Research Institutes. 268 distinct research centres from a large number of countries worldwide have participated in the IPAC 2015-2019 conferences. University institutes operating major research infrastructures, such as the MAX-IV Laboratory in Lund, are also included in this category. Figure 8.2.4(a) shows their distribution by continent. 55% of all participating institutes have been from Europe, 34% from Asia and 10% from America. Furthermore have participated two Australian and one African institutes, the latter being the only representation of the African continent observed in total. While the number of countries represented by research centres is for each continent higher than that represented by companies, the participation from the economically stronger countries is again prevailing. For America, also Brazilian and Mexican institutes have been attending, but more than 80% of all institutes have been US American. For Asia, Japan, China and Korea make up for 80% of all participants, but institutes from 11 countries across the whole continent have been present at the events. 77% of the European institutes are from the big countries Germany, France, Russia, Italy and UK, but in total 19 different countries are represented and Europe is thus the continent with the highest diversity of countries.

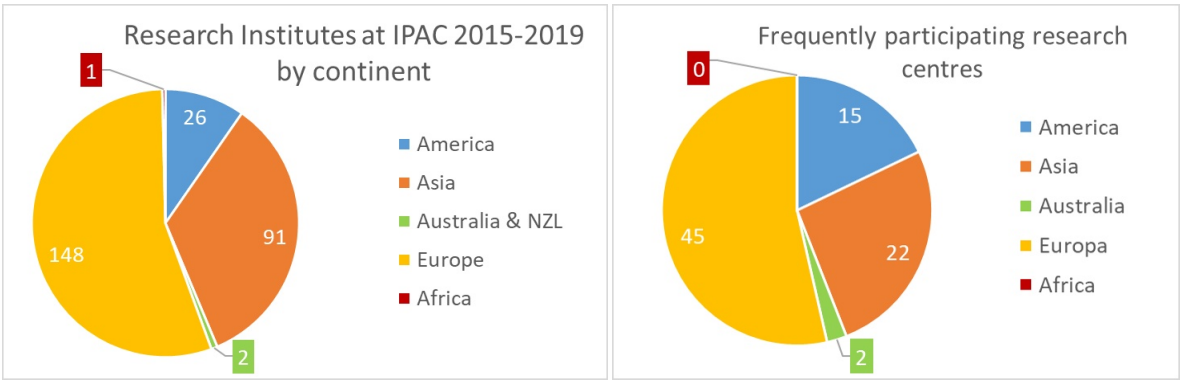

(a) Number of distinct research centres by continent. (b) Frequently participating centers by continent.

Figure 8.2.4.: Research Centers participating in the IPAC conferences 2015-2019.

84 research centres, which are 31% of the whole sample, have participated three or more times in the events. Figure 8.2.4(b) shows their distribution by continent. For America, 58% of the institutes in the sample have been frequent participators, for Asia 24%, for Australia 100%, for Europe 30% and for Africa 0%. A closer look reveals that almost all of these frequently attending institutions are running major national or international user facilities, such as particle sources, light sources, fusion reactors, or particle colliders. They include in particular all the very big accelerator-based installations worldwide. The majority, namely 69% of the sample, are however institutes participating only once in a while, which shows in particular that the whole community goes much beyond the huge installations with large public visibility.

Universities. The number of universities that have participated in the events is 242 and thus only slightly lower than the number of research centres (267). The data show a particular high participation of universities from all continents in the event in Australia and a high presence of American universities at their 'home event' in the USA. Apart from the peak attendance in Australia, the participation of Asian and European universities has not varied much with the venue of the event.

For Europe, the number of participating universities is 111 or 46% of all, and thus a bit lower than that of the European research centres. The same is observed for Asia with 58 participating universities (24%). The number of American universities (68, 28%) is instead almost three times higher than that of American research institutions, which reflects the different structure of the American research landscape. For Australia, all the numbers are low for obvious reasons and African universities have not been present. The geographic provenience of the universities within the continents is comparable to that of the research centres: Europe is represented by universities from 25 different, also small

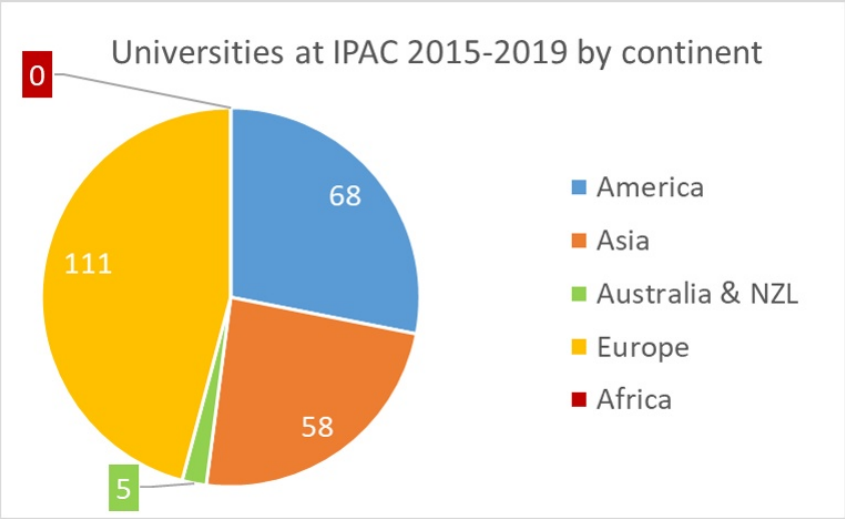

Figure 8.2.5.: Number of universities participating in the IPAC conferences 2015-2019 by continent.

countries across the continent, American universities have come from 5 countries with a very dominant US-American focus, while Asia has been represented by universities from 10 countries with large numbers from the strongest economies Japan, China and Korea. Finally, Australia and New Zealand have been represented by a rather high quote of five universities, while no African university has attended the meetings.

With 28% of all universities, the fraction of those that have participated three or more times during the analysed period is rather high and comparable to that for the research centres. This observation can be seen as an indication for a strong and consolidated community, in which also the universities play a significant and prominent role. This is an important observation, since their key role for the education and training of young researchers in the sector is certainly out of question.

Final Considerations. Large and very large research facilities, such as the giant colliders at CERN, the international fusion project ITER or the recent European projects XFEL, ELI and ESS serve international user communities and need to be planned, developed, and financed by big international partnerships, pooling knowledge and know-how from institutes, universities and companies around the world and money from several partner countries. Strong, skilled and experienced communities are required for the success of such projects, and the global accelerator community is certainly one of the flagships of global science in this respect.

The IPAC is the most important conference of this global community in the field of particle accelerators and it can be assumed that the participating research centres and universities represent together a large part of the public research sector in accelerator physics. Considering the attendance in the latest face-to-face editions of the conference in 2015-2019, these are in total 510 academic institutions worldwide, of which 94 are American (18%), 149 Asian (29%), 259 European (51%), while 7 are from Australia and New Zealand and 1 is from Africa. About 30% of the participating research centres are representing the global large-scale accelerator-based research infrastructures. Together with 30% of the universities, they are regularly participating in the events and can be considered the key players that constitute the core of the community, with a central role for its further development and integration in view of future challenges.

Additionally, the conferences have been attended by 355 distinct companies, but only a small fraction of them has regularly participated, while many have prevalently been present in events in their vicinity. For a large part of the companies the attendance of such events does not seem to be essential and there might be a considerable number of enterprises delivering high-tech supplies to a broader and diverse customer base that might benefit from new developments, which never show up in events like

IPAC. This concerns in particular also the field of small accelerator-based facilities for complementary use, for instance in industry and medicine. The complete number of concerned technology companies that could benefit from the development of new technologies and the construction of new infrastructures in the sector is therefore probably larger than those covered by the IPAC sample.

8.2.2. The Community of Accelerator-based Light Sources

After the first observation of synchrotron light at General Electrics in 1947 [284] and the subsequent recognition of its exceptional properties, scientists in the USA and Europe have started to use this new radiation for their research [285–289] and dedicated synchrotron laboratories have been constructed. Since then, accelerator-based light sources have been continuously further developed to produce light with always superior characteristics, triggering also the evolution of new experimental techniques and equipment. From its very beginning, the use of synchrotron radiation has been a real success story, which is still ongoing. It has recently led to the development of Free Electron Lasers, highly brilliant light sources with unique characteristics that complement synchrotrons and offer completely new research opportunities [50, 290, 291]. This chapter is dedicated to the global community of the accelerator-based light sources, namely the synchrotrons and free electron lasers.

8.2.2.1. Synchrotrons worldwide

An important part of the accelerator community discussed above is the community of the accelerator-based light sources producing synchrotron radiation, which is of particular interest for CompactLight. It has been analysed using the participation data from the IPAC conferences 2015-2019 presented in the last chapter above, which have been integrated with data and information collected from documents and facility websites. The results of this analysis are presented in detail in D7.2 and summarised in a more concise way in this section.

Among the institutions presented in Figure 8.2.4(b) as frequently participating in the analysed IPAC conferences are all the major FEL and synchrotron laboratories worldwide as well as representatives from major projects. Among them are also some FELs operating in the IR- and microwave region, which will however not been discussed in detail. The numbers of such light sources by continent that attended the analysed IPAC events are presented in Table 8.2.2.

Table 8.2.2.: FELs and Synchrotrons at IPAC 2015-2019 by continent.

Type	Africa	America	Asia	Australia	Europe	World
Synchrotrons	0	6	11	1	14	32
X-ray FELs	0	1	4	0	4	9
All Facilities	0	7	15	1	18	41
Host Countries	0	3	8	1	10	22

41 accelerator-based light sources from 22 host countries have participated in the events, which are most of the facilities in operation today. This underlines the importance of the IPAC for the community. The largest participation has come from Asia with 15 facilities in 8 countries and from Europe with 18 facilities in 10 countries. America has been represented by 7 facilities from 3 host countries and Australia by the Australian Synchrotron. A closer look shows that these have included 32 synchrotrons and major project from all continents except Africa and 9 FEL facilities from America, Asia and Europe.

Africa has currently no synchrotron laboratory, but Egypt is involved as a partner in SESAME and South Africa is an associated scientific partner of the European Synchrotron Radiation Facility ESRF.

European Synchrotrons. The European synchrotrons are listed in order of decreasing energy in Table 8.2.3. They are currently 16 facilities distributed in 11 distinct countries. Most of them are national light sources, except for the ESRF, which is a European facility managed by a consortium of partner countries. They offer together 298 beamlines to users, a number that will increase in the future. Based on information from the facilities, the number of annual users is estimated to over 37,000. Several European synchrotrons have been recently upgraded, are currently upgraded or are planning major upgrades.

Table 8.2.3 provides the numbers of European synchrotrons, host countries, available user beamlines, annual users as well as the electron energy range covered by these facilities.

Table 8.2.3.: Synchrotron Light Sources in Europe.

Facility	**Country**	**Operation**	**Energy (GeV)**	**Beamlines**	**Users/Year**
ESRF	France	1994	6	48	9,024
PETRA III	Germany	2010	6	25	4,300
ALBA	Spain	2012	3	10	1,766
Diamond	United Kingdom	2007	3	33	10,437
MAX IV	Sweden	2017	3	8	945
Soleil	France	2008	2.75	29	4,138
KISI-Kurchatov	Russia	1999	2.5	16	60 groups
SLS	Switzerland	2001	2.4	16	1,035
Elettra	Italy	1993	2.0 & 2.4	16	1,231
Bessy II	Germany	1998	1.72	46	3,200
DELTA	Germany		1.5	12	...
SOLARIS	Poland	2018	1.5	4	400
MAX IV	Sweden	2017	1.5	5	included above
MLS	Germany	2008	0.63	7	...
ASTRID 2	Denmark	2013	0.58	6	150
DAFNE	Italy	2000	0.51	5	30
16	**11**			**298**	**about 37,000**

Figure 8.2.6 maps the distribution of the European synchrotrons by country, using a color code for the number of synchrotrons in each country.

The figure shows that the synchrotrons are mostly distributed over the western part of Europe, while among the Eastern countries only Poland and Russia are hosting facilities. Except for the European light source ESRF in France, which is operated by a consortium of 12 European Countries, all synchrotrons

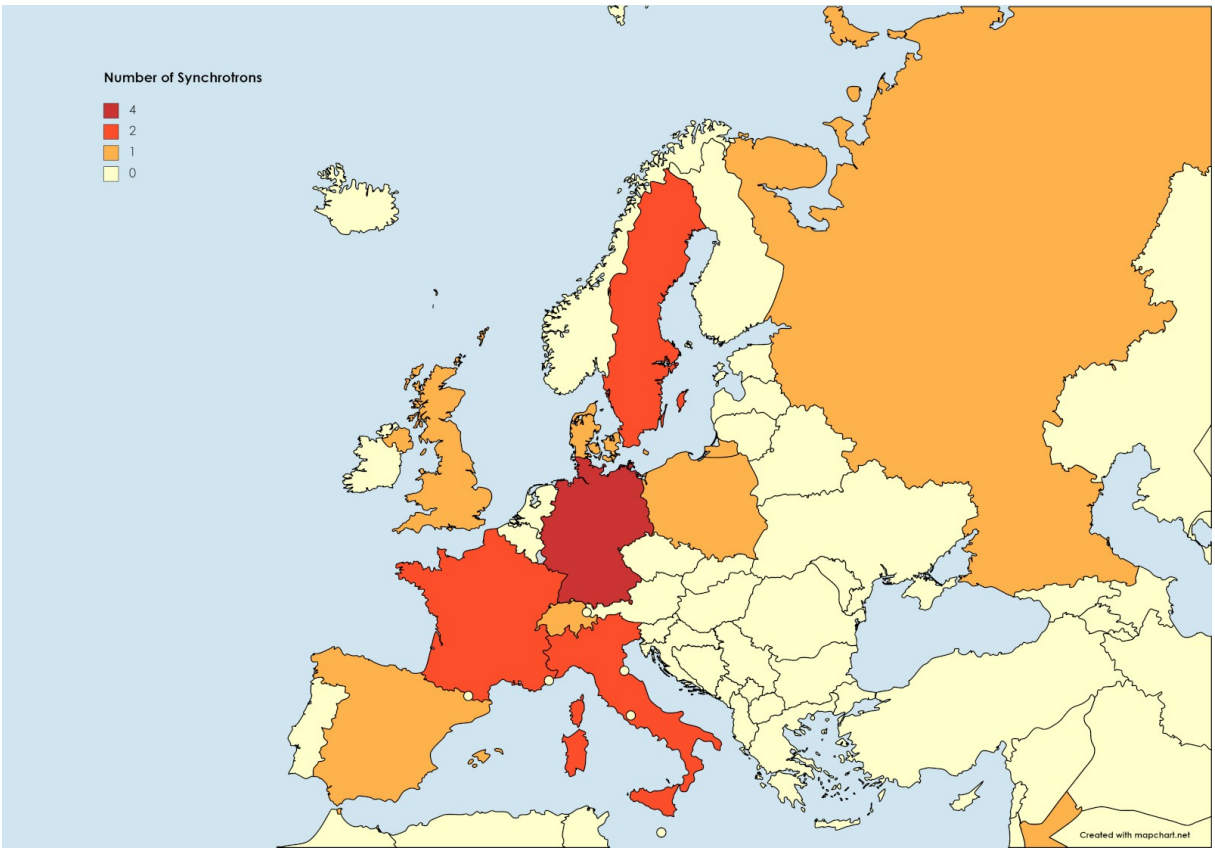

Figure 8.2.6.: Synchrotrons in European countries. Color code: dark read: 4 facilities, red: 2 facilities, orange: 1 facility, beige: no facility.

are national facilities and they are prevalently operated by the economically stronger countries. In particular the South and Central Eastern region of Europe is not hosting any such facility.

American & Australian Synchrotrons. A list of the 8 synchrotrons operating in America and Australia is available in Table 8.2.4. One of them is the Australian Synchrotron, which is the only light source in the Australian continent. In America, five facilities are hosted in the USA and one in Canada, while the Brazilian synchrotron Sirius is the only available large accelerator-based light source in Latin America. America offers currently 160 beamlines to its users, 10 beamlines are available at the Australian Synchrotron. Sirius and the Australian Synchrotron are planning to increase their numbers. The annual user visits are estimated to 5,000 in Australia and about 14,400 in America. Sirius is a new synchrotron that started operation in 2020, replacing the first Brazilian light source UVX. In the United States, the NSLS has been upgraded to NSLS II some years ago, while upgrading projects are currently in course for the ALS (ALS-U) and the APS (APS-U).

Asian Synchrotrons. The 15 Asian synchrotron laboratories are listed in Table 8.2.5. National synchrotron light sources exist in six countries, Iran is currently constructing a national facility. The Synchrotron SESAME in Jordan is operated by a collaboration of various Near and Middle Eastern partner states from Asia, Europe and Africa. As observed already for America, most of the available user facilities are operated by the economically strong countries in the far east, but with India, Jordan (SESAME partners: Cyprus, Egypt, Iran, Israel, Jordan, Pakistan, Palestine, Turkey) and Iran the geographic distribution is becoming broader and scientific users in more parts of the continent will gain access to synchrotron light. In Asia, 254 beamlines are currently available and serve more than 35,000 users

Table 8.2.4.: Synchrotron Light Sources in America and Australia.

Facility	Country	Operation	Energy (GeV)	Beamlines	Users/Year
APS	United States	1995	7	35/68	6,000
NSLS II	United States	2015	6	28	1,700
CHESS	Unites States	1980	6	7	1,000
SSRL II	United States	2004	3	27	1,700
AS	Australia	2007	3	10	5,000
Sirius	Brazil	2020	3	6	1,000
CLS	Canada	2004	2.9	17	1,000
ALS	United States	1994	1.9	40	2,000
8	**4**			**170**	**about 19,400**

annually.

Global view on synchrotrons. In this study have been identified 39 synchrotrons in operation worldwide on 4 continents and open for external users. Except for Africa, all continents offer users the possibility to do research with synchrotron light. 22 countries are operating such facilities, which is a very small number in a global context, and most of them are the economically stronger countries around the world. This means that users in large regions of the globe are still lacking important research possibilities today, in particular in Africa, Latin America, many Asian countries, and in South-east and East Europe. 740 beamlines are available worldwide and the size of the community is estimated to over 92,000 users per year.

8.2.2.2. X-ray FELs worldwide

The X-ray FELs in operation are currently 8, located in the economically strongest and scientifically most advanced countries of the northern hemisphere, namely in the United States, Japan, Korea, China, Germany, Switzerland and Italy. A list of these facilities is given in Table 8.2.6. The table includes also two projects that are supposed to start user operation in 2022, which are the LCLS II in the USA and the Chinese soft x-ray facility SXFEL in Shanghai.

American X-ray FELs. The national American X-ray FEL LCLS has started operation in 2009 as the first facility open for users worldwide. The NC accelerator has a final electron beam energy of 15 GeV, which allows to supply SX and HX photons in the energy range from 250 eV to 25 keV for research at 7 experimental beamlines. The facility has been used in average by 1,000 users annually.

The LCLS is currently integrated with the new LCLS II facility based on a SC accelerator with a final energy of 4 GeV. The electrons from the SC linac will feed two new undulator lines, one for operation with SX in the energy range 200 eV-1,300 eV, the second for operation with HX in the energy range from 1 keV to 5 keV. Both X-ray sources can operate simultaneously. Using the LCLS NC linac, which will remain in operation, the spectral range can be extended to 25 keV. The project is using existing infra-

Table 8.2.5.: Synchrotron Light Sources in Asia.

Facility	Country	Operation	Energy (GeV)	Beamlines	Users/Year
Spring-8	Japan	1997	8	56	15,000
PF-AR	Japan	2002	6.5	8	3,000 with PR ring
SSRF	China	2009	3.5	15	1,000
PLS-II	Korea	2012	3	35	1,300
TPS	Taiwan	2016	3	5	13,000 with TLS
PF ring	Japan	1982	2.5	40	see PF-AR
BSRF	China	1991	2.5	14	1,000
Indus II	India	2007	2.5	17	
SESAME	Jordan	2017	2.5	3	65 groups
TLS	Taiwan	1994	1.5	24	see TPS
SPS	Thailand	2003	1.2	10	
HLS	China	2014	0.8	10	
UVSOR-III	Japan	2012	0.75	14	
e HiSOR	Japan	1996	0.7	15	240
Indus I	India	1999	0.45	6	
15	**7**			**272**	**over 35,000**

structure at SLAC, which limits the project costs to 1,045 B$, including material, labour, civil construction and commissioning [14, 292].

Asian X-ray FELs. In Asia, X-ray FELs are operating in Japan, Korea and recently China. The Japanese light source SACLA started user operation in 2012 as the first FEL in Asia. It is a NC machine delivering electrons at a final energy of 8.5 GeV to three undulator lines for SX and HX operation, which feed 3 experimental beamlines with photos in the energy ranges of 40 eV-150 eV (SX) and 4 keV-20 keV [293] (see also Facility website for status of the experimental beamlines).

At the PAL XFEL in Korea the NC accelerator delivers electrons at 11 GeV to two FEL lines for SX and HX operation. The SX undulator produces photons in the range of 300 eV-1,200 eV for one experimental line, the HX undulator feeds two experimental lines with hard X-rays at 2.5 keV-13 keV [294].

The new Chinese soft X-ray FEL SXFEL in Shanghai will be open to users in 2022. The machine produces electrons at an energy of 0.84 GeV, which feed two undulator lines producing SX photons for currently two experimental lines which will become more in the future. The project is supposed to push also the Chinese project for a SC hard X-ray FEL Shine, for which commissioning is expected to start in 2025 [295, 296].

Table 8.2.6.: X-ray FELs worldwide.

Facility	Country	Operation since	Energy (GeV)	Photon Energy (keV)	FEL Lines	Exper. Lines
EU-XFEL	Germany	2017	17.5	0.25-25	3	6
LCLS LCLS II	Unites States	2009 2022	15 4	0.25-25 0.25-1.2, 1-5	2	6
PAL FEL	Korea	2017	11	0.3-1.2; 2.5-13	3	3
SACLA	Japan	2011	8	0.04-0.15; 4-20	3	3
SwissFEL	Switzerland	2019	5.8	0.25-12.4	2	5
FERMI	Italy	2012	1.5	0.015-0.31	2	6
FLASH	Germany	2005	1.25	0.014-0.310	2	7
SXFEL	China	2022	0.84	0.22-0.62	2	1
8	**7**				**19**	**37**

European X-ray FELs. In Europe, users are currently served by three national X-ray FELs and one European facility, which are located in Italy (FERMI), Switzerland (SwissFEL), and Germany (FLASH, European XFEL). Additionally, Sweden has a rather mature project for a national hard X-ray facility in Lund and also the scientific community in the UK has an advanced initiative for setting up an X-ray FEL in the country. The idea to create also a facility in Greece has recently emerged and will be further developed now.

The European XFEL is the largest X-ray FEL in the world, located in Germany and operated jointly by 12 European Countries. The facility, with an overall cost of 1.25 billion Euros (2005 cost level), started user operation in 2017. The unique SC linac of the EU XFEL is supplying three undulator lines with electrons at an energy up to 17.5 GeV, which produce SX and HX radiation for 6 experimental beamlines. The available photon energy range for SX photons is 0.26 keV to 3 keV, that for HX photons ranges from 3 keV to 25 keV. In 2019, 891 individual users have participated in experiments at the EU-XFEL, a number which decreased in 2020 to 364 individual users involved in experiments performed mostly in remote [8, 297–299].

The SwissFEL is a national X-ray FEL light source in Switzerland that started its regular user operation in 2019. The SwissFEL linac allows operation up to an electron energy of 5.8 GeV and two undulator lines produce SX and HX radiation in the photon energy ranges of 250 eV to 1,800 eV and from 2 keV to 12.4 keV, respectively. One end station for experiments with SX photons is open to users, a second one is currently under commissioning. For research with HX photons, two instruments are in operation and the commissioning of the third one is planned for 2022 [11, 282, 300].

The national Italian soft-X-ray FEL, FERMI, has been designed for producing high-quality photon pulses in the EUV and soft-X-ray spectral range. The facility, based on a NC linac that can operate up to 1.5 GeV, is serving external users since 2012. While most of the operational facilities are based on the SASE process (Self-Amplified Spontaneous Emission), where the FEL process is driven by spontaneous incoherent electron emission, characterized by lower shot-to-shot spectral and temporal stability and a limited longitudinal coherence, FERMI is the first user facility based on the HGHG scheme (High-Gain Harmonic Generation), where the FEL process is triggered by an external seed laser. This allows

to obtain full coherent photon pulses with stable central wavelength and an unprecedented spectral stability. FERMI has two undulator lines that produce soft X-ray radiation in the energy range from 15 eV to 310 eV and offers to users 6 experimental beamlines [4, 5].

FLASH, a national German facility, has been the first Soft X-ray FEL open to users. The facility, which started user operation in 2005, works at a final energy of 1.25 GeV and covers with two undulator lines a photon energy range from 14 eV to 310 eV. Additionally, it offers also the possibility to work with THz radiation. For operation with SX photons, Flash disposes of 2 undulator lines and 7 experimental beamlines [2, 301]. A major upgrade of FLASH, the FLASH 2020+ project, is currently in course, concerning both, machine and undulator lines. The upgrade will increase the electron energy range to 1.35 GeV and permit a fully parallel operation of the two FEL lines, which will increase both, user beamtime and experimental opportunities [302, 303].

8.2.2.3. European X-ray FEL Projects

Four major initiatives for new X-ray FELs exist currently in Europe: a Swedish FEL project at the MAX IV laboratory, the UK FEL project, a soft X-ray FEL initiative in Greece and the European project EuPRAXIA based on plasma accelerator modules. The most advanced of these projects are the Swedish one, which has already completed the conceptual design study, and the EuPRAXIA project, which is recently entered in the Preparatory Phase of the technical design report while the Greek project is in its very initial phase. Further European user communities are potentially interested in developing projects.

Sweden. Based on Sweden's strong tradition and huge expertise with the construction, operation and use of accelerator-based photon sources and after completing the world's first fourth generation storage ring MAX IV, Swedish accelerator scientists and users are now exploring the possibility of constructing at MAX IV a soft X-ray FEL called Soft X-ray Laser (SXL), an option already included at the design phase of the MAX IV facility.

In spring 2016 a user workshop on the scientific opportunities offered by a soft X-ray FEL was organized in Stockholm, where over 100 Swedish scientists formulated the scientific case report entitled SXL: "A Soft X-Ray Free Electron Laser beamline at the MAX IV facility". A conceptual design study of the SXL, funded by 3 Swedish universities, MAX IV and the private Swedish foundation "Knut and Alice Wallenberg Foundation" has been completed in 2021 and proposes a soft X-ray SASE FEL for studies of ultrafast processes in atomic and molecular science, chemistry, condensed matter physics and life science [304].

SXL will operate in the range of 1 - 5 nm (0.25 keV-1.2 keV), covering important absorption edges and offering element-specific selectivity. The facility will consist of (i) the already operating MAX IV 3 GeV linear accelerator, (ii) a new 40 m APPLE X type undulator, (iii) three photon beamlines and (iv) a set of experimental stations. The accelerator design will enable the generation of X-ray pulses down to sub-fs durations and the APPLE X type undulator will provide full polarization control of the photon beam and allow, for example, studies of magnetic circular dichroism. SXL will be able to operate in several modes, including double pulses with individually tunable wavelengths and delays for two-pulse two-color operation as well as flexible pump-probe operation schemes. The facility will provide a pink and a monochromatic photon beamline optimized for time resolution and energy resolution, respectively.

United Kingdom. The development of the Science Case for a UK XFEL was launched in 2019 under the auspices of STFC. The UK academic and industrial community carried out a wide consultation process over an extended period and this culminated in the Science Case being published in October 2020 [305]. The document articulates a strong motivation for building a UK XFEL and presented several potential facility options, which would be able to satisfy the user requirements to a greater or lesser extent. The CompactLight concept of generating soft X-rays at a high repetition rate and hard X-rays

at a lower repetition rate is explicitly mentioned as one of the options that will be considered when the Conceptual Design phase of this project commences, which is currently anticipated to be in early 2022.

The CLARA FEL Test Facility at the Daresbury Laboratory is a user facility dedicated to the demonstration of new accelerator technologies and advanced concepts for FEL operation, which has also the objective to pave the way for the UK XFEL. The facility is designed for at a maximum electron energy of 0.25 GeV, with the aim to enables photon energies in the range of 100 nm-400 nm in a future phase 3. The project is currently in phase 2 and first user experiments with high energy electrons have taken place in 2018/2019. The integration with an undulator line for the production of FEL radiation is planned in phase 3, which is however currently not yet funded [306–309].

Greece. The existing light sources and those under development in Europe are operating in the Northern and Western of the continent, while in the South-East European region no facility of this kind is currently running or in construction. CompactLight collaboration provides in the project's CDR a flexible design for a novel generation of innovative, relatively cheap and compact FEL facilities that can be adapted to the requirements of scientific, industrial and medical applications. This will facilitate the use of the CompactLight technologies and designs for constructing affordable and sustainable FEL light sources tailored to the specific needs and available resources of institutions and user communities in the different European regions, and such initiatives are explicitly supported by the partners through dedicated activities during and after the project.

Under this premise has been expressed the interest of Greece to develop, if possible in collaboration with other countries in the region, a case study aimed at the implementation of the CompactLight design for the construction of a soft X-ray FEL in the country. The initiative shall be enabled through close collaborations and dedicated knowledge and technology transfer activities between relevant CompactLight partners and Greek/South-Eastern European institutions.

The National Technical University of Athens (NTUA) has officially submitted a proposal for an FEL facility, for medical and industrial applications, to be installed and commissioned at the NTUA Technological and Cultural Part of Lavrion, about 60 km outside of Athens downtown. The area for the FEL installation will be provided for free by NTUA and all the necessary infrastructure exists already in this area due to other technological laboratories operating there.

The proposal is now under funding investigation by the Ministry of Development and the Ministry of Finance, with the idea that the main resources will be provided from the European recovery fund. Most of the participating institutes and laboratories in the CompactLight collaboration have expressed their will to support and cooperate for the installation and commissioning of such the FEL in Athens.

EuPRAXIA. It is widely accepted by the international scientific community that a fundamental milestone towards the realization of a plasma driven future Linear Collider will be the integration of high-gradient accelerating plasma modules in a short wavelength Free Electron Laser (FEL) user facility [310]. To this end the EuPRAXIA project (European Plasma Research Accelerator with eXcellence In Applications) is expected to provide by the end of 2028 the first European Distributed Research Infrastructure dedicated to demonstrate usability of plasma accelerators delivering high brightness beams up to 1-5 GeV for driving short wavelength Free Electron Laser User Facilities [311].

In its first implementation phase, the EuPRAXIA consortium will construct a Beam Driven Plasma Wakefield Accelerator facility (PWFA), named EuPRAXIA@SPARC-LAB at the LNF-INFN [312]. In its second phase, EuPRAXIA consortium will build a Laser Driven Plasma Wakefield Accelerator facility (LWFA) at a site to be chosen within the next 2 years between several options in Europe.

The PWFA facility will consist of a high brightness S-band RF photoinjector equipped with a hybrid compressor scheme based on both velocity bunching and magnetic chicane. The energy boost up to 1 GeV will be provided by chain of high gradient X-band RF cavities as the one developped in the framework of the XLS collaboration. At the linac exit a plasma accelerator section will be installed, which includes the plasma module (1 m long) and the required matching and diagnostics sections.

In the downstream tunnel an undulator chain will be installed able to provide SASE radiation source at 4 nm, in the spectral region called “water window”, as the one required to drive the biophysics user beam lines. Additional developments are also under investigation, including the one of particular interest for FEL user facilities such as high repetition rate plasma module (kHz range).

The EuPRAXIA project has received official government support from Italy, Czech Republic, Portugal, Hungary and UK. Financial support of 118 M€ has been already committed, mainly from Italy as lead country. The EuPRAXIA consortium includes in total 51 institutes from 15 countries. Finally the European Strategy Forum on Research infrastructures (ESFRI) has assessed the maturity of the EuPRAXIA project during a recent review of new research infrastructures for Europe, leading to the inclusion of EuPRAXIA in the ESFRI Roadmap 2021.

8.2.2.4. Some concluding considerations on X-ray FELs

Figure 8.2.7 shows the distribution of FELs in Europe, highlighting their frequency in a country by colors (dark red: 3 facilities, orange:1 facility, beige:no facility). The figure includes also the three European THz/Infrared FELs in hosted by France, Germany and the Netherlands, as well as the more advanced FEL projects in Sweden, Turkey and the United Kingdom (in green). The figure illustrated clearly that currently only the economically strongest countries in Europe can afford to construct and operate X-ray FELs, an observation confirmed at a global level also by Table 8.2.6. In Europe these countries are Germany, Italy and Switzerland today, in Asia Japan, China and Korea and in America the United States.

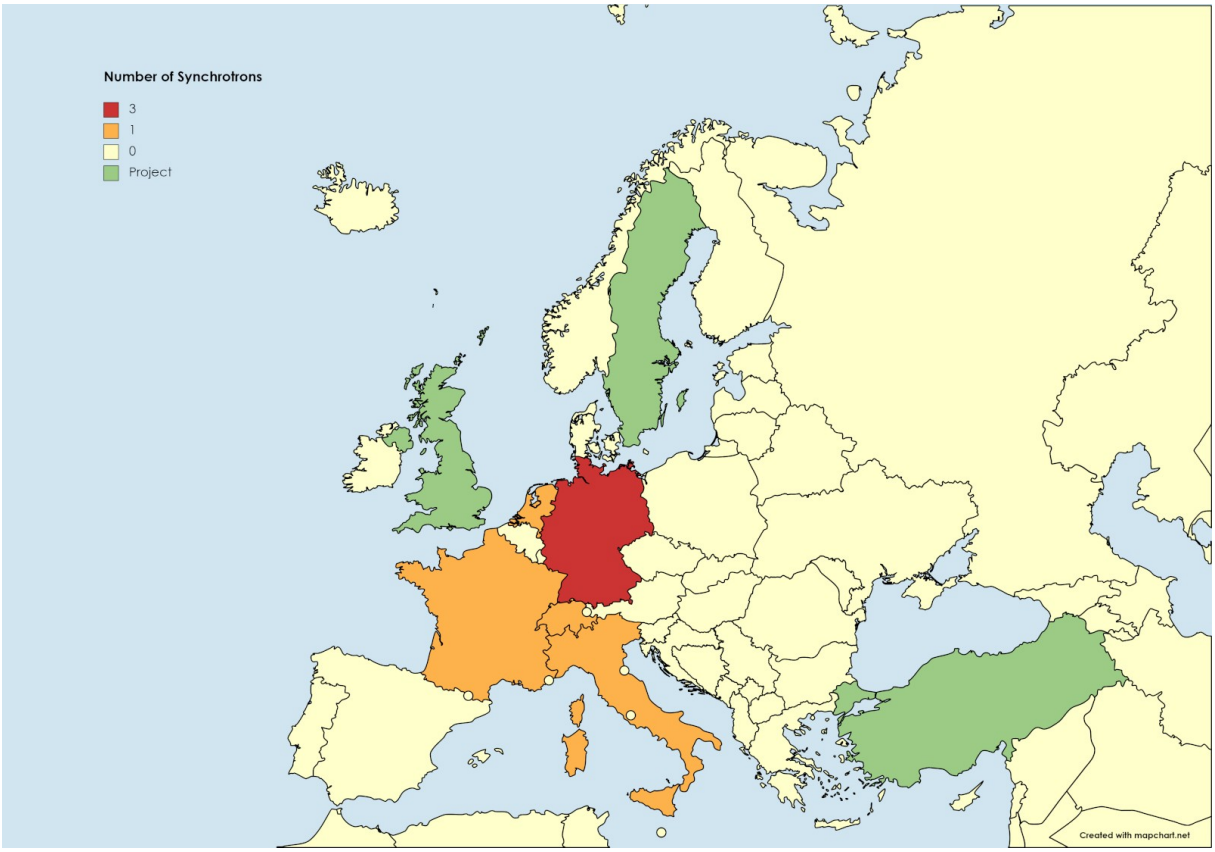

Figure 8.2.7.: Free Electron Lasers in European countries, including the THz/infrared FELs and major FEL projects (countries in green). Color code for the number of FELs per country: dark read - 3, orange - 1, beige - none.

These observations show in particular that access for researchers to important novel technologies

and to crucial scientific tools is still lacking in large parts of the world, especially in the southern hemisphere. Indeed, all X-FELs and synchrotrons for external users in the survey above are hosted by the economically strongest northern countries. This is even the case in Europe, with a strongly integrated research community and many national facilities and it applies also to the two big "European Facilities" ESRF and EU-XFEL, operated in France and Germany by consortia composed prevalently of the most developed, rich nations. And for other large accelerator-based facilities in Europe, such as CERN, FAIR, ESS, ITER, the situation is the same, with the only exception of ELI.

It is quite obvious that this is consolidating the existing economic status quo and widening the current knowledge and technology gap between stronger and weaker European countries. Given the importance of science and technology for the economic development, the consequence will even be a further increase of the economic gap, with no possibility for the weaker countries to catch up. Furthermore, it will very likely fuel the brain drain, since cutting-edge facilities are attracting the brightest minds of the continent and accumulating them in the most advanced and richest countries. Projects like SESAME can give hope in this scenario, but many more of them are needed in the underprivileged regions of the world. For this aim, technology must become more affordable and strong, altruistic support by the rich world countries for initiatives in poorer regions are required.

8.2.3. Users of Accelerator-based Light Sources

The Tables 8.2.3 - 8.2.5 of subsection 8.2.2 show, that 16 synchrotrons are currently operating in Europe and 23 in other continents. Furthermore, 8 X-ray FELs in three continents are serving the world-wide community at the moment. They are listed in Table 8.2.6 and are including the SXFEL in China, which has been announced to open user operation soon. The users of these facilities and their needs are in the focus of this chapter.

The trend in the number of proposals submitted every year by the users of synchrotrons and X-ray FELs and the fraction of them that have been allocated for beamtime provide information about how far the existing facilities can satisfy the demands from the scientific community. Proposal data from the Annual Reports of the European synchrotrons Elettra [313], ESRF [314], ALBA [315] and MAX IV [316] as well as the X-ray FELs FERMI and EU XFEL have been analysed to get some insights into this question.

8.2.3.1. Proposals and proposal allocation at European synchrotrons

Submitted proposals. The number of user proposals received annually in the years 2013 - 2020 by the four synchrotrons is illustrated in Figure 8.2.8. For Elettra, which is in operation since 1993, the number has been constantly between 800 and 900 per year in the period 2013-2019. The European Synchrotron Radiation Facility ESRF is open to users since 1994 and has just undergone a major upgrade, which required a shutdown in 2019. At ESRF, the number of received proposals has been about 2,500 during the last three years before the upgrade and roughly 2,000 in the years 2013-2015. At ALBA, which started user operation in 2012, the number of submitted user proposals has been continuously increasing over time and has now reached 600 per year. MAX IV, which has substituted the old synchrotron in Lund, restarted small-scale user operation during commissioning of the facility in 2017 and received about 450 proposals in 2019. In all facilities, the COVID-19 pandemic has affected user operation considerably and the 2020 data are not comparable to those of the years before.

Proposal allocation rates. Figure 8.2.9 shows the proposal allocation rates (number of allocated proposals as a percentage of the number of submitted proposals) for the period 2013 - 2020 at the synchrotrons Elettra, ESRF, ALBA, and MAX IV.

The data show that the facilities can satisfy the user demands in part. For Elettra and Alba, beamtime can be allocated to slightly more than half of the proposals submitted by the users with a bit of variation

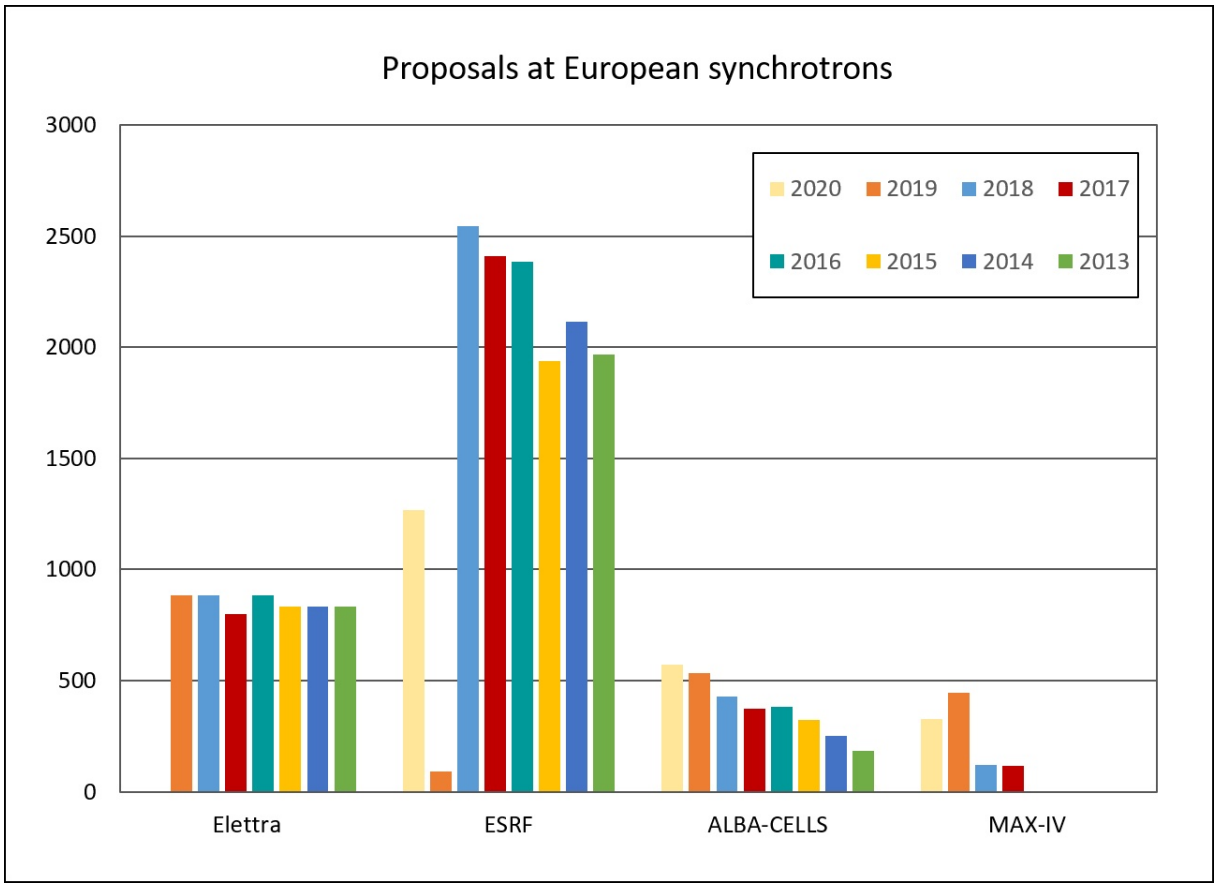

Figure 8.2.8.: User proposals submitted to European synchrotrons 2013 - 2020

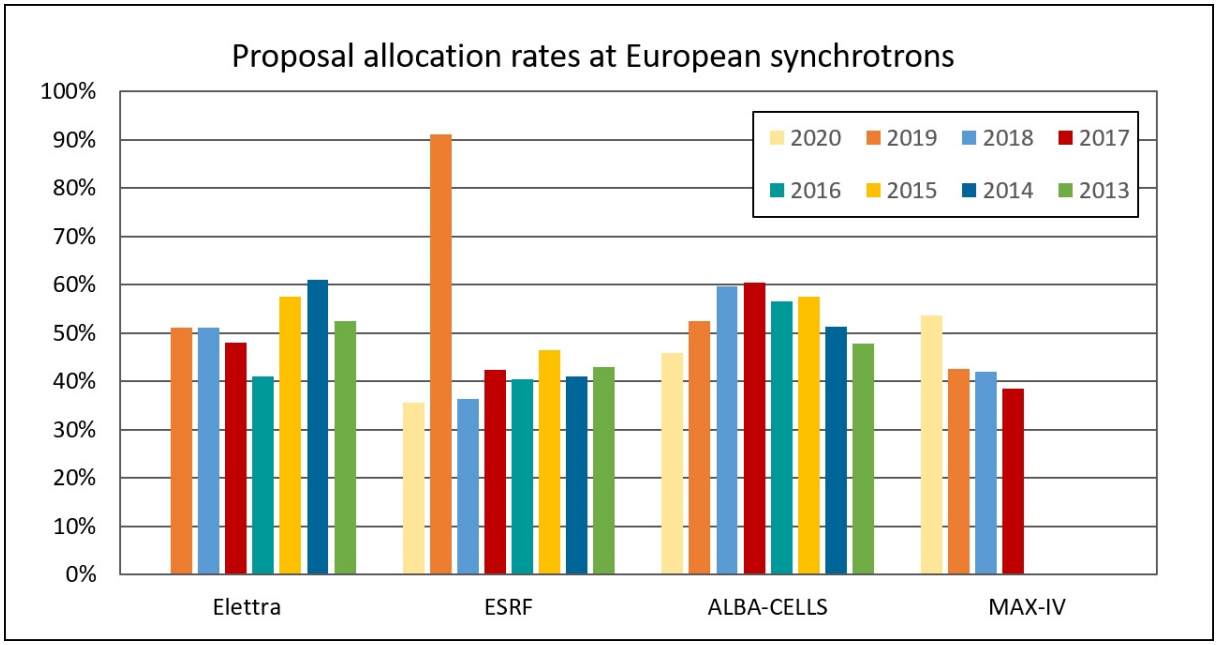

Figure 8.2.9.: Proposal allocation rates at European synchrotrons 2013 - 2020

from year to year. The average value over the considered period is 53% for both, Elettra and ALBA. At the ESRF, the indicated allocation rate for 2019 does not concern the X-ray beamlines that have been shut down due to the facility upgrade. Since the total number of received and allocated proposals has

therefore also been very small, this does not affect the average proposal allocation rate over the whole period, which is 41%. At MAX IV, user operation has just started in 2017 and proposal data are only available for a very short period since then, with an average proposal allocation rate of 46%.

8.2.3.2. Proposals and proposal allocation at European FELs

Submitted proposals. Figure 8.2.10(a) and Figure 8.2.10(b) show the number of submitted proposals at FERMI and the EU-XFEL, respectively. The data for FERMI stem from the annual reports of the laboratory [313], those for the European XFEL from their annual reports and presentations at their User Meetings [298, 299, 317–319]. They refer to the single calls for proposals of the facilities.

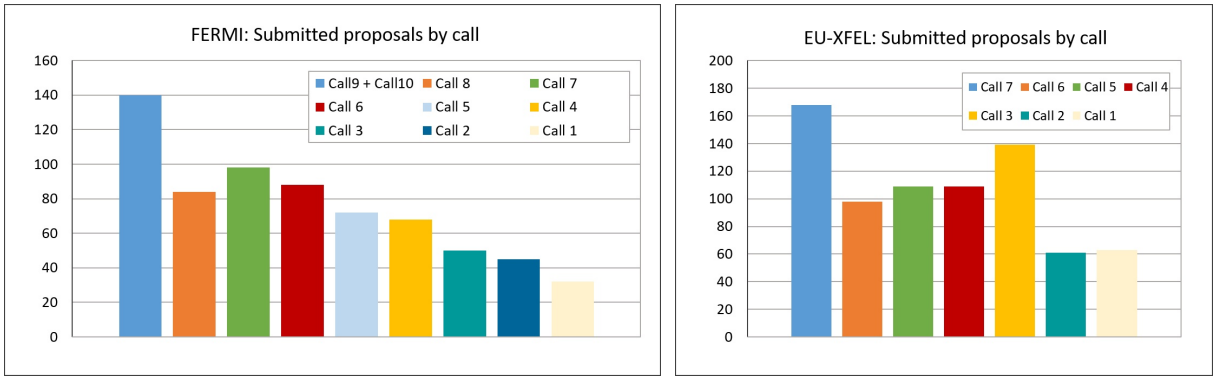

(a) Submitted proposals at FERMI.

(b) Submitted proposals at the EU XFEL.

Figure 8.2.10.: User proposals received at FERMI and EU XFEL by call.

The data for FERMI cover the calls of the years 2012 - 2019, in general one per year. A supplementary call in the end of 2017 has probably reduced the number of proposals received in 2018. The proposals of the two calls for 2019 are integrated in a single data point. The figure shows that the users' request for beamtime has been continuously increasing since the beginning of regular user operation at FERMI, a trend that is still ongoing today. Data for 2020 and 2021 that show the effects of COVID-19 are not available yet.

At the European XFEL there are two calls for user proposals every year, starting in 2017 with calls for 'user assisted commissioning' of the facility. Regular user operation began in 2018 and caused a huge request for beamtime in calls 3, when the availability of the user instruments, which are fully operational since summer 2019, was still reduced. The number of submitted proposals has settled down at about 100 per call before the COVID-19 emergency, which has required to cancel the first call in 2020. For the call in the end of 2020, a very high number of proposals has then been received.

SwissFEL started user operation with a first call for proposals in autumn 2018, dedicated to beamtime allocation in 2019. The start of user operation occurred thus just before the COVID-19 pandemic. PSI has informed on their website, that 73 proposals have been submitted and 10 (14%) have been allocated for experiments in 2019, while 71 have been submitted and 11 (15%) allocated in 2020 .

Proposal allocation rates. Figures 8.2.11(a) and 8.2.11(b) show for each call the rate of proposals allocated for beamtime at FERMI and the European XFEL. For FERMI these have been roughly 30% over the last years, an order of magnitude that has also been confirmed for call 8 - call 10, but yet without concrete numbers. The data for the European XFEL indicate an allocation rate of about 25%, which means that one proposal over 4 can be allocated for beamtime. At SwissFEL, the allocation rate for the first two calls is near 15%. These data show that at the European facilities the user demand for beamtime is considerably higher than the available capacity of the facilities. For the hard X-ray machines less than one request over 4 can be satisfied currently, with a trend towards even lower

allocation rates for the European X-FEL. Considering, that both facilities have started operation only recently and that their user communities will further develop, a further increase of beamtime applications can be expected. Personal discussions suggest also, that a considerable number of potential FEL users is currently not submitting applications due to the low success probabilities. The past experience with the synchrotrons indicates indeed that the development of user communities depends also on the availability of accessible infrastructures in their vicinity, and FELs exist in Europe currently only in Germany, Italy and Switzerland.

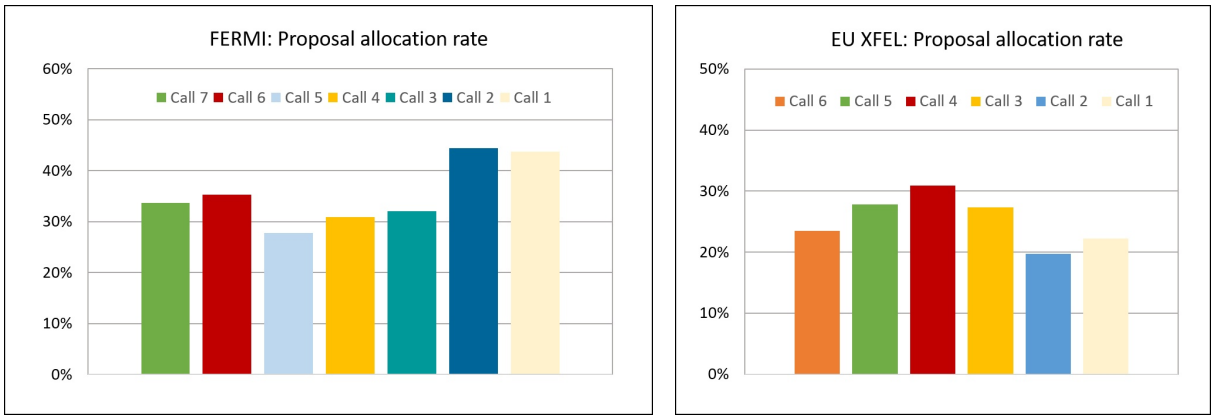

(a) Proposal allocation rate at FERMI.

(b) Proposal allocation rate at the EU XFEL.

Figure 8.2.11.: Proposal allocation rates at FERMI and EU XFEL by call.

8.2.3.3. Users of European photon sources

A strong and consolidated user community of photon sources has developed in the last decades in Europe, promoted through dedicated projects also by the transnational access programme of the European Commission. The users of many European counties are represented by national user organisations collaborating in the European Synchrotron and FEL User Organisation ESUO, as illustrated in the map of Figure 8.2.12. Considering the countries west of Russia, a lack of representation exists at the moment mainly in the Balkan region south-east of Croatia and in the Eastern European countries Romania, Moldova, Ukraine, and Belarus.

ESUO has estimated the size of the European community to more than 30,000 users [320]. At present, the largest part of them are users of synchrotron laboratories, which have a long history in Europe and developed their user communities over many decades, and only a minority are users of the few available European X-ray FELs, which started their user operation with the soft X-ray FEL Flash in 2005. Synchrotrons can accommodate a large number of beamlines where experiments can be done in parallel, while the possibilities for experiments in parallel are very limited at X-ray FELs. At European synchrotrons, 298 beamlines, of which more than 233 can work in parallel [321], are available for users today, while European X-ray FELs are offering only 11 FEL lines and 25 experimental lines, see section 8.2.2. At the moment it is difficult to estimate the size of the FEL community that is using European facilities, but the following data might give an indication.

The numbers indicate that the research at X-ray FELs involves even at a national facility, such as FERMI, a large number of countries. The 33 proposals allocated at FERMI for beamtime in 2019 have involved 148 individual users from 17 countries worldwide, 121 being European researchers from 12 European countries. The experiments at the EU XFEL have been performed by considerably larger collaborations. 56 research proposals have received beamtime in 2019 and 891 international researchers from 28 different countries around the globe have participated in the experiments, which yields an average of 16 researchers per project. 681 of these users of the EU XFEL have been European and they have come from 21 different countries in the continent.

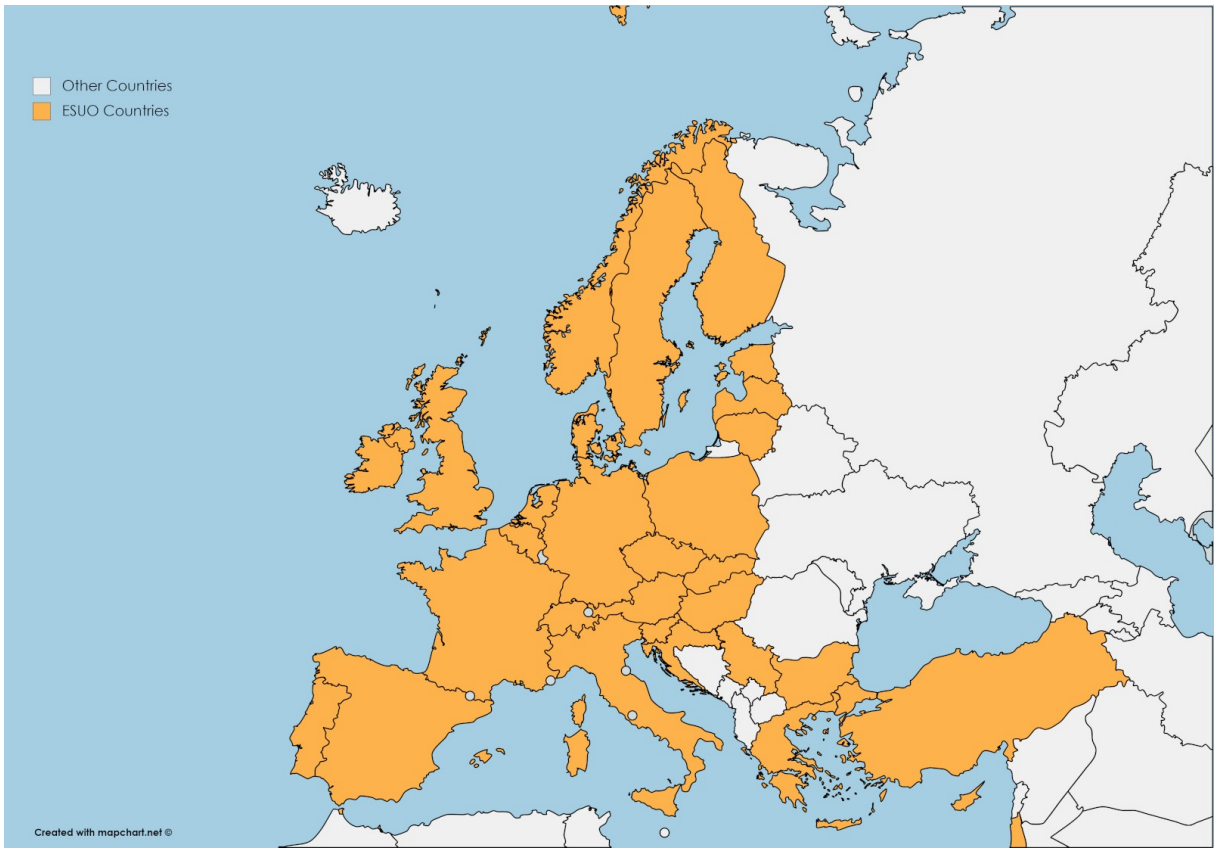

Figure 8.2.12.: Countries of the European Synchrotron and FEL User Organisation

Table 8.2.7.: Users 2019 at FERMI and EU XFEL.

Facility	Proposals	European Users	European Countries	All Users	All Countries
FERMI	33	121	12	148	17
EU XFEL	56	681	21	891	28

Given in years of normal operation a number of allocated proposals at FERMI in this range and a current proposal allocation rate of about 30%, and assuming that the situation is comparable for FLASH, the user community of the European soft X-ray FELs can be estimated to more than 1,000 individual users. For the EU X-FEL the data above and a proposal allocation rate of 25% suggest an active user community of a few thousand users already in their first year of operation, of which more than 75% are European. The size of the user community of European X-ray FELs will grow further in the next years, considering that numbers for the SwissFEL are not yet included, that both European hard X-ray FELs are still in a very early phase of their user operation, and that a couple of projects for setting up further facilities exist in Europe in these days.

8.2.3.4. Examples of users at European synchrotrons

Users from the European Union at Elettra. Figure 8.2.13 shows the countries of origin of the European users with allocated proposals at the Italian synchrotron Elettra in the years 2010 - 2018.

The color of each country corresponds to the number of users as indicated in the legend [322].

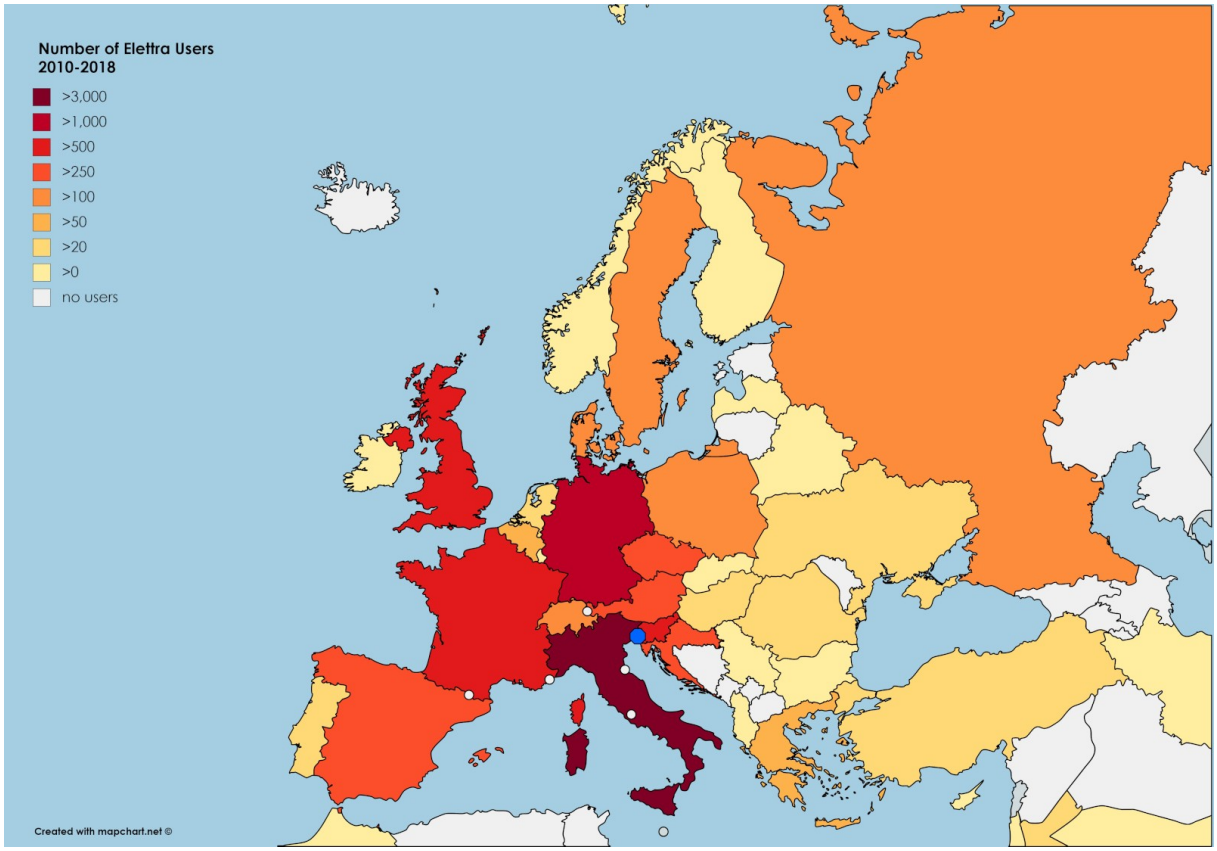

Figure 8.2.13.: Countries of origin of users from Europe and adjacent countries with allocated proposals at Elettra 2010-2018

The largest user community at Elettra is the Italian one with 3,874 users in the considered period, which are 41% of the European and 35% of all users. Large numbers of users are also observed for the big European countries Germany (1089 users), France (837 users), United Kingdom (525 users) and Spain (355 users), countries that are operating national and international synchrotron laboratories, and which have therefore consolidated national communities with relevant expertise.

In addition, a considerable number of users has come from smaller European countries with own light sources, namely Switzerland (188 users), Sweden (230 users), and Denmark (123 users). Also these scientists benefit from existing know-how, possibilities for skill development, and research opportunities offered by the light source in their own country.

For Poland, which has recently started user operation at the new national synchrotron laboratory Solaris, the user numbers at Elettra have increased after 2013, indicating that the Solaris project has pushed interest, skill development, and demand of the Polish scientific community, while they were looking forward to use also their own light source.

Countries without own national light source, but with a huge number of Elettra users in relation to their small populations are Austria (381 users), Czech Republic (282 users), Croatia (252 users), and Slovenia (518 users). Long lasting cooperations based on formal bilateral agreements and joint research activities between partner institutions in these countries and Elettra as well as the geographic vicinity have obviously facilitated the development of strong user communities in these countries. In the cases of Austria and the Czech Republic, the collaboration has included the construction of an Austrian beamline (SAXS) and a Czech beamline (Material Science) at Elettra, operated by permanent research groups from these countries located in Trieste. In the cases of Slovenia and Croatia it can be assumed that the location of Elettra on the Slovenian border and thus near to major research centres of these

partner countries has plays an important rule.

The low presence of EU researchers from Scandinavia and Western Europe at Elettra might be due to the geographic distance and enough research opportunities at synchrotrons in the regions and countries nearby.

Users from European non-EU countries at Elettra. Figure 8.2.14 illustrates the countries of origin of the 545 European users from non-EU countries at Elettra in the years 2010-2019 [313]. User numbers and percentages for countries below 1% are not indicated in the figure. The non-EU fraction of the European users has come from 11 different countries and makes up for 4% of all users and 5% of the European users in this period. They are thus a small minority, with major participation from Switzerland (40%, 216 users), Russia (37%, 200 users) and the Ukraine (11%, 59 users).

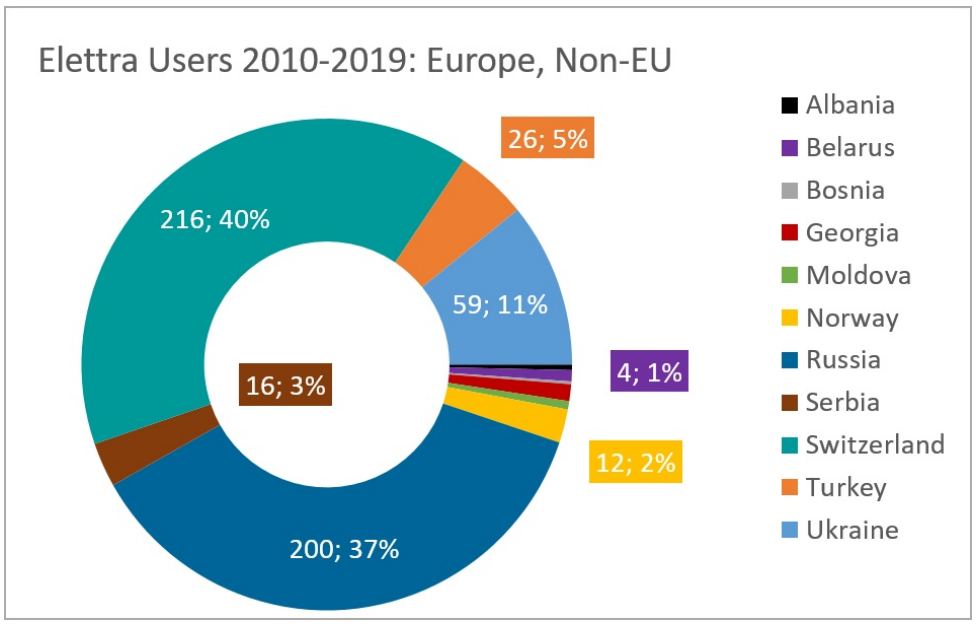

Figure 8.2.14.: European users from outside the European Union at Elettra in the period 2010-2019 by country [313]

The European regions with less users at Elettra are, despite their relative proximity, the Balkans with a few users from Serbia (16 users), Bosnia (1 user) and Albania (2 users). Also the Central and Eastern European countries have been hardly represented, with small numbers of users from Belarus (4 users), Georgia (6 users) and Moldova (3 users).

International users at the MAX IV Laboratory. The importance of geographic factors is also demonstrated by user data that have been published by the MAX IV Laboratory. Figure 8.2.15 shows the users at the MAX IV Laboratory by the country of origin of their institutions for the period 1 March 2019 to 29 February 2020 [316]. In this period, there have been 945 user visits involving 662 individual users from 30 different countries at the laboratory.

The figure indicates clearly that 75/,% of these users have come from the Nordic region, namely Sweden, Denmark, Norway, Finland and the Baltic countries. Particularly high is, with 14%, the participation of Danish users, which are rather near to Lund and dispose also of their own Synchrotron ASTRID2 in Aarhus. Furthermore, as also at Elettra, there are strong collaborations among these neighboring countries, which include the construction of a beamline jointly financed by Finland and Estonia (FinEstBeAMS) as well as one financed by Denmark (DanMAX).

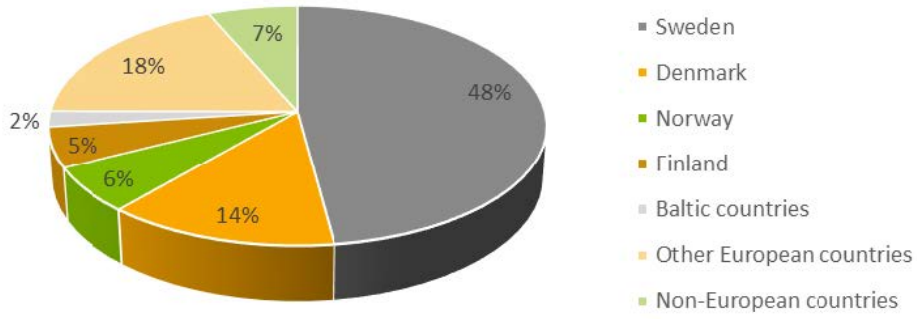

Figure 8.2.15.: Users at the MAX IV Laboratory 2019-2020 by country [316]

Non-European users at Elettra. European facilities are not only serving the European users, but also attracting users from other continents, as shown in Figure 8.2.15 for MAX IV and discussed in the following for Elettra. In Figure 8.2.16 it can be seen that between 2010 and 2019, 82% of Elettra's users have been from institutions in the European Union (9954 users) and 4% from other European countries (545 users), while 9% have come from Asia (1096 users), 3% from the Americas (419 users), and less than 1% from each, Africa (66 users) and Australia & New Zealand (90 users).

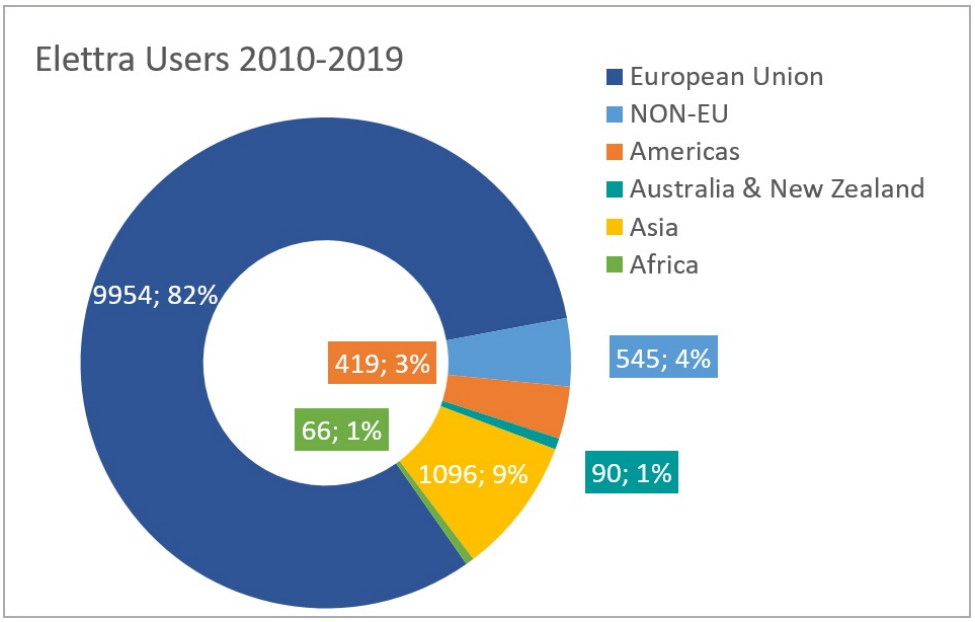

Figure 8.2.16.: Elettra users 2010-2018 by continent

Africa. Figure 8.2.17 indicates, that 66 African users have visited Elettra in the years 2010-2019 to perform experiments at the facility. The number of African users has thus been the lowest of all continents, even lower than that from the Australian one, although the Italian laboratory has been one

of the closest until the start of operation of SESAME, at least for the Northern Africa countries. Nearly two third of the African users at Elettra have however come from South Africa (43 users), most of the others from Egypt (20 users) and very few from Cameroon (2 users) and Morocco (1 user). At the moment, African users do not benefit from any light source in their continent, but without experience, proposal applications at facilities in other continents have a low probability of success. In addition, in the case of success, due to the large distances, the allocation of beamtime would also entails high costs in terms of time, money and effort. This is probably hindering the creation of consolidated user communities in African countries.

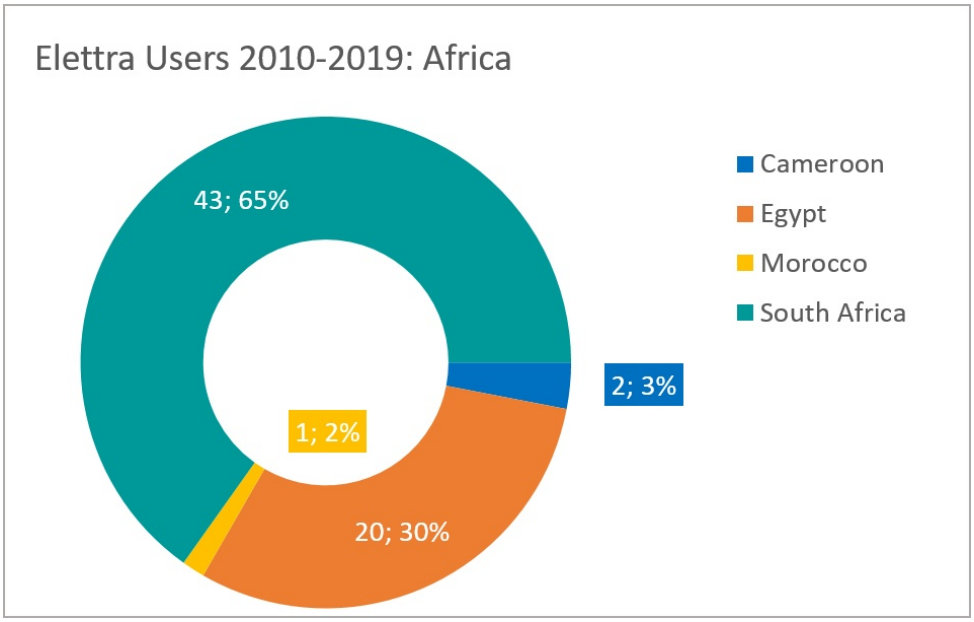

Figure 8.2.17.: Elettra users 2010-2019 from Africa

America. The home countries of the American users of Elettra in the years 2010-2019, which have been 419 in total, are depicted in Figure 8.2.18. The three major countries of origin are those with own national facilities, namely the USA with 48 % of the the American researchers (201 users), Canada with 17 % (70 users), and Brazil with 13 % (53 users). These countries make up for 78 % of all American users, the two northern countries USA and Canada alone for two third of them. Further users have come from Mexico (12 %, 50 users), Argentina (6 %, 27 users), Cuba (4 %, 16 users), Chile (1 user), and Peru (1 user).

Asia. The 1,096 Asia users have been the largest non-European user community at Elettra during the years 2010-2019 and also the geographically most diverse one, with 19 different home countries of the researchers. This can be seen in Figure 8.2.19, where user numbers and percentages are shown only for the major user countries. All countries in light yellow have user numbers below 1% of the Asian total. By far the largest share of Asian users is, with 622 users or 57%, the Indian one. This is the fruit of a long-lasting, very intense collaboration between Elettra Sincrotrone Trieste and Indian institutions, supported by the relevant ministries in both countries, which has led also to the construction of two Indo-Italian beamlines at Elettra. Furthermore, India is one of the Asian countries with own national synchrotron light sources. Japan (13 %, 137 users) and China (10 %, 111 users) reach quotes of 10 % and more and remarkable shares are also observed from Pakistan (7 %, 73 user's), Israel (4 %, 43 users), and Jordan (3 %, 30 users), three member countries of the new Middle-East synchrotron facility SESAME in Jordan. The large spectrum of countries in Figure 8.2.19 shows impressively that in Asia

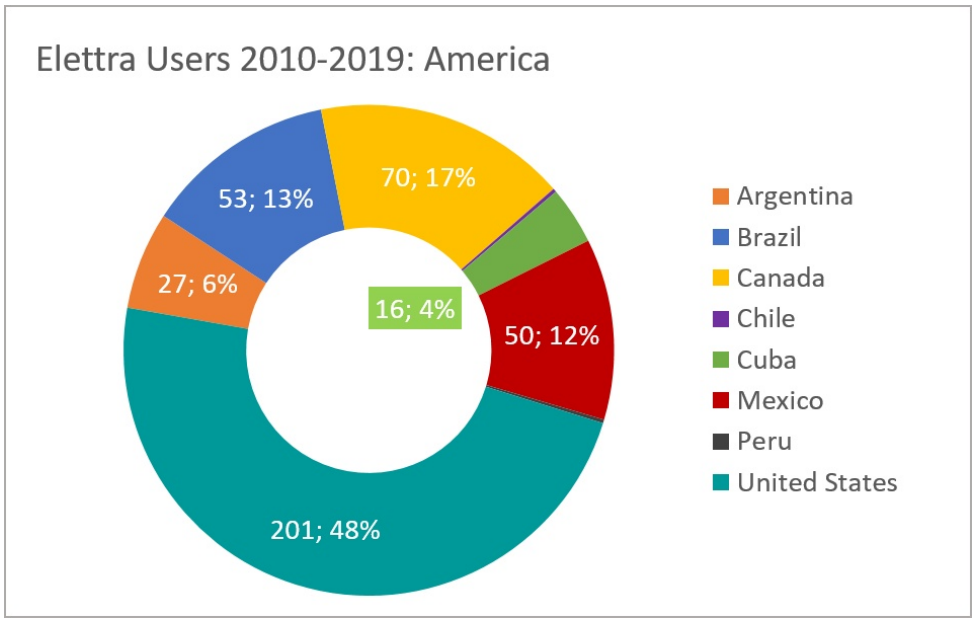

Figure 8.2.18.: Elettra users 2010-2019 from America

user communities have meanwhile developed, with few exceptions, across the whole continent, while however the availability of light sources is still scarce in many Asian regions.

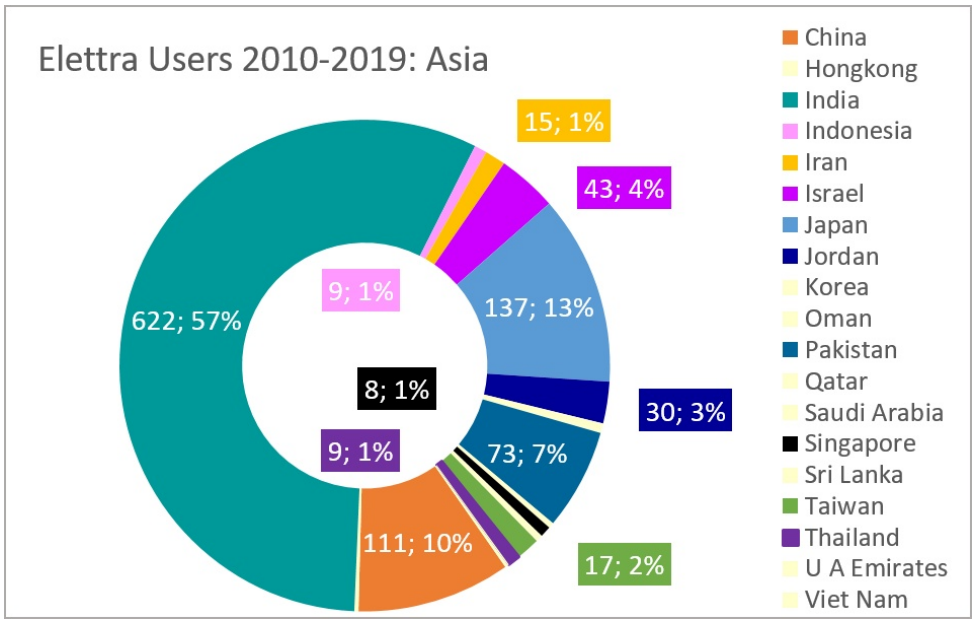

Figure 8.2.19.: Elettra users 2010-2019 from Asia

Australia & New Zealand. Finally, 90 users from the Australian continent have performed experiments at Elettra over the considered years. The large majority of them, namely 84% or 85 users, has been from Australia, the remaining part has come from New Zealand. Australia is operating a national light source, the Australian Synchrotron, and the community is closely collaborating with European institutions including Elettra, which facilitates probably also through joint research projects the exchange of users.

8.2.3.5. Examples of users at European Free Electron Lasers

FERMI. For the first years of operation of FERMI, namely the period 2014-2017, geographic data exist only for the proposer of the allocated proposals and not for all the users involved in the experiments at the facility. Since experiments at a FEL light source are usually international collaborations that involve researchers from different countries, these data do thus not provide a complete picture. In the years 2014-2017, 90% of 110 allocated proposals have come from European users (100 proposals), 5% from US-based users (5 proposals) and 5% from Japanese users (5 proposals). 78% of the allocated European proposals have been received from Italy (42 proposals) and Germany (36 proposals) and smaller numbers from Sweden (8 proposals), France (7 proposals), Switzerland (4 proposals), Slovenia (1 proposal), the United Kingdom (1 proposal), and the Netherlands (1 proposal) [313].

Figure 8.2.20 and Figure 8.2.21 present the number of users that have participated onsite in the research activities of the allocated proposals at FERMI in the years 2018-2019. The list of the European users in Figure8.2.20 contains 13 distinct countries, about double the number of the proposer countries of the period 2014-2017. Large numbers of users have come from Germany (110 users, 36%), France (44 users, 14%), Sweden (40 users, 13%), Italy (36 users, 12%), and Switzerland (27 users, 9%). The number of users from all other countries have been smaller, below 5%.

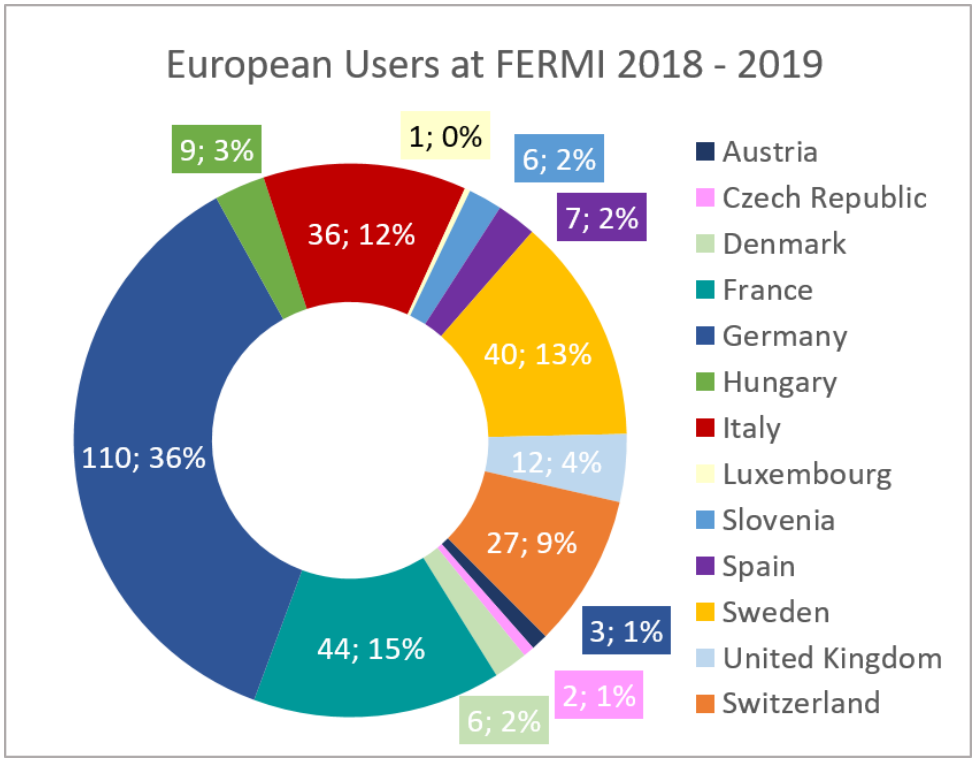

Figure 8.2.20.: European users at FERMI 2018-2019

The non-European users at FERMI have been 51 or roughly 14% of all users with allocated proposals in 2018-2019. Nearly two third of them have come from the USA, 15% from Japan and 6% from Korea. Further user countries have been Canada (4 users, 8%), Australia (2 users, 4%) and Singapore (1 user, 2%).

Except for one Slovenian user, all users that have submitted the allocated proposals of the period 2014-2017 have come from countries that are operating either own FEL facilities (Germany, Italy, Switzerland, USA, Japan), have user communities pushing own national FEL projects (Sweden, United Kingdom), or are member countries of the European XFEL (France). The major countries from which researchers have participated in experiments at FERMI in the years 2018-2019 are Germany hosting two FEL sources, Italy as the host country of FERMI, Sweden with a rather advanced soft X-ray FEL

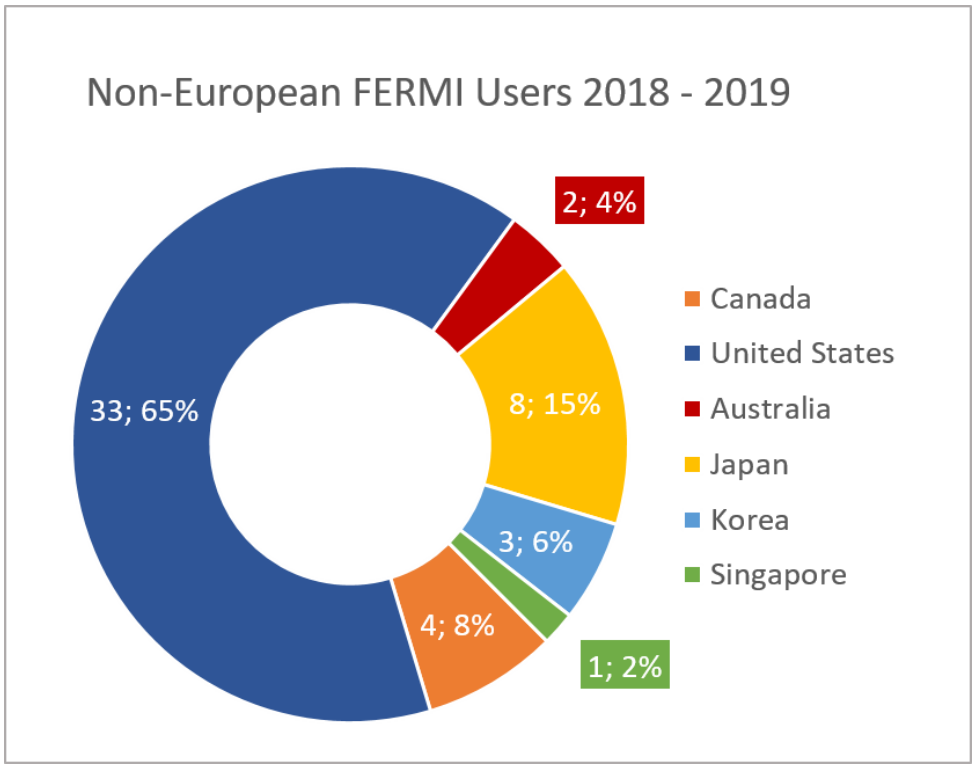

Figure 8.2.21.: Non-European users at FERMI 2018-2019

project, Switzerland hosting the SwissFEL that started operation in 2019 and France, strongly involved in the European X-FEL and with two synchrotrons available in the country. From the smaller countries, Denmark is is a major partner of the Swedish FEL project and Austria, Slovenia and Czech Republic are collaborating very closely with Elettra Sincrotrone Trieste. Concerning the non-European users 2018-2019, 86% have come from three countries with own X-ray FELs, namely the USA, which makes up for the large majority of these users, Japan and Korea.

The data show that the users with allocated proposals at FERMI have come to a large extent either from a small number of countries hosting, construction, or projecting FEL facilities, or are members of the European X-FEL, or have national synchrotron light sources, or they come from countries/institutions that have already been closely collaborating with Elettra Sincrotrone Trieste over a long period. These conditions seem to be success factors of particular importance for beamtime applications. This highlights the importance of experience, pertinent knowledge, skills, and expertise as indispensable preconditions for preparing a successful proposal and concluding the respective experiments with success. Gaining requested skills and experiences might however be difficult for researchers that do not have access opportunities in their own country, also in view of the limited number of available facilities and their current oversubscription.

8.3. Technology Transfer and Exploitation

CompactLight has not been a design study as usual, in the sense of a first phase to prepare the future construction of a concrete, well defined project for the implementation of a new Free Electron Laser somewhere in Europe. The fundamental idea underlying the project has been to create, based on the latest available technologies, the conceptual design of a Hard-X-ray FEL as a blueprint for a new generation of cost- and resource-efficient facilities with construction and operation costs that are affordable for a larger spectrum of countries and institutes. CompactLight follows a very flexible modular approach, with a cost-efficient basic design and two upgraded versions for the Hard X-ray FEL, that

can satisfy many of the various user requests identified during the user consultations. It can also be applied to smaller machines, such as the Soft-X-ray facility or the Inverse Compton Source for medical use presented in chapter 9 of this report, which can be adapted to the requirements of other, different applications, from material science to industrial use or radioactive waste processing.

In such a scenario, potential future applicants of the CompactLight technologies are in need of particular guidance and support in order to understand, how and on which timescale these technologies can be used. This chapter provides applicants in brief with this type of information concerning the use of XLS technologies and other created assets, the project's support measures for future users, and plans and initiatives for the further development of the CompactLight technologies. As a further support, the partners have published in the appendix of this document

- the parameter tables of the CompactLight baseline design containing the core parameters for the injector and the accelerators–see Appendix A.1
- the project's open data tables–see Appendix A.2
- the list of the CompactLight documents published by the end of the year 2021–see Appendix A.3,
- and the list of all the project's partner teams–see Appendix A.4.

For information, please contact us:

compactlight@elettra.eu

8.3.1. Technology development in and beyond CompactLight

An analysis of the technological and non-technological assets created by CompactLight, including the achieved progress and exploitation potential has been carried out in WP7 of the project. Detailed results of this study are provided in deliverable D7.2 of CompactLight. While the assets of WP1 and WP7, which are non-technological outcomes of the project (skills and know-how, XLS community, website, open data, publications, results of analyses, 3D-CAD, parameter list, cost analysis methodology etc.) are immediately available for potential users, most of the technological assets need a couple of years of further development to reach TRL9 and become market-ready.

The technological readiness levels achieved during the conceptual design phase for the major components and subsystems of the CompactLight machine are between TRL2 (Designs of the K-Band RF Linearizers for the high brightness injector and the Ka-Band RF sources) and TRL7 (Compact diagnostic design) and constitute a solid basis for further development activities towards an application in a real CompactLight machine. The estimated time required for these further development activities on subsystems and components towards their use in a concrete machine is on a 5-years scale, provided that the required activities are undertaken. CompactLight is fostering this process through a number of

initiatives that go beyond the project itself.

As follow-up initiatives for the further development of core technology, some CompactLight partners have launched dedicated activities for the creation and validation of CompactLight prototypes in the framework of WP7 of the I.FAST project (see: https://ifast-project.eu) and WP6 of LEAPS-INNOV (see: https://www.leaps-innov.eu/). Both projects started in spring 2021 with four years' duration.

Injector. Three XLS partners, among them one company and one new industrial partner will design, construct and test with RF power two different very high gradient, up to 200 MV/m on the cathode, C-band electron RF Guns: a Standing-Wave over-coupled cavity made of one and a half cell and a multi-cell traveling-wave accelerating section incorporating a photocathode in the very first cell. Both approaches are attractive, with different advantages to be exploited, and will be fully experimentally explored. The experimental demonstration of optimized prototypes will pave the way to the use of the guns in FEL radiation sources, Thomson/Compton photon sources and plasma based accelerators.

Accelerator. Six partners, among them three companies of which two have not been involved in CompactLight, will construct and test two prototypes of the 12 GHz accelerating structure developed for the basic design of the CompactLight Hard-X-ray machine. The construction of the two prototypes will be used to get a full validation of the XLS design at two RF operating regimes: a) high gradients/low pulse repetition rate (60 MV/m up to 100 Hz); b) low gradient/high pulse repetition rate (30 MV/m up to 1 kHz). Technical drawings for the prototype production and an overall analysis of the production process will be prepared and implemented by the partners. A pre-prototype and a full prototype will then be respectively constructed, tested and validated with low RF power measurements as well as high power RF tests, and characterized post-mortem.

Undulators. In LEAPS-INNOV, CompactLight Partners are involved in the further development of cheaper, more compact and sustainable undulators with larger flexibility and today unmatched performance. In the project, four undulator prototypes will be developed: (1) two short period, high field, planar undulators generating hard X-rays - a high temperature superconducting (HTS) undulator (SCU) and a cryogenic permanent magnet undulator (CPMU) with a period of the order of 1 cm and (2) two short period, high field elliptically polarizing undulators with a cryogenic in-vacuum APPLE-III system - a cryogenic APPLE III undulator and a cost-effective compact APPLE X undulator. Two novel measurement benches for testing the prototypes will also be developed. It is planned to carry out all activities in close collaboration with relevant companies, involving early and continuously all specialized European suppliers.

Activities for the development of prototypes based on CompactLight technologies are also taking place in the framework of two partner initiatives:

STFC/RAL. The teams working at the Rutherford Appleton Laboratory and Daresbury Laboratory on superconducting undulators for Light Sources have launched a project to develop a helical superconducting undulator, aimed towards parameters for the CompactLight design study. In a first step they are going to design and build a short 30 cm prototype of a helical device, and winding trials are already ongoing with copper wire. The aim is to develop a full-scale 2 m undulator, complete with other components required for installation on a FEL facility such as inter-undulator quadrupoles and phase shifters [323].

SINAP. During the last phase of CompactLight, SINAP has developed a 3.6-cell C-band photocathode gun and carried out high power tests to achieve a 150 MV/m gradient on the cathode. They have also developed two 0.6 m X-band accelerating structures redesigned from the original design of the Com-

pactLight project as linearizers for two FEL facilities, SXFEL and DCLS, in China. The manufacturing has been completed and the components are ready for installation.

8.3.2. Community activities and networking

From the very beginning, CompactLight has always tried to involve all the actors addressed by the scope of the project and required for a successful implementation of the developed technologies, also beyond the project itself. These are the potential applicants in terms of initiatives and projects for the construction of CompactLight facilities, the potential scientific and non-scientific users of such facilities, networks and founders in the field, and companies that have the expertise, capacities and potential to engage in the further development, manufacturing and supply of the required new high-tech components and systems.

XLS Community and Networking. The CompactLight Community will remain active and be consolidated and integrated with further relevant actors with the aim of fostering jointly the further development and application of the CompactLight technologies beyond the end of the project. Activities will include follow-up projects for technology development, also with additional partners, support and consulting for application projects and initiatives, organization of events and other dissemination activities in the accelerator science and light source communities, as well as general scientific networking and communication. This includes also to keep the project's website and Zenodo community updated as an information source for future applicants.

Companies. With VDL ETG, Kyma/KyTe and BNG, three industrial partners have been involved in the project that contributed expertise in the key fields of ultra-precision engineering and in permanent magnet as well as superconducting undulators. These companies are also participating in the I.FAST project, where they will push the further development of novel technologies for accelerators and light sources (see below). To support the transfer of the relevant technologies, the core team of XLS partners for the CompactLight related tasks of I.FAST has been integrated with further companies. The cutting-edge technologies employed by CompactLight require the availability of novel high-power RF systems for the accelerators. For this reason, contacts with companies operating in this sector and not directly involved in the XLS activities, have already been established early in the project. Information exchange about the objective and the proceeding of the work in CompactLight and relevant company activities on Klystrons has taken place during project meetings and it is planned to proceed with such activities also in the future.

Facility Users. Also an exchange with the scientific community that went beyond the presentation of the project results at conference and through scientific publications has taken place. After a first consolidation phase, CompactLight has conducted a user survey and a user meeting with key representatives of the FEL user community from different scientific fields. The purpose has been to take the decision on the technical characteristics of the CompactLight hard X-ray FEL on a well-founded basis established by the user requirements. The results of these activity can be reviewed in D2.1. Further face-to-face events planned with the facility users have been impeded by the COVID-19 emergency, but the partners are planning to organise further user events as soon as this will be possible again after the end of the project.

Projects and initiatives. CompactLight is in touch with a few initiatives potentially interested in developing an infrastructure project based on CompactLight technology. Interest has in particular been expressed by users in Finland and Greece. This dialogue will be intensified to discuss opportunities and further proceeding and verify how to promote and support such endeavors in the future through joint activities, dedicated collaborative projects and the transfer of knowledge, know-how, and technology. Interest of applying CompactLight technologies has also been expressed by the two already more

advanced European FEL projects that involve CompactLight partners, namely the Swedish soft X-ray FEL and the UK hard X-ray FEL. More information on these two projects as well as the Greek initiative has been given in part 8.2.2.3

Use Cases. CompactLight has investigated also into further, potentially less cost intensive application possibilities of the created technologies. These are in particular the Soft X-ray FEL and the Inverse Compton Source for medical applications presented in section 9. Knowledge exchange on such complementary use possibilities will be further stimulated through more dedicated activities, such as topical workshops for the scientific and technical exchange, awareness workshop for applicants, design or application projects, and investigations into other probabilities, for instance scientific or industrial use.

8.3.3. IPR, data, publications, and more

Given the purpose of CompactLight to foster a wide availability of FELs for research and other applications, which goes beyond the economically strongest countries, all results of the project are generally openly available, with exceptions in the case that the partners intend to use them as an input to projects for their own further development activities or the creation of IPR. Also the results of follow-up projects will in general be made openly available during the next years. The project's policies for access to information are briefly described in the following.

Intellectual Property Rights. Most of the results of CompactLight have been published or will be published in the form of copyright protected Intellectual Property. This includes the project website, the CompactLight logo, scientific and technical publications, reports and deliverables, newspaper articles, codes and software, data files and spreadsheets, technical drawings including the 3D CAD, photos and pictures, and similar items published by the project in electronic or paper format. IPRs owned by the project or some of its partners are usually protected by a CC-BY 4.0 or CC-BY 3.0 licenses. Other conditions, to be verified by the users, might apply in single cases and for scientific and technical papers published in scientific journals, in particular in green open access. Any use of results from CompactLight must respect the relevant licensing conditions, with proper reference to the work that will be used and to the CompactLight project.

Publications and Open Data. Generally, CompactLight publications have been published in open access. For papers published in green open access, the version of the paper published in a scientific journal is not available in open-access, but in these cases the Author Accepted Manuscript is made openly available. Links to all published documents, including papers, AAMs and deliverables, are provided on the project's website. These documents can be distinguished by their DOI and are also stored in a long-term repository, in most cases in Zenodo. A dedicated CompactLight Community in Zenodo allows to create easily a complete list of all project documents deposited in the repository searching simply with the keyword 'CompactLight'.

More detailed information about the project's open data policy and available open data are provided in the dedicated section on the CompactLight open data A.2 in the annex. Please refer also to the new version of the CompactLight Data Management Plan (Data Management Plan - v1.3), which will be published in early 2022 and made available on the project's website and in the CompactLight Community in Zenodo.

Website. The CompactLight website on https://www.compactlight.eu provides information about the

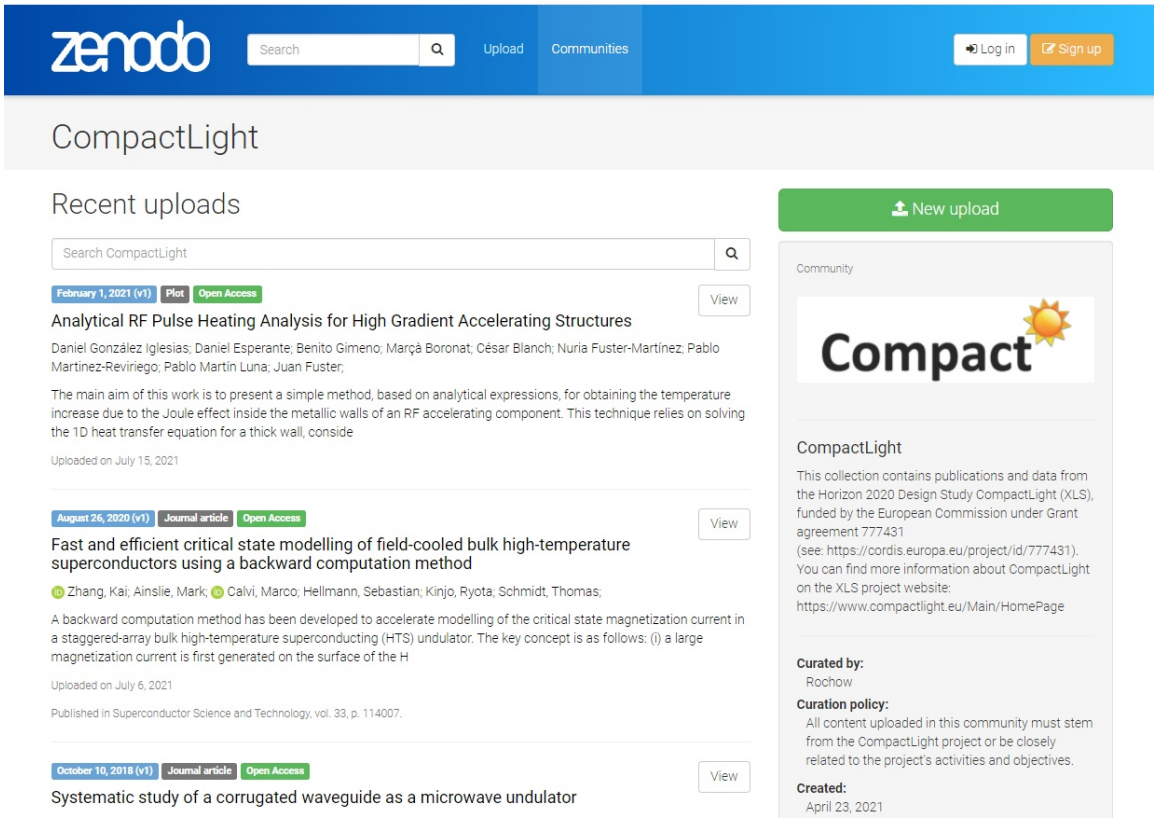

Figure 8.3.1.: Zenodo CompactLight Community: https://www.zenodo.org/communities/compactlight/.

project, such as objectives and results, partners and contacts, past and future events as well as links to deliverables, publications, repositories, and internal collaborative workspaces. It will remain active after the end of the project and be updated with information on relevant future activities concerning the further development of key components, follow-up projects, use cases, future workshops and events for the community, and more. The aim is to keep interested parties informed about all new development concerning CompactLight.

Further relevant information on these topics can also be found in the project's deliverable D7.2.

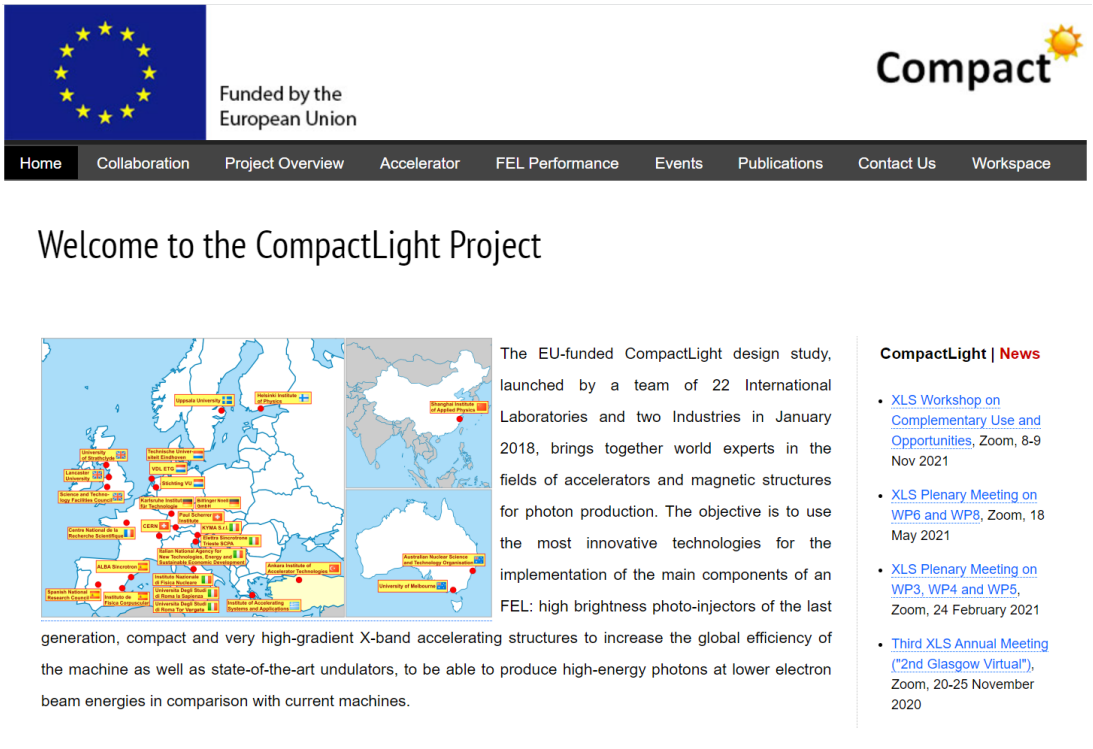

Figure 8.3.2.: CompactLight website

9. Examples of CompactLight Facilities

9.1. Soft X-Ray Facility

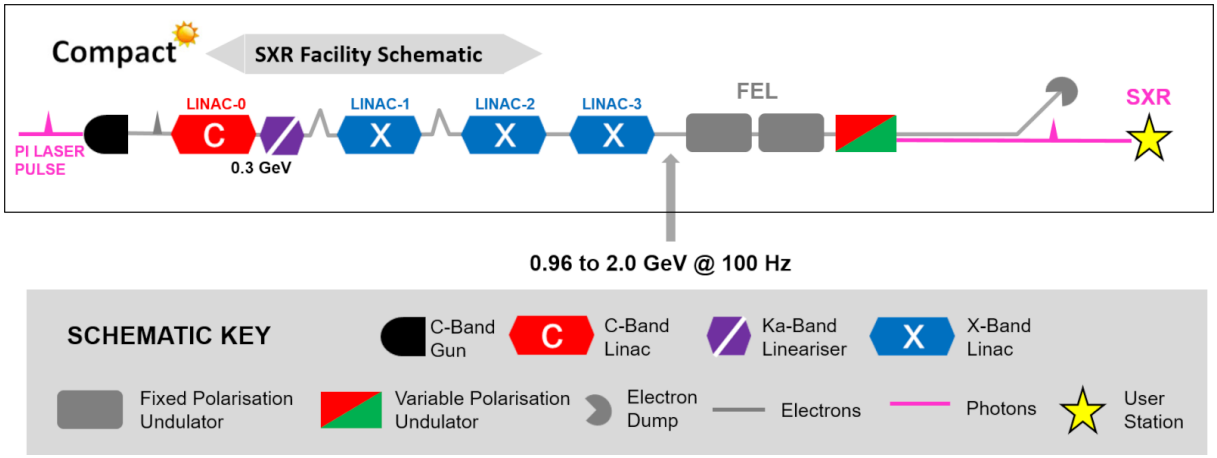

Figure 9.1.1.: Schematic layout of the SXR facility

The core electron binding energy of many important elements such as carbon (290 eV), nitrogen (400 eV), oxygen (530 eV), and all the 3d transition metals lies in the soft X-ray range. Soft X-ray spectroscopy techniques are element specific and allow revealing details of an atom's chemical bonding state. Specifically, absorption spectroscopy, photoemission spectroscopy, resonant inelastic X-ray scattering and Auger electron spectroscopy in the soft X-ray range are powerful core-level spectroscopy techniques for studying the nature of chemical bonding, local geometric structure and dynamics of electron transfer processes at the atomic site. The core-level spectroscopy techniques are well established at synchrotrons but soft X-ray FELs have opened a new research dimension in ultrafast soft X-ray science by providing access to the 1-100 fs time range with an unprecedented brightness of the X-ray beam. The access to ultrafast time scales allows studying, for example, how activation barriers are lowered by unusual bonding situations in reaction intermediates, which represent crucial bottle-necks for understanding and controlling the efficient conversion of solar energy into other forms of energy. To address the challenges of harnessing and storing of, for example, solar energy, direct time-resolved studies of charge-carrier dynamics at interfaces of new solar cells and energy storage devices are needed.

The strong needs for an ultrafast soft X-ray source justified the construction of a new generation of soft X-ray FELs such as the LCLS-II project – a high-repetition rate SXR FEL based on a superconducting accelerator. Note that the LCLS-II FEL provides a continuous train of FEL pulses with *uniform spacing* between the pulses. User end stations at LCLS-II are planned to provide the FEL beam at 100 kHz repetition rate. Also note that a high-repetition FEL with uniform pulse spacing will also be available in China as part of the hard X-ray FEL facility SHINE. In Europe only the Athos beamline at SwissFEL at 100 Hz repetition rate (currently under commissioning) provides the SXR FEL beam with uniform pulse spacing. The soft X-ray beamline of the European XFEL based on the SASE3 undulator operates in burst mode and is sub-optimal for many pump-probe experiments in condensed matter physics, where the sample must thermalise between pump pulses.

As evidenced from the FEL requirements Sec. 3.2, there is a clear need for SXR FELs with increased pulse stability and uniform spacing between the pulses. The operation mode of the FEL must be compatible with the type of pump-probe experiments, in which the non-equilibrium state of a sample must decay before the next pair of pump-probe pulses come. Furthermore, a repetition rate of 100 Hz

or 1 kHz is perfectly compatible very high power optical lasers used in some pump-probe experiments.

The CompactLight technology offers a unique capability of building a 100 Hz or even a 1 kHz FEL at a cost lower than that of a 100 Hz machine based on the previous generation C-band accelerator technology. *The compactness and cost efficiency of a 100 Hz standalone SXR FEL lowers the barrier for entering the world of femtosecond X-ray science for small national user communities.* In addition, an upgrade to the 1 kHz option would fill an important gap between the first and second generations of low and very high repetition rate FELs. On one hand, the 1-kHz FEL will provide a ten-fold increase in repetition rate, but on the other hand, it will still provide enough time between X-ray shots for sample replacement and preparation, such as for liquid droplet dispensers for exceptionally precious samples, or for measurements on solid surfaces where time is needed to deposit molecules.

9.1.1. Facility Layout

The facility design is a simplified version of the Baseline configuration, reduced to the essential components for 100 Hz SXR output over the photon energy range 0.25–2.0 keV from a single FEL. A schematic layout is shown in Figure 9.1.1. Note that, compared to the Baseline configuration, the facility is substantially more compact, for the following reasons:

- There is no need to reserve space between Linac-2 and Linac-3 for the deflecting cavity and spreader beamline required for Upgrade-2.
- Similarly, there is no need for space after Linac-3 for the deflecting cavity and spreader beamline to split the twin bunches into the twin FEL lines.
- There is no need for the timing chicane to tune the temporal separation of twin FEL pulses.
- The FEL undulator can be shorter because the saturation length in the SXR is less than that in the HXR.
- The photon beamline is shorter because the divergence of SXR output is larger, meaning that the first optical element can be placed closer to the undulator source without being damaged.

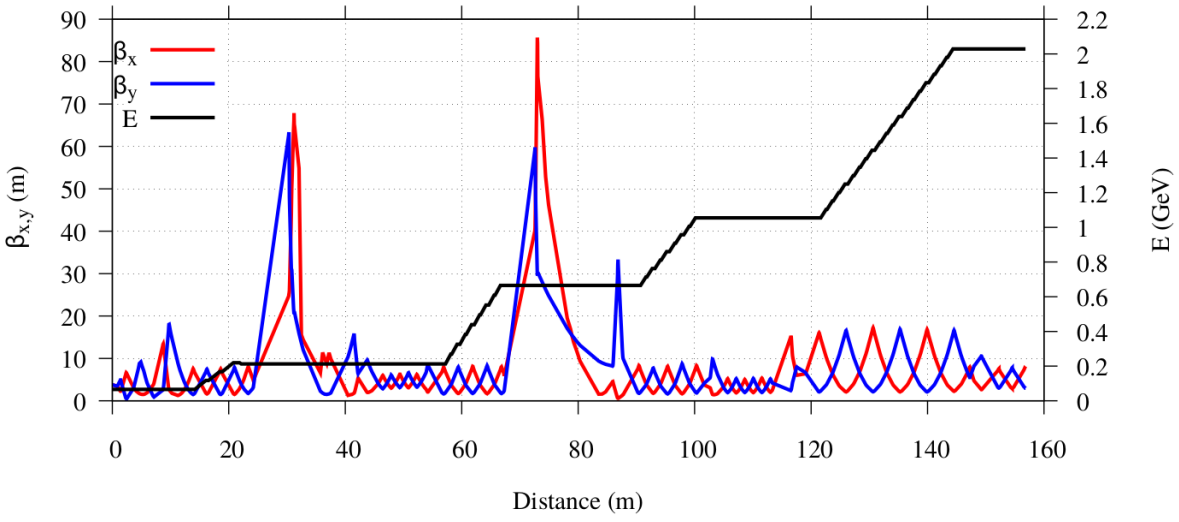

Figure 9.1.2.: Lattice β-functions and beam energy.

The accelerator and FEL lattices were reoptimised for standalone SXR operation. Starting from the injector all structures are used at their highest gradient—C-band structures in the injector are at

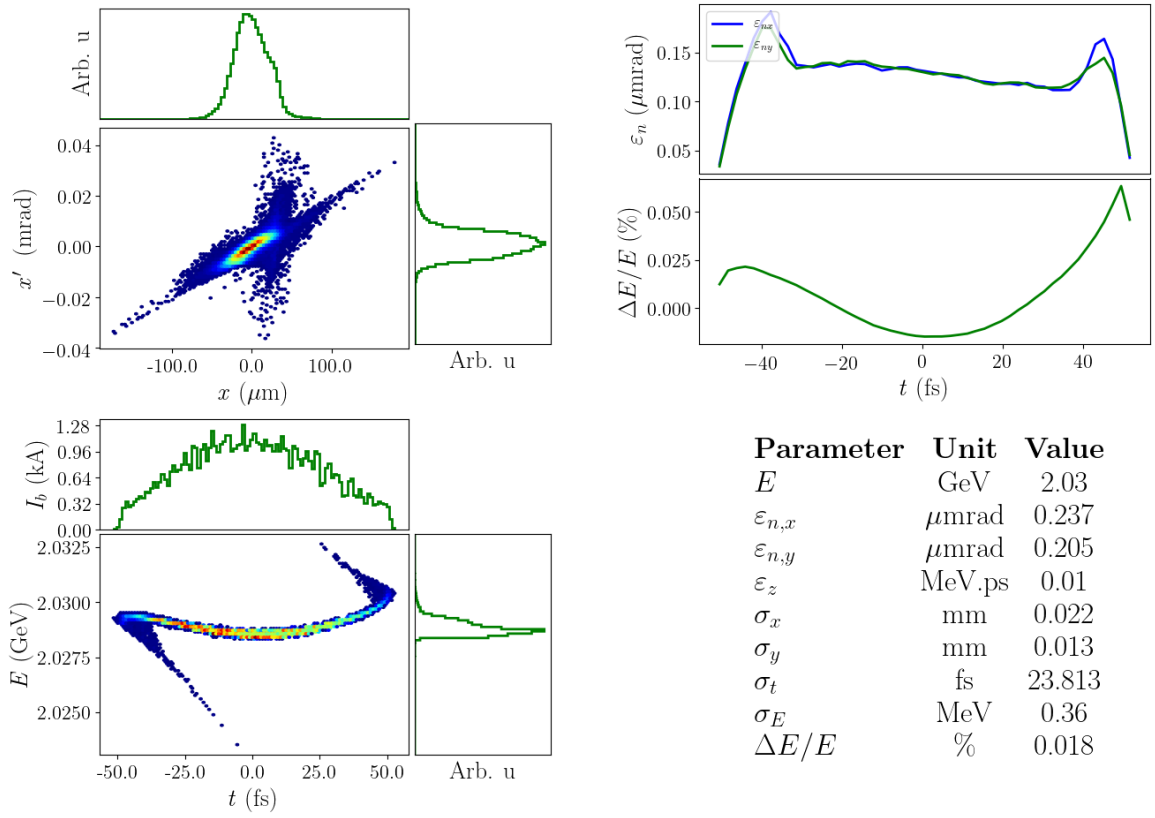

Parameter	Unit	Value
E	GeV	2.03
$\varepsilon_{n,x}$	μmrad	0.237
$\varepsilon_{n,y}$	μmrad	0.205
ε_z	MeV.ps	0.01
σ_x	mm	0.022
σ_y	mm	0.013
σ_t	fs	23.813
σ_E	MeV	0.36
$\Delta E/E$	%	0.018

Figure 9.1.3.: Properties of the simulated electron bunch used to drive the SXR FEL.

30 MV/m and the X-band structures are at 65 MV/m. A maximum beam energy of 2 GeV is attained at about 150 m with a peak current of 1 kA.

The lattice β-functions and beam energy are shown in Figure 9.1.2. The transverse and longitudinal phase spaces of the 2 GeV bunch are shown in Figure 9.1.3, together with the slice emittance and energy spread. The helical superconducting undulator period remains unchanged from the full CompactLight facility, at λ_u = 13 mm, so the undulator design is directly transferrable into the standalone SXR machine. At 2 GeV beam energy and with the FEL set to 2 keV photon output, the undulator parameter is a_w = 0.706. By tuning to maximum field the photon energy reduces to 1 keV. By operating at 1.35 GeV the tuning range covers 500 eV to 1 keV and to reach the lowest photon energies of 250–500 eV the beam energy is reduced to 0.96 GeV. The total undulator length is 19.75 m with the lattice comprising nine 2.75 m long SCU modules with 0.5 m gaps between them. After the SCU modules there are two variably polarising afterburner modules to provide selectable polarisation for users.

9.1.2. FEL Performance Estimates

The FEL simulation results are shown in Figure 9.1.4. Here the FEL is tuned to 2 keV photon output. The pulse energy saturates at a distance of 15.5 m through the undulator at a value of 90 μJ and the peak power is around 4 GW. The total undulator length of 19.75 m thus allows a reasonable contingency to ensure saturation is reached at 2 keV, and also allows the possibility of post-saturation tapering at lower photon energies for which the saturation length is shorter.

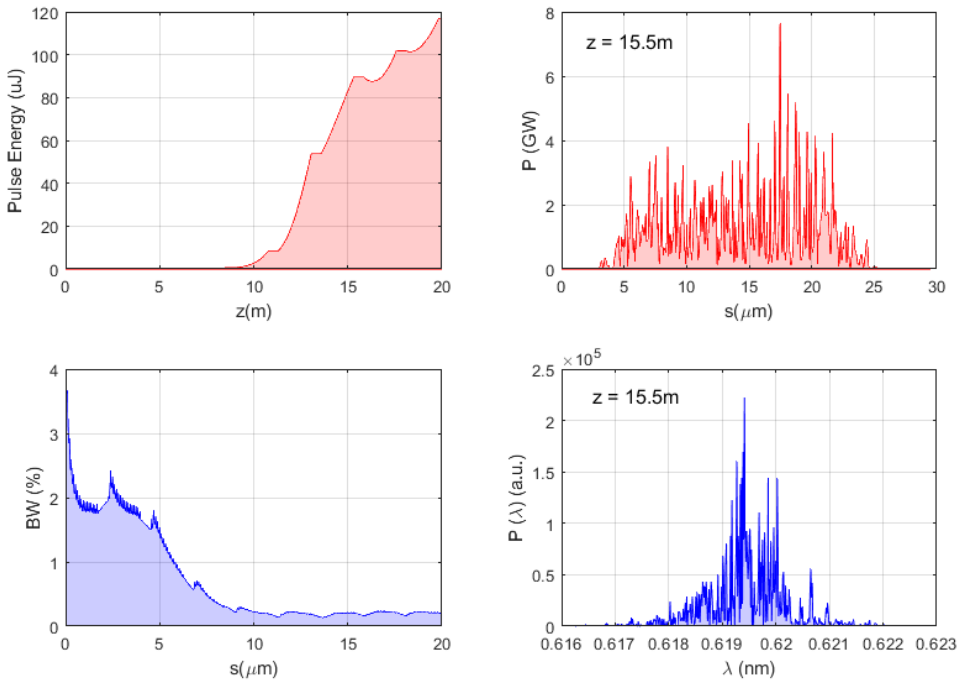

Figure 9.1.4.: FEL simulation results of the SXR FEL performance, showing (top left) pulse energy *vs* distance through the undulator z, (top right) power profile of output pulse at saturation, occurring at $z = 15.5$ m, (bottom left) rms bandwidth *vs* z, and (bottom right) pulse spectrum at saturation.

9.1.3. Photon Beamline

Compared to the Baseline configuration, the photon beamline design is greatly simplified as only one FEL line is serving user endstations. The optical layout of the photon transport is shown in Figure 9.1.5. The beamline starts with the front-end containing a bremsstrahlung collimator, a photon shutter and a set of photon diagnostics. The first optical element, a steering mirror, can direct the photon beam to one of the two beamlines: a pink beamline for time-resolved experiments or a mono beamline for photon energy-resolved experiments. The former provides broadband transmission and the temporal structure of FEL pulses is preserved. The pink beamline also includes a split-and-delay system for X-ray pump-probe experiments. Incoupling of external optical and UV lasers is foreseen for optical/UV pump – X-ray probe experiments with fs resolution. The mono beamline provides meV-energy resolution by employing a grating-based monochromator.

An important consideration in the photon beamline design is the choice of material for optical components as the beamline has to support transmission over a wide photon energy range from 0.25 to 2 keV. Figure 9.1.6 presents a comparison of the absorption coefficient vs photon energy for several materials commonly used in photon beamlines. Given the CompactLight parameters, Au is the preferred option even though the absorption level is as high as 20%. As a result, the transmission on the pink beamline composed of three mirrors is around 50%.

An example of the main output parameters of the beamlines at 250 eV (5 nm) and 2000 eV (0.62 nm) are presented in Table 9.1.1. Two grazing-incidence gratings are used to cover the entire photon energy range providing a good balance between photon energy resolution and pulse stretching due to the waveform tilt by the grating. The pink beamline contains no dispersive elements and preserves the FEL pulse bandwidth.

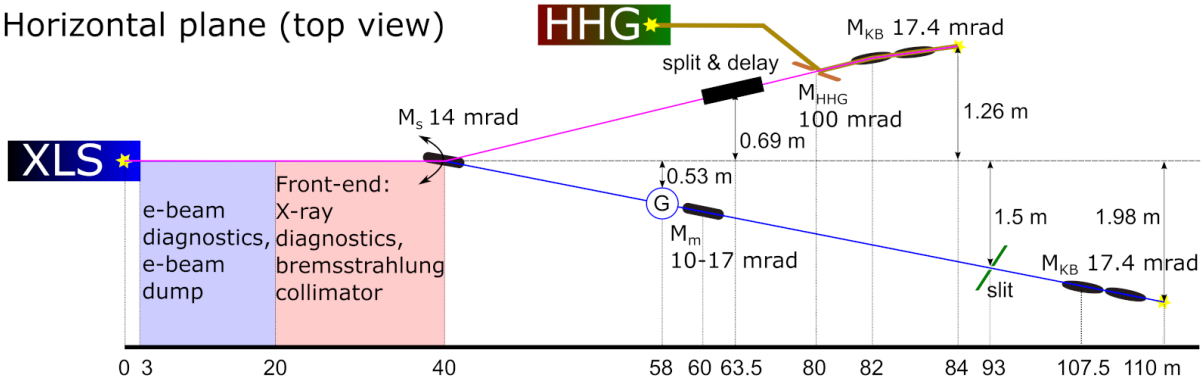

Figure 9.1.5.: Optical layout of the SXL beamlines. The position of the virtual FEL source (yellow star on the left) is taken as the origin. At 40 m downstream from the virtual source, the FEL beam is steered by means of a steering mirror M_s into one of the two main beamlines: a pink beamline (solid pink line) and a mono beamline (solid blue line). Other notations in the figure are: G stands for the monochromator grating, M_m for the monochromator mirror, M_{KB} for the set of KB mirrors, M_{HHG} for the holey mirror for incoupling of UV pulses from a high-harmonic generation (HHG) source. Typical operation angles of incidence are indicated next to the mirror symbol. The incoupling of HHG pulses and the split & delay-line are shown. The positions of the final FEL beam focus are depicted by the yellow stars.

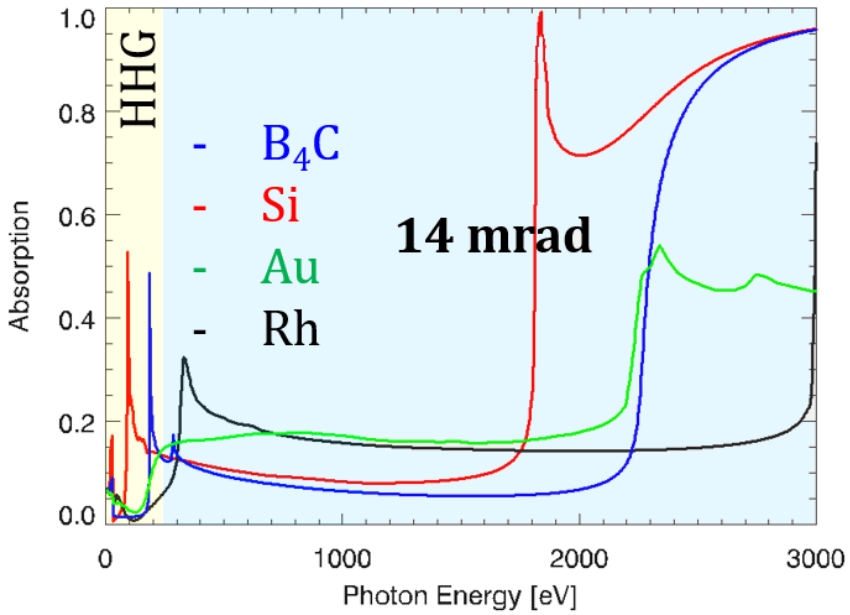

Figure 9.1.6.: Optical absorption for several materials vs photon energy at an incidence angle of 14 mrad.

9.1.4. Cost Estimate

Tables 9.1.2 and 9.1.3 show the breakdown of cost estimates for a 100 Hz and a 1 kHz option. The 1 kHz SXR FEL makes use of the full accelerator including the upgrade of RF power sources to provide the high repetition rate mode. The full-scale linac makes the 1 kHz SXR machine easily up-gradable to the 100 Hz HXR regime. Furthermore, comparing the cost per photon the proposed SXR FEL facility is clearly more cost efficient than the corresponding SXR FEL at SwissFEL.

Table 9.1.1.: Parameters of the FEL beam at the sample position in the experimental station. Distribution widths are FWHM.

Parameter	**Pink**		**Mono, high ph. energy**	**Mono, low ph. energy**
Grating	-	-	100 l/mm, 0.25^{o} blaze	50 l/mm, 0.15^{o} blaze
Wavelength (nm)	0.62	5	0.62	5
Photon energy (eV)	2000	250	2000	250
Transmission (%)	60	55	3.15	1.33
Pulse energy (μJ)	54	83	2	2.84
Beam size ($\mu m \times \mu m$)	2×1	2.8×1.1	3.2×1.6	4×2.4
Pulse stretching (fs)	-	-	10	200
Resolution (meV)	-	-	450	47

Table 9.1.2.: Cost breakdown for the standalone 100 Hz SXR FEL. The uncertainty of the total cost amounts to around 20-30% and depends on specific scientific requirements on the FEL pulse-length, stability, photon energy resolution, polarization control and other parameters.

Section of the facility	**Cost (MEURO)**
Injector	15.4
Linac 1	12
Linac 2-3	12.7
Bunch Compressors 1 and 2	1.6
Machine Timing, Controls and Protection	4
FEL 1	16
Photon Beamline	18
Civil Engineering	18
Electrical System	2.9
Cooling and Ventilation	4.4
TOTAL	105

Table 9.1.3.: Cost breakdown for the standalone 1-kHz SXR FEL. The uncertainty of the total cost amounts to around 20-30%.

Section of the facility	**Cost (MEURO)**
Injector	15.4
Linac 1	12
Linac 2-3	54.2
Bunch Compressors 1 and 2	1.6
Machine Timing, Controls and Protection	4
FEL 1	16
Photon Beamline	18
Civil Engineering	40
Electrical System	6
Cooling and Ventilation	10
TOTAL	138

9.2. Inverse Compton Sources

Inverse-Compton Scattering (ICS) sources offer the potential to achieve quasi-monochromatic X-ray beams of tunable energy at room-size laboratories. Typical applications of ICS sources include medical imaging (using K-edge subtraction or phase-contrast techniques), analyses of cultural heritage, irradiation therapy, protein crystallography, and nuclear waste management, depending on the flux and on the energy of the generated X-rays. The attractiveness of ICS sources rests on their small footprint and reduced cost, which make them ideal tools for institutions such as universities, hospitals, and museums.

The number of ICS sources worldwide has been steadily increasing over the last years. Most ICS designs are based on storage rings, since the circular layout of a storage ring maximises the repetition rate and the flux. This comes at the cost of needing significantly large facilities. Moreover, collective effects in storage rings lead to larger normalised emittances, which limit the maximum brilliance. In the years 2000's, Energy Recovery Linacs (ERLs) have also garnered interest and there exist several ICS designs based on ERLs. However, these sources are normally based on superconducting technology, which is not feasible for use in hospitals or small laboratories due to the handling of cryogenics. Normal-conductive, low-emittance linacs like that of CompactLight can also be adapted for compact ICS designs. Linac-based ICS sources tend to exhibit lower fluxes, since the electron bunches are used only once, but offer higher brilliance due to the lower emittance obtained from the photoinjector. One example of such a design is Smart*Light in Eindhoven, which is part of the CompactLight consortium. A summary of designed, commissioned, and already existing ICS sources is visible in Figure 9.2.2.

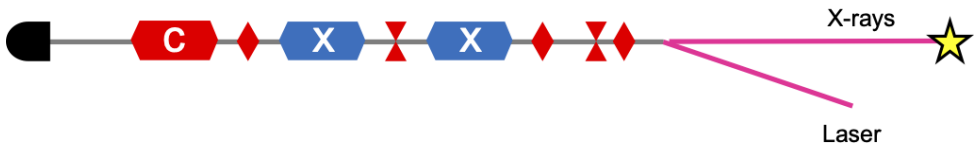

Figure 9.2.1.: Schematic layout of an ICS source based on the CompactLight C-band gun and a short X-band linac.

Recent developments in high power compact lasers, combined with the high-intensity electron beams provided by the CompactLight technology, enable the conception of a new generation of very compact ICS sources. CompactLight's technology, based on X-band high-gradient normal-conductive RF combined with high-rep-rate, low-emittance injectors, has the potential to provide both high fluxes and high brilliance. This chapter examines the preliminary parameters of an ICS source based on CompactLight technology. Figure 9.2.1 short a schematic layout of an ICS source.

9.2.1. ICS Parameters Optimisation

The parameters that characterise an ICS source in terms of X-rays are its photon flux, i.e., the number of emitted photons per second, the brilliance, which indicates the coherency of the source, and the energy bandwidth. The photon flux is the number of scattered photons, N_γ, produced in a collision between a bunch of N_e electrons and a laser pulse of N_l photons:

$$N_\gamma = \sigma_C \frac{N_e N_l \cos(\phi/2)}{2\pi\sigma_y \sqrt{\sigma_x^2 \cos^2(\phi/2) + \sigma_z^2 \sin^2(\phi/2)}}, \tag{9.1}$$

where σ_C is the Compton scattering cross-section, $\sigma_i^2 = \sigma_{e,i}^2 + \sigma_{l,i}^2$ is the convoluted spot size of the electron and laser beam in each direction $i = x, y, z$, and ϕ is the crossing angle (typically 2 deg). The total flux is defined as,

$$\mathscr{F}_{\text{total}} = \dot{N}_\gamma \text{ [ph/s]}, \tag{9.2}$$

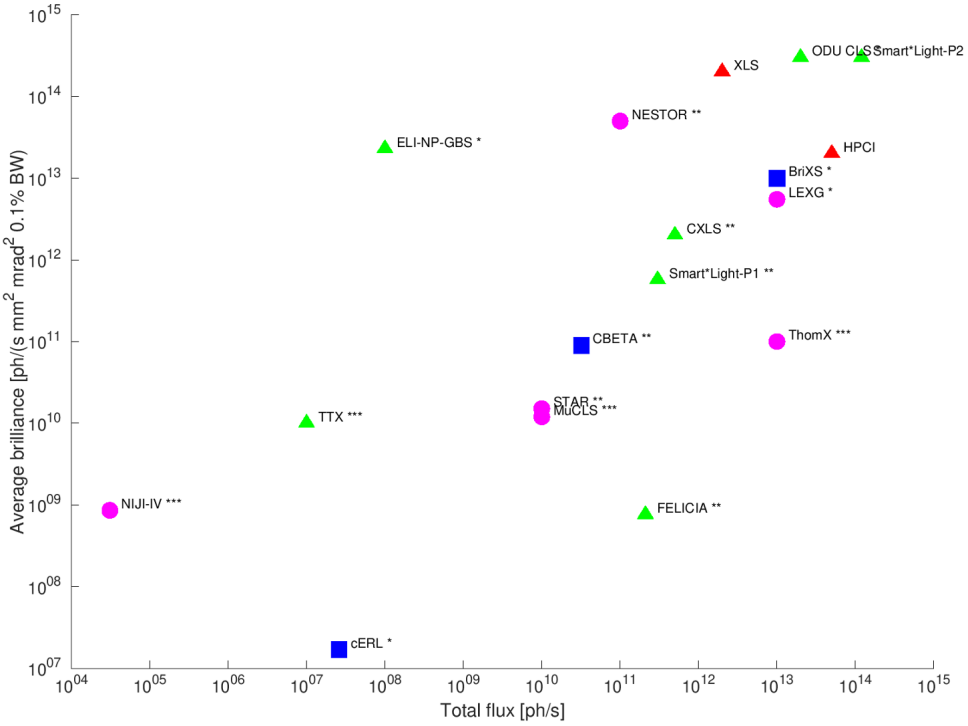

Figure 9.2.2.: Landscape of ICS sources. Circles indicate storage-ring-based sources, triangles indicate linac-based sources, squares energy-recovery-linac-based sources. Stars indicate: $\star$, design study; $\star\star$, under commissioning; $\star\star\star$, existing.

and depends on the number collisions per second occurring. The flux within a 0.1% bandwidth at the Compton edge is defined as:

$$\mathscr{F}_{0.1\%} \simeq 1.5 \times 10^{-3} \dot{N}_\gamma \text{ [ph/s]}. \tag{9.3}$$

The brilliance, in the non-diffraction limit where the electron and the laser beams have similar spot size and comparable divergence, is defined as:

$$\mathscr{B} \simeq \frac{\gamma^2 \mathscr{F}_{0.1\%}}{4\pi^2 \varepsilon_x^N \varepsilon_y^N}, \tag{9.4}$$

where ε_i^N is the normalised emittance in the direction $i = x, y$, and γ is the Lorentz factor of the electrons.

The energy bandwidth is defined as

$$\frac{\sigma_{E_\gamma}}{E_\gamma} = \sqrt{\left(\frac{\sigma_{E_\theta}}{E_\theta}\right)^2 + \left(2\frac{\sigma_{E_e}}{E_e}\right)^2 + \left(\frac{\sigma_{E_l}}{E_l}\right)^2 + \left(\frac{\sigma_{E_\varepsilon}}{E_\varepsilon}\right)^2}, \tag{9.5}$$

where appear:

- The contribution from the small collection angle, θ

$$\frac{\sigma_{E_\theta}}{E_\theta} = \frac{1}{\sqrt{12}} \frac{\gamma^2\theta^2}{1+\gamma^2\theta^2/2}. \tag{9.6}$$

- The contribution from the beam emittance:

$$\frac{\sigma_{E_\varepsilon}}{E_\varepsilon} = \frac{2\gamma^2\varepsilon}{\beta}. \tag{9.7}$$

- The relative energy spread of the electron and of the laser beam:

$$\frac{\sigma_{E_e}}{E_e}, \text{ and } \frac{\sigma_{E_l}}{E_l}. \tag{9.8}$$

Eqn. 9.1 shows the direct proportionality between the flux and the rate of electron-laser collisions. The flux can be maximised by increasing both the electron beam current and the laser pulse energy. Equation 9.4 shows that the brilliance is maximised by reducing the normalised electron beam emittance in both the horizontal and vertical axes.

The output X-ray energy depends on the electron beam's relativistic factor γ, the laser's photon energy E_L, the crossing angle ϕ between the electron beam and laser, and the scattering angle θ between the generated X-rays and the electron beam

$$E_X = 2\gamma^2 E_L \frac{1+\cos\phi}{1+\gamma^2\theta^2}. \tag{9.9}$$

In head-on collisions, ϕ can be approximated to 0, which leads to a maximum X-ray energy of $E_{X,\text{max}} = 4\gamma^2 E_L$.

The CompactLight linac module enables electron beam energies that can easily reach hundreds of MeV. A parametric scan of the laser wavelength against the electron beam energy up to 300 MeV, shown in Figure 9.2.3, confirms the larger X-ray energy achievable using XLS technology with respect to other sources. X-ray energies of the order of several MeV can be obtained.

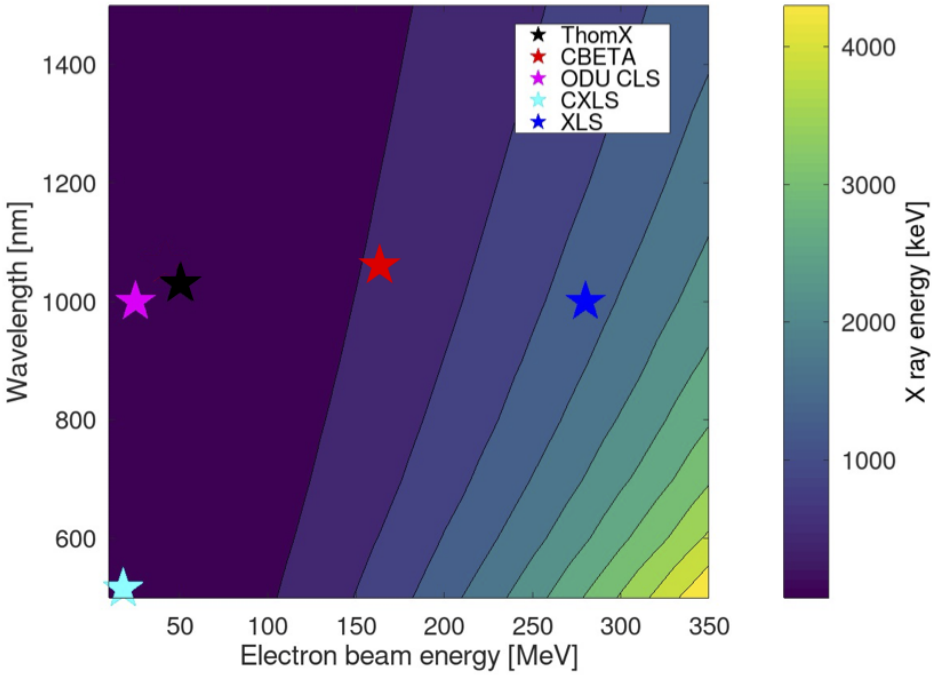

Figure 9.2.3.: Parametric scan of wavelength against electron beam energy with color coded X-ray energy. The scan confirmed the square dependence on the electron beam energy, and the linear dependence on E_{laser}.

9.2.2. Facility Layout

9.2.2.1. The Electron Gun

The 2-bunch train at 1 kHz of the CompactLight injector provides insufficient average current to make a CompactLight-based ICS competitive with respect to existing designs. The effective bunch repetition

rate f_{eff} was maximised by increasing the number of bunches per train, while the single-bunch charge was increased from 75 to 200 pC. Due to the larger charge extracted from the cathode, it was assumed that the electron beam normalised emittance would increase from 0.15 mm mrad to 0.3 mm mrad. Table 9.2.1 summarises the beam parameters for the ICS.

Table 9.2.1.: Baseline parameters of CompactLight ICS electron beam.

Parameter	**Symbol**	**Value**	**Unit**
Bunch repetition rate	f	1	kHz
Nb of bunches per train	n_b	50	
Effective nb of bunches per second	f_{eff}	50×10^3	
Bunch length	σ_z	1	ps
Bunch charge	Q	200	pC
Bunch spacing		5	ns
Normalised emittance	$\varepsilon_{x,y}^N$	0.3	mm mrad
Final energy	E	100 – 300	MeV

9.2.3. The Linac

The electron beam is then be accelerated in a short linac. The CompactLight baseline injector reaches 300 MeV, whereas typical applications of ICS X-rays require beam energies below 100 MeV. The performance estimates thus considered two electron beam energies: 100 MeV, for a very compact facility; and 300 MeV, to explore to potential of more energetic X-rays. The energy of 100 MeV could be easily achieved directly using the baseline XLS injector upstream of the laser heater. To reach 300 MeV, while maintaining compactness, one could consider the alternative injector designs proposed for CompactLight, for instance, the full X-band solution where both gun and linac are in X-band.

9.2.3.1. The Laser System

The performance estimates used the TRUMPF's 1 kW Dira 1000 [324]. The Dira 1000 is a state of the art high power compact laser with a pulse-length of 0.6 ps and wavelength of 1 µm.

Considering the XLS injector running with a repetition rate of 1 kHz as in Table 9.2.1, a 1 kW laser power would lead to a pulse energy per train of 1 J. Given that each pulse consists of a train of 50 bunches, a modest 20 mJ pulse energy would be available for the laser-electron beam scattering. To increase the pulse energy, an optical enhancement cavity should be used.

An optical enhancement cavity suitable to sustain the 1 kHz repetition rate of the XLS injector and a bunch spacing of 5 ns, would need to operate in CW mode. In CW mode, considering the Dira 1000's 1 kW laser and a 200 MHz cavity, the laser pulse energy per bunch would be of 5 µJ, requiring an enhancement factor of at least 4×10^3 is required to match the "no cavity" intensity. Recent developments in enhancement cavities allow for factors up to 10^5–10^6, however, assumed here is a conservative factor of 10^4 for safety considerations, which results in a final pulse energy of 50 mJ.

A different electron beam time structure could also be considered, with lower rep-rates and longer trains (e.g., 10 Hz repetition rate, and 1000 bunches per train). This configuration would enable the use of the enhancement cavity in burst mode. Preliminary simulations revealed that, for a total laser burst duration of 0.5 µs, the individual laser pulse energy would amount to 66 mJ. With an enhancement factor 100, 6.6 J of laser pulse energy would be available to the single-bunch interaction, attaining very high X-ray fluxes.

9.2.4. Performance Estimates

Considering a crossing angle of 2 degrees between electron beam and laser, preliminary parametric scans to determine the dependence of the flux in a 1.5 mrad cone, and of the bandwitdh, on electron and laser spot sizes have been performed. Figure 9.2.4 shows that peak fluxes of excess of 10^{11} ph/s are achievable, and the corresponding X-ray energy bandwidth.

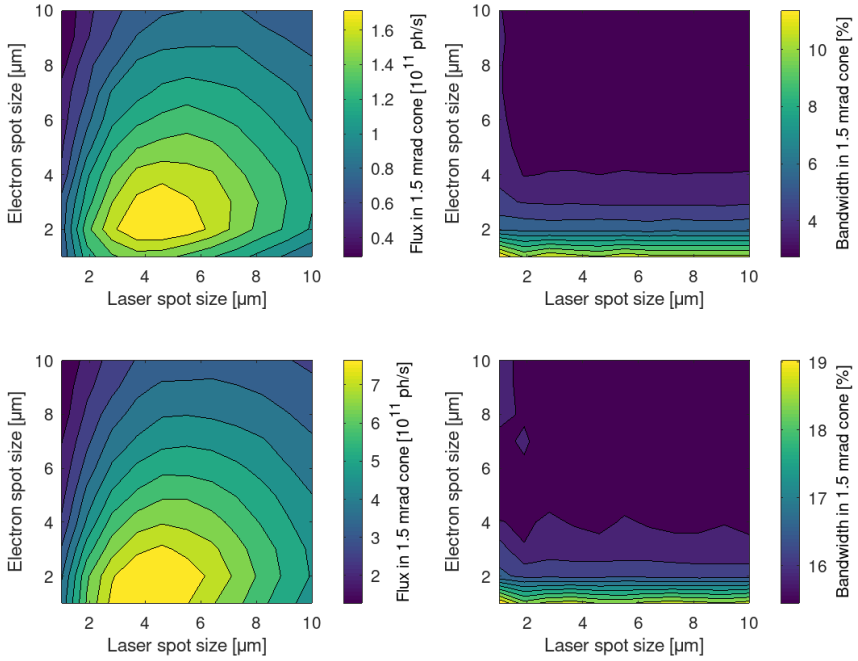

Figure 9.2.4.: Parametric scan of electron spot size versus laser spot size. The flux and the bandwidth are calculated in a cone with 1.5 mrad aperture. The two top plots refer to an electron beam energy of 100 MeV; the two bottom plots refer to an electron beam energy of 300 MeV.

9.2.5. Preliminary Cost Estimate

A preliminary cost estimate for the ICS source was obtained scaling the cost of the CompactLight injector, which can provide electron beams up to 300 MeV. It must be noted that the injector for the ICS source should be a modified version of the CompactLight injector presented in this document, since for ICS operation 50 bunches per train are needed, and not just 2 like the CompactLight baseline. A multi-bunch operation would certainly require a partial redesign of the RF system, to include for example high-order-modes damping. Table 9.2.2 summarised this preliminary cost estimate. The cost of the laser system for ICS includes the control system and locking electronics of the laser to the cavity and an external reference. The final cost will depend on the final repetition rate and average power requirements. The cost of the laser beam delivery includes vacuum chamber, optomechanics, optics, windows, motors eventually, beam pointing stabilisation and Basler cameras for beam visualisations. The Fabry-Pérot cost estimate includes granite table, vacuum chamber, optics, motorisations. Vacuum pumping, gauges and related safety are not included in this estimate.

Table 9.2.2.: Preliminary cost estimate for a CompactLight-based Inverse-Compton Scattering source.

Sub-system	**Estimated Cost (kEURO)**
1-kHz Gun laser and photo cathode system	1,800
C-band RF	3,500
Magnets	509.5
Beam instrumentation	317
Vacuum	300
Laser system for ICS	600
Laser beam delivery system	200
Fabry-Pérot enhancement cavity	210
TOTAL	7,436.5

10. Alternative Technology Solutions

10.1. X-Band RF Injector Option

10.1.1. An X-band Travelling Wave RF Photogun

A fully X-band injector is a natural progression in the development of an even more compact light-source. Using an X-band standing-wave (SW) RF photogun is one possibility and, as such, is under investigation as part of the CompactLight project. However, the strict mechanical tolerances of SW photoguns, and the necessity of using a high power RF circulator, make it a challenging task. An alternative to a conventional standing-wave RF photogun is the travelling-wave (TW) RF photogun. A TW photogun was first proposed in 1991 but never gained popularity in the injector community. The development of high-gradient linear accelerators has made the TW RF photogun a more feasible option. Here we present a brief overview of the electromagnetic design of an X-band, high-gradient TW RF photogun based on one of the CLIC structures. This work is still in its preliminary stages and merely aims to demonstrate possible alternatives in future compact light-sources.

10.1.1.1. Electromagnetic Design

The RF design for the TW photogun was based on the CLIC-G Open structure which was a CLIC prototype fabricated from milled halves. The choice of this style of accelerating structure was due to the unique gap in the geometry which is used to couple-in the photo-cathode laser. The RF design of the TW RF photogun is illustrated in Figure 10.1.1.

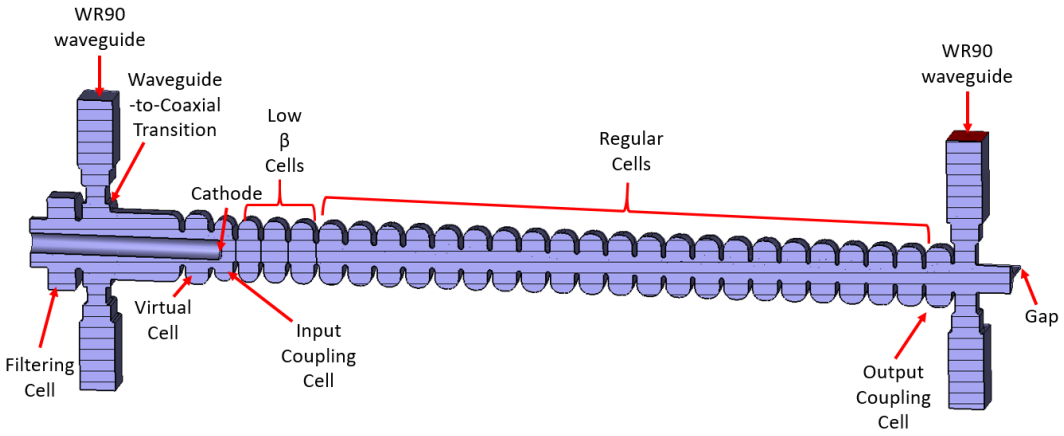

Figure 10.1.1.: The vacuum design of the RF photogun based on the CLIC-G Open.

A coaxial input coupler is used to correct the quadrupole field component induced by the dual-feed RF input couplers. All cells in the structure use a racetrack geometry, primarily for fabrication reasons, although it is possible to further reduce the quadrupole fields through an adjustment of the cells' relative horizontal and vertical dimensions. At the end of the input coupling cell, the electron velocity is 0.8 c. Consequently, the first three cells are adjusted in length to match the beta of the electrons, given the accelerating gradient expected in each respective cell for an input power of 28 MW. The remainder of the RF photogun downstream of these cells keep the geometry of the CLIC-G Open accelerating structure. Whether the structure should be shortened to allow for further emittance compensation techniques downstream is to be investigated further.

The vacuum model was simulated in CST using the frequency domain solver. Figure 10.1.2 displays the magnitude of the electric field distribution. The new coaxial input coupler is observed to have surface

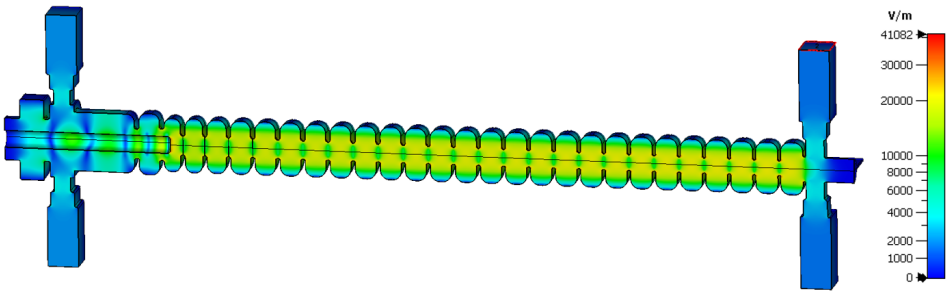

Figure 10.1.2.: Magnitude of the electric field distribution in the TW RF photogun.

electric fields lower than in the remainder of the structure which is important for the gun's high power RF performance. The magnitude of the field distribution along the beam axis is plotted in Figure 10.1.3. The field on the cathode is observed to peak at 113 MV/m. The low-beta cells have a reduced peak axial field which is to be expected from their shortened length. The remainder of the RF photogun is observed to have similar behaviour to the CLIC-G Open structure as would be expected. A summary of the properties of the TW RF photogun are demonstrated in Table 10.1.1.

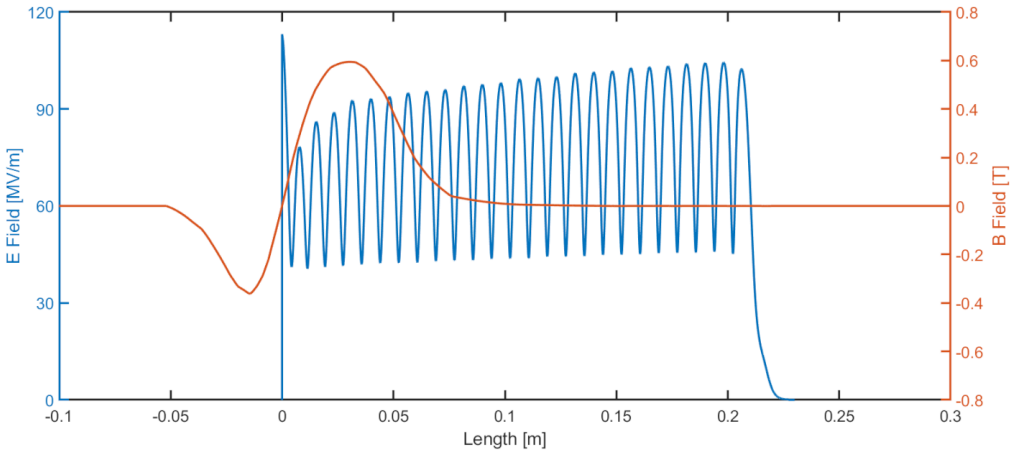

Figure 10.1.3.: The magnitude of the axial Electric field in the z-direction.

10.1.1.2. Beam Dynamics

Using the one-dimensional axial field distributions, preliminary beam dynamics calculations of the RF photogun were modelled using GPT to understand what beam quality was possible. These calculations give an idea of the possibility of a TW photogun but do not demonstrate the specific effects of the unique design choices, such as the two halves design. The cathode was modelled as a Gaussian distribution cut off at 2σ with a beam waist of 250 μm and an intrinsic emittance of 0.5 mm mrad/mm. The main solenoid, bucking coil and an additional solenoid downstream were modelled utilising the 1D axial magnetic field. A CLIC-style X-band accelerating structure was placed 10 cm downstream of the end of the RF photogun. Figure 10.1.4 illustrates the beam parameters over the length of the fully TW photoinjector.

The injector simulation demonstrates the ability to achieve a 32 MeV electron bunch in less than 0.6 m with an energy spread of 0.1%. The emittance for an 80 pC bunch is 0.5 mm mrad which greater than the requirement for CompactLight although further developments are expected to yield similar results to a SW photogun.

Table 10.1.1.: Main parameters of the travelling-wave gun.

Parameter	**Value**	**Unit**
Length	216	mm
Regular Cells	24	
Phase Advance	120	°
Frequency	11.994	GHz
Attenuation	-2.26	dB
Power	28	MW
Fill time	50.2	ns
Gradient	79	MV/m
Peak Cathode field	113.2	MV/m
Peak Surface E field	216	MV/m
Pulsed Surface Heating (τ = 50 ns)	7.7	K
Repetition Rate	1	kHz
Flow Rate	15	L/min

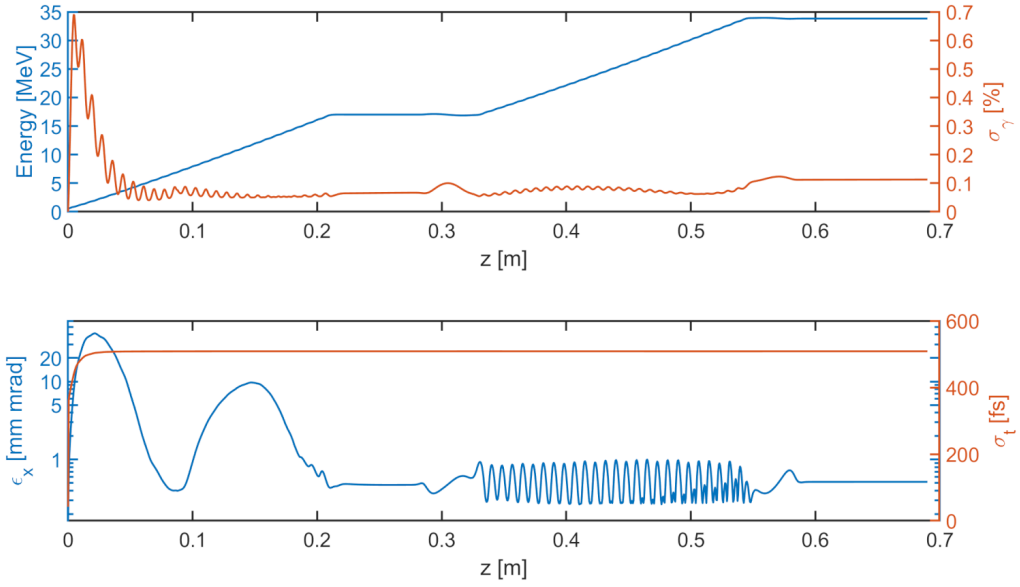

Figure 10.1.4.: Beam dynamics of the electron bunch produced by the TW RF photogun.

10.1.1.3. Discussion

The preliminary RF model demonstrates the feasibility of a fully X-band TW RF photoinjector. Such a concept is desirable as this would reduce the complexity of the RF system, given that the gun could be driven using the same RF infrastructure as the X-band linac. For such a structure to achieve the emittance requirement of CompactLight, some steps would need be taken. Particularly the concept of emittance compensation, which is vital to low emittance injectors, still needs to be investigated in detail. It is expected that a shorter accelerator would lead to better emittance compensation. A lower emittance is deemed feasible as this has already been achieved in a TW RF photogun model developed at C-band [325]. Further simulations using the full three-dimensional field-maps are recommended.

10.1.2. X-band Standing Wave RF Photoinjector

Another option for the RF photoinjector is based on a 5.6-cell Standing-wave RF gun intended to operate at an RF frequency of 11.994 GHz with a high-gradient RF electric field at the cathode of 200 MV/m. The injector is intended to generate an electron beam with low emittance and a final kinetic energy of nearly 300 MeV. To reach this aim, it will be necessary to add a solenoid to compensate the beam emittance growth due to the space-charge forces during the early stages of the beam acceleration. Since the beam's kinetic energy at the output of the 5.6-cell RF gun is typically a few MeV, seven RF accelerating sections will be required after the gun in order to achieve the goal of reaching an energy of 300 MeV. The travelling-wave (TW) structures downstream of the gun would also operate at 12 GHz . Thus, the total length of the photoinjector layout is 8.2 m and is schematized in Figure 10.1.5. The main parameters of the photoinjector prototype are summarized in Table 10.1.2 and will be discussed in detail in the next section.

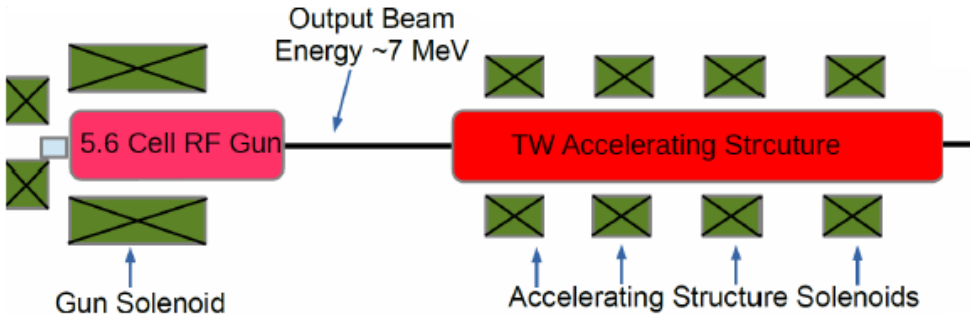

Figure 10.1.5.: Partial view of the RF photoinjector layout. After the 5.6-cell RF gun seven identical TW accelerating structures are added to accelerate the beam (in the current scheme only the first of the seven TW structures is shown). Only the first TW section includes solenoids.

Table 10.1.2.: Main parameters of the X-band SW photoinjector.

Parameter	**Value**	**Unit**
Frequency f_π	GHz	11.994
RF Electric Cathode field	MV/m	200
Maximum superficial RF electric field (for 1 MV/m at cathode)	MV/m	0.998
Coupling factor, β		1.008
Mode separation, Δf	MHz	27.1
Filling time, τ	ns	112.5
Required magnetic field to suppress multipactor	mT	360
Breakdown Rate, BDR (for pulse of 400 ns)	bpp/m	5.6×10^{-6}
Pulse heating (for pulse of 400 ns), ΔT	$^\circ$C	31

10.1.2.1. Electromagnetic Design of the RF Gun

The cross-section of the RF gun geometry is shown in Figure 10.1.6. It consists of six accelerating cavities, each with length $\lambda/2$ (λ being the wavelength of the RF electromagnetic wave in vacuum), except for the first cell, which has a length of 0.6 times the others—this has been optimized over several beam dynamic iterations similar to the approach in [326]. The cells are coupled by means of elliptical irises, instead of circular ones, in order to reduce the RF electric field at the surface of the gun [327,

328], thus reducing the rate of RF breakdown. The material chosen for the bulk of the photoinjector is copper. The photoinjector is connected to the RF generator's external circuit by means of a coaxial coupler with a door-knob geometry [329]. Due to the choice of this coupling scheme, the entire RF gun structure is axisymmetric, allowing the use of the free distribution software SUPERFISH [330] for the electromagnetic design of the gun. SUPERFISH is a 2D eigenmode solver applicable for geometries with cylindrical axisymmetry, and it has the advantage of being much faster than 3D codes.

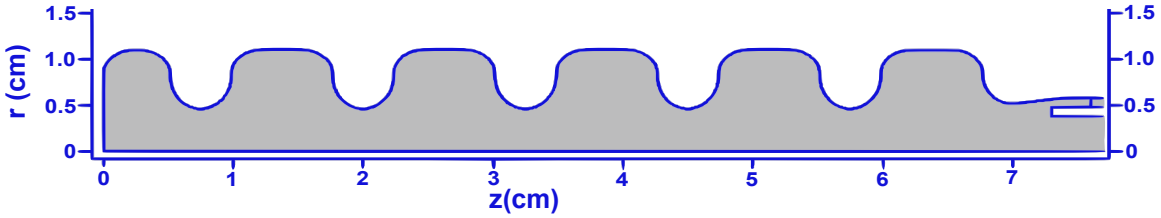

Figure 10.1.6.: Scheme of the longitudinal section of the 5.6 cell RF photoinjector with the coaxial coupler. The structure has symmetry of revolution around the z axis.

In the design, the shape of the main cell is tuned to minimize the RF electric field on the surface relative to the corresponding value on the cathode surface. Also, the gun geometry is intended to maximize the separation between the operating π-mode and the nearest neighbour mode in order to avoid the residual excitation of such a mode during RF transients. The effect of this undesirable neighbour mode on the gun RF electric field pattern has also been taken into account in the design process, by using an equivalent circuit model to characterize the system consisting of the gun cavity plus the coaxial coupler, following a procedure similar to that described in [80].

After the gun optimization, for the final prototype it was found that the maximum value of the surface electric field is 0.998 MV/m, assuming a cathode RF electric field amplitude of 1 MV/m. Other relevant gun parameters are the coupling factor, $\beta = 1.008$, the separation between the π-mode and the nearest neighboring mode, $\Delta f = 27.1$ MHz, and the gun cavity filling time, $\tau = 112.5$ ns. These results, obtained with SUPERFISH in combination with the circuit model, were benchmarked at the design frequency with the 3D numerical electromagnetic field solver HFSS [331]. The steady-state HFSS result is also plotted in Figure 10.1.7 and agrees well with the model. The comparison thus validates the theoretical approach employed for the RF gun design.

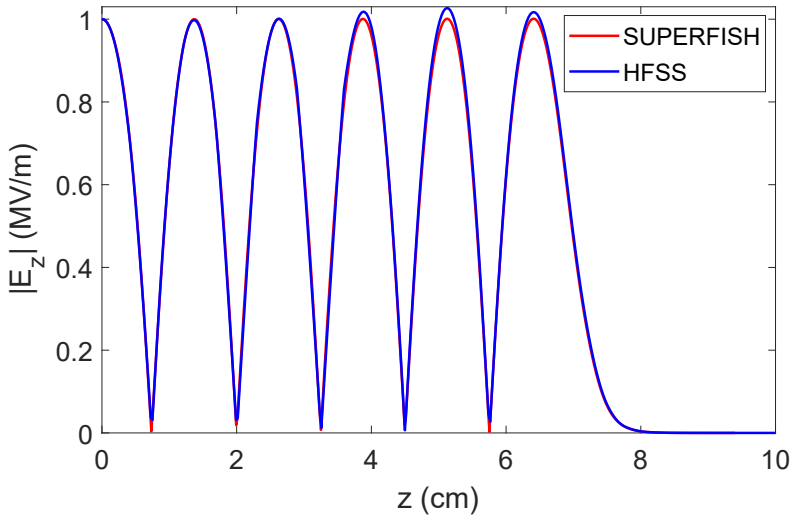

Figure 10.1.7.: RF electric field along the axis of the RF gun, normalized for 1 MV/m at the cathode, computed with SUPERFISH plus a circuit model for the neighboring modes (red curve), and with HFSS (blue curve).

10.1.2.2. Multipactor Analysis in the Coaxial Coupler

During RF gun operation the coupler coaxial line will be exposed to high-power RF electromagnetic fields that may cause the appearance of multipactor discharges. The multipactor phenomenon is an electron avalanche-like discharge occurring in components operating under vacuum conditions and high-power RF electromagnetic fields [332]. This process can lead to an exponential increase of the electron population which degrades the component's performance and can physically damage the structure.

To assess the multipactor risk in the coaxial coupler, a set of multipactor numerical simulations were performed to determine the susceptibility zones in which the discharge is expected to occur. The multipactor numerical simulations for the coaxial line were carried out with an in-house developed code based on the Monte Carlo method which relies on the single effective electron model [333]. This technique is based on 3-D tracking a set of effective electrons governed by the electromagnetic field. Each effective electron describes a particular electron population that evolves in time by colliding with the coaxial metallic walls of the waveguide (inner and outer coaxial conductors).

According to the results of the numerical simulations for the coaxial coupler of the photoinjector, which is intended to operate with a cathode RF electric field of 200 MV/m, there are two multipactor bands within the operating range. These bands, in terms of RF peak voltage in the coaxial waveguide, correspond to the intervals 0.891-3.565 kV and 5.219-8.388 kV. At the RF power level required to operate the gun, the RF voltage in the coaxial line is 13.2 kV, which is above the second multipactor window, and hence no multipactor discharge is expected at this operating point. However, when the RF power is turned on, there will be a transient increase in the RF electromagnetic field, both in the coaxial line and in the RF gun cavity, until the field reaches steady-state. In fact, during the filling of the cavity there will be two time intervals of 15 ns and 23 ns (corresponding to the first and second window, respectively) in which multipactor discharges are expected to occur. Similarly, multipactoring will appear during the emptying of the cavity in two time spans of 53 ns and 156 ns.

Despite the multipactor risk, it does not represent an insurmountable problem since it can be suppressed by means of an external magnetic field. This method was theoretically and experimentally demonstrated for coaxial lines in [334]. In our case, the numerical simulations reveal that a static magnetic field equal to or higher than 360 mT suppresses the discharge. Accordingly, a solenoid will be included in the RF photoinjector layout for multipactor mitigation in the coupler coaxial line, as well as for beam emittance compensation purposes.

10.1.2.3. RF Breakdown Risk

RF breakdown is a phenomenon that appears in RF accelerating structures at high electric surface field gradients [335]. During breakdown, an electric current is emitted from the walls of the device forming a plasma that causes a sudden increase in the vacuum pressure level. The risk of RF breakdown is characterized by a normalized breakdown rate (BDR), which is defined as the expected number of breakdowns per pulse per meter length of the structure. According to [75], the BDR can be roughly estimated based on the maximum of a modified Poynting vector, S_c, that is computed along the device's surface. The relationship between modified Poynting vector, BDR and the RF pulse-length t_{on} is given by the empirical expression

$$BDR = \frac{S_c^{15} t_{on}^5}{C} \tag{10.1}$$

where $C = 9.765625 \times 10^{27}\ \mathrm{W^{15}ns^5}\mu\ \mathrm{m^{-30}bpp^{-1}m}$ is a constant found from measured breakdown rate data provided in [75]. The above expression allows one to estimate the BDR during a period when the gradient is constant. However, this is not the case for the RF gun where the gradient varies during the filling and emptying of the cavities. For the RF gun case, the modified Poynting vector will vary with time, and this effect must be taken into account to calculate properly the BDR for the RF pulse in the

gun. To do this, the pulse is split into the sum of many short pulses, assuming that for each of them the corresponding BDR is given by the uniform S_c amplitude case

$$\mathrm{BDR}_{\mathrm{pulse}} = \frac{1}{C}\lim_{n\to\infty}\sum_{k=1}^{n} S_c^{15}(t_k)\left(\frac{T_p}{n}\right)^5 = \frac{5}{C}\int_0^{T_p} S_c^{15}(t)\,t^4 \mathrm{d}t \tag{10.2}$$

where $T_p = nt_p$ is the total pulse-length, n is the number of short pulses into which the total pulse is divided, and t_p is the length of each of the short pulses. Figure 10.1.8 shows the resulting BDR in the RF gun as a function of the pulse-length. The BDR predictions corresponding to the constant gradient case are also included for comparison. There is a significant difference between the two curves, which shows the importance to taking into consideration the transient effect. For $t_{\mathrm{on}} \gg \tau$ the transient result approaches that of the constant gradient case as expected.

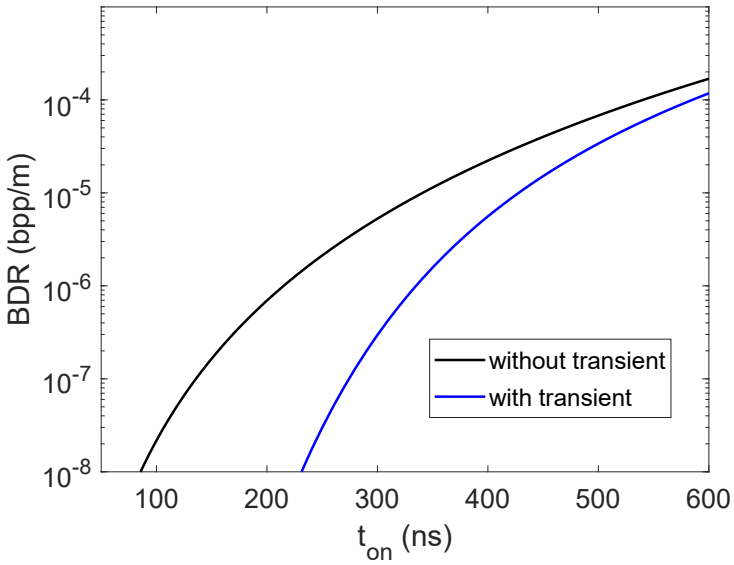

Figure 10.1.8.: BDR in the gun as a function of the RF pulse-length for a constant cathode electric field of 200 MV/m.

10.1.2.4. RF Pulse Heating

The surface currents associated with the RF fields in a structure induce Ohmic losses on the walls that increase the metal's temperature. Pulsed temperature increases over 50°C-60°C are known to significantly increase the BDR in copper structures [336]. Thus one wants to avoid operating at gradients and pulse-lengths that produce such peak temperature rises during the RF pulse.

The temperature increase during an RF pulse in the photoinjector can be estimated by means of a 1D model that solves analytically the heat transfer differential equation for a metallic wall where the wall boundaries are assumed to be thermally isolated. Given these assumptions, the 1D heat transfer equation can be solved analytically following a similar procedure to that described in [161] and [337]. For our calculations, the equations given in [337] are employed since they take into account the effect of the RF pulse transient. In Figure 10.1.9 (left), the maximum temperature increase during the RF pulse in the photoinjector walls is shown as a function of the pulse-length, and Figure 10.1.9 (right) shows a color map of the peak temperature rise in the gun for t_{on} = 400 ns. For a pulse-length of t_{on} = 400 ns the maximum temperature rise is ΔT = 31°C, which is below the limit of 50°C - 60°C.

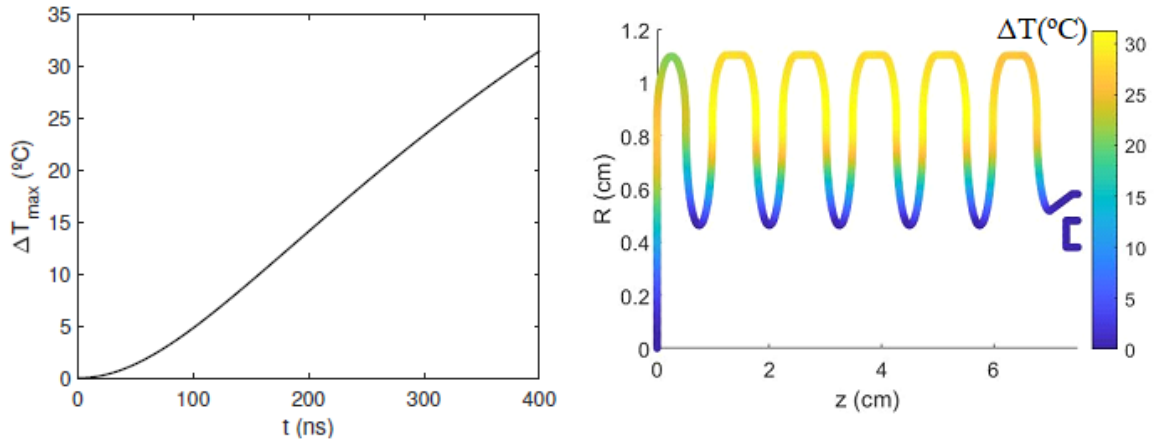

Figure 10.1.9.: Left: Maximum temperature increase in the RF gun copper walls as a function of the pulse duration for a steady state cathode electric field of 200 MV/m. Right: Maximum temperature increase in the RF gun copper surfaces when operating with a steady state cathode field of 200 MV/m and t_{on} = 400 ns.

10.1.2.5. RF Power System

The proposed RF gun is intended to operate with a high-gradient cathode field of 200 MV/m when the laser beam hits the cathode to generate the electron beam. In order to achieve this field at the cathode, an input RF power of 11.58 MW must be delivered at the coaxial coupler port. During the RF transient phase, a significant amount of RF power is reflected back to the klystron. In order to protect the klystron, a delay-line between the klystron and the RF gun has been added, thus ensuring that when the reflected power starts to arrive, the RF pulse has finished and the klystron is switched off. For our design the intended pulse duration (t_{on} = 400 ns) would require a length of L = 50.24 m to protect the klystron. However, taking into account the attenuation of the standard copper WR-90 rectangular waveguide (α_{at} = 0.11 dB/m) operating with the fundamental TE_{10} mode, this will result in a total attenuation of 5.52 dB, which implies that nearly 72 % of the input power is lost before reaching the RF gun, and hence results in a very inefficient design. A solution to that problem is to shorten the RF pulse and excite the gun with a square-step RF pulse [80]. The initial part of the RF pulse has a power ΛP_{in}, P_{in} being the RF input power required to obtain the desired RF electric field amplitude at cathode (after the filling transient) for the RF gun operation and $\Lambda > 1$ is the power magnification factor at the first part of the RF pulse. At the time t_h there is a sharp change in the RF power to the value P_{in}, which is maintained for the rest of the pulse. It is chosen that $\Lambda = 4$ ($\Lambda P_{in} = 46.32 MW$) and t_h = 77.2 ns. Using such an RF pulse, it is found that for a time of t_{inj} = 85 ns, the axial pattern of the RF electric field matches well with the steady state case and with the desired amplitude of 200 MV/m at cathode, hence the electron beam must be injected at this time. For this case, the length of the delay-line is L = 10.67 m and a total RF power of 60.7 MW must be finally delivered by the klystron to feed the photoinjector circuit (taking into account the power losses of the delay-line).

To achieve this RF power, a layout similar to that existing in Xbox 3 at CERN is proposed [338]. The layout is composed of four combined Toshiba E37113 klystrons and SLED pulse-compressors. Each of the klystrons can provide an RF pulse with a peak power of 6 MW and a pulse-length of up to 4-5μs. Thus, combining the four klystrons a pulse with a peak power of 24 MW and pulse-length up to 4-5μs can be obtained. Now, if this combined pulse is compressed by means of a SLED pulse-compressor with a compression factor between 3 and 4, a final output pulse with peak power in the range between 70-80 MW, pulse-length of up to 300 ns, and a maximum repetition rate of 400 Hz can be achieved [338]. A pulse with such characteristics would be suitable for feeding the proposed RF gun.

10.1.2.6. Photoinjector Beam Dynamics

The beam simulations of the photoinjector have been carried out with the simulation codes GPT [168], ASTRA [339] and RF-Track [340]. 20k macro-particles were used to simulate a 75 pC bunch charge that is excited by a uniform laser which has a 0.3 ps long flat pulse with with a 0.25 mm rms transverse width. It was also assumed that the particles emerging from cathode at room temperature have kinetic energy of E_k = 0.05 eV with intrinsic emittance of ε = 0.06 μm rad.

In order to examine the performance of the RF photoinjector, an optimization procedure was carried to achieve a bunch with good properties (low emittance, small uncorrelated energy spread, etc.) at the injector output. Beam dynamics modeling was carried out by optimizing the overall photoinjector design, in particular, by adjusting the bunch phase, solenoid strength, the accelerating TW phase, and the spacing between the gun and the first TW structure in order to achieve the best emittance compensation. An exploration of different combinations of the above parameters was required to find the optimum working point. The spacing between the gun to accelerating structure is chosen according to the Ferrario's working point [179], which states that the entrance to the accelerating structure after the gun must be at the position where the beam size has a minimum, and the emittance is optimized for minimum at the end of the first TW structure. The optimum set of parameters was obtained using the code GPT that produced a minimum projected emittance at the end of the first TW structure.

The results from the GPT simulations have been benchmarked with the codes ASTRA [339] and RF-Track [340], finding a good agreement between them, and thus giving confidence in the simulations. The energy gain and length of the bunch in the X-band gun and TW structures are shown in Figure 10.1.10 (right). The evaluation of rms emittance as well as the transverse beam size along the injector are shown in Figure 10.1.10 (left).

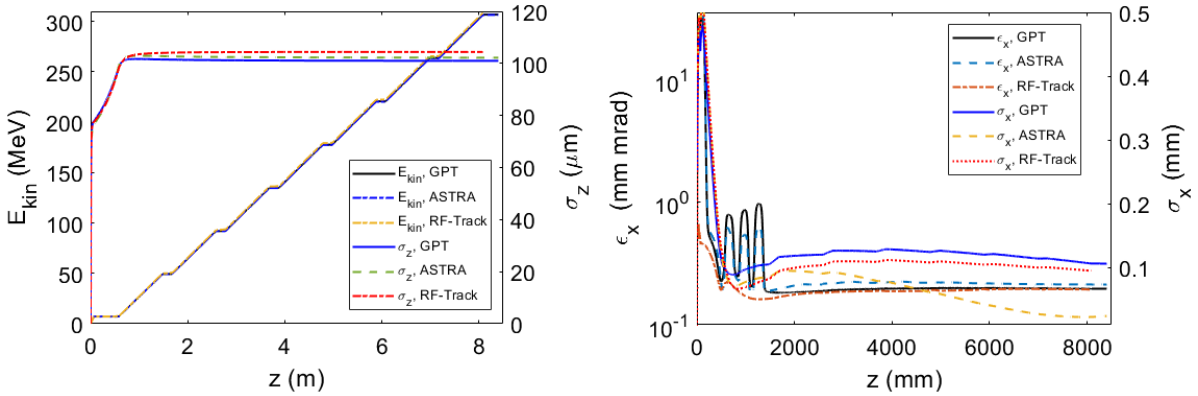

Figure 10.1.10.: Left: Energy gain and the bunch length evolution along the injector. Right: Projected normalized horizontal emittance and transverse RMS beam size along the injector.

The final beam properties obtained with each code are listed in the Table 10.1.3.

Table 10.1.3.: Electron beam properties at the output of the photoinjector.

Parameter	Units	GPT	ASTRA	RF-Track
Kinetic energy	MeV	307	306	308
Bunch length	fs	337	341	348
Energy spread	%	0.50	0.56	0.43
Peak current	A	64	64	62
Rms norm. emittance	mm-mrad	0.20	0.21	0.19
Transverse size	mm	0.10	0.02	0.09

Page 297 Undulator Option

undulator technology, the performance of the magnetic field can be drastically improved.

10.2. Undulator Option

II. CRYOGENIC PERMANENT MAGNET UNDULATORS

NdFeB magnets with high coercivity of Sm_2Co_{17} magnets are generally used in in-vacuum undulators because of their resistance against demagnetization due to electron beam irradiation. In addition, in the case of storage ring, thermal stabilization and vacuum bakeout at high temperatures around 420 K are necessary for the magnets; high coercivity magnets are also favored to minimize thermal demagnetization during these processes [12]. However, if the undulator is operated at a cryogenic temperature, the outgassing rate from the magnets becomes very low or the magnets are even expected to work as cryopumps, so that it is no more necessary to expose the magnets to high temperatures. Supposing a cryogenic temperature operation, NdFeB magnets with high remanent fields, normally showing low coercivity at room temperature, can exhibit sufficiently high coercivity and resistivity against electron beam irradiation. This gives us an opportunity to create a new undulator concept called the cryogenic permanent magnet undulators (CPMUs).

Since the magnet arrays of an in-vacuum undulator are placed under good thermal isolation with vacuum, the undulator operation at the cryogenic temperature of liquid nitrogen or higher simply needs some additional refrigerant channels or cryocoolers. Figure 1 shows two examples of the CPMU design, both of which resemble the ordinary in-vacuum undulator design [12] except having refrigerant channels 1(a) or cryocoolers 1(b) attached to the magnet beams.

The most important advantage of the CPMUs is to avoid a very high heat load of several hundred watts, which can be covered by a compact cryocooler of a cooling capacity of a few watts. The estimated amount of heat flowing in through the shafts of the magnet beams is about 100 W and thermal radiation from the inner surface of the vacuum chamber is about 5 W. The heat generated by the resistive wall effect and synchrotron radiation from upstream bending magnets is normally smaller, for instance about 10 W in the case of the 203-bunch operation in SPring-8 at a 3 mm gap. These heat loads can be covered by one cryocooler, for example, the Suzuki Shokan RF90S having a cooling capacity higher than 200 W at 80 K.

The CPMUs offer further advantages over SCUs, with the saving of electricity and a stable operation without any quench. In addition, all techniques of magnetic field correction developed for permanent magnet undulators can be applied to the CPMUs without any significant modification.

III. CHARACTERISTICS OF NdFeB MAGNETS AT CRYOGENIC TEMPERATURES

Sintered NdFeB magnets exhibit negative dependence of remanent fields against temperature, typically $-0.1\%/\mathrm{K}$ around room temperature. According to this

10.2.1. Cryogenic Permanent Magnet Undulators

The helical SCU solution adopted as the baseline undulator discussed in Section 6.1.1, has open issues that cannot be addressed in detail at this conceptual design stage. The engineering challenges are the main factors that have, to date, prevented SCUs from being widely adopted, especially at FEL user facilities. The following issues are mentioned on a qualitative level:

- The mechanical tolerances are tight and have to be maintained as the coils are cooled down from room temperature to about 4K.
- Any heat transfer due to wakefields or synchrotron radiation from the electron beam has be minimised to prevent magnet quenching.
- Concerning the phase error, conventional field correction schemes used for permanent magnet devices cannot be directly applied to SCUs.

These considerations suggest that an alternative option for the main radiator should be considered as a precaution.

Such an option is the cryogenic permanent magnet undulator (CPMU) in which permanent magnets are cooled by means of either refrigerant channels or cryocoolers, down to the temperature of liquid nitrogen.

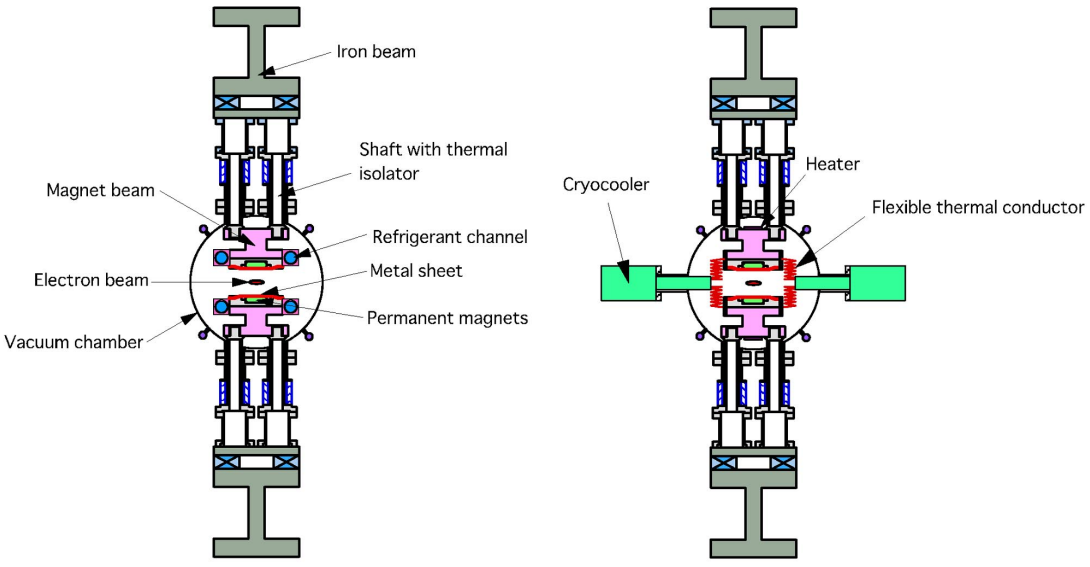

Figure 10.2.1.: Diagram of a typical CPMU structure with two different cooling schemes. Left: refrigerant channels with liquid nitrogen. Right: cryocooler coldheads. Reproduced from [341].

FIG. 1. (Color) Design examples of a CPMU with refrigerant channels (a) or with cryocoolers (b).

The operation of the magnet blocks at cryogenic temperatures provides a three-fold benefit:

a) It removes the need to bake the magnets at high temperature

b) It enhances the coercive force of the magnets, making them more resistant to demagnetising effects

c) It increases the remanence of the magnets, with the subsequent increase of the undulator magnetic peak field.

This scheme can be easily adapted to currently existing in-vacuum undulators and the magnetic field strength is improved over room temperature devices by $\sim$ 30% for pure permanent magnet types and $\sim$ 50% for hybrid types. Compared to a room temperature in-vacuum undulator of equivalent spectral range, the flux performance is enhanced thanks to the field increase and to the additional number of periods for a given module length. In summary CPMUs fit well the demand of short period undulators.

Unlike SCUs operating around the liquid helium temperature where the heat load budget is a few watts, with CPMUs there is no big technological issue such as the thermal shield so a heat load as high as several hundred watts is allowed. In addition, existing field correction techniques are applicable to the CPMUs, and since there is no quench possibility CPMUs have a similar reliability to conventional permanent magnet undulators.

Figure 10.2.1 shows two available schemes for magnet cooling. The most straightforward one is using refrigerant channels with liquid nitrogen. This solution provides a cooling capacity of more than a kW, and it is the solution used at the first directly cooled CPMU to be operated at 77 K, built at SOLEIL [342]. The other cooling concept is based on coldheads, each providing a cooling capacity at 77 K of $\sim$ 180-200 W [249]. Nevertheless, several CPMU key components need to be adapted, in particular the cooling system, the magnet girder and the gap measurement systems. Moreover, the magnetic field characterisation of cryogenic undulators is challenging, given that magnetic measurements have to be performed inside the vacuum chamber at cryogenic temperature in order to optimise the undulator in the final operation conditions. More technical considerations as well as details on risk, benefit and cost challenges are reported on the deliverable document D5.1 [343].

10.2.2. Comparison of SCU and CPMU

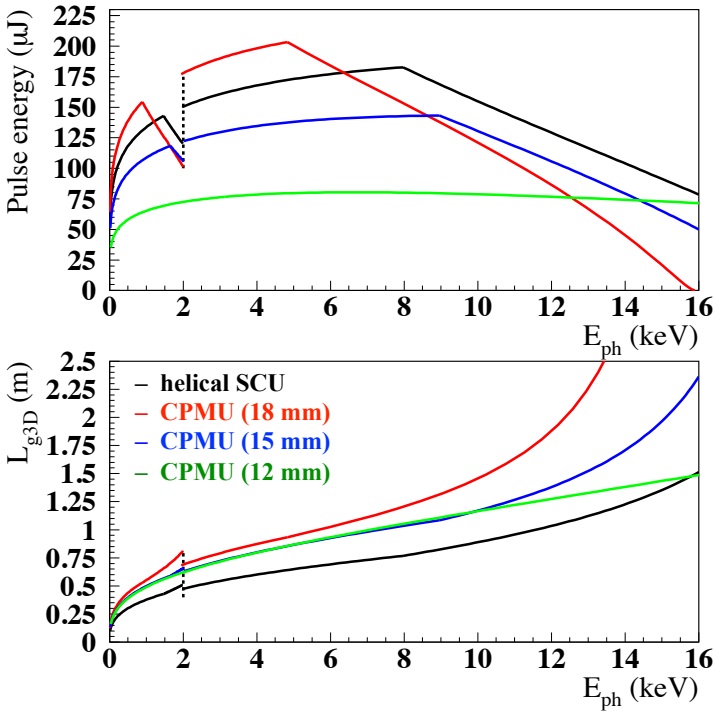

Figure 10.2.2.: Semi-analytical performance calculations, showing comparison between the helical 13 mm SCU period (baseline choice) and the CPMU with 18 mm, 15 mm and 12 mm periods, showing pulse energy (top) and gain length (bottom) as a function of the FEL photon energy.

Following the method of the study presented in Section 6.1.2.2 which determined the optimal undu-

lator period of the helical SCU in order to balance the FEL output across the whole Soft and Hard X-ray tuning range, the semi-analytical Xie model [64] is used to evaluate the performance. This model is widely adopted as it yields quick calculations of the FEL parameters, accounting for the main effects

Table 10.2.1.: Reference electron beam parameters.

Parameter	**Value**	**Units**
Beam energy	5.5	GeV
Peak current	5	kA
Normalised emittance	0.2	mm mrad
RMS slice energy spread	0.01	%
Average β function	9	m

deteriorating the gain performance due to energy spread, emittance and finite transverse bunch size, and as it provides reliable comparisons among different undulator period and strength configurations. Calculations assume the average electron beam parameter values listed in Table 10.2.1. The analysed quantities are the gain length L_{g3D}, whose evaluation is improved in the Xie model by the aforementioned effects over the 1-dimension estimate of eq.(3.6) (see Section 3.3.2.1), and the pulse energy as defined in Section 6.1.2.2. The FEL saturation length is estimated approximately as $20\,L_{g3D}$.

Figure 10.2.2 shows the comparison, as a function of the FEL resonant photon energy E_{ph}, of pulse energy and L_{g3D}, between the baseline helical SCU with period $\lambda_u = 13$ mm and three planar CPMUs with the specified undulator periods and the related colour code. In particular, the CPMUs under consideration are those designed at Soleil [344, 345].

Following the same definitions discussed in Section 6.1.2.2, the pulse energy increases with E_{ph}, as the photon energy is sustained by increasing the beam energy at fixed tuning, for each undulator line.

Once the beam energy of 2.36 GeV is reached, namely the maximum value allowed to operate in the Soft X-ray regime at 1 kHz repetition rate, the pulse energy decreases as the E_{ph} increase is provided by the magnetic strength decrease with the subsequent FEL gain decrease. This is the explanation of the turning points located at $E_{ph} < 2$ keV values. The 12 mm CPMU period is the only exception as this configuration provides a regular resonant photon energy increase for the whole beam energy range under consideration within this project. For photon energies larger than 2 keV, a similar behaviour occurs for beam energies up to 5.5 GeV, resulting in a turning point located around 5 keV for the 12 mm CPMU period after which the pulse energy drops. In this range, the pulse energy behaviour of the 15 mm CPMU period is very similar to the baseline SCU choice, with the turning point located between 8 and 9 keV. The gain length of the 12 mm and 15 mm CPMU periods is basically the same up to $E_{ph} \simeq 10$ keV values, with about 50% better length performance at larger photon energies, for the shorter period.

In conclusion, while the gain length does not make any substantial difference between 12 mm and 15 mm CPMU periods, the pulse energy comparison tends to favour the latter one, as it is better balanced along the full E_{ph} range to be covered, very similar to that of the baseline helical SCU, at the price of an overall 25% loss in the output FEL pulse energy.

References

[1] W. Ackermann et al.,
Operation of a free-electron laser from the extreme ultraviolet to the water window,
Nature Photonics **1** (2007) 336, ISSN: 17494885, DOI: 10.1038/nphoton.2007.76.

[2] DESY, *FLASH Free Electron Laser*, URL: https://flash.desy.de/accelerator/.

[3] *SACLA X-ray Free Electron Laser*, URL: http://xfel.riken.jp/eng/.

[4] Elettra Sincrotrone Trieste, *FERMI Conceptual Design Report*, tech. rep., 2007,
URL: https://www.elettra.eu/files/Documents/FERMI%20Machine/Machine/CDR/FERMI_CDR.pdf.

[5] Elettra Sincrotrone Trieste, *FERMI Website*,
URL: https://www.elettra.eu/lightsources/fermi.html.

[6] Stanford Linear Accelerator Center,
Linac Coherent Light Source (LCLS) Conceptual Design Report, Slac-R-593 (2002),
DOI: 10.2172/1029479.

[7] *Linac Coherent Light Source | SLAC National Accelerator Laboratory*,
URL: https://lcls.slac.stanford.edu/.

[8] European XFEL, *European XFEL: Overview*, 2021,
URL: https://www.xfel.eu/facility/overview/index_eng.html.

[9] Altarelli M et al., *The European X-Ray Free-Electron Laser - Technical design report*, tech. rep.,
Hamburg: DESY, 2007, 646.

[10] M. Pedrozzi, *SwissFEL Injector Conceptual Design Report*, tech. rep., PSI, 2010.

[11] SwissFEL, *SwissFEL | Paul Scherrer Institut (PSI)*, 2021,
URL: https://www.psi.ch/en/swissfel.

[12] *Pohang Accelerator Laboratory*, URL: https://pal.postech.ac.kr/paleng/Menu.pal?method=menuView&pageMode=paleng&top=7&sub=6&sub2=1&sub3=0.

[13] Z. Y. Zhu et al., *SCLF: An 8-GeV CW SCRF Linac-Based X-Ray FEL Facility in Shanghai*,
Proceedings of the 38th International Free-Electron Laser Conference, FEL 2017 (2018) 182,
DOI: 10.18429/JACOW-FEL2017-MOP055.

[14] J. N. Galayda, *The LCLS-II: a high power upgrade to the LCLS* (2018),
DOI: 10.18429/JACoW-IPAC2018-MOYGB2.

[15] *LCLS-II | Linac Coherent Light Source*,
URL: https://lcls.slac.stanford.edu/lcls-ii.

[16] M. Aicheler et al.,
A Multi-TeV Linear Collider Based on CLIC Technology: CLIC Conceptual Design Report,
CERN Yellow Reports: Monographs, CERN, Geneva, 2012,
DOI: 10.5170/CERN-2012-007, URL: http://cds.cern.ch/record/1500095.

[17] CompactLight Partnership, *CompactLight Project Website*, 2018,
URL: http://www.compactlight.eu/Main/HomePage%20%5Ccite%7BXLS%7D.

[18] J. M. Rodenburg et al., *Hard-X-ray lensless imaging of extended objects*,
Physical Review Letters **98** (2007) 034801, ISSN: 00319007,
DOI: 10.1103/PHYSREVLETT.98.034801/FIGURES/3/MEDIUM, URL: https://journals.aps.org/prl/abstract/10.1103/PhysRevLett.98.034801.

[19] S. Boutet et al.,
High-Resolution Protein Structure Determination by Serial Femtosecond Crystallography,
Science **337** (2012) 362, ISSN: 10959203,
DOI: 10.1126/SCIENCE.1217737/FORMAT/PDF,
URL: www.sciencemag.org/cgi/content/full/science.1217737/DC1.

[20] T. Masuda et al.,
Atomic resolution structure of serine protease proteinase K at ambient temperature,
Scientific Reports **7** (2017), ISSN: 20452322, DOI: 10.1038/SREP45604,
URL: /pmc/articles/PMC5374539/%20/pmc/articles/PMC5374539/?report=abstract%20https://www.ncbi.nlm.nih.gov/pmc/articles/PMC5374539/.

[21] M. O. Wiedorn et al., *Megahertz serial crystallography*,
Nature Communications 2018 9:1 **9** (2018) 1, ISSN: 2041-1723,
DOI: 10.1038/s41467-018-06156-7,
URL: https://www.nature.com/articles/s41467-018-06156-7.

[22] M. L. Grünbein et al.,
Megahertz data collection from protein microcrystals at an X-ray free-electron laser,
Nature Communications 2018 9:1 **9** (2018) 1, ISSN: 2041-1723,
DOI: 10.1038/s41467-018-05953-4,
URL: https://www.nature.com/articles/s41467-018-05953-4.

[23] B. Henrich et al.,
The adaptive gain integrating pixel detector AGIPD a detector for the European XFEL,
Nuclear Instruments and Methods in Physics Research Section A: Accelerators, Spectrometers, Detectors and Associated Equipment **633** (2011) S11, ISSN: 0168-9002,
DOI: 10.1016/J.NIMA.2010.06.107.

[24] R. Neutze et al., *Potential for biomolecular imaging with femtosecond X-ray pulses*,
Nature 2000 406:6797 **406** (2000) 752, ISSN: 1476-4687, DOI: 10.1038/35021099,
URL: https://www.nature.com/articles/35021099.

[25] Z. Sun et al., *Current status of single particle imaging with X-ray lasers*,
Applied Sciences (Switzerland) **8** (2018), ISSN: 20763417, DOI: 10.3390/APP8010132.

[26] D. Milathianaki et al.,
Femtosecond visualization of lattice dynamics in shock-compressed matter,
Science **342** (2013) 220, ISSN: 10959203,
DOI: 10.1126/SCIENCE.1239566/SUPPL{_}FILE/MILATHIANAKI.SM.PDF,
URL: https://www.science.org/doi/abs/10.1126/science.1239566.

[27] M. G. Gorman et al., *Direct Observation of Melting in Shock-Compressed Bismuth with Femtosecond X-ray Diffraction*, Physical Review Letters **115** (2015) 095701, ISSN: 10797114,
DOI: 10.1103/PHYSREVLETT.115.095701/FIGURES/4/MEDIUM, URL: https://journals.aps.org/prl/abstract/10.1103/PhysRevLett.115.095701.

[28] D. Kraus et al.,
Nanosecond formation of diamond and lonsdaleite by shock compression of graphite,
Nature Communications 2016 7:1 **7** (2016) 1, ISSN: 2041-1723,
DOI: 10.1038/ncomms10970,
URL: https://www.nature.com/articles/ncomms10970.

[29] J. Kern et al., *Simultaneous femtosecond X-ray spectroscopy and diffraction of photosystem II at room temperature*, Science (New York, N.Y.) **340** (2013) 491, ISSN: 1095-9203,
DOI: 10.1126/SCIENCE.1234273,
URL: https://pubmed.ncbi.nlm.nih.gov/23413188/.

[30] P. Salén et al., *Experimental verification of the chemical sensitivity of two-site double core-hole states formed by an x-ray free-electron laser*, Physical Review Letters **108** (2012) 153003, ISSN: 00319007, DOI: 10.1103/PHYSREVLETT.108.153003/FIGURES/2/MEDIUM, URL: https://journals.aps.org/prl/abstract/10.1103/PhysRevLett.108.153003.

[31] N. Berrah et al., *Double-core-hole spectroscopy for chemical analysis with an intense X-ray femtosecond laser*, Proceedings of the National Academy of Sciences **108** (2011) 16912, ISSN: 0027-8424, DOI: 10.1073/PNAS.1111380108, URL: https://www.pnas.org/content/108/41/16912%20https://www.pnas.org/content/108/41/16912.abstract.

[32] S. E. Canton et al., *Visualizing the non-equilibrium dynamics of photoinduced intramolecular electron transfer with femtosecond X-ray pulses*, Nature Communications 2015 6:1 **6** (2015) 1, ISSN: 2041-1723, DOI: 10.1038/ncomms7359, URL: https://www.nature.com/articles/ncomms7359.

[33] P. Wernet et al., *Orbital-specific mapping of the ligand exchange dynamics of Fe(CO)5 in solution*, Nature 2015 520:7545 **520** (2015) 78, ISSN: 1476-4687, DOI: 10.1038/nature14296, URL: https://www.nature.com/articles/nature14296.

[34] H. Öström et al., *Probing the transition state region in catalytic CO oxidation on Ru*, Science **347** (2015) 978, ISSN: 10959203, DOI: 10.1126/SCIENCE.1261747/SUPPL{_}FILE/PAP.PDF, URL: https://www.science.org/doi/abs/10.1126/science.1261747.

[35] M. Dell'Angela et al., *Real-time observation of surface bond breaking with an X-ray laser*, Science **339** (2013) 1302, ISSN: 10959203, DOI: 10.1126/SCIENCE.1231711/SUPPL{_}FILE/DELLANGELA-SOM.PDF, URL: https://www.science.org/doi/abs/10.1126/science.1231711.

[36] D. J. Higley et al., *Femtosecond X-ray magnetic circular dichroism absorption spectroscopy at an X-ray free electron laser*, Review of Scientific Instruments **87** (2016) 033110, ISSN: 0034-6748, DOI: 10.1063/1.4944410, URL: https://aip.scitation.org/doi/abs/10.1063/1.4944410.

[37] K. Yamamoto et al., *Ultrafast demagnetization of Pt magnetic moment in L10-FePt probed by magnetic circular dichroism at a hard x-ray free electron laser*, New Journal of Physics **21** (2019) 123010, ISSN: 1367-2630, DOI: 10.1088/1367-2630/AB5AC2, URL: https://iopscience.iop.org/article/10.1088/1367-2630/ab5ac2%20https://iopscience.iop.org/article/10.1088/1367-2630/ab5ac2/meta.

[38] T. Wang et al., *Femtosecond single-shot imaging of nanoscale ferromagnetic order in co/pd multilayers using resonant x-ray holography*, Physical Review Letters **108** (2012) 267403, ISSN: 10797114, DOI: 10.1103/PHYSREVLETT.108.267403/FIGURES/4/MEDIUM, URL: https://journals.aps.org/prl/abstract/10.1103/PhysRevLett.108.267403.

[39] C. E. Graves et al., *Nanoscale spin reversal by non-local angular momentum transfer following ultrafast laser excitation in ferrimagnetic GdFeCo*, Nature Materials 2013 12:4 **12** (2013) 293, ISSN: 1476-4660, DOI: 10.1038/nmat3597, URL: https://www.nature.com/articles/nmat3597.

[40] A. X. Gray et al.,
Ultrafast terahertz field control of electronic and structural interactions in vanadium dioxide,
Physical Review B **98** (2018) 045104, ISSN: 24699969,
DOI: 10.1103/PHYSREVB.98.045104/FIGURES/7/MEDIUM, URL: https://journals.aps.org/prb/abstract/10.1103/PhysRevB.98.045104.

[41] R. Mankowsky et al.,
Nonlinear lattice dynamics as a basis for enhanced superconductivity in YBa2Cu3O6.5,
Nature 2014 516:7529 **516** (2014) 71, ISSN: 1476-4687, DOI: 10.1038/nature13875,
URL: https://www.nature.com/articles/nature13875.

[42] F. Perakis et al.,
Coherent X-rays reveal the influence of cage effects on ultrafast water dynamics,
Nature Communications 2018 9:1 **9** (2018) 1, ISSN: 2041-1723,
DOI: 10.1038/s41467-018-04330-5,
URL: https://www.nature.com/articles/s41467-018-04330-5.

[43] A. Gorel et al., *Two-colour serial femtosecond crystallography dataset from gadoteridol-derivatized lysozyme for MAD phasing*, Scientific Data **4** (2017) 1, ISSN: 20524463,
DOI: 10.1038/sdata.2017.188,
URL: www.nature.com/scientificdata%20https://www.nature.com/articles/sdata2017188.

[44] S. Serkez et al.,
Opportunities for two-color experiments in the soft X-ray regime at the European XFEL,
Applied Sciences (Switzerland) **10** (2020) 2728, ISSN: 20763417,
DOI: 10.3390/APP10082728,
URL: www.mdpi.com/journal/applsci%20https://www.mdpi.com/2076-3417/10/8/2728/htm%20https://www.mdpi.com/2076-3417/10/8/2728.

[45] P. Abbamonte et al., *New Science Opportunities Enabled by LCLS-II X-Ray Lasers* (2015),
DOI: 10.2172/1630267,
URL: https://www.osti.gov/servlets/purl/1630267/.

[46] E. Weckert, *The potential of future light sources to explore the structure and function of matter*,
IUCrJ **2** (2015) 230, ISSN: 20522525, DOI: 10.1107/S2052252514024269,
URL: http://www.ncbi.nlm.nih.gov/pubmed/25866660%20http://www.pubmedcentral.nih.gov/articlerender.fcgi?artid=PMC4392416.

[47] J. M. J. Madey, *Stimulated Emission of Bremsstrahlung in a Periodic Magnetic Field*,
Journal of Applied Physics **42** (1971) 1906, ISSN: 0021-8979, DOI: 10.1063/1.1660466.

[48] L. R. Elias et al., *Observation of Stimulated Emission of Radiation by Relativistic Electrons in a Spatially Periodic Transverse Magnetic Field*, Physical Review Letters **36** (1976) 717,
ISSN: 0031-9007, DOI: 10.1103/PhysRevLett.36.717,
URL: https://link.aps.org/doi/10.1103/PhysRevLett.36.717.

[49] D. A. G. Deacon et al., *First Operation of a Free-Electron Laser*,
Physical Review Letters **38** (1977) 892, DOI: 10.1103/PhysRevLett.38.892.

[50] B. W. Mcneil, N. R. Thompson, *X-ray free-electron lasers*, 2010,
DOI: 10.1038/nphoton.2010.239.

[51] W. A. Barletta et al., *Free electron lasers: Present status and future challenges*,
Nuclear Instruments and Methods in Physics Research, Section A: Accelerators, Spectrometers, Detectors and Associated Equipment **618** (2010) 69, ISSN: 01689002,
DOI: 10.1016/J.NIMA.2010.02.274,

URL: https://www.researchgate.net/publication/223787179_Free_electron_lasers_Present_status_and_future_challenges.

[52] E. A. Seddon et al., *Short-wavelength free-electron laser sources and science: A review*, 2017, DOI: 10.1088/1361-6633/aa7cca.

[53] Z. Huang, K. J. Kim, *Review of x-ray free-electron laser theory*, Physical Review Special Topics - Accelerators and Beams **10** (2007) 34801, ISSN: 10984402, DOI: 10.1103/PhysRevSTAB.10.034801, URL: https://link.aps.org/doi/10.1103/PhysRevSTAB.10.034801.

[54] Institute of Free Electron Laser Osaka University, *Free Electron Laser figure*.

[55] R. Bonifacio, C. Pellegrini, L. M. Narducci, *Collective instabilities and high-gain regime in a free electron laser*, Optics Communications **50** (1984) 373, ISSN: 00304018, DOI: 10.1016/0030-4018(84)90105-6, URL: https://www.sciencedirect.com/science/article/pii/0030401884901056?via%3Dihub.

[56] R. Bonifacio et al., *Spectrum, temporal structure, and fluctuations in a high-gain free-electron laser starting from noise*, Physical Review Letters **73** (1994) 70, ISSN: 00319007, DOI: 10.1103/PhysRevLett.73.70.

[57] E. L. Saldin, E. A. Schneidmiller, M. V. Yurkov, *Statistical and coherence properties of radiation from x-ray free-electron lasers*, New Journal of Physics **12** (2010) 035010, ISSN: 13672630, DOI: 10.1088/1367-2630/12/3/035010, URL: http://www.njp.org/%20http://stacks.iop.org/1367-2630/12/i=3/a=035010?key=crossref.1d6a11bf3834ba2332f40daa9164e0a6.

[58] D. Ratner et al., *Second and third harmonic measurements at the linac coherent light source*, Physical Review Special Topics - Accelerators and Beams **14** (2011) 60701, ISSN: 10984402, DOI: 10.1103/PhysRevSTAB.14.060701.

[59] P. Schmüser et al., *Free-Electron lasers in the ultraviolet and x-ray regime: Physical principles, experimental results, technical realization*, vol. 258, Springer International Publishing, Switzerland, 2014, 3, DOI: 10.1007/978-3-319-04081-3.

[60] R. Ischebeck et al., *Study of the transverse coherence at the TTF free electron laser*, Nuclear Instruments and Methods in Physics Research, Section A: Accelerators, Spectrometers, Detectors and Associated Equipment **507** (2003) 175, ISSN: 01689002, DOI: 10.1016/S0168-9002(03)00866-0.

[61] I. A. Vartanyants et al., *Coherence properties of individual femtosecond pulses of an x-ray free-electron laser*, Physical Review Letters **107** (2011) 144801, ISSN: 00319007, DOI: 10.1103/PhysRevLett.107.144801.

[62] F. Lehmkühler et al., *Single shot coherence properties of the free-electron laser SACLA in the hard x-ray regime*, Scientific Reports **4** (2014) Article no: 5234, ISSN: 20452322, DOI: 10.1038/srep05234.

[63] S. Di Mitri, *On the importance of electron beam brightness in high gain free electron lasers*, Photonics **2** (2015) 317, ISSN: 23046732, DOI: 10.3390/photonics2020317.

[64] M. Xie, *Exact and variational solutions of 3D eigenmodes in high gain FELs*, Nuclear Instruments and Methods in Physics Research Section A: Accelerators, Spectrometers, Detectors and Associated Equipment **445** (2000) 59, ISSN: 0168-9002, DOI: 10.1016/S0168-9002(00)00114-5, URL: https://www.sciencedirect.com/science/article/pii/S0168900200001145.

[65] Ming Xie, *Design optimization for an X-ray free electron laser driven by SLAC linac*, Procedures of IEEE Particle Acceleration Conference, Dallas, TX, USA, 2002, 183, DOI: 10.1109/pac.1995.504603.

[66] S. Reiche, *GENESIS 1.3: a fully 3D time-dependent FEL simulation code*, Nuclear Instruments and Methods in Physics Research Section A: Accelerators, Spectrometers, Detectors and Associated Equipment **429** (1999) 243, ISSN: 0168-9002, DOI: 10.1016/S0168-9002(99)00114-X, URL: https://www.sciencedirect.com/science/article/pii/S016890029900114X?via%3Dihub.

[67] S. Reiche, *Update on the FEL code Genesis1.3*, Proceedings of FEL Conference, 2014, TUP019, ISBN: 9783954501335, URL: http://accelconf.web.cern.ch/AccelConf/FEL2014/papers/tup019.pdf.

[68] J. Feldhaus et al., *Possible application of X-ray optical elements for reducing the spectral bandwidth of an X-ray SASE FEL*, Optics Communications **140** (1997) 341, ISSN: 0030-4018, DOI: 10.1016/S0030-4018(97)00163-6.

[69] D. Ratner et al., *Experimental demonstration of a soft x-ray self-seeded free-electron laser*, Physical Review Letters **114** (2015) 054801, ISSN: 10797114, DOI: 10.1103/PHYSREVLETT.114.054801/FIGURES/5/MEDIUM, URL: https://journals.aps.org/prl/abstract/10.1103/PhysRevLett.114.054801.

[70] J. Amann et al., *Demonstration of self-seeding in a hard-X-ray free-electron laser*, Nature Photonics 2012 6:10 **6** (2012) 693, ISSN: 1749-4893, DOI: 10.1038/nphoton.2012.180, URL: https://www.nature.com/articles/nphoton.2012.180.

[71] S. Serkez et al., *Grating monochromator for soft X-ray self-seeding the European XFEL*, FEL 2013: Proceedings of the 35th International Free-Electron Laser Conference (2013) 667, URL: https://arxiv.org/abs/1303.1392v1.

[72] G. Geloni, V. Kocharyan, E. Saldin, *A novel self-seeding scheme for hard X-ray FELs*, https://doi.org/10.1080/09500340.2011.586473 **58** (2011) 1391, ISSN: 09500340, DOI: 10.1080/09500340.2011.586473, URL: https://www.tandfonline.com/doi/abs/10.1080/09500340.2011.586473.

[73] E. Prat, S. Reiche, S. D. J. Dunning, *Self-Seeding Design for SwissFEL* ().

[74] E. Prat, S. Reiche, *SELF-SEEDING DESIGN FOR SwissFEL* ().

[75] A. Grudiev, S. Calatroni, W. Wuensch, *New local field quantity describing the high gradient limit of accelerating structures*, Physical Review Special Topics - Accelerators and Beams (2009), DOI: 10.1103/physrevstab.12.102001.

[76] V. A. Dolgashev, *High magnetic fields in couplers of X-band accelerating structures*, Proceedings of the IEEE Particle Accelerator Conference, vol. 2, IEEE, 2003, 1267, ISBN: 0-7803-7738-9, DOI: 10.1109/pac.2003.1289674, URL: http://ieeexplore.ieee.org/document/1289674/%20https://ieeexplore.ieee.org/document/1289674.

[77] C. Nantista, S. Tantawi, V. Dolgashev,
Low-field accelerator structure couplers and design techniques,
Physical Review Special Topics - Accelerators and Beams (2004), ISSN: 10984402,
DOI: 10.1103/PhysRevSTAB.7.072001.

[78] C. Limborg et al., *RF Design of the LCLS Gun*, tech. rep., 2005, URL: https://www-ssrl.slac.stanford.edu/lcls/technotes/lcls-tn-05-3.pdf.

[79] D. Alesini et al.,
New technology based on clamping for high gradient radio frequency photogun,
Physical Review Special Topics - Accelerators and Beams (2015), ISSN: 10984402,
DOI: 10.1103/PhysRevSTAB.18.092001.

[80] D. Alesini et al., *Design, realization, and high power test of high gradient, high repetition rate brazing-free S -band photogun*, Physical Review Accelerators and Beams (2018),
ISSN: 24699888, DOI: 10.1103/PhysRevAccelBeams.21.112001.

[81] *ANSYS Electronics Desktop website*, URL: http://www.ansys.com/products/electronics/ansys-electronics-desktop.

[82] G. Castorina et al., *A TM01 mode launcher with quadrupole field components cancellation for high brightness applications*, Journal of Physics: Conference Series, vol. 1067, 8,
Institute of Physics Publishing, 2018, DOI: 10.1088/1742-6596/1067/8/082025.

[83] M. Croia et al., *High gradient ultra-high brightness C-band photoinjector optimization*,
Journal of Physics: Conference Series, vol. 1596, 1, 2020,
DOI: 10.1088/1742-6596/1596/1/012031.

[84] D. Alesini et al., *Design of a Full C-Band Injector for Ultra-High Brightness Electron Beam*,
10th International Particle Accelerator Conference (IPAC2019), 2019, ISBN: 9783954502080,
DOI: 10.18429/JACoW-IPAC2019-TUPTS024.

[85] D. Palmer, *The next generation photoinjectors*,
PhD thesis, Stanford Linear Accelerator Center, Stanford University, Stanford, CA 94309, 1998,
URL: https://slac.stanford.edu/pubs/slacreports/reports16/slac-r-500.pdf.

[86] *CML link*, URL: https://www.cmlengineering.com/.

[87] J. L. e. a. Warren, *Reference manual for the POISSON/SUPERFISH Group of Codes*,
tech. rep. LA-UR-87-126, 1987, DOI: 10.2172/10140827.

[88] H. Busch, *Berechnung der Bahn von Kathodenstrahlen im axialsymmetrischen elektromagnetischen Felde*, Annalen der Physik **386** (1926) 974,
DOI: https://doi.org/10.1002/andp.19263862507, URL: https://onlinelibrary.wiley.com/doi/abs/10.1002/andp.19263862507.

[89] J. Scifo,
The characterization of metal photo-cathode for high brightness electron beam photoinjectors,
PhD thesis, 2018,
URL: http://www.infn.it/thesis/PDF/getfile.php?filename=13205-Scifo-dottorato.pdf.

[90] K. Flöttmann, *ASTRA particle tracking code* (2016),
URL: https://www.desy.de/~mpyflo/.

[91] A. Bacci, V. Petrillo, M. Rossetti Conti,
GIOTTO: A Genetic Code for Demanding Beam-dynamics Optimizations, Proceedings of the 7th International Particle Accelerator Conference (IPAC 2016), Busan, Korea, 2016, 8,
URL: https://accelconf.web.cern.ch/ipac2016/papers/wepoy039.pdf.

[92] E. Telali, *Photoinjector study of a novel XFEL in the CompactLight Collaboration*, PhD thesis, National Technical University of Athens, 2019, URL: https://inspirehep.net/literature/1819658.

[93] K. Tzanetou, *FEL photocathode/laser studies*, PhD thesis, National Technical University of Athens, 2020.

[94] M. B. Danailov et al., *Performance of the FERMI FEL photoinjector laser*, Proceedings of FEL, 2007, 358, URL: https://accelconf.web.cern.ch/f07/PAPERS/WEPPH014.PDF.

[95] R. W. Assmann et al., *EuPRAXIA Conceptual Design Report*, The European Physical Journal Special Topics **229** (2020) 3675, URL: https://syncandshare.desy.de/index.php/s/HziDk32RjEAwss7.

[96] E. Prat et al., *Measurements of copper and cesium telluride cathodes in a radio-frequency photoinjector*, Physical Review Special Topics-Accelerators and Beams **18** (2015) 43401, URL: https://inspirehep.net/literature/1359078.

[97] *Amplitude laser link*, URL: https://amplitude-laser.com/products/lasers-for-science/arco/.

[98] F. Zhou, *Recent photocathode R\&D for the LCLS injector*, tech. rep., SLAC National Accelerator Lab., Menlo Park, CA (United States), 2018, URL: https://accelconf.web.cern.ch/FEL2014/papers/thp030.pdf.

[99] B. E. Carlsten, *New photoelectric injector design for the Los Alamos National Laboratory XUV FEL accelerator*, Nuclear Inst. and Methods in Physics Research, A (1989), ISSN: 01689002, DOI: 10.1016/0168-9002(89)90472-5.

[100] R. Ganter et al., *SwissFEL cathode load-lock system*, Proc. 35th Int. Free-Electron Laser Conf., New York, NY, USA, 2013, 259, URL: https://accelconf.web.cern.ch/FEL2013/papers/tupso21.pdf.

[101] M. Diomede et al., *Preliminary RF design of an X-band linac for the EuPRAXIA at SPARC_LAB project*, Nuclear Instruments and Methods in Physics Research, Section A: Accelerators, Spectrometers, Detectors and Associated Equipment (2018), ISSN: 01689002, DOI: 10.1016/j.nima.2018.01.032.

[102] R. Zennaro, *C-band RF Pulse Compressor for SwissFEL*, In Proc. of IPAC 2013, Shanghai, China, 2013, URL: https://s3.cern.ch/inspire-prod-files-f/f5ceba03e3c25c245a77a8de4032b2e6.

[103] E. Saldin, E. Schneidmiller, M. Yurkov, *Klystron instability of a relativistic electron beam in a bunch compressor*, Nuclear Instruments and Methods in Physics Research Section A: Accelerators, Spectrometers, Detectors and Associated Equipment **490** (2002), ISSN: 01689002, DOI: 10.1016/S0168-9002(02)00905-1.

[104] E. Saldin, E. Schneidmiller, M. Yurkov, *Longitudinal space charge-driven microbunching instability in the TESLA Test Facility linac*, Nuclear Instruments and Methods in Physics Research Section A: Accelerators, Spectrometers, Detectors and Associated Equipment **528** (2004), ISSN: 01689002, DOI: 10.1016/j.nima.2004.04.067.

[105] Z. Huang et al., *Measurements of the linac coherent light source laser heater and its impact on the x-ray free-electron laser performance*,
Physical Review Special Topics - Accelerators and Beams **13** (2010), ISSN: 1098-4402,
DOI: 10.1103/PhysRevSTAB.13.020703.

[106] G. Stupakov, *Centripetal Transverse Wakefield in Relativistic Beam*, tech. rep., 2019,
URL: http://arxiv.org/abs/1901.10745.

[107] M. Diomede, *High-gradient structures and RF systems for high-brightness electron linacs*,
PhD thesis, Sapienza University of Rome, 2020,
URL: https://iris.uniroma1.it/retrieve/handle/11573/1357033/1347035/Tesi_dottorato_Diomede.pdf.

[108] Z. D. Farkas et al., *SLED: A METHOD OF DOUBLING SLAC's ENERGY*,
Proceedings of the 9th International Conference on High-Energy Accelerators, 1976, 576,
URL: https://inspirehep.net/literature/94052.

[109] LAPOSTOLLE ED PM, SEPTIER ED AL, *LINEAR ACCELERATORS*, North-Holland Publ Co, Amsterdam, Neth, and Wiley Interscience Div, John Wiley & Sons, Inc (1970),
DOI: 10.1007/978-3-642-16483-5{_}3364.

[110] R. B. Neal, *Design of Linear Electron Accelerators with Beam Loading*,
Journal of Applied Physics **29** (1958) 1019, ISSN: 0021-8979, DOI: 10.1063/1.1723355,
URL: http://aip.scitation.org/doi/10.1063/1.1723355.

[111] M. Diomede et al., *RF Design of the X-band Linac for the EuPRAXIA at SPARC_LAB Project*,
Proc. 9th International Particle Accelerator Conference (IPAC'18), Vancouver, BC, Canada, 29 April-04 May 2018, International Particle Accelerator Conference 9,
JACoW Publishing, Geneva, Switzerland, 2018, 4422, ISBN: 978-3-95450-184-7,
DOI: doi:10.18429/JACoW-IPAC2018-THPMK058,
URL: http://jacow.org/ipac2018/papers/thpmk058.pdf.

[112] R. M. Jones et al., *Wakefield damping in a pair of X-band accelerators for linear colliders*,
Physical Review Special Topics - Accelerators and Beams **9** (2006), ISSN: 10984402,
DOI: 10.1103/PhysRevSTAB.9.102001.

[113] R. M. Jones, *Wakefield suppression in high gradient linacs for lepton linear colliders*,
Physical Review Special Topics - Accelerators and Beams **12** (2009), ISSN: 1098-4402,
DOI: 10.1103/physrevstab.12.104801.

[114] M. Dehler, I. H. Wilson, W. Wuensch, *A tapered damped accelerating structure for CLIC*,
Proc. of 19th International Linear Accelerator Conference, Chicago, 1998, 1987,
URL: https://cds.cern.ch/record/364530.

[115] C. Achard et al., *An Asset Test of the CLIC Accelerating Structure*,
Proc. of the 7th European Particle Accelerator Conference, Vienna Austria, 2000,
URL: https://cds.cern.ch/record/452944.

[116] R. Jones et al., *Dipole wakefield suppression in high phase advance detuned linear accelerators for the JLC/NLC designed to minimise electrical breakdown and cumulative BBU*,
Proc. of the 2001 Particle Accelerator Conference, Chicago, 2001, 3810,
DOI: 10.1109/PAC.2001.988261.

[117] *CPI website*, URL: http://www.cpii.com/.

[118] W. Wuensch et al., *Experience Operating an X-band High-Power Test Stand at CERN*, Proc. 5th International Particle Accelerator Conference (IPAC'14), Dresden, Germany, June 15-20, 2014, International Particle Accelerator Conference 5, JACoW, Geneva, Switzerland, 2014, 2288, ISBN: 978-3-95450-132-8, DOI: https://doi.org/10.18429/JACoW-IPAC2014-WEPME016, URL: http://jacow.org/ipac2014/papers/wepme016.pdf.

[119] W. Wuensch, *High-Gradient RF Development and Applications*, Proc. of Linear Accelerator Conference (LINAC'16), East Lansing, MI, USA, 25-30 September 2016, Linear Accelerator Conference 28, JACoW, Geneva, Switzerland, 2017, 368, ISBN: 978-3-95450-169-4, DOI: https://doi.org/10.18429/JACoW-LINAC2016-TU2A04, URL: http://jacow.org/linac2016/papers/tu2a04.pdf.

[120] *Canon website*, URL: https://etd.canon/en/product/category/microwave/klystron.html.

[121] N. C. Lasheras et al., *Commissioning of XBox-3: A Very High Capacity X-band Test Stand*, Proc. of Linear Accelerator Conference (LINAC'16), East Lansing, MI, USA, 25-30 September 2016, Linear Accelerator Conference 28, JACoW, Geneva, Switzerland, 2017, 568, ISBN: 978-3-95450-169-4, DOI: https://doi.org/10.18429/JACoW-LINAC2016-TUPLR047, URL: http://jacow.org/linac2016/papers/tuplr047.pdf.

[122] *Scandinova website*, URL: https://scandinovasystems.com/.

[123] N. C. Lasheras et al., *High Power Conditioning of X-Band RF Components*, Proc. 9th International Particle Accelerator Conference (IPAC'18), Vancouver, BC, Canada, April 29-May 4, 2018, International Particle Accelerator Conference 9, JACoW Publishing, Geneva, Switzerland, 2018, 2545, ISBN: 978-3-95450-184-7, DOI: doi:10.18429/JACoW-IPAC2018-WEPMF074, URL: http://jacow.org/ipac2018/papers/wepmf074.pdf.

[124] G. Riddone et al., *Engineering Design and Fabrication of X-band RF Components*, Conf. Proc. C **110904** (2011), ed. by C. Petit-Jean-Genaz 196, URL: https://accelconf.web.cern.ch/ipac2011/papers/mopc052.pdf.

[125] G. L. D'Alessandro, *Development of X-band high-power RF load for CLIC applications using additive manufacturing techniques*, PhD thesis, Salento U., 2015, URL: http://cds.cern.ch/record/2139981.

[126] H. Zha et al., *Design of a variable X-band RF power splitter*, Nuclear Instruments and Methods in Physics Research, Section A: Accelerators, Spectrometers, Detectors and Associated Equipment **859** (2017) 47, ISSN: 01689002, DOI: 10.1016/j.nima.2017.04.006, URL: https://inspirehep.net/literature/1418054.

[127] H. Zha et al., *Design of a variable X-band RF power splitter*, Nuclear Instruments and Methods in Physics Research, Section A: Accelerators, Spectrometers, Detectors and Associated Equipment, vol. 859, 2017, 47, ISBN: 9783954501687, DOI: 10.1016/j.nima.2017.04.006, URL: https://inspirehep.net/literature/1418054.

[128] P. Wang et al.,
The RF Design of a Compact, High Power Pulse Compressor with a Flat Output Pulse, Proc. of International Particle Accelerator Conference (IPAC'16), Busan, Korea, May 8-13, 2016, International Particle Accelerator Conference 7, JACoW, Geneva, Switzerland, 2016, 3591, ISBN: 978-3-95450-147-2, DOI: doi:10.18429/JACoW-IPAC2016-THPMW022, URL: http://jacow.org/ipac2016/papers/thpmw022.pdf.

[129] B. Woolley, I. Syratchev, A. Dexter, *Control and performance improvements of a pulse compressor in use for testing accelerating structures at high power*,
Physical Review Accelerators and Beams (2017), ISSN: 24699888,
DOI: 10.1103/PhysRevAccelBeams.20.101001.

[130] M. Aicheler et al., *A primary electron beam facility at CERN – eSPS Conceptual design report* (2020), DOI: 10.23731/CYRM-2020-008.

[131] M. Aicheler et al., *The Compact Linear Collider (CLIC) - Project Implementation Plan*,
tech. rep., 2019, DOI: 10.23731/CYRM-2018-004.

[132] G. A. Loew, O. H. Altenmueller,
DESIGN AND APPLICATIONS OF R.F. DEFLECTING STRUCTURES AT SLAC, tech. rep., SLAC, 1965, URL: https://s3.cern.ch/inspire-prod-files-c/c1be43e925db8226d80778005361b3a7.

[133] D. Alesini et al., *RF deflector design and measurements for the longitudinal and transverse phase space characterization at SPARC*,
Nuclear Instruments and Methods in Physics Research, Section A: Accelerators, Spectrometers, Detectors and Associated Equipment **568** (2006) 488, ISSN: 01689002,
DOI: 10.1016/j.nima.2006.07.050.

[134] S. Jiaru et al., *A three-cell superconducting deflecting cavity design for the ALS at LBNL*,
Proceedings of the IEEE Particle Accelerator Conference, vol. 2005, 2005, 4287,
ISBN: 0780388593, DOI: 10.1109/PAC.2005.1591795.

[135] D. Esperante et al.,
Construction and commissioning of the S-Band high gradient RF laboratory at IFIC,
Journal of Physics: Conference Series, vol. 1067, 8, Institute of Physics Publishing, 2018,
DOI: 10.1088/1742-6596/1067/8/082024.

[136] R. W. Assmann et al., *A 3 TeV e+e- Linear Collider Based on CLIC Technology*, CERN, 2000, 83, ISBN: 92-9083-168-5, URL: http://cds.cern.ch/record/461450.

[137] K. Bane, *Short range dipole wakefields in accelerating structures for the NLC*,
SLAC-PUB-9663 (2003), URL: https://inspirehep.net/literature/614846.

[138] J. C. Cai, I. Syratchev, G. Burt,
Design Study of a High-Power Ka-Band High-Order-Mode Multibeam Klystron,
IEEE Transactions on Electron Devices **67** (2020) 5736, ISSN: 15579646,
DOI: 10.1109/TED.2020.3028348.

[139] K. R. Chu, *The electron cyclotron maser*, 2004, DOI: 10.1103/RevModPhys.76.489.

[140] L. Wang et al., *Design of a Ka-band MW-level high efficiency gyroklystron for accelerators*,
2017 10th UK-Europe-China Workshop on Millimetre Waves and Terahertz Technologies, UCMMT 2017, Institute of Electrical and Electronics Engineers Inc., 2017,
ISBN: 9781538627204, DOI: 10.1109/UCMMT.2017.8068506.

[141] L. J. Nix et al.,
Demonstration of efficient beam-wave interaction for a MW-level 48 GHz gyroklystron amplifier,
Physics of Plasmas (2020), ISSN: 10897674, DOI: 10.1063/1.5144590.

[142] *Magnet Gyrotron link*, URL: http://www.cryogenic.co.uk/sites/default/files/product_files/sms_series_sample_users_manual.pdf.

[143] *Power Modulator link*, URL: https://scandinovasystems.com/content/uploads/2020/04/scandinova-productsheet-k100-200421.pdf.

[144] P. B. Wilson, Z. D. Farkas, R. D. Ruth,
SLED II: A NEW METHOD OF RF PULSE COMPRESSION,
Proceedings of the Linear Accelerator Conference 1990, Albuquerque, New Mexico, USA, 1990, URL: https://inspirehep.net/literature/298685.

[145] J. W. Wang et al., *Development for a supercompact X -band pulse compression system and its application at SLAC*, Physical Review Accelerators and Beams **20** (2017), ISSN: 24699888, DOI: 10.1103/PhysRevAccelBeams.20.110401.

[146] R. Ruth et al., *A High-Power SLED II Pulse Compression System*,
Proceedings of the 3rd European particle accelerator conference, 1992,
URL: https://www.researchgate.net/publication/236524267.

[147] I. Syratchev, *Status of 30 GHz High Power RF Pulse Compressor for CTF3*,
Proceedings of EPAC 2006, Edinburgh, Scotland, 2006,
URL: https://accelconf.web.cern.ch/e06/PAPERS/TUPCH163.PDF.

[148] S. G. Tantawi, *Multimoded reflective delay lines and their application to resonant delay line rf pulse compression systems*,
Physical Review Special Topics - Accelerators and Beams **7** (2004) 13, ISSN: 10984402,
DOI: 10.1103/PhysRevSTAB.7.032001.

[149] S. Tantawi et al., *STATUS OF HIGH-POWER TESTS OF DUAL MODE SLED-II SYSTEM FOR AN X-BAND LINEAR COLLIDER*, tech. rep., 2004,
URL: https://www.researchgate.net/publication/238792134.

[150] S. G. Tantawi et al.,
High-power multimode X-band rf pulse compression system for future linear colliders,
Physical Review Special Topics - Accelerators and Beams **8** (2005) 88, ISSN: 10984402,
DOI: 10.1103/PhysRevSTAB.8.042002.

[151] *GdfidL*, URL: www.gdfidl.de.

[152] G. E. Reuter, E. H. Sondheimer, *Theory of the anomalous skin effect in metals [6]*, 1948,
DOI: 10.1038/161394a0.

[153] A. D. Cahill et al.,
High gradient experiments with X -band cryogenic copper accelerating cavities,
Physical Review Accelerators and Beams **21** (2018), ISSN: 24699888,
DOI: 10.1103/PhysRevAccelBeams.21.102002.

[154] B. E. Carlsten et al., *High-Brightness Beam Technology Development for a Future Dynamic Mesoscale Materials Science Capability*, Instruments **3** (2019), ISSN: 2410-390X,
DOI: 10.3390/instruments3040052.

[155] J. B. Rosenzweig et al., *An ultra-compact x-ray free-electron laser*,
New Journal of Physics **22** (2020), ISSN: 13672630, DOI: 10.1088/1367-2630/abb16c.

[156] M. Behtouei et al., *Initial Design of a High-Power Ka-Band Klystron*,
Journal of Physics: Conference Series, vol. 1596, 1, 2020,
DOI: 10.1088/1742-6596/1596/1/012023.

[157] A. D. Cahill et al., *Rf losses in a high gradient cryogenic copper cavity*, Physical Review Accelerators and Beams **21** (2018), ISSN: 24699888, DOI: 10.1103/PhysRevAccelBeams.21.061301.

[158] Spataro B., *RF parameters and Wakefielkds estimations on the structure at F = 35.982 GHz for the Compact light XLS project*, tech. rep., Barcelona: INFN-LNF, 2018.

[159] M. Behtouei et al., *A Ka-band linearizer TW accelerating structure for the Compact Light XLS project*, Journal of Physics: Conference Series, vol. 1596, 1, 2020, DOI: 10.1088/1742-6596/1596/1/012021.

[160] K. N. Sjobak, A. Grudiev, E. Adli, *New Criterion for Shape Optimization of Normal-Conducting Accelerator Cells for High-Gradient Applications*, Proceedings, 27th Linear Accelerator Conference, LINAC2014, 2014, MOPP028, URL: https://inspirehep.net/literature/1363323.

[161] D. P. Pritzkau, *RF Pulsed Heating*, PhD thesis, Stanford University, CA, USA, 2001, URL: http://inspirehep.net/record/569074/files/.

[162] A. Grudiev, W. Wuensch, *A new local field quantity describing the high gradient limit of accelerating structures*, Proceedings of the 24th Linear Accelerator Conference, LINAC 2008, 2009, DOI: 10.1103/physrevstab.12.102001.

[163] D. P. Pritzkau, R. H. Siemann, *Experimental study of rf pulsed heating on oxygen free electronic copper*, Physical Review Special Topics - Accelerators and Beams **5** (2002), ISSN: 10984402, DOI: 10.1103/PhysRevSTAB.5.112002.

[164] O. A. Ivanov et al., *Active microwave pulse compressor using an electron-beam triggered switch*, Physical Review Letters **110** (2013), ISSN: 00319007, DOI: 10.1103/PhysRevLett.110.115002.

[165] A. Aksoy et al., *XLS Deliverable D6.1: Computer codes for the facility design*, tech. rep., CompactLight Collaboration, 2019, URL: https://www.compactlight.eu/uploads/Main/D6.1_XLS_Computer%20Codes%20for%20Facility%20Design.pdf.

[166] L. Serafini, J. B. Rosenzweig, *Envelope analysis of intense relativistic quasilaminar beams in rf photoinjectors: A theory of emittance compensation*, Physical Review E **55** (1997) 7565, ISSN: 1063-651X, DOI: 10.1103/physreve.55.7565.

[167] K. Flöttmann, *Astra: A space charge tracking algorithm*, 2011.

[168] *General Particle Tracer*, URL: http://www.pulsar.nl/gpt/.

[169] M. Ferrario, *Instabilities in Linacs*, CERN Accelerator School : 5th Advanced Accelerator Physics Course, ed. by S. Turner, CERN, Geneva, 2011, 459, URL: https://cas.web.cern.ch/sites/cas.web.cern.ch/files/lectures/chios-2011/ferrariowf.pdf.

[170] P. B. Wilson, *Introduction to wakefields and wake potentials*, AIP Conference Proceedings, vol. 184, 1, AIP Publishing, 2008, 525, DOI: 10.1063/1.38045, URL: http://aip.scitation.org/doi/abs/10.1063/1.38045.

[171] A. W. Chao et al., *Handbook of Accelerator Physics and Engineering*, ed. by A. W. Chao et al., WORLD SCIENTIFIC, Singapore, 2013, chap. 2.4.4, 133, ISBN: 978-981-4415-84-2, DOI: 10.1142/8543, URL: https://www.worldscientific.com/worldscibooks/10.1142/8543.

[172] A. Latina, *The 1D tracking code, Track1D*, Geneva, Switzerland, 2020, URL: https://gitlab.cern.ch/XLS-Git/WP6/-/tree/master/simulation_codes/beam_dynamics/Track1D.

[173] K. L. F. Bane, P. Emma, *LiTrack: A fast longitudinal phase space tracking code with graphical user interface*, Proceedings of the IEEE Particle Accelerator Conference, 2005, ISBN: 0780388593, DOI: 10.1109/PAC.2005.1591786.

[174] C. Mitchell, J. Qiang, P. Emma, *Longitudinal pulse shaping for the suppression of coherent synchrotron radiation-induced emittance growth*, Physical Review Special Topics - Accelerators and Beams (2013), ISSN: 10984402, DOI: 10.1103/PhysRevSTAB.16.060703.

[175] M. Borland, *ELEGANT: A flexible SDDS-compliant code for accelerator simulation*, tech. rep., 2000, DOI: 10.2172/761286.

[176] S. Di Mitri, M. Cornacchia, S. Spampinati, *Cancellation of coherent synchrotron radiation kicks with optics balance*, Physical Review Letters **110** (2013), ISSN: 00319007, DOI: 10.1103/PhysRevLett.110.014801.

[177] T. Hara et al., *High peak current operation of x-ray free-electron laser multiple beam lines by suppressing coherent synchrotron radiation effects*, Physical Review Accelerators and Beams **21** (2018) 040701, ISSN: 24699888, DOI: 10.1103/PhysRevAccelBeams.21.040701, URL: https://journals.aps.org/prab/abstract/10.1103/PhysRevAccelBeams.21.040701.

[178] A. Latina et al., *Recent improvements in the tracking code placet*, EPAC 2008 - Contributions to the Proceedings (2008) 1750, URL: https://inspirehep.net/literature/794917.

[179] M. Ferrario et al., *HOMDYN study for the LCLS RF photoinjector*, 2nd ICFA Advanced Accelerator Workshop on the Physics of High Brightness Beams, World Scientific, 2000, 534, URL: https://inspirehep.net/literature/524888.

[180] M. Ferrario et al., *Direct measurement of the double emittance minimum in the beam dynamics of the sparc high-brightness photoinjector*, Physical review letters **99** (2007) 234801, URL: https://journals.aps.org/prl/abstract/10.1103/PhysRevLett.99.234801.

[181] A. Cianchi et al., *High brightness electron beam emittance evolution measurements in an rf photoinjector*, Physical Review Special Topics-Accelerators and Beams **11** (2008) 32801, URL: https://journals.aps.org/prab/abstract/10.1103/PhysRevSTAB.11.032801.

[182] C. Kim et al., *Stripline beam position monitor for X-ray free electron laser of Pohang Accelerator Laboratory*, Review of Scientific Instruments **90** (2019) 93306, URL: https://aip.scitation.org/doi/10.1063/1.5109421.

[183] A. Heo, E. S. Kim, H. Hitoshi, *Status of cold cavity beam position monitor for STF*, IPAC 2011 - 2nd International Particle Accelerator Conference (2011) 1236, URL: https://inspirehep.net/literature/1183396.

[184] C. Simon et al., *Production process for the european XFEL re-entrant cavity BPM*, International Beam Instrumentation Conference, IBIC 2014, 2014, URL: https://accelconf.web.cern.ch/IBIC2014/papers/tupf05.pdf.

[185] B. Keil et al., *Status of the Swissfel BPM system*, Proceedings of the 4th International Beam Instrumentation Conference, IBIC 2015 **13** (2015) 497, DOI: 10.18429/JACoW-IBIC2015-TUPB065.

[186] G. Kube, C. Behrens, W. Lauth, *Resolution studies of inorganic scintillation screens for high energy and high Brilliance electron beams*, IPAC 2010 - 1st International Particle Accelerator Conference (2010) 906, URL: https://www.google.com/url?sa=t&rct=j&q=&esrc=s&source=web&cd=&cad=rja&uact=8&ved=2ahUKEwi3iOykkb_xAhUBtRoKHefWCdcQFnoECAQQAA&url=https%3A%2F%2Faccelconf.web.cern.ch%2Faccelconf%2FIPAC10%2Fpapers%2Fmopd088.pdf&usg=AOvVaw1_okXOjF26QbnGljfOAUO5.

[187] H. Loos et al., *Observation of coherent optical transition radiation in the LCLS LINAC*, 30th International Free Electron Laser Conference, FEL 2008, 2008, 485, URL: https://www.google.com/url?sa=t&rct=j&q=&esrc=s&source=web&cd=&cad=rja&uact=8&ved=2ahUKEwjkg7y7kb_xAhVH1hoKHakFAaMQFnoECBMQAA&url=https%3A%2F%2Faccelconf.web.cern.ch%2Ffel2008%2Fpapers%2Fthbau01.pdf&usg=AOvVaw0yJzpLhtwzxZLi-nBWVrqn.

[188] S. Matsubara et al., *Improvement of screen monitor with suppression of coherent-OTR effect for SACLA*, IBIC 2012 - Proceedings of the 1st International Beam Instrumentation Conference, 2013, 34, ISBN: 9783954501199, URL: https://www.google.com/url?sa=t&rct=j&q=&esrc=s&source=web&cd=&cad=rja&uact=8&ved=2ahUKEwiz-eHakb_xAhVSxhoKHdpTBTwQFnoECAQQAA&url=https%3A%2F%2Faccelconf.web.cern.ch%2FIBIC2012%2Fpapers%2Fmocc04.pdf&usg=AOvVaw1Evt8V0sbpXAECIHoUSfsA.

[189] P. Emma, J. Frisch, P. Krejcik, *A transverse RF deflecting structure for bunch length and phase space diagnostics*, LCLS Technical Note **12** (2000), URL: https://www-ssrl.slac.stanford.edu/lcls/technotes/lcls-tn-00-12.pdf.

[190] C. Behrens et al., *Measurement and Control of the Longitudinal Phase Space at High–Gain Free–Electron Lasers*, Proc. of 33rd International Free Electron Laser Conference, Shanghai, China, 2011, URL: https://accelconf.web.cern.ch/FEL2011/talks/thoci1_talk.pdf.

[191] C. Behrens et al., *Few-femtosecond time-resolved measurements of X-ray free-electron lasers*, Nature Communications **5** (2014) 3762, ISSN: 2041-1723, DOI: 10.1038/ncomms4762, URL: http://www.nature.com/articles/ncomms4762.

[192] A. Cianchi, *Diagnostics Examples from lepton-linacs and FELs*, arXiv preprint arXiv:2005.07469 (2020), URL: https://arxiv.org/abs/2005.07469.

[193] P. Craievich et al., *Novel X-band transverse deflection structure with variable polarization*, Physical Review Accelerators and Beams **23** (2020) 112001, URL: https://journals.aps.org/prab/abstract/10.1103/PhysRevAccelBeams.23.112001.

[194] B. Marchetti et al., *Experimental demonstration of novel beam characterization using a polarizable X-band transverse deflection structure*, Scientific reports **11** (2021) 1, URL: https://inspirehep.net/literature/1846654.

[195] D. Dowell et al., *Analysis of slice emittance measurements for the slac gun test facility*, Proceedings of the 2003 Bipolar/BiCMOS Circuits and Technology Meeting (IEEE Cat. No.03CH37440), vol. 3, 1-2, IEEE, 2003, 2104, ISBN: 0-7803-7738-9, DOI: 10.1109/PAC.2003.1288795, URL: http://ieeexplore.ieee.org/document/1288795/.

[196] Y. Ding et al.,
Results From the Lcls X-Band Transverse Deflector With Femtosecond Temporal Resolution,
SLAC Publication (2014) 2, URL: http://inspirehep.net/record/1363526/.

[197] T. J. Maxwell et al., *Coherent-radiation spectroscopy of few-femtosecond electron bunches using a middle-infrared prism spectrometer*, Physical Review Letters **111** (2013) 184801, ISSN: 00319007, DOI: 10.1103/PhysRevLett.111.184801.

[198] S. Wesch et al., *A multi-channel THz and infrared spectrometer for femtosecond electron bunch diagnostics by single-shot spectroscopy of coherent radiation*,
Nuclear Instruments and Methods in Physics Research, Section A: Accelerators, Spectrometers, Detectors and Associated Equipment **665** (2011) 40, ISSN: 01689002, DOI: 10.1016/j.nima.2011.11.037.

[199] Q. Q. Su et al., *Temporal diagnostics of femtosecond electron bunches with complex structures using sparsity-based algorithm*, Physical Review Accelerators and Beams **21** (2018) 112801, ISSN: 24699888, DOI: 10.1103/PhysRevAccelBeams.21.112801.

[200] D. Mihalcea et al., *Longitudinal electron bunch diagnostics using coherent transition radiation*, Proceedings of the IEEE Particle Accelerator Conference **2005** (2005) 4254, DOI: 10.1109/PAC.2005.1591782.

[201] M. K. Bock, *Measuring the electron bunch timing with femtosecond resolution at FLASH*, 2013, URL: https://bib-pubdb1.desy.de/record/139310/files/.

[202] M. Viti et al., *The bunch arrival time monitor at FLASH and European XFEL*,
Proceedings of the 16th International Conference on Accelerator and Large Experimental Physics Control Systems (ICALEPCS 2017): Barcelona, Spain, October 8–13, 2017, URL: https://inspirehep.net/literature/1656225.

[203] A. Mostacci et al., *Chromatic effects in quadrupole scan emittance measurements*,
Physical Review Special Topics - Accelerators and Beams **15** (2012) 82802, ISSN: 10984402, DOI: 10.1103/PhysRevSTAB.15.082802.

[204] *Design report of the optimized RF units XLS Deliverable D4.2*, tech. rep.

[205] *Menhir timing system*, URL:
https://menhir-photonics.com/applications/timing-distribution/.

[206] K. Şafak et al., *Synchronous multi-color laser network with daily sub-femtosecond timing drift*, Scientific Reports **8** (2018), ISSN: 20452322, DOI: 10.1038/s41598-018-30348-2, URL: https://pubmed.ncbi.nlm.nih.gov/30093636/.

[207] *Cyclelasers*, 2021, URL: https://www.cyclelasers.com/.

[208] K. L. F. Bane, M. Sands, *The Short-Range Resistive Wall Wakefields*, 2008, DOI: 10.1063/1.50300.

[209] K. L. Bane, G. Stupakov, *Resistive wall wakefield in the LCLS undulator*,
Proceedings of the IEEE Particle Accelerator Conference, 2005, ISBN: 0780388593, DOI: 10.1109/PAC.2005.1591481.

[210] K. Bane, G. Stupakov, *Using surface impedance for calculating wakefields in flat geometry*, Physical Review Special Topics - Accelerators and Beams (2015), ISSN: 10984402, DOI: 10.1103/PhysRevSTAB.18.034401.

[211] H. Henke, O. Napoly, *Wake fields between two parallel resistive plates*,
2nd European Particle Accelerator Conference, 1990, 12, URL: https://cds.cern.ch/record/202863.

[212] B. Podobedov, *Resistive wall wakefields in the extreme anomalous skin effect regime*, Physical Review Special Topics - Accelerators and Beams (2009), ISSN: 10984402, DOI: 10.1103/PhysRevSTAB.12.044401.

[213] G. Stupakov et al., *Resistive wall wakefields of short bunches at cryogenic temperatures*, Physical Review Special Topics - Accelerators and Beams (2015), ISSN: 10984402, DOI: 10.1103/PhysRevSTAB.18.034402.

[214] J. Qiang, *Suppression of wakefield induced energy spread inside an undulator through current shaping*, FEL 2013: Proceedings of the 35th International Free-Electron Laser Conference, 2013, ISBN: 9783954501267, URL: https://accelconf.web.cern.ch/fel2013/papers/mopso65.pdf.

[215] S. Reiche, *GENESIS 1.3 User Manual*, tech. rep., URL: http://genesis.web.psi.ch/download/documentation/genesis_manual.pdf.

[216] A. A. Lutman, J. P. MacArthur, M. Ilchen, *Polarization control in an X-ray free-electron laser*, Nature Photonics **10** (2016) 468, ISSN: 1749-4885, DOI: 10.1038/nphoton.2016.79, URL: http://www.nature.com/articles/nphoton.2016.79.

[217] E. A. Schneidmiller, M. V. Yurkov, *Obtaining high degree of circular polarization at x-ray free electron lasers via a reverse undulator taper*, Physical Review Special Topics - Accelerators and Beams **16** (2013) 110702, ISSN: 1098-4402, DOI: 10.1103/PhysRevSTAB.16.110702, URL: https://link.aps.org/doi/10.1103/PhysRevSTAB.16.110702.

[218] F. Nguyen et al., *Design Studies for the Undulator, XLS-CompactLight Deliverable D5.2*, tech. rep., 2021, 71, URL: https://espace.cern.ch/compactlight/Shared%20Documents/D5.2_XLS_Final.pdf.

[219] P. Emma et al., *A plan for the development of superconducting Undulator prototypes for LCLS-II and future FELs*, en, Proceedings of the 36th International Free Electron Laser Conference, FEL 2014 (2014) 649, URL: https://escholarship.org/uc/item/5hs0h07j.

[220] J. D. Fuerst et al., *Review of New Developments in Superconducting Undulator Technology at the APS*, Proc. 60th ICFA Advanced Beam Dynamics Workshop (FLS'18), Shanghai, China, JACoW Publishing, Geneva, Switzerland, 2018, DOI: https://doi.org/10.18429/JACoW-FLS2018-MOA2PL03, URL: http://jacow.org/fls2018/papers/moa2pl03.pdf.

[221] M. Leitner et al., *SCU Segmented Cryostat Concept*, 2014, URL: https://portal.slac.stanford.edu/sites/ad_public/FEL_RandD/scu_rd/_layouts/mobile/dispform.aspx?List=10182c32-8d3b-4c87-b668-e805a44ecab4&View=d6924684-e4ca-4239-b6ef-9a323f73942e&RootFolder=%2Fsites%2Fad_public%2FFEL_RandD%2Fscu_rd%2Fshared_docs%2FLCLS-I.

[222] J. A. Clarke, *The Science and Technology of Undulators and Wigglers*, Oxford University Press, 2004, DOI: 10.1093/acprof:oso/9780198508557.001.0001.

[223] S. D. Chen et al., *Phase shifter design for iSASE*, Proceedings of the 36th International Free Electron Laser Conference, FEL 2014, 2014, ISBN: 9783954501335, URL: https://accelconf.web.cern.ch/FEL2014/papers/mop045.pdf.

[224] H. H. Lu et al.,
A Permanent Magnet Phase Shifter for the European X-Ray Free Electron Laser,
Nuclear Instruments and Methods in Physics Research, Section A: Accelerators, Spectrometers, Detectors and Associated Equipment (2009), ISSN: 01689002,
DOI: 10.1016/j.nima.2009.03.217,
URL: https://flash.desy.de/sites2009/site_vuvfel/content/e403/e1642/e2410/e2411/infoboxContent2414/TESLA-FEL2009-01.pdf.

[225] M. Tischer et al., *Phase shifters for the FLASH2 FEL*,
IPAC 2014: Proceedings of the 5th International Particle Accelerator Conference, 2014,
ISBN: 9783954501328,
URL: https://accelconf.web.cern.ch/ipac2014/papers/wepro032.pdf.

[226] H. P. Freund, *Phase-matching segmented wigglers in free-electron lasers*, Physical Review E - Statistical Physics, Plasmas, Fluids, and Related Interdisciplinary Topics (2004),
ISSN: 1063651X, DOI: 10.1103/PhysRevE.70.015501.

[227] G. Parisi et al., *PHase shifters for the sparc undulator system*,
Proceedings of the 27th International Free Electron Laser Conference, FEL 2005, 2005,
URL: http://accelconf.web.cern.ch/f05/PAPERS/MOPP056.PDF.

[228] J. Pflüger, M. Tischer,
A Prototype Phase Shifter for the Undulator Systems at the TESLA X-Ray FEL, tech. rep.,
2000, URL: https://flash.desy.de/sites2009/site_vuvfel/content/e403/e1642/e810/e704/infoboxContent791/fel2000-08.pdf.

[229] L. Rossi, L. Bottura, *Superconducting magnets for particle accelerators*,
Reviews of Accelerator Science and Technology: Volume 5 2012 Applications of Superconducting Technology to Accelerators, 2013, ISBN: 9789814449953,
DOI: 10.1142/9789814449953{_}0003.

[230] E. Todesco, *Magnetic design of superconducting magnets*,
CAS-CERN Accelerator School: Superconductivity for Accelerators - Proceedings, 2014,
ISBN: 9789290834052, DOI: 10.5170/CERN-2014-005.269.

[231] Cobham Technical Services, *Opera (2d/3d) Vector Fields Software*, Oxford, UK, 2018.

[232] D. Nölle,
The diagnostic system at the European XFEL: Commissioning and first user operation,
Proceedings of the 7th International Beam Instrumentation Conference, IBIC 2018, 2018,
ISBN: 9783954502011, DOI: 10.18429/JACoW-IBIC2018-tuoa01.

[233] Cryomech Inc., *PT420 Cryooolers*, 2021,
URL: https://www.cryomech.com/products/pt420/.

[234] P. Emma et al.,
Conceptual Design of a Superconducting Undulator System for the LCLS-II Hard-X-Ray FEL, 2014,
URL: https://portal.slac.stanford.edu/sites/ad_public/FEL_RandD/scu_rd/shared_docs/LCLS-II%20Conceptual%20Design/SCU-CDR.docx.

[235] Linde Kryotechnik AG, *L-Series: The new standard for helium liquefiers and refrigerators*,
2021, URL: https://www.linde-kryotechnik.ch/wp-content/uploads/2016/10/Linde_Kryotechnik_Produktbrosch_L-Series.pdf.

[236] G. Venkatarathnam, *Fundamental principles and processes*,
Cryogenic Mixed Refrigerant Processes, 2008, 1,
DOI: 10.1007/978-0-387-78514-1{_}1,
URL: http://link.springer.com/10.1007/978-0-387-78514-1_1.

[237] T. Kochenburger,
Kryogene Gemischkältekreisläufe für Hochtemperatursupraleiter-Anwendungen,
PhD thesis, Karlrsuhe Institute of Technology, 2018, ISBN: 978-3-8439-3987-4,
URL: https://publikationen.bibliothek.kit.edu/1000093562.

[238] E. Shabagin, S. Grohmann,
Development of 10 kA Current Leads Cooled by a Cryogenic Mixed-Refrigerant Cycle,
IOP Conference Series: Materials Science and Engineering, 2019,
DOI: 10.1088/1757-899X/502/1/012138.

[239] D. Gomse, *Development of heat exchanger technology for cryogenic mixed-refrigerant cycles*,
PhD thesis, Karlsruhe Institute of Technology, 2019,
URL: https://publikationen.bibliothek.kit.edu/1000119417.

[240] E. Gluskin, P. Emma, Y. Ivanyushenkov,
A Superconducting Helical Undulator-Based FEL Prototype Cryomodule, 2016, URL: https://portal.slac.stanford.edu/sites/ad_public/FEL_RandD/scu_rd/shared_docs/SCU-Phase-II/FEL%20SCU%20Prototype%20proposal.pdf.

[241] Y. Xu et al., *Integrated thermal analysis of the FRIB cryomodule design*,
IPAC 2012 - International Particle Accelerator Conference 2012, 2012, ISBN: 9783954501151,
URL: https://www.osti.gov/servlets/purl/1047739.

[242] J. Arnsberg, *Wärmelastberechnung CompactLight SCU, Internal Technical Report*, tech. rep.,
Karlsruhe Institute of Technology, 2021.

[243] S. Reiche, *Tolerance studies for the hard X-ray beamline of SwissFEL*,
FEL 2009 - 31st International Free Electron Laser Conference, 2009,
URL: https://accelconf.web.cern.ch/FEL2009/papers/wepc58.pdf.

[244] E. A. Schneidmiller, M. V. Yurkov, *Reverse undulator tapering for polarization control and background-free harmonic production in XFELs: Results from FLASH*,
Proceedings of the 38th International Free-Electron Laser Conference, FEL 2017, 2017,
ISBN: 9783954501793, DOI: 10.18429/JACoW-FEL2017-MOP032.

[245] T. Schmidt, M. Calvi, *APPLE X Undulator for the SwissFEL Soft X-ray Beamline Athos*,
Synchrotron Radiation News **31** (2018) 35, DOI: 10.1080/08940886.2018.1460174.

[246] S. Sasaki et al.,
Design of a new type of planar undulator for generating variably polarized radiation,
Nuclear Inst. and Methods in Physics Research, A (1993), ISSN: 01689002,
DOI: 10.1016/0168-9002(93)90153-9.

[247] Y. Ivanyushenkov et al., *Status of the Development of Superconducting Undulators for Storage Rings and Free Electron Lasers at the Advanced Photon Source*,
Proceedings, 2nd North American Particle Accelerator Conference (NAPAC2016): Chicago, Illinois, USA, October 9-14, 2016, 2017, THA1CO06,
DOI: 10.18429/JACoW-NAPAC2016-THA1CO06.

[248] I. Kesgin et al., *Development of short-period Nb3Sn superconducting planar undulators*,
IEEE Transactions on Applied Superconductivity **29** (2019) 1, ISSN: 15582515,
DOI: 10.1109/TASC.2019.2897645.

[249] J. Bahrdt, E. Gluskin, *Cryogenic permanent magnet and superconducting undulators*, Nuclear Instruments and Methods in Physics Research, Section A: Accelerators, Spectrometers, Detectors and Associated Equipment, Advances in Instrumentation and Experimental Methods (Special Issue in Honour of Kai Siegbahn) **907** (2018) 149, ISSN: 0168-9002, DOI: 10.1016/j.nima.2018.03.069.

[250] J. Bahrdt, S. Grimmer, *In-vacuum APPLE II undulator with force compensation*, AIP Conference Proceedings **2054** (2019) 030031, ISSN: 15517616, DOI: 10.1063/1.5084594.

[251] O. Chubar, P. Elleaume, J. Chavanne, *A three-dimensional magnetostatics computer code for insertion devices*, Journal of Synchrotron Radiation **5** (1998) 481, ISSN: 0909-0495, DOI: 10.1107/s0909049597013502.

[252] M. Calvi et al., *Transverse gradient in Apple-type undulators*, Journal of Synchrotron Radiation **24** (2017) 600, DOI: 10.1107/s1600577517004726.

[253] P. Baumgärtel et al., *RAY-UI: New features and extensions*, AIP Conference Proceedings, vol. 2054, 1, American Institute of Physics Inc., 2019, 60081, ISBN: 9780735417823, DOI: 10.1063/1.5084665, URL: https://doi.org/10.1063/1.5084712.

[254] M. Störmer, F. Siewert, H. Sinn, *Preparation and characterization of B4C coatings for advanced research light sources*, Journal of Synchrotron Radiation, vol. 23, 1, International Union of Crystallography, 2016, 50, DOI: 10.1107/S1600577515020901, URL: http://dx.doi.org/10.1107/S1600577515020901.

[255] H. M. Castañeda Cortés et al., *Optical beam quality analysis of the CLARA test facility using second moment analysis*, Proceedings of the 38th International Free-Electron Laser Conference, FEL 2017, JACoW Publishing, 2017, 543, ISBN: 9783954501793, DOI: 10.18429/JACoW-FEL2017-WEP062.

[256] E. L. Saldin, E. A. Schneidmiller, M. V. Yurkov, *A simple method for the determination of the structure of ultrashort relativistic electron bunches*, Nuclear Instruments and Methods in Physics Research, Section A: Accelerators, Spectrometers, Detectors and Associated Equipment **539** (2005) 499, ISSN: 01689002, DOI: 10.1016/j.nima.2004.11.002.

[257] *FEL gratings — Inprentus*, URL: https://www.inprentus.com/fel-gratings.

[258] P. Heimann et al., *Linac Coherent Light Source soft x-ray materials science instrument optical design and monochromator commissioning*, Review of Scientific Instruments **82** (2011) 093104, ISSN: 0034-6748, DOI: 10.1063/1.3633947, URL: https://doi.org/10.1063/1.3633947.

[259] R. Soufli et al., *Development and calibration of mirrors and gratings for the Soft X-ray Materials Science beamline at the Linac Coherent Light Source free-electron laser*, Applied Optics **51** (2012) 2118, ISSN: 15394522, DOI: 10.1364/AO.51.002118, URL: https://www.osapublishing.org/viewmedia.cfm?uri=ao-51-12-2118&seq=0&html=true%20https://www.osapublishing.org/abstract.cfm?uri=ao-51-12-2118%20https://www.osapublishing.org/ao/abstract.cfm?uri=ao-51-12-2118.

[260] K. Tiedtke et al., *Gas detectors for x-ray lasers*, Journal of Applied Physics **103** (2008) 94511, ISSN: 00218979, DOI: 10.1063/1.2913328, URL: https://doi.org/10.1063/1.2913328.

[261] T. Tschentscher et al.,
Photon Beam Transport and Scientific Instruments at the European XFEL,
Applied Sciences **7** (2017), ISSN: 2076-3417, DOI: 10.3390/app7060592,
URL: https://www.mdpi.com/2076-3417/7/6/592.

[262] C. J. Milne et al., *SwissFEL: The Swiss X-ray Free Electron Laser*, Applied Sciences **7** (2017), ISSN: 2076-3417, DOI: 10.3390/app7070720,
URL: https://www.mdpi.com/2076-3417/7/7/720.

[263] J. Grünert et al., *X-ray photon diagnostics at the European XFEL*,
Journal of Synchrotron Radiation **26** (2019) 1422, DOI: 10.1107/S1600577519006611,
URL: https://doi.org/10.1107/S1600577519006611.

[264] J. Laksman et al., *Commissioning of a photoelectron spectrometer for soft X-ray photon diagnostics at the European XFEL*, Journal of Synchrotron Radiation **26** (2019) 1010,
DOI: 10.1107/S1600577519003552,
URL: https://doi.org/10.1107/S1600577519003552.

[265] E. Allaria et al.,
Control of the Polarization of a Vacuum-Ultraviolet, High-Gain, Free-Electron Laser,
Phys. Rev. X **4** (2014) 41040, DOI: 10.1103/PhysRevX.4.041040,
URL: https://link.aps.org/doi/10.1103/PhysRevX.4.041040.

[266] J. Rehanek et al.,
A compact and versatile tender X-ray single-shot spectrometer for online XFEL diagnostics,
Journal of Synchrotron Radiation **25** (2018) 16, DOI: 10.1107/S1600577517012796,
URL: https://doi.org/10.1107/S1600577517012796.

[267] N. Kujala et al.,
Hard x-ray single-shot spectrometer at the European X-ray Free-Electron Laser,
Review of Scientific Instruments **91** (2020) 103101, DOI: 10.1063/5.0019935,
URL: https://doi.org/10.1063/5.0019935.

[268] M. Harmand et al., *Achieving few-femtosecond time-sorting at hard X-ray free-electron lasers*,
Nature Photonics **7** (2013) 215, ISSN: 17494885, DOI: 10.1038/nphoton.2013.11,
URL: www.nature.com/naturephotonics.

[269] M. R. Bionta et al.,
Spectral encoding method for measuring the relative arrival time between x-ray/optical pulses,
Review of Scientific Instruments **85** (2014) 083116, ISSN: 10897623,
DOI: 10.1063/1.4893657, URL: http://dx.doi.org/10.1063/1.4893657].

[270] N. Hartmann et al.,
Sub-femtosecond precision measurement of relative X-ray arrival time for free-electron lasers,
Nature Photonics **8** (2014) 706, ISSN: 17494893, DOI: 10.1038/nphoton.2014.164,
URL: www.nature.com/naturephotonics.

[271] R. Ivanov et al.,
FLASH free-electron laser single-shot temporal diagnostic: Terahertz-field-driven streaking,
Journal of Synchrotron Radiation, vol. 25, 1, International Union of Crystallography, 2018, 26,
DOI: 10.1107/S160057751701253X,
URL: https://pubmed.ncbi.nlm.nih.gov/29271747/.

[272] N. Hartmann et al., *Attosecond time-energy structure of X-ray free-electron laser pulses*,
Nature Photonics **12** (2018) 215, ISSN: 17494893, DOI: 10.1038/s41566-018-0107-6,
URL: https://doi.org/10.1038/s41566-018-0107-6.

[273] J. Duris et al.,
Tunable isolated attosecond X-ray pulses with gigawatt peak power from a free-electron laser,
Nature Photonics **14** (2020) 30, ISSN: 17494893, DOI: 10.1038/s41566-019-0549-5,
URL: https://doi.org/10.1038/s41566-019-0549-5.

[274] Y. Liu et al., *High-accuracy wavefront sensing for x-ray free electron lasers*,
Optica **5** (2018) 967, ISSN: 2334-2536, DOI: 10.1364/optica.5.000967,
URL: https://doi.org/10.1364/OPTICA.5.000967.

[275] *Home Imagine Optic*, URL: https://www.imagine-optic.com/.

[276] S. Schulz et al., *Femtosecond all-optical synchronization of an X-ray free-electron laser*,
Nature Communications **6** (2015) 1, ISSN: 20411723, DOI: 10.1038/ncomms6938,
URL: www.nature.com/naturecommunications%20https://www.nature.com/articles/ncomms6938.

[277] I. Bustinduy, J. Munoz, *ESS Bilbao - Technical Design Report: Magnet for the ESS MEBT*,
2015, URL: https://www.essbilbao.org/st_docs/technical-design-report-ess-bilbao-rfq/.

[278] B. Marchetti et al., *X-Band TDS Project*, Proceedings of IPAC2017, Copenhagen, Denmark,
European Spallation Source, 2017, ISBN: 9783954501823.

[279] P. Lebrun, P. H. Garbincius, *Assessing risk in costing high-energy accelerators: From existing projects to the future linear collider*,
IPAC 2010 - 1st International Particle Accelerator Conference, 2010, ISBN: 9789290833529.

[280] P. e. a. Lebrun, *The CLIC programme: towards a staged ee-linear collider exploring the terascale: CLIC conceptual design report*, ed. by Lebrun P et al., CERN-2012-005,
CERN, Geneva, 2012, ISBN: 9789290833772.

[281] P. Christensen et al., *18R-97: Cost Estimate Classification System - As Applied in Engineering, Procurement, and Construction for the Process Industries*, tech. rep., 2005.

[282] R. (Ganter, *SwissFEL Conceptual Design Report*, tech. rep., 2012.

[283] JACoW.org, *JACoW Website*, 2021, URL: https://www.jacow.org/.

[284] Elder et al., *Radiation from Electrons in a Synchrotron*, Physical Review **71** (1947) 829,
DOI: 10.1103/PhysRev.71.829.5,
URL: https://link.aps.org/doi/10.1103/PhysRev.71.829.5.

[285] K. Codling, *Atomic and Molecular Physics Using Synchrotron Radiation - the Early Years*,
Jornal of Synchrotron Radiation **4** (1997) 316, DOI: 10.1107/S090904959701162X,
URL: https://doi.org/10.1107/S090904959701162X.

[286] Frascati National Laboratory, *ADONE*,
URL: http://www.lnf.infn.it/acceleratori/adone/.

[287] Daresbury Laboratory, *Daresbury Timeline - Science and Technology Facilities Council*,
URL: https://stfc.ukri.org/public-engagement/activities-for-the-public/visit-daresbury-laboratory/daresbury-open-week/daresbury-timeline/.

[288] E. Lohrmann, P. Söding,
Von schnellen Teilchen und hellem Licht - 50 Jahre Deutsches Elektronen Synchrotron DESY,
2nd, Wiley VCH Verlag, Weinheim, 2013, ISBN: 9783935702713.

[289] G. Margaritondo, *Synchrotron light: a success story over six decades*,
Rivista del Nuovo Cimento **40** (2017) 411, DOI: 10.1393/ncr/i2017-10139-3,
URL: https://www.sif.it/riviste/sif/ncr/econtents/2017/040/09/article/0.

[290] P. Emma et al., *First lasing and operation of an ångstrom-wavelength free-electron laser*, Nature Photonics **4** (2010) 641, ISSN: 17494885, DOI: 10.1038/nphoton.2010.176.

[291] C. Pellegrini, *The history of X-ray free-electron lasers*, European Physical Journal H **37** (2012) 659, ISSN: 21026459, DOI: 10.1140/epjh/e2012-20064-5.

[292] LCLS, *LCLS-II Final Design Report DRAFT*, tech. rep., 2014.

[293] Y. Otake, *Overview of SACLA Machine Status* (2012).

[294] C. Kim, *Operation Status of PAL-XFEL*, 2021.

[295] Z. Zhao et al., *Status of the SXFEL Facility*, Applied Sciences **7** (2017) 607, ISSN: 2076-3417, DOI: 10.3390/app7060607.

[296] ShanghaiTech University, *Shanghai-XFEL Beamline Project (SBP) an..* (2021).

[297] H. Weise, *THE EUROPEAN XFEL-STATUS AND COMMISSIONING**, 2017, ISBN: 9783954501816, URL: www.xfel.eu.

[298] R. Feidenhans'l, *Welcome to the 2019 European XFEL Users Meeting - the 13th Users Meeting, presentation, 23/01/2019*, Hamburg, 2019.

[299] R. Feidenhans'l, *European_XFEL_Annual_Report_2020* (2020).

[300] H.-H. Braun, *SwissFEL C-band Linac and S-band Linac for FERMI*, Brussels, 2019.

[301] DESY, *FLASH Beamlines*, URL: https://photon-science.desy.de/facilities/flash/beamlines/index_eng.html.

[302] DESY, *FLASH2020+ Project*, URL: https://photon-science.desy.de/facilities/flash2020_project/index_eng.html.

[303] K. Tiedtke et al., *FLASH2020+ Making FLASH brighter, faster and more flexible Conceptual Design Report Deutsches Elektronen-Synchrotron DESY FLASH 2020 + Making FLASH brighter, faster and more fl exible Conceptual Design Report Deutsches Elektronen-Synchrotron DESY A Research Centre of the Helmholtz Association*, tech. rep., 2020.

[304] A. Vorozhtsov et al., *The Soft X-ray Laser @ MAX IV - Conceptual Design Report*, tech. rep., 2021.

[305] Marangos J et al, *UK XFEL Science Case*, tech. rep., 2020.

[306] J. A. Clarke et al., *CLARA conceptual design report*, Journal of Instrumentation **9** (2014) T05001, ISSN: 1748-0221, DOI: 10.1088/1748-0221/9/05/T05001, URL: http://stacks.iop.org/1748-0221/9/i=05/a=T05001?key=crossref.0b621eebec5f698828483b62e41fce6d.

[307] ASTEC, *CLARA FEL Test Facility*, 2021, URL: https://www.astec.stfc.ac.uk/Pages/CLARA-FEL-Test-Facility.aspx.

[308] E. Snedden, *High gradient acceleration at the CLARA Test Facility*, 2021.

[309] STFC, *UK-first experiments at CLARA play key role in radiotherapy research - Science and Technology Facilities Council*, 2019, URL: https://stfc.ukri.org/news-events-and-publications/whats-happening/uk-first-experiments-at-clara-play-key-role-in-radiotherapy-research/.

[310] D. Roadmap, *European Strategy for Particle Physics*, tech. rep., 2022.

[311] R. W. Assmann et al., *EuPRAXIA Conceptual Design Report*, The European Physical Journal Special Topics **229** (2020) 3675, URL: https://syncandshare.desy.de/index.php/s/HziDk32RjEAwss7.

[312] M. Ferrario, D. Alesini, M. P. Anania,
EuPRAXIA at SPARC_LAB Design study towards a compact FEL facility at LNF,
Nuclear Instruments and Methods in Physics Research, Section A: Accelerators,
Spectrometers, Detectors and Associated Equipment (2018), ISSN: 01689002,
DOI: 10.1016/j.nima.2018.01.094.

[313] Elettra Sincrotrone Trieste,
Facts and Figures: Users at Elettra, in: Elettra Highlights 2010-2020, 2021,
URL: http://www.elettra.trieste.it/science/highlights.html.

[314] ESRF - European Synchrotron Radiation Facility, *ESRF Highlights (different years)*, 2021,
URL: http://www.elettra.trieste.it/science/highlights.html.

[315] ALBA CELLS, *ALBA: Activity Reports (different years)*, 2021,
URL: https://www.cells.es/en/media/corporate-publications.

[316] MAX IV Laboratory, *MAX IV: Annual Reports*, 2021,
URL: https://www.maxiv.lu.se/science/reports/.

[317] R. Feidenhans'l, *European_XFEL_Annual_Report_2018* (2018).

[318] R. Feidenhans'l, *Welcome to the 2018 European XFEL Users Meeting*, tech. rep., 2018.

[319] R. Feidenhans'l, *Welcome to the Users Meeting 2021, Status 2020 - Outlook for 2021*,
tech. rep., 2021.

[320] ESUO, *European Synchrotron and FEL User Organisation*, 2021,
URL: http://www.wayforlight.eu/en/users/esuo/.

[321] LEAPS, *LEAPS Landscape Analysis*, tech. rep.,
League of European Accelerator-based Photon Sources, 2019, 1,
URL: https://leaps-initiative.eu/about/leaps-documents/.

[322] R. Rochow et al., *XLS - D7.1: CompactLight Global Integration and Cost Analysis* (2021),
DOI: 10.5281/ZENODO.5024680,
URL: https://www.zenodo.org/record/5024680.

[323] B. Shepherd, *ASTEC Superconducting Undulators for Light Sources*,
URL: https://www.astec.stfc.ac.uk/Pages/Superconducting-Undulators-for-Light-Sources.aspx.

[324] T. Metzger, *Ultrafast Thin-Disk Amplifiers*, Source Workshop, Amsterdam, Netherlands, 2019,
S55, URL: https://www.euvlitho.com/2019/S55.pdf.

[325] M. Schaer et al., *rf traveling-wave electron gun for photoinjectors*, Phys. Rev. AB (2016) 72001,
URL: https://inspirehep.net/literature/1477108.

[326] A. E. Vlieks et al., *Development of an X-band RF Gun at SLAC*,
AIP Conference Proceedings **625** (2002) 107,
URL: https://arxiv.org/ftp/hep-ph/papers/0208/0208116.pdf.

[327] A. E. Vlieks et al., *X-band RF gun development*,
Proceedings of IPAC'10, Kyoto, Japan (2010) 3816,
URL: https://accelconf.web.cern.ch/IPAC10/papers/thpea063.pdf.

[328] R. A. Marsh et al., *Modeling and design of an X-band rf photoinjector*,
Phys. Rev. ST Accel. Beams **15** (2012) 102001,
DOI: 10.1103/PhysRevSTAB.15.102001,
URL: https://link.aps.org/doi/10.1103/PhysRevSTAB.15.102001.

[329] F. B. Kiewiet, *Generation of ultra-short, high brightness relativistic electron bunches*,
PhD thesis, Technische Universiteit Eindhoven, 2003,
DOI: https://doi.org/10.6100/IR571240.

[330] K. Halbach, R. F. Holsiger,
SUPERFISH - A Computer Program for Evaluation of RF Cavities with Cylindrical Symmetry,
Particle Accelerators, **7** (1976) 213,
URL: https://inspirehep.net/literature/116636.

[331] *Ansys High Frequency Simulation Studio*,
URL: https://www.ansys.com/products/electronics/ansys-hfss.

[332] J. R. M. Vaughan, *Multipactor*, IEEE Transactions on Electron Devices **35** (1988) 1172,
URL: https://ieeexplore.ieee.org/document/3387.

[333] A. M. Perez et al., *Prediction of Multipactor Breakdown Thresholds in Coaxial Transmission Lines for Traveling, Standing, and Mixed Waves*,
IEEE Transactions on Plasma Science **37** (2009) 2031,
URL: https://riunet.upv.es/handle/10251/61218.

[334] D. Gonzalez-Iglesias et al.,
Multipactor Mitigation in Coaxial Lines by Means of Permanent Magnets,
IEEE Transactions on Electron Devices **61** (2014) 4224,
URL: https://ieeexplore.ieee.org/document/6926820.

[335] J. Shao, *Investigations on rf breakdown phenomenon in high gradient accelerating structures*,
PhD thesis, Tsinghua U., Beijing, Dept. Eng. Phys., 2016,
DOI: 10.1007/978-981-10-7926-9.

[336] M. Behtouei, *Design and Measurements of the High Gradient Accelerating Structures*,
PhD thesis, Universita di Roma 'La Sapienza', 2019,
DOI: 10.13140/RG.2.2.16781.90086.

[337] D. Gonzalez-Iglesias et al.,
Analytical RF Pulse Heating Analysis for High Gradient Accelerating Structures,
IEEE Transactions on Nuclear Science **68** (2021) 78, DOI: 10.1109/TNS.2021.3049319.

[338] B. J. Woolley, *High Power X-band RF Test Stand Development and High Power Testing of the CLIC Crab Cavity*, PhD thesis, Lancaster U., 2015,
URL: https://inspirehep.net/literature/1679128.

[339] K. Flöttmann, *Astra: A space charge tracking algorithm*, 2011,
URL: https://www.desy.de/~mpyflo/.

[340] A. Latina, *RF-Track Reference Manual*, DOI: 10.5281/zenodo.3887085,
URL: https://doi.org/10.5281/zenodo.3887085.

[341] T. Hara et al., *Cryogenic permanent magnet undulators*,
Physical Review Special Topics - Accelerators and Beams2 **7** (2004) 050702,
DOI: 10.1103/PhysRevSTAB.7.050702.

[342] C. Benabderrahmane et al., *Development of Pr2Fe14B cryogenic undulator CPMU at SOLEIL*,
Proceedings of IPAC2011, JACoW, San Sebastián, Spain, 2011, THPC149.

[343] F. Nguyen et al.,
Technologies for the CompactLight undulator, XLS-CompactLight Deliverable D5.1, tech. rep., 2019, 97,
URL: https://www.compactlight.eu/uploads/Main/D5.1_XLS_Final.pdf.

[344] A. Ghaith et al., *EuPRAXIA deliverable 6.1: Report on state-of-the-art short period undulators*,
tech. rep., 2016, URL: https://theuniversityofliverpool.sharepoint.com/:b:/r/sites/eupraxia/Shared%20Documents/Deliverables/Reports/EuPRAXIA%20Deliverable%206%20Report%20SOLEIL%2020161031_D6.1.pdf?csf=1&web=1&e=eMZvC6.

[345] M. Valleau et al., *Development of cryogenic permanent magnet undulators at SOLEIL*, Synchrotron Radiation News **31** (2018) 42, DOI: 10.1080/08940886.2018.1460175.

A. Appendices

A.1. Parameter Tables

This section shows a snapshot of the central parameter list taken directly from Microsoft Excel. The lists are included here as they appear and are used by the project partners as tools, so the format is slightly different from the rest of the current deliverable.

Here the notion of the Project Break-Down Structure (PBS) is used to fully categorize and uniquely identify each component of the machine. This PBS is harmonized all over the project as well as in the data storage tools and allows for easy retrieval of information.

XLS Parameter List

XLS-000001

Compact

Index

Revision History

Revision	Issued	Changes
R1	27-04-21	V7 of Initial **Draft Issue R1**
R2	14-12-21	V7 updated numbers to final lattice

XLS Performance Parameters

Targeted features of baseline CompactLight FEL

Parameter	Soft X-rays	Hard X-rays	Unit
Max. repetition rate	1	0.1	kHz
Photon energy	0.25 - 2.0	2.0 - 16.0	keV
Wavelength	5.0 - 0.6	0.6 - 0.08	nm
FEL tuning range at fixed energy	x 2	x 2	
Peak brilliance @ 16 keV	10^{31}	10^{33}	(*)
Pulse duration	0.1 - 50	1 - 50	fs
Polarization	variable, selectable		
Two-pulse delay	± 100	± 100	fs
Two-colour separation	20	10	%
Synchronization	< 10	< 10	fs

(*) The unit for peak brilliance is ph/s/mm^2/mrad^2/0.1%BW

XLS Layout

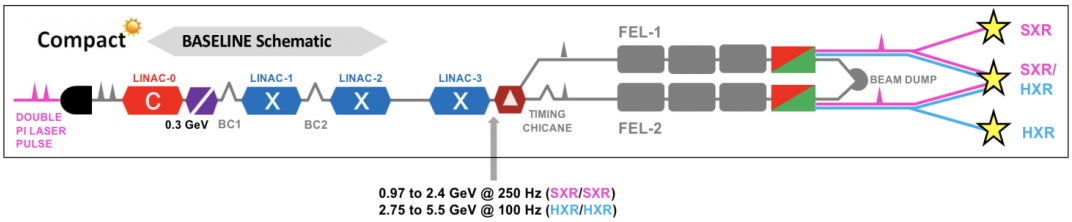

XLS Symbol Table

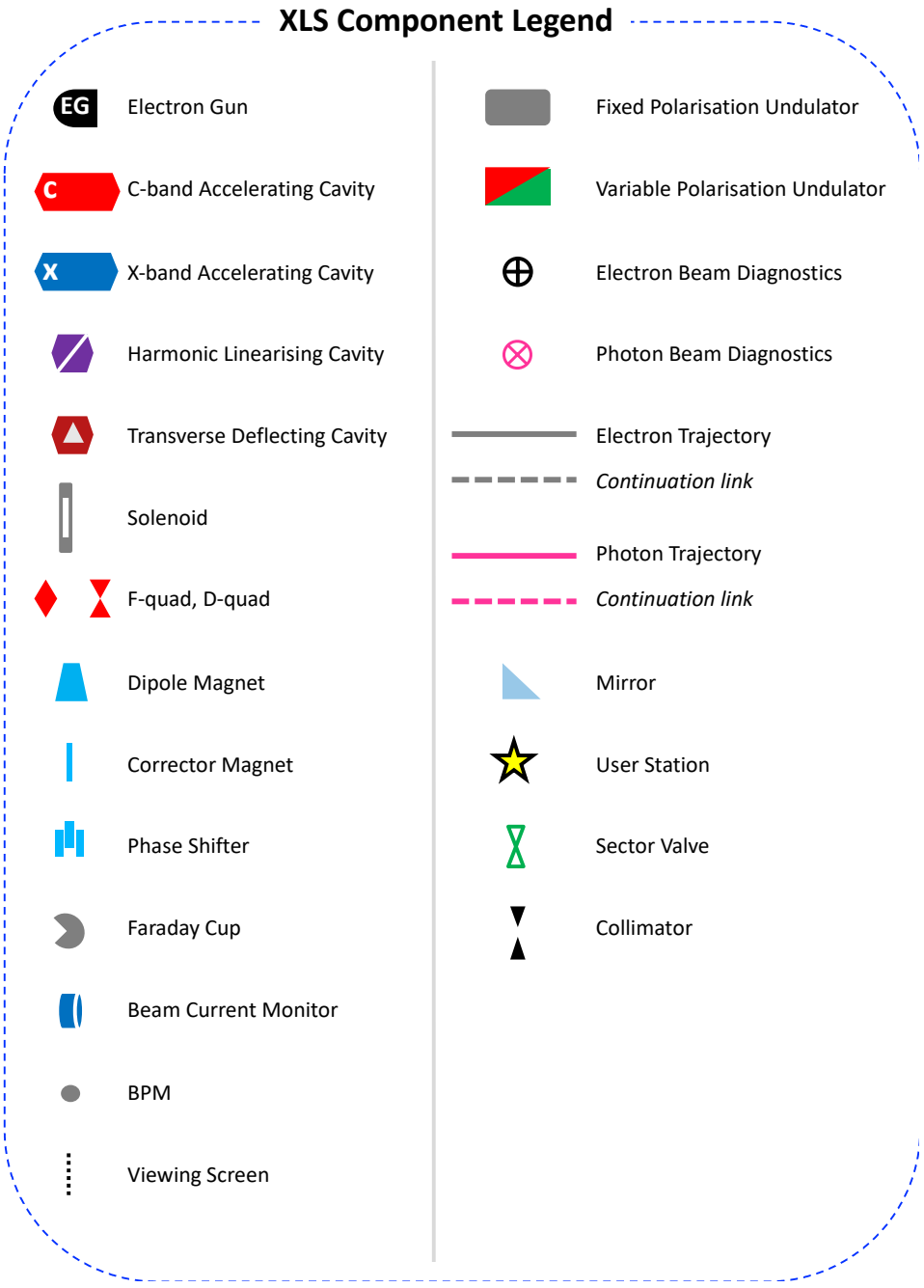

Compact Light
XLS Parameter List

Injector, Linac0 and BC1 Parameter List

Date 14-12-21 Based on XLS Baseline Accelerator Lattice Vxxx

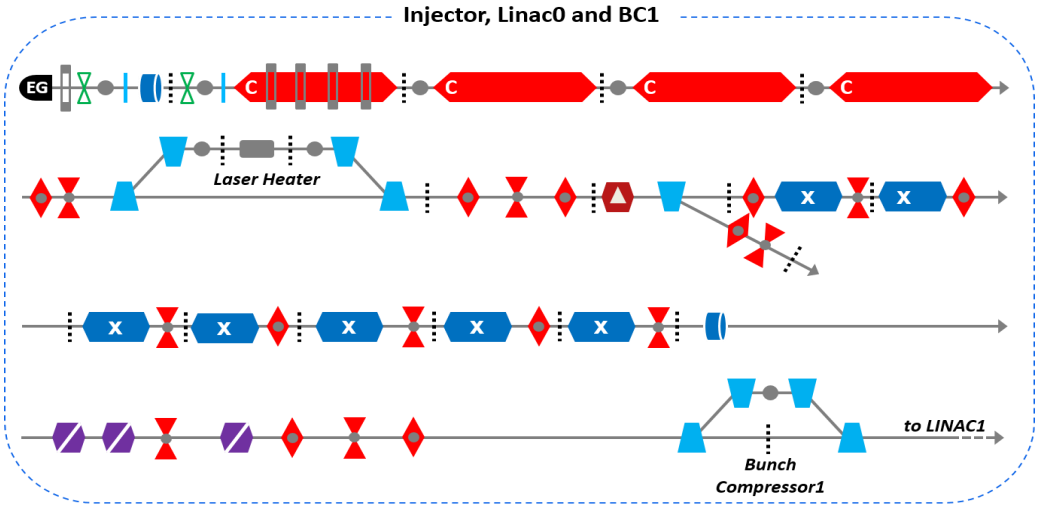

PBS	Parameter	Qty or Type	Qty or Type	Unit	Comments
	Injector Length		25.0	m	Starting from the Egun cathode surface
	Output Energy		0.320	GeV	
1	**Injector**				C band
	Beam properties				Properties at the injector output
	Bunch charge (Q)		75	pC	
	Beam Emittance		331	mm.mrad	
	Beam Emittance, rms, norm.		0.2	mm.mrad	Slice emittance in X, Y at injector output
	Beam Emittance, rms, norm.		0.2	mm.mrad	Projected emittance in X, Y at inj. output
		w/o BC	with BC		BC=Bunch Compression
	Bunch length	295	105	µm	
	Bunch length, rms (σ_t)		350	fs	VB
	Beam Energy		320	MeV	
	Peak current	22	60	A	Q/(√12 σ_t)
	Beam energy spread	0.6	1.4	%	
	Beam energy spread, rms		0.5	%	Corresponds to 2 keV
1.1.	Photocathode System		1		
	Cathode peak field		160	MV/m	
	Cathode material		Cu		Cs_2Te is considered as alternative option
1.2.	Laser System		1		TiSa laser
	Laser spot size		294	µm	Uniform
	Laser rms length		13.4	ps	
	Rise time laser pulse		600	fs	
1.6.	Vacuum System				
	Pressure			Torr	operating vacuum
	Beam line gate valves		2		

Compact Light
XLS Parameter List

Injector, Linac0 and BC1 Parameter List (continued)

Date 14-12-21 Based on XLS Baseline Accelerator Lattice Vxxx

PBS	Parameter	Qty or Type	Qty or Type	Unit	Comments
	Injector (continued)				
1.3.3.1.	RF gun cavity		1		C band structure
	Number of cells		2.5		
	Resonant frequency		5.712	GHz	
	RF input power		40	kW	18 MW peak
	Repetition rate		100 - 1000	Hz	
	$E_{cath}/\sqrt{P_{diss}}$		52	$MV/(mMW^{0.5})$	
	Quality factor		11800		
	Filling time		150	ns	
	Coupling coefficient		3		
	RF pulse length		180	ns	
	Mode separation 0 - π			MHz	
	Pulsed heating		< 40	℃	
	Average did. Power		200	W	
1.7.1.	Gun solenoid		1		
	Solenoid coils		2		One main and one bucking coil
	Main solenoid Field			T	
	Bucking coil Field			T	
1.7.3.	Gun solenoid PS		1		
1.8.	Beam Instrumentation System				
1.8.1.	Beam Current Transformer		1		
1.8.2.	In-quad Beam Position Monitor				
1.8.3.	Beam Position Monitor		2		Injector type stripline BPM
1.8.4.	Viewing Screen (type VS1)		1		
1.8.7.	Faraday cup				
1.7.6.	Corrector magnets		2		Correct in H and V planes
1.7.7.	Corrector magnet PS		4		
1.3.	RF system				RF system for E gun
1.3.1.	Klystron Modulator System		1		20 MW, 300 ns, 1 kHz
1.3.2.	RF Power Distribution System		1		
1.3.4.	Low Level RF & Timing		1		
	Output Beam Energy		7	MeV	Beam energy out of the gun
1	**Linac0**				
	Linac0 length			m	
	Input Beam Energy		7	MeV	Input energy to C band cavities
	Beam Emittance, rms, norm.		0.1	mm.mrad	H slice emittance at C band cavities input
1.3.3.2.	C band cavities		4		
	Cavity length		2	m	
	Effective accelerating length		1.9	m	at 1 kHz operation
	RF Frequency		5.712	GHz	
	Electric field		15	MV/m	
	Modulation factor				
	Number of cells				
	Synchronous phase			deg	
	Quality factor				
	Power (minimum required)			kW	
		w/o BC	with BC		BC=Bunch Compression
	Output Beam Energy	170	107	MeV	At output of C band cavities

Injector, Linac0 and BC1 Parameter List (continued)

Date 14-12-21 Based on XLS Baseline Accelerator Lattice Vxxx

PBS	Parameter	Qty or Type	Qty or Type	Unit	Comments
	Linac0 (continued)				
1.7.2.	Number of solenoids (type S1)		4		Only the first C band cavity has solenoids
	Length		0.5	m	
	Field		0.22	T	
1.7.3.	Number of solenoid PS				
1.2.3.	Laser Heater				
	Section length		1.5	m	
1.2.3.1.	Laser		1		Includes source and transport
	Wavelength		0.5 to 1	µm	
	Power		≈ 10	mW	
1.2.3.3.	Dipole (type D1)		4		Dipoles for diagnostics section dog leg
	Bending angle		5	deg	
	Nominal field		0.34	T	0.4 T peak field
	Arc length		0.1	m	
1.2.3.3.	Dipole (type D1) PS				
1.2.3.4.	Fixed Polarisation Undulator		1		
	Length		0.32	m	
	Number of periods		8		
	Period length		40	mm	
	Peak field		0.4	T	
1.2.3.5.	View screen		2		Diagnostics part of laser heater
1.2.3.6.	BPM		2		
	Induced uncorr. rms energy spread		< 10	keV	Induced by laser heater
1.8.	Beam Instrumentation System				
1.8.1.	Beam Current Transformer				
1.8.2.	In-quad Beam Position Monitor		18		
1.8.3.	Beam Position Monitor		3		Injector type stripline BPM
1.8.4.	Viewing Screen (type VS1)		10		
	Transverse Deflecting Cavity		1		PolariX
	ICCD Screen Station		1		
1.3.	RF system				RF system for C band cavities
1.3.1.	Klystron Modulator System				100 Hz @ 50 MW
1.3.1.1.	Modulator		1		
1.3.1.2	Klystron		1		1 klystron drives 4 C band cavities
1.3.2.	RF Power Distribution System				
1.3.4.	Low Level RF & Timing		1		
1.6.	Vacuum System				
	Pressure			Torr	operating vacuum
	Beam line gate valves				

Compact Light
XLS Parameter List

Injector, Linac0 and BC1 Parameter List (continued)

Date 14-12-21 Based on XLS Baseline Accelerator Lattice Vxxx

PBS	Parameter	Qty or Type	Qty or Type	Unit	Comments
	Linac0 (continued)				
		w/o BC	with BC		BC=Bunch Compression
	Input Beam Energy	170	107	MeV	Input to X band cavities
	Beam Emittance, rms, norm.		0.1	mm.mrad	H slice emittance at X band cavities input
1.4.3.1.	X band cavities		7		
	Cavity length		0.916	m	Structure length
	RF Frequency		11.994	GHz	
	Phase advance per cell		2π/3	rad	
	Waveguide power attenuation		≈10	%	
	Average iris radius **<a>**		3.5	mm	
	Iris radius **a**		4.3 - 2.7	mm	
	Number of cells		109		
	Accelerating cell length		8.332	mm	
	Unloaded SLED Q-factor Q_0		180000		
	External SLED Q-factor Q_E		23200		
	Shunt impedance **R**		85 - 111	MΩ/m	
	Effective shunt impedance $\mathbf{R_s}$		349	MΩ/m	
	Group velocity v_g/c		4.7 - 0.9	%	
	Filling time		146	ns	
	Average accelerating gradient(@100		65	MV/m	30 MV/m at 250 and 1000 Hz
	Output Beam Energy		320	MeV	
1.4.	X-band RF system				RF system for X-band cavities
	RF pulse length @100, 1000 Hz		1.5	μs	0.15 @ 250 Hz
1.4.1.	Klystron Modulator System				
1.4.1.1.	Modulator		2		
1.4.1.2	Klystron		2		1 klystron drives 4 X-band cavities
	Available Pout @ 100, 250 Hz		50	MW	10 MW @ 1000 Hz
	Net power @ 100, 250 Hz		44	MW	9 MW @ 1000 Hz
1.4.2.	RF Power Distribution System				
1.4.4.	Low Level RF & Timing		2		
1.7.4.	Quadrupole magnets		18		Quads with integrated BPM and corrector
1.7.5.	Quadrupole magnets PS		18		
1.7.6.	Corrector magnets		1		Correct in H and V planes
1.7.7.	Corrector magnet PS		2		
	Harmonic Linearising Cavity		2		K-band linearizer
	Frequency		36	GHz	
	Structure length		30	cm	
	Ri		2.00	mm	
	Li		0.60	mm	
	Voltage		12.75	MV	
	Phase		-180	deg	
	Ep		108	MV/m	

Injector, Linac0 and BC1 Parameter List (continued)

Date 14-12-21 Based on XLS Baseline Accelerator Lattice Vxxx

PBS	Parameter	Qty or Type	Qty or Type	Unit	Comments
	Bunch Compressor 1				
4.1.2.1.	Quadrupole magnets		2		Quads with integrated BPM and corrector
4.1.2.2.	Quadrupole magnets PS		2		
4.1.1.1.	Dipole (type D2)		4		Dipoles for Bunch Compressor 1
	Bending angle			deg	
	Nominal field			T	
4.1.1.2.	Dipole (type D2) PS		4		
4.1.3.1.	Corrector magnets		7		Correct in 1 plane
4.1.3.2.	Corrector magnet PS		7		
4.1.4.	Beam Instrumentation System				
	Beam Position Monitor		2		Injector type stripline BPM
4.1.4.1.	Beam Current Transformer				
4.1.4.2.	In-quad Beam Position Monitor		2		
4.1.4.3.	Viewing Screen (type VS1)		1		
4.1.4.4.	Transverse Deflecting Cavity		1		PolariX
4.1.4.5.	ICCD Screen Station		1		
4.1.5.3.	Collimator		1		Not yet in ideogram
	X-band RFD		1		RF (transverse) Deflector

Compact Light XLS-000001-R1 Page 10 of 15
XLS Parameter List

Linac1 and BC2 Parameter List

Date 14-12-21 Based on XLS Baseline Accelerator Lattice Vxxx

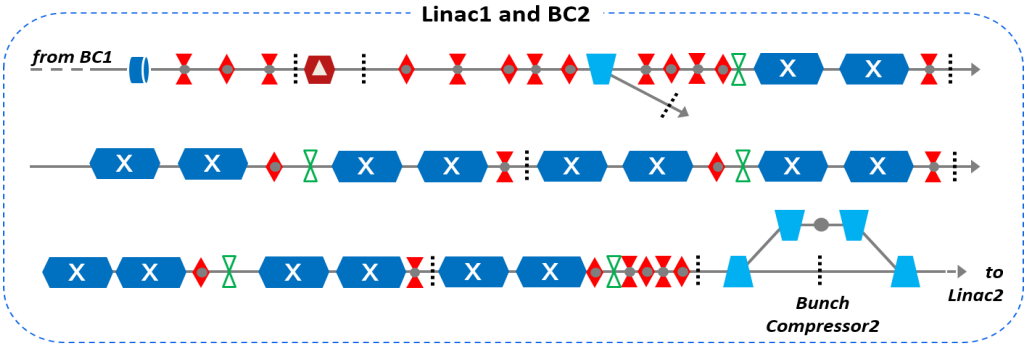

PBS	Parameter	Qty or Type	Qty or Type	Unit	Comments
	Linac1 Length			m	
	Input Energy		0.320	GeV	
	Output Energy		0.994	GeV	
2	**Linac1**				
2.1.3.1.	X band cavities		16		
	Cavity length		0.916	m	Structure length
	RF Frequency		11.994	GHz	
	Phase advance per cell		2π/3	rad	
	Waveguide power attenuation		≈10	%	
	Average iris radius **<a>**		3.5	mm	
	Iris radius **a**		4.3 - 2.7	mm	
	Number of cells per structure		109		
	Accelerating cell length		8.332	mm	
	Unloaded SLED Q-factor Q_0		180000		
	External SLED Q-factor Q_E		23200		
	Shunt impedance **R**		85 - 111	MΩ/m	
	Effective shunt impedance $\mathbf{R_s}$		349	MΩ/m	
	Group velocity v_g/c		4.7 - 0.9	%	
	Filling time		146	ns	
	Average accelerating gradient(@100		65	MV/m	30 MV/m at 250 and 1000 Hz
2.3.	Linac1 Vacuum System				
	Pressure			Torr	operating vacuum
	Beam line gate valves		5		
2.1.	RF system				RF system for X band cavities
	Required klystron power (@100 Hz)		44	MW	SLED on
	Required klystron power (@250 Hz)		44	MW	SLED off
	Required klystron power (@1000 Hz)		9	MW	SLED on
2.1.1.	Klystron Modulator System				
2.1.1.1.	Modulator		4		
2.1.1.2	Klystron		4		1 klystron drives 4 X-band cavities
2.1.2.	RF Power Distribution System				
2.1.4.	Low Level RF & Timing		4		

Linac1 and BC2 Parameter List (continued)

Date 14-12-21 Based on XLS Baseline Accelerator Lattice Vxxx

PBS	Parameter	Qty or Type	Qty or Type	Unit	Comments
	Linac1 (continued)				
2.4.1.1.	Quadrupole magnets		24		Quads with integrated BPM
2.4.1.2.	Quadrupole magnets PS		24		
2.4.2.1.	Corrector magnets		24		Correct in H and V planes
2.4.2.2.	Corrector magnet PS		24		
2.5.	Beam Instrumentation System				
2.5.1.	In-quad Beam Position Monitor		24		
2.5.2.	Viewing Screen (type VS1)		7		
	Bunch Compressor 2				
4.2.2.1.	Quadrupole magnets		4		Quads with integrated BPM
4.2.2.2.	Quadrupole magnets PS		4		
4.2.1.1.	Dipole (type D3)		4		Dipoles for Bunch Compressor 2
	Bending angle		2.1	deg	
	Nominal field			T	
4.2.1.2.	Dipole (type D3) PS		4		
4.2.3.1.	Corrector magnets		10		
4.2.3.2.	Corrector magnet PS		10		
4.2.4.	Beam Instrumentation System				
4.2.4.1.	Beam current monitor				
4.2.4.2.	In-quad Beam Position Monitor		4		Stripline BPM
4.2.4.3.	Viewing Screen (type VS1)				
4.2.4.4.	Transverse Deflecting Cavity		1		PolariX
4.2.5.3.	Collimator		1		Not yet in ideogram

Compact Light XLS-000001-R1 Page 12 of 15

XLS Parameter List

Linac2 Parameter List

Date 14-12-21 Based on XLS Baseline Accelerator Lattice Vxxx

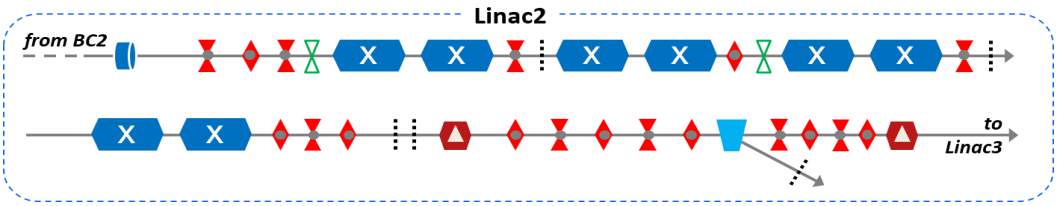

PBS	Parameter	Qty or Type	Qty or Type	Unit	Comments
	Linac2 Length			m	
	Input Energy		0.994	GeV	
	Output Energy		1.442	GeV	
	Linac2				
3.1.3.1.	X band cavities		8		
	Cavity length		0.916	m	Structure length
	RF Frequency		11.994	GHz	
	Phase advance per cell		2π/3	rad	
	Waveguide power attenuation		≈10	%	
	Average iris radius **<a>**		3.5	mm	
	Iris radius **a**		4.3 - 2.7	mm	
	Number of cells per structure		109		
	Accelerating cell length		8.332	mm	
	Unloaded SLED Q-factor Q_0		180000		
	External SLED Q-factor Q_E		23200		
	Shunt impedance **R**		85 - 111	MΩ/m	
	Effective shunt impedance $\mathbf{R_s}$		349	MΩ/m	
	Group velocity v_g/c		4.7 - 0.9	%	
	Filling time		146	ns	
	Average accelerating gradient(@100		44	MV/m	30 MV/m at 250 and 1000 Hz
3.3.	Linac2 and Linac3 Vacuum System				
	Pressure			Torr	operating vacuum
	Beam line gate valves		4		
3.1.	RF system				RF system for X band cavities
	Required klystron power (@100 Hz)		44	MW	SLED on
	Required klystron power (@250 Hz)		44	MW	SLED off
	Required klystron power (@1000 Hz)		9	MW	SLED on
3.1.1.	Klystron Modulator System				
3.1.1.1.	Modulator		2		
3.1.1.2.	Klystron		2		1 klystron drives 4 X-band cavities
3.1.2.	RF Power Distribution System				
3.1.4.	Low Level RF & Timing		2		
3.4.1.1.	Quadrupole magnets		18		Quads with integrated BPM
3.4.1.2.	Quadrupole magnets PS		18		
3.4.2.1.	Corrector magnets				Correct in H and V planes
3.4.2.2.	Corrector magnet PS				

Linac2 Parameter List (continued)

Date 14-12-21 Based on XLS Baseline Accelerator Lattice Vxxx

PBS	Parameter	Qty or Type	Qty or Type	Unit	Comments
	Linac2 (continued)				
	Dipole (type D3)		4		Dipoles for Bunch Compressor 2
	Bending angle		2.1	deg	
	Nominal field			T	
	Harmonic Linearising Cavity		1		
	Transverse Deflecting Cavity		1		
3.5.	Beam Instrumentation System				
3.5.1.	In-quad Beam Position Monitor		18		Stripline BPM
3.5.2.	Viewing Screen (type VS1)		2		
3.5.3.	Coherent Transition Radiation Monitor				
3.5.4.	ICCD Screen Station				

Compact Light XLS-000001-R1 Page 14 of 15
XLS Parameter List

Linac3 Parameter List

Date 14-12-21 Based on XLS Baseline Accelerator Lattice Vxxx

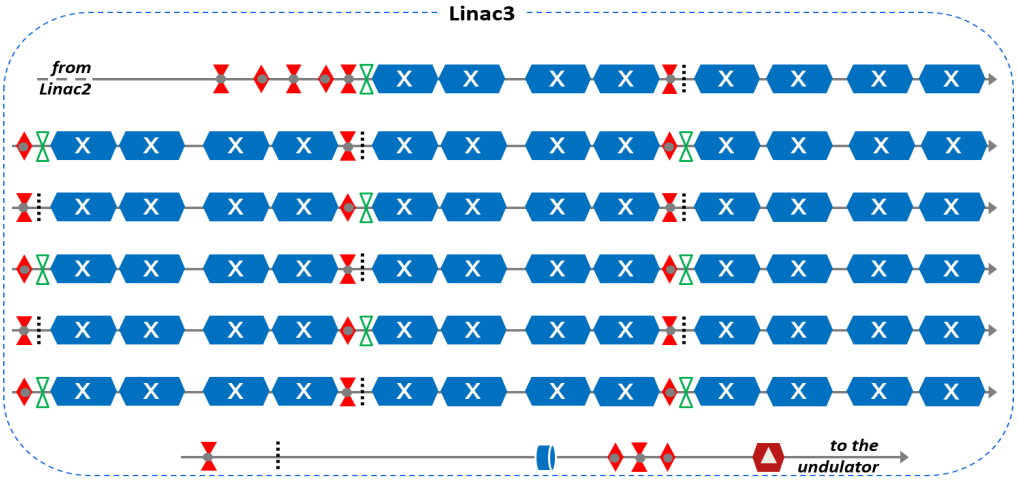

PBS	Parameter	Qty or Type	Qty or Type	Unit	Comments
	Linac3 Length			m	
	Input Energy		1.442	GeV	
	Output Energy		5.666	GeV	
	Output peak current		≈ 5	kA	
	Bunch duration (rms)		≈ 2	fs	
		X	Y		
	Beam Emittance, rms, norm.	0.2	0.2	mm.mrad	Slice emittance at output
	Beam Emittance, rms, norm.	< 0.4	< 0.3	mm.mrad	Projected emittance at output
		SX	HX		
	Final mean energy	4.5	7	GeV	Based on Table 1 Deliverable 3.4
	Total energy spread (rms)	< 2	< 8	MeV	At the output
	Slice energy spread (rms)	< 0.03	< 0.03	%	Relative, at the output
	Linac3				
3.1.3.1.	X band cavities		68		
	Cavity length		0.916	m	Structure length
	RF Frequency		11.994	GHz	
	Phase advance per cell		2π/3	rad	
	Waveguide power attenuation		≈ 10	%	
	Average iris radius **<a>**		3.5	mm	
	Iris radius **a**		4.3 - 2.7	mm	
	Number of cells per structure		109		
	Accelerating cell length		8.332	mm	
	Unloaded SLED Q-factor Q_0		180000		
	External SLED Q-factor Q_E		23200		
	Shunt impedance **R**		85 - 111	MΩ/m	
	Effective shunt impedance $\mathbf{R_s}$		349	MΩ/m	
	Group velocity v_g/c		4.7 - 0.9	%	
	Filling time		146	ns	
	Average accelerating gradient(@100		44	MV/m	30 MV/m at 250 and 1000 Hz

Linac3 Parameter List (continued)

Date 14-12-21 Based on XLS Baseline Accelerator Lattice Vxxx

PBS	Parameter	Qty or Type	Qty or Type	Unit	Comments
	Linac3 (continued)				
3.3.	Linac2 and Linac3 Vacuum System				
	Pressure			Torr	operating vacuum
	Beam line gate valves		9		
3.1.	RF system				RF system for X band cavities
	Required klystron power (@100 Hz)		44	MW	SLED on
	Required klystron power (@250 Hz)		44	MW	SLED off
	Required klystron power (@1000 Hz)		9	MW	SLED on
3.1.1.	Klystron Modulator System				
3.1.1.1.	Modulator		17		
3.1.1.2.	Klystron		17		1 klystron drives 4 X-band cavities
3.1.2.	RF Power Distribution System				
3.1.4.	Low Level RF & Timing		17		
3.4.1.1.	Quadrupole magnets		25		Quads with integrated BPM
3.4.1.2.	Quadrupole magnets PS		25		
3.4.2.1.	Corrector magnets				Correct in H and V planes
3.4.2.2.	Corrector magnet PS				
3.5.	Beam Instrumentation System				
3.5.1.	In-quad Beam Position Monitor		25		Stripline BPM
3.5.2.	Viewing Screen (type VS2)		9		
3.5.3.	Coherent Transition Radiation Monitor				
3.5.4.	ICCD Screen Station				

A.2. Open Data and Documentation

A.2.0.1. CompactLight Open Data Policy

The data in CompactLight include basically the results of the project created from scratch through research and development activities, based prevalently on the knowledge and know-how of the involved researchers and technicians. In particular, no hardware has been created during the design study and the creation of hardware will be the objective of follow-on projects.

CompactLight data are in general open data, in order to facilitate a widespread use of the project results. However, further development activities, for instance prototyping, are required before the technology is ready to be actually applied in projects for the construction of X-ray FELs and small facilities. The CompactLight partners have already started such activities and are planning to start others, also in collaboration with new partners including companies. Critical data for these activities, in particular if they are expected to lead to exploitable IPRs in the future, are not open at the moment. The following tables describe the types and formats of the created project data and provide information on access and re-use possibilities by interested external users. In case of doubt, interested parties can contact the project partners using the indicated contact information.

A.2.0.2. List of CompactLight Data

1. Deliverable D1.1	
Type	Website
Format	Website
Description	CompactLight website with information about the project, partners, events, documents, and related future activities
Sharing	Public (PU)
Owners	CompactLight project partners
License	CC-BY
Reuse	The project partners will keep the website active in order to communicate with the community and inform about future events, follow-up projects, new developments and everything else concerning CompactLight technologies and infrastructures
Archiving	Not applicable
Preservation	About 5 years
Access	https://www.compactlight.eu/Main/HomePage
Information	compactlight@elettra.eu
Comments	None

2. Other Deliverables	
Type	Report
Format	
Description	Technical reports of the various work packages describing the work performed and results achieved by the date of delivery
Sharing	Public (PU)
Owners	CompactLight project partners
License	CC-BY
Reuse	The deliverables describe in detail the work and the achieved results in the different work packages in detail and create therefore the basis for any future activity for the further the development of the technologies and their use in application projects
Archiving	All CompactLight deliverables have been archived in the CompactLight Community in Zenodo, including standard metadata
Preservation	Long-term preservation is ensured in Zenodo
Access	https://www.zenodo.org/search?page=1&size=20&q=CompactLight https://www.compactlight.eu/Main/HomePage
Information	compactlight@elettra.eu; corresponding authors
Comments	A complete list of all deliverables accepted by the end of 2021 can be found in the Annex of the CompactLight CDR and on the project's website

3. Scientific Publications	
Type	Scientific articles
Format	
Description	Scientific papers describing the work performed and the results achieved by the project
Sharing	Open access
Owners	Authors of the publications
License	CC-BY
Reuse	The publications describe the work and the achieved results in detail and can be used by other researchers in the field for further scientific activities based on the published project results
Archiving	All CompactLight publications have been archived in the CompactLight Community in Zenodo, including standard metadata
Preservation	Long-term preservation is ensured in Zenodo
Access	https://www.zenodo.org/search?page=1&size=20&q=CompactLight https://www.compactlight.eu/Main/HomePage
Information	Corresponding authors of the publications
Comments	A complete list of all publications published by the end of 2021 can be found in the Annex of the CompactLight CDR and on the project's website

4. Design parameters	
Type	Data files
Format	spreadsheet
Description	Detailed parameters of the CompactLight design collected in the CompactLight Parameter List
Sharing	Open access
Owners	CompactLight project partners
License	CC-BY
Reuse	The data can be reused to understand the CompactLight design in more detail and to develop concrete design studies for facilities based on the CompactLight technologies; the CompactLight Parameter List can also be used as a template for parameter lists in general
Archiving	The CompactLight Parameter List is included in format in the CompactLight CDR and in D7.2, which will both be archived in the CompactLight Community in Zenodo after acceptance by the European Commission; a spreadsheet version for easy reuse will be attached as an open data file in spreadsheet format for easy reuse
Preservation	Long-term preservation is ensured in Zenodo
Access	https://www.zenodo.org/search?page=1&size=20&q=CompactLight https://www.compactlight.eu/Main/HomePage
Information	compactlight@elettra.eu
Comments	The CompactLight parameter list will also be available on the project's website

5. Simulation Data	
Type	Data files
Format	Specific formats
Description	Input and output data of the simulations performed for the CompactLight design study
Sharing	Partly open access, partly restricted access
Owners	Project partners that have performed the design studies; CompactLight partners
License	Open data: CC-BY; others: as indicated by the owners
Reuse	The data will be reused by the CompactLight partners for further development activities; they can be used by interested applicants as starting point for their own design studies; upon request and agreement with the project partners
Archiving	The simulation data are archived in the CompactLight GIT space
Preservation	Long-term preservation is ensured in GIT
Access	https://www.zenodo.org/search?page=1&size=20&q=CompactLight https://www.compactlight.eu/Main/HomePage https://gitlab.cern.ch/XLS-Git
Information	compactlight@elettra.eu; owners of the data
Comments	None

6. Cost Analysis Data	
Type	Data files
Format	pdf, spreadsheet
Description	Input data and output data of the CompactLight cost analysis; the data have been organized by means of a costing tool that was originally developed to estimate the CLIC project cost at CERN. The tool provides the interface to a large database where the information is stored and secured. The CERN Advanced Information Systems team (AIS) has provided a dedicated interface specifically prepared for the CompactLight project.
Sharing	Open access (on request)
Owners	Project partners involved in the cost analysis; CompactLight partners
License	CC-BY
Reuse	The data can be used by interested applicants as the basis for the cost analysis of their own projects and by the CompactLight partners for updates based on further development activities
Archiving	Core results of the cost analysis are published in the CompactLight CDR and D7.2 in format; these documents will be archived in Zenodo and on the project's website. The input data are stored in the CERN Advanced Information Systems AIS
Preservation	Long-term preservation is ensured in Zenodo and in the CERN AIS
Access	Publications on cost analysis results: https://www.zenodo.org/search?page=1&size=20&q=CompactLight https://www.compactlight.eu/Main/HomePage Cost analysis input data: The database of the cost analysis data will remain accessible for consultation in a simplified form upon request by interested users, see contact information below
Information	compactlight@elettra.eu; corresponding authors; owners of the data
Comments	None

7. Landscape Analysis Data	
Type	Statistical data
Format	spreadsheet
Description	Community, facility and user data collected as an input to the landscape analysis
Sharing	Open access
Owners	Project partners involved in the cost analysis; CompactLight partners
License	CC-0
Reuse	The data can be reused for further investigations into the topic, in particular for long term trend and community analyses; they will be reused by the CompactLight partners for this purpose and can be useful for accompanying strategic documents of research infrastructure projects
Archiving	Data will be attached as data files in spreadsheet format to all relevant CompactLight publications (CompactLight CDR, D7.2, scientific papers on these results) and archived in the CompactLight Community in Zenodo
Preservation	Long-term preservation is ensured in Zenodo
Access	https://www.zenodo.org/search?page=1&size=20&q=CompactLight https://www.compactlight.eu/Main/HomePage
Information	compactlight@elettra.eu; corresponding authors
Comments	None

8. Software	
Type	Computer codes
Format	Specific programming languages
Description	Computer codes developed / further developed by the partners for the simulations required in the course of the study
Sharing	Confidential
Owners	Authors of the codes
License	Trade Secret
Reuse	The software will be used at the moment by the owners for further R&D activities; it might become open later on
Archiving	By authors
Preservation	By authors
Access	Potentially through collaborations with the authors, depends on the single case
Information	compactlight@elettra.eu; corresponding authors
Comments	None

A.3. Publications

Selected Scientific Articles

M. Behtouei, B.Spataro, L. Faillace, M. Carillo, A. Leggieri, L. Palumbo, and M. Migliorati, Relativistic Versus Nonrelativistic Approaches to a Low Perveance High Quality Matched Beam for a High Efficiency Ka-Band Klystron, Instruments 2021, 5, 33, (2021).
doi: 10.3390/instruments5040033
https://doi.org/10.3390/instruments5040033

D. González-Iglesias, D. Esperante, B. Gimeno, M. Boronat, C. Blanch, N. Fuster-Martínez, P. Martinez-Reviriego, P. Martín-Luna, and J. Fuster, Analytical RF Pulse Heating Analysis for High Gradient Accelerating Structures, IEEE Transactions on Nuclear Science, vol. 68, no. 2, pp. 78-91, (2021).
doi: 10.1109/TNS.2021.3049319
https://roderic.uv.es/handle/10550/79894 (AAM)

M. Behtouei, B. Spataro, F. Di Paolo, and A. Leggieri, The Ka-Band High Power Klystron Amplifier Design Program of INFN, v.2, Vacuum 191, 110377, (2021).
doi: 10.5281/zenodo.5062317
https://arxiv.org/abs/2011.12809 (AAM)

M. Behtouei, B. Spataro, F. Di Paolo and A. Leggieri, Simulations for a low-perveance high-quality beam matching of a high efficiency Ka-band klystron (v.1, 2020).
doi: 10.5281/zenodo.5062151
https://arxiv.org/abs/2012.03737 (Manuscript, v.1)

L. Zhang, L.J. R. Nix, and A. W. Cross, Magnetron injection gun for high-power gyroklystron, IEEE Transactions on Electron Devices, 67 (11), pp. 5151-5157 (2020).
doi:10.1109/TED.2020.3025747
https://strathprints.strath.ac.uk/73952/ (AAM)

K. Zhang, M. Ainslie, M. Calvi, S. Hellmann, R. Kinjo, and T. Schmidt, Fast and efficient critical state modelling of field-cooled bulk high-temperature superconductors using a backward computation method, 33/11, 114007, IOP Publishing (2020);
doi:10.1088/1361-6668/abb78a
https://zenodo.org/record/5074857#.YOQSeOjwhjE

K. Zhang, S. Hellmann, M. Calvi, T. Schmidt, and L. Brouwer, Magnetization Current Simulation of High Temperature Bulk Superconductors Using A-V-A Formulation and Iterative Algorithm Method: Critical State Model and Flux Creep Model, IEEE Transactions on Applied Superconductivity 31, 2 (2021).
doi: 10.1109/TASC.2020.3037964
https://arxiv.org/abs/1908.04640v2

S. Di Mitri, A. Latina, M. Aicheler, A. Aksoy, D. Alesini, G. Burt, A. Castilla, J. Clarke, H. M. Castañeda Cortés, M. Croia, G. D'Auria, M. Diomede, D. Dunning, M. Ferrario, A. Gallo, A. Giribono, V. Goryashko, A. Mostacci, F. Nguyen, R. Rochow, J. Scifo, B. Spataro, N. Thompson, C. Vaccarezza, A. Vannozzi, X. Wu, and W. Wuensch, Scaling of Beam Collective Effects with Bunch Charge in the CompactLight Free-Electron Laser, Photonics 7/4, 125, MDPI Publishing (2020).

doi: 10.3390/photonics7040125
https://zenodo.org/record/5070178#.YOLv_ejwhjE

M. Behtouei, L. Faillace, M. Ferrario, B. Spataro, and A. Variola, Initial Design of a High-Power Ka-Band Klystron, Journal of Physics: Conference Series - 4th European Advanced Accelerator Concepts Workshop 1596, 012023, IOP Publishing (2020).
doi:10.1088/1742-6596/1596/1/012023
https://zenodo.org/record/5069989#.YOLchejwhjE

M. Behtouei, L. Faillace, M. Ferrario, B. Spataro, and A. Variola, A Ka-band linearizer TW accelerating structure for the Compact Light XLS project, Journal of Physics: Conference Series - 4th European Advanced Accelerator Concepts Workshop 1596, 012021, IOP Publishing (2020).
doi:10.1088/1742-6596/1596/1/012021
https://zenodo.org/record/5061782#.YN8pDujwhjE

S. Di Mitri, G. Perosa, A. D. Brynes, I. Setija, S. Spampinati, P. Williams, A. Wolski, E. Allaria, S. Brussaard, L. Gianessi, G. Penco, P. R. Rebernik, and M. Trovò, Experimental Evidence of Intrabeam Scattering in a Free-Electron Laser Driver, New J. Phys. (2020).
doi: 10.1088/1367-2630/aba572
https://zenodo.org/record/5060921#.YN8jRujwhjE

L. Nix, L. Zhang, W. He, C. Donaldson, K. Ronald, A. Cross, and C. Whyte , Demonstration of efficient beam-wave interaction for a MW-level 48 GHz gyroklystron amplifier, Physics of Plasmas, vol. 27, no. 5, p. 053101, (2020).
doi:10.1063/1.5144590
https://strathprints.strath.ac.uk/72253/ (AAM)

L. Zhang, W. He, C. R. Donaldson, J. Clarke, K. Ronald, A. D. R. Phelps and A. W. Cross, Coupling structure for high Q corrugated cavity as a microwave undulator, IEEE Trans. Electron Devices, Vol. 66, No. 10. pp. 4392-4397, (2019).
doi:10.1109/TED.2019.2933557
https://strathprints.strath.ac.uk/69243/ (AAM)

M. Calvi, M. D. Ainslie, A. Dennis, J. H. Durrell, S. Hellmann, C. Kittel, D. A. Moseley, T. Schmidt, Y. Shi and K. Zhang, A GdBCO bulk staggered array undulator, Superconductor Science and Technology 33, Number 1 - Focus on Processing and Application of Superconducting Bulk Materials 2019, IOP Publishing (2019).
doi: 10.1088/1361-6668/ab5b37
https://zenodo.org/record/5054451#.YN20bujwiHs

S. Di Mitri, G. De Ninno, R. Fabris, S. Spampinati, and N. R. Thompson, Simple and Robust Free Electron Laser Double, Phys. Rev. Accel. Beams 22, 100701 (2019).
doi: 10.1103/PhysRevAccelBeams.22.100701
https://zenodo.org/record/5054237#.YN2t7OjwiHs

S. Di Mitri, G. De Ninno, R. Fabris, S. Spampinati, and N. R. Thompson, Simple and Robust Free Electron Laser Doubler, Proceedings of the 39th Free Electron Laser Conference FEL 2019, JACoW Publishing, Geneva (2019).
doi:10.18429/JACoW-FEL2019-THP010
https://zenodo.org/record/5040921#.YNsf1OjwiMo

G. D'Auria et al., Status of the CompactLight Project, Proceedings of the 39th Free Electron Laser Conference FEL 2019, JACoW Publishing, Geneva (2019).
doi:10.18429/JACoW-FEL2019-THP078
https://zenodo.org/record/5040435#.YNr8gujwiMo

H. M. Castañeda Cortés, N. R. Thompson, and D. J. Dunning, Linear polarisation via a Delta Afterburner for the CompactLight Facility Proceedings of the 39th Free Electron Laser Conference FEL 2019, JACoW Publishing, Geneva (2019).
doi:10.18429/JACoW-FEL2019-WEP101
https://zenodo.org/record/5040404#.YNrsKujwiMo

N. Gazis, E. Tanke, Th. Apostolopoulos, K. Pramatari, R. Rochow, and E. Gazis, Light Sources in Europe - Case Study: The CompactLight Collaboration, Instruments 2019, 3, 43, Special Issue "Physics and Applications of High Brightness Beams" (2019).
doi:10.3390/instruments3030043
https://zenodo.org/record/5040261#.YNri3-jwiMo

M. Ferrario and R. W. Assmann, From Dreams to Reality: Prospects for Applying Advanced Accelerator Technology to Next Generation Scientific User Facilities, Proceedings of the 10th International Particle Accelerator Conference IPAC 2019, JACoW Publishing, Geneva (2019).
doi:10.18429/JACoW-IPAC2019-MOXPLM2
https://zenodo.org/record/5007127#.YNCtCejwhjE

D. Zhu, Y. R. E. Tan, L. Zhang, and A. Cross, The Conceptual Design of a 36 GHz RF Undulator Proceedings of the 10th International Particle Accelerator Conference IPAC 2019, JACoW Publishing, Geneva (2019).
doi: 18429/JACoW-IPAC2019-TUPRB002
https://zenodo.org/record/5007026#.YNCo9ejwhjE

D. Alesini, G. Castorina, M. Croia, M. Ferrario, A. Gallo, B. Spataro, C. Vaccarezza, A. Vannozzi, A. Giribono, and F. Cardelli, Design of a Full C-Band Injector for Ultra-High Brightness Electron Beam, Proceedings of the 10th International Particle Accelerator Conference IPAC 2019, JACoW Publishing, Geneva (2019).
doi:10.18429/JACoW-IPAC2019-TUPTS024
https://zenodo.org/record/5005996#.YNB2cOjwhjE

E. Marin, R. Muñoz Horta, F. Pérez, A. Aksoy, S. Di Mitri, A. Latina, and S.B. van der Geer, Start-to-End Simulations of the Compact Light Project Based on an S-Band Injector and an X-Band Linac, Proceedings of the 10th International Particle Accelerator Conference IPAC 2019, JACoW Publishing, Geneva (2019).
doi:10.18429/JACoW-IPAC2019-TUPRB074
https://zenodo.org/record/5006503#.YNCQ1OjwhjE

J.M. Arnesano, A. Mostacci, L. Palumbo, M. Diomede, M. Marongiu, L. Ficcadenti, Design of an X-Band Constant Impedance LINAC for Compact Light Project, Proceedings of the 10th International Particle Accelerator Conference IPAC 2019, JACoW Publishing, Geneva (2019).
doi:10.18429/JACoW-IPAC2019-WEPRB105
https://zenodo.org/record/5005680#.YNB3R-jwhjE

A. Castilla, G. Burt, W.L. Millar, A. Latina, X. Liu, W.L. Millar, X.W. Wu, and W. Wuensch, Ka-Band Linearizer Studies for a Compact Light Source, Proceedings of the 10th International Particle Accelerator Conference IPAC 2019, JACoW Publishing, Geneva (2019), CompactLight Design Study, Proceedings of the 10th International Particle Accelerator Conference IPAC 2019, JACoW Publishing, Geneva (2019).
doi:10.18429/JACoW-IPAC2019-WEPRB068
https://zenodo.org/record/doi:10.18429/JACoW-IPAC2019-WEPRB068

G. D'Auria et al., CompactLight Design Study, Proceedings of the 10th International Particle Accelerator Conference IPAC 2019, JACoW Publishing, Geneva (2019).
doi:10.18429/JACoW-IPAC2019-TUPRB032
https://zenodo.org/record/5006656#.YNCjvOjwhjE

L. Zhang, W. He, J. Clarke, K. Ronald, A. D. R. Phelps, and A. W. Cross, Microwave undulator using a helically corrugated waveguide, IEEE Trans. Electron Devices, vol. 65, no. 12, pp. 5499-5504, (2018).
doi: 10.1109/TED.2018.2873726
https://strathprints.strath.ac.uk/65580/ (AAM)

A. Latina et al., CompactLight Design Study, Proceedings of the 60th ICFA Advanced Beam Dynamics Workshop on Future Light Sources FLS2018, JACoW Publishing, Geneva (2018).
doi:10.18429/JACoW-FLS2018-WEP1WC02
https://zenodo.org/record/4720630#.YNBbbOjwhjE

XLS Deliverables

XLS - D7.1: CompactLight global integration and cost analysis, R. Rochow, M. Aicheler, G. D'Auria, E. Gazis, R. Geometrante, R. Hoekstra, A. Latina, F. Perez, H. Priem, and C. Rossi, on behalf of the CompactLight Collaboration; 26 December 2019.
doi: 10.5281/zenodo.5024529
https://zenodo.org/record/5024529#.YNRCPOjwhjE

XLS - D6.1: Computer codes for the facility design, A. Aksoy, A. Giribono, A. Latina, H. M. Castañeda Cortés, N. Thompson, F. Nguyen, and E. Marin, on behalf of the CompactLight Collaboration; 27 June 2019.
doi: 10.5281/zenodo.5024680
https://zenodo.org/record/5024680#.YNRG_OjwhjE

XLS - D5.1: Technologies for the CompactLight undulator, F. Nguyen, A. Aksoy, A. Bernhard, M. Calvi, J. Clarke, H. M. Castañeda Cortés, A. Cross, G. Dattoli, D. Dunning, R. Geometrante, J. Gethmann, S. Hellmann, M. Kokole, J. Marcos, Z. Nergiz, F. Perez, A. Petralia, S. Richter, T. Schmidt, D. Schoerling, N. Thompson, K. Zhang, L. Zhang, and D. Zhu, on behalf of the CompactLight Collaboration; 27 June 2019.
doi: 10.5281/zenodo.5024409
https://zenodo.org/record/5024409#.YNQ-K-jwhjE

XLS - D4.1: Report on the computer code and simulation tools which will be used for RF power unit design and cost optimization, W. Wuensch, M. Diomede, A. Gallo, D. Alesini, C. Rossi, A. Cross, L. Zhang, L. Nix, and X. Wu, on behalf of the CompactLight Collaboration; 27 June 2019.

doi: 10.5281/zenodo.5018877
https://zenodo.org/record/5018877#.YNNcAujwhjE

XLS - D3.2: Review report on bunch compression techniques and phase space linearization, J. M.s Arnesano, M. Croia, S. Di Mitri, L. Ficcadenti, An. Faus-Golfe, A. Giribono, Y. Han, A. Latina, X. Liu, E. Marin Lacoma, R. Muñoz Horta, A. Mostacci, L. Palumbo, B. Spataro, and C. Vaccarezza, on behalf of the CompactLight Collaboration; 27 June 2019.
doi: 10.5281/zenodo.5018303
https://zenodo.org/record/5018303#.YNNWZOjwhjE

XLS - D3.1: Preliminary assessments and evaluations of the optimum e-gun and injector solution for the CompactLight design, M. Ferrario, D. Alesini, F. Cardelli, G. Castorina, M. Croia, M. Diomede, A. Gallo, A. Giribono, J. Scifo, B. Spataro, C. Vaccarezza, A. Vannozzi, S. Di Mitri, R. Rochow, A. Latina, M. D. Kelisani, S. Doebert, D. Angal-Kalinin, J. Clarke, E. Gazis, A. Aksoyk, J. Luiten, A. Rajabi, X. Stragier, A. Faus-Golfe, Y. Han, D. Esperante, M. Boronat, C. Blanch, J. Fuster, and B. Gimeno, on behalf of the CompactLight Collaboration; 27 June 2019.
doi: 10.5281/zenodo.5016578
https://zenodo.org/record/5016578#.YNM9POjwhjE

XLS - D2.2: FEL design with accelerator and undulator requirements, S. Di Mitri, A. Aksoy, A. Bernhard, H. M. Castañeda Cortés, J. Clarke, G. D'Auria, D. Dunning, M. Ferrario, A. Latina, E. Marin, F. Nguyen, T. Schmidt, N. Thompson, and W. Wuensch, on behalf of the CompactLight Collaboration; 22 December 2019.
doi: 10.5281/zenodo.5013771
https://zenodo.org/record/5013771#.YNLiY-jwhjF

XLS - D2.1: FEL Science Requirements and Facility Design, A. Mak, P. Salén, V. Goryashko, and J. Clarke, on behalf of the CompactLight Collaboration; 20 December 2018.
doi: 10.5281/zenodo.5013682
https://zenodo.org/record/5013682#.YNIAUOjwhjE

XLS - D1.2: Data Management Plan - v1.2, G. D'Auria, E. Gazis, A. Latina, R. Rochow, and M. Aicheler, on behalf of the CompactLight Collaboration; 21 December 2019.
doi: 10.5281/zenodo.5013663
https://zenodo.org/record/5013663#.YNH7zOjwhjE

XLS - D1.2: Data Management Plan - v1.1, G. D'Auria, E. Gazis, A. Latina, R. Rochow, and M. Aicheler, on behalf of the CompactLight Collaboration; 08 April 2019.
doi: 10.5281/zenodo.5013614
https://zenodo.org/record/5013614#.YNH6b-jwhjE

XLS - D1.2: Data Management Plan - v1.0, G. D'Auria, E. Gazis, A. Latina, and R. Rochow, on behalf of the CompactLight Collaboration; 29 June 2018.
doi: 10.5281/zenodo.5013499
https://zenodo.org/record/5013499#.YNH3yejwhjE

A.4. XLS Collaboration

ST

CO: Elettra Sincrotrone Trieste (Italy)
Elettra Sincrotrone Trieste is a multidisciplinary research center operating two advanced large-scale light sources: the synchrotron laboratory Elettra and the Free Electron Laser FERMI. Located in Trieste (Italy), Elettra ST is producing light beams with unique characteristics for an international community of scientific and industrial users, enabling scientific research and development at the frontiers of science. As the Coordinator of CompactLight, Elettra ST has been involved in all work packages of the project, leading WP1 (Management) and WP7 (Global Integration).

Team: Gerardo D'Auria, Regina Rochow, Simone Di Mitri, Marco Zangrando, Miltcho Danailov, Mario Ferianis, Caterina Tabacco, Renato Gioppo.

Website: http://www.elettra.eu

CERN

BE2: European Organization for Nuclear Research (Geneva)
CERN is the world's largest particle physics centre and operates the world's largest complex of particle accelerators. The 60-year history of CERN is marked with numerous achievements in the construction and operation of powerful linear and circular accelerators. At the end of 2009, CERN brought into operation the Large Hadron Collider (LHC). CERN has experience in managing the largest world accelerator infrastructures and by its very nature of International Organization the expertise in leading large-scale collaborations involving a large number of institutes from all over the world. In Compactlight, CERN has been leading WP4 (RF Systems) and actively contributed to all the other work packages.

Team: Andrea Latina, Walter Wuensch, Carlo Rossi, Steinar Stapnes, Daniel Schulte, Xiaowei Wu, Xingguang Liu, Daniel Schoerling, Sebastian Richter, Vlad Musat, Serge Deleval, Mario Parodi, Yongke Zhao.

Website: http://www.cern.ch

STFC

BE3: Science and Technology Facilities Council (United Kingdom)
STFC is one of the UK's seven publicly funded Research Councils, providing access to international facilities such as CERN and ESRF, and national facilities such as the Diamond Light Source, ISIS spallation source and Central Laser facility. Preparation for future FEL facilities is a significant theme of STFC research. STFC is contributing to Work Packages 1, 5, 6, 7, and 8 and leading WP2 (FEL Science Requirements and Facility Design).

Team: Jim Clarke, Neil Thompson, David Dunning, Louise Cowie, Hector Castaneda Cortes, Ben Shepherd, Peter Williams, Alex Hinton, James Jones, Minerva Maheshwari.

Website: https://www.ukri.org/councils/stfc/

BE4: Shanghai Institute of Applied Physics (China)

SINAP

SINAP is a multidisciplinary research Institute, in particular operating two advanced large-scale light sources: the Shanghai Synchrotron Radiation Facility (SSRF) and the Soft X-ray Free Electron Laser Facility (SXFEL). Located in Shanghai (China P. R.), SINAP is producing light beams with unique characteristics for an international community of scientific and industrial users, enabling scientific research and development at the frontiers of science. As the participator of CompactLight, SINAP has been involved in two work packages: WP2 (FEL) and WP4 (LINAC and RF system), and meanwhile SINAP has also done much work to develop the advanced RF gun and injector in WP3.

Team: Wencheng Fang, Zhentang Zhao, Xiaoxia Huang, Jianhao Tan, Cheng Wang, Qiang Gu.

Website: http://english.sinap.cas.cn/

BE5: Institute of Accelerating Systems and Applications (Greece)

IASA

The Institute of Accelerating Systems and Applications (IASA) was founded in 1994, affiliated of the National and Kapodistrian University of Athens and the National Technical University of Athens. IASA is charged with pursuing research and promoting graduate studies in particle accelerators and related technologies. Its cross disciplinary character and its superb infrastructure in enabling technologies have proven to provide particularly attractive and fertile ground for a number of technology driven scientific fronts. In XLS IASA is involved in WP1 (data management), WP3 (laser/photocathode for injector) and WP7 (3D CAD model, parameters list, economic analyses, technology transfer).

Team: Evangelos Gazis, Nikolaos Gazis, Eugene Tanke, Emmanouil Trachanas, Andrea Bignami.

Website: https://www.iasa.gr/

BE6: Uppsala University (Sweden)

UU

UPPSALA UNIVERSITET

Uppsala University, with its accelerator and instrumentation center at the FREIA Laboratory, is designing, operating and pushing the performance of accelerators beyond continuously expanding limits, thus enabling science to reach previously inaccessible domains (LHC, CLIC, ESSnuSB). The Freia Laboratory is involved in the development of the accelerator based neutron sources and synchrotron light sources (ESS, MaxIV) as well as free-electron lasers to enable materials- and life-sciences to develop new materials and then probe them with unprecedented spatial and temporal resolution. UU has contributed to the work in WP2, WP4 and WP6 of the project.

Team: Roger Ruber, Vitaliy Goryashko, Marek Jacewicz, Peter Salén, Alan Mak, Georgii Shamuilov.

Website: https://www.physics.uu.se/research/freia-lab/

BE7: The University of Melbourne, ARC Centre of Excellence for Particle Physics (Australia)

UoM

The ARC Centre of Excellence for Particle Physics of UoM's School of Physics - Experimental Particle Physics is a university group with activities in particle physics including ATLAS, Belle II and SABRE. The group has recently expanded into accelerator physics development under the leadership of Dr Suzie Sheehy. The work of relevance to CompactLight involves installation of the CERN XBOX3, X-band RF facility for its further development and application. Accelerator work, especially development of compact linear accelerators, in the group is carried out in close collaboration with the Australian Synchrotron, situated in the outskirts of Melbourne.

Team: Geoffrey Taylor, Suzie Sheehy, Roger Rassool, Matteo Volpi, Jacinta Yap. Students with Accelerator Projects (2021): Frank Zhang, Greg Peiris, Scott Lindsay, Hannah Norman, Adam Steinberg, Paarangat Pushkarna.

Website: https://www.coepp.org.au/

BE8: Australian Nuclear Science and Technology Organisation (Australia)

ANSTO

ANSTO is a Australian government research organisation that is the home of Australia's most significant landmark and national infrastructure for research. These include a modern nuclear research reactor, OPAL; a comprehensive suite of neutron beam instruments at the Australian Centre for Neutron Scattering; a 3rd Generation Light Source at the Australian Synchrotron; the National Imaging Facility Research Cyclotron; and several ion beam accelerators at the Centre for Accelerator Science. As a partner in this project, ANSTO has been active in XLS WP5 and WP6.

Team: Rohan Dowd, Rebecca Auchettl, David Zhu.

Website: http://www.ansto.gov.au/

BE9: Ankara University, Institute of Accelerator Technology (Turkey)

UA-IAT

The Institute of Accelerator Technology of Ankara University is hosting the TARLA (Turkish Accelerator Research LAboratory), which is a multidisciplinary advanced research laboratory established for promoting accelerator based research in Turkey. Its mission is to build and open to public use the first accelerator based user facility in the country. In the first instance the facility will produce Bremsstrahlung and infrared radiation from electrons accelerated to 40 MeV using superconductor technology. TARLA will not only serve the academic and industrial community through production of radiation, but it will also contribute to the development of advanced technology infrastructure and know-how in the country.

Team: Avni Aksoy, Zafer Nergiz.

Websites: http://www.tarla.org.tr , http://hte.en.ankara.edu.tr/

ULANC

BE10: Lancaster University (United Kingdom)

Lancaster University is the lead institute in the Cockcroft Institute of Accelerator science and technology, based at Daresbury Laboratory. Daresbury is home to the CLARA accelerator, an FEL technology testbed. Lancaster's Engineering group has decades of experience in high power RF systems for accelerators. In CompactLight Lancaster has been leading the development of Ka-band harmonic RF systems in WP3 and WP4.

Team: Joel Bedolla, Graeme Burt, Alejandro Castilla, Jinchi Cai, Robert Apsimon.

Website: https://www.lancaster.ac.uk

VDL-ETG

BE11: VDL Enabling Technologies Group (Netherlands)

VDL Enabling Technologies Group (VDL ETG) is a tier 1 contract manufacturer serving customers in the semiconductor, medical, and analytical segment. The company's main competences are engineering, precision machining, vacuum, chambers, stages, (clean room) assembly, module / system qualification and test. With over 900 M€ sales and approximately 3.500 employees it is one of the largest European contact manufacturer. VDL ETG has factories in Netherlands, Singapore, China, Switzerland, and USA. For already more than 30 years VDL is active in science-related projects and collaborations: astronomy (ESO), space (ESA), and accelerators (eg. CERN, Elettra, PSI). Enabling science. We believe science drives the high-tech innovation and considers accelerator-related research and collaboration a strategically important activity. VDL ETG has been involved in WP4 and WP7 of CompactLight.

Team: Miranda van den Berg, Mathieu Breukers, Hans Priem.

Website: http://www.vdletg.com/

TU/e

BE12: Eindhoven University of Technology (Netherlands)

Eindhoven University of Technology (TU/e) is a technical university, located in Netherlands, with over a decade of experience electron gun physics and design, charged particle tracking simulations, and ultrafast electron diffraction and microscopy. In recent years, TU/e has entered the field of high gradient acceleration through the Smart*Light compact inverse Compton X-ray source. As a contributor to CompactLight, TU/e has been involved in WP3, which was an investigation into options for the electron gun and injector.

Team: Thomas Lucas, Xavier Stragier, Peter Mutsaers and Jom Luiten.

Website: https://www.tue.nl/en/

BE13: Istituto Nazionale di Fisica Nucleare (Italy)

INFN

INFN is a research institute aimed to the study of the fundamental constituents of matter, which conducts theoretical and experimental research in the fields of sub-nuclear, nuclear, astro-particle and particle accelerator physics. The Laboratori Nazionali di Frascati (LNF) is one of the four main laboratories of INFN. INFN has also addressed its R&D to high gradient acceleration techniques in the framework of the EuPRAXIA@SPARC_LAB project that plans using an X-band rf linac as energy booster. INFN has been involved in Compact Light as coordinator of WP3 and participant in WP1, WP2, WP4, WP6, and WP7.

Team: David Alesini, Mostafa Behtouei, Marco Bellaveglia, Fabio Cardelli, Michele Croia, Marco Diomede, Massimo Ferrario, Alessandro Gallo, Anna Giribono, Luigi Pellegrino, Luca Piersanti, Stefano Pioli, Jessica Scifo, Bruno Spataro, Cristina Vaccarezza, Alessandro Vannozzi.

Website: http://w3.lnf.infn.it/

BE14: Kyma S. p. A. (Italy)

Kyma

Kyma is an Italian-Slovenian high-tech company, established in 2007 as a joint-venture between Elettra Sincrotrone Trieste SCpA, Cosylab dd. and Euromisure Srl, bringing together world-class expertise in insertion devices, magnetic design and characterisation, mechanical manufacturing, quality control, project management and control systems. Located in Trieste, KyMa is projecting, manufacturing, and delivering advanced permanent magnets devices for light source applications to customers worldwide. In CompactLight, Kyma has been involved in WP5 (Undulators) and WP7 (Global Integration).

Team: Raffaella Geometrante, Roberto Pavlica.

Website: https://kyma-undulators.com/

BE15: Sapienza - University of Rome (Italy)

SAPIENZA

Sapienza, University of Rome consists of 23 Faculties and about 5000 employees. The Department of Basic and Applied Sciences for Engineering and Physics (SBAI) joins researchers in the field of general, atomic and nuclear physics, in recent years focusing on FEL photoinjectors for the new generation of coherent radiation sources and laser-based secondary sources. The Accelerator team of the SBAI department is heavily involved in theoretical studies, in modelling and numerical simulations, in studying the electron beam dynamics in novel particle accelerators. URLS is contributing to all SPARC_LAB experiments on novel applications of high brightness beams. The SBAI team contributed to WP3 activity.

Team: L. Ficcadenti, Mauro Migliorati, A. Mostacci, and L. Palumbo.

Website: https://www.uniroma1.it/en/

ENEA

BE16: Agenzia Nazionale per le Nuove Tecnologie, l'Energia e lo Sviluppo Economico Sostenibile ENEA - Centro Ricerche Frascati (Italy)

ENEA is a leading Italian center for R&D on Nuclear Fusion, Laser and Accelerator Physics. The Frascati Research Center pioneered the Free Electron Laser design since the beginning, building its track record and expertise in core fields: FEL design, realization and applications; Undulators design and development; advanced accelerator technologies; coherent intense radiation sources; Microwave cavities, Laser optics. ENEA has coordinated XLS WP5 on undulators and light production, contributing also to the WPs on beam dynamics, diagnostics and global integration.

Team: Federico Nguyen, Giuseppe Dattoli, Alberto Petralia, Mariano Carpanese, Elio Sabia, Ivan P. Spassovsky.

Website: www.enea.it

ALBA-CELLS

BE17: Consorcio para la Construccion Equipamiento y Explotacion del Laboratorio de Luz Sincrotron (Spain)

ALBA is the Spanish Synchrotron Light facility, a complex of electron accelerators producing synchrotron light in the soft and hard X-ray range. This allows the visualization of the atomic structure of matter and the study of its properties in fields from bio- to material sciences. Each year, this large infrastructure provides more than 2.000 researchers from academics and industrial with 6.000 hours of beam time. ALBA is committed to scientific excellence and the promotion of well-being and progress in society. ALBA has been involved in all work packages except WP4.

Team: Francis Perez, Raquel Muñoz, Eduardo Marin, Jordi Marcos, Daimí Perez.

Website: http://www.cells.es/

CNRS

BE18: Centre National de la Recherche Scientifique (France)

The French National Centre for Scientific Research is among the world's leading research institutions. The Laboratoire de Physique des 2 Infinis Irène Joliot-Curie IJCLab, one of the largest physics laboratories of CNRS and the University Paris-Saclay (UPSaclay), has scientific expertise in many fields from particle physics to cosmology. UPSaclay is legally linked to the CNRS, with research centres and higher education institutions for 5.000 doctoral students, 45% foreigners. IJCLab's pole for Accelerator Physics has numerous unique facilities and cutting-edge technologies. The CNRS team has contributed to XLS WP2, WP3, and WP4.

Team: Angeles Faus-Golfe, Bruno Mercier, Yanliang Han, Pierre Lepercq.

Website: https://www.ijclab.in2p3.fr/en/home/

KIT

BE19: Karlsruhe Institut für Technologie (Germany)

KIT, the Research University in the Helmholtz Association, combines the traditions of a renowned technical university and a major large scale research facility in a very unique way. It is one of the largest, most prestigious, and leading engineering and technology universities in Germany. KIT hosts the Accelerator Technology Platform (ATP) which combines accelerator-relevant infrastructures, technologies and research in a unique way, taking advantage of the wide-spread expertise of KIT institutes to advance accelerator science and technology. KIT has been involved in WP5 of the CompactLight Project as task leader for superconducting undulators.

Team: Axel Bernhard, Julian Gethmann, Steffen Grohman, Samira Fatehi, Jonas Arnsberg, Bennet Krasch, Sebastian Claus Richter.

Website: http://www.kit.edu/english/

PSI

BE20: Paul Scherrer Institute (Switzerland)

The Paul Scherrer Institute is the largest research institute for natural and engineering sciences in Switzerland, conducting cutting-edge research in three main fields: matter and materials, energy and the environment and human health. PSI develops, builds and operates complex large research facilities, the Swiss Light Source SLS, the free-electron X-ray laser SwissFEL, the SINQ neutron source, the SμS muon source and the Swiss research infrastructure for particle physics CHRISP. PSI is committed to the training of future generations. Therefore about one quarter of our staff are apprentices, post-graduates or post-docs. SwissFEL is so far the most compact FEL source for hard- and soft x-rays and acts as benchmark for CompactLight. In CompactLight PSI has been contributing to WP5.

Team: Marco Calvi, Kai Zhang, Thomas Schmidt, Sven Reiche.

Website: https://www.psi.ch/en

CSIC

BE21: Consejo Superior de Investigaciones Científicas (Spain)

The Instituto de Física Corpuscular (IFIC) is a joint centre between the Spanish Research Council (Consejo Superior de Investigaciones Científicas, CSIC) and the University of Valencia devoted to research in Nuclear, Particle and Astroparticle Physics and its applications to Medical Physics and to other fields of Science and Technology. In the new institute converged experimental and theoretical physicists and, in addition to the lecturers and professors of the University of Valencia, this institute was joined in the following years by Spanish and foreign researchers who worked in several institutions from abroad. IFIC has collaborated in the framework of WP3, focusing on the design of an X-band RF electron gun injector.

Team: Daniel Gonzalez-Iglesias, Daniel Esperante Pereira, Benito Gimeno Martinez, Juan Fuster.

Website: https://webific.ific.uv.es/web/en

UH/HIP

BE22: University of Helsinki - Helsinki Institute of Physics (Finland)
The Helsinki Institute of Physics is very active in carrying out and facilitating research in basic and applied physics as well as in physics research and technology development at international accelerator laboratories. The Institute has a proven experience in material science and breakdowns in high-gradient structures, in particular development of mechanical design for next generation of CLIC module taking into account the full life cycle - from manufacturing over the assembly, rf-conditioning, transportation, installation, alignment, the operation to failure scenarios and industrial collaboration. for the development of manufacturing CLIC accelerating structures and other RF components. UH-HIP has been involved in WP1, WP4 and WP7 of CompactLight.

Team: Markus Aicheler, Jukka Vainola.

Website: https://www.hip.fi/

VU

BE23: Free University Amsterdam (Netherlands)
The Vrije Universiteit Amsterdam is one of Europe's most prominent research-led universities. It is leading in laser techniques to generate EUV and soft-X-ray laser light, which is to be used for FEL seeding. VU is a partner in the public-private partnership ARCNL (Advanced Research Center for Nanolithography), a Joint Research Unit founded in 2014 together with the Netherlands Organisation for Scientific Research (NWO), the University of Amsterdam (UvA), and the semiconductor equipment manufacturer ASML which is the launching platform of FEL-NL. VU's research group is embedded in ARCNL and their project activities are performed there. The team has contributed to XLS WP6 and WP7.

Team: Ronnie Hoekstra, Thomas Lucas.

Website: https://www.vu.nl/en

USTR

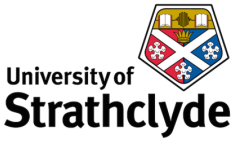

BE24: The University of Strathclyde (Scotland,UK)
The Atoms, Beams and Plasmas (ABP) research group in the Department of Physics, University of Strathclyde has 30 years' experience of fast wave oscillators (gyrotrons) and amplifiers (gyro-travelling-wave amplifiers and gyro-klystrons). The range of capabilities for the generation of high power (multi-MWs), ka-band (36GHz) radiation includes: theoretical analysis; numerical simulation; experimental demonstration; and manufacturing realization. To provide the rf power source design for a harmonic linearizer, the ABP group has been involved in WP3 (which has overlap with WP4) of the project.

Team: Adrian W. Cross, Liang Zhang, Laurence Nix and Jack Easton.

Website: http://reld.phys.strath.ac.uk/

UniToV

BE25: University of Rome 'Tor Vergata' (Italy)

Tor Vergata University of Rome is a public research university in Rome, Italy. The university consists of six schools: Economics, Engineering, Humanities, Law, Mathematics, Physics and Natural Sciences, and Medicine & Surgery, further divided into departments. It offers 32 PhD programs, 51 Master's degree programs, 55 undergraduate Bachelor's degree programs, and 7 single-cycle degree programs. Moreover, The university's 20 international degree courses (3 Bachelor 15 Master, single-cycle degree courses) are taught in English. UniToV has coordinated XLS WP8 (diagnostics) and been also involved in WP1, WP3 and WP7.

Team: Alessandro Cianchi.

Website: https://web.uniroma2.it/home/

BNG

BE26: Bilfinger Noell GmbH (Netherlands)

Bilfinger Noell GmbH (BNG) is operating worldwide in the product areas of nuclear service, nuclear technology and magnet technology. In collaboration with the Karlsruhe Institute of Technology (KIT), Noell develops and designs superconducting undulators and wigglers. BNG has delivered SCU15 and SCU20 to KIT. With the design of SCU20 Noell made the step from prototype to product with superconducting insertion devices. BNG has supplied components for large-scale projects like dipole magnets for CERN, or the non-planar coils for the fusion experiment W7-X in Greifswald. By supporting the cost calculation, giving advice on technological and economical aspects of the CDR, BNG is involved in WP5.

Team: Achim Hobl, Marcel Breitenbach, Philipp Revilak.

Website: https://www.noell.bilfinger.com/en/

XLS Third Parties

Oslo

3P1: Oslo University (Norway)

The University of Oslo has been supporting as a third party of the project the activities of CERN.

Team: Erik Adli.

Website: https://www.uio.no/english/

ARCNL

3P2: Advanced Research Center for Nanolithography (Netherlands)
The Advanced Research Center for Nanolithography is a joint Dutch public-private unit engaged also in research on FELs. The ARCNL team, closely collaborating with the VU researchers in CompactLight and introduced already above (VU), has been contributing to the project as a third party of VU. The joint activities of the two groups have been carried out on their premises.

Team: Thomas Lucas, Ronnie Hoekstra.

Website: https://arcnl.nl/

NTUA

National Technical University of Athens

3P3: National Technical University of Athens (Greece)
The National Technical University of Athens is an outstanding and internationally recognized public university of science and technology in Greece. The NTUA is structured according to the continental European system for training engineers, with an emphasis on solid background of mathematics and physics. NTUA has participated in CompactLight as a third party of IASA, supporting the partner in WP3 and WP6.

Team: Theodoros Alexopoulos, Dimitrios Bantekas, Irini Telali, Katerina Tzanetou, Rafaella Kotitsa.

Website: https://www.ntua.gr/en/

AUEB

3P4: Athens University of Economics and Business (Greece)
The Athens University of Economics and Business is the premier Economics and Business University in Greece and the third oldest University in the country. Its 3 Schools (8 Departments) offer state-of-the-art studies in areas such as Economics, IR, Management, Accounting, Marketing, Informatics and Statistics. The AUEB has provided their specific expertise as a third party of IASA, contributing to their activities in WP7.

Team: Dimosthenis Kotsopoulos, Angeliki Karagiannaki, Katerina Pramatari.

Website: https://www.aueb.gr/en

KyTe

3P5: Kyma Tehnologija d.o.o. (Slovenia)
Kyma Tehnologija is a technology company 100% owned by the CompactLight partner Kyma, specialised in advanced high-tech permanent magnet devices for light source accelerators. The KyTe team has supported the project as a linked third party of Kyma with their specific expertise on undulators provided in WP5.

Team: Mirko Kokole, Jure Pockar, Tadej Milharcic, Uros Primozic, Jaka Mahnic.

Website: https://kyma-undulators.com/dove-siamo/